MODELING THE IMPACT OF LANDUSE/LANDCOVER AND CLIMATE VARIABILITY ON FLOODING WITHIN THE LOWER NIGER BASIN USING REMOTE SENSING AND MACHINE LEARNING

By

Orobosa ORIAKHI

PG/ENG0801687

A PROJECT SUBMITTED IN PARTIAL FULFILLMENT OF THE REQUIREMENT FOR THE AWARD OF DOCTOR OF PHILOSOPHY (PhD) DEGREE

IN

THE DEPARTMENT OF CIVIL ENGINEERING, FACULTY OF ENGINEERING, UNIVERSITY OF BENIN, BENIN CITY, NIGERIA

NOVEMBER, 2025

CERTIFICATION

This is to certify that this study was carried out by Orobosa ORIAKHI of the Department of Civil Engineering (Water Resources and Environmental Health Engineering), Faculty of Engineering, University of Benin, in partial fulfilment of the requirements for the award of PhD in Civil Engineering.

Engr. Prof. J.O Ehiorobo (SUPERVISOR)	Date
Engr. Dr. A.I Agbonaye (CO-SUPERVISOR)	Date
Engr. Prof. (Mrs) N.Ihemekpen (HEAD OF DEPARTMENT)	Date

CERTIFICATION OF THESIS PLAGIARISM

This is to attest and declare that the thesis by Orobosa ORIAKHI (with Mat. Number PG/ENG0801687) titled: MODELING THE IMPACT OF LANDUSE/LANDCOVER AND CLIMATE VARIABILITY ON FLOODING WITHIN THE LOWER NIGER BASIN USING REMOTE SENSING AND MACHINE LEARNING has successfully passed anti-plagiarism test and does not violate any copyright regulation.

SUPERVISOR:

Engr. Prof. J.O Ehiorobo Date

CO-SUPERVISOR

Engr. Dr. A.I Agbonaye Date

HEAD OF DEPARTMENT

Engr. Prof. (Mrs) N.Ihemekpen Date

DECLARATION

I hereby declare that this thesis titled "Modeling the Impact of Landuse/Landcover and Climate Variability on Flooding Within the Lower Niger Basin Using Remote Sensing and Machine Learning" was carried out by me in the Department of Civil Engineering under the supervision of Engr. Prof. J.O Ehiorobo and Engr. Dr. A.I Agbonaye. The information derived from the literature has been duly acknowledged in the text and in the form of references provided. No part of this work has been produced for another degree or diploma at any institution.

DEDICATION

I dedicate this work to GOD Almighty and my immediate family for the enabling strength and zeal to carry out this research.

ACKNOWLEDGEMENT

I am deeply grateful to the Almighty God for his wisdom and strength granted to me for consistency on the completion of this research. I want to express my profound gratitude to my supervisor; Engr. Prof. J.O Ehiorobo, former Deputy Vice Chancellor (Admin), University of Benin, for his trust and undying encouragement he gave me to commence this research work in the Department of Civil Engineering and my Co-Supervisor Engr. Dr. A.I. Agbonaye for his detail scrutiny, support and directions in the course of this research work. I will also want to extend my gratitude to the Head of Department; Engr. Prof. (Mrs) N.I Ihemekpen and the post graduate coordinator Engr. Prof. O.R. Ogirigbo. My grantitude gose to all the academic staff of this great department who have been of great support in the course of this project; Engr. Prof. O.C. Izinyon, Engr. Prof. O.U. Orie, Engr. Prof. S.O. Osuji, Engr. Prof. J.O Okovido, Engr. Prof. H.A.P. Audu, Engr. Prof. N. Kayode Ojo, Engr. Prof. S.D. Iyeke, Engr. Dr. L.O. Bobor, Engr. Dr. A. Rawlings, Engr. Dr. R. Ilaboya, Engr. Dr. E. S. Okonofua, Engr. Dr. U.Ukeme, Engr. Prof. R.I Umasabor, Engr. K.N. Oghoyafedo, Engr. Dr. P. Nowamagbe, Engr. Dr. S.A. Adegbemileke, Engr. B. E. Omosefe, Engr. O. Osasu, Engr. E, Oria Usifo. I also owe my gratitude to the Labouratory staff of Cviil Engineering Department, amongst who are Engr. N. Uwaila, Engr. I. Sani, Mr. A.A. Ehiogie. My heart fell thanks goes also to all the non-academic staff of the department who have contributed to the success of this research work.

I also owe my father, mentor and guidance Mr. David Ehiozuwa Oriakhi whom inspite of all circumstances still believes in me and never get tired encouraging me to keep fighting until success is attained. I will not fail to also mention my beloved mother, Mrs. Elizabeth E. Oriakhi, for her patience and support. I want to also extend my deepest gratitude to my siblings, Itohan Oriakhi (Sister), Nosa Oriakhi (Brother), Osaretine Oriakhi (Brother), Osamudiame Oriakhi (Brother). My sincere thanks go to my immediate family: Mrs. Omosigho S. Oriakhi (my lovely Wife), Eliora and Eliana (Children), for their patience and understanding in the course of this program.

ABSTRACT

Flooding remains one of the most pressing environmental challenges in the Niger Delta region of Nigeria, where rapid urbanization, land degradation, and climate variability interact to intensify hydrological extremes. This study evaluates the combined impact of land use/land cover (LULC) changes and climate variability on flooding in the Lower Niger Region, focusing on Edo, Delta, Bayelsa, and Rivers States.

An integrated methodological framework was developed using remote sensing (RS) and machine learning (ML) techniques implemented on the Google Earth Engine (GEE) platform. Rainfall and temperature datasets were obtained from multiple satellite products, CHIRPS, PERSIANN-CDR, PERSIANN-CCS, ERA5, and CPC, and validated against observations from the Nigerian Meteorological Agency (NiMET). LULC classification was conducted using Random Forest (RF) and Support Vector Machine (SVM) algorithms applied to Sentinel-2 and Landsat-8 imagery, generating five major land cover classes: water bodies, forest, barren land, vegetation, and built-up areas. Flood dynamics were assessed using multiple spectral indices, including AWEI, FWI, NDWI, MNDWI, WRI, and NDVI, evaluated across different temporal scales to capture hydrological variations.

The results reveal significant interannual and seasonal rainfall variability, with the Standardized Precipitation Index (SPI) effectively identifying alternating wet and dry cycles, although long-term annual rainfall trends were largely non-significant. There is, however, evidence of increasing frequency of extreme rainfall events, particularly in Delta and Rivers States. Temperature analysis (1971–2023) indicates a statistically significant warming trend, with minimum temperatures rising faster than maximum temperatures—most notably during the dry season (DJF). LULC assessment confirmed the superior performance of the RF classifier over SVM and showed a consistent pattern of urban expansion at the expense of vegetation and wetlands. Flood analysis revealed a persistent hotspot occurring along river corridors, low-lying floodplains, and southeastern basins. Overall, the findings demonstrate that while climate variability influences hydrological extremes, LULC transformations, particularly urban encroachment into natural flood buffers, have been a more decisive factor driving flood vulnerability in the Lower Niger Region.

TABLE OF CONTENTS

LIST OF TABLES

LIST OF FIGURES

LIST OF ABBREVIATIONS

Abbreviation	Full Form
AHP	Analytical Hierarchy Process,
ANN	Artificial Neural Network,
ARIMA	Autoregressive Integrated Moving Average Model,
AUC	Area Under the Curve,
AWEI	Automated Water Extraction Index,
CC	Correlation Coefficient
CDC	Centers for Disease Control and Prevention
CH4	Methane
CHIRPS	Climate Hazards Group InfraRed Precipitation with Station data,
CMIP5	Coupled Model Intercomparison Project phase 5
CNN	Convolutional Neural Network,
CO_2	Carbon Dioxide
CPC	Climate Prediction Center (Temperature Dataset),
DEM	Digital Elevation Model,
DJF	December–January–February (Climatological Season)

DL	Deep Learning
ERA5	ECMWF Reanalysis 5th Generation (Temperature Dataset),
FMA	Flood Mapping Algorithm
FWI	Flood Water Index
GCMs	Global Climate Models
GDP	Gross Domestic Product
GEE	Google Earth Engine,
GHG(s)	Greenhouse Gas(es),
GIS	Geographic Information System,
GHSL	Global Human Settlement Layer
GLDAS	Global Land Data Assimilation System
GPW	Gridded Population of the World
HFCs	Hydrofluorocarbons
IGBP	Indo-Gangetic-Brahmaputra plains
IPCC	Intergovernmental Panel on Climate Change
ITD	Intertropical Discontinuity
JJA	June–July–August (Climatological Season)
K	Kappa Coefficient

KGE	Kling–Gupta Efficiency
LCM	Land Change Modeler
LOOCV	Leave-One-Out Cross-Validation
LR	Logistic Regression
LST	Land Surface Temperature,
LULC	Land Use/Land Cover,
MAE	Mean Absolute Error,
MAM	March–April–May (Climatological Season)
MAPE	Mean Absolute Percentage Error
MBE	Mean Bias Error
MID	Middle-Infrared
ML	Machine Learning,
MLR	Multivariate Linear Regression
MNDWI	Modified Normalized Difference Water Index,
MODIS	Moderate Resolution Imaging Spectroradiometer,
MSE	Mean Squared Error
N_2O	Nitrous Oxide
NDMI	Normalized Difference Moisture Index

NDVI	Normalized Difference Vegetation Index,
NDWI	Normalized Difference Water Index,
NIR	Near-Infrared (Band)
NiMET	Nigerian Meteorological Agency,
NSE	Nash–Sutcliffe Efficiency
OA	Overall Accuracy,
O_3	Ozone
OLI	Operational Land Imager (Landsat 8 Sensor),
PCC	Pearson Correlation Coefficient
PCA	Principal Component Analysis
PFCs	Perfluorocarbons
PERSIANN-CDR	Precipitation Estimation from Remotely Sensed Information using Artificial Neural Networks - Climate Data Record,
PERSIANN-CCS	Precipitation Estimation from Remotely Sensed Information using Artificial Neural Networks - Cloud Classification System,
PhD	Doctor of Philosophy
QGIS	Quantum GIS
R^2	Coefficient of Determination

RCP4.5, RCP8.5	Representative Concentration Pathways (Emission Scenarios),
RF	Random Forest,
RMSE	Root Mean Square Error,
ROC	Receiver Operating Characteristic Curve,
RS	Remote Sensing,
SAR	Synthetic Aperture Radar,
SDR	Standard Deviation Ratio
SGD	Stochastic Gradient Descend
SLR	Sea Level Rise
SNHT	Standard Normal Homogeneity Test,
SON	September–October–November (Climatological Season)
SPI	Standardized Precipitation Index
SRTM	Shuttle Radar Topography Mission,
SUDS	Sustainable Urban Drainage Systems
SVM	Support Vector Machine
SWIR	Short-wave Infrared
Tmax	Maximum Temperature,

Tmin Minimum Temperature

TRMM Tropical Rainfall Measuring Mission,

TVDI Temperature–Vegetation Dryness Index,

TWI Topographic Wetness Index

UAVs Unmanned Aerial Vehicles

VV Vertically transmitted Vertically received (SAR Polarization Data),

WRI Water Ratio Index,

CHAPTER ONE

INTRODUCTION

1.1 Background to the study

Flooding is a major natural hazard that affects many regions around the world, including the Lower-Niger region of Nigeria. It has been proven to be one of the most common environmental hazards which is mostly caused by either man-made or natural events (Twumasi et al., 2017). While flooding caused by rainstorm is usually attributed to climate change (Akeh and Mshelia, 2016; Yaw A. et al., 2017). When rainfall exceeds absorption capacity of the soil, which in turn causes significant environmental consequences (Nwachukwu et al., 2018; Umar and Gray, 2022). (Peduzzi et al., 2009; Umar and Gray, 2022) maintained that 'the rate of flood occurrence in recent times has been unprecedented, with over 70 million people globally exposed to flooding every year, and more than 800 million living in flood-prone areas. (Rentschler and Salhab, 2020) estimate that 1.47 billion people, or 19% of the world population, are directly exposed to substantial risks during 1-in-100-year flood events.

In developing countries, flooding results from climate extreme, excessive precipitation, building on waterways, sea-level rise, and soil moisture regime, dam operations, especially along borders, uncontrolled rapid population growth, inadequate preparedness, and lack of political will (Dalil et al., 2015; Innocent Abbas, 2013; Olanrewaju et al., 2019; Umar and Gray, 2022) which is common in Nigeria. Flooding is cause by either natural or human events. (MacLeod et al., 2021) identified excessive levels of precipitation as the main natural cause of flooding, caused by climate change while (Tramblay et al., 2021) link flood occurrence to maximum level of soil moisture rather than maximum precipitation. Nigeria, like many other countries, is experiencing high population density, rapid urbanization, and significant land use changes.

These changes have led to various environmental and climate issues such as loss of agricultural land, land degradation, water shortage, and pollution (Onilude, 2023). Studies have been conducted to analyze the spatio-temporal trends of land use/land cover (LULC) changes in different regions of Nigeria. For example, research in Lagos and Nguru has shown significant urban expansion and a decrease in green areas, highlighting the need for sustainable land-use management and strategies (Hassan and Syakir, 2023; Kadiria et al., 2023). Similarly, studies in Etsako West LGA and Abuja have observed the increase in built-up areas, decline in forestland, and the need for eco-friendly strategies to ensure sustainable urban growth (Chukwurah et al., 2022). Nigeria like many other country is characterized by a high population density, rapid urbanization, and significant land use changes, which, when combined with climate change impact can cause significant effect on flood patterns and severity. With the increase in rainfall duration and intensity, there have been records of large surface runoffs and flooding in many places in Nigeria. Rainfall variation is projected to continue to increase, with precipitation in southern areas expected to rise and sea levels expected to exacerbate flooding and submersion of coastal lands (Richard and Okeke, 2023). On the other hand, the northern regions are expected to suffer from droughts due to a decline in precipitation and rise in temperature (Ekpeni et al., 2023). Additionally, lakes in the country, including Lake Chad, are drying up and at risk of disappearing (Abaje, 2023). These findings highlight the significant impact of climate change on Nigeria, with increased flooding in some areas and droughts in others. The changing climate patterns pose challenges for water resources management and agricultural practices in the country.

Remote sensing and big data are powerful tools that can be used to study the complex interactions between land use/land cover, climate change, and flooding in Nigeria. Remote sensing provides a synoptic view of the earth's surface and can be used to detect and monitor changes in land use/land cover, precipitation, surface temperature and water bodies, such as NDWI (Normalized Difference Water Index) (Gao, 1996). Big data, on the other hand, provides a vast amount of information that can be used to model and predict flooding patterns.

As computational technology and techniques improve, researchers now have access to a greater set of resources, including big data and machine learning techniques. These advancements have increased the means of retrieving data for analysis, providing insights into various environmental attributes and events. For example, machine learning and big data can help address major knowledge and methodological gaps in ecosystem service research, filling data gaps and quantifying uncertainty estimates (Manley et al., 2022). Additionally, big data and computational methods can be used to analyze mediated environmental communication, allowing researchers to measure variables such as the salience of communication and framing (Amirmahani et al., 2021). In the field of animal movement ecology, big data approaches have revolutionized the understanding of animal movement and its ecological implications, facilitating improved opportunities for conservation and insights into the movements of wild animals (Nathan et al., 2022). Furthermore, the evaluation of land use and land cover changes using remote sensing data and machine learning algorithms has aided in understanding landscape dynamics and framing sustainable land use policies (Ramachandra et al., 2023). Finally, machine learning tools can be used to make predictions and develop applications for environmental intelligence, such as continuous monitoring and alerting for public health purposes (Malakar, 2022). Big data in the real world comprises more on geospatial data, and it is expected to keep growing rapidly at a rate of about 20% every year. As such, handling these data explosion requires high-end computing techniques, modeling, architecture, methodologies, storage and solutions. Geospatial big data (GBD) refers to spatial data sets which surpass the current capacity of computing systems and demand advanced methods for acquisition, storage, processing, analysis, and visualization to extract meaningful information in a timely manner. (Wahap et al., 2020)

Machine learning techniques have been shown to be an important technique in science due to the data driven attributes (i.e. empirically modeled data with little or no assumptions) as well as the efficacy and efficiency when handling big data. Several researches and researchers have applied Machine learning and remote sensing techniques for land use and climate change analysis (Avand et al., 2020; Govender et al., 2022; Nasiri et al., 2022; Saarinen et al., 2017). Google Earth Engine is a cloud-based platform for planetary-scale geospatial analysis that brings Google's massive computational capabilities to bear on a variety of high-impact societal issues including deforestation, drought, disaster, disease, food security, water management, climate monitoring and environmental protection. (Gorelick et al., 2017). The combination of remote sensing and big data can be used to evaluate the impact of land use/land cover and climate change impact on flooding in the Lower-Niger Delta region of Nigeria.

1.2 Statement of Problem

Flooding is a major natural hazard that affects many regions around the world, including the Lower-Niger Delta region of Nigeria. The Lower-Niger Delta region is characterized by a high population density, rapid urbanization, and significant land use changes. The population of this region has grown by about 3% annually over the past decade, and this has led to an increase in the demand for housing, infrastructure, and other services. This, in turn, has led to a decline in green spaces and an increase in surface runoff, which is exacerbating the problem of flooding in the region. Climate variability, such as changes in precipitation and temperature, can also have a significant impact on flooding patterns and severity.

Recent examples of devastating floods in Nigeria include the 2012 flooding, which was caused by heavy rainfall and the release of excess waters from lagdo in Cameroon. This led to the overflow of the Niger and Benue rivers, resulting in the destruction of thousands of hectares of farmland, homes, and infrastructure including lives and properties. The flooding in 2011 and 2012 caused a high number of casualties and left many farmers and residents in dire financial straits. The devastating effects of climate change, excessive rainfall, overflowing local rivers, and the flooding have all been linked, but the underlying causes and contributing factors remain poorly understood. This makes it difficult for decision-makers, resource planners, and administrators to make informed decisions about land use and flood management in the Lower-Niger Delta region.

This fundamental problem is compounded by a persistent data gap of which developing countries like Nigeria suffer from limited or a lack of sufficient high-quality ground-based Meteor-hydrological data, necessitating the use of alternative sources. Consequently, there is a recognized research gap marked by a lack of scientific work systematically investigating the correlative relationship among LULC changes, climate elements (rainfall and temperature), and flood events in the lower Niger region, alongside a limitation on the use of advanced machine learning algorithms for accurately modeling and predicting flooding patterns in this specific area.

1.3 Aim and Objectives

This research aims to evaluate the impact of land use/land cover (LULC) changes and climate variability on flooding in the Lower Niger States of Nigeria by leveraging remote sensing technology and machine learning algorithms.

The specific objectives for the research include;

1. Evaluate rainfall patterns in the region using remote sensing data on the Google Earth Engine platform and gauge data.
2. Collect and process remote sensing data to detect and analyze changes in surface temperature.
3. Analyze and assess LULC time series changes in the study area utilizing remote sensing techniques on the Google Earth Engine platform and machine learning algorithms.
4. Estimate flooding patterns in the Lower Niger region through various remote sensing indices for flood detection.
5. Conduct trend analysis of flooding patterns using the remotely sensed dataset.

1.4 Scope of Study

The research boundary for this work is hinged on the research application of remote sensing and Machine learning algorithm to estimate the impact of changes in land use land cover and climate on flooding in the lower Niger Delta Region of Nigeria.

I. This research will adopt remotely sensed data sets with ground thrusted data used as validation dataset where available. Due to the size and the processing power need for the computation, cloud based system will be adopted for this analysis.

II. Google Earth Engine will be used for the, computation as it houses a huge volume of remotely sensed data set and has the capacity to compute large satellite images within a short time period.

III. Open sourced Geographic information system such as the quantum GIS (QGIS) will be used to produce the various maps.

IV. Due to the difficulty in gathering high quality Metero-hydrological dataset in the study area, in terms of space and time, the availability of station data will be used to define the time period for this study so as to produce a consistent result.

V. The result output will be generated based on the data availability and computation capability of the system. Land use/land cover category will be defined based on the reflectance values of the most prevailing land use class in the study area.

VI. This will lead to creating groups such as classifying buildings, roads, concreted floors etc. as residential areas.

VII. Climate change variable will be based on rainfall and temperature which are the most prevailing climate variables affecting flooding event in the study area.

1.5 Justification of the study

Flooding is a major natural hazard that affects many regions around the world, including the Lower-Niger Delta region of Nigeria. This research will provide valuable insights into the complex interactions between land use/land cover change, climate change and flooding in the study region. The use of remote sensing and big data in this research will provide a synoptic view of the earth's surface and a vast amount of information that can be used to model and predict flooding patterns. This will help to improve flood management and mitigation in the Lower-Niger region.

The study area is known to have suffered flooding of different magnitude. Some flood event with severe impacts recorded in the lower Niger Delta region which includes the 2012 flooding that is known to have been caused by heavy rainfall and the release of excess waters from dams in Nigeria and Cameroon and have also been attributed to the overflow of the Niger and Benue rivers, leading to the destruction of thousands of hectares of farmland, homes, and infrastructure. This research seeks to identify the underlying causes and contributing factors to flooding in the Lower-Niger Delta region, which will help decision-makers, resource planners, and administrators to make informed decisions about land use and flood management in the region.

The use of Google Earth Engine and machine learning algorithms in this research will provide an efficient and cost-effective way to access and process large amounts of remote sensing data, and to model and predict flooding patterns. This will help to improve the accuracy and reliability of flood management and mitigation in the Lower-Niger Delta region. As such, this project will be beneficial to the country as it will provide recommendations for flood management and mitigation in the Lower-Niger Delta region, which will help to reduce the impact of flooding on the people and infrastructure in the region and help reduce environmental and economic and social impacts of flood events.

CHAPTER TWO

LITERATURE REVIEW

2.1 Flooding and Flood Risk in Nigeria

Flooding is a recurring environmental phenomenon that poses significant challenges to societies worldwide, and Nigeria is no exception. Understanding the causes, impacts, and management strategies related to flooding is crucial for effective disaster preparedness and response. This literature review examines a wide range of studies conducted on flooding in Nigeria, exploring the causes of flooding, its impacts on various sectors, and the existing flood management strategies.

Flooding in Nigeria can be attributed to a combination of natural and human-induced factors. The Nigeria Hydrological Services Agency (NHSA) identifies several major causes of flooding, including soil moisture, extreme weather events resulting from climate change, dam operations (particularly those near the country's borders), and topography (Adegboyega et al., 2018). Changes in land use, such as urbanization, have also been identified as significant triggers for flooding. Inadequate drainage systems and poor urban planning are major contributors to flooding in Nigerian cities (Mfon et al., 2022). A study by (Akoteyon, 2022) conducted in Lagos, Nigeria, identified blockage of canals, inadequate drainage systems, torrential rain, and encroachment as the main causes of flooding in the city. Additionally, anthropogenic activities such as dumping of refuse in waterways, building on waterways, and dam overflow further exacerbate flood risk (Brisibe and Brown, 2020). Several studies have highlighted the role of climate change in increasing flood frequency and intensity in Nigeria. (Muruganandam et al., 2023) emphasize excessive or heavy precipitation as a major cause of flooding, along with climate change and anthropogenic activities. (Merz et al., 2021) found heavy downpours and river storms to be natural causes of flooding, while broken water pipes, inadequate drainage systems, and dam overflow were identified as anthropogenic causes.

Flooding in Nigeria has severe impacts on the built environment, affecting infrastructure, human lives, and socio-economic conditions. The rapid population growth in urban areas, combined with poor governance and inadequate drainage facilities, amplifies vulnerability to flood-related hazards (Douglas, 2017). (Olanrewaju et al., 2019) highlighted the widespread destruction of properties worth billions of naira, loss of lives, spread of diseases, and displacement of people as consequences of flooding in Nigeria. The impacts of flooding extend beyond immediate damages. (Roy et al., 2023) emphasize the economic toll on downstream populations whose means of livelihood are disrupted by floods. The long-term consequences include increased poverty, decreased productivity, and reduced access to basic services. The built environment's resilience to flooding is essential for mitigating these impacts and ensuring the well-being of communities.

Flood risk management in Nigeria faces several challenges that hinder effective preparedness, response, and recovery. (Oladokun and Proverbs, 2016) highlighted the absence of an integrated flood risk management system, inadequate inter-agency coordination, substandard and weak infrastructure, inadequate drainage networks, high urban poverty, low literacy levels, cultural barriers, and weak institutions as major challenges. These issues collectively limit the capacity to mitigate flood risks and increase vulnerability to future flooding events.

Improved flood mapping and modeling techniques are crucial for effective flood risk management. (Ighile et al., 2022) emphasize the need for accurate flood modeling in the northern regions of Nigeria, which are particularly susceptible to flooding. They suggest employing Bayesian and machine learning approaches alongside remote sensing data and Geographic Information System

(GIS) techniques to enhance flood modeling accuracy. Such advancements can provide valuable insights for effective flood risk assessment, emergency response planning, and infrastructure development. Another challenge in flood risk management is the lack of comprehensive land-use planning and enforcement. Uncontrolled urbanization and encroachment on floodplains contribute to increased vulnerability to flooding (Qian and Eslamian, 2022). It is crucial to integrate flood risk considerations into urban development policies, zoning regulations, and building codes to ensure that future constructions are resilient to flood hazards (Hemmati et al., 2020). Inadequate early warning systems and communication networks pose significant challenges in flood preparedness and response. Timely dissemination of accurate and reliable flood forecasts and warnings is essential to alert vulnerable communities, facilitate evacuation plans, and enable effective emergency response (Perera et al., 2020). Investments in weather monitoring technologies, early warning systems, and community awareness campaigns are necessary to improve flood preparedness and reduce the loss of lives and properties during flooding events. Socio-economic factors, including poverty and limited access to resources, exacerbate the impacts of flooding and hinder effective flood risk management. Poor households are more likely to settle in flood-prone areas due to affordability constraints, leading to increased exposure to flood hazards (Perera et al., 2020). Addressing poverty and improving the livelihoods of vulnerable communities can enhance their resilience to flooding and enable them to adapt to future climate-related challenges.

Furthermore, institutional capacity and governance play a critical role in flood risk management. Strengthening institutional frameworks, establishing clear responsibilities, and promoting multi-stakeholder collaboration are essential for effective flood risk governance (Gerkensmeier and Ratter, 2018). Enhancing the capacities of government agencies, local authorities, and community-based organizations in flood risk assessment, planning, and response is crucial for building resilience at all levels. Successful flood risk management requires a holistic approach that combines structural and non-structural measures. Structural measures include the construction of flood control infrastructure such as dams, levees, and flood retention basins (Chan et al., 2020). Non-structural measures focus on policies, regulations, and community-based approaches, such as land-use planning, early warning systems, public awareness campaigns, and capacity building (Chan et al., 2020). Integrating both approaches can enhance the overall effectiveness and sustainability of flood risk management strategies.

Flooding in Nigeria is a complex and multifaceted challenge influenced by natural and human-induced factors. Inadequate drainage systems, poor urban planning, climate change, and anthropogenic activities contribute to increased flood risk. The impacts of flooding on the built environment are significant, affecting infrastructure, human lives, and socio-economic conditions. Challenges in flood risk management include the need for improved flood mapping and modeling techniques, inter-agency coordination, resilient infrastructure, early warning systems, poverty alleviation, and institutional capacity building. Addressing these challenges requires a comprehensive and integrated approach that encompasses structural and non-structural measures, effective governance, community participation, and long-term planning. By implementing appropriate flood risk management strategies, Nigeria can reduce the vulnerability of communities to flooding, mitigate the impacts on the built environment, and promote sustainable development in the face of future climate-related challenges. Continued research and knowledge sharing are essential for advancing flood risk management practices and fostering resilience in Nigeria's flood-prone areas.

2.2 Flooding in the Lower-Niger Region of Nigeria.

Floods have a significant impact on human life and its surrounding environment which makes it a feared natural disaster. Leading to this, the occurrence worldwide has claimed the lives of many, rendering many places deserted, degradation of farmlands, destruction of properties, natural resources, forest and wetlands. According to (Wood, 2001) unlike any other natural disaster, it is the most frequent occurring natural disaster worldwide and its distribution have led to significant economic and social damage.

The Niger River Basin covers 2.27 million km^2, with the active drainage area comprising less than 50% of the total (Oyebande and Odunuga, 2010). At 4200 km in length, the Niger is the third longest river in Africa and the world's ninth largest river system. The basin is shared among 10 countries as indicated in Figure 2.1: Nigeria (27 %), Mali (26 %), Niger (24 %), Algeria (8 %), Benin, Burkina Faso, Cameroon, Chad, Cote d'Ivoire and Guinea (each <5 %). The study area falls within the Nigeria section and include the Benue (the Niger major tributary) that join it at Lokoja. Figure 2.1 shows Niger basin and its tributary, Benue River in West African respectively. Annual rainfall ranges from about 1100mm in the upstream basement complex area, to about 1400mm south of Lokoja (Odunuga et al., 2015).

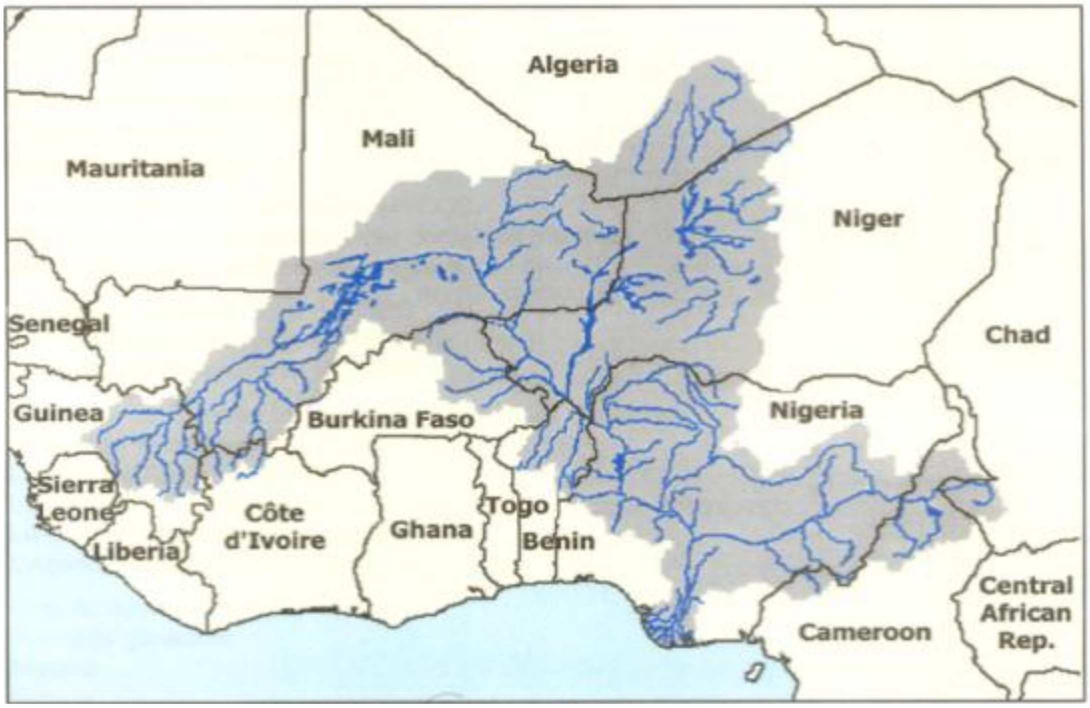

Figure 2.1: Niger and Benue in West Africa

The fresh and saline water ecosystems which inhabit the lower Niger region maintain a dynamic equilibrium thereby making the rich biodiversity ecosystem relatively fragile. As seen in Figure 2.2, the interaction of the hydro-ecological processes with the environment at the same time has resulted in the development of different ecological zones whose boundaries are constantly adjusting to the balance of upstream discharge and tidal flows.

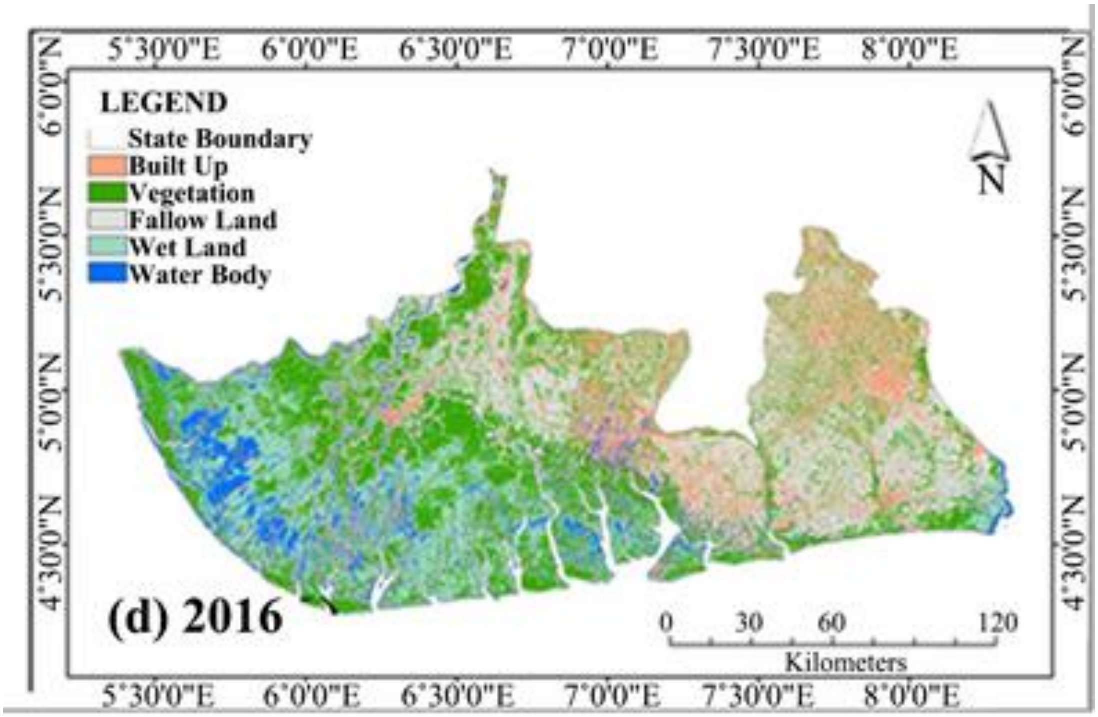

Figure 2.2: Spatiotemporal changes in ecosystem in the Niger Delta Region *(Elekwachi et al., 2021)*

The extent of the variation is usually heavily influenced by topography, soil type and discharge. Any alteration in these factors has the potential of changing the geo-ecological equilibrium and boundaries. (Abam, 2001) stated that, the change from one geomorphic zone to the other can be imperceptible in the field since in actuality, there exists in the field, a transitional zone of variable width, characterized by mixed attributes.

The geographical area of the Niger Delta covering some 38 km^2 is the receptacle of water and sediments from the vast catchment area of approximately 2 million km^2 of the Niger River system. The continuous deposition of sediments for several millions of years together with other delta development processes have resulted in the formation of a gently sloping prolific sedimentary basin characterized by a crisscrossing river and creek network (Figure 2.3).

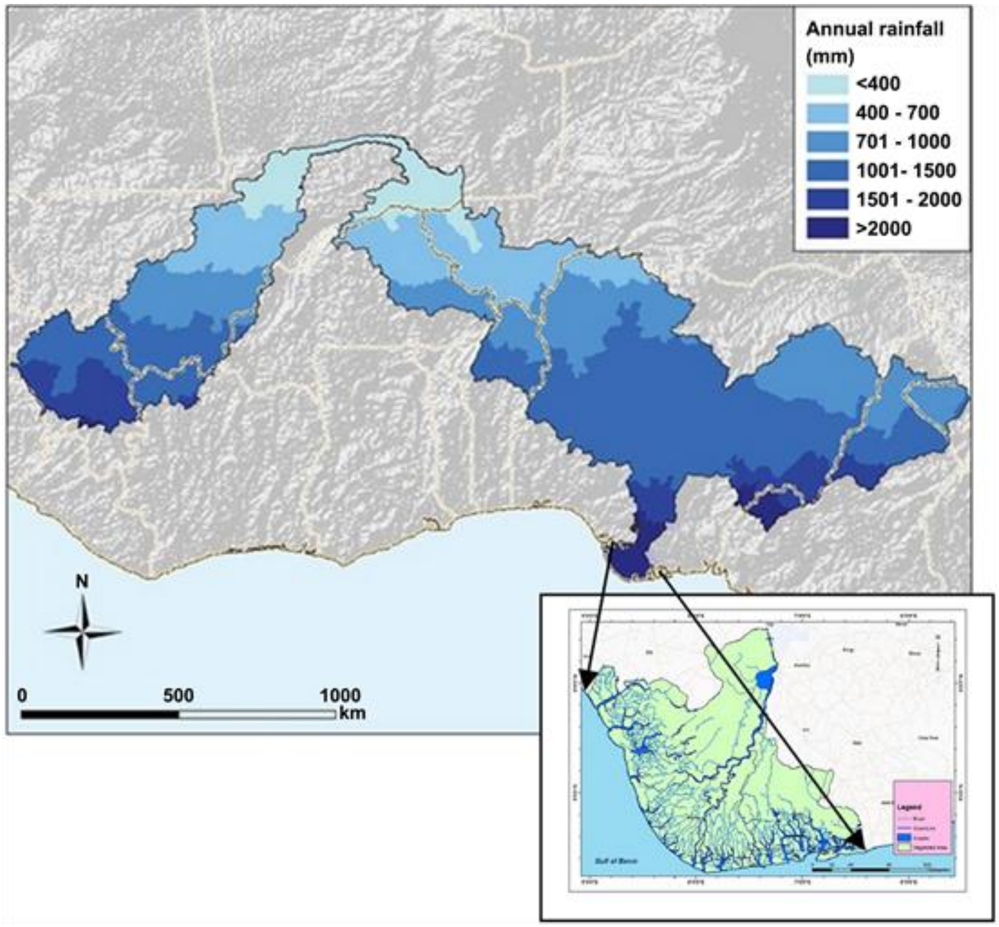

Figure 2.3: Drainage catchment area of the Niger Delta.

The Niger River floodplain on the other hand exhibits medium and high vulnerability levels from Jederbode to Lokoja (Table 2.1). It can therefore be explained that, any year that hydrological processes especially the peak flow event is above the long term historical average on the Niger, settlements between Jederbode and Lokoja in Nigeria will experience flood and the reservoir (Kainji dam) on the Niger within this segment will receive enough to operate at full capacity. However, if best practices in dam operation and reservoir optimization are not used, the downstream population will be highly impacted. The severity of impact may be much higher if corresponding high flow comes from the Benue River as it occurred in year 2012. Also, the floodplain vulnerability of Niger around the confluence and downstream of Lokoja to the acute delta will probably be very high class.

Table 2.1: Vulnerability Index of the Lower Niger–Benue Floodplain (Source: Shuaibu, 2020)

Location	River	Floodplain Vulnerability Levels (km^2)			
		Low	Medium	High	Very High
Worobokri–Makurdi	Benue		270.36	1370.08	
Makurdi–Lokoja	Benue			5417.06	1163.07
Lokoja–Jebba	Niger		698.07	1916.62	
Jebba–Jederbode	Niger		2779.52	1554.17	

As the flow progresses towards the ocean, the ecological zones are further dissected by a dense network of rivers and creeks that convey water and sediments through the numerous estuaries to support the dynamic equilibrium of the coastal hydrological processes. Due to estuarine processes and the combined influence of tides and ocean currents on the sediments, the original river outlets may frequently be blocked, forcing the creation of new outlets. Consequently, the form, shape and size of the chain of coastal islands bordering the shoreline continue to change over time. Recent changes in the shoreline during the last 100 years against the background of conflict between forces of Nature and Humans were described by (Dada et al., 2018)

There has been the slow poisoning of the waters of this country and the destruction of vegetation and agricultural land by oil spills which occur during petroleum exploration and exploitation. But since the inception of the oil industry in Nigeria, more than 25 years ago, there has been no concerted and effective effort on the part of the government, l*et. al*one the oil operators, to control environmental problems associated with the industry (Powell, 2009).

It is estimated that:

I. 1.5% of the country is at risk from direct flooding from the sea.

II. About 7% of the country is likely to flood at least once every 100 years from rivers.

III. 1.7million homes and 130,000 commercial properties, worth more than £200 billion, are at risk from river or coastal flooding in England (Powell, 2009).

2.3 Types of Flooding

There are different types of flooding which include the following;

2.3.1 Tidal flooding

Both sea and river defenses may be overtopped or breached by a combination of low-pressure weather systems and peak high tides. Storms with high wind speeds cause tall and powerful waves, and low-pressure fronts cause sea levels to rise above normal levels (Spencer et al., 2015). High tide levels vary through the lunar and solar cycle, and when superimposed upon other tidal variations, exceptionally high tides result (Mfon et al., 2022). The onset of flooding from the sea and tidal rivers is often sudden, and the extreme forces driving it present a significant danger to life ("Flood risk management," 2014). The east coast storm surge of 1953 claimed 307 people's lives in the UK and 1,835 in Holland. A similar storm surge tide in September 2007 came within a few centimeters of breaching a number of the UK's coastal defenses (Hall et al., 2003; Spencer et al., 2015). It is often possible to forecast, with reasonable accuracy, this type of flooding due to the predictability of the tide and trackability of low-pressure systems (Lasat et al., 2018). The duration of this type of flooding is also limited by the cycle of the tides where drainage is available (Dance and Hynes, 1980).

2.3.2 Fluvial Flooding

Flooding occurs in the floodplains of rivers when the capacity of watercourses is exceeded as a result of rainfall or snow and ice melts within catchment areas further upstream (Environment Agency, 2022). Blockages of watercourses and flood channels or tide locking may also lead to ponding and rising water levels (Mfon et al., 2022). River defenses may then be overtopped due to increased water levels or breached by large objects of debris carried at high water velocities (Dysarz, 2020). Flooding from rivers has in recent years been experienced in the Severn Valley, in Sheffield, in Hull from the River Humber in 2007, and Carlisle on the River Eden in 2006 (Hall et al., 2003). The onset can be quite slow in some catchments with steadily rising water levels (Kamara, 2019).

2.3.3 Flash Flooding

Flash flooding can occur in steep catchments and is far more immediate (Kamara, 2019). Flooding from rivers, particularly in recognized floodplains, can usually be predicted with good accuracy (Hall et al., 2003). However, flash floods from sudden downpours, such as those in Carlisle, continue to challenge the capability of detection and forecasting systems (Cologna et al., 2017). Water over about 250 mm in depth may carry debris, particularly in urban locations, and can also be very cold. Even when travelling at low speeds, this can make it extremely hazardous to people caught in it (Cologna et al., 2017).

2.3.4 Ground Water

Low-lying areas situated over aquifers may periodically experience groundwater flooding when the water table rises above the surface. This typically occurs after prolonged periods of rainfall when the ground becomes saturated, and the capacity of underlying aquifers is exceeded (Lasat et al., 2018). Unlike surface or fluvial flooding, groundwater flooding tends to have a delayed onset, sometimes occurring days or even weeks after heavy rainfall. It is often seasonal in nature and is most common during late winter or early spring due to cumulative recharge of aquifers over the wet season (Cologna et al., 2017).

Although it develops slowly, groundwater flooding can persist for extended periods weeks or even months making it particularly disruptive to agriculture, infrastructure, and underground services (Akhtar et al., 2021). The predictability of seasonal patterns and aquifer behavior allows for relatively accurate forecasting and early warning in some regions, particularly where long-term monitoring systems are in place (Lasat et al., 2018). However, due to its diffuse nature, it can be difficult to manage with traditional flood defenses.

2.3.5 Pluvial Flooding

Surface water flooding is caused by rainwater run-off from urban and rural land with low absorbency. Increased intensity of development in urban areas has given rise to land with a larger proportion of non-permeable surfaces, a problem often exacerbated by overloaded and outdated drainage infrastructure (Akhtar et al., 2021). These circumstances, combined with intense rainfall, can give rise to localized flooding. This type of flooding often occurs outside of recognized floodplains and, because it is driven by highly localized weather conditions, it is very difficult to forecast (Lasat et al., 2018). Its onset can also be very rapid and the level of flooding very severe, especially in areas where surface drainage is inadequate or blocked by debris (Amoako and Frimpong Boamah, 2015).

In the summer of 2007, much of the flooding experienced in Gloucestershire and Yorkshire was not directly caused by rivers but by surface water. Large volumes of rainfall early in the year saturated the ground, and intense rainfall later caused both urban and rural areas to flood (J. Huang et al., 2022). This event highlighted the urgent need for improved surface water management strategies and greater investment in sustainable urban drainage systems (SUDS).

2.3.6 Flooding from Sewers

Flooding from sewers can occur where there are combined storm and foul sewer systems and their capacity is exceeded due to large volumes of surface water run-off within a short period, particularly during intense or prolonged rainfall events (Environment Agency, 2022). These combined systems, which are common in older urban areas, are especially vulnerable during storm surges when the volume of water entering the system far surpasses its design capacity. Poor cleaning and maintenance can exacerbate the situation by allowing debris, fats, oils, and non-biodegradable waste to block the sewer pipes, thereby reducing flow capacity and increasing the likelihood of localized flooding (Ayilara et al., 2020).

This type of flooding is especially concerning because it often results in the discharge of untreated wastewater into streets, homes, and public spaces. Consequently, sewer flooding poses significant public health risks, including exposure to pathogens and waterborne diseases (Islam and Islam, 2020). The sudden and unpredictable nature of sewer flooding also makes it difficult to forecast and manage effectively, especially in areas with aging or poorly mapped infrastructure (Islam and Islam, 2020). As climate change leads to more frequent extreme rainfall events, the risk of sewer system overload and subsequent flooding is expected to rise unless proactive adaptation strategies and infrastructure upgrades are implemented.

2.3.7 Flooding from Manmade Infrastructure

Canals, reservoirs, and other manmade water-retaining structures such as embankments and levees can fail, leading to catastrophic flooding in downstream areas. Structural failures may result from overtopping during extreme rainfall events, internal erosion (piping), poor maintenance, or aging infrastructure that no longer meets modern safety standards (Concha Larrauri et al., 2023). In the event of a breach or uncontrolled release of water, downstream communities can be severely impacted within minutes, with little or no warning. Such events can cause extensive property damage, disruption to services, and significant risk to life, particularly where early warning systems or emergency action plans are absent or ineffective (Concha Larrauri et al., 2023).

In addition to structural failures, industrial activities, water mains, and pumping stations can also contribute to flooding, especially when mechanical or electrical systems malfunction. Failures in pumping stations—critical for managing drainage and sewage in low-lying areas—can rapidly lead to localized flooding if water cannot be discharged or redirected (Islam and Islam, 2020). Similarly, burst water mains, often due to age-related deterioration or high-pressure surges, can release large volumes of water onto roads and into buildings, disrupting transportation and utilities (Serafeim et al., 2024).

As climate change increases the frequency and intensity of extreme weather events, the reliability of manmade flood defense systems and infrastructure is being tested more frequently. This highlights the need for regular inspection, risk assessment, and reinforcement of critical water infrastructure to ensure resilience and public safety (Ridha et al., 2022).

2.4 Causes and Types of Flooding, Their Types and Effects

Flooding can result from a variety of natural processes and human activities. The following sections outline the main categories of flooding and their respective causes.

a) Natural and Human-Induced Causes of Flooding

Prolonged or intense rainfall can exceed the capacity of natural and artificial drainage systems, causing widespread surface or fluvial flooding. In a similar way, rapid snowmelt—particularly when it coincides with rainfall, can saturate the soil, significantly raising water levels and leading to overflow. Strong winds over large water bodies may push waves and water inland, and when combined with unusually high tides or storm surges during cyclonic events, the result is often severe coastal flooding. Tsunamis or the failure of critical manmade structures such as dams, levees, or retention ponds can also trigger sudden and destructive floods in downstream areas. Human activities further contribute to flood risk, especially in urban areas where widespread development leads to the replacement of natural land cover with impervious surfaces. This reduces the ground's capacity to absorb water, resulting in higher surface runoff. Additionally, vegetation loss caused by wildfires or deforestation diminishes the land's natural ability to retain water, thereby increasing vulnerability to flooding (Concha Larrauri *et. al*., 2023, Serafeim *et. al*., 2024).

b) Slow-Onset Flooding

Flooding can gradually develop as a result of prolonged rainfall or rapid snowmelt, often driven by seasonal weather patterns such as monsoons, hurricanes, or tropical depressions. In some cases, the accumulation of water is further intensified by obstructions within drainage systems such as landslides, ice jams, or debris that block the normal flow of water, leading to upstream flooding. Although these types of floods progress slowly, offering more time for evacuation and emergency response, they often persist for extended periods. Their prolonged nature can cause significant disruption to agriculture, transportation networks, and critical infrastructure ("Flood risk management," 2014).

c) Fast-Onset Flooding (Flash Floods)

Flash floods often occur with little warning, typically triggered by short, intense bursts of rainfall, especially in steep or poorly drained landscapes. In addition to heavy precipitation, sudden releases of water from failed dams, glacier collapses, or landslide-blocked reservoirs can lead to rapid and dangerous downstream flooding. Coastal areas are also highly vulnerable to storm surges caused by tropical or extra-tropical cyclones, which can drive seawater inland and inundate communities with minimal notice. Furthermore, seismic activity such as earthquakes and volcanic eruptions can result in abrupt water displacement, leading to severe flash flooding. Urban environments face heightened risk due to the extensive coverage of impermeable surfaces, which prevents infiltration and causes rainwater to accumulate rapidly, overwhelming drainage systems (Amoako and Frimpong Boamah, 2015).

d) Muddy Floods and Repeated Storm Events

Muddy floods typically occur in agricultural areas where heavy rainfall causes surface runoff to detach and carry loose topsoil downslope. This sediment-laden water often reaches inhabited areas, particularly when the land is tilled, poorly vegetated, or situated on a gradient. Unlike mudflows, which are caused by mass movements of saturated soil, muddy floods result from the flow of water across the land surface. The situation can be worsened when multiple storms strike the same region in rapid succession, leaving the ground fully saturated and unable to absorb additional rainfall, which significantly increases the severity and extent of flooding ("Flood Disaster Hazards; Causes, Impacts and Management," 2021).

e) Influence of Urban Planning

Recent studies have examined the underlying causes of persistent flooding in Lagos, aiming to propose sustainable management strategies. Comprehensive analyses incorporating climate data, drainage infrastructure conditions, and urban planning regulations have been carried out, complemented by field inspections and consultations with key stakeholders, including government agencies, academic institutions, and local residents. Findings indicate that, contrary to widespread belief, climate change or unusually heavy rainfall is not the primary driver of flooding in Lagos. Instead, rapid urbanization, weak enforcement of physical planning regulations, and inadequate drainage infrastructure are the main contributors to the city's recurrent flood challenges. Research suggests that effective, long-term solutions must focus on integrating sustainable drainage systems (SuDS) into existing flood management frameworks. This integration should be prioritized and implemented through forward-looking urban planning and governance reforms (Geekiyanage *et. al*., 2020, Mar *et. al*., 2022).

2.4.1 Climate Change

Climate Change is an attributed cause of flooding because when the climate is warmer it results to:

i. Heavy rains.
ii. Relative sea level will continue to rise around most shoreline.
iii. Extreme sea levels will be experienced more frequently.

Climate change is expected to significantly and progressively increase flood risk across the globe. Low-lying coastal regions are especially vulnerable due to sea level rise, while areas not historically prone to fluvial or tidal flooding are increasingly at risk as more intense and frequent rainfall events result in surface water runoff and overwhelmed drainage infrastructure (Ridha et al., 2022). These changes are closely linked to the growing concentration of greenhouse gases (GHGs) in the atmosphere, largely from anthropogenic sources such as fossil fuel combustion, agriculture, and industrial processes.

Efforts to reduce GHG emissions have included strategies to limit methane release, one of the most potent greenhouse gases. Methane, which is over 25 times more effective than carbon dioxide in trapping heat over a 100-year period, is often released during oil and gas production, as well as through the decomposition of organic waste in landfills (Magazzino et al., 2024). In recent years, methane capture and combustion systems have been adopted in many developing countries to convert methane to carbon dioxide and water, thereby reducing its climate impact. Under international frameworks like the Kyoto Protocol and the more recent Paris Agreement, carbon credit incentives have been provided for such mitigation efforts (Mar et al., 2022).

The greenhouse effect itself is a natural process, but human activity has intensified it significantly. Greenhouse gases such as carbon dioxide (CO_2), methane (CH_4), nitrous oxide (N_2O), ozone (O_3), and synthetic compounds like hydrofluorocarbons (HFCs) and perfluorocarbons (PFCs) trap outgoing infrared radiation, leading to warming of the Earth's surface and lower atmosphere. Scientific advancements over the past century have allowed for detailed monitoring and modeling of these gases, with recent studies focusing on the impact of anthropogenic emissions on long-term climate change, including their role in altering ocean chemistry. The increase in atmospheric CO_2 levels is also contributing to ocean acidification, which poses a serious threat to marine ecosystems and biodiversity. This, in turn, has implications for sea level rise, which can exacerbate coastal flooding (Mar et al., 2022).

2.4.2 Factors Which Determine the Effects of Flooding:

Flood impacts vary greatly depending on a range of physical and social factors. The extent of destruction and the ability of individuals and communities to respond are influenced by several interrelated conditions, as outlined below.

I.) Level of Predictability

The predictability of a flood plays a critical role in shaping its consequences. Accurate and timely forecasting determines how effectively warnings can be issued and communicated. When floods are predictable, early warning systems and emergency responses can be activated to reduce harm to life and property. On the other hand, unpredictable events leave less time for preparation, increasing vulnerability and potential damage (Intergovernmental Panel On Climate Change (Ipcc), 2023).

II.) Rate of Onset

The speed at which floodwaters arrive and rise influences how much time people have to prepare and respond. A rapid onset limits evacuation and protective actions, increasing the potential for injuries, fatalities, and property loss. Slow-onset floods, while often prolonged, provide more opportunity for mitigating measures and coordinated emergency response (Borowska-Stefańska et al., 2023).

III.) Speed and Depth of Water

The velocity and depth of floodwater are crucial in determining the physical force exerted on people, buildings, and infrastructure. Even shallow water, when moving quickly, can be difficult to wade through, and depths of over one meter can carry vehicles and large debris. Fast-flowing water significantly increases the risk of injury or death and can cause extensive structural damage to homes, bridges, and utilities (Borowska-Stefańska et al., 2023).

IV.) Duration of Flooding

The length of time a flood persists directly affects its long-term impact. Prolonged flooding can cause deeper psychological, economic, and infrastructural damage. Extended waterlogging disrupts livelihoods, displaces communities, damages crops, and leads to the spread of waterborne diseases. Recovery is often slower when flooding is sustained over days or weeks (Borowska-Stefańska et al., 2023).

2.4.3 The Effects of Flooding

Flooding has wide-ranging consequences that can be categorized into primary and secondary effects. These impacts can be immediate and visible or long-term and systemic, affecting not just the built environment but also human health, ecosystems, and local economies.

a) Primary Effects

Primary effects refer to the direct physical consequences of flooding. These include the immediate damage caused to infrastructure such as roads, bridges, railways, canals, buildings, vehicles, and underground facilities like sewerage systems and water pipelines. Structures may be submerged, undermined, or completely destroyed by fast-moving floodwaters, particularly when debris or sediment increases the destructive force of the water. In urban areas, the breakdown of essential infrastructure such as power supply, communication networks, and transportation can paralyze economic activity and delay emergency response efforts. In rural regions, flooding may destroy crops, livestock, and irrigation systems, severely affecting food security and local livelihoods (Mfon et al., 2022).

b) Secondary Effects

Secondary effects are the indirect or delayed consequences that emerge following the initial flood event. A critical secondary effect is the contamination of water supplies. When floodwaters mix with sewage, chemicals, industrial waste, or decaying organic matter, they pollute rivers, reservoirs, and groundwater. This leads to a scarcity of safe drinking water and compromises public health. The lack of clean water, coupled with unhygienic conditions in flooded areas, often contributes to the outbreak and spread of waterborne diseases such as cholera, dysentery, typhoid, and leptospirosis. Additionally, stagnant water becomes a breeding ground for mosquitoes, increasing the risk of vector-borne diseases such as malaria and dengue. These health challenges place a strain on already limited healthcare infrastructure, particularly in developing countries (Mar et al., 2022). Beyond health, secondary effects also include psychological trauma, displacement of people, and long-term disruption of education and livelihoods.

2.4.4 Receptors and Impacts of Flooding

Flooding affects a wide range of “receptors” that is, the people, environments, and systems that experience the consequences of flood events. These impacts can be immediate or long-term and may affect both natural and human-made systems.

I. Human Impact and Social Consequences

Flooding can result in tragic loss of human life, particularly in regions where preparedness and response systems are inadequate. In southwest Nigeria, for instance, over 100 lives were lost during floods around the city of Ibadan, underscoring the devastating human toll (Zade et al., 2021). In northeastern Nigeria, the 2011 floods caused widespread destruction of homes and livestock, with children making up a significant number of casualties. Beyond physical harm, flooding also brings profound emotional and social consequences. These include displacement, loss of personal belongings, emotional trauma, and ongoing fear or anxiety among affected populations (Fothergill et al., 2021).

II. Public Health and Water Contamination

Potable water supplies are often compromised during flood events. Contamination from floodwater can lead to the spread of waterborne diseases affecting both humans and animals. Poor sanitation, especially in low-income areas, can exacerbate these health risks. Floodwaters may carry pathogens, toxic substances, and untreated sewage, posing direct threats to public health and safety (Erickson et al., 2019).

III. Economic Impact and Livelihood Disruption

Flooding can severely disrupt local and national economies. Businesses may suffer from the loss of inventory, data, and physical assets, leading to reduced productivity and income. Infrastructure failures such as the disruption of electricity, transportation, and water services can create ripple effects that affect commerce, agriculture, and tourism. Farming and livestock activities are also highly vulnerable to flood-related destruction, often leading to food insecurity and economic instability (Douglas, 2009)

IV. Damage to the Built Environment and Infrastructure

Buildings, roads, bridges, and public spaces are frequently damaged or destroyed by flooding. The cost of repairs can be immense, and recovery periods are often prolonged. Debris, silt, and other contaminants left behind after floods also degrade the public realm. Moreover, floodwaters can transport hazardous substances, causing land contamination. Flooding of electrical substations, gas facilities, and telecommunications infrastructure can lead to widespread outages and severely hinder communication and rescue efforts (National Infrastructure Commission, 2022).

V.) Emergency Response and Clean-up Hazards

Post-flood clean-up activities carry significant risks. Emergency responders and volunteers may face hazards such as electrical shocks, exposure to hazardous materials, carbon monoxide poisoning, musculoskeletal injuries, and drowning. Flood zones often contain unstable debris, exposed wires, and potentially contaminated water. To mitigate these risks, safety equipment like hard hats, waterproof boots, gloves, and life jackets are essential (Sarkar et al., 2020).

VI.) Water Quality and Aquatic Ecosystems

Floods contribute significantly to water pollution through the transport of sediments, chemicals, and biological contaminants. These changes alter the physical and chemical characteristics of water, thereby affecting aquatic biodiversity. The suitability of aquatic environments for fish and other organisms depends on variables such as temperature, dissolved oxygen, turbidity, and pH levels. Monitoring these variables is crucial for maintaining healthy aquatic ecosystems, particularly in small water bodies used for fish production and rural livelihoods (George *et. al*., 2020).

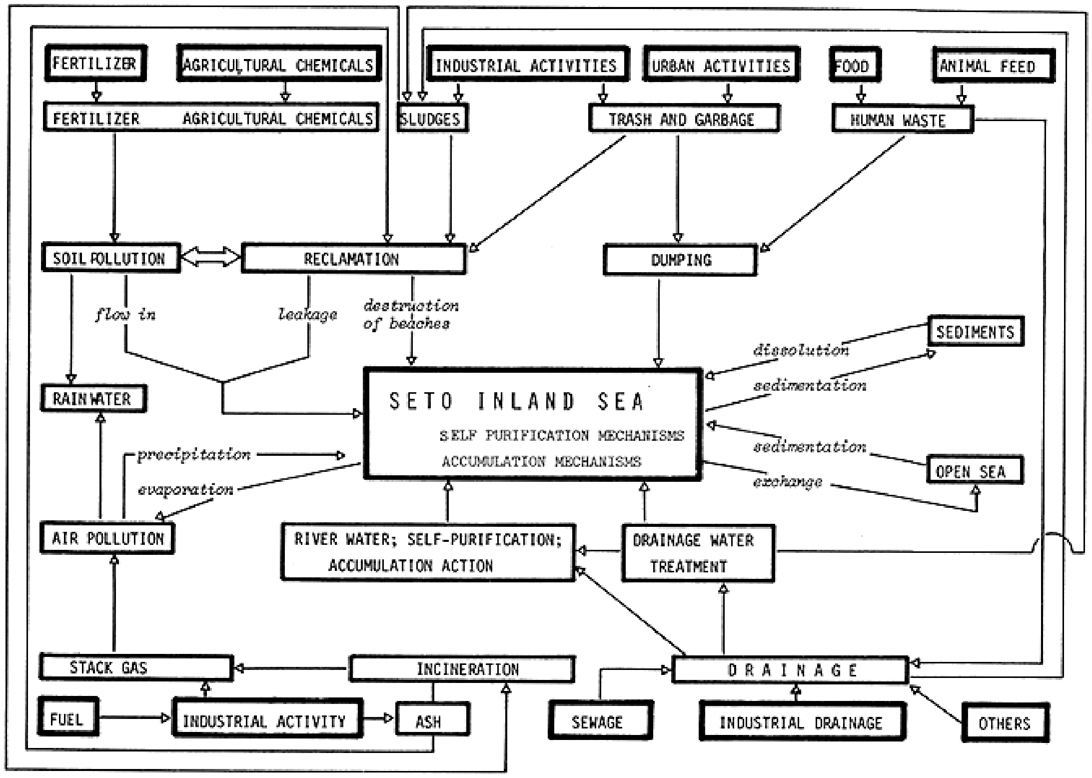

Figure 2.4: Various Forms of Pollution Carried by Flooding

2.5 Influence of Water Quality, Sediment, and Agricultural Activity on Aquatic Ecosystems

I. Impact of Water Quality Variability on Fish Production

Water quality plays a crucial role in maintaining the health of aquatic ecosystems, especially in fish farming. Variability in water parameters such as temperature, salinity, pH, and concentrations of dissolved oxygen, carbon dioxide, ammonia, and hydrogen ions (H^+) directly affects fish growth, metabolism, and survival. Pollution from sources such as market effluents, abattoir waste, street runoff, and flushed sewage alters the chemical composition of water bodies, disrupting aquatic life. Without effective water quality management, fish yield is significantly compromised. Regular monitoring and regulation of environmental conditions are essential to maintain optimal productivity in aquaculture systems (Okon *et. al*., 2021; Udo & Emeka, 2020).

II. Availability of Nutrients and Role of Plankton

The growth of plankton microscopic plants and animals that serve as the base of aquatic food chains is vital for the nutrition of cultured fish. The availability of key nutrients like nitrogen, phosphorus, and carbon compounds influences plankton abundance. These nutrients are, however, sensitive to external inputs from pollution or agricultural runoff, which can cause imbalances and result in eutrophication or oxygen depletion. This, in turn, impacts fish health and mortality (Adesina & Nwosu, 2022; Eze & Obinna, 2023).

III. Sediment Composition and Its Ecological Functions

Sediment comprising silt, sand, and organic matter settles at the bottom of water bodies and serves as a critical habitat for benthic macroinvertebrates. These organisms are essential to aquatic productivity as they aid in the breakdown of organic matter and nutrient cycling. Bacteria in the sediment facilitate decomposition, while the interchange of macronutrients like nitrogen and phosphorus between sediment and water supports aquatic food webs. However, excessive sedimentation from anthropogenic sources can degrade this habitat (Ibrahim *et. al*., 2020; George & Ezeonu, 2021).

IV. Agricultural Land Use and Sediment Load Impact

Intensive agricultural activities such as land clearing, tilling, and stream channelization increase sediment load in adjacent water bodies. These sediments often carry agrochemicals like pesticides and fertilizers that disrupt aquatic ecosystems. High sediment levels reduce light penetration, smother benthic habitats, and lower water quality. Drainage modifications from agricultural lands also alter water temperature and chemistry, leading to a decline in macroinvertebrate diversity and fish populations (Olayemi *et. al*., 2019; Yusuf & Anyaoha, 2021).

V. **Sediment Structure and Benthic Organism Distribution**

The physical and chemical structure of sediments in aquatic environments influences the distribution and abundance of benthic species. Factors such as grain size, salinity, dissolved oxygen, pH, and organic carbon determine habitat suitability. Benthic organisms often show preferences for specific sediment types, and changes in sediment characteristics due to pollution or erosion can result in reduced species diversity. Proper sediment management is therefore essential for maintaining ecological balance in aquatic environments (Nwankwo & Okoro, 2020; Omokpariola & Alade, 2022).

Table 2.2: Effects of flooding on surface water quality *(Golladay and Battle, 2002)*

Parameter	Flooding effects
Surface water temperature	Increases
Salinity	Reduces
Dissolved oxygen	Increases
Conductivity	Increases
Turbidity	Increases
Ph	Increases
Biochemical Oxygen Demand BOD)	Increases
Total dissolved solids in water	Increases
Depth	Increases
Waves	Increases
Current	Increases
Planktons	Reduces
Nektons	Reduces

Table 2.2 presents the observed effects of flooding on various water quality parameters. During flood events, several indicators of water quality including surface water temperature, dissolved

oxygen (DO), electrical conductivity, turbidity, pH, biochemical oxygen demand (BOD), total dissolved solids (TDS), water depth, wave height, and current velocity tend to increase in intensity. This is largely attributed to the influx of runoff carrying organic and inorganic matter, the agitation of sediments, and increased water mixing. Conversely, flood intensity tends to reduce salinity levels due to freshwater dilution, while biological components such as plankton and nekton populations decline, likely due to habitat disruption, increased turbidity, and displacement (Adesanya & Ekechukwu, 2020; Nnaji *et. al*., 2021).

In addition to hydrological impacts, flooding significantly alters soil composition. Mineral soils typically consist of inorganic particles known as soil separates**,** which include sand, silt, and clay. These particles are defined by their sizes, with the texture of soil being a function of their relative proportions, particularly those below 2 mm in diameter. Sand is coarse and gritty, silt is smooth and flour-like, and clay is fine-textured and sticky when wet. This textural classification greatly influences the soil's porosity, permeability, and microbial activity. The microbiological population within a given soil profile is highly dependent on its texture class, which governs biological and biochemical processes critical to nutrient cycling and pollutant breakdown (Okonkwo & Adebanjo, 2019; Umeh *et. al*., 2022).

Floodwaters also serve as vectors for nutrient loading in aquatic environments. Key nutrients particularly phosphates, nitrates, and sulphates enter water bodies via runoff from agricultural lands and urban waste discharge. Phosphates are especially significant, as large volumes originate from phosphate fertilizers and detergents. Their presence in high concentrations can lead to eutrophication**,** a process that promotes excessive algal growth, depletes oxygen levels, and ultimately disrupts aquatic ecosystems (Olayinka & Abimbola, 2021; Etim & Ibe, 2023).

2.6 Climate Change and Variability

The Niger Delta region of Nigeria is a complex, yet fragile environment consisting of upland, wetland and fishing communities. Almost all oil production activities in Nigeria, with their attendant negative effects on the environment take place in this region. The area is highly degraded due to oil exploration and exploitation activities, oil spills and gas flaring. Farming and fishing are the major livelihood activities of inhabitants of the region. Records from National Bureau of Statistics and Central Bank of Nigeria reveal that not less than 70% of the population depends on agriculture and fishing for their livelihood, producing food and fiber for human consumption and industrial use respectively (Wu et al., 2014). Agriculture is largely rain-fed and crop cultivation as well as livestock production depends on the availability of water from rainfall. Thus, agriculture in the Niger delta region is highly influenced by annual and inter-annual variations in rainfall and other climatic factors.

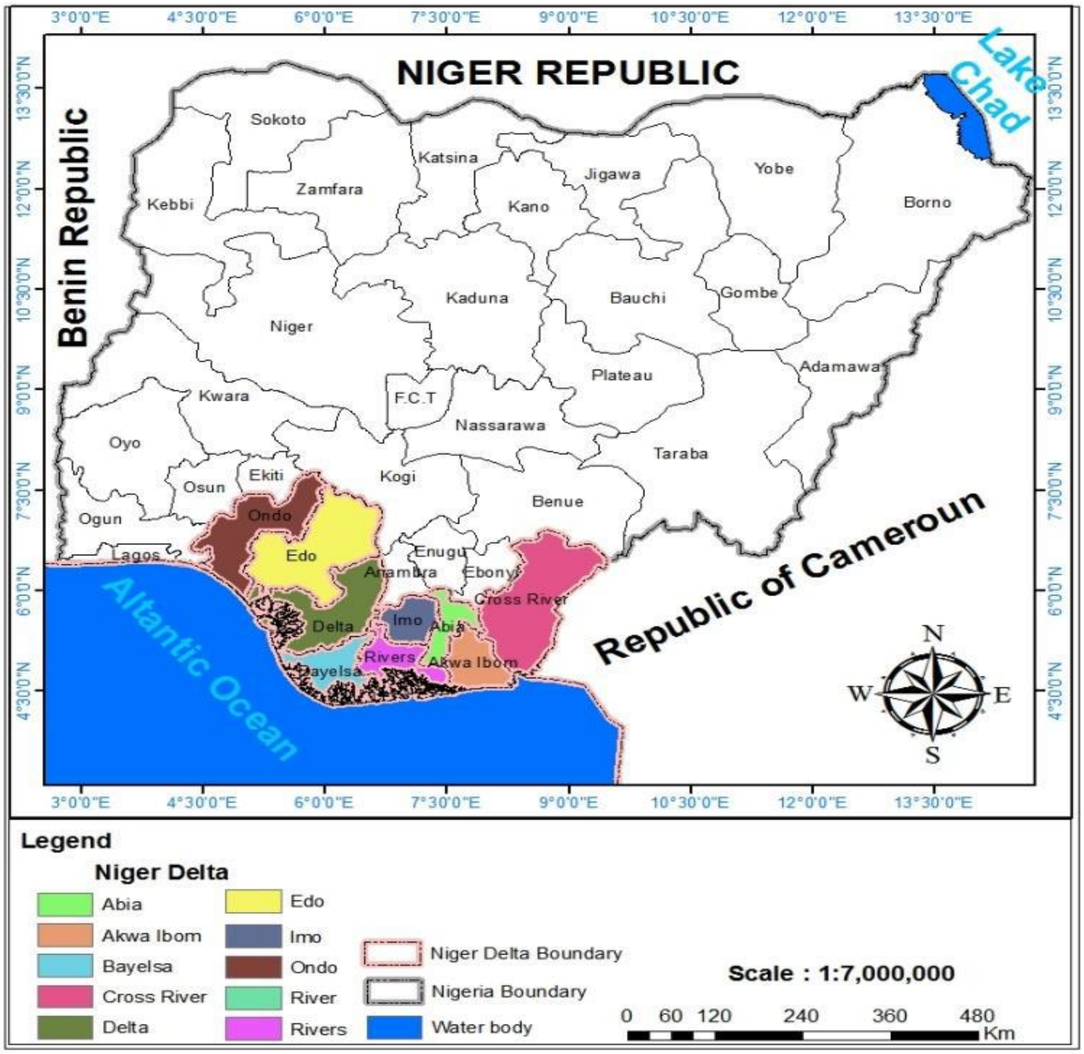

Figure 2.5: Map of Nigeria showing the Niger Delta Region [Source: Authors' GIS Lab 2020 (extracted using LST and NDVi for the states)]

Accordingly, Climate change is referred to as statistically significant variation in the mean state of the climate or the long-term changes in climate conditions observable over several decades or longer (Watson and Team, 2001). Climate variability on the other hand is the deviations of climate statistics over a given period of time from the long-term climate statistics relating to the corresponding calendar period or short-term variations in climate over periods of days, months, years and decades (Watson and Team, 2001).

Before the turn of the 21st century, when global warming and climate change began to dominate scientific discussions, many people—including policymakers—regarded climate change as unreal or a mere myth. This skepticism explains why several nations were reluctant, and in some cases remain unwilling, to ratify international agreements such as the Kyoto Protocol. Today, however, the effects of climate change are evident across almost every part of the world, manifesting in both beneficial and harmful ways (Nashier & Lakra, 2020). Consequently, climate change has emerged as one of the most urgent and complex environmental challenges confronting humanity, demanding immediate and coordinated responses. It is a long-term problem rooted in over two centuries of human activity, and very few aspects of modern life remain untouched by it.

Its impacts are increasingly visible through extreme hydrological and weather events such as floods and droughts, particularly in sensitive regions like the Niger Delta River Basin. These changes are expected to intensify, undermining sustainable development and exerting significant pressure on the economies of developing nations, their social systems, natural resources, and physical infrastructure. The consequences extend beyond local impacts, shaping global patterns of livelihood, especially in countries with low adaptive capacity, fragile ecosystems, and heavy dependence on river basin resources. In addition, climate change has the potential to heighten global insecurity by driving migration and fueling conflicts over scarce resources (Scheffran & Battaglini, 2011).

A further challenge lies in the disparity between those primarily responsible for greenhouse gas emissions and those who bear the brunt of their consequences. This imbalance has long complicated international climate negotiations and slowed global action. Nowhere is this inequity more pronounced than in Africa, particularly West Africa, where countries contribute minimally to global emissions yet face some of the harshest consequences of climate variability and change.

Even though, there is no consensus amongst the Global Climate Models (GCMs) over the future climate of the West Africa (Christensen *et. al*., 2007), the region's experience so far, starkly demonstrates the development setbacks and high level of vulnerability of the area to impacts of climate change; ranging from recurrent droughts, Niger River zero flow of 1984 and 1985 at Malaville and Niamey (Benin and Niger) respectively, to shrinkage and disappearance of Lake Chad, devastation of Abuja National stadium velodrome, collapse of connecting Nukkai and Sokoto bridges, in 2003, 2005 and 2010 respectively (all in Nigeria) (Juddy et al., 2013). This is because; the current climate of the region is strongly characterized by climatic variability and extreme events (floods and droughts) that already have serious implications on economic development of the region.

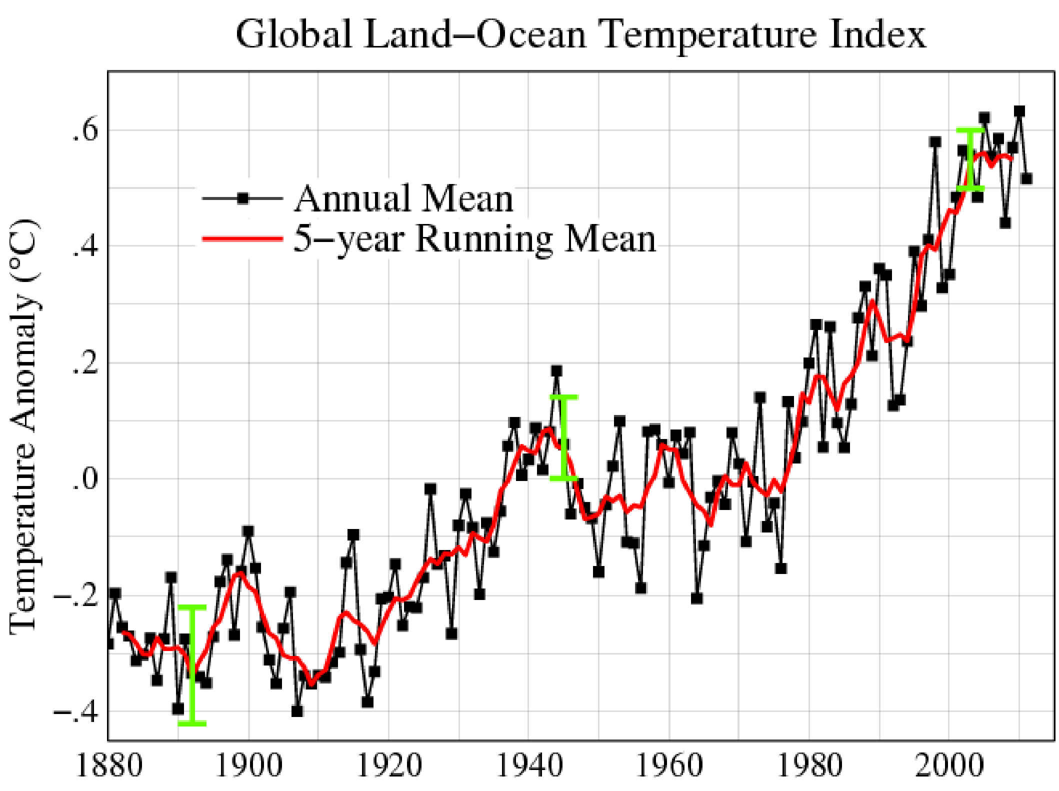

Figure 2.6: Global Temperature Anomaly 1880-2010 (Sources NASA, 2011)

It is now very obvious too that an inherent characteristic of climate is change, and a period of change is already underway which has the potential to threaten the fabric of human society and its development across the globe both at present and in the future. Climate, development, and the water-resource systems of a river basin are intricately linked, as water availability is governed by the hydrological cycle, which itself forms part of the Earth's climate system driven by solar energy (Yang et al., 2021). The phenomenon now referred to as global warming—marked by the rise in average atmospheric and oceanic temperatures since the late 19th century and projected to continue—has largely been triggered by human activity. Rather than coexisting with natural systems, human efforts to dominate and exploit nature have accelerated this warming trend, making it the primary driver of climate change.

Human influence has therefore altered weather and climate patterns, which in turn exert significant effects on human society through the increasing occurrence of extreme events (Handmer et al., 2012). This has heightened the urgency to study, evaluate, and quantify the potential impacts of climate change on climate-sensitive sectors of national economies and on hydrological systems. As a result, decision-makers across multiple sectors—such as water, agriculture, energy, fisheries, health, forestry, transport, tourism, and disaster risk management—are becoming increasingly concerned about the growing risks associated with climate change. However, many of these sectors remain poorly equipped to effectively address the challenges posed by these adverse impacts.

Figure 2.7: Reaping Extreme Hydrological disasters due to climatic Variability and changing climate (Nigeria experience in the lower Niger Sub-basin) (Juddy et al., 2013)

2.7 Effects of Climate Change and Variability on the Niger River Basin

Climate change, driven by the rising concentration of greenhouse gases, is projected to intensify existing climatic variability and extreme weather conditions in the Niger Delta Basin. This intensification poses significant challenges to water resource availability, agricultural productivity, and food security, not only within the basin itself but also across the broader West African subregion.

I. Impacts on Water Resources and Agriculture

The warming climate, driven by rising concentrations of greenhouse gases, is expected to intensify existing climatic variability and extremes in the Niger River Basin. This shift poses significant implications for water resource availability and food production throughout West Africa. The region's predominant livelihoods rain-fed agriculture and nomadic pastoralism—are especially vulnerable to increased temperature volatility. As summertime heat becomes more erratic, crop yields are likely to decline, particularly in key grain-growing regions. Additionally, the projected intensification of the hydrological cycle may lead to more frequent and severe droughts or floods (Intergovernmental Panel on Climate Change (IPCC), 2021).

II. Socioeconomic Vulnerabilities and Livelihood Dependence

The Niger Delta River is more than a water source; it serves as a vital cultural and economic artery for the region. It supports migration, trade, and is a central component of identity for many communities. With an annual population growth rate of approximately 2.8%, pressure on water resources continues to grow. Many communities within the basin experience chronic poverty, exacerbating their vulnerability to climate-induced stressors such as food and water insecurity, malnutrition, and livelihood disruption (Naz & Saleem, 2024). Addressing these risks requires adaptive and integrated water resource management practices, especially in the face of demographic and land use pressures (Connell, 2017)

2.7.1 Environmental Pressures in the Niger Delta

The Niger River and its tributaries serve as vital arteries for hydropower generation, domestic use, irrigation, and ecological sustainability.

a) Petroleum Activities and Environmental Degradation

The Niger Delta is geologically rich in petroleum-bearing sedimentary formations, which contribute over 90% of Nigeria's export revenues. However, the intensive exploration and production of petroleum in the region has resulted in frequent gas flaring, which severely degrades local air quality, soil fertility, and public health. The environmental footprint of these extractive industries poses long-term risks to both ecological sustainability and human development in the Delta (Kuenzer & Renaud, 2012)

b) Livelihoods and Vegetation Dynamics

Local economies in the Niger Delta rely heavily on subsistence activities such as farming, fishing, and small-scale trade. These livelihoods are sensitive to changes in rainfall patterns, soil health, and vegetation cover. Recent studies affirm that climate is a dominant driver of vegetation change in the region, with temperature and precipitation influencing plant growth, carbon storage, and species distribution (Pugnaire et al., 2019). Consequently, managing climate impacts on vegetation is crucial for maintaining biodiversity, food security, and rural livelihoods.

Table 2.3: Impact of sea level rise in the Niger Delta (source: Musa *et. al*., 2016)

Type of impact	**Unit of measure**	**Present**	**1m SLR**	**2m SLR**
Erosion rate	m/year	10-15	16-19	20-25
Area lost to erosion	Km2	26-45	55-120	130-230
Inundation and erosion	Km2	3,000	7,000	15,000
Percent of area lost	%	15	35	75
Villages impacted	No	50	200	350
People displaced	Million	0.15	1-2	1-2

Table 2.3 contains impacts of sea level rise in the Niger Delta (Awosika et al., 1992). The report indicates that between 26 and 45 meters of land are lost annually to erosion in the Niger Delta, representing approximately 15% of the region's total land area. This phenomenon has already affected around 50 villages and displaced an estimated 150,000 people. Projections suggest that continued sea level rise could displace between 2 and 3 million inhabitants in the future. Without urgent and practical interventions, large portions of the Niger Delta may be submerged, leading to widespread human displacement.

Mitigation measures such as the construction of embankments to safeguard coastal areas, afforestation and re-vegetation programs, as well as the promotion of sustainable land management practices, are necessary to slow the rate of land loss. Furthermore, raising awareness and strengthening the capacity of farmers and local communities to adopt climate change adaptation strategies will be critical in minimizing the impacts of sea level rise. Given that the Niger Delta covers an estimated 2 million hectares, protecting this landmass is vital not only for the environment but also for the socio-economic wellbeing of the region's population (Kuenzer et al., 2014).

Figure 2.8: Debris of brick building destroyed by sea level rise in Ibaka, Mbo LGA, Akwa Ibom State (source : Solomon *et. al*., 2015).

The recent experiences of unusual weather events in the region clearly demonstrate the reality of climate variability and change. For rural farmers with limited adaptive capacity, these changes present a severe shock, exposing the vulnerability of both the Niger River Basin and its inhabitants to hydrological extremes such as droughts, floods, and even landslides. At present, droughts and floods have become the most frequent natural disasters in the basin, often resulting in the loss of human lives, destruction of property, and damage to agricultural land.

Climate variability and change are also altering the timing of rainfall, with noticeable shifts in the onset and cessation of the rainy season, as currently being observed in Nigeria. Most droughts in the region are linked to late onset and early withdrawal of rains, which substantially shortens the rainy season and, consequently, the length of the growing season. This has serious implications for food security, rural livelihoods, and the overall resilience of farming communities in the basin. Number of studies in the Niger basin have shown significant trends towards a false onset (a situation where the rainy season starts normally and then ceases abruptly, creating a dry period between the false onset and the true onset), late or delayed onset (a situation where the expected start of the rainy season is delayed) and early cessation (a situation where the rainy season stops far ahead of the expected time of the summer rains) (Camberlin and Diop, 2003).

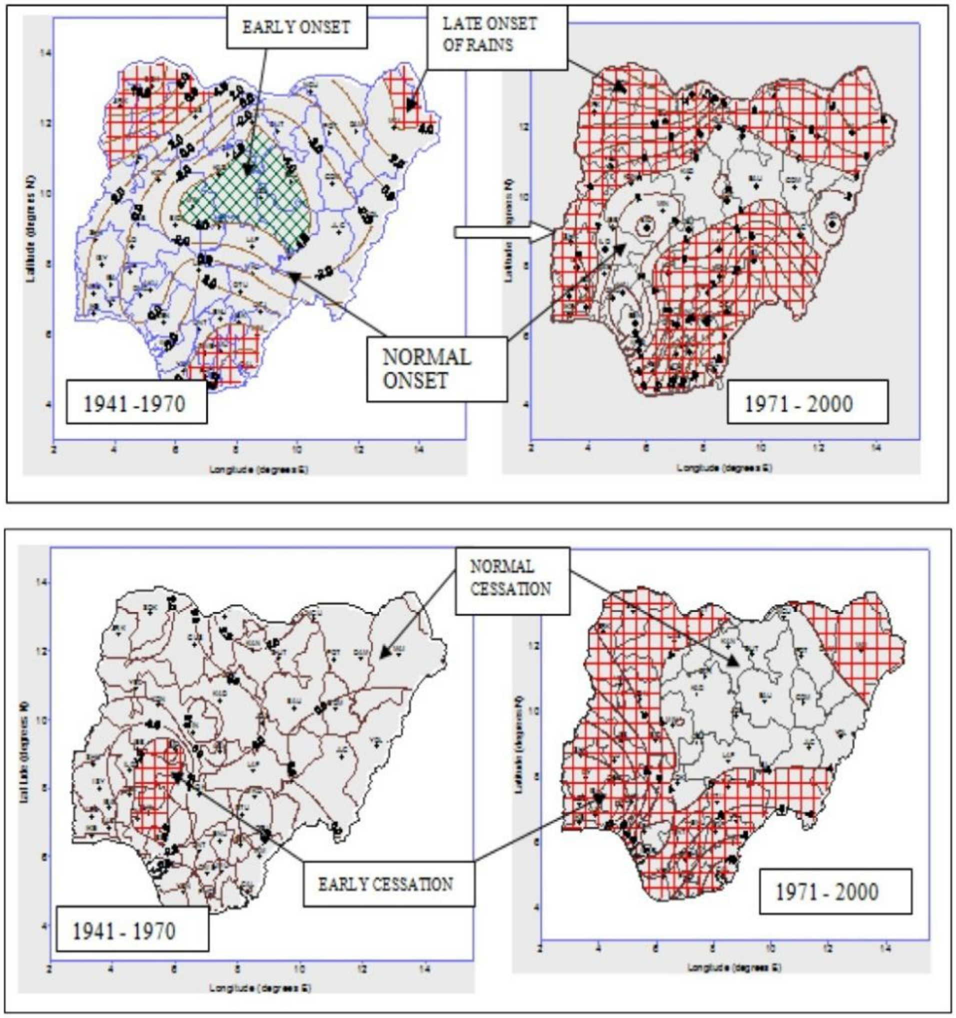

Figure 2.9: Changes in Onset (top) and Cessation (bottom) Dates of Rainy Season (Nigeria)

(Source: Nigeria Meteorological Agency (NIMET, 2007))

With increasing climatic variability, climate change will impose additional pressures on the water availability, water accessibility and water demand in the region; although the scant available data in the region make it presently difficult to predict these changes with recognizable certainty (Rummukainen, 2010). Also, observed is the consequent collapse of the region’s ecological zones from 6 zones (Table 2.5) to 5 zones (Figure 2.10), as a result of decline in rainfall; there has been 200km southward shift in isohyets (Figure 2.11). Following the decline in average annual rainfall, before and after 1970, with ranges from 15% to over 30% depending on the location within the Niger basin (Oyebande and Odunuga, 2010), the savanna zone (interface of desert and forest) is resultantly pushed further south with the desert advancing at a fast rate of 700m per annual on the average. Hence, we now have the Sudano/Sahel extending to about latitude 10.5N from latitude 12.5N, covering about 35% of the landmass of the country (Okpara et al., 2013).

Table 2.4: Characteristics of the ecological zones over West Africa (Source: Okpara *et. al*., 2013)

Ecological Zones	**Altitude in(m)**	**Mean Monthly Temperature(°C)**	**Mean Annual Rainfall(mm)**	**Type of Rainfall Distribution**	**Length of Rainy Season (days)**
Mangrove Forest and/ Freshwater Swamp Forest	< 100	28 – 25	> 2000	Extended Modal	300 – 360
Rain Forest	100	28 – 24	1200 - 2000	Bimodal	250 – 300
Derived Savanna and /Southern Guinea Savanna	< 500	30 – 26	1100 - 1400	Bimodal	200 - 250
Northern Guinea Savanna	400-500	30 – 23	1000 - 1300	Unimodal	150 – 200
Sudan Savanna	<300- >600	31 – 21	600 - 1000	Unimodal	90 – 150
Sahel Savanna	300-400	32 – 25	400 - 600	Unimodal	90

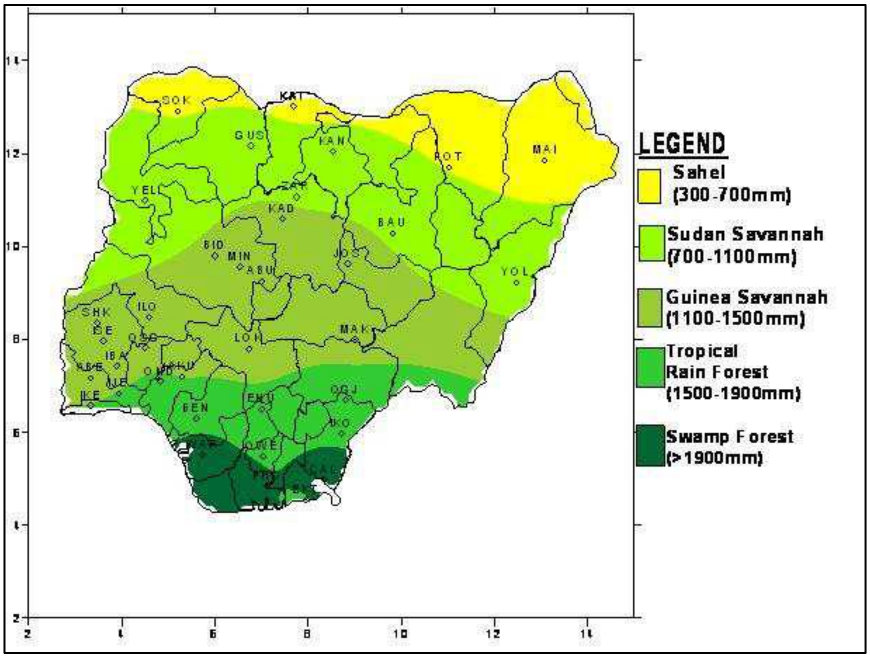

Figure 2.10: Collapsed Ecological Zone of Nigeria from 6 in table 1 to 5 zones due to changing climate

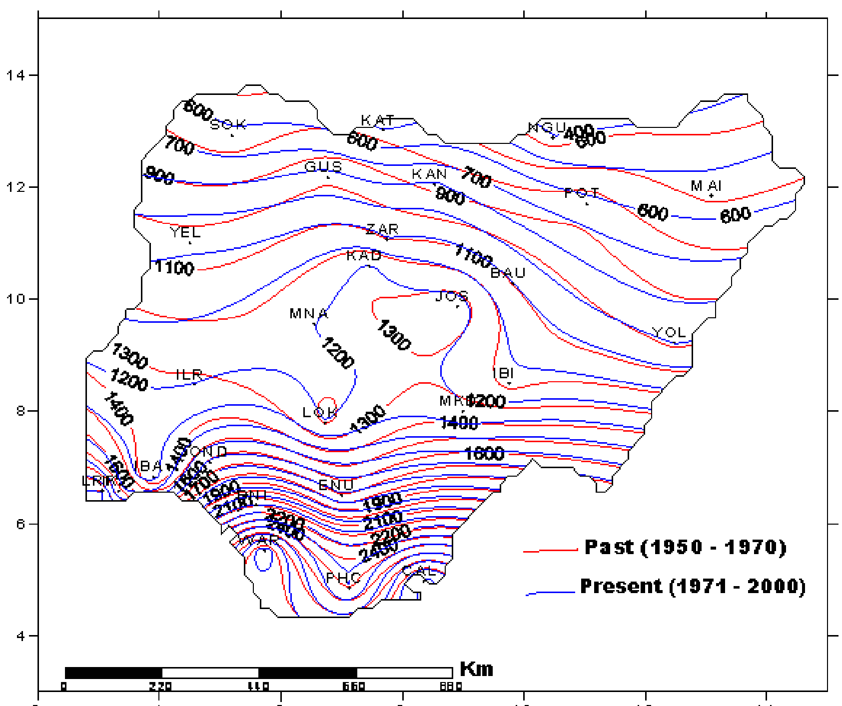

Figure 2.11: Isohyets shift due to southward advancing of aridity

Additional evidence of climate change and its influence on regional hydrology is reflected in long-term streamflow records of the Niger River. Observations from 1907 to 2000 reveal a significant decline in discharge across the basin, a trend largely attributed to rising temperatures. In fact, a zero-flow condition was documented in 1985 at the Niamey gauging station in Niger, located upstream of Nigeria (Olomoda, 2006). Even within the humid lower Niger sub-basin, the mean river discharge for the more recent period (1982–2000) is considerably lower compared to the earlier reference period (1960–1981) (Table 6). Such reductions in precipitation and river flow inevitably alter both the timing and magnitude of hydrological regimes, with important implications for water availability, agriculture, and ecosystem stability.

Table 2.5: Discharge Characteristics of River Niger (Source: Archives of HYDRONIGER)

Station	**River**	**Period**	**Qmean (m^3/s)**	**Qmax (m^3/s)**	**Year**	**Qmin (m^3/s)**	**Year**
Koulikoro (Mali)	Niger	1907-2000	1385	9670	1925	13	1973 and 1982
Niamey (Niger)	Niger	1928-2000	870	2360	1968	0	1985
Lokoja (Nigeria)	Niger	1915-2000	5590	26,300	1956	599	1974

Table 2.6: Lower Niger River Flow Characteristics

Station	River	Period	Qmean (m^3/s)	Qmax (m^3/s)	Year	Qmin (m^3/s)	Year
Lokoja	Niger	1960-1981 1982-2003	68936.5 58646.9	94790 (1960-2003)	1969	25760	2003
Onitsha	Niger	1960-1981 1982-2003	71136.64 59721.14	87810 (1960-2003)	1999	25760	2003
Makurdi	Benue	1960-1981 1982-2000	41369.21 34660.84	61869 (1960-2000)	1969	20378	1983
Jebba	Niger	1960-1976 1977-1997	18122.53 11275.74	23377 (1960-1997	1963	6253	1991

Another major concern in the Lower Niger sub-basin is the practice of gas flaring, which has been ongoing in the Niger Delta for more than four decades (Figure 13). Gas flaring not only contributes significantly to global warming—the primary driver of climate change—but also results in a wide range of environmental degradations, including air pollution, soil contamination, and adverse impacts on human health and livelihoods. Today there are about 123 flaring sites in the region, making Nigeria one of the highest emitter of greenhouse gases in Africa (Odionu, 2018). For example, some 45.8 billion kilowatts of heat are discharged into the atmosphere of the Niger Delta from flaring 1.8 billion cubic feet of gas every day (Agbola and Olurin, 2003). Gas flaring has raised temperatures and rendered large areas uninhabitable. Between 1970 and 1986, a total of about 125.5 million cubic meters of gas was produced in the Niger Delta region, about 102.3 (81.7%) million cubic meters were flared while only 2.6 million cubic meters were used as fuel by oil producing companies and about 14.6 million cubic meters were sold to other consumers (Awosika, 1994).

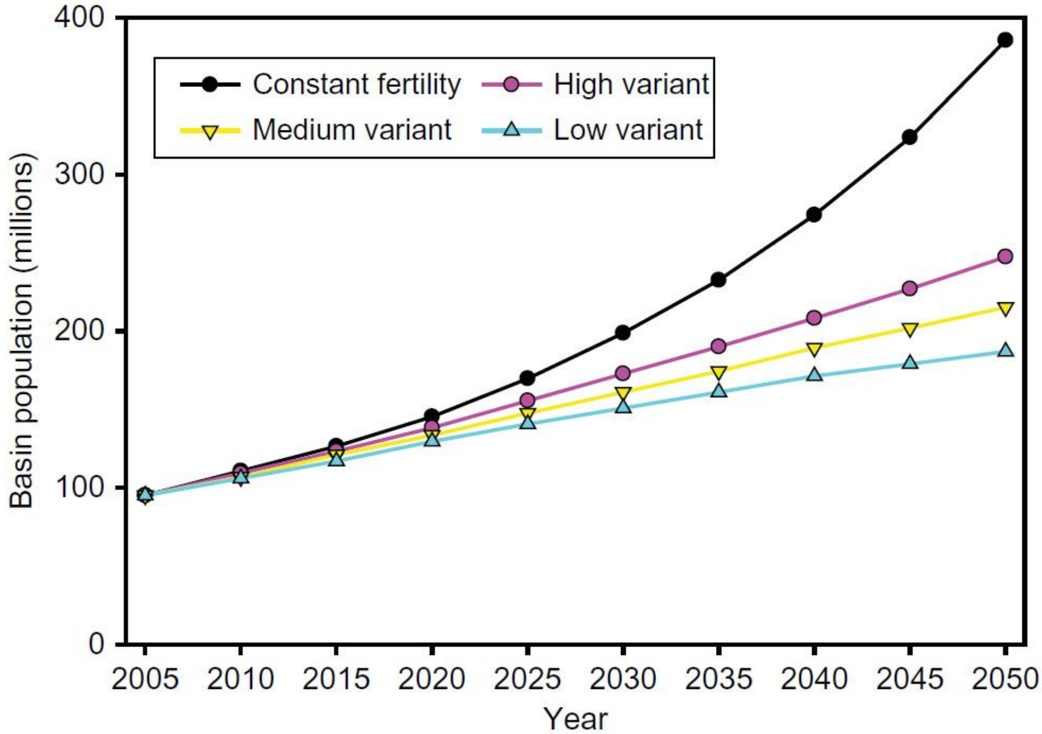

Figure 2.12: The evolution of Niger River Basin population 2005-2050(Source: based on *(Secretary-General, 2007)*

Gas flaring, together with other oil exploration and production activities, has been a major driver of environmental degradation in the Niger Delta. One of its notable consequences is the occurrence of acid rain, with studies suggesting that rainfall in the region exhibits higher acidity levels compared to areas farther away, although further research is needed to fully establish these patterns. Gas flaring has also contributed to ecological changes, including the replacement of native vegetation with resilient species such as elephant grass, which thrives under harsh conditions. Despite the well-documented negative impacts of gas flaring on both the environment and local livelihoods, multinational oil companies operating in Nigeria have continued these harmful practices with little restraint.

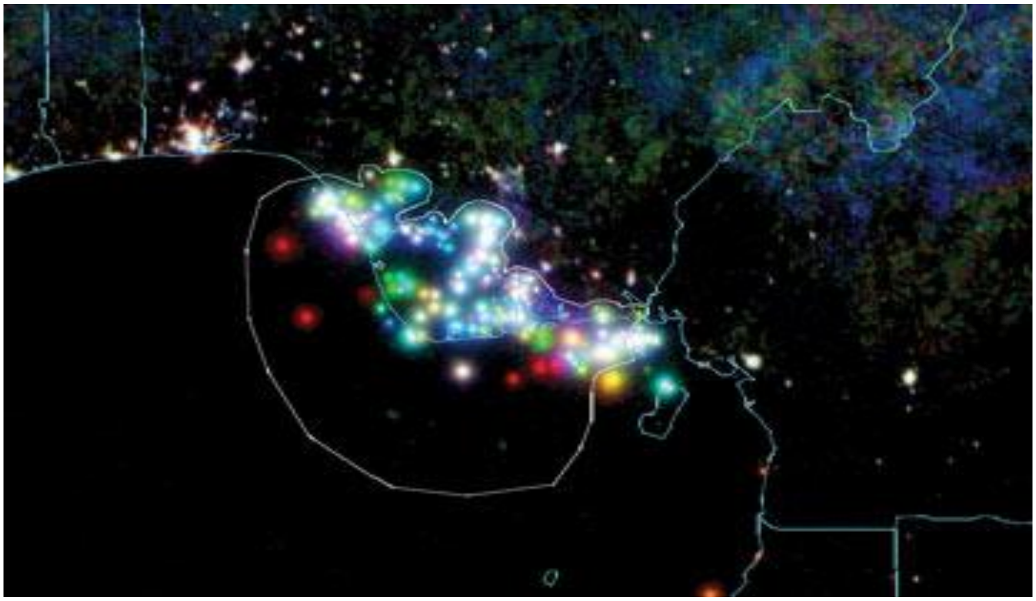

Figure 2.13: Satellite image shows Nigeria's coastline burning bright with gas flares at night. The red dots represent gas flared in 2006, the green dots represent 2000 and the blue dots represent 1992. The white line encircles the flares associated with Nigeria.

2.8 Projected Greenhouse Gas Effects and Research Gaps

Although recent research indicates that elevated greenhouse gas (GHG) concentrations—up to 550 ppm—may potentially increase the robustness of West Africa's rainfall regime and reduce the frequency and persistence of droughts (Bradshaw *et. al*., 2020), there remains a critical need to assess the scale of future changes on local and regional water resources. While global attention toward climate change impacts on hydrology and water systems has accelerated, the Niger Basin remains under-researched in this context. Most available studies focus on climate variability in the Sahelian zone (10°N–20°N), while data from the more humid portions of the basin, including the Lower Niger sub-basin, remain limited (Goulden *et. al*., 2019). This imbalance underscores the necessity of further hydrological and socio-economic assessments in the more vulnerable southern sections of the basin.

2.8.1 Hydrological Implications and Modeling Needs

The majority of climate impact assessments in the basin still lack quantitative evaluations of future hydrological extremes and socio-economic repercussions. Research also reveals that the region's vulnerability to climate change is compounded by its dependence on rain-fed agriculture and limited water infrastructure. The need for comprehensive modeling and long-term climate projections for the humid sub-basins is urgent, given the region's role in national water supply and hydropower generation (Ayanlade et al., 2019).

2.8.2 Regional Temperature and Rainfall Shifts

Climatic variations have been documented in the Benin–Owena River Basin in southwestern Nigeria, revealing rainfall and streamflow fluctuations every 2–3 years, alongside a positive temperature trend of approximately 0.37°C per decade (Okpara *et. al*., 2020). In the Lake Chad Basin, a sustained decrease in rainfall has been observed, with climate change alongside anthropogenic factors such as irrigation being identified as the primary driver of the lake's drastic reduction from 25,000 km² in the 1960s to about 2,000 km² today (Okpara *et. al*., 2020).

2.8.3 Uncertainty in Climate Models and Water Security Risks

There is no consensus among global climate models (GCMs) on the future direction of West Africa's rainfall. Of the 21 models assessed by the Intergovernmental Panel on Climate Change (IPCC), half project an increase in rainfall, while the others predict a decrease (Christensen *et. al*., 2018). However, most models agree that climate variability is likely to increase. Consequently, water, food, and human security are at heightened risk due to the anticipated intensification of climate extremes. The lower Niger sub-basin, located in the humid tropical zone of southern Nigeria, already experiences high levels of temperature, evapotranspiration, and precipitation, indicating elevated sensitivity to climate dynamics. Recent modeling suggests a strong correlation between rainfall and runoff patterns in the region, highlighting the urgent need for localized adaptation strategies (Ayanlade et al., 2019).

2.8.4 Homogeneity Tests

Hydrological and climatological studies require that the data be homogeneous as such a number of techniques have been used for analyzing homogeneity of hydrological and meteorological variables such as the Pettitt test, Buishand test, Standard normal homogeneity test (SNHT) and the double mass Curve (Bickici Arikan and Kahya, 2019).

I. Pettitt Test

(Pettitt, 1979) introduced a non-parametric test for detecting change points within a time series. The method can be applied at both monthly and annual scales to identify the timing of a potential shift. In this framework, the null hypothesis assumes that the observations are independently and randomly distributed, whereas the alternative hypothesis suggests the presence of an abrupt change. The Pettitt test, being a rank-based non-parametric procedure, is widely used due to its robustness and ability to detect a single point of change without requiring assumptions about the underlying distribution of the data. In order to calculate the statistics for the pettitt test, the ranks $r_1 \ldots r_n$ of the $y_1 \ldots y_n$ are used (Pettitt, 1979);

$$X_k = 2\sum_{i=1}^{k} r_1 - k(n+1), \qquad k = 1 \dots n \tag{2.1}$$

If there is a break in year K, the statistic is maximal or minimal near the year k = K:

$$X_k = \max_{1 \le k \le n} |X_k| \tag{2.2}$$

The statistical significance for a probable level α is given as;

$$X_{k\alpha} = [-\ln \alpha(n^3 + n^2)/6]^{1/2} \tag{2.3}$$

If the X_k values do not exceed the critical values, the H_0 hypothesis is accepted; that is to say, it is homogeneous.

II. Buishand Test

The Buishand test operates under the assumption that the data follow a normal distribution and that, under the null hypothesis (H0H_0H0), the observations are independently and randomly distributed. The test is particularly sensitive to detecting breaks that occur near the middle of a time series, making it a useful tool for identifying inhomogeneities in climatological and hydrological datasets. (Wijngaard et al., 2003).

$$S_0^* = 0;\ S_0^* = \sum_{i=1}^{k}(X_i - \bar{X}), k = 1, 2, \dots, N \tag{2.4}$$

Where;

$\bar{X}$: the mean of the time series observations $(X_1, X_2, \dots, X_N)$

K : the number of the observation at which a break point has occurred.

Rescaled adjusted partial sums are obtained by dividing the S_0^* by the sample standard deviation which becomes;

$$\boldsymbol{S_0^* = S_0^*/D_{X,}\, k = 1, 2, \ldots, N} \quad \textbf{(2.5)}$$

Where;

$$\boldsymbol{D_X = \sqrt{\frac{\sum_{i=1}^{N}(x_i - \bar{x})^2}{N}}} \quad \textbf{(2.6)}$$

The statistic that can be used to analyze homogeneity is expressed as follows:

$$\boldsymbol{Q = \max_{0 \le k \le N} |S_k^*|} \quad \textbf{(2.7)}$$

$Q/\sqrt{N}$ value is compared with the critical values given by (Buishand, 1982). If a calculated value is less than the critical value then the null hypothesis is accepted; otherwise the null hyptesis should be rejected (Bickici Arikan and Kahya, 2019).

III. Standard Normal Homogeneity Test (SNHT)

SNHT is a homogeneity test that has been used frequently in climate studies. This method which was developed by Alexandersson, has successfully been used in testing many climatic and hydrological scales (Alexandersson, 1986). This method is flexible and simple to use. Alexandersson divides the reference point of the examined series by a “k” point and calculates T(k).

$$\boldsymbol{T(k) = k\bar{z}^2 + (n - k), k = 1, 2, \ldots, n} \quad \textbf{(2.8)}$$

Where;

$$\bar{z}_1 = \frac{1}{k}\frac{\sum_{i=1}^{k}(Y_i - \bar{Y})}{s} \tag{2.9}$$

And

$$\bar{z}_2 = \frac{1}{n-k}\frac{\sum_{i=k+1}^{n}(Y_i - \bar{Y})}{s} \tag{2.10}$$

If the breal is located at the point k, T(k) reaches its maximum value at k = K. the test statistic T_0 is defined as;

$$T_0 = \max(T(k)) \;\; for\ 1 \leq k \leq n \tag{2.11}$$

Alternatively, the following equation based on this test can be used;

$$T_0 = \frac{n(T(n))^2}{n - 2 + (T(n))^2} \tag{2.12}$$

If T_0 exceeds the test statistic valus, the null hypothesis is rejected. Critical values of this test are given by (Wijngaard et al., 2003).

IV. Basis of The Double Mass Curve Method

The double mass curve method is used to analyze changes in runoff and sediment trends in the basin by first calculating the continuous cumulative values of basin runoff and sediment transport over time during the same period (Guoshuai et al., 2023);

$$Q' = \sum_{i=1}^{n} Q_i \tag{2.13}$$

$$S' = \sum_{i=1}^{n} S_i \tag{2.14}$$

In Equation (2.13), Q' is the continuous cumulative value of watershed runoff ($10^8\ m^3$), Qi is the watershed runoff in the ith year of the statistical series ($10^8\ m^3$), and n is the number of samples in the statistical series. In Equation (2.14), S' denotes the continuous cumulative value of sediment transport in the basin ($10^8\ t$), while Si represents the sediment transport in the basin in the ith year of the statistical series ($10^8\ t$), The double mass curve is shown in Figure 2.14, using the cumulative values of runoff and sediment load as the horizontal and vertical axes, respectively. The double mass curve, illustrated in Figure 2.14, is constructed by plotting the cumulative runoff values on the horizontal axis and the cumulative sediment load on the vertical axis. The slope of this curve reflects the ratio between runoff and sediment load within the basin, thereby providing insights into changes in their relationship over time. (Ashagrie et al., 2006; Guoshuai et al., 2023; Pirnia et al., 2019).

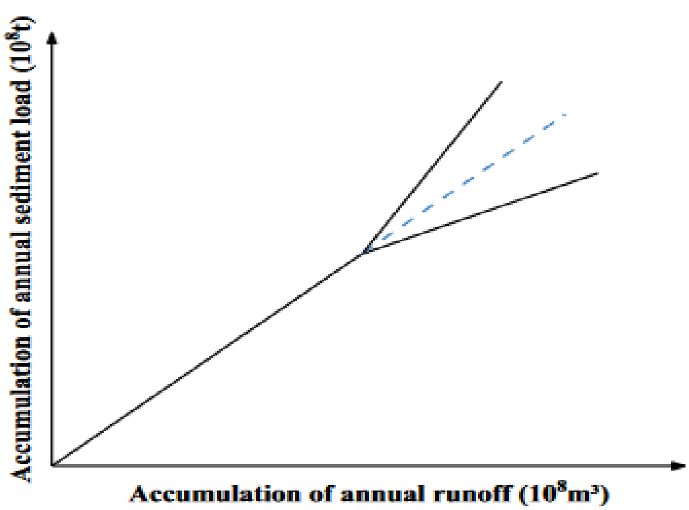

Figure 2.14: Double Mass Curve

$$\boldsymbol{S' = a\,Q' + b} \qquad \textbf{(2.15)}$$

$$S' = a' Q' + b' \quad (2.16)$$

In Equation (2.15), a and b represent the slope and intercept of the double mass curve during the natural variation period, and in Equation (2.16), a′ and b′ are the slope and intercept of the double mass curve during the runoff–sediment response period, respectively. As the slope change of the double mass curve, the external factor leads to the change in the runoff–sediment load relationship in the basin, including anthropogenic or extreme climatic events. The changing process of runoff and sediment load can be divided into two periods, the early period and the response period, based on the change point in the double mass curve. In the response period, the relative difference in the accumulation of sediment load, between the original trend extension line and the response curve, is used to calculate the contribution of the external factor to sediment load change.

$$y = \frac{a'Q' + b'}{a\,Q' + b} - 1 \quad (2.17)$$

In Equation (2.17), γ is the contribution of the external factor to the change in consistency of runoff and sediment load. When γ is greater than 0, the double mass curve is upwardly skewed, indicating that external factors increase the sediment transport capacity; when γ is less than 0, the double mass curve is downwardly skewed, indicating that the sediment transport capacity of the basin decreases under the same runoff conditions (Guoshuai et al., 2023).

2.9 Land Use/Land Cover

Since the discovery of oil in commercial quantities, the Niger Delta region of Nigeria has undergone profound eco-environmental changes. Intensive anthropogenic activities associated with resource exploration and exploitation have significantly altered the natural land use/land cover (LULC), which in turn is believed to have influenced land surface temperature (LST) dynamics. From the 1970s onwards, satellite remote sensing has provided substantial advantages for monitoring environmental change, particularly in detecting LULC transformations and retrieving LST data. The availability of long-term, time-series remote sensing datasets has further enhanced the ability to investigate environmental processes such as LULC change and surface temperature variation. According to (Orhan et al., 2014), remote sensing is an invaluable tool for analyzing spatio-temporal land cover dynamics in relation to key physical properties, including surface radiance and emissivity

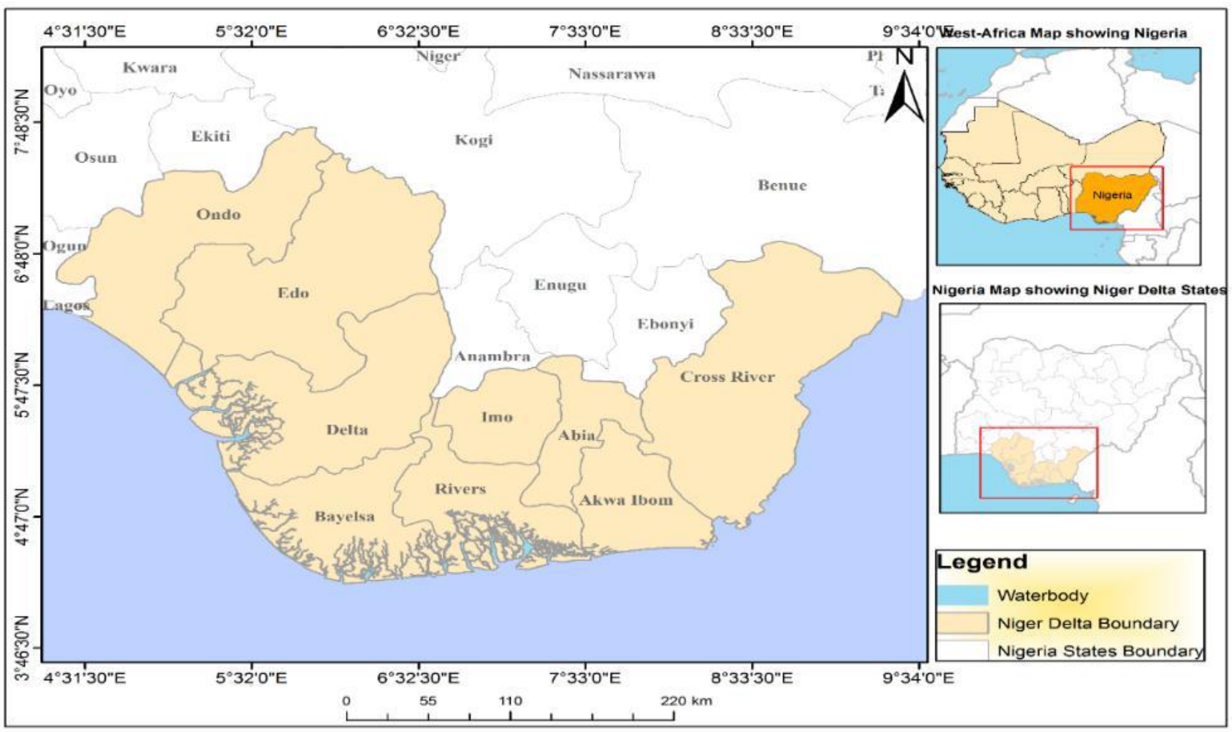

Figure 2.15: Study Area in relation to West Africa and Nigeria

The Niger Delta Region (shown in Figure 2.15) lies in the southern part of Nigeria where the River Niger divides into numerous tributaries ending at the edge of the Atlantic Ocean. It is bordered to the south by the Atlantic Ocean and to the east by Cameroon. It lies between longitude 4º 30’ - 9º 50’E and Latitude 4º 10’ - 8º 0’N. The temperature in the region is between 24°C to 32°C throughout the year, rainfall ranges from 3000- 4500mm. The region has two seasons: dry season (starting around December- February) and the rainy season (starting around July- September) (Nwilo and Badejo, 2006). The region covers seven southern states namely: Cross River, Akwa Ibom, River, Bayelsa, Delta, Edo and Ondo state with more than 40 ethnic groups and has about 250 different dialects. The region is the sole oil producing basin since the discovery of oil in commercial quantity in 1965. The region is asserted to be the main source of export earnings to Nigeria. Records has it that oil and gas earnings from the region funds 85% of the Nation's yearly budget; and contribute about 95% of Gross Domestic Product (GDP) (Dokubo, 2004; Ebegbulem et al., 2013; Ringim et al., 2016). A United Nations' report indicates that there are more than 7,000kilometres of pipelines, 5,284 oil wells, 275 flow stations, 10 Gas plants, and 10 Export Terminals operated by more than 13 oil companies (Jenkins and Sugden, 2006).

Land cover just like in any other part of the global environments results mostly from combination of natural and anthropogenic influences. The main natural force of the change remains rainfall changes induced by climatic variability. This has been found to often reduce the natural regeneration rate of land resources in the area. Table 2.7 shows the percentage of changes that took place between 1976 and 1995 in Nigeria (Fasona and Omojola, 2005).

Table 2.7: Typical Land use/land cover changes in Niger River Basin from 1976-1995 (lower Niger Basin) (Source: *(Fasona and Omojola, 2005)*

S/n	Ecology	Area_km2 (1976)	Area_km2 (1995)	Change_1976-1995	Percent change
1	Agricultural Tree Crop Plantation	824.15	1,656.88	832.73	101.0
2	Alluvial	523.61	282.38	-241.23	-46.1
3	Discontinuous grassland dominated by grasses and bare surfaces	7,614.72	12,517.23	4,902.51	64.4
4	Disturbed Forest	14,677.70	19,491.29	4,813.59	32.8
5	Dominantly grasses with discontinuous shrubs and scattered trees	13,053.77	12,487.62	-566.15	-4.3
6	Dominantly shrubs and dense grasses with a minor tree component	118,529.55	85,020.98	-33,508.57	-28.3
7	Dominantly trees/woodlands/shrubs with a subdominant grass component	154,933.40	83,281.15	-71,652.25	-46.2
8	Extensive (grazing, minor row crops) Small Holder Rainfed Agriculture	170,837.55	192,892.33	22,054.77	12.9
9	Extensive Small Holder Rainfed Agriculture with Denuded Areas	4,417.88	10,118.47	5,700.58	129.0
10	Floodplain Agriculture	9,671.81	21,576.03	11,904.21	123.1
11	Forest Plantation	1,000.85	1,581.24	580.39	58.0
12	Forested Freshwater Swamp	18,564.71	16,696.51	-1,868.20	-10.1
13	Graminoid/Sedge Freshwater Marsh	5,882.74	1,136.51	-4,746.22	-80.7
14	Grassland	1,196.74	8,146.74	6,950.00	580.7
15	Gullies	125.35	19,070.48	18,945.13	15,113.2
16	Intensive (row crops	329,227.97	373,481.34	44,253.37	13.4
17	Irrigation Project	148.85	1,008.86	860.01	577.8
18	Livestock Project	51.02	139.65	88.63	173.7
19	Major Urban	1,102.58	1,362.37	259.79	23.6
20	Mangrove Forest	10,157.12	10,067.31	-89.81	-0.9
21	Minor Urban	958.69	4,022.98	3,064.29	319.6
22	Montane Forest	7,900.02	8,053.76	153.74	1.9
23	Montane grassland	2,502.27	3,898.15	1,395.88	55.8
24	Natural Waterbodies: Ocean	6,766.53	15,588.36	8,821.83	130.4
25	Rainfed Arable Crop Plantation	15.92	521.38	505.46	3,174.9
26	Reservoir	1,331.41	2,901.16	1,569.75	117.9
27	Riparian Forest	7,506.46	5,330.46	-2,176.01	-29.0
28	Rock Outcrop	1,445.15	2,647.96	1,202.81	83.2
29	Saltmarsh/Tidal Flat	18.84	596.92	578.08	3,067.5
30	Sand Dunes/Aeolian	1,032.77	5,428.30	4,395.53	425.6
31	Shrub/Sedge/Graminoid Freshwater Marsh/Swamp	17,749.63	10,251.68	-7,497.95	-42.2
32	Teak/Gmelina Plantation	624.44	1,156.43	531.99	85.2
33	Undisturbed Forest	28,022.42	13,477.90	-14,544.52	-51.9
34	Canal		30.76	30.76	
35	Mining Areas		61.15	61.15	

The Niger Delta Region has undergone severe environmental alterations since the pre oil boom era of 1975 due to several anthropogenic activities directed at exploring and exploiting the natural resources in the region. This alteration has caused unquantifiable environmental changes to natural land cover, land surface temperature, vegetation health, etc.; and has led to soil and water degradation, air pollution, decreasing biodiversity, increased urban heat, and erosion. In essence both land use and cover changes are products of prevailing interacting natural and anthropogenic processes by human activities. (Eyoh & Okwuashi, 2017) observed that land cover and land use patterns are basic data used for physical planning and environmental evaluation. Therefore, periodic land use change patterns are needed for many applications including map revision and updating, natural resources inventory and management, urban planning, agricultural land development, forestry and wide life management and demographic studies.

Also, Land Use Land Cover (LULC) change analysis is very important for environmental management purposes as it helps the decision maker in planning for future changes that may occur in that area and it also helps the decision maker realize the effects of these changes on humans and their environment. Over the years, Land use/Land cover has been a key indicator for the evaluation of environmental impacts. According to (Foley et al., 2005; Matthews et al., 2004; Turner et al., 2007) global and regional assessments on land cover and land use status and changes are fundamentally important for climate and environmental change studies. Thus, the evaluation of the spatial and temporal dynamics of Land use/Land cover (LULC) of a region like Niger Delta that has experienced serious environmental alteration is very essential.

Table 2.8: Land Use / Land Cover (LULC) Classes and Description (Source: Ikiel *et. al*., 2012)

LULC Class Name	Description
Water body	All the water bodies, ocean, rivers, stream, lagoons, creeks, etc.
High density Built up	City centers, commercial/industrial areas, high density residential settlements.
Low Density built up /Exposed Surface	All low density settlements and bare/exposed surfaces
Forest	Primary Evergreen forested areas and forest reserves.
Sand Deposit	Sand bars and sediment deposit without any vegetation
Vegetation	Lightly forested areas, cultivated lands and farmlands mixed with light forestation.
Mangrove	Mangrove, swamps/wetlands.

2.9.1 Land Use/Land Cover Distribution/Magnitude

The classified land use/land cover distribution maps of the respective years are presented in Figures 2.15, 2.16 and 2.17. While the magnitude and percentages of LULC are presented in Table 2.9, 2.10, and 2.11 respectively. The spatial distribution of land use/land cover types were presented in Figure 2.15. Figure 2.15 showed that a large magnitude of forest could be clearly seen in Ondo, Edo, Akwa Ibom, Cross River and the boundary between Delta, Imo and Rivers states. Figure 2.15 and Table 2.9 showed the initial distribution of LULC of in 1986 and their spatial extent across the study area.

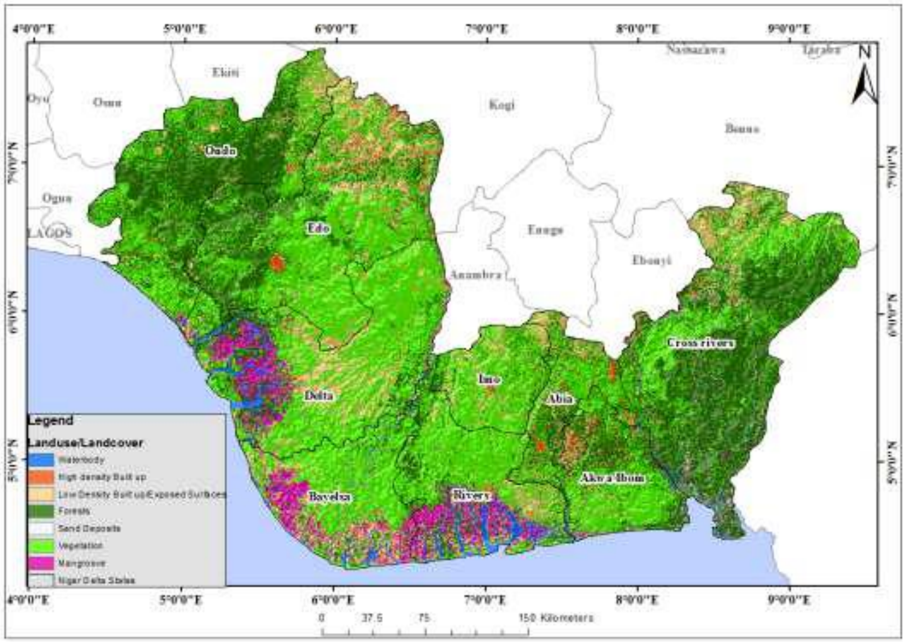

Figure 2.16: 1986 Land use/Land cover Map of Niger Delta Region, Nigeria

Table 2.9: 1986 percentage and Spatial Extent of LULC of Niger Delta Region, Nigeria

Land Use/Land Cover	Area (Hectares)	Area (%)
Water body	266031.95	2.406
High density Built up	145068.13	1.312
Low Density built up /Exposed Surface	1427240.42	12.908
Forest	3743465.42	33.856
Sand Deposit	23883.17	0.216
Vegetation	4940609.21	44.683
Mangrove	510723.85	4.619

Comparing the 1986 land use/land cover Map of study area shown in Figure 2.15 and the spatial distribution of land use/land cover for 2002 shown in Figure 2.16, it could be seen clearly that there has been alteration particularly the forested area and the mangrove. Table 2.10 depicted the spatial distribution and percentages of LULC for 2002 (Eyoh & Okwuashi, 2017).

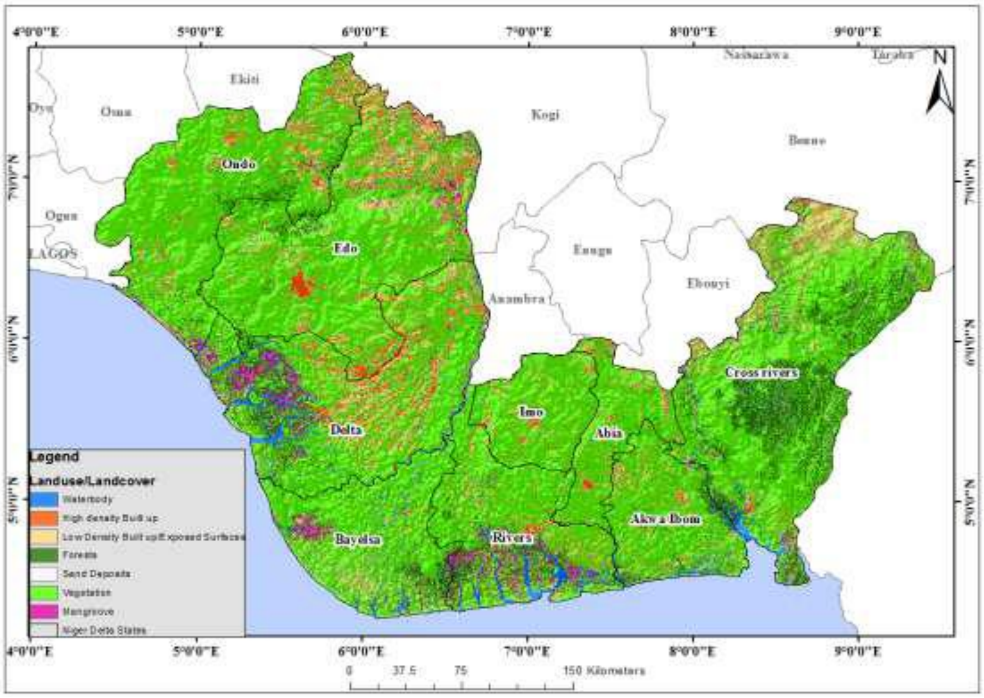

Figure 2.17: 2002 Land use/Land cover Map of Niger Delta Region, Nigeria

Table 2.10: 2002 percentage and Spatial Extent of LULC of Niger Delta Region, Nigeria

Land Use/Land Cover	Area (Hectares)	Area (%)
Water body	282506.916	2.555
High density Built up	423373.3782	3.829
Low Density built up /Exposed Surface	1242256.439	11.235
Forest	1026865.647	9.287
Sand Deposit	23219.74652	0.21
Vegetation	7724214.536	69.858
Mangrove	334585.4903	3.026

The results presented in Figure 2.16 and Table 2.10 indicated that the spatial extent of high density built up, low density built up/exposed surface, water, sand deposit and vegetation increased whereas, the forested area suffered depletion mostly in Ondo, Edo, Akwa Ibom, Cross River and the boundary between Delta, Imo and Rivers states. The mangrove was depleted mostly in the core oil producing states of Bayelsa, Rivers, Akwa Ibom and Delta States as a result of over two thousand incidents of oil spill that occurred between 1997 and 2002 (Eyoh & Okwuashi, 2017).

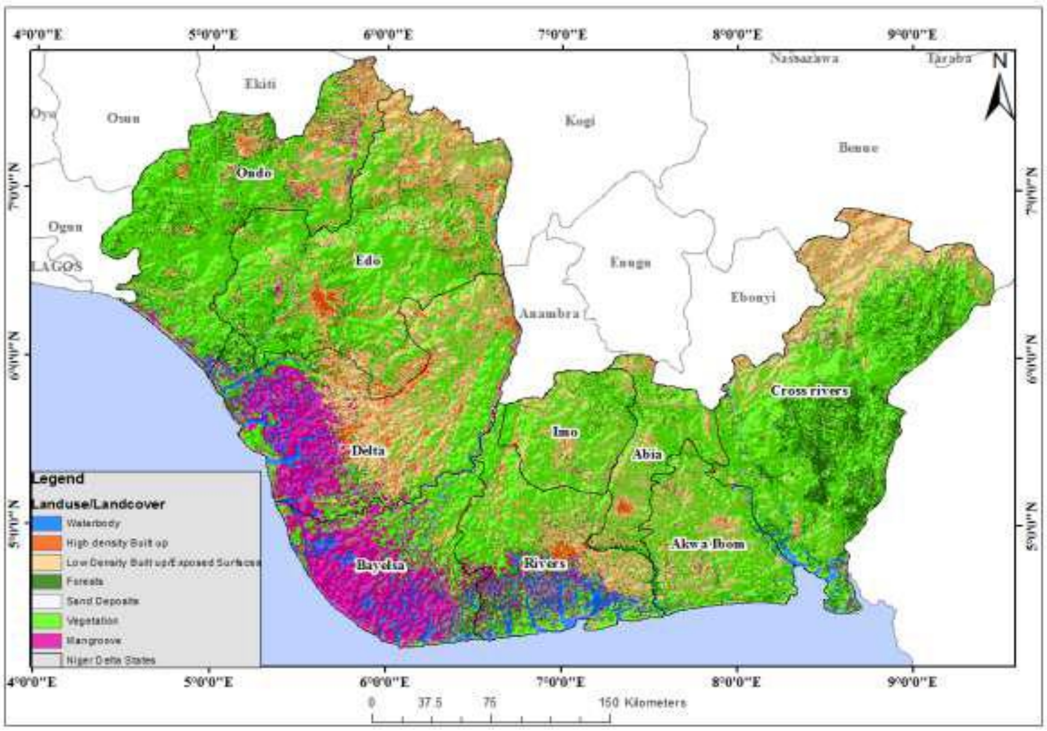

Figure 2.18: 2016 Land use/Land cover Map of Niger Delta Region, Nigeria

Table 2.11: 2016 Percentage and Spatial Extent of LULC of Niger Delta Region, Nigeria

Land Use/Land Cover	Area (Hectares)	Area (%)
Water body	454111.90	4.107
High density Built up	442280.89	4
Low Density built up /Exposed Surface	2684866.12	24.282
Forest	774323.26	7.003
Sand Deposit	4312.24	0.039
Vegetation	5553721.09	50.228
Mangrove	1143406.66	10.341

In 2016, almost similar trend of increase in 2002 occurred. Figure 2.17 and Table 2.11 showed that high density built up and low density built up/exposed surface continued to increase and the depletion of the forest continued in virtually all the states. But vegetation magnitude this time was reduced in all the states as a result of settlement sprawl. Mangrove surprisingly increased in all the coastal states probably due to improved strategy of oil spillage amelioration and amnesty intervention that reduced the incident of pipeline vandalism (Eyoh & Okwuashi, 2017).

2.10 Remote Sensing

Remote Sensing is known as a science and art that contain large information about the physical object on the surface of the earth being captured with a device without physical contact with that object in the environment (Campbell and Wynne, 2011). Remote sensing technology is used in various fields, including urban planning, agriculture, geology, hydrology, weather forecasting, environmental study, natural hazards study, and resource exploration etc. (Yao et al., 2019).

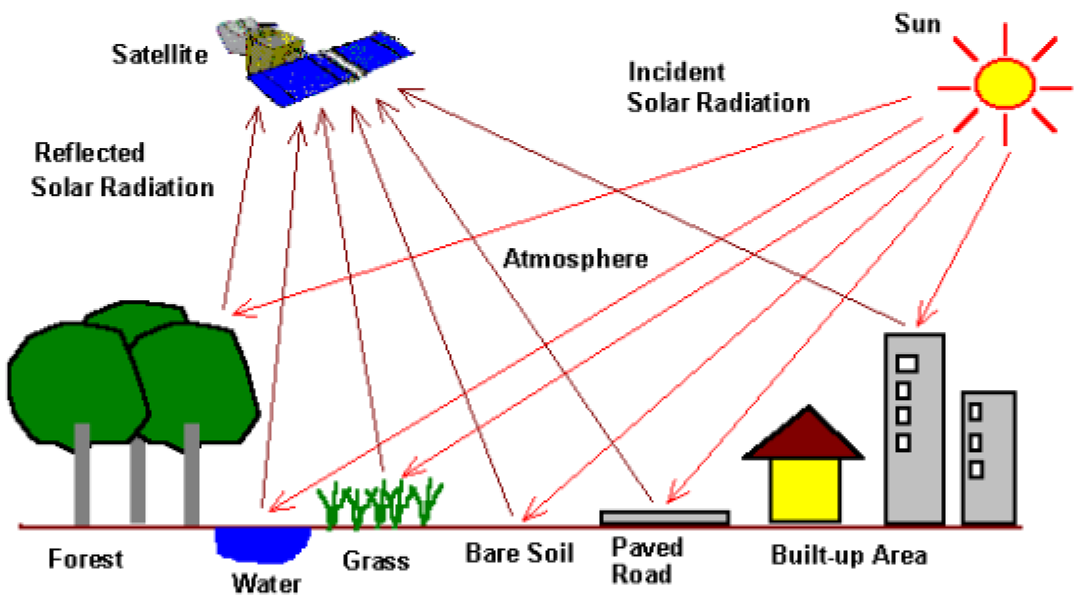

Figure 2.19: An Image showing the remote sensing application and its processes from the platform and incoming solar radiation to the earth's surface, (source; Aggarwal, 2004)).

Remote sensing has very powerful functionalities that include many applications and processing satellite images for a specific operation in the process of producing substantive results from input raster images (Campbell and Wynne, 2011). It is used to gather information and imaging remotely and can be done using devices such as cameras placed on the ground, ships, aircraft, satellites, or even spacecraft (Navalgund et al., 2007). There are two type of remote sensing classified based on their source of signal the use to explore object, which are;

2.10.1 Passive Remote Sensing

Passive remote sensing is based on detecting available (background) electromagnetic energy from natural sources, such as sunlight. Passive sensors detect energy emitted or reflected from an object and include different types of radiometers and spectrometers. Most passive systems used in remote sensing applications operate in the visible, infrared, thermal infrared, and microwave portions of the electromagnetic spectrum (Earth Science Data Systems, 2021). Passive remote sensors include multispectral or hyperspectral imagers, which measure the natural radiation emitted or reflected by the target at various wavelengths to determine its temperature, colour, and chemical composition (Woodhouse, 2017).

2.10.2 Active Remote Sensing

Active remote sensing relies on an artificial "light" source, such as radar, LiDAR to illuminate the scene. These active sensors emit a pulse of energy and detect the changes in the return signal. They operate in the microwave portion of the electromagnetic spectrum, allowing them to penetrate the atmosphere under most conditions. Examples of active sensors include radar, lidar, and laser fluorosensors (Alexandru TUDOR, 2023). The Tropical Rainfall Measuring Mission (TRMM) satellite, equipped with the TRMM Precipitation Radar (PR), was the first spaceborne weather radar and provided valuable observations of three-dimensional precipitating cloud structure (Marghany, 2022). The CloudSat W-band radar and the Cloud-Aerosol Lidar and Infrared Pathfinder Satellite Observations (CALIPSO) lidar enabled the profiling of the vertical structure of various clouds (Misra, 2022). The Dual-frequency Precipitation Radar (DPR) aboard the Global Precipitation Measurement (GPM) core observatory improved the capability to detect light and frozen precipitation (Masunaga, 2022).

2.10.3 Satellite Images

Satellite sensors are capable of covering a vast spatial and temporal area. As a result, satellite photos have become extremely popular for disaster management and mapping (Lewis, 2009). After NASA openly published their longest-running satellite program, Landsat (Green et al., 1994), satellite photographs became even more accessible. Private companies such as Planet Labs and Digital Globe also contribute to large-scale datasets such as the EuroSAT-Dataset (Helber et al., 2019) and the ImageCLEFF Remote-Dataset (Ionescu et al., 2017).

However, a variety of spacecraft with varying sensors and characteristics acquire earth observation data. These datasets have various resolutions, including geographical, radiometric, spectral, and temporal resolutions. Understanding the benefits and weaknesses of various forms of sensor data is critical when selecting a dataset for a certain application. Several studies have been undertaken to characterize the key categories of satellite data (Althausen, 2002; Barnsley, 1999; Estes and Loveland, 1999; Wulder and Franklin, 2012). Table 2.5 outlines the features of some of the most common satellite sensors used for danger mapping and monitoring. Different types of satellite sensors can provide different forms of data due to their unique properties. Researchers have employed almost all of them to harness their individual benefits. For flood detection and monitoring, high resolution (IKONOS) and medium resolution (e.g., Landsat TM) satellite imagery have been employed in (Brivio et al., 2002; Dewan et al., 2006; Frazier and Page, 2000; Jain et al., 2005; Nghiem et al., 2000; Sanyal and Lu, 2004; Shakeel et al., 2015). Moderate resolution (e.g., MODIS) pictures have also been used to detect, map, and measure floods (Brakenridge and Anderson, 2006; Ticehurst et al., 2009). However, with the deployment of the European Space Agency's (ESA) 'Copernicus' satellites, Sentinel-1, Sentinel-2, Sentinel-3, and Sentinel-4, high resolution multispectral photos are being used more for catastrophe assessment, such as flooding (Minh et al., 2019; Wu et al., 2019; Zhang et al., 2021).

Researchers now have more options when choosing a suitable satellite dataset for a particular study, depending on the requirements, thanks to the easy availability of data from numerous sensors. For instance, as it necessitates a fine-scale classification method, high spatial resolution data is appropriate for local categorization. On the other hand, medium spatial resolution data are most commonly used at the regional scale. Furthermore, on a continental or global scale, the coarse spatial resolution data are preferred (Lu and Weng, 2007). However, since not all satellite data is publicly available, the state of the economy frequently has the greatest impact on the data selection process (Lu and Weng, 2007).

Satellites observe solar energy that is naturally reflected by the Earth's surface across various spectral bands, both visible and invisible. Landsat 8, for instance, captures data in nine spectral bands, with bands 1 to 7 and 9 exhibiting a spatial resolution of 30 meters, while the panchromatic band (band 8) offers a higher resolution of 15 meters. Thermal bands 10 and 11 play a crucial role in enhancing the accuracy of surface temperature measurements, with a spatial resolution of 100 meters (Barsi et al., 2014). The spectral distribution of Landsat 8 images is summarized in Table 2.12. The near infrared (NIR) band stands out as particularly effective in detecting water surfaces due to its strong absorption by water and reflection by land (Klemas, 2015). Consequently, satellite imagery can effectively delineate inundated areas, provided that clouds, trees, and vegetation do not obscure the water surface.

Table 2.12: Summary of the characteristics of popular satellite sensors used in natural disaster monitoring

Satellite	Sensor	Swath(km)	Nadir Spatial Resolution	Revisit time (days)
Worldview-2	Panchromatic	16.4	0.46	1.1
	Multispectral	16.4	1.82	
Quickbird	Panchromatic	16.5	0.6	1.5-3
	Multispectral	16.5	2.4	
Ikonos	Panchromatic	11	1	1.5-3
	Multispectral	11	4	
Landsat-7	ETM+ Panchromatic	185	15	16
	ETM+ Multispectral	185	30	
	ETM+ Thermal	185	60	
Landsat-8	OLI+ Panchromatic	185	15	
	OLI+ Multispectral	185	30	16
	TIRS	185	30(100)	
PlanetScope	FThree-band frame or four-band frame images	16.4	3	Variable
Sentinel 2	Multispectral	290	10	10

2.11 Application of Remote Sensing for Flood Modeling

Remote sensing plays a crucial role in flood modeling by providing valuable data for accurate predictions and mapping of flood-prone areas. Various studies highlight the significance of remote sensing in flood management. For instance, research in North Kazakhstan utilized Earth remote sensing data and GIS technologies to model flooding scenarios and prevent flood events (Shugulova et al., 2023). Similarly, studies in Chile and Russia emphasized the use of remote sensing to create detailed digital terrain models for hydraulic modeling and flood estimation, showcasing the effectiveness of UAV-derived data in flood studies (Clasing et al., 2023; Stoyanova, 2023). Furthermore, a study in Bulgaria demonstrated the application of satellite data for flood mapping, emphasizing the importance of timely and precise flood modeling for hazard analysis and risk assessment (Krasnopeyev et al., 2022). These findings collectively underscore the critical role of remote sensing in enhancing flood modeling accuracy and preparedness.

2.11.1 Water Detection using Satellite Images

Several methods have been developed for detecting water in remote sensing photos. Land cover classification with remote sensing data, for example, is a popular technique for identifying water, vegetation, wildlife, and other features (Hepner et al., 1990; Liu et al., 2016). However, the spectrum reflectance of water bodies in satellite pictures is substantially lower than that of other land cover categories, hence image segmentation techniques based on spectral indices generated from multiple bands are often successful for this purpose (Klemas, 2015). Several spectral indices have been created throughout the years to detect water in multispectral images. These indices are created by merging several visible and invisible bands. They are intended to highlight a phenomenon involving water and other land use groups, which may then be classified.

2.11.2 Multispectral indexes

A few common spectral indexes for water detection are mentioned below:

I. Normalized Difference Water Index

Light in the Near-Infrared (NIR) band is heavily absorbed by water but reflected by land; thus, the NIR band is highly useful for delimiting water (Klemas, 2015). NDWI takes advantage of this NIR band feature and is thus widely used for detecting water in satellite pictures (McFeeters, 2013; Mueller et al., 2016; Ogashawara et al., 2013; Ticehurst et al., 2009). The NDWI of a pixel can be determined using the following equation:

$$\boldsymbol{NDWI = \frac{GREEN - NIR}{GREEN + NIR}} \qquad \textbf{(2.18)}$$

Where GREEN is a band that includes reflected green light, and NIR is the reflection of the near-infrared band. Water has positive NDWI values. McFeeters proposed this spectral measure in 1996, which was then used to identify non-urban surface water linked with wetlands (McFeeters, 1996). However, throughout time, other modified versions of NDWI were proposed.

II. **Normalized Difference Moisture Index**

The Normalized Difference Moisture Index (NDMI) is a modified version of the NDWI (Wilson and Sader, 2002). This index likewise takes advantage of the fact that the NIR band is strongly absorbed by water; however, instead of the green band, the middle-infrared (MID) band is used, and the calculation is as follows.

$$\boldsymbol{NDMI = \frac{NIR - MIR}{NIR + MIR}} \qquad \textbf{(2.19)}$$

Water has positive NDMI values.

III. Modified Normalized Difference Water Index

Modified Normalized Difference Water Index (MNDWI) has positive values for water pixels.

$$MNDWI = \frac{GREEN - MIR}{GREEN + MIR} \tag{2.20}$$

It uses Green and NIR bands for water identification and is calculated by equation 2.20 (Xu, 2006).

IV. Water Ratio Index

Shen et, al. proposes an index called Water Ratio Index (Shen and Li, 2010). This index uses Green, Red, NIR and MIR bands and is expressed as:

$$WRI = \frac{GREEN - RED}{NIR + MIR} \tag{2.21}$$

The authors argue that this index generates values greater than 1 for water bodies and therefore, does not require to set a threshold.

V. Normalized Difference Vegetation Index

The Normalized Difference Vegetation Index was first introduced in 1973 (Freden et al., 1974), and it has since become widely used for land classification and change detection, particularly vegetation identification (DeFries and Townshend, 1994; Gandhi et al., 2015; Yue et al., 2007). However, because water bodies often have negative NDVI values, this index can also be used to detect water in satellite photos.

$$NDVI = \frac{NIR - RED}{NIR + RED} \tag{2.22}$$

VI. Automated Water Extraction Index

Another spectral index called Automated Water Extraction Index was introduced in 2013 (Feyisa et al., 2014) for water body detection. This index was proposed for improving classification accuracy in water extraction in presence of environmental noise and to offer a stable threshold value.

$$\boldsymbol{AWEI = 4 * (GREEN - MIR) - (0.25 * NIR + 2.75 * SWIR)} \qquad \textbf{(2.23)}$$

AWEI uses green, MIR, NIR and Short-wave Infrared (SWIR) band and effective in mountainous area, where deep shadows impose challenges to accurate classification. Water bodies have positive AWEI values. Research shows that NDWI typically performs better compared with other indexes for water surface detection using Landsat images (Rokni et al., 2014). In addition, an efficient classifier is required that can utilize these indexes and detect water in satellite images.

2.12 Machine Learning and Deep Learning Models

Machine Leaning refers to the mechanism by which machines learn from observations or data collected from experimentation considering the uncertainties on that data. Another well elaborated by (Liyew and Melese, 2021)"A computer program is said to learn from experience E with respect to some class of tasks T and performance measure P, if its performance at tasks in T, as measured by P, improves with experience E". to relate this quote in applying ML to flood prediction, we can say that to predict the future flood events (Task T), we can process through machine learning algorithms with available historical data (Experience E) and when it is effectively "learned", then the model will predict better for future flood events with better performance measurement (P). It comprises a set of methods, sometimes inspired by how biological systems learn from their interaction with other systems in the surrounding environment. It belongs to the intersection of computer science, statistics, data science, among others. Through inference, relations between a set of representative input features X and a set of output targets Y is learned, thus generating a prediction model. These models express the dependencies between input and outputs. Some common machine leaning models include the followings;

2.12.1 Multilinear regression model

Multivariate linear regression (MLR) is one of the most common statistical algorithms that uses predictors to predict a target variable (Maulud and Abdulazeez, 2020). Feng *et. al*. (2017) studied contact temperature prediction using MLR and concluded that the MLR model achieved high accuracy. Liu *et. al*. (2020) also indicated the effectiveness of MLR for drought monitoring.

MLR refers to the linear regression model of more than one predictor variable. The MLR equation is given in equation (2.24) where β is the regression coefficients; i represents the number of features and ε the random error term (Montgomery et i al., 2021).

$$Y_i = \beta_0 + \beta_1 x_{i1} + \beta_2 x_{i2} + \cdots + \beta_{p-1} x_{i,p-1} + \varepsilon_i \quad \textbf{(2.24)}$$

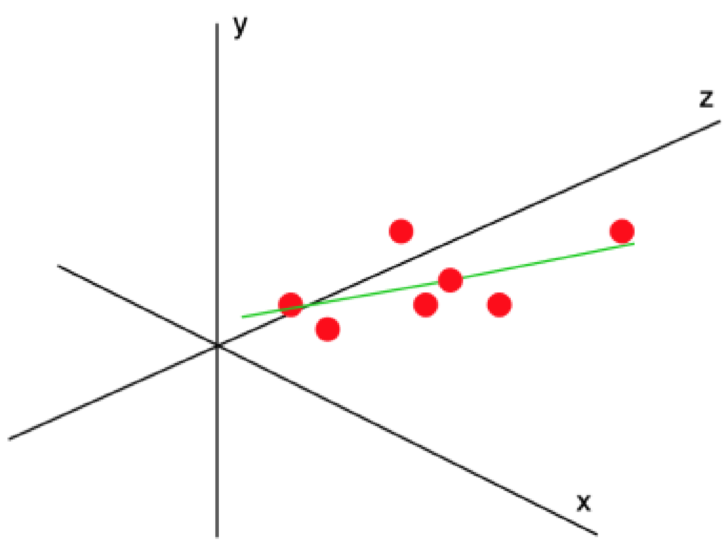

Figure 2.20: Multilinear regression

2.12.2 Support Vector Machine Model

The original method of SVM developed by Cortes & Vapnik (1995) aims to classify labeled datasets by finding an optimal separating hyperplane that discriminates classes in agreement with the training data with the largest margin. The generalization of this method to construct as optimal hyperplane in non-separable training data became known as the SVNs (Vapnik, 2006). The term optimal hyperplane is used for the decision edge that reduces misclassifications and the training data. Support vector regression is the SVM extended version for solving regression models (Basak et al., 2007). This is based on the structural risk minimization principle by finding a separating hyperplane with minimized loss(Ref). This is represented empirically as shown below;

$$\boldsymbol{f(x) = < w, x_j > + b = y} \qquad \textbf{(2.25)}$$

Where x is the input features, y is the output target, w is the weight, and b is the bias. W and b are defined in the equation 2.25 and 2.26 (Roy et al., 2021):

$$\textbf{Minimize}\ \boldsymbol{\frac{1}{2}\|w\|^2 + c\sum_{i=1}^{l}(\xi_i + \xi_i{}^*)} \qquad \textbf{(2.26)}$$

Subject to

$$\boldsymbol{\{y_i - < w, x_j > - b \ \le \varepsilon + \xi_i < w, x_j > + b - y_i \le \varepsilon + \xi_i{}^* \xi_i \xi_i{}^* \ge 0, i = 1, 2, 3 \ldots N\}} \qquad \textbf{(2.27)}$$

Where C is the constant, $\xi_i\ and\ \xi_i{}^*$ are slack variables, and ε represents the boundary value. Several kernel types including linear, polynomial, radial basis function (RBF), sigmoid and precomputed can be applied in the SVR. SVR is more sensitive to the outlier value and insensitive to the inner data point group.

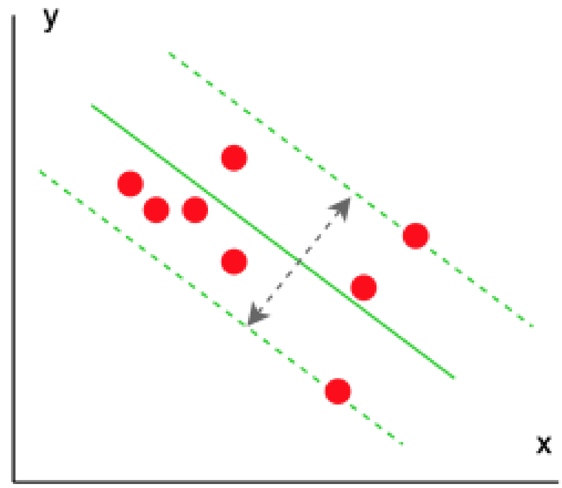

Figure 2.21: Support Vector regression

2.12.3 Decision Tree Model

Decision tree (DT) is widely used in decision making with a tree-like graph (Navada, 2011). It consists of nodes and branches that break down datasets into smaller subsets regarding the features by splitting, stopping and pruning (Nourani and Molajou, 2017; Song *et. al*., 2015). Decision Tree model can separate data group that is nonlinear.

Several decision tree algorithms include iterative dichotomiser 3 and classification and regression tree (CART) can be implemented.

2.12.4 Random Forest Model

Random forest model consist of a multitude of decision trees that is independent and uncorrelated (Lei et al., 2019). Generalization of the model is achieved by these independent decision trees through randomness (Ho, 1995). This can be inferred from this example, in a training data set.

$$\mathbf{S} = \{\boldsymbol{X^m}, \boldsymbol{Y^m}\}^{\boldsymbol{m}}{}_{(\boldsymbol{M-1})} \qquad \textbf{(2.28)}$$

X has the input features such as elevation, slope while Y is the multidimensional space taking m as the sample number. The subset S_t of the training set S has the same number of samples as S that randomly includes around one third of the duplicate samples and around one third of the original samples are removed.

Both Decision Tree and Random Forest are classification-based Machine Learning Models algorithm. Random forest has widely been applied in remote sensing research and shows a great performance in meteorological, land use/land cover and other water resources research. The advantages of the random forest model are high computing speed and high accuracy (Yates and Islam, 2021).

2.12.5 Autoregressive Integrated Moving Average Model (ARIMA)

Autoregressive integrated moving average (ARIMA) is one of the most commonly applied time series machine leaning models developed by Box and Jenkins in 1976 (Lee and Tong, 2011). It has the ability to predict greater time-related information by finding the past data pattern with the moving average and forecasting based on time-related changes. ARIMA model is a combination of the autoregressive model (AR) and moving average model (MA). AR uses the past value to make the prediction by the following equation (Babu and Reddy, 2014).

$$\boldsymbol{Y_t} = \propto + \boldsymbol{\beta_1 Y_{t-1}} + \boldsymbol{\beta_2 Y_{t-2}} + \cdots + \boldsymbol{\beta_p Y_{t-p}} + \boldsymbol{\epsilon_i} \qquad \textbf{(2.29)}$$

MA uses the past errors to make predictions and is expressed as

$$\gamma_{t=} \propto+\epsilon_t+\phi_1\epsilon_{t-1}+\phi_2\epsilon_{t-2}+\cdots+\emptyset_p\epsilon_{t-p} \quad \textbf{(2.30)}$$

AR and MA can be only used on stationary data. Stationary data is defined as data with a constant mean or no trend over time. And by adding differencing of data series, ARIMA extends to non-stationary data (Cheng et al., 2015). In the form of ARIMA(p,d,q)(P,D,Q)s, (p,d,q) is the non-seasonal part while (P,D,Q) is the seasonal part. p is the order of non-seasonal AR, d is the differencing number, and q is the order of non-seasonal MA, respectively (Silva et al., 2021).

2.12.6 Artificial Neural Network Model

Artificial neural network (ANN) is an information processing system that structures and operates like a human brain (Abraham, 2005). An ANN model comprises of three kinds of layers which are input layers, hidden layers and output layers (Abdolrasol et al., 2021). The processing units in an ANN model are referred to as neurons that can store the experience knowledge (Shanmuganathan, 2016). The relations between the input neurons and the hidden layer neurons are expressed mathematically as given below (Shanmuganathan, 2016).

$$\boldsymbol{net_j} = \sum_{i=1}^{p}(\boldsymbol{w_{ji}x_i} + \boldsymbol{b_j}) \quad \textbf{(2.31)}$$

Where x is the input value, w is the weight and b is the bias, i,j,k respectively represents the neurons in the input layers, hidden layers and output layers. Functions such as transfer and activation are applied to the network values net_j for the output from the hidden layer neurons. It is generated as (Sharma et al., 2017);

$$\boldsymbol{y_j} = \boldsymbol{f}(\boldsymbol{net_j}) = \boldsymbol{f_h}(\sum_{i=1}^{p}(\boldsymbol{w_{ji}x_i} + \boldsymbol{b_j})) \quad \textbf{(2.32)}$$

The relationship between the hidden layer neurons and the output neurons is represented mathematically as (Panchal et al., 2011);

$$\boldsymbol{net_k} = \sum_{i=1}^{q} \boldsymbol{f_o}(\boldsymbol{y_j})\boldsymbol{w_{ki}} + \boldsymbol{b_k} \tag{2.33}$$

The output relationship with the output neurons are given as (Panchal et al., 2011);

$$\boldsymbol{y_k} = \boldsymbol{f}(\boldsymbol{net_k}) = \boldsymbol{f_o}(\sum_{i=1}^{p}(\boldsymbol{w_{ki}}\boldsymbol{f_h}(\boldsymbol{w_{ji}}\boldsymbol{x_i} + \boldsymbol{b_j})) + \boldsymbol{b_k}) \tag{2.34}$$

2.13 Application of Machine Learning Models for Flood Modeling

Machine learning models have been effectively applied in flood modeling to enhance prediction accuracy and mitigate the impact of floods (Avand et al., 2020; Fidan et al., 2023; Langhammer, 2023; Piraei et al., 2023; Saikh and Mondal, 2023; Yu Han et al., 2023). These models utilize various data sources such as remotely sensed imagery, historical flood inventory data, and topographic variables to predict flood susceptibility, inundation extent, and timeline. Different machine learning algorithms like Random Forest, Support Vector Machine, and Stacked Generalization have been employed, showing significant improvements in flood prediction accuracy, with some models achieving high F1 scores and AUC values. The use of machine learning models not only aids in identifying areas at risk of flooding but also helps in understanding the impact on infrastructure like bridges, crops, and transportation systems, thereby enabling better disaster management strategies.

2.14 Summary of Previous Work Done

Several research works have been done on flooding in Nigeria due to the severity of its impact to the environment. (Agbonkhese et al., 2014) carried a study on Flood Menace in Nigeria: Impacts, Remedial and Management Strategies. This study revealed the causes of flooding in Nigeria such as rapid population growth, poor governance, poor drainage facilities and decaying infrastructures, lack of proper environmental planning and management strategies, poor practice of dumping waste/refuse and climate change coupled with inadequate preparedness have been traced and among others, human activities. He also pointed the flood incedent caused by the release of water from the Lagdo Dam in Cameroon. The research provides an overview of how Nigerian cities have been affected by flood menace incidences by conducting a review of literature on flood menace.

Another study by (Chukwuma et al., 2018) carried out a comparative analysis of flooding in Warri and Port Harcourt urban areas of the Niger Delta region in southern Nigeria with a view to isolate effective policies and strategies which may prove valuable for flood mitigation. Data used in the study comprised of field measurements, observations, interviews, and questionnaire administration. These data were analyses using descriptive statistical tools. The results revealed the flood characteristics, impacts, coping mechanisms and risk-oriented planning which is essential for protection of floodplain occupants is neglected in the areas. It also showed that urban drainage systems are inadequate; the existing ones underperform and the municipal authorities have no well-articulated policies/arrangements through which repairs/maintenance/clearance of the drains would be regularly and speedily provided to ensure that they function properly and sustainably.

(Chukwu, 2023) worked on A novel Account of Flooding Devastation and Consequences in Kogi State, Nigeria. The paper discusses the impact of flooding in Kogi State, Nigeria, specifically the devastation caused by flooding in 2022. It applied a structured questionnaire for interviewing 300 people who are residents of these states. validation of the instrument was done through peer review and pilot testing and the data were collected and analyzed using frequency, percentages and Linkert scaling test. The results showed that 94% of the respondents agreed that flooding destroyed their livestock and farm products, blocked their roads, submerged their buildings and rendered many homeless. This in turn affected daily road transportation, businesses were distorted, thereby impacting negatively on their economy.

(Egbiki et al., 2020) employed Adaptive Neuro-Fuzzy Inference System (ANFIS) to simulate and forecast daily discharge of the Ikpoba River in Edo State. Their study utilized hydrological and climatic data covering the period 1991–1995, including discharge, temperature, and rainfall. Five models were developed in MATLAB, with Models 1–4 relying solely on discharge data, while Model 5 integrated temperature and precipitation to account for climate change influences. Performance was evaluated using five statistical criteria: correlation coefficient (R), coefficient of determination (R^2), mean square error (MSE), model efficiency (E), and index of agreement (IOA). While all models predicted river discharge with reasonable accuracy, the climate-informed Model 5 demonstrated superior performance, with minimal overestimation errors (0.043% during training and 0.044% during testing), well within the ±10% tolerance threshold. This research underscores the potential of neuro-fuzzy systems in forecasting river flows and highlights their utility for integrated water resources planning in the Niger Delta.

The development of intensity–duration–frequency curves has been widely adopted as a key tool for rainfall prediction and flood risk planning. (Ilaboya and Nwachukwu, 2022) analyzed 40 years (1974–2013) of annual maximum rainfall data for selected states in South-West Nigeria to generate IDF curves. Data homogeneity was confirmed using residual mass curves and hypothesis testing, while rainfall intensities for durations ranging from 2 to 320 minutes were estimated using the Indian Meteorological Department's reduction formula and MATLAB curve fitting. The Gumbel probability distribution was used to determine rainfall frequency factors for return periods of 2–100 years. Four empirical IDF models—Talbot, Bernard, Kimijima, and Sherman—were evaluated, with Talbot's equation proving to be the best fit due to its lowest root mean square error values (5.67E-07 and 6.42E-07). The study demonstrated the effectiveness of IDF models in predicting rainfall intensities for ungauged catchments and provides critical input for stormwater and hydraulic design.

(Okeke and Ehiorobo, 2017) Rainfall frequency studies have also been conducted in other parts of the Niger Delta. Okeke and Ehiorobo (2017) assessed rainfall frequency in Patani, Delta State, using 33 years of peak monthly rainfall data (1981–2013). Several probability distributions were tested, including Normal, Log-Normal, Log-Pearson, Gumbel, and Foster's Type I. The rainfall series was analyzed for return periods ranging from 2 to 200 years. Goodness-of-fit analysis revealed that the Gumbel distribution was most suitable for the dataset, followed by Foster's Type I, while the Normal distribution performed poorly. These findings demonstrate that frequency analysis is an essential tool in estimating extreme rainfall events for flood control and infrastructure planning in flood-prone regions.

(Akpejiori et al., 2017) investigated flood hazards in Agenebode, Edo State, through probability modeling and geospatial analysis. Using rainfall records from 1983–2010 and probability distributions such as Log-Normal, Log-Pearson Type III, and Gumbel, the Log-Normal model was identified as the most appropriate for projecting river discharge at different return periods. Flood hazard mapping was conducted with ArcGIS, integrating topographic data, Shuttle Radar Topographic Mission (SRTM) digital elevation models, and historical flood records. The analysis revealed that approximately 72% of the built-up area (1.8 km^2) was at risk of flooding, directly threatening about 481 residents. This study highlights the importance of hazard mapping in identifying vulnerable communities and guiding the allocation of disaster response resources.

(Ehiorobo and Uso, 2014) examined flood frequency along the River Niger at the Onitsha Bridge Head using annual maximum discharge data for the period 1960–1991. Five probability distributions—Normal, Gumbel, Log-Normal, Log-Pearson Type III, and Pearson Type III—were used to estimate discharge at return periods of 2 to 200 years. Comparative analysis showed that the Gumbel distribution provided the most reliable fit, producing discharge estimates from 21,998 m^3/s (2-year return period) to 37,390 m^3/s (200-year return period). Other distributions yielded comparatively lower or less consistent estimates, with the Normal distribution found to be the least reliable. The study concluded that Gumbel distribution is the most appropriate model for flood prediction in the Lower Niger Basin, reinforcing its suitability for hydrological risk analysis across Nigeria.

(Ehiorobo et al., 2012) examined changes in flow regimes within the mangrove and tropical rainforest regions of West Africa. Their findings highlighted significant alterations in discharge patterns, pointing to the vulnerability of these ecosystems to climate variability and extreme hydrological events. Similarly, (Ehiorobo and Izinyon, 2011) focused on the documentation and measurement of flood events in the Niger Delta, with an emphasis on erosion monitoring and control. Their work emphasized the need for continuous monitoring and proactive management strategies to mitigate the impacts of floods on communities and infrastructure.

(Echendu, 2023) studied Human factors vs climate change; experts' view of drivers of flooding in Nigeria. This research utilized experts' judgements in the field of flood risk management in

Nigeria. It employed an in-depth qualitative case study by administering semi-structured interviews as the primary data collection tool. The result from this research acknowledged the influence of climate change on flooding which is as a result of increase in rainfall intensity, frequency and duration. However, they also attributed the flooding being experienced in the study location to be due to more controllable human factors which include lack of infrastructure, poor urban planning and governance, and weak implementation and enforcement of laws and policies.

(Okunola and Werners, 2023) worked on Recovery Pathways from Extreme Flood Events: Lessons and Experiences of Flooding in Lagos, Nigeria. This study focused on understanding flood recovery process after previous events to build resilient equitable futures in this low-lying city. It adopted a multi-methods approach, which includes in-depth interviews, grey materials, and policy document analysis. These were adopted to assess the impacts of flood risks, recovery experiences, as well as conceptualize and identify recovery indicators and governance strategies in the study area. Of particular interest is the exploration of the extent to which the current existing institutions and policy frameworks have been a barrier or enabler for climate-resilient recovery and what we can learn from this about how institutions and policy frameworks can build resilience after extreme events. This research argued that institutions and the associated policy frameworks and political will play an essential role in building holistic and comprehensive climate-resilient recovery to extreme weather events.

(Badamosi et al., 2023) studied Socioeconomic impacts of flooding and its coping strategies in Nigeria: Evidence from Dagiri community, Gwagwalada area council of Abuja. This study focuses on the socioeconomic implications of the 2020 flood in the Dagari community. To achieve the specific objectives, a number of methodologies were employed such as map analysis, questionnaire survey, oral interviews, and site observations. Presentation of results was done using percentages, tables, bar graphs, pie charts, and photos. The land cover is mostly residential with urban infrastructures. A flood hazard map was created from which analysis revealed that about 87% of the area is at risk of flooding, though the severity of vulnerability varies from low vulnerable areas to highly vulnerable risk zones. The socioeconomic impacts were duly measured using some sustainable development indicators, and the result revealed that flooding had numerous socio-economic impacts on the community, ranging from income, education, agriculture, sanitation, infrastructures, and properties. The coping strategies adopted by some community members were also very inadequate, while a high number of them are not employing any coping strategies at all.

(Danhassan et al., 2023) investigated *Flood Policy and Governance: A Pathway for Policy Coherence in Nigeria*, with the aim of assessing how flood governance is structured and how policy coherence is achieved through institutional design and implementation in the country. The study revealed that Nigeria does not have a dedicated national flood policy, which has led to a lack of clear focus, objectives, and coordinated strategies for flood governance, prevention, control, and management. This absence also weakens the government's commitment to developing both short- and long-term flood mitigation solutions. The research further highlighted poor synergy and coordination among institutions involved in flood governance. Since the establishment of the Federal Ministry of Environment in 1999, floods and climate-related hazards have been given relatively low priority. As a result, state and local governments bear the primary responsibility for managing flood disasters and emergencies, while federal intervention occurs only when the magnitude of flooding surpasses the response capacity of subnational authorities.

(Richard and Okeke, 2023) worked on Climate change and urban flooding in South-South Nigeria from 1990 – 2020. this study was aimed at evaluating the impact of climate change and urban development on urban flooding in South – South Nigeria using geospatial techniques. Datasets utilized for the study included; land use/ land cover derived from Landsat satellite data, soil map, slope model, soil infiltration rate, impervious surface derived from vegetation indices, distance from river, precipitation, and surface temperature data. These datasets were processed into common coordinate system. Landsat data of four epochs (1990 – 2020) were used to map urbanization. Accordingly, the variations in climate variables were investigated using NiMET reports and the satellite derived values. Flood vulnerability zones were determined using multi-criteria analysis implemented in ArcGIS weighted overlay tool. The study observed that urbanization increases from 1990 to 2020, which also increase impervious surfaces, making the area more vulnerable to flooding. In addition, wetland and vegetation cover are being replaced by built-up thereby decreasing the ability of wetland to retain flood water. The lowest rainfall was in 1990 with value 293.70mm and the highest was in 2000 with value 454.90mm. There is general variation of rainfall and temperature from 1990 – 2020 due to climate change. Total built-up at risk was 8873.55ha with most of them situated along the river banks. Geospatial technology is suitable for urban flood vulnerability modeling.

(Malachy et al., 2022) studied Flooding in Nigeria, towards prioritizing mental health and psychosocial support. The paper focused on the impact of flooding in Nigeria on mental health and the importance of integrating mental health support in emergency response. The result revealed that Flooding in Nigeria has worsened in the past decade. And that mental health impact of flooding has gotten to a significant level.

(Mast et al., 2023) studied Linking remote sensing data and online engagement in flood events in Nigeria. This research examines whether the online attention received by flood-affected states in Nigeria is correlated with the physical impact of the floods in these states. The method measured the online attention using data gathered from Twitter and Google and relate it to the flood impact on settlements derived from remote sensing data on flood extent, settlements, and population. The result showed that at the level of states, online attention and the flood impact on settlements are not correlated. It is likely that other factors, such as the distribution of social media users or habituation towards extreme events, influence online attention to a similar or higher degree than the physical impact of floods on settlements.

(Idowu et al., 2021) conducted a study on Land Use and Land Cover Change Assessment in the Context of Flood Hazard in Lagos State, Nigeria. The research emphasized the importance of assessing LULC changes over time for effective flood hazard mapping, with the aim of identifying possible drivers of increasing flood risk in the state. Four dominant land cover categories—water, wetland, vegetation, and developed land—were mapped and analyzed over a 35-year period. The study applied a post-classification, map-matrix-based change detection approach to evaluate multi-year land cover transitions between 1986–2000, 2000–2016, 2016–2020, and 1986–2020. Seven key factors were identified as potential contributors to rising flood hazards, and their relative importance was quantified using a hybrid weighting technique that combined the Analytical Hierarchy Process (AHP) with Shannon Entropy. The resulting hazard classification categorized areas into very high, high, moderate, low, and very low flood risk zones. Findings revealed that much of the LULC transformation involved the conversion of wetland areas into developed land, alongside widespread unplanned urban expansion within moderate to high flood-prone zones. Over the study period, wetlands declined by 69%, while developed areas expanded by 94%. Whereas wetlands were a dominant land cover in 1986, by 2020 they had become the least represented. These patterns strongly suggest that the observed LULC changes are a major factor driving the increasing flood hazards in Lagos State.

(Ighile et al., 2020) carried out a study on the effects of land use change on flooding risks in Nigeria. This research aimed at identifying the drivers of land use change and their effects on flood risks in Nigeria. The method applied on this research identified the factors responsible for land use changes in Nigeria between 2000 and 2013 and their effects on the level of flooding risks. A multinomial logistic regression was used to model the probability of land use changes impact on flooding risks, as a function of explicit independent variables. The results show that Economic, biophysical, demographic and climatic variables were the significant determinants of land use change. Additionally, while assessing the relationship between the changes in land use and flood risks, agricultural, settlement and forest land use had the most significant contributions to the changes in the level of flood risks.

(Ibitoye et al., 2020) worked on analysis of vulnerable urban properties within river Ala floodplain in Akure, Southwestern Nigeria. The study assessed the impact of flooding on some elements at risk along Ala River in Akure, Ondo State, Nigeria, using Remote Sensing and GIS techniques. The land use/land cover change detection of Ala River catchments was carried out using 1984, 2000 and 2015 Landsat images with each of the classes and the positional accuracy of the river were validated using GPS (Garmin78SC). Buffers were generated around the river channels using high resolution Google Images as input data. The result of LULC showed that there was positive increase in built up land use from 17.65% in 1984 to 24.96% in 2000 and 65.67% in 2015. While that of the buffering analysis showed that 105, 214 and 554 buildings with the estimated population of 2520, 5136 and 13,296, fall within 10 m, 20 m and 30 m distance to the river.

(Musa et al., 2019) used geographic information system to evaluate land use and land cover affected by flooding in Adamawa State, Nigeria. This study evaluated land use and land cover affected by flooding along Benue River in Adamawa State, Nigeria. The method comprises of retrieving of satellite imageries of land use, vegetation, settlements and drainage basins, from the National Space Research and Development Agency, Abuja, and the National Centre for Remote Sensing, Jos. The imageries were collected for the study period: 2002, 2012 and 2014, all between October and November. These imageries were used to generate a LULC map of the study areas. Land cover and/or land use and flood inundation analysis was carried out using Integrated Land and Water Information System image processing and Earth Resources Data Analysis (ERDAS 9.2) image processing geographic information system software. A supervised classification was done using the LULC samples collected on the field. This final product generated a LULC map for the entire study area. Six LULC classes were generated: waterbodies, farmland, vegetation, settlement, alluvial deposits and bareland. The study revealed that in 2002 floods affected 38% farmland and 53% vegetation of the total inundated areas. In 2012, it affected 56% farmland cover and 35% vegetation, while in 2014, it affected 51% farmland cover and 42% vegetation cover of the total inundated area of Adamawa State.

(Adelalu et al., 2021) studied Quantitative and qualitative evidence of anthropogenic fingerprint in flooding in Taraba State of Nigeria. This research provides technical proof of anthropogenic impression in the incessant flooding in the area. The research adopted both spatial and hydro-climatic data in addition to designed questionnaire. Hydro and climatic data were collected from Upper Benue River Basin Development Agency, Yola. Correlation matrix was used to show the extent of climatic variation and GIS depicts the land use change. The result revealed that rainfall has not related well with excess channel flow while the coefficient of variation in rainfall and runoff is not pronounced. R- Factor in all the gauging stations is very low. Built up area occupied just 2.8% of the area accounting for 806.9 hectares. Cultivated area and the bare land was about 13146.2 hectares, which account for about 46.3% of the area. Vegetation cover occupied more than half of the study area making about 50.1% of the land mass of the catchment. The farmers' assessment agreed with the scientific analysis. The runoff volumes that traverse the state three decades ago without much disturbance now pose a serious ache. Though Inter catchment link and discharge thereof is a factor, the cogwheel pinpoints land use change and encroachment of floodplain. Parastatals involved in the land survey and planning of the state should wake up to the challenge.

(Umar et al., 2021) Umar *et. al*. (2021) examined the detection and prediction of land use change impacts on streamflow regimes in a Sahelian river basin in northwestern Nigeria. The study employed ENVI software for LULC change detection and utilized the Cellular Automata (CA)–Markov model within the IDRISI environment for LULC projection. Streamflow trends and variability were analyzed using the Mann–Kendall (MK) trend test alongside the Inverse Distance Weighting (IDW) method. Prior to modeling and projecting LULC for the year 2030, supervised classification was conducted for the years 1990, 2000, and 2010. The modeling results demonstrated a strong correlation between LULC dynamics and streamflow variations. The decade 1990–2000 was characterized by extensive forest clearance, which coincided with elevated streamflow levels and severe flooding events. By contrast, the period 2000–2010 was marked by significant land use expansion, particularly construction activities, which accounted for approximately 3.4% of the observed changes.

(Anugwa et al., 2022) Assessing climate change-related losses and damages and adaptation constraints to address them: Evidence from flood-prone riverine communities in Southern Nigeria. A multistage sampling procedure was utilized in selecting 240 households within eight riverine communities in Southern Nigeria. A mixed methods research approach was used in eliciting responses from the respondents. Data were analyzed using descriptive statistics. The market cost approach was used to value the losses and damages due to climate change. The respondents identified flooding as the major climate change hazard in the study location. The major effects of flooding on the livelihood of the respondents were loss of crops (98.6%) and rise in food prices (92.8%), among others. In response to increased climatic threats, farmers have adopted various risk management strategies such as income diversification, adjusting planting dates, soil and water conservation techniques, among others. The estimated average monetary value of losses and damages in community infrastructure, employment, personal properties, crops and livestock were $28,409.09, $3,095.23, $1,583.52, $824.60 and $224.16, respectively.

(Ekwueme and Ekwueme, 2021) studied the quantification of effects of climate change on flood in tropical river basins. This study investigated the extent to which climate change contributes to flooding in the river basins of southeastern Nigeria. A Climate–Flood model equation was formulated using the time-series autoregressive modeling technique. With the aid of Minitab software, long-term mean annual values of key climatic variables were analyzed. Runoff estimates derived from the Climate–Flood model, based solely on annual climatic records, were further examined alongside geological conditions, infiltration capacity, drainage patterns, and the digital elevation model (DEM) of the area.

The results revealed that persistent variations in climatic parameters significantly influence flood occurrence. Among the locations studied, Owerri recorded the highest positive change in evaporation (0.11%) with a corresponding rainfall change of 0.03%. Awka showed the largest increase in sunshine hours and rainfall (0.41%), while Umuahia experienced the greatest change in solar radiation (0.08). Enugu exhibited the highest increase in air temperature (0.12). When runoff variation attributable to climate change was quantified, Enugu again ranked highest with an estimated 1.68 m^3/s, whereas Owerri recorded the lowest contribution at 0.04 m^3/s.

Hassan *et. al*., (2020) examined the Potential Impacts of Climate Change on Extreme Weather Events in the Niger Delta Region of Nigeria, focusing on projected changes in meteorological extremes between 2010 and 2099. The study employed four Coupled Model Intercomparison Project Phase 5 (CMIP5) global climate models (GCMs) under Representative Concentration Pathways (RCP 4.5 and RCP 8.5) emission scenarios. Extreme events were assessed using the Standardized Precipitation Index (SPI) at 1-month and 12-month time scales. The findings suggest a general increase in rainfall across all projection periods and under both emission scenarios, with the most pronounced increases expected during the final three decades of the century. Under the RCP 8.5 scenario, rainfall at Port Harcourt and Yenagoa stations is projected to rise by approximately 2.47% and 2.62% respectively, while Warri station may experience an increase of about 1.39% toward the century's end. Moreover, the 12-month SPI projections under both RCP 4.5 and RCP 8.5 indicate exceedances of the extreme wet threshold (SPI > 2) across all locations and future periods, pointing to a higher likelihood of prolonged and severe flooding events in the Niger Delta.

(Ayotamuno, 2020) studied Changes of Key Climatic Parameters and Flooding in Rivers State, Nigeria. This research aimed at determining the impact of changing climatic parameters on the recently observed flooding events in many of the communities. The method adopted comprises of retrieving key climatic parameters in Rivers State, Nigeria, such as temperature, atmospheric vapour and rainfall spanning a period of 30 years (1988-2018), from the Nigerian Meteorological Agency (NIMET). The data was statistically analyzed and the results show that there has been a gradual increase in the amount of rainfall with increasing temperature and decreasing atmospheric pressure within the period of study (1988-2018).

(Jumbo et al., 2023) worked on Flood risk assessment, climate change adaptations and mitigation strategies of communities in Edo State, Nigeria. The study carried out a flood risk assessment, climate adaptation and mitigation strategies of communities in Edo State, Nigeria. With the aid of questionnaires and GIS techniques, the flood risk level of communities within Edo states were analysed by capturing all the components of flood risk which include exposure and vulnerability. All analysis was carried out using descriptive statistics and Analytical Hierarchy Process (AHP) to determine the extent of the communities' flood. The extent of risk showed that 778 communities were captured in risk analysis, 503 (64.65%) of the communities were found within low flood risk level while 150 (19.28%) communities and 125 (16.07%) communities were found to be within medium and high flood risk level respectively. The climate variables showed some level of fluctuation while the adopted adaptation measures such as expansion of floodplain and wetlands was based on political will of administrators, and the measure was perceived less effective. There was high level of awareness about government mitigation measures in the area and the main mitigation measure by government is construction of drainage system which was perceived to be effective. It was therefore concluded that all the adopted attributes contributed to the establishment of flood risk of Edo State and was categories into high, medium and low flood risk level.

(Kehinde, 2022) studied The effect of global warming in Nigeria: Flood in perspective. This research examines some causes and effects of the global warming in Nigeria, while paying particular attention to floods as one of its effects. The aim of the research is to answer the question why is Nigeria so much affected with the effects of global warming especially flooding. This research adopted both primary and secondary research sources for retrieving data. Various laws regulating environmental protection, both local and international, were considered. The Internet sources as well as Nigerian newspapers articles related to the research topic are also essential to this work. The result revealed that there are inadequacies in the existing laws regulating environmental protection.

(Rashidiyan and Rahimzadegan, 2024) Rashidiyan and Rahimzadegan (2024) carried out a study on the Investigation and Evaluation of Land Use–Land Cover Change Effects on Current and Future Flood Susceptibility in the Talar watershed, Iran. The research aimed to predict future LULC using the Land Change Modeler (LCM) and to evaluate how these changes influence flood susceptibility through the application of machine learning (ML) algorithms. The models applied included Artificial Neural Networks (ANN), Logistic Regression (LR), Random Forest (RF), and Support Vector Machine (SVM). Nine flood-influencing factors—altitude, slope, distance from rivers, land use/land cover, topographic wetness index, stream power index, profile curvature, rainfall, soil type, along with 200 flood and non-flood location data points—were incorporated into the analysis. Model performance was assessed using root mean square error (RMSE) and the coefficient of determination (R^2). Results showed strong predictive accuracy across the models, with RMSE values of 0.125 (SVM), 0.175 (LR), 0.192 (RF), and 0.2834 (ANN), and corresponding R^2 values of 0.9373, 0.8773, 0.8667, and 0.8525, respectively. The findings confirmed the effectiveness of LCM in forecasting future LULC patterns, while also demonstrating the robustness of the applied ML algorithms in generating reliable flood susceptibility maps for the watershed.

(Vu et al., 2023) conducted a study on *Predicting Land Use Effects on Flood Susceptibility Using Machine Learning and Remote Sensing in Coastal Vietnam*. The research assessed how climate and land use changes influence flood susceptibility in Thua Thien Hue Province by applying machine learning models—Support Vector Machine (SVM) and Random Forest (RF)—in combination with remote sensing data. A flood inventory comprising 1,864 flood locations and 11 conditioning factors for the years 2017 and 2021 served as the input dataset.

The predictive performance of the models was evaluated using the area under the curve (AUC), root mean square error (RMSE), and mean absolute error (MAE). Both models achieved high accuracy, with AUC values greater than 0.95. Among them, the RF model (AUC = 0.98) slightly outperformed the SVM model (AUC = 0.97). The analysis also revealed that flood-prone areas expanded between 2017 and 2021, primarily due to the increase in built-up land cover.

(Hariyono et al., 2023) studied Land use and land cover change analysis of flood prone area using remote sensing data and machine learning in Malang Raya, East Java, Indonesia. To reduce flood risk, this study uses remote sensing data to analyze changes in land use and land cover. The research location is Malang Raya, one of the locations prone to flooding in East Java. The method analyzes the results of processing satellite image data with the machine learning tools available at Google Earth Engine (GEE). This method provides convenience in accelerating the object classification in satellite image data. The study results indicate that using satellite image data analysis and machine learning processes is beneficial in accelerating object classification and approaching the actual conditions, making it easier to make a policy in handling disaster risk reduction.

(Ilaboya et al., 2023) develop a flood susceptibility map around Ikpoba catchment in Benin City, Nigeria. Ten thematic maps namely; Topographic wetness index (TWI) map, Elevation map, Slope map, Precipitation map, Land use land cover map, Normalized difference vegetation index (NDVI) map, Distance from river map, Distance from road map, Drainage density map and soil map were employed for the study. The thematic maps were thereafter reclassified in order to obtain a uniform scale. To obtain the percentage weight of influence for each of the data, analytical hierarchy process (AHP) was employed to generate a pairwise comparison matrix which validated using the index of consistency. Thereafter weighted overlay method was employed to stack the reclassify maps in order to generate the final flood map. To determine the areas with high flood risk, the flood map was converted to kml file and thereafter projected to google. The outcome revealed that some communities pose a very high risk of flooding compared to other which pose a high risk of flooding.

(Ehiorobo and Izinyon, 2013) carried out a study on flood frequency analysis on annual maximum discharge data of River Oshun at Iwo in Osun State, Nigeria for the period 1985 to 2002 utilizing three probability distribution models namely: Extreme EVI (value Type-1), LN (Log normal) and LPIII (Log Pearson Type III). The models were used to predict and compare corresponding flood discharge estimates at 2, 5, 10, 25, 50, 100 and 200 years return periods. The results indicated that Extreme Value Type 1 distribution predicted discharge values ranging from 26.6 m3 /s for two years to 431.8 m3 /s for 200 years return periods; the Log Pearson Type III distribution predicted discharge values ranging from 127.2 m3 /s for two years to 399.54 m3 /s for 200 years return periods and the Log normal distribution predicted discharge values ranging from 116.2 m3 /s for two years to 643.9 m3 /s for 200 years return periods. From the results, it was concluded that for lower return periods ($T \leq 50$ yrs) Extreme Value Type 1 and Log Pearson Type III could be used to estimate flood quantile values at the station while for higher return periods ($T > 50$ yrs) Log Normal probability distribution model which gives higher estimates could be utilized for safe design in view of the short length of discharge records used for the analysis.

(Nguyen et al., 2022) proposed a novel hybrid framework for flood susceptibility assessment that integrates machine learning with land use change analysis. Their study, conducted in the Gianh

River watershed of Quang Binh Province, Central Vietnam, applied the Relevance Vector Machine (RVM) model in combination with the Coyote Optimization Algorithm (COA). Model performance was evaluated using statistical indices such as the area under the curve (AUC). The findings demonstrated that the COA significantly enhanced the predictive capacity of the RVM, achieving an AUC of 0.99. This performance was superior to several benchmark models, including Support Vector Machine (AUC = 0.98), Gradient Boosting Machine (AUC = 0.97), Random Forest (AUC = 0.99), Extra Trees Regressor (AUC = 0.98), and AdaBoost (AUC = 0.96). When applied alongside land use maps, the enhanced model effectively highlighted the role of urbanization in increasing flood susceptibility. Results indicated that between 2005 and 2020, urban development expanded by 110% in low and very low flood susceptibility zones, and by 30–40% in high to very high risk areas, underscoring the interaction between demographic growth and exposure to flood hazard.

(Wang et al., 2020) explored the application of convolutional neural networks (CNNs) for flood susceptibility mapping (FSM) in Shangyou County, China. The study introduced CNN frameworks for both classification and feature extraction, applying them to flood susceptibility assessment. Three different data presentation approaches were incorporated into the CNN architecture to optimize the two proposed frameworks. A total of 13 flood-triggering factors, derived from historical flood events in the study area, were used as model inputs. The effectiveness of the CNN-based methods was evaluated against the traditional Support Vector Machine (SVM) classifier using multiple performance metrics. Results showed that all CNN-based approaches produced more reliable and practical flood susceptibility maps compared to SVM. Specifically, the CNN classifiers outperformed SVM, achieving improvements in area under the curve (AUC) values ranging from 0.022 to 0.054. These findings underscore the potential of deep learning techniques, particularly CNNs, in enhancing flood susceptibility assessments.

(Islam et al., 2020) investigated Flood Susceptibility Modelling Using Advanced Ensemble Machine Learning Models in the Teesta River Basin, northern Bangladesh. Given the highly dynamic and complex nature of flash floods, predicting vulnerable sites remains a major challenge. To address this, the study applied and evaluated two hybrid ensemble approaches—Dagging and Random Subspace (RS)—combined with Artificial Neural Network (ANN), Random Forest (RF), and Support Vector Machine (SVM). These were compared with several benchmark machine learning models for flood susceptibility mapping. The models incorporated twelve flood-influencing factors alongside 413 current and historical flood locations, integrated within a GIS framework. To assess the relationships between flooding events and influencing factors, the study employed information gain ratio and multicollinearity diagnostic tests. Model performance and predictive capability were validated using statistical appraisal methods such as the Friedman test, Wilcoxon signed-rank test, paired t-tests, and the Receiver Operating Characteristic (ROC) curve. All models achieved strong predictive accuracy, with AUC values exceeding 0.80. Among them, the Dagging ensemble approach performed best, followed by RF, ANN, SVM, and RS. The findings demonstrate the potential of ensemble-based machine learning methods to enhance the reliability of flood susceptibility assessments. The methodology and practical outputs provide valuable guidance for policymakers and local authorities in mitigating flood risks and developing targeted adaptation measures to minimize potential damage.

(Roy et al., 2021) studied Climate and land use change induced future flood susceptibility assessment in a sub-tropical region of India. This research work presents flood-prone areas in the Ajoy River basin of India, considering the “Support Vector Machine”, “Extremely Randomize

Trees” and “Biogeography Based Optimization” (BBO) method in GIS platform. “Area Under Curve” (AUC) values of “Receiver Operating Characteristics” were used to validate and determine the accuracy of the predicted models. AUC shows the state or nature of the flooding. If the outcome of AUC values indicates more than 0.95, then the likelihood of flooding will be high BBO gave us the most optimal outcomes in this research out of these models (AUC = 0.98) and assured us that BBO is an influential tool for assessing flood-prone areas in eastern India and helps to take measures for strategic management and preparing for progress.

(Roy et al., 2020) investigated the Threats of Climate and Land Use Change on Future Flood Susceptibility in the Ajoy River Basin, India. The study employed three machine learning approaches—Support Vector Machine (SVM), Random Forest (RF), and Biogeography-Based Optimization (BBO)—within a GIS environment to map flood-prone areas. The models incorporated a range of flood susceptibility factors, including topographic, hydrological, soil, environmental, and geological characteristics. Model performance was assessed using the Receiver Operating Characteristic (ROC) curve and the Area Under the Curve (AUC) metric, which indicates the probability of flood occurrence under given conditions. Results showed that the BBO model achieved the highest predictive accuracy with an AUC of 0.985, followed by RF (0.925) and SVM (0.896). Based on these results, the study concluded that the BBO approach provides a highly reliable method for identifying flood-prone areas, particularly in the eastern part of India.

(Hao et al., 2019) examined Land Use Change and Climate Variation in the Three Gorges Reservoir Catchment (TGRC) from 2000 to 2015 using the Google Earth Engine (GEE) platform. Leveraging GEE’s cloud-based system and its extensive geoscience and remote sensing archives, the study analyzed both land use/land cover change (LULCC) and climate variation in the catchment. GlobeLand30 data were employed to assess spatial land dynamics for 2000–2010, while Landsat 8 OLI imagery was used for 2015. Interannual variations in land surface temperature (LST) and seasonally integrated normalized difference vegetation index (SINDVI) were derived from MODIS products. In addition, climate variables including air temperature, precipitation, and evapotranspiration were obtained from the Global Land Data Assimilation System (GLDAS). The results showed that between 2000 and 2015, cultivated land and grassland decreased by 2.05% and 6.02%, respectively, whereas forest, wetland, artificial surfaces, shrubland, and water bodies increased by 3.64%, 0.94%, 0.87%, 1.17%, and 1.45%. The SINDVI rose by 3.209 during the period, while the LST declined by 0.253 °C between 2001 and 2015. However, LST increased in urbanized areas while declining in forested zones, with Chongqing City consistently exhibiting the highest LST. Similarly, reductions in SINDVI were most pronounced in urbanized regions, while higher vegetation indices were observed in the eastern TGRC, particularly in Wuxi, Wushan, and Xingshan counties. Climate trends during 2000–2015 revealed increases in air temperature (0.0678 °C/year), precipitation (1.0844 mm/year), and evapotranspiration (0.4105 mm/year). Although LULCC influenced local climate patterns, its effect was relatively minor compared to broader regional climate drivers in Southwest China. The study also established a significant negative correlation between LST and SINDVI across most of the TGRC, particularly in areas experiencing urban expansion and forest growth.

(Zurqani et al., 2018) studied Geospatial analysis of land use change in the Savannah River Basin using Google Earth Engine. The objectives of this study are to: 1) determine the classes and the distribution of land cover in the Savannah River basin; 2) identify the spatial and the temporal change of the land cover that occurs as a consequence of land use change in the area; and 3) discuss the potential effects of land use change in the Savannah River basin. The land cover maps were produced using random forest supervised classification at four time periods for a total of thirteen common land cover classes with overall accuracy assessments of 79.18% (1999), 79.41% (2005), 76.04% (2009), and 76.11% (2015). The major land use change observed was due to the deforestation and reforestation of forest areas during the entire study period. The change detection results using the normalized difference vegetation index (NDVI) indicated that the proportion areas of the deforestation were 5.93% (1999–2005), 4.63% (2005–2009), and 3.76% (2009–2015), while the proportion areas of the reforestation were 1.57% (1999–2005), 0.44% (2005–2009), and 1.53% (2009–2015).

(Pandey et al., 2022) examined the application of *Google Earth Engine (GEE) for Large-Scale Flood Mapping Using SAR Data and Impact Assessment on Agriculture and Population in the Ganga-Brahmaputra Basin*. The study focused on the severe flood events that occurred between July and September 2020, which heavily impacted Bihar, West Bengal, and Assam in India, as well as neighboring Bangladesh. Using Sentinel-1A Synthetic Aperture Radar (SAR) data within the GEE platform, the researchers mapped flood extents and quantified inundation. The total flooded area during the study period was estimated at 25,889.1 km² in Bangladesh, 20,837 km² in Bihar, 17,307.1 km² in West Bengal, and 13,460.1 km² in Assam.

The Copernicus Global Land Cover dataset was employed to identify affected agricultural lands and settlements, showing that floods inundated 23.68–28.47% of farmland and 5.66–9.15% of settlement areas. To assess human impacts, the Gridded Population of the World (GPW) density data and the Global Human Settlement Layer (GHSL) were utilized, revealing that approximately 23.29 million people were directly affected by flooding in the basin. The highest population impacts were observed in Bihar, where communities live predominantly in low-lying valleys and riverbanks due to their dependence on river water. Bangladesh also recorded severe impacts owing to its high population and settlement densities.

(Mehmood et al., 2021) studied Mapping of Flood Areas Using Landsat with Google Earth Engine Cloud Platform. This study employed Landsat 5, 7, and 8 imageries to delineate flood inundation areas, with data processing carried out in Google Earth Engine (GEE) through the implementation of a Flood Mapping Algorithm (FMA). The FMA approach is based on constructing a "data cube," which integrates spatially overlapping pixels from Landsat imagery acquired over multiple time periods. Using this cube, temporary and permanent water bodies were distinguished by applying the Modified Normalized Difference Water Index (MNDWI), alongside site-specific elevation and land use data.The accuracy of the method was evaluated through a confusion matrix across nine global flood events. Results demonstrated a high true positive detection rate of 71–90% and overall accuracy between 74–89%. These findings highlight the potential of the FMA in GEE as a rapid and reliable tool for mapping flood inundation. Moreover, the approach offers valuable applications for training artificial intelligence (AI) models and strengthening ongoing initiatives in flood mitigation, monitoring, and management.

(Loukika et al., 2021) studied Analysis of Land Use and Land Cover Using Machine Learning Algorithms on Google Earth Engine for Munneru River Basin, India. With the increasing demand for reliable LULC mapping from remotely sensed data, it is essential to evaluate the performance of different machine learning classifiers. The present study aimed to classify LULC within the Google Earth Engine (GEE) platform using three machine learning algorithms—Support Vector Machine (SVM), Random Forest (RF), and Classification and Regression Trees (CART)—and to compare their effectiveness through accuracy assessments. A supervised classification approach was adopted, with the inclusion of vegetation and water indices (NDVI and NDWI) to enhance classification precision. Multitemporal datasets from Sentinel-2 (10 m resolution) and Landsat-8 (30 m resolution) for the years 2016, 2018, and 2020 were utilized to generate LULC maps, categorizing the area into five primary classes: water bodies, forest, barren land, vegetation, and built-up areas. The average overall classification accuracies obtained for Landsat-8 imagery were 90.88% (SVM), 94.85% (RF), and 82.88% (CART), while Sentinel-2 imagery yielded accuracies of 93.8% (SVM), 95.8% (RF), and 86.4% (CART). These results clearly demonstrate that the RF classifier consistently outperforms both SVM and CART in terms of accuracy, making it a more robust choice for LULC classification in this context.

(Lal et al., 2020) worked on Google Earth Engine for concurrent flood monitoring in the lower basin of Indo-Gangetic-Brahmaputra plains. The research work focused on the recent flood inundation (July 2020) that occurred in the lower Indo-Gangetic-Brahmaputra plains (IGBP) using concurrent C-band Sentinel-1A Synthetic Aperture Radar images in Google Earth Engine. The study exhibited that a substantial proportion of IGBP (40,929 km2) was inundated primarily in Bangladesh (9.09% of the total inundation), Assam (8.99%), and Bihar (6.29%) during June–July 2020. The severe impact of flood inundation was observed in croplands (4.41% of the total cropland), followed by settlements (20.98% of the total settlements) that affected a large population (~ 10,046,262) in IGBP. The prevailing COVID-19 pandemic has debilitated the efforts of mitigation and responses to flooding risks. The study necessitates adopting an integrated, multi-hazard, multi-stakeholder approach with an emphasis on self-reliance of the community for sustenance with local resources and practices.

(Pham et al., 2021) studied Specifying the relationship between land use/land cover change and dryness in central Vietnam from 2000 to 2019 using Google Earth Engine. This research presents a first attempt to specify the relationship between LULC change and dryness in a region of Vietnam that is profoundly affected by climate change. Using the temperature–vegetation dryness index (TVDI), we specified the relationships and changes underway in Vietnam's Ba river basin, one of the largest river systems in the South Central Coast. Using Google Earth Engine, we extracted land use data from Landsat images and calculated TVDI values from Moderate Resolution Imaging Spectroradiometer (MODIS) data for 2000 to 2019. We found, first, that agricultural area and deforestation rose by 7.2% and 2.4% annually, respectively. These changes were driven by economic development, rising crop prices, illegal logging, wildfires, and emergence of new agricultural areas. Second, areas classified in the driest TVDI intervals (dry and very dry) occupied 57% of the basin in 2019, 70% of which was agricultural lands and 20% other (mainly urban and bare lands). These driest land categories expanded at an average rate of 0.08% to 0.1% per year. Moreover, 90% of areas classified as "very wet" and "wet" were forest. We observed a strong relationship between LULC change and TVDI.

(Shilengwe et al., 2023) investigated *Synthetic Aperture Radar and Optical Sensor Techniques Using Google Earth Engine for Flood Monitoring and Damage Assessment: A Case Study of Mumbwa District, Zambia*. The study analyzed the December 2020 flood event using both radar- and optical-based satellite sensors. Sentinel-1B Synthetic Aperture Radar (SAR) data were processed on the Google Earth Engine (GEE) platform to generate image mosaics covering the period from December 2020 to May 2021, which were then used to delineate flood extents. Flood mapping employed a local histogram thresholding and change detection approach based on image ratios, where an intensity value of 1.26 dB—tailored specifically for the study area—proved more effective than the global threshold of 1.25 dB.

To refine the flood extent, areas inundated during the flood were filtered using auxiliary datasets. The HydroSHEDS Digital Elevation Model (DEM) excluded regions with slopes greater than 7%, while the Global Surface Water Layer removed zones of permanent water bodies. Once the inundation areas were accurately identified, Sentinel-2 optical data were used to produce a Land Use Land Cover (LULC) map for August 2020, allowing the flood extents to be overlaid with land cover features. The LULC classification, conducted in GEE using the Random Forest algorithm, achieved an overall accuracy of 0.957 and a Kappa coefficient of 0.915. These results were then applied in carrying out detailed flood analysis and damage assessment for the affected district. The quantitative damages to Landcover were found to be: Wetland 6,338.97 Ha (33.27%), Shrubland 5,117.75 Ha (26.89%), Biochar Soil 3,660.47 Ha (19.21%), Trees 3,466.37 Ha (18.19%), Bare soil 273.47 Ha (1.44%), Crop Fields 190.69 Ha (1%) and Built-Up 4.13 Ha (0.02%).

(DeVries et al., 2020) studied Rapid and robust monitoring of flood events using Sentinel-1 and Landsat data on the Google Earth Engine. This research presents an algorithm that exploits all available Sentinel-1 SAR images in combination with historical Landsat and other auxiliary data sources hosted on the GEE to rapidly map surface inundation during flood events. This algorithm relies on multi-temporal SAR statistics to identify unexpected floods in near real-time. Additionally, historical Landsat-based surface water class probabilities are used to distinguish unexpected floods from permanent or seasonally occurring surface water. The algorithm was further assessed over three recent flood events using coincident very high- spatial resolution imagery and operational flood maps. Using very high resolution optical imagery, an area-normalized accuracy of 89.8 ± 2.8% (95% c.i.) was estimated over Houston, Texas following Hurricane Harvey in late August 2017, representing an improvement of between 1.6% and 9.8% over flood maps derived from a simple backscatter threshold. Additionally, comparison of the results with SAR-derived Copernicus Emergency Management Service (EMS) maps following devastating floods in Thessaly, Greece and Eastern Madagascar in January and March 2018, respectively, yielded overall agreement rates of 98.5% in both cases.

(Moharrami et al., 2021) studied Automatic flood detection using sentinel-1 images on the google earth engine. This research present flood event monitoring by Sentinel-1 images. The Otsu thresholding algorithm was applied to separate flooded areas from remaining land covers. The threshold value of −14.9 dB was derived and applied to each scene to delineate flooded areas. There was high variability of the inundated area; however, the presented threshold correctly represented the variation of the flood. The resultant maps were further verified by independent datasets. The overall accuracies were higher than 90%, confirming the applicability of the Otsu automatic thresholding method in flood mapping.

(Tiwari et al., 2020) studied Flood inundation mapping- Kerala 2018; Harnessing the power of SAR, automatic threshold detection method and Google Earth Engine. In the present study, Sentinel-1 Synthetic Aperture RADAR (SAR) data and Otsu method were utilized to map flood inundation areas. Google Earth Engine (GEE) was used for implementing Otsu algorithm and processing Sentinel—1 SAR data. The results were assessed by (i) calculating a confusion matrix; (ii) comparing the submerge water areas of flooded (Aug 2018), non-flooded (Jan 2018) and previous year's flooded season (Aug 2016, Aug 2017), and (iii) analyzing historical rainfall patterns to understand the flood event. The overall accuracy for the Sentinel-1 SAR flood inundation maps of 9th and 21st August 2018 was observed as 94.3% and 94.1% respectively. The submerged area (region under water) classified significant flooding as compared to the non-flooded (January 2018) and previous year's same season (August 2015–2017) classified outputs.

(Akpejiori et al., 2017) carried out a study that analyses flood risk potential in Agenebode, Edo state, Nigeria. Flood frequency analysis was carried out on discharge data from the River Niger at Onitsha from 1960-2006 as the discharge from this river is the primary cause of flooding of the study area. Log-Normal, Log-Pearson Type III and Gumbel probability distribution models were used to test for the most appropriate projection for discharge for different return periods. From the analysis, Log-normal distribution was selected as the most appropriate probability distribution for the series in order to determine projected flows for the river for different return periods. The rainfall pattern for the study area was analyzed using gauge values for the period 1983-2010. Flood hazard assessment was carried out with the aid of ArcMap using the topographical feature data of the area, Digital Elevation Model obtained from Shuttle Radar Topographical Mission (SRTM) hole-filled seamless data and historical records of the previous flood occurrence. A flood hazard map produced indicated that about 1.8 km2 (72% of the total built-up area) of the area is at risk of flooding putting approximately 481 people at direct risk of flooding.

Based on the literature review conducted on the topic of this research, it is observed that flood analysis is an active research area which have cut the attention of the scientific environment. This can be deduced from the fact that the corresponding environmental impact of flood event is overwhelming and has a significant economic and social effect. In spite of these, it can be concluded that there is limited research on the use of remote sensing and Machine learning for analyzing the impact of land use/land cover change and climate change on flooding in the lower Niger region of Nigeria. Although, there have been studies on the of remote sensing and machine learning for flood management and mitigation in other region of the world. With the proliferation of Machine learning algorithms in most research work, there are still great limitation on the use of machine learning algorithm for modeling and predicting flooding pattern in the lower Niger region of Nigeria. On the basis of climate change, land use and land cover changes it becomes imperative for in-depth research to be conducted on the correlative relationship between these environmental elements and flood event in the lower Niger Region of Nigeria. From the list of reviewed literatures for this research work, it can be observed that there are lack of scientific work done in this aspect.

2.15 Research Gap

Although numerous studies have examined rainfall variability, land use/land cover (LULC) dynamics, and flooding in Nigeria, a careful review of the literature reveals several unresolved issues and methodological limitations, particularly concerning the Lower Niger Region. These gaps are as follows;

Limited Integration of Multi-Source Datasets: Most previous hydrological and climate studies in Nigeria have relied on either gauge-based or single-source satellite rainfall datasets, such as TRMM or CHIRPS, without comprehensive cross-validation against in-situ observations. This limits the reliability of spatio-temporal rainfall trend detection, especially in areas with sparse or inconsistent ground data. There remains a gap in studies that integrate multiple remotely sensed rainfall datasets (e.g., CHIRPS, PERSIANN-CDR, TRMM) and validate them with NiMET gauge data to ensure accuracy and representativeness.

Inadequate Long-Term Climate Trend Analysis for the Lower Niger Region: While some studies have assessed rainfall trends in northern and southwestern Nigeria, very few have provided a multi-decadal (1981–2023) hydroclimatic analysis for the Lower Niger Region. The existing studies often use short or fragmented time series, which fail to capture long-term variability and potential climate-induced shifts in rainfall and temperature patterns. This leaves a substantial temporal gap in understanding the evolving hydroclimatic regime of the region.

Limited Use of Cloud-Based Platforms for Spatio-Temporal Analysis: The use of cloud-computing environments like Google Earth Engine (GEE) for large-scale hydrological analysis remains underexplored in Nigeria. Many prior works employed conventional desktop GIS and image processing tools, which restrict data volume, temporal depth, and processing efficiency. There is a lack of integrated, GEE-based workflows capable of handling multi-sensor data for rainfall, LULC, and flood assessment simultaneously.

Insufficient Application of Advanced Machine Learning Models for Flood Susceptibility Mapping: Although flood mapping studies in Nigeria have traditionally used empirical or statistical methods (e.g., frequency analysis, logistic regression, AHP), the application of machine learning algorithms such as Random Forest (RF) and Support Vector Machine (SVM) remains limited. These models offer superior predictive capabilities for flood susceptibility and spatial risk assessment, yet few studies have leveraged their full potential to model flood dynamics in the Lower Niger Basin.

Lack of Integrated Assessment Linking LULC, Temperature, and Flood Dynamics: Existing studies often treat rainfall variability, land cover change, and flood incidence as separate research themes. However, the interconnected nature of these processes, where land conversion intensifies runoff and temperature rise affects evapotranspiration and rainfall regimes, has not been comprehensively evaluated in the Lower Niger Region. A multi-variable correlation analysis linking LULC change, surface temperature variation, and flood patterns remains largely absent.

Inadequate Empirical Data for Flood Risk Decision Support: The absence of continuous monitoring and open-access flood datasets has limited the development of spatial decision-support systems for flood management in the region. Most flood management strategies rely on anecdotal or event-based data rather than systematic spatio-temporal modeling. Therefore, there is a need for data-driven, machine-learning-supported frameworks that can predict flood susceptibility zones and guide climate-resilient planning.

Despite numerous studies on flooding and climate variability in Nigeria, there remains a significant research gap in understanding the combined influence of land use/land cover (LULC) changes, climate variability, and flooding, particularly within the Lower Niger region. Most prior research has focused on either hydrological modeling, rainfall frequency, or flood hazard mapping in isolation, without integrating these factors into a comprehensive analytical framework.

CHAPTER THREE

MATERIALS AND METHODOLOGY

3.1 Description of Study Area

This research methodology is designed to respond to the research objectives. Thus, it is arranged to fit the various objectives. Figure 3.1 present the Study area map for this research work. The study area is the Lower Niger Region of Nigeria, specifically consisting of four states which are Edo, Delta, Bayelsa, and Rivers States. These states form part of the Southern geopolitical zone of Nigeria and are strategically situated within the Lower Niger River Basin, a region that is highly sensitive to climate variability and land use/land cover (LULC) changes. The region lies approximately between latitude 4°00′N to 7°30′N and longitude 5°00′E to 8°00′E. The region is characterized by a humid tropical climate, due to its high rainfall events, especially during the monsoon season which is from April to October. The average annual rainfall ranges from 2,000 mm to 3,500 mm, with significant spatial and temporal variation influenced by proximity to the Atlantic Ocean and prevailing wind patterns. The terrain consists largely of low-lying floodplains, mangrove swamps, rainforests, and riverine environments, making it highly vulnerable to recurrent flooding events, especially during peak rainy months.

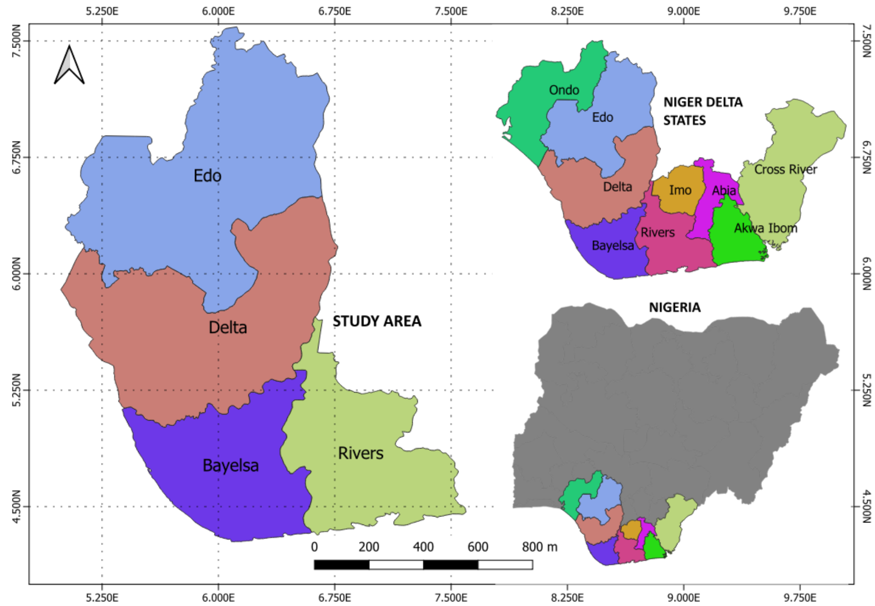

Figure 3.1: Study Area for the Research

Edo State, located in the northern part of the study area, is a transitional zone between the savanna and rainforest belts. This state serves as an important upstream area where land use dynamics—especially urban expansion, deforestation, and agricultural activities—have serious downstream hydrological impacts (Ridha et al., 2022). The state is also home to several rivers and tributaries feeding into the Lower Niger system, making it ecologically significant in regional watershed functioning.

Delta State, which lies centrally in the study area, plays a critical role in the Niger Delta hydrological system. It is traversed by multiple tributaries of the Niger River and is highly susceptible to flooding due to its low elevation, poorly drained soils, and dense river networks (Jerome Glago, 2021)("Flood Disaster Hazards; Causes, Impacts and Management," 2021). Rapid LULC changes in the state, driven by urbanization, oil exploration, and agricultural encroachment, have significantly altered natural drainage patterns and increased surface runoff, thereby amplifying flood risks (Prokešová et al., 2022).

Bayelsa State, located in the southernmost part of the study area, is characterized by extensive wetlands, tidal inlets, and creeks. It ranks among the most flood-prone states in Nigeria due to its coastal location, low relief, and fragile deltaic environment (Dalil et al., 2015). The dominance of aquatic vegetation, mangrove ecosystems, and waterlogged soils provides a unique ecological system that is highly sensitive to both climatic stressors and anthropogenic alterations, such as oil spills and infrastructure development (Onyena and Sam, 2020).

Rivers State lies to the southeast of the study area and is also significantly influenced by the Atlantic Ocean. The state features a complex hydrological system consisting of interconnected rivers, estuaries, and creeks. With rapid industrialization, port expansions, and population growth, Rivers State has experienced significant LULC transformations, which have altered its flood regime by increasing impermeable surfaces and disrupting natural waterways (Dan-Jumbo et al., 2018).

The study area, situated within the broader context of Southern Nigeria, occupies a significant portion of the Niger Delta, Nigeria's largest river delta and one of the most ecologically diverse wetlands globally. This region serves as a convergence point for major tributaries of the Niger River before draining into the Atlantic Ocean. Its hydrological positioning makes it particularly suitable for studies on flood modeling and climate interaction. The selection of this region is informed by its high vulnerability to flooding, shaped by dynamic interactions among land use transitions, climate variability, and hydrological sensitivity (Aich et al., 2016). The states chosen for analysis represent a gradient from upstream to downstream conditions and encompass a diverse mix of urban, peri-urban, agricultural, forested, and wetland ecosystems. This diversity is crucial for understanding the spatial and temporal variability of flood patterns and the role of human-induced and climatic drivers in modifying them.

3.2 Data Collection

This section outlines the various datasets employed in the study for rainfall analysis, land use/land cover (LULC) mapping, and flood inundation assessment. Ground-based daily rainfall data was sourced from the Nigerian Meteorological Agency (NiMet) and other institutions, with thorough checks for consistency and station stability. Complementary satellite-based rainfall datasets—including CHIRPS, PERSIANN-CDR, and PERSIANN-CCS were accessed using Google Earth Engine for the period spanning 1985 to 2023. For LULC classification, time-series imagery from Landsat 8 OLI and Sentinel-2 were utilized, offering high spectral and temporal resolution. Flood extent mapping incorporated Sentinel-1 SAR (VV polarization), which is favored for its superior accuracy in inundation detection. Additionally, administrative boundaries and historical water level records were obtained from relevant authorities to support spatial analysis and flood modeling.

3.2.1 Dataset

Daily rainfall data was retrieved from the Nigeria Meteorological Agencies (NiMet) and other relevant agencies. The gauge characteristics which include, coordinates, elevation and description were also collected so as to provide a base point for correlating satellite datasets. The gauge data were checked for consistency and homogeneity in terms of duration and ensure there have not been relocation of station within the period of the study and to ascertain the fitness of datasets from different agencies.

Remotely sensed data was retrieved from CHIRPS, PERSIANN-CDR and PERSIANN-CCS satellite-based data sources. These datasets were extracted using the Google Earth Engine (GEE) web-based remote sensing platform for the period of 1985 to 2023. The CHIRPS data is a combination of in-situ, satellite and global precipitation system which will be derived from the climate Hazard Group website with the help of GEE via the CHRS data portal. The PERSIANN-CDR has provided a near-global precipitation dataset for almost 40 years starting from January 1983 to date. It provides daily rainfall measurement at 0.25^0 x 0.25^0 scales. While the PERSIANN-CCS is a real-time high resolution global product providing precipitation estimate at 0.04^0 x 0.04^0 scale.

Sentinel 2 and Landsat 8 Operational Land Imager (OLI) time series data were used to map LULC classes. The L-8 OLI consists of nine spectral bands (costal: 443nm, blue: 485nm, green: 563nm, red: 655nm, panchromatic: 640nm, NIR: 865nm, short-wave infrared1 (SWIR1): 1610nm, SWIR2: 2200nm, and cirrus: 1375nm). The S2 provides high temporal resolution data with a rich spectral configuration, including 13 spectral bands. It has six land monitoring bands that are comparable with Landsat-8 (blue: 490nm, green: 560nm, red: 665nm, NIR: 842nm, SWIR1: 1910nm, SWIR2: 2190nm) and three additional bands covering the red-edge part of the spectrum which are centered at 705nm, 740nm, and 783nm and NIR narrow band at 865nm.

In order to estimate the flood pattern for the study area, remote sensing indices were used for the period. Administrative boundaries of the whole area and other spatial features were retrieved.

Table 3.1: Dataset Requirement for this research

S/N	Data	Source	Purpose
1	Daily rainfall data	CHIRPS, PERSIANN-CDR and PERSIANN-CCS	Rainfall Analysis
2	Rainfall Data	Meteorological Agencies and other relevant agencies	Validation of Remotely Sensed Rainfall Data
3	sentinel 2	Google Earth Engine: https://developers. google.com - Acquisition date: 29 October 2021	LULC Analysis
4	Landsat 8 Operational Land Imager (OLI) time series	Google Earth Engine: https://developers. google.com - Acquisition date: 29 October 2021	LULC Analysis
5	Shapefile of the Study Area	River Basin Development Authorities and other relevant agencies	Administrative boundaries and other Geological Feature of Niger Delta Region.

3.2.2 Digital Elevation Model (DEM)

The elevation and slope of the study area were extracted from the Shuttle Radar Topography Mission (SRTM) Digital Elevation Model (DEM) band. The SRTM-DEM provides elevation data at a resolution of 1 arc second (approximately 30m). it is a near-global DEM which covers a range of 60^0N to 56^0S latitude, built on the data collected by a specially modified radar system onboard the space shuttle Endeavour (SSE) during 11 days in February 2000 (Yang et al., 2011).

3.2.3 Reference\Training Datasets and LULC Classes

A high classification accuracy of remotely sensed datasets requires a substantial volume of training and validation samples, which serve as reference data to improve model reliability (Garcia-Salgado et al., 2020; Ma *et. al*., 2019). Therefore, this study adopted the visual inspection of high-resolution satellite imagery to manually extract both training and validation samples, ensuring the reference data reflect real-world land cover accurately (Zhou *et. al*., 2020).

The land use/land cover (LULC) analysis focuses on classifying five dominant classes: water bodies, forest, barren land, vegetation, and built-up areas. Agricultural plantations and other cultivated green areas were also categorized under vegetation, while features such as rivers and ponds were classified as water bodies. To perform the classification, a Random Forest (RF) algorithm was used, which is a widely adopted ensemble learning method known for its high accuracy, robustness against overfitting, and suitability for remote sensing applications (Rodriguez-Galiano *et. al*., 2018; Liu *et. al*., 2020). The accuracy of the classification were evaluated using established metrics such as the Overall Accuracy (OA), Kappa Coefficient, User's Accuracy, and Producer's Accuracy, following best practices outlined in recent literature (Li *et. al*., 2022).

Furthermore, data acquisition is a critical component of scientific research and must be guided by theoretical soundness, systematic procedures, and rigorous quality control and error correction techniques (Petropoulos *et. al*., 2019). For this study, two types of rainfall data were retrieved: gauge rainfall data and satellite-based rainfall data. Gauge data offers localized, point-based and real-time observations, while satellite-derived rainfall data provide a spatially distributed time-series representation, enabling a more comprehensive and robust analysis of rainfall dynamics (Ashouri *et. al*., 2015; Zambrano-Bigiarini *et. al*., 2019). The integration of both datasets enhances the spatial and temporal resolution of the analysis and supports the development of more accurate flood and rainfall models (Awange *et. al*., 2020).

3.3 Data Preprocessing and Statistical Application

3.3.1 Rainfall Data Validation and Homogeneity Testing

Rainfall data from observed gauge stations were utilized to validate the accuracy of remotely sensed rainfall datasets. This validation ensures the reliability and suitability of the satellite products and supports the selection of the best-fitting dataset for the study area.

To perform this validation, several well-established statistical tests were employed:

- Pettitt's Test
- Buishand's Range Test
- Standard Normal Homogeneity Test (SNHT)
- Double Mass Curve (DMC)

These methods are commonly used for detecting breakpoints and testing the homogeneity of hydro-meteorological data over time (Lin *et. al*., 2020). Ensuring data homogeneity is crucial for accurate trend analysis and climate assessments.

3.3.2 Retrieval, Aggregation, and Evaluation of Satellite-Based Rainfall Data

Monthly, seasonal, and annual gridded rainfall products were retrieved using the Google Earth Engine (GEE) platform. The data extraction utilized the ee.ImageCollection function along with ee.Filter.calendarRange to define the time period of interest (Gorelick *et. al*., 2017). The spatial extent of the analysis was controlled using the clip function to align the data with the study area.

To harmonize the satellite gridded data with ground-based gauge observations, a nearest-neighbor pixel approach was applied. This method extracts rainfall values from the closest pixel to each station location for consistent comparison (Dinku *et. al*., 2018).

For long-term rainfall trend analysis, the Sen's Slope Estimator was implemented via ee.Reducer.senSlope. This non-parametric method estimates monotonic trends in time series data and is preferred for climate studies due to its resistance to outliers (Zhang *et. al*., 2021).

Daily rainfall values were also aggregated to:

- Seasonal totals (Rainy and Dry seasons)
- Annual totals

To validate the satellite data against gauge observations, the following statistical metrics were used:

- Correlation Coefficient (CC): Measures the linear relationship between datasets.
- Root Mean Square Error (RMSE): Quantifies overall differences between observed and estimated values.
- Mean Absolute Error (MAE): Provides the average magnitude of the errors.
- Mean Error (ME): Indicates the bias in estimates.

These statistical indices offer comprehensive insights into the performance of satellite rainfall products (Nury *et. al*., 2021; Khosravi *et. al*., 2020).

3.4 Change Detection Analysis Over the Niger Delta

The most suitable rainfall data set were retrieved and processed for change analysis. Spatial analysis was carried out for the region using specific time period. This was used to study the area distribution of rainfall pattern in the study area. In order to analyze rainfall change pattern, rainfall variability index was calculated. Rainfall index is commonly computed as the standardize precipitation departure and helps to separate the available rainfall time series into different climate regime such as very dry climatic year, normal climatic year and wet or very wet climatic year. The equation for estimating rainfall variability index is given as (Y. F. Huang et al., 2022);

$$\boldsymbol{\delta_i = {(P_i - \mu)}/{\sigma}} \qquad \textbf{(3.1)}$$

Where δ_i is rainfall variability index for year i, P_i is annual rainfall for year $i, \mu\ and\ \sigma$ are the mean rainfall and standard deviation for the period between the time period.

Trend analysis was also carried out using the Mann-Kendall non-parametric test. This method is commonly used in the hydro-climatological time series (Ogunrinde et al., 2023), to test for the presence of trends. The Mann-Kendall rank correlation statistic τ is derived from the following equation (Hamed, 2009; McLeod, 2005);

$$\boldsymbol{\tau = \frac{4\sum_{i=1}^{N-1} n_i}{N(N-1)} - 1} \qquad \textbf{(3.2)}$$

The Mann-Kendall test has two parameters that are of particular importance for trend detection. These parameters are the slope magnitude estimate. This indicated the direction and magnitude of the trend. A positive value in the test result indicates an upward trend while a negative value indicates a downward trend.

3.5 Land Use/Land Cover Analysis Using Machine Learning Algorithm

3.5.1 Digital Elevation Model (DEM)

The elevation and slope of the study area were extracted from the Shuttle Radar Topography Mission (SRTM) Digital Elevation Model (DEM) band. The SRTM-DEM provides elevation data at a resolution of 1 arc second (approximately 30m). it is a near-global DEM which covers a range of 60^0N to 56^0S latitude, built on the data collected by a specially modified radar system onboard the space shuttle Endeavour (SSE) during 11 days in February 2000 (Yang et al., 2011).

3.5.2 Reference\Training Datasets and LULC Classes

A high classification accuracy of the remotely sensed datasets requires large sets of training and validation samples which were used as reference datasets. Thus, a visual inspection of high-resolution satellite imagery method was used to extract training and validation samples for this research. LULC analysis was done by identifying and classifying five LULC classes; water bodies, forest, barren land, vegetation and build-up areas. Agricultural and Plantations and other green farmlands were considered as vegetation while river and pond were considered as water bodies. A support vector machine (SVM and the random forest (RF) classifier were used to produce LULC maps and the classification accuracy were obtained.

3.5.3 Time Series Analysis

The Google Earth Engine (GEE) cloud computing platform was used to create image collections and process time series data from 2013 to 2023. Landsat 8 (L8) imagery over the study area was processed to extract spectral-temporal metrics used as predictors for Land Use/Land Cover (LULC) classification. Images with less than 15% cloud cover were selected. Cloud, cloud shadow, and snow were masked using the Function of Mask (FMASK) algorithm. During the masking process, the results were visually inspected, and all parameters were iteratively refined until optimal results were achieved.

3.5.4 Land Use Land Cover Classification Accuracy Assessment

The extracted polygons for the various LULC classes were used to train both the Random Forest (RF) and Support Vector Machine (SVM) classifiers. RF is an ensemble learning method that combines multiple decision trees, offering advantages such as reduced processing time, fewer parameter adjustments, and minimal manual intervention. SVM, on the other hand, is a supervised learning algorithm known for its high accuracy but typically requires more fine-tuning and computational resources.

For the RF classification, 500 decision trees (i.e., *ntree* = 500) were used. Both classifiers were trained and tested on the respective datasets to generate the LULC classifications. Classification accuracy was assessed by comparing the classified outputs from the testing phase with ground-truth polygon samples using confusion matrices. From the confusion matrices, global accuracy metrics such as Overall Accuracy (OA) and the Kappa Coefficient (K) were computed to evaluate and compare the performance of the RF and SVM classifiers on the LULC classification task.

$$\boldsymbol{Overall\ Accuracy\ (OA)} = \frac{\boldsymbol{Number\ of\ Correctly\ Classified\ Samples}}{\boldsymbol{Number\ of\ Total\ Samples}} \quad \textbf{(3.3)}$$

$$\boldsymbol{kappa\ (k)} = \frac{\boldsymbol{Overall\ accuracy - Estimated\ Chnace\ Agreement}}{\boldsymbol{1 - Estimated\ Chance\ Agreement}} \quad \textbf{(3.4)}$$

3.6 Estimating Land Surface Temperature

To validate the use of remotely sensed maximum temperature datasets in this study, a comparative analysis was conducted using satellite-derived temperature data and ground-based observations from the Nigerian Meteorological Agency (NiMET) station in Benin City, Edo State. This validation was necessary to ensure the suitability of the satellite datasets for temperature trend analysis, particularly in a region like Nigeria where ground station coverage is limited.

Two widely used gridded temperature datasets ERA5 and CPC were selected for evaluation due to their global availability and accessibility on Google Earth Engine. The maximum temperature values from both datasets were extracted for the exact coordinates of the NiMET station in Benin City, covering the period from 1971 to 2023. The observed daily temperature records from NiMET were collected, cleaned, and aggregated to match the temporal resolution of the satellite data to ensure consistency in the comparison. Preprocessing involved aligning the satellite and observed datasets to the same time scale, handling any missing values through linear interpolation, and spatially averaging the satellite data over the station location. Once harmonized, both satellite datasets were evaluated using seven statistical metrics: Mean Bias Error (MBE), Mean Absolute Error (MAE), Root Mean Square Error (RMSE), Pearson Correlation Coefficient (PCC), Nash–Sutcliffe Efficiency (NSE), Kling–Gupta Efficiency (KGE), and the Coefficient of Determination (R^2). Willmott's Index of Agreement (d) and the Mean Absolute Percentage Error (MAPE) were also calculated to provide a more comprehensive performance assessment.

In addition to the numerical analysis, scatter plots were generated to visually assess the relationship between the observed and satellite-derived maximum temperature values. These plots provided a clear visual representation of the strength of correlation and the degree of error dispersion between datasets. The performance of each dataset was then assessed based on these statistical indicators and visual observations. The CPC dataset exhibited lower RMSE, MAE, and bias values, as well as higher values for Willmott's d and MAPE, indicating a better overall match with the observed Tmax data. However, the ERA5 dataset demonstrated a stronger correlation and a better ability to capture temporal variability in the temperature data.

3.7 Estimating Flood Indices

To assess the spatial and temporal patterns of flooding in the study area, this research employed a multi-index remote sensing approach using satellite-derived flood indices over a 24-year period (2000–2023). The methodology was designed to integrate both time series analysis and spatial distribution mapping, enabling a comprehensive understanding of surface water dynamics, flood-prone areas, and hydrological variability across the state.

Satellite imagery was accessed and processed using the Google Earth Engine (GEE) platform, which enabled the generation of consistent, cloud-free composites and index calculations over the long-term study period. A suite of spectral indices commonly used in flood monitoring and surface water detection were selected based on their scientific robustness and relevance in tropical regions. These indices included:

a) Automated Water Extraction Index (AWEI)
b) Flood Water Index (FWI)
c) Modified Normalized Difference Water Index (MNDWI)
d) Normalized Difference Vegetation Index (NDVI)
e) Normalized Difference Water Index (NDWI)
f) Water Ratio Index (WRI)

Each index was computed annually from 2000 to 2023 to capture the temporal dynamics of surface water and flooding. These values were then aggregated and visualized using time series plots to identify major flood years and assess temporal variability. Additionally, spatial annual average maps for each index were generated to visualize the distribution of flood-prone and water-logged areas across the study area. In order to carry out temporal analysis, annual mean values of each index were plotted in multi-year time series charts to observe long-term trends, peak flood years, and hydrological anomalies. Also, annual average of each index over the entire study period was mapped to reveal persistent patterns of surface water presence, floodplain extent, and wetland dynamics for the spatial analysis.

3.8 Modelling and predicting flooding patterns in the Lower-Niger region by using machine leaning algorithms

Flood pattern modeling using Machine Learning Algorithm consists of the generation and application of the model constrains which are obtained from results of previous objectives. The methodological procedure for developing a machine learning model requires data pre-processing which include data scaling, training and testing.

3.8.1 Feature Selection

Feature selection is an essential process used to reduce data dimensionality prior to model development. This preprocessing step involves identifying the most informative variables from all the collected metrics, thereby improving model efficiency and accuracy. Several methodologies can be employed for feature selection, including expert domain knowledge, variance-based filtering, mutual information, and recursive feature elimination (Kuzudisli et al., 2023). Selecting relevant features not only improves the interpretability of models but also reduces overfitting and training time.

3.8.2 Feature Scaling

Feature scaling, also known as normalization, ensures that variables are brought to a comparable scale, which is critical for algorithms sensitive to the magnitude of data, such as gradient descent or k-nearest neighbors. Two commonly used techniques include:

- **Min-Max Scaling**:

Transforms each feature to a range [0,1] using the formula: $\frac{x-x_{min}}{x_{max}-x_{min}}$.

- **Standardization (Z-score normalization)**:

Centers the features around zero with unit variance using the formula $\frac{x-m_x}{s_x}$, Choosing an inappropriate normalization method can introduce bias and affect the model's predictive performance (Kuzudisli et al., 2023).

3.8.3 Dimensionality Reduction

Dimensionality reduction helps mitigate the "curse of dimensionality" by transforming high-dimensional data into a lower-dimensional form while retaining its key characteristics. Common strategies include correlation analysis to remove redundant features, and transformation-based techniques like Principal Component Analysis (PCA). PCA projects the data into a new coordinate system, where the first principal component captures the direction of greatest variance, followed by subsequent orthogonal components (Demšar et al., 2013; Jaadi, 2022). Dimensionality reduction improves computational efficiency, reduces noise, and enhances model generalization.

3.8.4 Model Training

Model training refers to the process of using input-output data to allow the algorithm to learn the underlying relationships through a learning process. Two common optimization strategies include:

- **Loss Minimization**: Reduces the error between the predicted and actual outputs using a loss function (e.g., MSE, Cross-Entropy).

- **Likelihood Maximization**: Maximizes the probability that the observed data fits a proposed statistical model through a probability density function.

To avoid overfitting, data used for training should be different from that used for validation (Jabbar & Khan, 2015)Gradient Descent is a widely adopted algorithm for optimizing the cost function during training by iteratively adjusting model parameters in the direction of the steepest descent (Saad Hikmat Haji & Adnan Mohsin Abdulazeez, 2021)

$$\boldsymbol{\hat{\theta} = arg_{\theta} minj(\theta), \qquad j(\theta) = \frac{1}{n}\sum_{i=1}^{n} L(x_i, y_i, \theta)} \tag{3.5}$$

The set of parameters θ to adjust during the training process defines the search space during the optimization process while searching for the minimum loss model and it is given by (Alibrahim and Ludwig, 2021):

$$\boldsymbol{\theta = [\beta_o, \beta_1, \dots, \beta_i]^T} \tag{3.6}$$

The general gradient decent algorithm proceeds as follows;

Algorithm 1: Gradient Descent

Input: Learning rate γ

Output: Model parameters θ

$$\theta \leftarrow \theta_0;$$

Repeat;

$$\boldsymbol{\theta_{t+1} = \theta_t - \gamma g_t, g_t = \nabla_{\theta} J(\theta);} \tag{3.7}$$

$$\boldsymbol{t \leftarrow t + 1;}$$

Unit convergence;

The parameter γ or learning rate is adjusted in such a way that if the error gets worse or if its value oscillates then γ should be reduced and if the error slowly gets better then this values shoud be increased. While the optimization process tries to reach the minimum, the gradient ∇ has to be calculated which could lead to high computational demand, especially for Artificial Neural Networks (ANN) made up of several hidden layers, large datasets where the number of samples n is very larger. In order to improve the efficiency of these calculations, the chain rule is used in the so called Back-propagation Algorithm. The Stochastic Gradient Descend (SGD) also introduces an efficiency improvement regarding the number of samples used for computing the gradient, thus using a smaller dataset at each iteration. From these, three main approaches during the training or learning process can be used (Haji and Abdulazeez, 2021):

3.8.5 Model Validation

Validating machine learning (ML) models is critical to ensure their generalizability and prevent overfitting. There are several standard approaches to validating ML models, each with its unique advantages and trade-offs (El Naqa et al., 2018).

I. Validation Set Approach

This approach involves randomly dividing the dataset into two subsets: a training set and a validation (or test) set. The training set is used during the model learning stage, while the validation set evaluates model performance on unseen data. Although simple and efficient, this method can lead to high variance in performance estimation depending on how the data is split (Tsamardinos et al., 2014).

II. K-Fold Cross-Validation

In k-fold cross-validation, the dataset is divided randomly into k equal-sized subsets or "folds". The model is trained k times, each time using $k - 1$ folds for training and the remaining fold for validation. The final performance metric is obtained by averaging the results from all folds. This method provides a more stable and reliable estimate of model performance compared to the simple validation set approach (Tsamardinos et al., 2014).

III. Leave-One-Out Cross-Validation (LOOCV)

LOOCV is a special case of k-fold cross-validation where $k = n$, with n being the total number of data samples. In each iteration, a single sample is used for validation while the remaining $n - 1$ samples are used for training. While LOOCV provides an almost unbiased estimate of model performance, it is computationally intensive for large datasets (Cheng et al., 2021).

CHAPTER FOUR

RESULTS AND DISCUSSION

The results for each of the four states; Edo, Delta, Bayelsa and Rivers State are presented as follows. The first analysis was to check for homogeneity between old and new NIMET station data which were available for Edo and Rivers state only.

4.1 Statistical Test Results for Change Point Detection in Edo State

The rainfall data sets for Edo state were checked for presence of any significant changes which defines level of homogeneity between the old and new rainfall data using various statistical test such as the Pettitt test, Buishand test, SNHT (Standard Normal Homogeneity Test) and the Double Mass Curve. The results for each test are presented in table 4.1:

Table 4.1: Summary of Change Point Detection Results for Edo State Rainfall Data

Test Parameters	Pettitte Test	Buishand Test	SNHT
Test Hypothesis (h)	False	False	False
Change Point (cp)	136	136	205
p-value (p)	0.6783	0.3911	0.4404
U-statistic (U)	1196.0	1.2254	4.8764
Average values before change point (μ1)	188.72	188.72	199.42
Average values after change point (μ2)	228.88	228.88	373.47

4.1.1 Pettitt Test

The Pettitt test was applied to detect a change point in the time series. It is a non-parametric method for identifying a shift in the median of a dataset (Pettitt, 1979). The test result showed a p-value of 0.6783. The null hypothesis states that no significant change exists. Since the p-value is greater than 0.05, we fail to reject the null hypothesis. This means that there is no statistically significant change detected in the series.

The identified change point was at position 136 while the test statistic (U) was 1196.0. The mean value before the change point was 188.72 while the mean value after the change point was 228.88. Although the means differ, but the change is not statistically significant as such the time series remains stable over the period analyzed.

4.1.2 Buishand Test

The Buishand Range Test was also used to detect a change point in the time series. It assesses the cumulative sum of deviations from the mean (Buishand, 1982). The test returned a p-value of 0.3911. The null hypothesis assumes no significant change. Since the p-value is greater than 0.05, we fail to reject the null hypothesis. This indicates that there is no statistically significant change in the dataset.

The change point occurred at position 136. The test statistic (R) was 1.2254. The mean value before the change point was 188.72. After the change point, it was 228.88. Although the mean values differ, the change is not statistically significant as such the time series shows temporal consistency over the period examined.

4.1.3 SNHT (Standard Normal Homogeneity Test)

The Standard Normal Homogeneity Test (SNHT) was also used to check for a shift in the mean of the time series. This test is commonly applied for detecting breaks in climatological and hydrological records (Alexandersson, 1986). The p-value from the test was 0.4404. The null hypothesis assumes no significant change. Since the p-value is above 0.05, the null hypothesis is not rejected. This implies that no significant change is present in the series.

The detected change point was at position 205. The test statistic (T) was 4.8764. The mean before the change point was 199.42. The mean after the change point increased to 373.47. Despite the large difference in mean values, the result is not statistically significant. This suggests that the observed shift could be due to random variation.

4.1.4 Double Mass Curve

The double mass curve analysis provides compelling visual evidence that confirms the homogeneity test results obtained from the other statistical tests. As shown in Figure 4.1, the plot of cumulative rainfall from the new dataset against the old dataset at Benin NIMET Station demonstrates a remarkably consistent linear relationship throughout the entire record period.

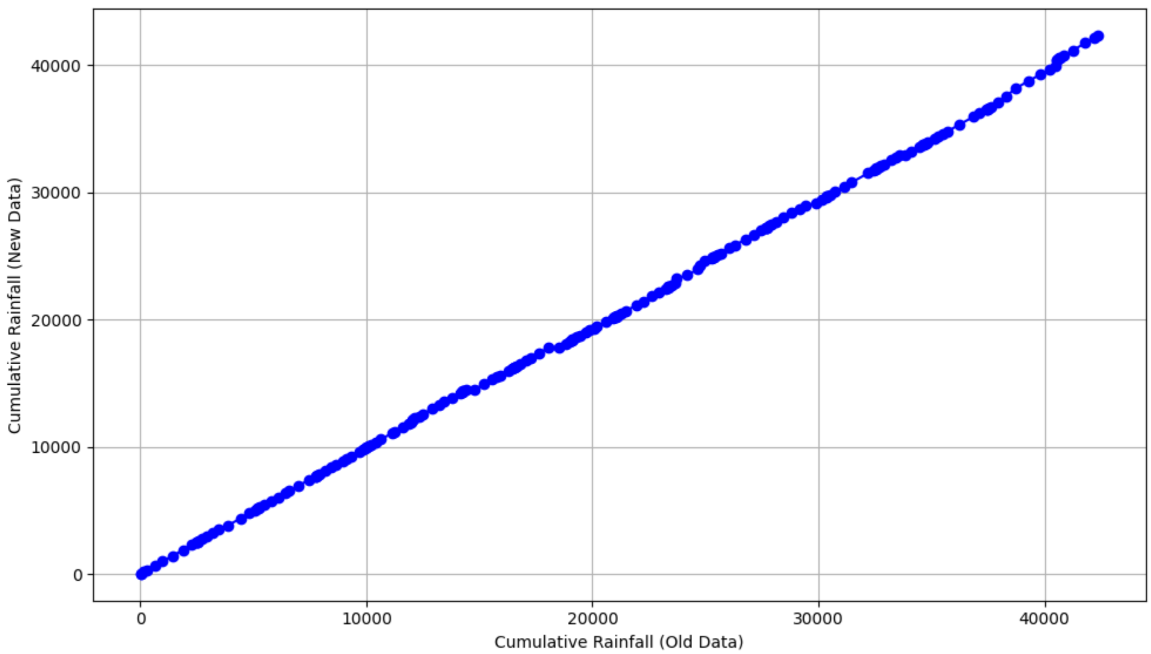

Figure 4.1: Double Mass Curve of New and Old Rainfall Data for Benin City Station

The double mass curve shows that there are no significant breakpoints or changes in slope that would indicate inhomogeneities in the rainfall records. This visual confirmation strongly supports the statistical findings from the Pettitt, Buishand Range, and SNHT tests, which all failed to reject the null hypothesis of stationarity ($p > 0.05$).

The near-perfect linearity observed in the double mass curve aligns with the high p-values (0.678, 0.391, and 0.440) obtained from the change-point tests. While the statistical tests identified potential change points at observations 136 (Pettitt and Buishand) and 205 (SNHT), the double mass curve confirms this represented natural variability rather than true discontinuities in the data collection or measurement processes.

The consistent slope throughout the entire cumulative rainfall record (from 0 to over 40,000 units) demonstrates that the proportionality between old and new datasets remains stable. This stability is particularly valuable for validating the integrity of the rainfall dataset prior to further climatological analyses, suggesting that any trends or patterns detected in subsequent analyses likely represent genuine climate signals rather than artifacts of data inhomogeneity.

This combined approach employing both statistical tests and graphical techniques provides robust confirmation of data homogeneity, strengthening the foundation for subsequent hydro-climatological analyses in this thesis.

4.2 Statistical Test Results for Change Point Detection in Rivers State Rainfall Data

In order to evaluate potential structural changes in the rainfall pattern for Rivers State, the same statistical test which are Pettitt's Test, Buishand's Range Test, and the Standard Normal Homogeneity Test (SNHT), were applied to the long-term old and new rainfall datasets.

Table 4.2: Summary of Change Point Detection Results for Rivers State Rainfall Data

Test Parameters	Pettitte Test	Buishand Test	SNHT
Test Hypothesis (h)	False	False	False
Change Point (cp)	39	39	39
p-value (p)	0.2154	0.30055	0.3935
U-statistic (U)	571.0	1.2624	1.2624
Average values before change point ($\mu 1$)	156.32	156.32	156.32
Average values after change point ($\mu 2$)	218.70	218.70	218.70

As presented in Table 4.2, all three tests returned consistent outcomes. For each method, the test hypothesis (h) was false, indicating that no statistically significant change point was detected in the rainfall data. Although a common change point (cp) was identified at time step 39, corresponding to a transition in average rainfall from 156.32 mm ($\mu 1$) to 218.70 mm ($\mu 2$), the observed difference was not statistically significant.

4.2.1 Pettitt's Test

The Pettitt's Test produced a p-value of 0.2154 and a U-statistic of 571.0, both of which fall outside the conventional 0.05 significance level. This suggests that the increase in mean rainfall after the change point is likely due to natural variability rather than a true structural break. This outcome is consistent with findings from previous climatological studies where Pettitt's Test was applied to rainfall series in humid tropical regions (Animashaun et al., 2020; Jenifer and Jha, 2021).

4.2.2 Buishand's Range Test

Buishand's Range Test returned a p-value of 0.30055 with a range statistic of 1.2624, reinforcing the conclusion that no significant inhomogeneity exists in the time series. Just like the pettitt's test, the buishand test has also been previously applied in various hydroclimatic studies to detect inhomogeneities and confirm rainfall stability over time (Ajibola et al., 2021; De La Casa et al., 2018; Y. Wu et al., 2023), and the results support the hypothesis of homogeneity in the Rivers State rainfall dataset.

4.2.3 SNHT (Standard Normal Homogeneity Test

The SNHT also showed no evidence of change, with a p-value of 0.3935 and a T-statistic of 4.7735. Like the other tests, SNHT identified the same change point but failed to confirm its statistical significance. The results from all three tests shows that the rainfall datasets in Rivers State has remained statistically stable over the study period. Although fluctuations in annual rainfall totals may exist which may appear to fall within the bounds of natural variability rather than indicating any abrupt or systematic shifts. This has significant implications for long-term hydrological modeling and flood management, as it implies that observed rainfall changes are gradual and potentially driven by seasonal dynamics rather than abrupt climate-induced changes.

4.2.4 Double Mass Curve Analysis

In addition to the statistical homogeneity tests, a Double Mass Curve (DMC) analysis was conducted to visually assess the consistency and homogeneity between the "Old" and "New" rainfall datasets. The DMC is a widely used graphical tool in hydrology and climatology to compare cumulative data series, and it helps identify discrepancies that may arise from changes in measurement methods or environmental influences (X. Wu et al., 2023).

The plotted DMC as presented in Figure 4.2, revealed an overall linear relationship between the cumulative rainfall of the two datasets, indicating that the "Old" and "New" series are generally consistent and exhibit similar rainfall patterns over time. This linearity supports the findings from the statistical tests, reinforcing that the rainfall data are largely homogeneous and reliable for trend analysis. Similar observations have been reported in other hydrological studies where DMC linearity confirmed the compatibility of merged or updated rainfall datasets (Garba and Udokpoh, 2023; Machiwal et al., 2022).

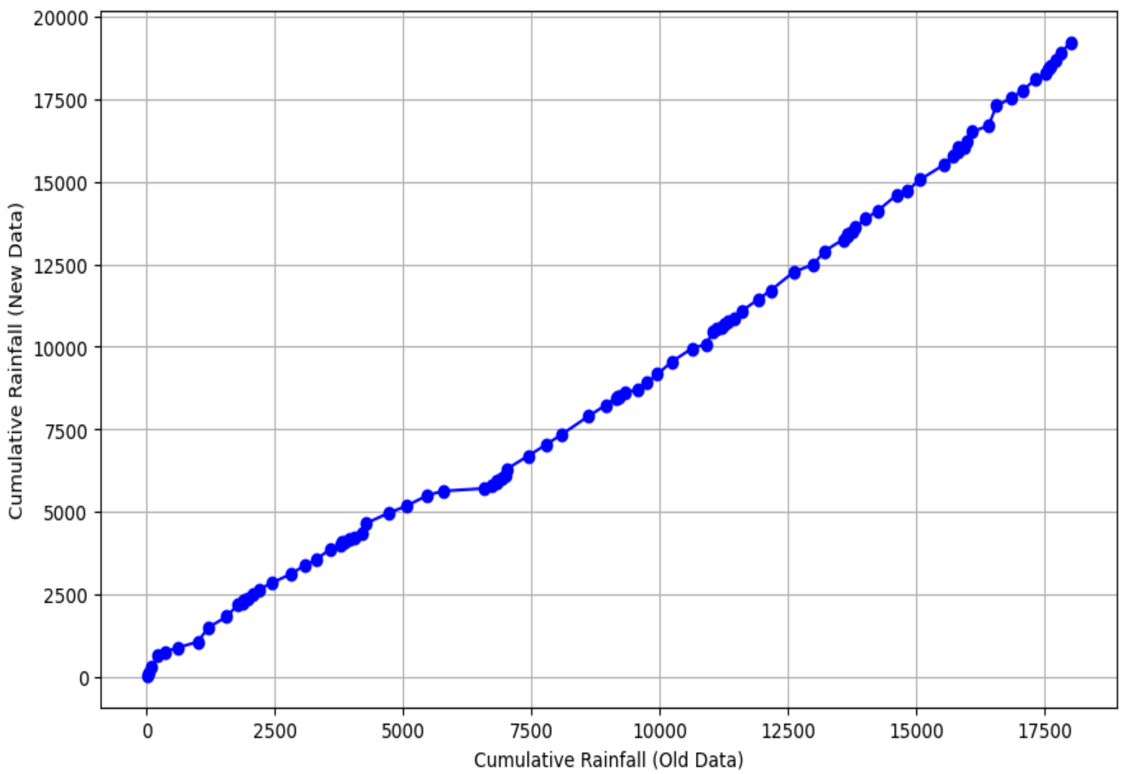

Figure 4.2: Double Mass Curve of New and Old Rainfall Data for Rivers Station

However, the curve showed slight deviations in slope around certain cumulative rainfall values, particularly 5000 mm and 7500 mm on the x-axis (corresponding to the “Old” data series). These subtle slope changes suggest minor inconsistencies between the datasets, which may stem from several factors. Possible causes include changes in instrumentation, such as the replacement or recalibration of rain gauges that can introduce measurement biases (Shedekar et al., 2016). Station relocation is another common source of such discrepancies, as even small geographic shifts can affect rainfall recordings due to local topographical or microclimatic variations (Shedekar et al., 2016)

4.3 Validation of Remotely Sensed Rainfall Dataset.

This section presents the statistical results for validating satellite rainfall datasets against the ground-based rain gauge data for the study areas which are Edo, Delta and Rivers State. Bayelsa State was not included due to lack of station dataset. The analysis was carried out on the monthly temporal and state spatial scales. In order to ascertain the accuracy and performance of these data sets, eight statistical methods were used on satellite datasets relative to the rain gauge data. The evaluation metrics used included Mean Squared Error (MSE), Root Mean Squared Error (RMSE), Mean Absolute Error (MAE), Bias, Coefficient of Determination (R^2), Correlation, Nash-Sutcliffe Efficiency (NSE), and Willmott's Index of Agreement (d). These metrics have been widely adopted in hydrological and climate studies for evaluating the performance of satellite precipitation products (Vu et al., 2018; Willmott et al., 2012; Ye et al., 2022). As such, these methods provide a comprehensive assessment of the accuracy, reliability, performance and acceptability of the satellite datasets in reproducing the gauge datasets. The results are presented as follows;

4.3.1 Validation of Satellite Rainfall Data for Edo State.

The result for Edo State is presented in Table 4.3;

Table 4.3: Evaluation Metrics for the validation of Satellite Rainfall data for Edo State.

Station against Satellite	**MSE**	**RMSE**	**MAE**	**Bias**	**R2**	**Correlation**	**NSE**	**Willmott_d**
CHIRPS	7900.18	88.88	57.61	-17.42	0.65	0.82	0.65	0.89
PERSIANN_CDR	10950.88	104.65	66.93	-43.86	0.51	0.78	0.51	0.82
TRMM	44058.62	209.90	161.37	-159.54	-0.96	0.46	-0.96	0.50

From Table 4.2, it was observed that the CHIRPS dataset exhibited the best performance among the three satellite products. It provides the lowest MSE of 7900.18, RMSE of 88.88, and MAE 57.61 which indicate the lowest deviations from observed rainfall. The bias value of -17.42 suggests a slight underestimation of rainfall but is still within an acceptable range for climate-related studies (Berhanu et al., 2016). The R^2 value of 0.65 and correlation coefficient of 0.82 demonstrate a strong linear relationship with observed data. Furthermore, the NSE of 0.6481 indicates good predictive power, while the Willmott d index of 0.89 reflects a high level of agreement between CHIRPS and ground observations. these results align with findings by (Bamweyana et al., 2021), who reported that CHIRPS is one of the most reliable rainfall datasets over Africa due to its integration of satellite and station data.

The PERSIANN-CDR dataset on the other hand also performed reasonably well but was slightly less accurate compared to CHIRPS. It showed higher MSE of 10950.88, RMSE of 104.65, and MAE of 66.93, with a more significant negative bias of -43.86. The R^2 value of 0.513 and correlation coefficient of 0.78 indicate a moderate correlation with observed rainfall. The NSE value of 0.513) and Willmott d of 0.82 suggest that although PERSIANN-CDR captures the general rainfall pattern, it tends to underestimate actual rainfall, possibly due to limitations in capturing convective rainfall typical in the tropics (Ghajarnia et al., 2018).

From the analysis it can be concluded that the TRMM dataset showed the weakest performance. It had the highest errors, with an MSE of 44058.62, RMSE of 209.90, and MAE of 161.37, which point to significant deviation from observed rainfall. The very high negative bias of -159.54 indicates a substantial underestimation. Additionally, the negative R^2 of -0.96 and NSE of -0.96 values, coupled with a low correlation of 0.46 and Willmott d indices of 0.50, demonstrate that TRMM fails to reliably replicate the observed rainfall trends at the Benin station. These poor results are consistent with reports by (Nicholson et al., 2003), who identified TRMM's limitations in accurately estimating rainfall in West Africa due to its coarse spatial resolution and potential inadequacy in capturing localized rainfall events.

4.3.2 Validation of Satellite Rainfall Data for Delta State.

The result for Delta State satellite rainfall validation is presented in Table 4.4

Table 4.4: Evaluation Metrics for the validation of Satellite Rainfall data for Delta State.

Station against Satellite	MSE	RMSE	MAE	Bias	R2	Correlation	NSE	Willmott_d
CHIRPS	12652.75	112.48	79.10	16.92	0.58	0.78	0.58	0.87
PERSIANN_CDR	16522.41	128.54	89.01	-21.48	0.45	0.69	0.45	0.77
TRMM	46608.85	215.89	152.98	-147.51	-0.56	0.44	-0.56	0.52

As shown in Table 4.4, the CHIRPS dataset outperformed both PERSIANN-CDR and TRMM in most of the statistical indicators. It gave the lowest MSE of 12,652.75, RMSE of 112.48 and MAE of 79.10. it showed a modest positive bias of 16.92 while a R^2 value of 0.5778 and correlation coefficient of 0.7753 indicating a strong linear association and moderate predictive ability. Moreover, the NSE value of 0.58 and Willmott's index of 0.87 confirm CHIRPS' better agreement with observed rainfall data, consistent with findings from other regions in West Africa (Bamweyana et al., 2021).

The PERSIANN-CDR satellite dataset gave the second best results, with an MSE of 16,522.41, RMSE of 128.54 and MAE of 89.01. It produced a negative bias of -21.48, suggesting a tendency to underestimate rainfall amounts. Although its correlation coefficient of 0.69 and R^2 of 0.45 were lower than those of CHIRPS, they still indicate moderate reliability. This dataset gave an NSE of 0.45 and d-index of 0.77 values which show that PERSIANN-CDR is reasonably effective for hydrological assessments in the region. These outcomes align with other studies that have reported moderate performance of PERSIANN products in tropical and sub-humid environments (Ghajarnia et al., 2018).

The TRMM satellite rainfall dataset produced weakest performance among other metrics. It had the highest MSE of 46,608.85, RMSE of 215.89, and MAE of 152.98. this dataset gave a significantly large negative bias of -147.51, indicating major underestimation of rainfall. Its R^2 of -0.56 and NSE of -0.56 values reflect a poor ability to reproduce observed rainfall dynamics, and its Willmott d-index of 0.52 further confirms its low level of agreement. Although TRMM has shown acceptable performance in other parts of Africa (Nicholson et al., 2003), its coarse spatial resolution and limitations in detecting light rainfall may contribute to its poor performance in coastal, high-precipitation areas such as Delta State.

4.3.3 Validation of Satellite Rainfall Data for Rivers State

Rivers states gauge dataset was used to validate the corresponding satellite dataset. The summary of the statistical performance of each dataset is presented in Table 4.5.

Table 4.5: Evaluation Metrics for the validation of Satellite Rainfall data for Rivers State.

Station against Satellite	MSE	RMSE	MAE	Bias	R2	Correlation	NSE	Willmott_d
CHIRPS	9163.67	95.73	66.86	22.85	0.54	0.79	0.54	0.88
PERSIANN_CDR	9548.64	97.72	67.88	4.92	0.52	0.73	0.52	0.85
TRMM	40930.66	202.31	155.54	-152.95	-1.08	0.33	-1.08	0.50

As observed in Table 4.4, the CHIRPS rainfall datas*et. al*so outperformed other datasets in representing rainfall patterns over Rivers State. It recorded the lowest error statistics which are MSE of 9,163.66, RMSE of 95.73, and MAE of 66.86. Although it slightly overestimated rainfall with a bias of 22.85 mm, the CHIRPS data showed a strong correlation coefficient of 0.79 and R^2 value of 0.54. Additionally, the NSE of 0.54 and Willmott's index of 0.88 confirm its adequate predictive performance and reliability in capturing rainfall variability in this region. These findings are consistent with previous validations of CHIRPS across sub-Saharan Africa, where it has demonstrated reliable spatial and temporal performance (Bamweyana et al., 2021).

The PERSIANN-CDR dataset on the other hand showed reasonable performance with a slightly lower results compared to the CHIRPS dataset. It produced an MSE of 9,548.64, RMSE of 97.72, and MAE of 67.88, with a very low bias of 4.92, indicating near-unbiased estimates. The R^2 value of 0.52 and correlation coefficient of 0.73 suggest moderate to strong agreement with observed data. Similarly, NSE of 0.52 and Willmott's d-index of 0.85 confirm its viability for hydrological applications in Rivers State. Prior studies such as (Ghajarnia et al., 2018) have also shown that PERSIANN-CDR performs better in humid tropical zones with consistent rainfall patterns.

Conversely, the TRMM dataset showed the weakest performance across all metrics. It produced a very high MSE of 40,930.66, RMSE of 202.31, and MAE of 155.54. Notably, it underestimated rainfall significantly with a negative bias of -152.95. It gave a negative R^2 and NSE values (-1.08 and -1.08 respectively, which indicate a very poor agreement with observed rainfall, suggesting limited applicability in Rivers State. Finally, its Willmott's index of 0.50 was the lowest among the three products, confirming that TRMM may not be reliable for operational rainfall estimation in this high-rainfall coastal region. This aligns with conclusions by (Nicholson et al., 2003), who noted that TRMM often struggles in areas with intense convective systems and high precipitation variability.

4.4 Spatio-Temporal Rainfall Trend Analysis

This section presents a comprehensive analysis of rainfall patterns in the study area which includes Edo, Delta, Bayelsa, and Rivers States using high-quality satellite-derived data. The satellite dataset with the best performance obtained during the validation step against ground observations was selected for assessing long-term trends, monthly distributions, extremes, and seasonal characteristics from 1981 to 2023. Statistical methods such as the Mann-Kendall trend test and Sen's slope estimator were employed to quantify trends and determine their significance, consistent with methods widely used in recent climatological studies (Saikh and Mondal, 2023). Additionally, indices like the Standardized Precipitation Index (SPI) and analysis of extreme rainfall events were used to capture both the magnitude and variability of rainfall extremes, following frameworks used in contemporary hydroclimatic assessments (Kamruzzaman et al., 2022). These approaches offer robust insights into both long-term climatic shifts and short-term extremes, which are critical for developing adaptive strategies under climate variability in the Niger Delta region.

4.4.1 Rainfall Trend Analysis for Edo State

Figure 4.3 present the annual rainfall trend in Edo State from 1981 to 2023. The time series plot shows noticeable year-to-year variability, with annual rainfall values fluctuating between approximately 1450 mm and 2250 mm. A linear trend line with a calculated Sen's slope of 0.2405 mm/year is superimposed, suggesting a very slight upward trend in annual rainfall over the study period. The Mann-Kendall trend test indicates an increasing trend, however, the associated p-value of 0.9201 suggests that this trend is not statistically significant at the 95% confidence level. This implies that although there is a marginal positive slope, there is insufficient evidence to confirm a consistent or meaningful long-term increase in rainfall in Edo State during this period.

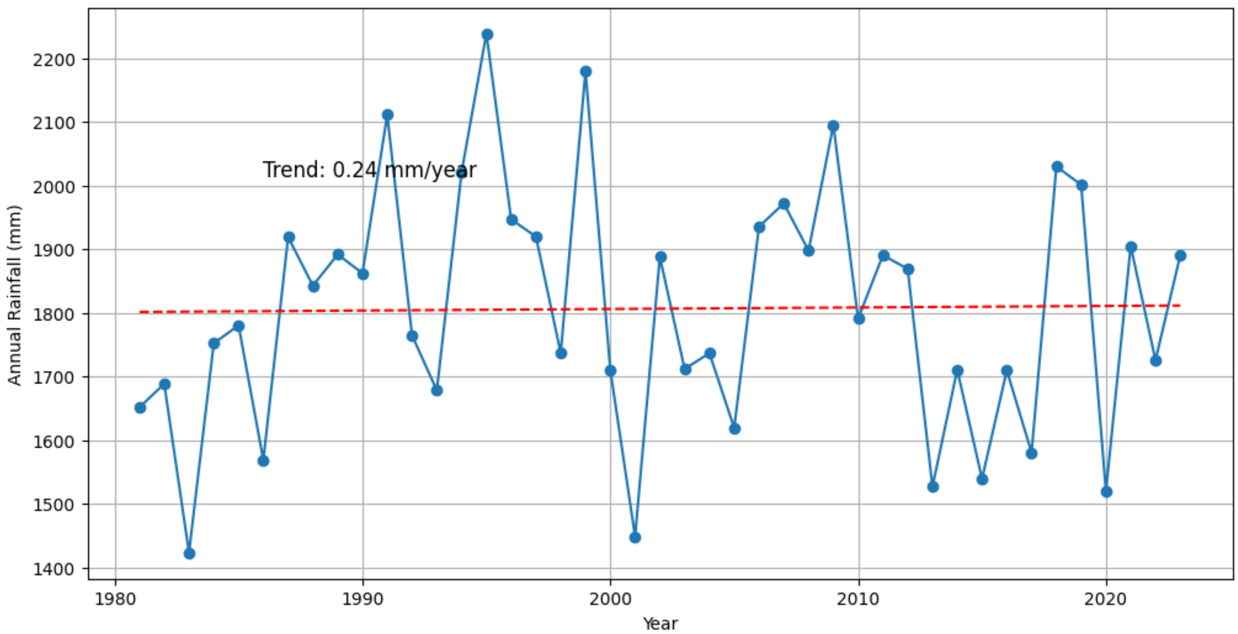

Figure 4.3: Annual Rainfall Trend Analysis for Edo State from 1981 to 2023

The presence of substantial inter-annual variability and periods of both high and low rainfall may be attributed to natural climate oscillations and regional climatic factors influencing rainfall distribution in the area (Nicholson, 2017; Synodinos et al., 2018). The non-significant trend may also be linked to short-term variability and potential errors or uncertainties inherent in the rainfall dataset.

1. Monthly Rainfall Patterns and Extremes

Figure 4.4 presents the decadal average monthly rainfall distribution in Edo State for four-time intervals: 1981–1990, 1991–2000, 2001–2010, and 2011–2023. The seasonal rainfall pattern across decades shows a unimodal distribution with a peak during September, which is consistent with the West African Monsoon season (Nicholson, 2017).

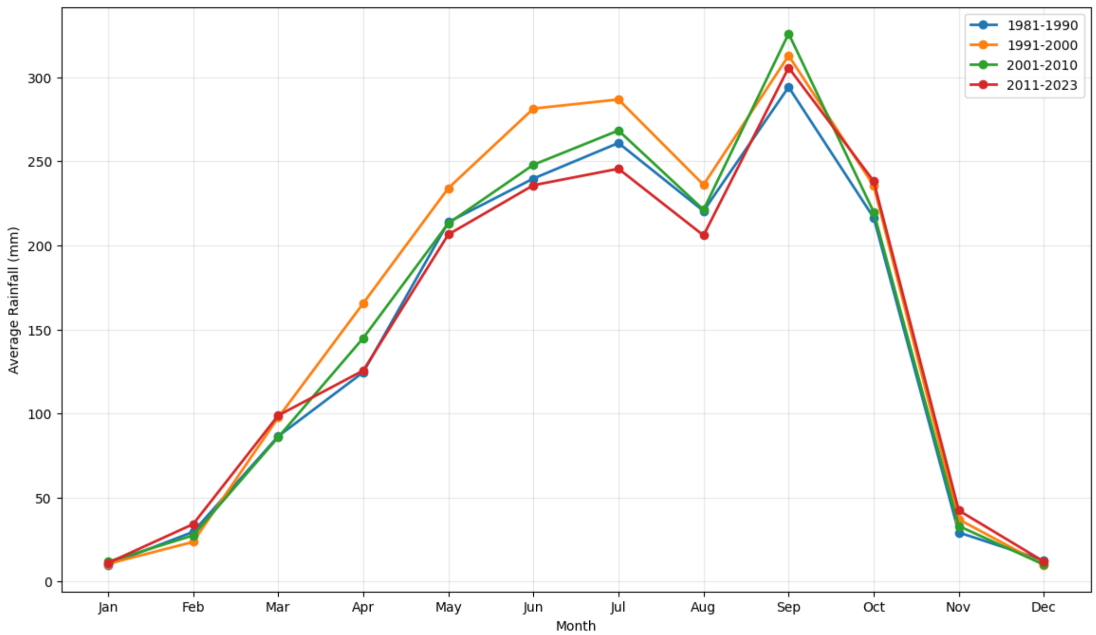

Figure 4.4: Average Monthly Rainfall by Decade from 1981 to 2023

While the overall monthly trend remains similar across decades, it is evident that the 1991–2000 period recorded the highest average monthly rainfall, particularly between April and October, indicating a wetter decade. Conversely, the most recent period, 2011–2023, shows a slight decline in rainfall in several key months, especially in August, where the average is noticeably lower compared to previous decades. This suggests a potential shift or irregularity in the intra-annual rainfall distribution, which may be linked to changes in atmospheric circulation patterns or localized climate variability.

The early onset of rainfall in March and prolonged wet season up to October is typical of southern Nigeria and is critical for agriculture, water resource planning, and flood risk management

(Animashaun et al., 2020). The fluctuations in monthly patterns across decades also underscore the need to integrate climate resilience in water infrastructure and agricultural planning.

I. 12-Month Standardized Precipitation Index (SPI) for Edo State (1981-2023)

Figure 4.5 shows the 12-month Standardized Precipitation Index (SPI) for Edo State, which is a widely used indicator of meteorological drought and wetness. The SPI values fluctuate between -2 and +2, reflecting periods of both significant drought and excess rainfall. Notably, several years fall below the -1 threshold, which indicate that there is moderate to severe drought conditions, while others surpass +1, reflecting unusually wet years. The overall trend line suggests a slight increase in SPI values over time, implying a marginal tendency toward wetter conditions, but with persistent high inter-annual variability. This variability underscores the ongoing risk of both drought and flood events in the region.

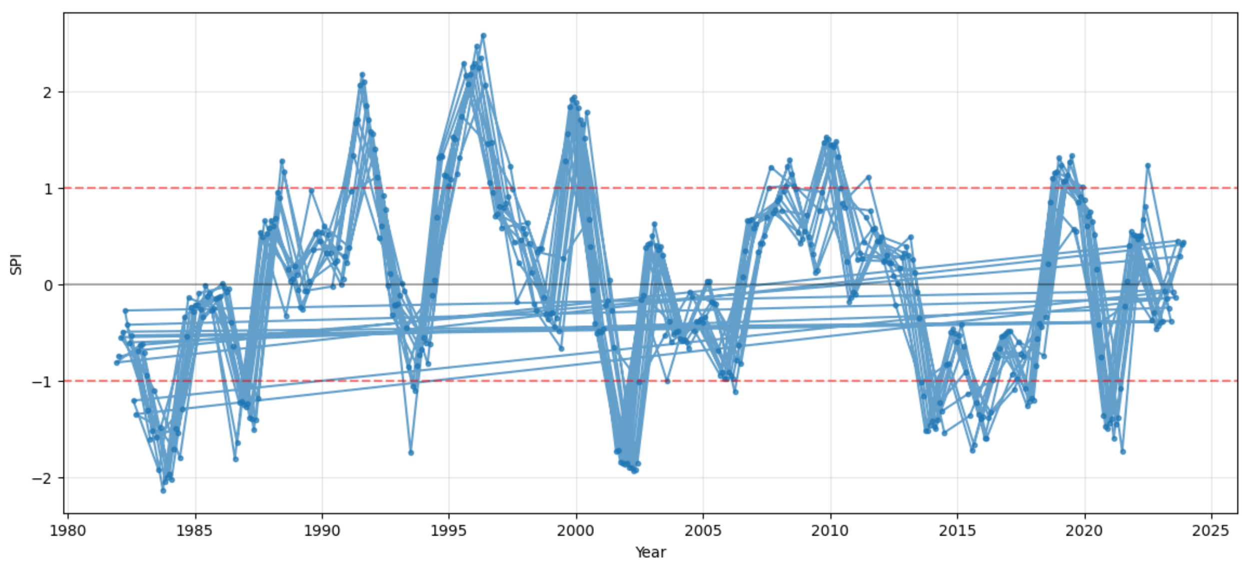

Figure 4.5: 12 Months Standardized Precipitation Index (SPI) for Edo State

II. Inter-annual Rainfall Extremes and Drought Risk

Figure 4.6 present the annual trend in the number of extreme rainfall days, defined as days exceeding the 95th percentile of daily rainfall from 1981 to 2023. The time series exhibits high inter-annual variability, with the number of extreme events ranging from than 10 to over 25 days per year. While the visual trend appears relatively stable overall, slight oscillations suggest that extreme rainfall events have persisted throughout the period with no clear increasing or decreasing pattern.

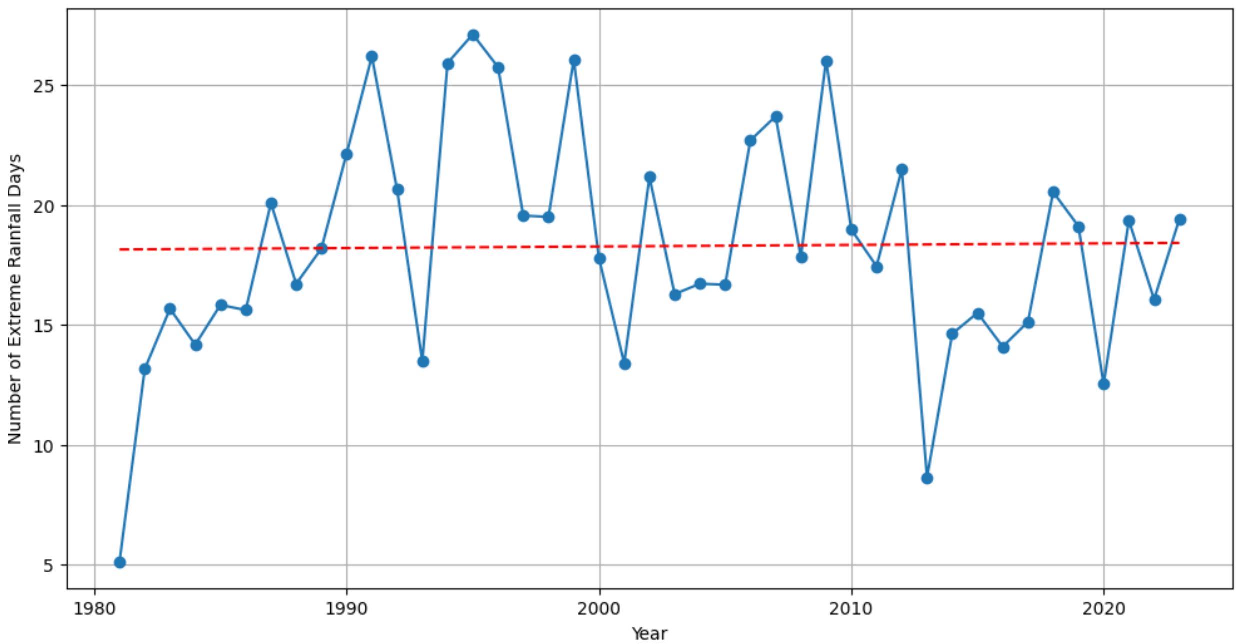

Figure 4.6: Inter-annual Rainfall Extremes for Edo State from 1983 - 2023

The dashed line representing the linear trend suggests a slightly positive slope, though any inference about statistical significance would require a test such as the Mann-Kendall trend test. Nonetheless, the consistent recurrence of extreme events highlights the potential for localized flooding, especially in urban areas with poor drainage systems. The variability in extreme events aligns with findings in other parts of West Africa, where changes in rainfall intensity, rather than total amounts, are increasingly affecting flood risks (Wasko et al., 2021).

III. Monthly Rainfall Variability

The analysis of monthly rainfall variability in Edo State from 1981 to 2023, as illustrated in Figure 4.7, reveals a pronounced seasonal pattern characteristic of the region's humid tropical climate. Rainfall is minimal during the dry season months (December–February), with median values consistently below 50 mm. A rapid increase is observed from March, culminating in a peak between June and September, where median monthly rainfall exceeds 200 mm and reaches up to 300 mm in certain months. Notably, July, August, and September exhibit the greatest interquartile ranges and the presence of outliers, indicating heightened variability and the occurrence of extreme rainfall events during the core wet season.

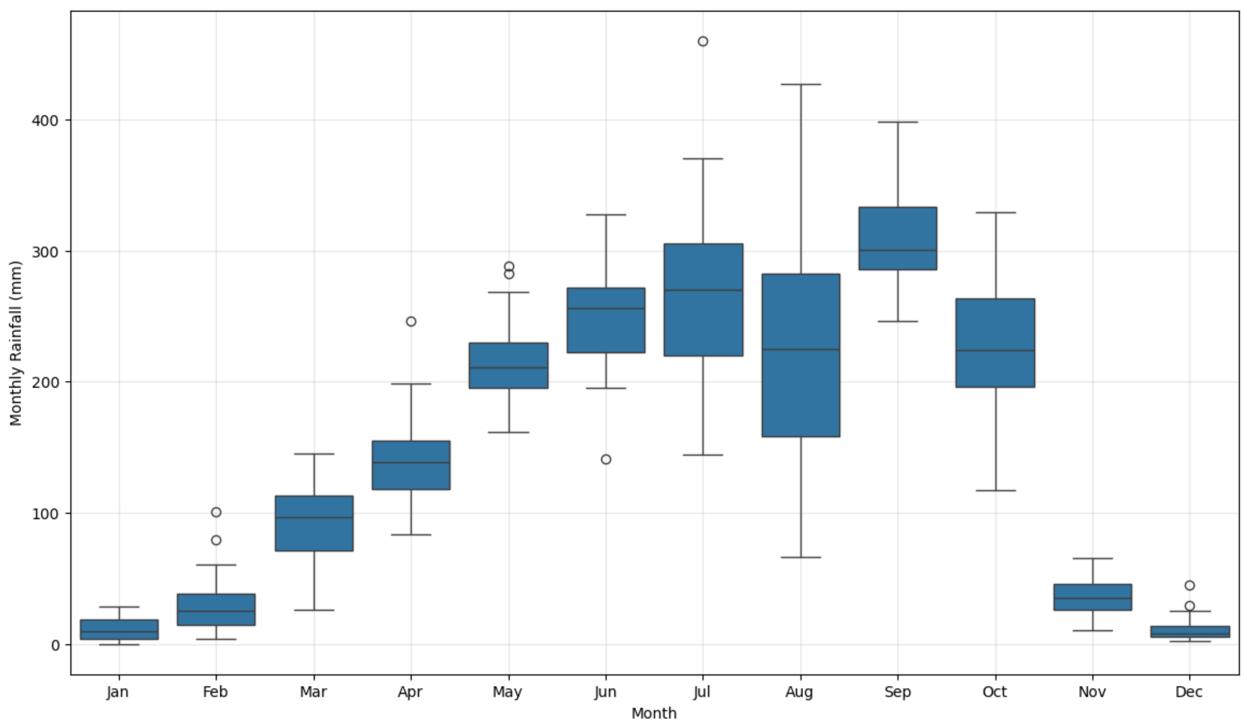

Figure 4.7: Monthly Rainfall Variability in Edo State from 1981 to 2023.

This pattern aligns with previous studies that attribute the seasonal rainfall distribution in southern Nigeria to the influence of the West African monsoon and the movement of the Intertropical

Discontinuity (ITD) (Ayanlade et al., 2019). The sharp decline in rainfall after September, returning to dry conditions by November and December, further underscores the distinctiveness of the wet and dry seasons in the study area.

IV. Seasonal Rainfall Trends

Figure 4.8 presents the seasonal rainfall trends for four climatological periods: Dry (December–February), Early Wet (March–May), Peak Wet (June–August), and Late Wet (September–November). The Peak Wet season (June–August) consistently records the highest rainfall, with seasonal totals frequently exceeding 800 mm and displaying substantial inter-annual variability.

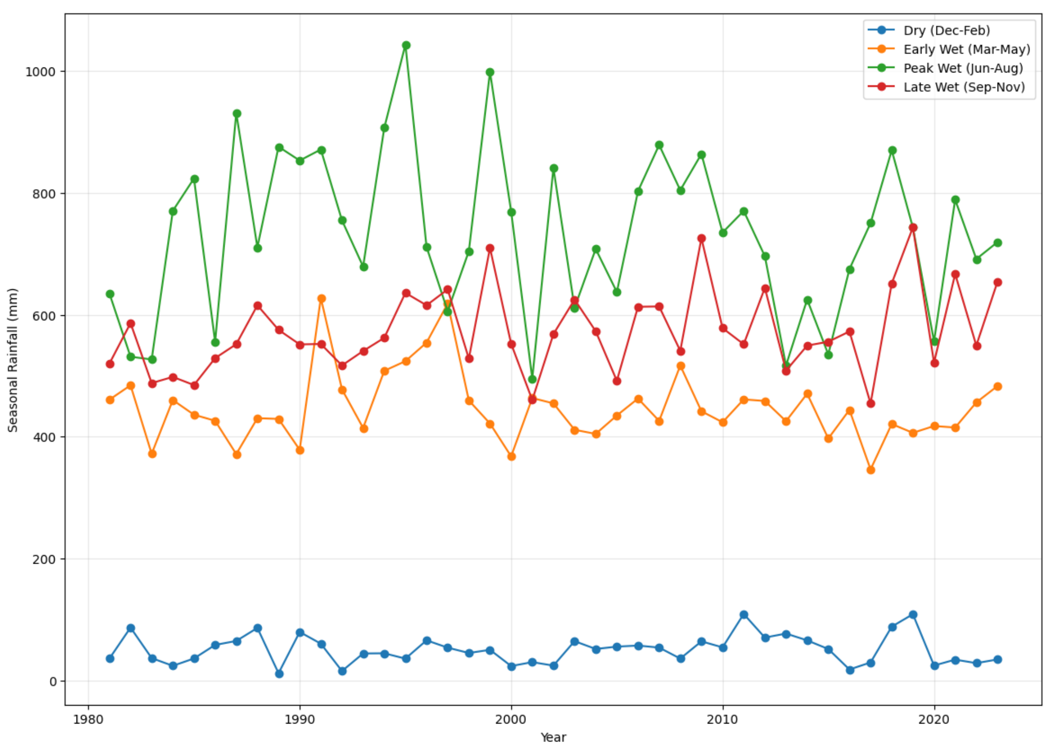

Figure 4.8: Seasonal Rainfall Trends in Edo State from 1981 to 2023.

Both the Early Wet and Late Wet seasons exhibit moderate rainfall, while the Dry season remains persistently low across the study period. Importantly, no significant long-term trend either increasing or decreasing is evident in the Peak Wet season, suggesting that while inter-annual fluctuations are marked, the underlying seasonal rainfall regime has remained relatively stable over the past four decades (Figure 4.8). This finding is consistent with the work of NIMET (2018), which reported similar stability in the seasonal rainfall structure across southern Nigeria.

V. Wet Season Onset and Duration Trends

Figure 4.9 provides insight into the temporal dynamics of the wet season's onset and duration. The upper panel shows that the onset of the wet season generally occurs in March, with occasional outlier years exhibiting a later onset.

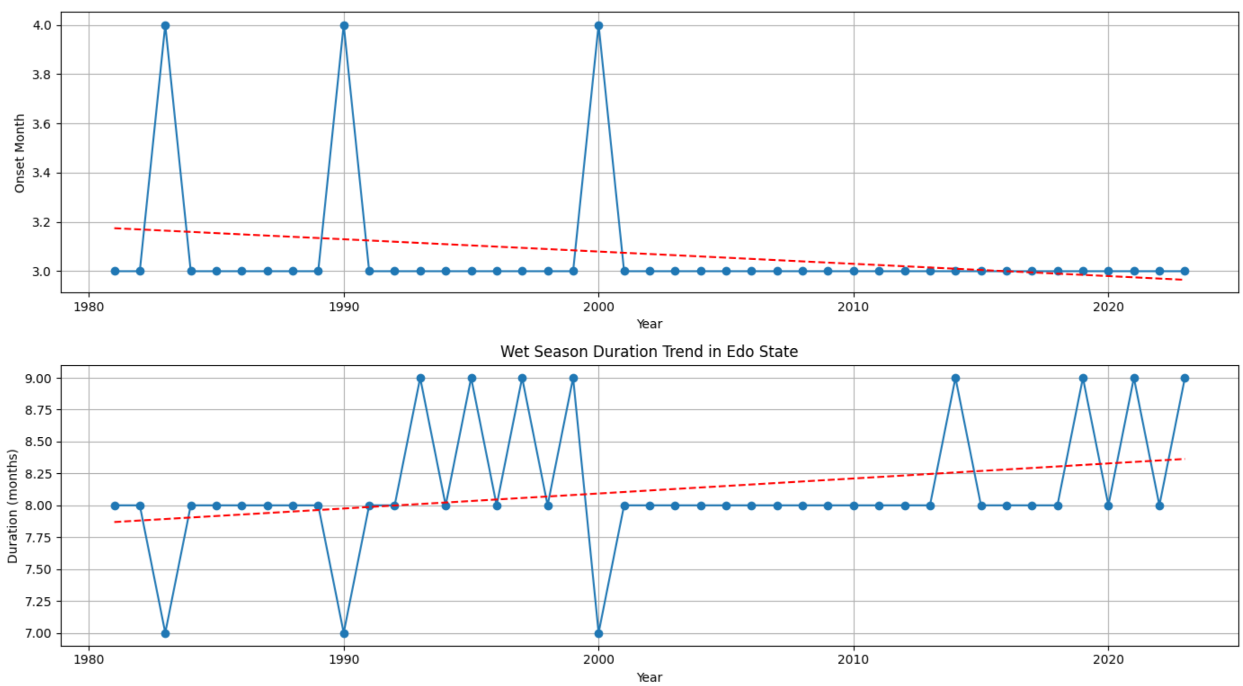

Figure 4.9: Wet Season Onset Trend in Edo State from 1983 to 2023

The trend line indicates a marginal delay in onset over the study period. The lower panel of Figure 4.9 demonstrates that the duration of the wet season typically ranges from 7.5 to 9 months, with a subtle but discernible increasing trend. This suggests a tendency toward a lengthening wet season, even as onset becomes slightly delayed. Such trends are consistent with recent regional analyses indicating that climate variability may be contributing to shifts in the timing and length of the rainy season in West Africa (Animashaun et al., 2020; Ayanlade et al., 2019).

4.4.2 Rainfall Trend Analysis for Delta State

The annual rainfall trend in Delta State from 1981 to 2023, as depicted in Figure 4.10, reveals considerable inter-annual variability. Superimposed on this fluctuation is a statistically non-significant decreasing trend, as indicated by the Mann-Kendall trend test (Trend: decreasing, p-value = 0.9364). This finding is further quantified by Sen's slope estimate of -0.2627 mm/year, suggesting a very slight average decrease in annual rainfall over the study period.

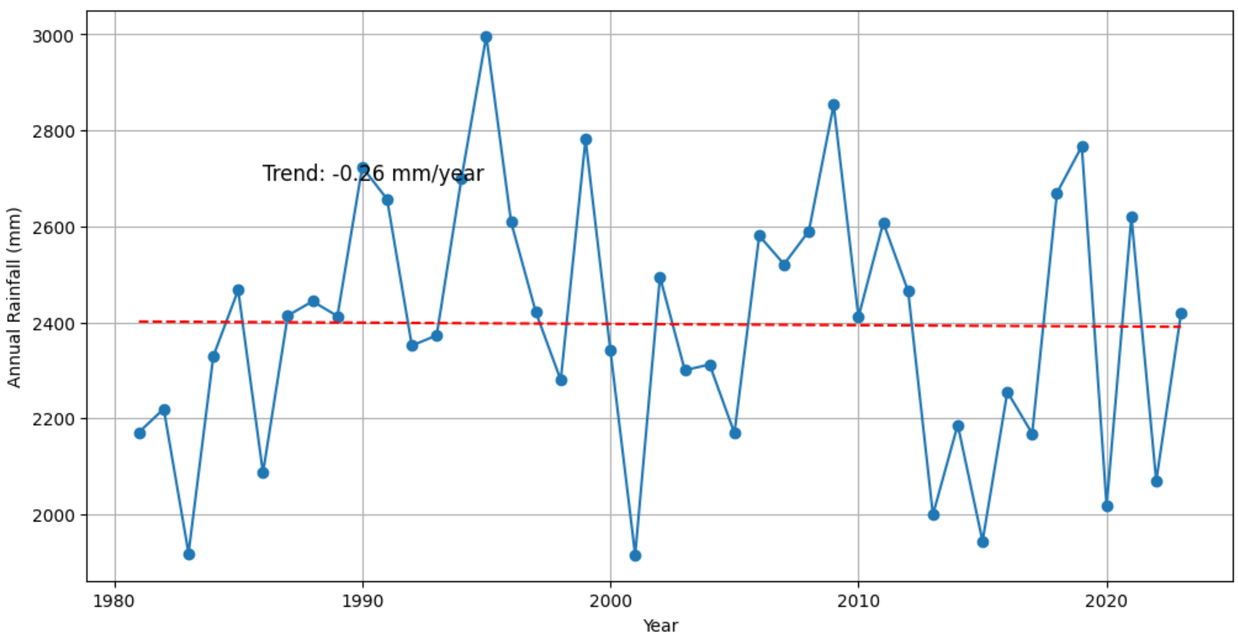

Figure 4.10: Annual Rainfall Trend Analysis for Delta State from 1981 to 2023

The high p-value (0.9364), well above the conventional significance level of 0.05, implies that we fail to reject the null hypothesis of no trend. Therefore, while the Sen's slope suggests a marginal decrease in rainfall, this trend is not statistically significant within the observed timeframe. This suggests that natural climatic variability might be the primary driver of the observed fluctuations in annual rainfall in Delta State during this period, rather than a consistent directional change.

The pronounced inter-annual variability, characterized by periods of higher and lower rainfall, is consistent with the known climate dynamics of the Niger Delta region, which is influenced by the West African monsoon system and associated atmospheric circulation patterns. Factors such as changes in sea surface temperatures in the Atlantic and Indian Oceans, as well as regional land-atmosphere interactions, can contribute to these year-to-year fluctuations (Lu, 2009).

Despite the lack of a statistically significant trend over the entire period, the visual inspection of Figure 1 reveals some interesting patterns. For instance, the period around the mid-1990s appears to exhibit higher rainfall compared to the early 1980s or the early 2000s. However, these visual observations need to be interpreted with caution in light of the non-significant trend identified by the Mann-Kendall test. Short-term fluctuations are inherent in climate data and do not necessarily indicate a long-term directional change.

The non-significant decreasing trend observed in this study contrasts with some projections of future climate change that suggest potential alterations in rainfall patterns in the region (Ilori and Ajayi, 2020a). However, it is important to note that this study focuses on historical data and a specific timeframe. Longer-term analyses and climate model projections, considering various emission scenarios, might reveal different trends. Furthermore, the magnitude of the Sen's slope (-0.2627 mm/year) is relatively small. Over the 43-year study period, this would amount to a total decrease of approximately 11.3 mm, which is minor compared to the substantial inter-annual variability observed in the annual rainfall amounts, which range from approximately 1900 mm to 3000 mm.

In conclusion, the analysis of annual rainfall data for Delta State between 1981 and 2023 indicates substantial year-to-year variability but no statistically significant long-term trend. While a slight decreasing tendency is suggested by Sen's slope, it is overshadowed by the natural fluctuations inherent in the regional climate. Further research, potentially incorporating higher temporal resolution data and exploring the influence of specific climate drivers, could provide a more nuanced understanding of rainfall dynamics in the region.

I. Monthly Rainfall Patterns and Extremes

Figure 4.11 illustrates the average monthly rainfall distribution in Delta State, segmented by decades (1981-1990, 1991-2000, 2001-2010, and 2011-2023). This decadal analysis provides a more granular perspective on the temporal patterns of rainfall.

The figure clearly demonstrates the seasonal nature of rainfall in Delta State, with a distinct wet season typically spanning from April to October, characterized by significantly higher average monthly rainfall. Peak rainfall is generally observed during the months of July, August, and September across all decades. The dry season, from November to March, experiences considerably lower rainfall amounts. This seasonal pattern aligns with the broader climatic regime of the West African monsoon, which dictates the precipitation patterns in the region.

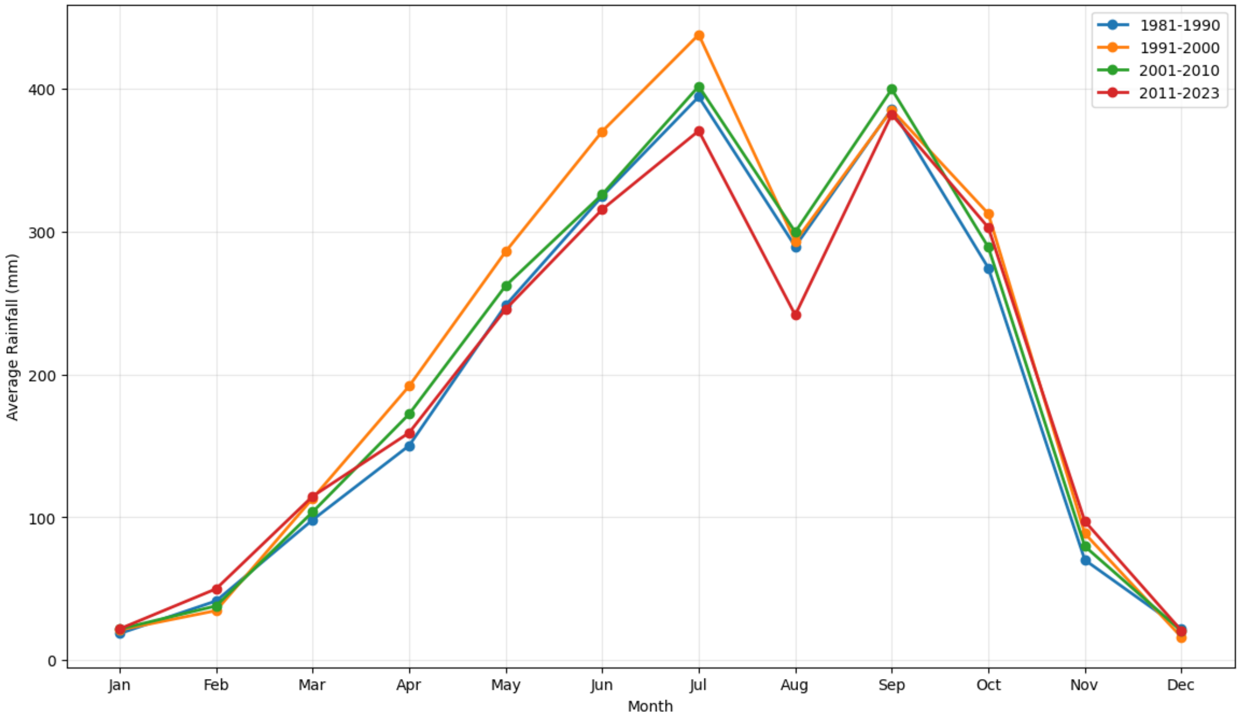

Figure 4.11: Average Monthly Rainfall by Decade for Delta State from 1981 to 2023

The figure clearly demonstrates the seasonal nature of rainfall in Delta State, with a distinct wet season typically spanning from April to October, characterized by significantly higher average monthly rainfall. Peak rainfall is generally observed during the months of July, August, and September across all decades. The dry season, from November to March, experiences considerably lower rainfall amounts. This seasonal pattern aligns with the broader climatic regime of the West African monsoon, which dictates precipitation patterns in the region (Khalil Ahmad et al., 2022; Sian et al., 2025).

Comparing the decadal averages reveals some interesting variations in the monthly rainfall distribution. For instance, the decade of 2001–2010 appears to exhibit slightly higher average rainfall during the peak wet season months (July–September) compared to the other decades. Conversely, the earlier decades (1981–1990 and 1991–2000) seem to have experienced relatively lower rainfall during these peak months. These inter-decadal differences are consistent with findings from recent climatological studies that highlight the influence of global and regional climatic drivers such as Atlantic sea surface temperature variability and anthropogenic changes on West African rainfall patterns (Mohino et al., 2011).

Interestingly, while Figure 4.11 indicated a statistically non-significant decreasing trend in annual rainfall, this decadal analysis suggests a more complex picture. The shifts in average monthly rainfall across decades, particularly during the wet season, imply that the overall annual trend might be a result of subtle changes in the intensity and distribution of rainfall within the year, rather than a uniform decrease across all months. For example, a slight increase in rainfall during some months might be offset by a decrease in others, resulting in a non-significant annual trend (Animashaun et al., 2020).

The most recent decade (2011–2023) shows a tendency towards lower average rainfall during the early part of the wet season (April–June) compared to the 2001–2010 period. However, the peak rainfall months still exhibit substantial amounts. This highlights the dynamic nature of rainfall patterns and the importance of examining sub-annual variations to fully understand climate trends. The observed inter-decadal variability in monthly rainfall could have significant implications for various sectors in Delta State, including agriculture, water resource management, and flood risk assessment. Shifts in the timing and intensity of rainfall can affect crop yields, water availability for domestic and industrial use, and the likelihood of flooding events (Cai et al., 2015a).

II. 12-Month Standardized Precipitation Index (SPI) for Delta State (1981-2023)

Figure 4.12 displays the 12-month Standardized Precipitation Index (SPI) for Delta State from 1981 to 2023. The SPI is a widely used index to quantify precipitation deficits or surpluses at different time scales, providing insights into drought severity and frequency.

The fluctuating nature of the 12-month SPI in Figure 4.12 indicates periods of both wetter-than-average (positive SPI values) and drier-than-average (negative SPI values) conditions across the study period. Notably, the index frequently crosses the +1 and -1 thresholds (indicated by the red dashed lines), which typically signify moderately wet and moderately dry conditions, respectively.

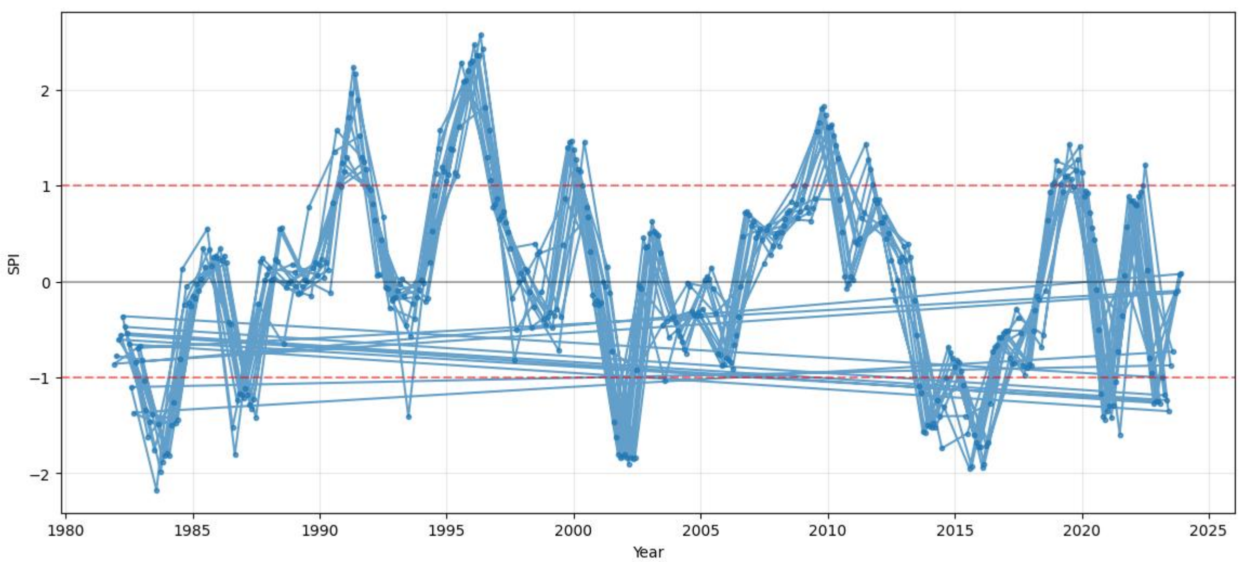

Figure 4.12: 12-Month Standardized Precipitation Index (SPI) for Delta State (1981-2023)

Several periods of prolonged negative SPI values, indicating potential drought episodes, can be observed. For instance, there appear to be extended dry periods in the late 1980s, around the early 2000s, and again in the mid-2010s. The magnitude of the negative SPI values during these periods suggests the occurrence of moderate to severe drought conditions in Delta State. Conversely, periods with sustained positive SPI values, such as the mid-1990s and around 2012, indicate prolonged periods of above-average wetness.

Connecting these observations to the annual rainfall trend discussed in Figure 4.10, the lack of a statistically significant long-term trend in annual rainfall does not preclude the occurrence of significant inter-annual and multi-year variations in water availability, as highlighted by the SPI. Even without a consistent decrease in total annual rainfall, shifts in the timing and distribution of rainfall within the year (as suggested by Figure 4.10) can lead to periods of prolonged moisture deficit reflected in the SPI.

Furthermore, the SPI analysis provides a different perspective compared to simply looking at total rainfall amounts. The SPI normalizes precipitation data to account for the long-term mean and standard deviation, allowing for a more standardized assessment of wetness and dryness across different time periods and locations.

The occurrence of both wet and dry spells, as indicated by the SPI, underscores the hydroclimatic variability experienced in Delta State. These fluctuations can have significant implications for water resources management, agriculture, and ecological systems in the region. Understanding the frequency and severity of these events is crucial for developing effective adaptation strategies to mitigate the impacts of both water scarcity and excess.

In conclusion, the 12-month SPI analysis for Delta State reveals significant inter-annual variability in moisture conditions, with notable periods of both drought and wetness between 1981 and 2023. While the annual rainfall trend was not statistically significant, the SPI highlights the occurrence of prolonged dry periods, emphasizing the importance of considering drought indices in assessing water resource availability and potential risks in the region. Future research could explore the relationship between these SPI fluctuations and specific climate drivers or their impacts on different sectors within Delta State.

III. Inter-annual Rainfall Extremes and Drought Risk

Figure 4.13 illustrates the trend in the number of extreme rainfall days in Delta State from 1981 to 2023. Here, extreme rainfall days are defined as those exceeding the 95th percentile of daily rainfall during the baseline period. Analyzing the frequency of such extreme events is crucial for understanding potential increases in flood risk and the intensity of precipitation, even if the total annual rainfall does not show a significant trend (as seen in Figure 10).

The time series in Figure 4.13 exhibits considerable inter-annual variability in the number of extreme rainfall days. We observe periods with a higher frequency of these events, such as the early 1990s and around 2010, and periods with fewer extreme rainfall days, such as the mid-1980s and the early 2000s.

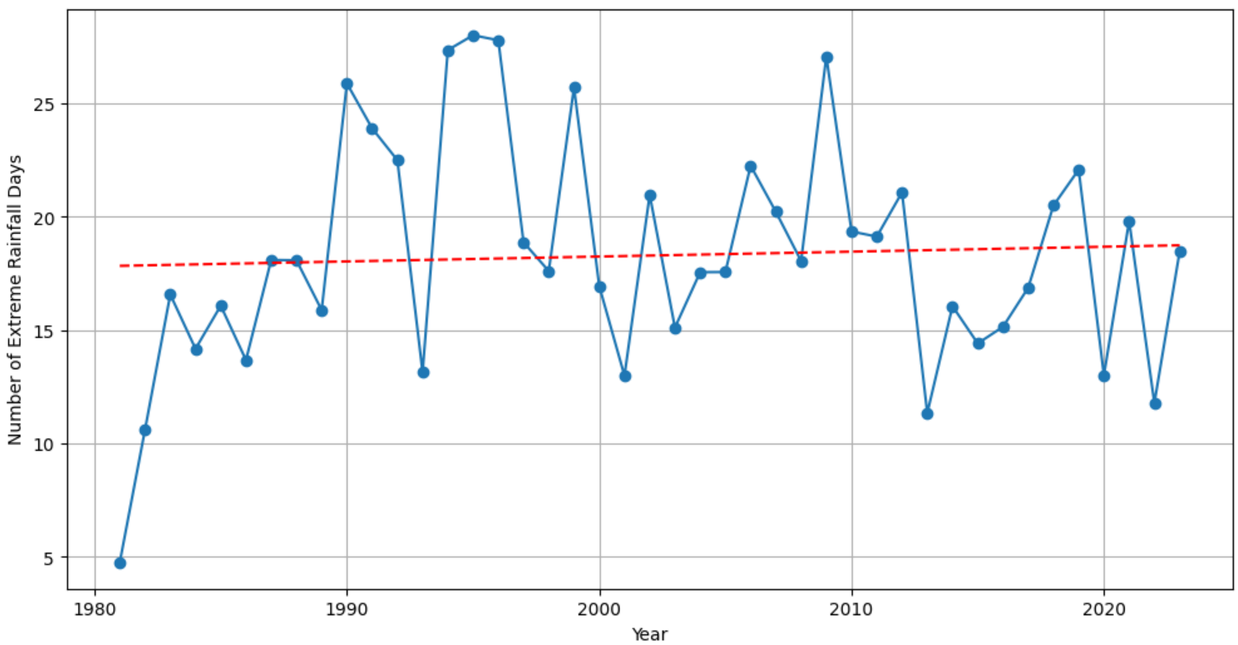

Figure 4.13: Inter-annual Rainfall Extremes for Delta State from 1983 - 2023

Superimposed on the inter-annual fluctuations is a slightly increasing trend line (red dashed line). To statistically assess the significance of this visual trend, a more formal trend analysis such as the non-parametric Mann-Kendall test is necessary. However, the upward slope of the trend line suggests a potential increase in the frequency of extreme rainfall events over the study period. Recent studies have similarly highlighted emerging trends of increasing rainfall intensity in West Africa, even in the absence of consistent increases in total rainfall (Sylla et al., 2016; Tano et al., 2023).

This potential increase in extreme rainfall days, even without a significant trend in total annual rainfall, has important implications. It suggests that while the overall amount of rainfall may not have changed drastically, the intensity of rainfall events could be rising. This can lead to a heightened risk of localized flooding, soil erosion, and infrastructure damage, especially as urban drainage systems may not be designed to handle such short bursts of intense precipitation

(Shortridge, 2019). These hydrological challenges are increasingly relevant for urban and peri-urban areas in Nigeria, where land cover changes compound climate-related vulnerabilities.

Connecting this to the decadal analysis of monthly rainfall (Figure 4.11), shifts in the distribution of rainfall within the wet season could contribute to an increase in the number of extreme rainfall days. For instance, if the peak rainfall months are experiencing more intense rainfall events, even if the duration of the wet season or the rainfall in other months' changes only slightly, it could result in a higher count of days exceeding the extreme threshold. This supports previous observations that changes in intra-seasonal rainfall characteristics often play a more critical role in hydrological impacts than annual totals alone (Sylla et al., 2016).

The observed variability in the number of extreme rainfall days may be linked to shifts in atmospheric circulation patterns, warming sea surface temperatures in the Gulf of Guinea, and other regional climate drivers that influence convective activity in the tropics (Palmer et al., 2023). Further research could explore these relationships to better understand the mechanisms driving the potential increase in extreme rainfall events and help inform adaptation planning across vulnerable sectors.

IV. Monthly Rainfall Variability

Figure 4.14 presents the monthly rainfall variability in Delta State from 1981 to 2023 using boxplots. Each boxplot summarizes the distribution of monthly rainfall for a specific month across all 43 years of data. This visualization allows us to understand not only the central tendency (median) of rainfall in each month but also the spread (interquartile range) and the presence of outliers, indicating the range of rainfall conditions experienced throughout the year (Ishak et al., 2025).

As anticipated from the decadal averages shown in Figure 4.11, the boxplots clearly illustrate the distinct wet and dry seasons in Delta State. The months from April to October exhibit significantly higher median rainfall (the horizontal line within each box) and a much larger interquartile range (the height of the box), indicating greater variability in rainfall amounts during these months. The peak rainfall months, particularly July, August, and September, show the highest median rainfall and the widest spread, reflecting substantial differences in rainfall amounts across different years during the core of the wet season (Song et al., 2011).

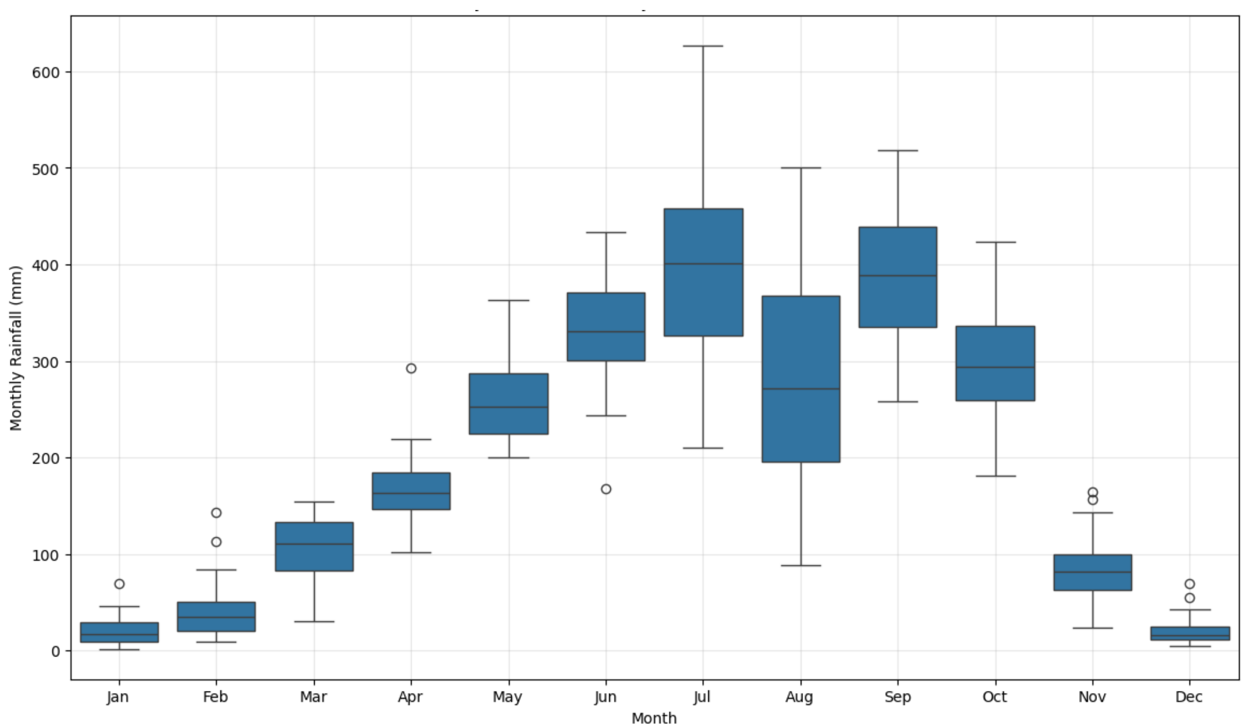

Figure 4.14: Monthly Rainfall Variability in Delta State from 1981 to 2023.

Conversely, the months from November to March show considerably lower median rainfall and a much smaller interquartile range, indicating consistently drier conditions with less year-to-year variation. This confirms the pronounced seasonality driven by the West African monsoon system, which is the primary determinant of rainfall patterns in this region (Nicholson, 2017).

The whiskers extending from each box represent the range within which the majority of the data points fall (typically 1.5 times the interquartile range). The circles outside the whiskers represent outliers, indicating months in which the rainfall was exceptionally high or low compared to the typical range for that month. The presence of outliers, particularly during the wet season months, highlights the occurrence of unusually wet or dry conditions within those months across the study period.

Comparing the boxplots across different months reveals the gradual onset of the wet season from April, peaking in the July-September period, and then a gradual decline towards the dry season starting in November. The asymmetry of some boxplots (where the median is not in the center of the box, or the whiskers are of unequal length) suggests a skewness in the rainfall distribution for those months, indicating that rainfall amounts are more concentrated towards either the higher or lower end of the spectrum.

This detailed view of monthly rainfall variability complements the annual trend analysis (Figure 4.10) and the decadal averages (Figure 4.11). While the annual trend might be non-significant, and the decadal averages show shifts in monthly rainfall, this boxplot provides a comprehensive picture of the range of rainfall conditions experienced in each month over the long term. It underscores the inherent variability within each month and highlights the potential for both very wet and relatively dry conditions, particularly during the wet season.

Understanding this monthly variability is crucial for various applications, including agricultural planning (e.g., planting and harvesting times), water resource management (e.g., reservoir operations), and disaster preparedness (e.g., anticipating flood risks during months with high variability and extreme rainfall events, as discussed in Figure 4) (Masson-Delmotte et al., 2021).

In conclusion, the boxplots of monthly rainfall in Delta State from 1981 to 2023 effectively illustrate the strong seasonal pattern and the substantial inter-annual variability within each month, particularly during the wet season. This detailed understanding of monthly rainfall distribution and the presence of outliers provides valuable insights into the hydro-climatic regime of the region.

V. Seasonal Rainfall Trends

Figure 4.15 presents the seasonal rainfall trends in Delta State from 1981 to 2023, dividing the year into four distinct seasons: Dry (December-February), Early Wet (March-May), Peak Wet (June-August), and Late Wet (September-November). Analyzing rainfall trends at this seasonal scale can reveal nuances that might be masked when considering only annual totals (as in Figure 4.10) or monthly averages (as in Figure 4.14).

The Dry season (December-February), represented by the blue line, consistently shows the lowest rainfall amounts across the entire period, which is expected for this region influenced by the dry harmattan winds (Khalil Ahmad et al., 2022). The variability in rainfall during this season appears relatively low, with no clear long-term trend discernible by visual inspection.

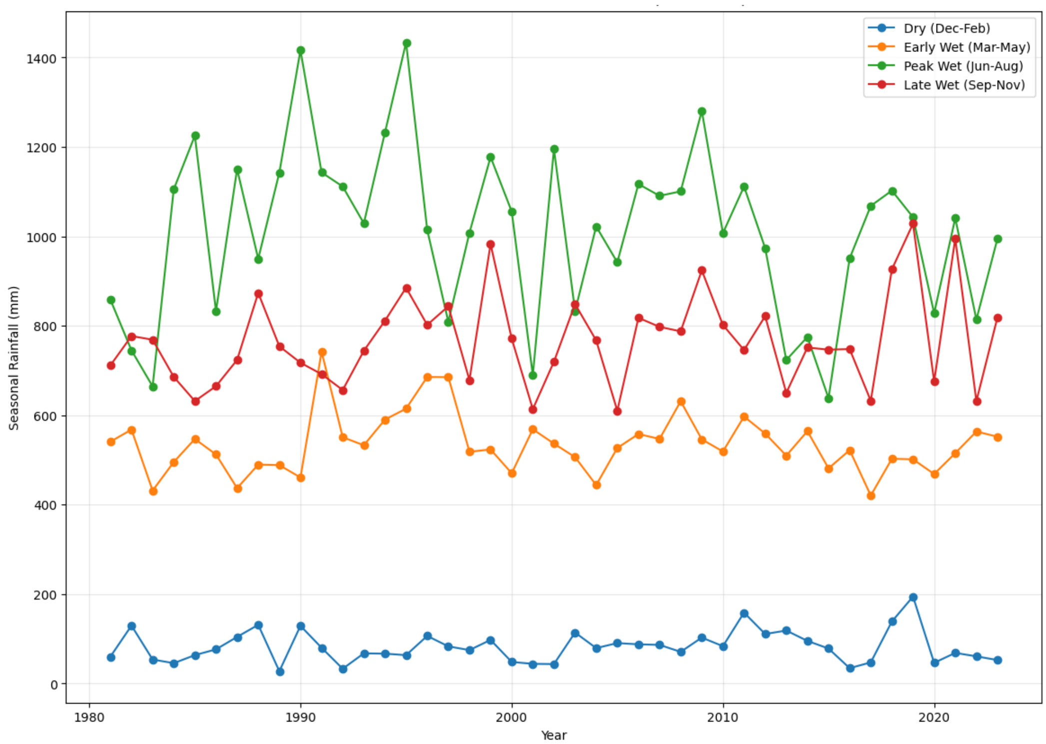

Figure 4.15: Seasonal Rainfall Trends in Delta State from 1981 to 2023.

The Early Wet season (March–May), depicted by the orange line, shows a gradual increase in rainfall compared to the dry season, marking the transition into the main wet period. There appears to be some inter-annual variability, but again, a strong long-term trend is not immediately obvious from the graph. This transitional period aligns with broader West African monsoon dynamics and is consistent with findings from recent regional climate assessments (Cook and Vizy, 2019).

The Peak Wet season (June–August), represented by the green line, exhibits the highest rainfall amounts and the most significant inter-annual variability. This supports earlier observations from the monthly boxplots (Figure 4.14), which highlighted July and August as the months with the highest median rainfall and the widest spread. Visual inspection suggests substantial fluctuations from year to year, with some notably high rainfall years in the late 1980s and around 2012. Such variability in the core monsoon months has been associated with shifts in sea surface temperatures and changing atmospheric circulation patterns that drive West African precipitation.

The Late Wet season (September–November), shown by the red line, indicates a decrease in rainfall compared to the peak wet season as the monsoon begins to retreat. This season also displays considerable inter-annual variability. Interestingly, there might be a visual suggestion of a decreasing trend in rainfall during the late wet season, particularly in the latter part of the study period, although this would require statistical validation. These observations are consistent with the projected shortening or weakening of wet seasons reported in CMIP6 climate model outputs for the West African region (Yahaya et al., 2024).

Comparing these seasonal trends provides a more detailed understanding of the rainfall dynamics in Delta State. While the annual rainfall trend (Figure 4.10) was non-significant, these seasonal analyses suggest that changes might be more pronounced within specific seasons. For example, a potential decrease in rainfall during the Late Wet season, if statistically significant, could affect late-season agriculture and reduce water availability toward the dry months, impacting food security and water resource management (Shukla et al., 2021).

Similarly, the high variability in the Peak Wet season is crucial for understanding flood risks and planning adequate water storage infrastructure. The lack of a strong trend across all seasons suggests that the overall non-significant annual trend may result from complex intra-annual interactions and potentially opposing tendencies. For instance, a slight increase in rainfall during one season may be counterbalanced by a decrease in another. Further statistical analysis—such as the Mann-Kendall trend test and Sen's slope estimation should be applied to each seasonal time series to determine the significance and magnitude of any underlying trends. This would provide a more nuanced and robust understanding of how seasonal rainfall patterns have evolved over the past four decades.

VI. Wet Season Onset and Duration Trends

Figure 4.16 presents the trends in the wet season onset (top panel) and wet season duration (bottom panel) in Delta State from 1981 to 2023. The wet season onset is indicated by the month number (e.g., 3 for March, 4 for April), while the duration is measured in months. Changes in these phenological indicators of the rainy season can have significant implications for agricultural practices, natural ecosystems, and water availability (Hajek and Knapp, 2022).

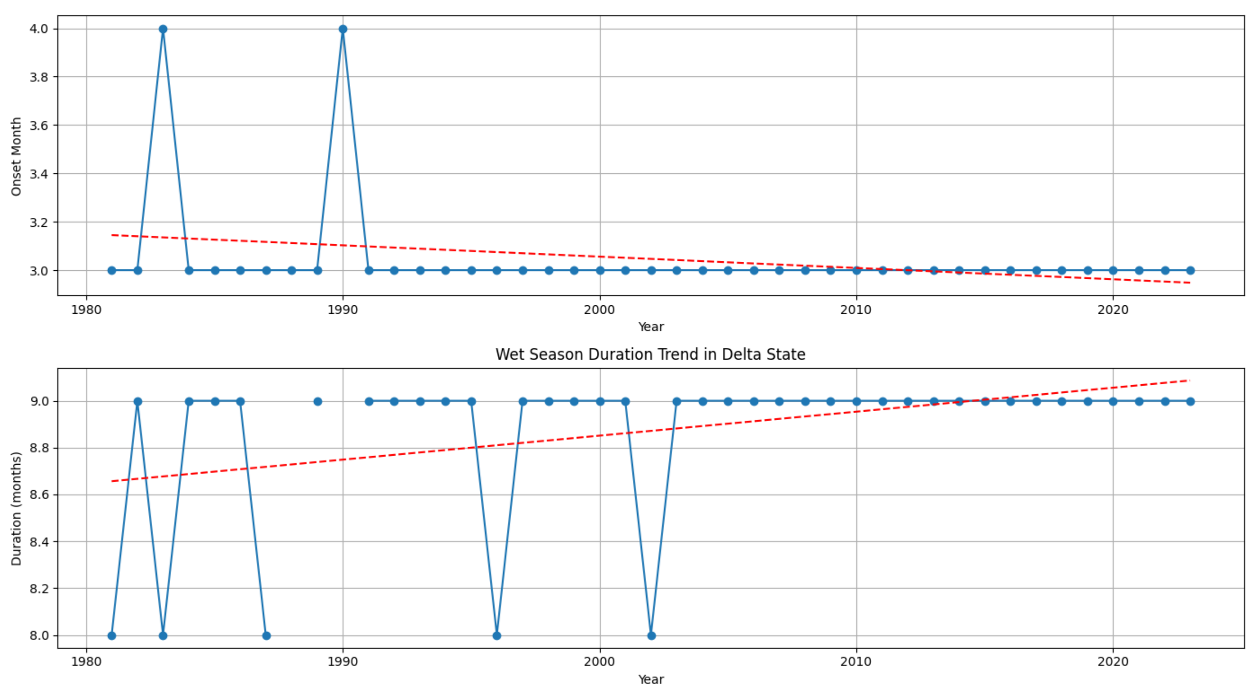

Figure 4.16: Wet Season Onset Trend in Delta State from 1983 to 2023

i. Wet Season Onset:

The top panel shows considerable inter-annual variability in the onset of the wet season. The onset appears to fluctuate between March (month 3) and April (month 4) for most of the study period, with a few instances of a later onset in May (month 5). Superimposed on this variability is a slightly decreasing trend line (dashed line). While the fluctuations are prominent, the downward slope of the trend line suggests a tendency towards an earlier onset of the wet season over the study period. However, as with the trend in extreme rainfall days (Figure 4.13), a formal statistical test would be needed to confirm the significance of this visual trend. These observed shifts in the timing of wet season onset are consistent with regional studies indicating changes in monsoon dynamics across West Africa under a changing climate (Hagos and Cook, 2007). An earlier onset of the wet season could have implications for planting schedules and the overall length of the growing season, which is crucial for optimizing crop productivity and agricultural planning (Sylla et al., 2018).

ii. Wet Season Duration:

The bottom panel illustrates the trend in the duration of the wet season. Similar to the onset, the duration also exhibits inter-annual variability, ranging primarily between approximately 8 and 9 months. There are some years with shorter durations. The superimposed trend line (dashed line) shows a slight upward slope, suggesting a tendency towards a longer wet season over the study period. Again, statistical analysis would be necessary to determine the significance of this trend. A longer wet season could potentially increase total rainfall amounts over the year and have implications for water resources and flood risk.

The observed trends in wet season onset and duration could be linked to broader changes in atmospheric circulation patterns and the timing of the West African monsoon (Thorncroft et al., 2011). Shifts in these large-scale climate drivers can influence the arrival and retreat of the rainy season in the region.

The potential earlier onset and longer duration of the wet season, if statistically significant, could have both positive and negative consequences. A longer growing season might benefit agriculture, but it could also lead to changes in the timing of agricultural activities and potentially increase the risk of flooding during extended periods of rainfall. Understanding these changes is crucial for developing appropriate adaptation strategies.

4.4.3 Rainfall Trend Analysis for Bayelsa State

The annual rainfall pattern in Bayelsa State from 1981 to 2023, as depicted in Figure 4.17, reveals considerable inter-annual variability. Visual inspection of the time series plot indicates fluctuations in total annual rainfall over the study period, ranging from a low of approximately 2250 mm to a high of nearly 3800 mm. To statistically assess the presence and direction of a long-term trend, the non-parametric Mann-Kendall trend test was applied to the annual rainfall data.

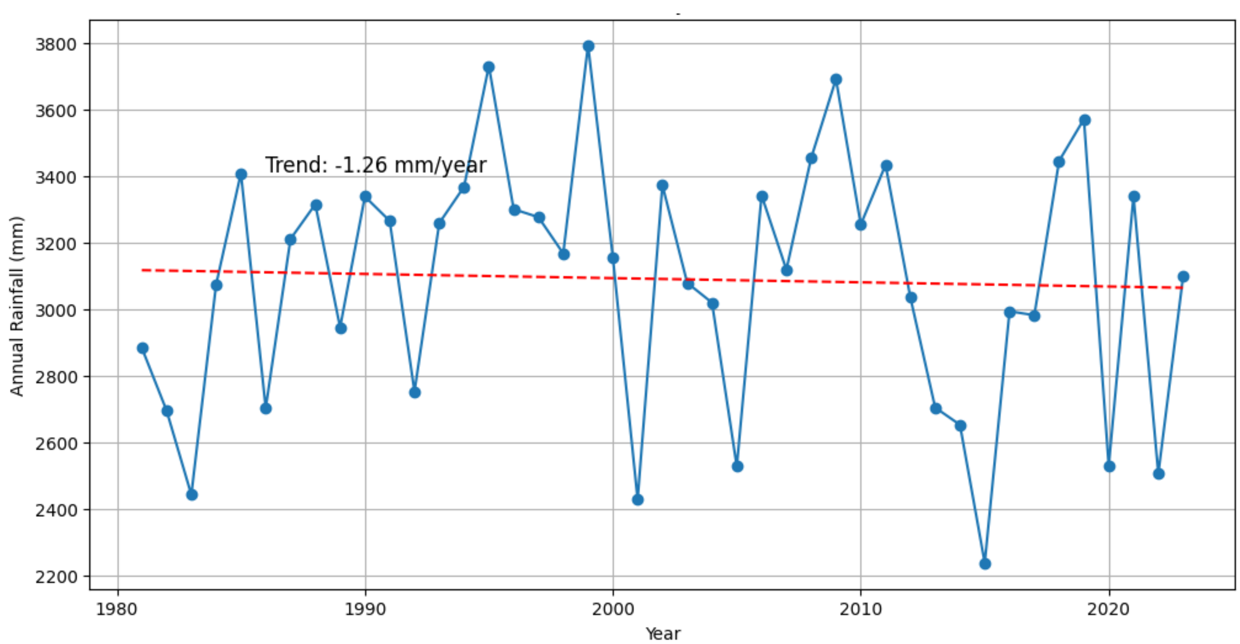

Figure 4.17: Annual Rainfall Trend Analysis for Bayelsa State from 1981 to 2023

The results of the Mann-Kendall trend test indicate a decreasing trend in annual rainfall in Bayelsa State over the period 1981–2023. However, this trend was found to be statistically insignificant, with a p-value of 0.7897, which is considerably higher than the conventional significance level of 0.05. This suggests that while there is a calculated downward slope, it is not statistically robust enough to conclude a significant long-term decline in annual rainfall during the study period. Further analysis using Sen's slope estimator quantified the magnitude of this non-significant downward trend at −1.2555 mm/year. This value suggests that, on average, the annual rainfall in Bayelsa State has decreased by approximately 1.26 mm per year over the past four decades. This is visually represented in Figure 4.17 by the dashed red trend line, which exhibits a slight negative slope across the time series.

The observed inter-annual variability, coupled with the statistically insignificant long-term trend, highlights the complex nature of rainfall patterns in the region. While the Sen's slope suggests a gradual drying trend, the high p-value from the Mann-Kendall test implies that this observed decrease could be attributed to natural climate variability rather than a systematic long-term change. These findings are consistent with studies in other tropical coastal regions that often exhibit high rainfall variability and complex responses to broader climate signals (Akeh and Mshelia, 2016; Ciemer et al., 2019). It is important to consider the potential implications of even a non-significant decreasing trend, particularly in a region like Bayelsa State that is susceptible to the impacts of both flooding and potential future water scarcity. Continued monitoring of rainfall patterns and further investigation into the underlying climatic drivers are warranted to better understand the long-term hydrological changes in the region (Hoffmann and Spekat, 2021; Sylla et al., 2018).

I. Monthly Rainfall Patterns and Extremes

Figure 4.18 presents the average monthly rainfall in Bayelsa State, segmented by decade from 1981 to 2023. This decadal analysis provides a detailed view of the seasonal rainfall distribution and highlights potential shifts in these patterns over time. The figure clearly illustrates a consistent unimodal rainfall regime across all four decades, with a distinct wet season centered around the months of June, July, August, and September. Peak average monthly rainfall consistently occurs during these months, indicating a strong seasonality in the hydrological cycle of Bayelsa State (Okoro and Ofordu, 2025; Sylla et al., 2018). The drier months are typically from November to April, characterized by significantly lower average rainfall.

Comparing the average monthly rainfall across the decades reveals some interesting variations in the magnitude of rainfall during different parts of the year. Notably, the decade of 1991–2000 generally exhibits the highest average rainfall during the peak wet season months of June and July, reaching approximately 510 mm and 540 mm, respectively. In contrast, the most recent decade (2011–2023) appears to have experienced slightly lower average rainfall during these peak months compared to the 1991–2000 period. For instance, the average rainfall in July during 2011–2023 is around 470 mm. These decadal variations in peak rainfall may reflect the influence of broader climate variability and changing atmospheric circulation patterns affecting West Africa (Ciemer et al., 2019; Khalil Ahmad et al., 2022).

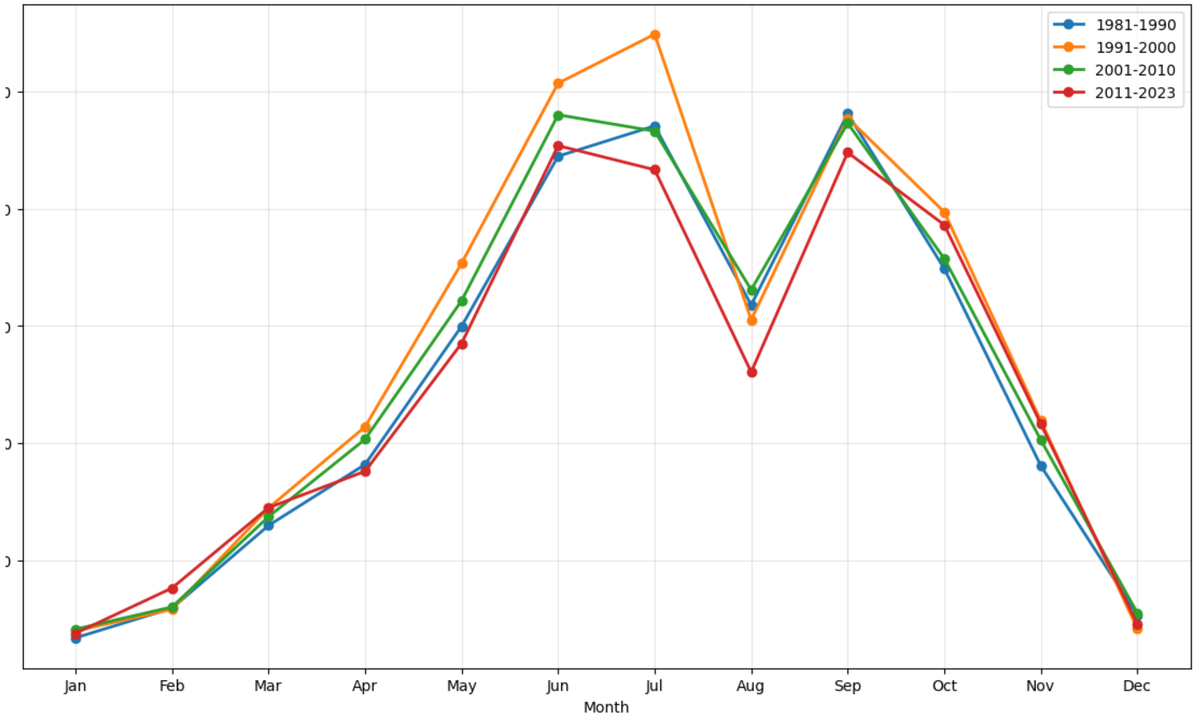

Figure 4.18: Average Monthly Rainfall by Decade for Bayelsa State from 1981 to 2023

Furthermore, there are observable differences during the transition months. For example, the average rainfall in May shows a general increase from the earliest decade (1981–1990) to the 1991–2000 period, followed by a slight decrease in the subsequent decades. Similarly, the retreat of the wet season, as seen in October, shows some variability in average rainfall amounts across the decades. The observed inter-decadal variations in average monthly rainfall, while not statistically tested here, suggest potential shifts in the intensity and temporal distribution of rainfall within the year. These changes could have implications for various sectors, including agriculture, which is highly dependent on the predictable onset and duration of the wet season (Hassan and Syakir, 2023; Yanto et al., 2016). Shifts in peak rainfall timing or a reduction in rainfall during critical growth periods could impact crop yields (Aji Suraji et al., 2022).

Moreover, understanding these decadal changes in monthly rainfall is crucial for water resource management and flood risk assessment. A decrease in rainfall during the peak wet season in recent decades, if statistically significant, could have implications for water availability during the dry season. Conversely, changes in the intensity of rainfall during peak months could affect the frequency and magnitude of flooding in this low-lying coastal state. Continuous monitoring and climate-resilient planning are therefore essential to mitigate the potential socio-economic impacts of changing rainfall dynamics.

II. Inter-annual Rainfall Extremes and Drought Risk

Figure 4.19 illustrates the annual number of extreme rainfall days in Bayelsa State from 1981 to 2023, where extreme rainfall is defined as exceeding the 95th percentile of daily rainfall. The time series plot reveals considerable year-to-year variability in the frequency of these extreme events. Visual inspection of Figure 4.19 suggests a potential increasing trend in the number of extreme rainfall days over the study period. While there are notable fluctuations, with periods of both high and low numbers of extreme rainfall days, the general tendency appears to be upward. This is further supported by the dashed trend line, which exhibits a positive slope across the time series.

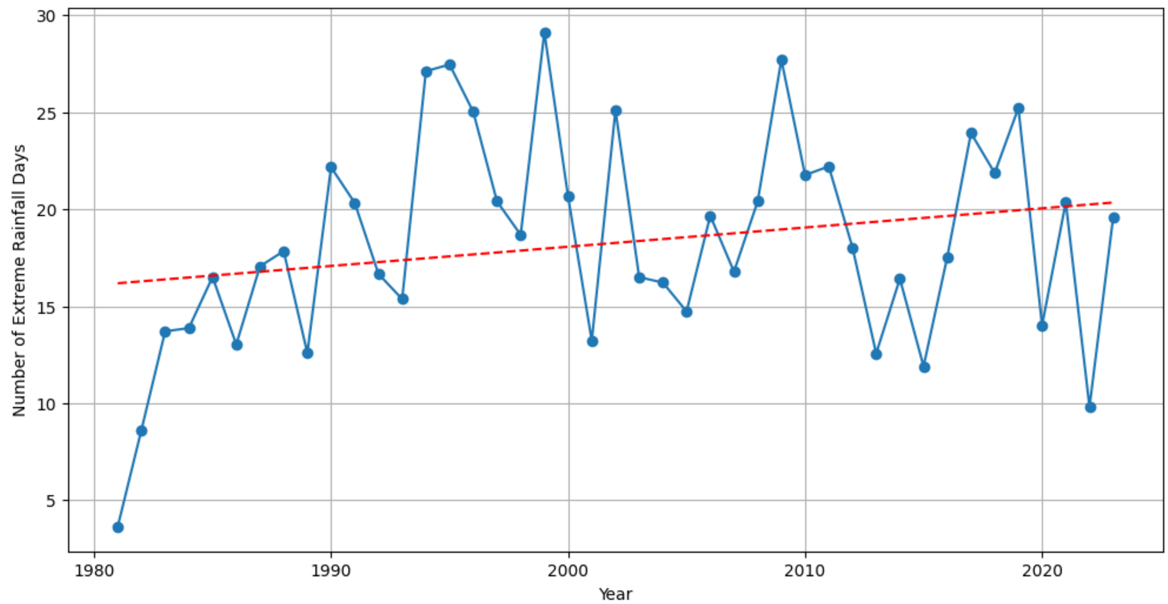

Figure 4.19: Inter-annual Rainfall Extremes for Bayelsa State from 1983 - 2023

The increasing frequency of extreme rainfall days has significant implications for a low-lying coastal region like Bayelsa State. More frequent high-intensity rainfall events can exacerbate the risk of flooding, leading to damage to infrastructure, displacement of communities, and disruption of livelihoods (Douglas, 2017; Otto et al., 2023). This is particularly concerning given the existing vulnerability of the region to flooding due to its topography and proximity to the coast (Roy and Blaschke, 2015).

The observed trend in extreme rainfall days could be linked to broader climate change patterns, which are projected to increase the intensity and frequency of extreme weather events in many parts of the world. Changes in atmospheric circulation patterns, increased atmospheric moisture holding capacity due to warming, and the influence of regional climate drivers could all contribute to this trend.

Further analysis could explore potential correlations between the number of extreme rainfall days and other climatic variables, such as sea surface temperatures or regional wind patterns, to better understand the underlying mechanisms driving this trend. Additionally, assessing the spatial distribution of these extreme events within Bayelsa State could provide valuable insights for targeted adaptation and mitigation strategies.

III. Monthly Rainfall Variability

Figure 4.20 provides a comprehensive overview of the monthly rainfall variability in Bayelsa State over the period 1981-2023. The box plots for each month illustrate the distribution of monthly rainfall amounts, including the median, quartiles, and potential outliers, offering insights into both the central tendency and the spread of rainfall across different months.

The box plots clearly demonstrate the pronounced seasonal rainfall pattern in Bayelsa State. The months of June, July, August, and September exhibit the highest median monthly rainfall, consistent with the wet season identified in the decadal analysis (Figure 4.20). July shows the highest median rainfall, exceeding 500 mm, and also displays a wide interquartile range, indicating substantial variability in rainfall amounts during this peak wet season month across different years.

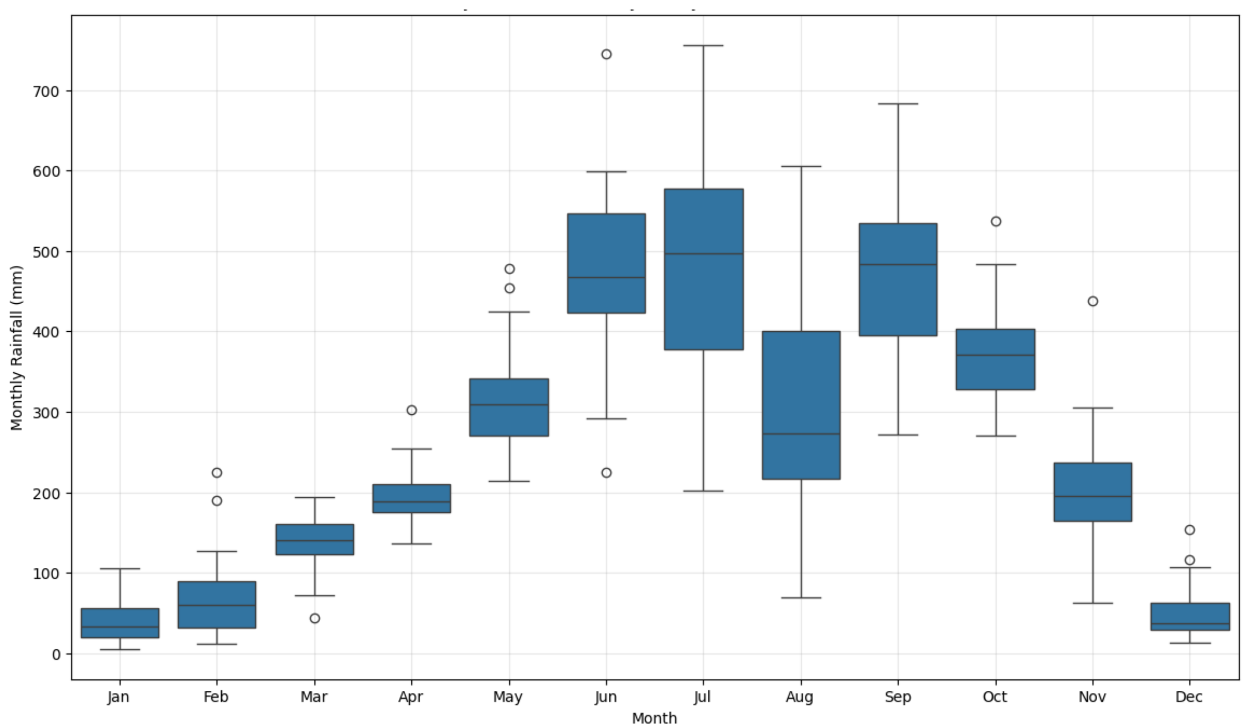

Figure 4.20: Monthly Rainfall Variability in Bayelsa State from 1981 to 2023.

Conversely, the months from November to March show significantly lower median monthly rainfall, highlighting the dry season. January and December have the lowest median rainfall, typically below 50 mm, with relatively compact box plots suggesting less inter-annual variability during these dry months.

The length of the boxes, representing the interquartile range (IQR), provides a measure of the spread of the central 50% of the data for each month. Months with longer boxes, such as June, July, August, and September, indicate greater variability in monthly rainfall from year to year during the wet season. This suggests that while these months consistently receive the highest rainfall, the exact amount can differ considerably between years (Khalil Ahmad et al., 2022; Yanto et al., 2016).

The whiskers extending from the boxes represent the range of the data within 1.5 times the IQR. The presence of circles beyond the whiskers indicates potential outliers, representing years with exceptionally high or low rainfall for a particular month compared to the long-term average. For instance, several months, particularly during the wet season (May to October), show outliers on the higher end, indicating instances of extreme monthly rainfall.

The information presented in Figure 4.20 is crucial for understanding the reliability and predictability of rainfall across different times of the year. The high variability during the wet season has implications for water management, agriculture planning (e.g., planting and harvesting schedules), and disaster preparedness for flooding (Cherinet et al., 2022; Sikka et al., 2016). The relatively lower variability during the dry season suggests a more consistent period of low rainfall, relevant for water resource management and irrigation needs (Khalil Ahmad et al., 2022).

IV. Seasonal Rainfall Trends

Figure 4.21 presents the trends in seasonal rainfall amounts in Bayelsa State from 1981 to 2023, dividing the year into four distinct seasons: Dry (December-February), Early Wet (March-May), Peak Wet (June-August), and Late Wet (September-November). This disaggregation allows for a more nuanced understanding of how rainfall patterns have evolved across different parts of the year.

The plot clearly shows that the Peak Wet season (June-August) consistently receives the highest amount of rainfall compared to the other seasons throughout the study period. The seasonal rainfall during this period fluctuates considerably from year to year, ranging from approximately 1200 mm to over 1750 mm. This dominance of the June-August rainfall aligns with the monthly analysis, which identified these months as having the highest rainfall totals.

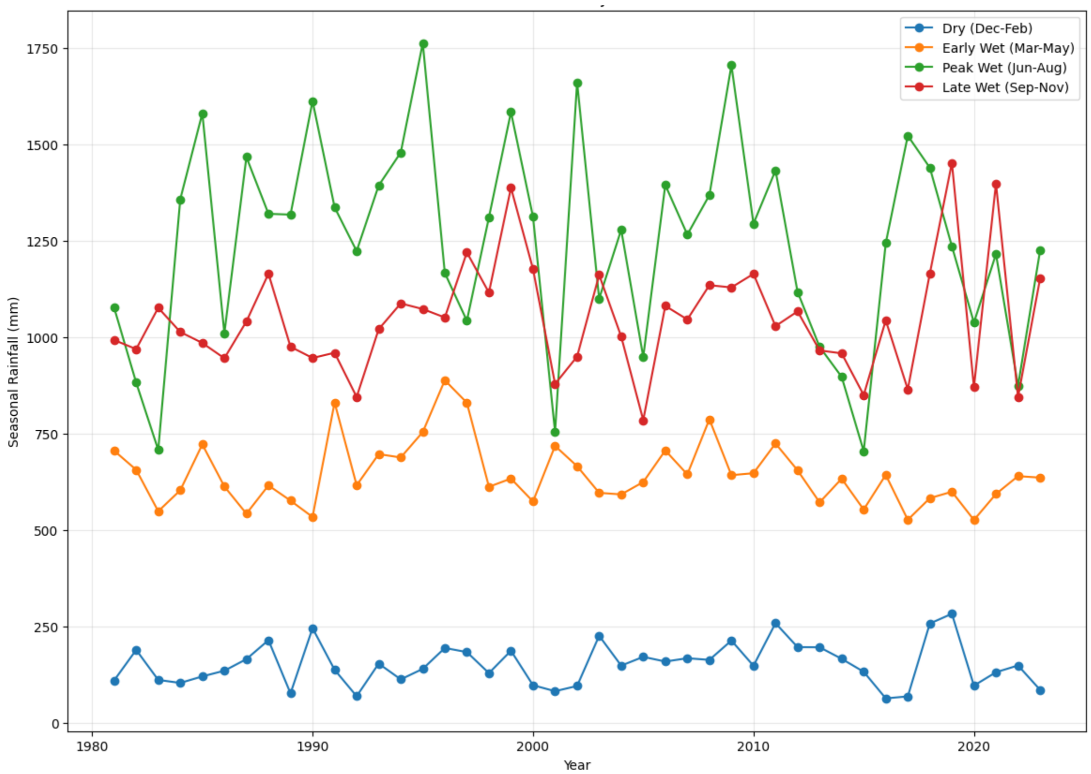

Figure 4.21: Seasonal Rainfall Trends in Bayelsa State from 1981 to 2023.

The Late Wet season (September–November) also contributes significantly to the annual rainfall, with amounts generally ranging between 800 mm and 1400 mm. Similar to the Peak Wet season, this period exhibits substantial inter-annual variability. In contrast, the Early Wet season (March–May) receives a moderate amount of rainfall, typically between 500 mm and 850 mm, with noticeable fluctuations across the years. The Dry season (December–February) consistently experiences the lowest rainfall amounts, generally staying below 300 mm and often below 200 mm, which is expected for a region with a distinct wet and dry season cycle (Sylla et al., 2018).

Visual inspection of the trends for each season does not reveal strong, consistent long-term increases or decreases across all seasons. However, some observations can be made. For instance, the Peak Wet season shows considerable variability without a clear upward or downward trend discernible by eye. Similarly, the Late Wet and Early Wet seasons exhibit fluctuations without a pronounced directional change over the study period. The Dry season also shows inter-annual variability, but the overall amounts remain consistently low (Animashaun et al., 2023). To rigorously determine the presence and significance of trends in each season, statistical trend tests such as the Mann-Kendall test and Sen's slope estimation (as applied to the annual rainfall in Figure 4.17) would be necessary for each seasonal time series. These tests would quantify the magnitude and statistical significance of any potential long-term changes in seasonal rainfall amounts.

Understanding the trends in seasonal rainfall is crucial for assessing potential shifts in the hydrological regime of Bayelsa State. Changes in the timing or intensity of rainfall during critical agricultural seasons (often coinciding with the Early and Peak Wet seasons) can impact crop production (Zeppel et al., 2014). Similarly, variations in rainfall during the Late Wet season can influence the frequency and severity of late-year flooding (Li et al., 2022). The consistently low rainfall during the Dry season is important for water resource management and planning for potential water stress (Pedro-Monzonís et al., 2015).

V. Wet Season Onset and Duration Trends

Figure 4.22 displays the annual trends in the onset (top panel, measured in terms of the month of the year, where 3 represents March, 4 represents April, etc.) and duration (bottom panel, measured in months) of the wet season in Bayelsa State from 1981 to 2023. Understanding the temporal characteristics of the wet season is crucial for various climate-sensitive sectors, particularly agriculture and water resource management.

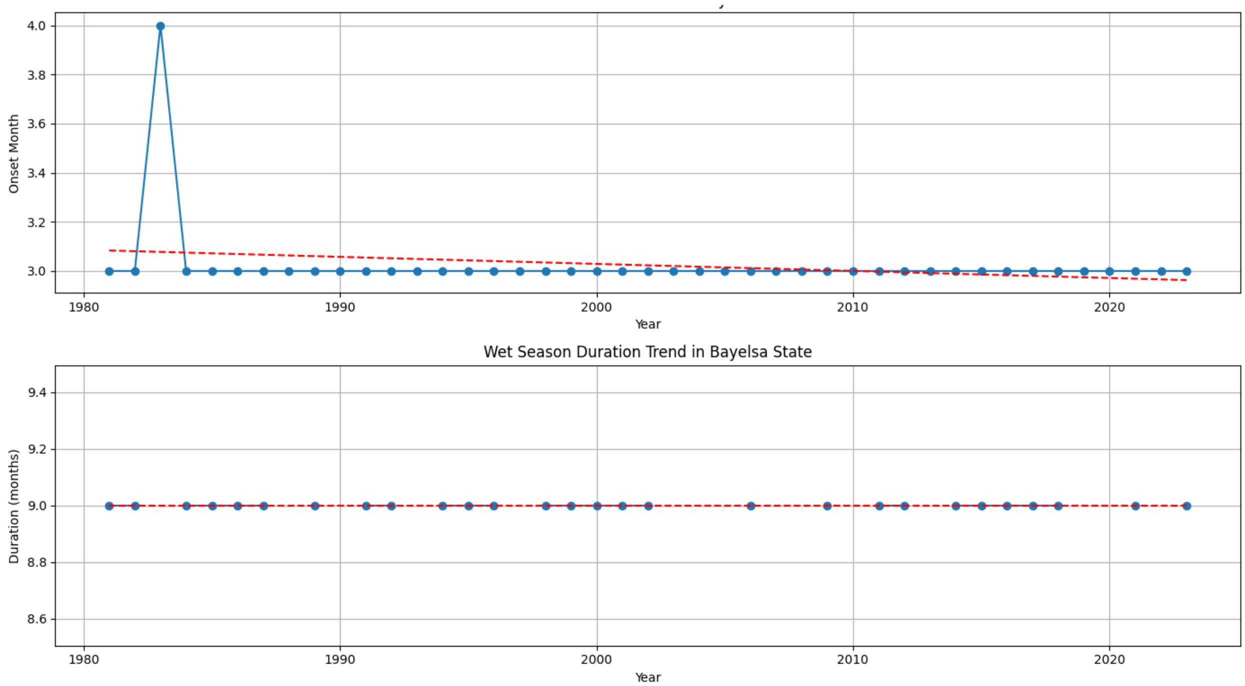

Figure 4.22: Wet Season Onset Trend in Bayelsa State from 1983 to 2023

The top panel of Figure 4.22 illustrates the inter-annual variability in the onset of the wet season. For the majority of the study period, the wet season onset appears to occur consistently around the beginning of April (month 4). However, there is a notable early onset in the initial years, particularly in 1982, where the onset appears to be in March (month 3). After this early onset, the onset seems to stabilize around April for a considerable period. Towards the end of the record, there might be a subtle suggestion of a slightly later onset in some years, although the variability remains relatively low. The dashed red trend line indicates a very slight, almost negligible, trend towards a later onset of the wet season over the study period. Statistical analysis using a trend test would be needed to confirm if this minor visual trend is significant (Sylla et al., 2018).

The bottom panel of Figure 4.22 shows the trend in the duration of the wet season. This panel reveals a remarkable consistency in the length of the wet season in Bayelsa State over the 1981–

2023 period. For almost all years, the wet season duration appears to be consistently around 9 months. There is very little inter-annual variability observed in the duration, with the data points clustering tightly around the 9-month mark. The dashed red trend line in this panel is virtually horizontal, indicating no discernible long-term trend in the duration of the wet season.

The relative stability in both the onset and duration of the wet season, as depicted in Figure 6, has important implications. A consistent wet season onset around April provides a predictable timeframe for agricultural planning activities such as planting. Similarly, a consistent wet season duration of approximately 9 months allows for relatively stable water availability periods, crucial for both rain-fed agriculture and water resource management (Wani et al., 2009a).

However, it is important to note that while the onset and duration might be relatively stable, the intensity and distribution of rainfall within the wet season can still exhibit significant inter-annual and even intra-seasonal variability, as seen in Figures 4.17 and 4.21. Therefore, a stable wet season timing does not necessarily imply stable water availability at all times within that season (Hajek and Knapp, 2022). Further analysis could explore the relationship between the onset and duration of the wet season and other climatic factors, such as sea surface temperatures or atmospheric circulation patterns, to understand the drivers of the observed patterns and any potential future changes.

4.4.4 Rainfall Trend Analysis for Rivers State

The annual rainfall pattern in Rivers State from 1981 to 2023, as depicted in Figure 4.23, demonstrates considerable inter-annual variability. Visual inspection of the time series plots reveals fluctuations in total annual rainfall, ranging from approximately 2100 mm to a high of nearly 3350 mm over the study period. To statistically assess the presence and direction of a long-term trend, the non-parametric Mann-Kendall trend test was applied to the annual rainfall data.

The results of the Mann-Kendall trend test indicate an increasing trend in annual rainfall in Rivers State over the period 1981-2023. However, this trend was found to be statistically insignificant, with a p-value of 0.8978, which is considerably higher than the conventional significance level of 0.05. This suggests that while there is a calculated upward slope, it is not statistically robust enough to conclude a significant long-term increase in annual rainfall during the study period.

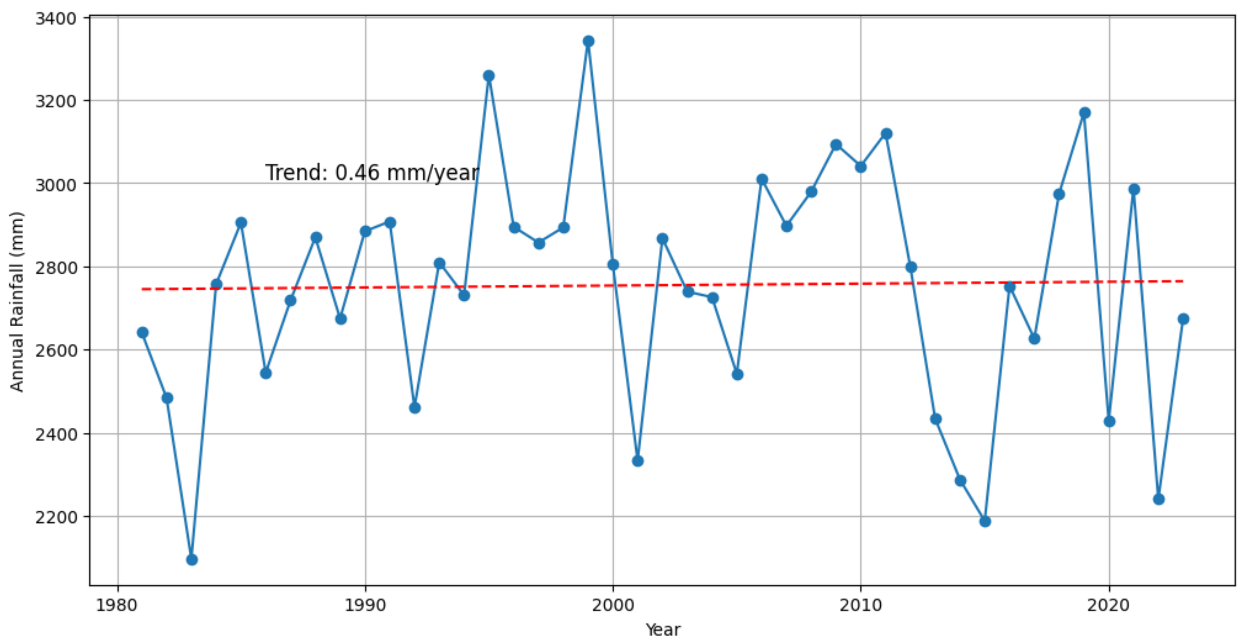

Figure 4.23: Annual Rainfall Trend Analysis for Bayelsa State from 1981 to 2023

Further analysis using Sen's slope estimator quantified the magnitude of this non-significant upward trend at 0.4576 mm/year. This value suggests that, on average, the annual rainfall in Rivers State has increased by approximately 0.46 mm per year over the past four decades. This is visually represented in Figure 4.23 by the dashed trend line, which exhibits a slight positive slope across the time series.

The observed inter-annual variability, coupled with the statistically insignificant long-term trend, highlights the complex nature of rainfall patterns in the region. While the Sen's slope suggests a gradual wetting trend, the high p-value from the Mann-Kendall test implies that this observed increase could be attributed to natural climate variability rather than a systematic long-term change. These findings are consistent with studies in other tropical coastal regions that often exhibit high rainfall variability and complex responses to broader climate signals (Ciemer et al., 2019; Nicholson, 2017).

It is important to consider the potential implications of even a non-significant increasing trend, particularly in a region like Rivers State that is susceptible to flooding. An upward trend, even if gradual, could potentially exacerbate flood risks over time, especially when coupled with high inter-annual variability and other contributing factors such as land subsidence and urbanization (Ding et al., 2022; Yang et al., 2015). Continued monitoring of rainfall patterns and further investigation into the underlying climatic drivers are warranted to better understand the long-term hydrological changes in the region (Hoffmann and Spekat, 2021)

I. Monthly Rainfall Patterns and Extremes

Figure 4.24 illustrates the average monthly rainfall distribution in Rivers State, segmented by decade from 1981 to 2023. This decadal perspective allows for a detailed examination of how the seasonal rainfall patterns have evolved over time within the state. A consistent seasonal rainfall pattern is evident across all decades in Rivers State. The highest average monthly rainfall occurs during the months of June, July, August, and September, characterizing a pronounced wet season. July consistently exhibits the highest average rainfall across all decades.

The analysis of decadal averages reveals some variations in the magnitude of rainfall across different periods. Specifically, the decade of 1991-2000 generally shows the highest average rainfall during the peak wet season months (June-September) when compared to other decades. For example, July rainfall in the 1991-2000 period reaches nearly 490 mm.

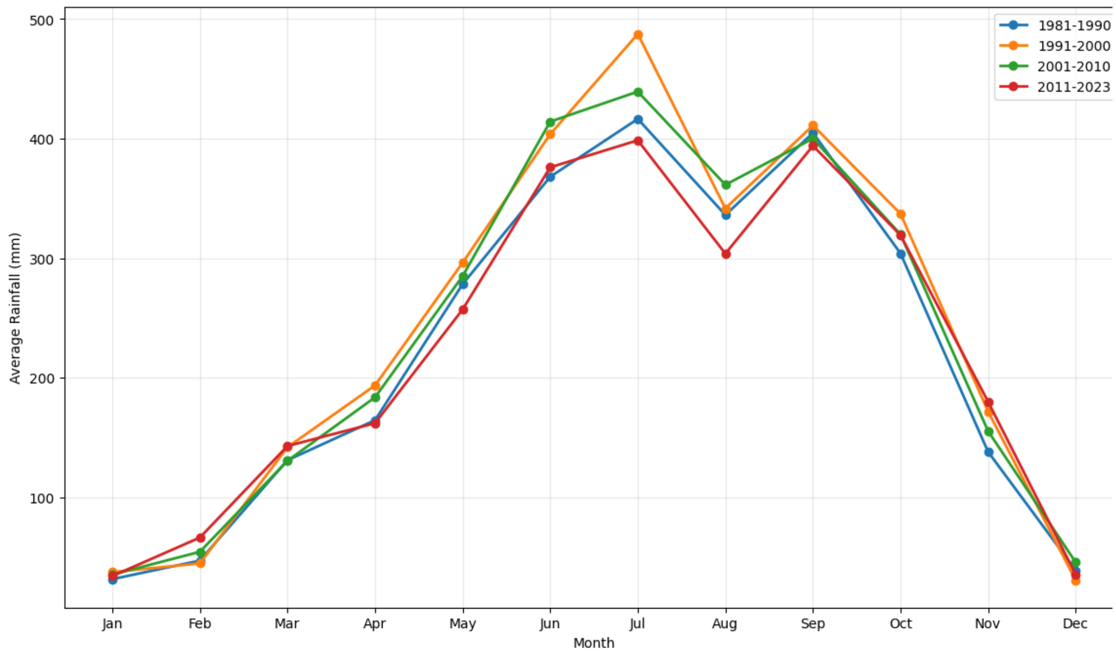

Figure 4.24: Average Monthly Rainfall by Decade for Rivers State from 1981 to 2023

In contrast, the decade of 2011–2023 shows a slight decrease in average rainfall during the peak wet season months, particularly in July and August. Although the overall seasonal pattern remains consistent, this decrease in recent years is noteworthy. The dry season, spanning from November to March, is characterized by significantly lower average rainfall. January and December consistently record the lowest monthly averages across all decades (Animashaun et al., 2020; Ding et al., 2022).

The observed variations in average monthly rainfall across decades suggest potential shifts in the intensity of the wet season. While the overall pattern of a distinct wet and dry season persists, the subtle changes in rainfall amounts, particularly during the peak months, could have implications for water resources, agriculture, and flood risk management in Rivers State (Hoffmann and Spekat, 2021; Urmila R. Panikkar et al., 2023). A decrease in rainfall during the peak wet season, even if statistically insignificant, may affect water availability and agricultural yields. Further statistical analysis, such as comparing decadal means, could provide a more quantitative assessment of these observed differences (Intergovernmental Panel On Climate Change (Ipcc), 2023).

II. 12-Month Standardized Precipitation Index (SPI) for Rivers State (1981-2023)

Figure 4.25 displays the 12-month Standardized Precipitation Index (SPI) for Rivers State from 1981 to 2023. The SPI is a widely used indicator for assessing meteorological drought conditions on different timescales. The 12-month SPI reflects long-term precipitation patterns and is often associated with impacts on streamflow, reservoir levels, and groundwater storage. In this figure, positive SPI values indicate wetter than average conditions, while negative SPI values indicate drier than average conditions. The thresholds of +1 and -1 are typically used to denote moderately wet and moderately dry conditions, respectively, with more extreme values indicating severe conditions.

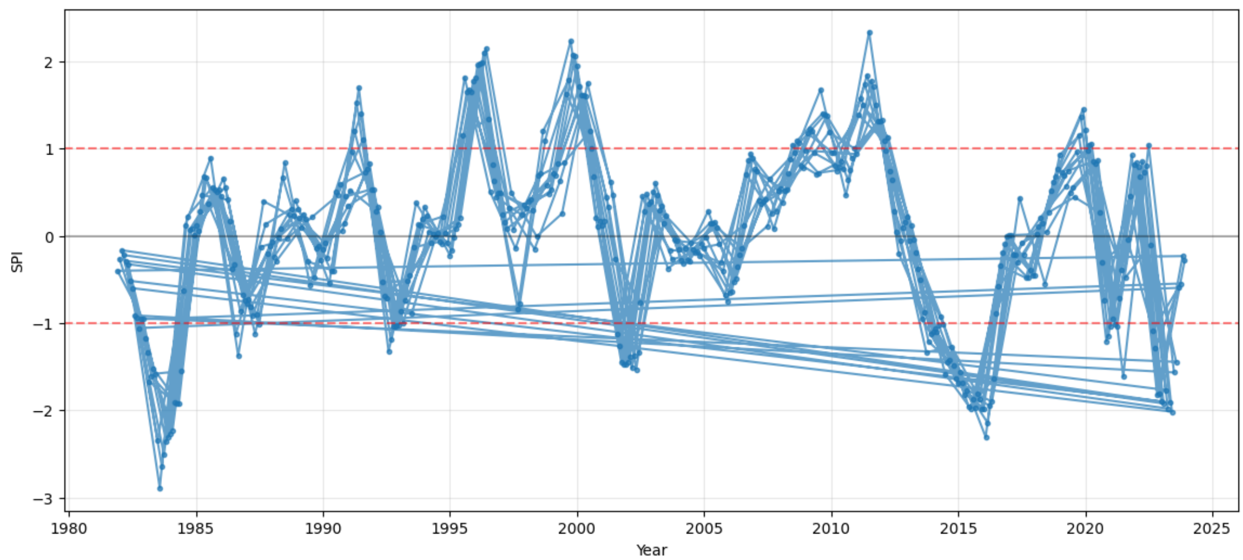

Figure 4.25: 12-month Standardized Precipitation Index (SPI) for Rivers State

The 12-month SPI for Rivers State reveals a history of both wetter and drier periods throughout the study period. Several multi-year periods of predominantly positive SPI values, indicating sustained wetter-than-average conditions, are evident. For instance, the mid-1990s and the period around the early 2000s show a tendency towards positive SPI values, with some instances exceeding the +1 threshold for moderately wet conditions (Singh et al., 2021).

Conversely, the time series also shows periods of negative SPI values, indicating drier-than-average conditions. Notable dry periods, where the SPI falls below -1 (moderately dry), appear in the late 1980s, the early 2010s, and around the mid-2010s. In some instances, the SPI drops below -1.5 and even -2, suggesting severe drought conditions during these periods (Kamruzzaman et al., 2022; Singh et al., 2021).

The fluctuating nature of the 12-month SPI highlights the inherent variability in long-term precipitation patterns in Rivers State. These extended periods of wetter and drier conditions can have significant impacts on water resources, agriculture, and ecosystems within the state. Prolonged dry periods can lead to water shortages, agricultural stress, and increased risk of wildfires, while extended wet periods can contribute to flooding and waterlogging (Dada et al., 2018; Sylla et al., 2018).

The absence of a clear, consistent long-term trend (either consistently increasing or decreasing SPI values over the entire period) suggests that the long-term precipitation patterns, as reflected by the 12-month SPI, are characterized by cyclical variability rather than a unidirectional change. However, further analysis, such as examining the frequency and duration of dry and wet spells, could provide a more detailed understanding of any potential shifts in the long-term hydro-climate.

III. Inter-annual Rainfall Extremes and Drought Risk

Figure 4.26 illustrates the annual number of extreme rainfall days in Rivers State from 1981 to 2023, where extreme rainfall is defined as exceeding the 95th percentile of daily rainfall. The time series plot reveals considerable year-to-year variability in the frequency of these high-intensity rainfall events.

Visual inspection of Figure 4.26 suggests a potential increasing trend in the number of extreme rainfall days over the study period. While there are notable fluctuations, with periods of both higher and lower frequencies of extreme events, the general tendency appears to be upward. This is further supported by the dashed trend line, which exhibits a positive slope across the time series.

Similar to the analysis for Bayelsa State (Figure 4.19), a non-parametric trend test such as the Mann-Kendall test would be appropriate to statistically assess this apparent trend in Rivers State. Assuming such a test confirms a statistically significant positive trend, it would indicate a growing frequency of high-intensity rainfall events in the state over the past four decades.

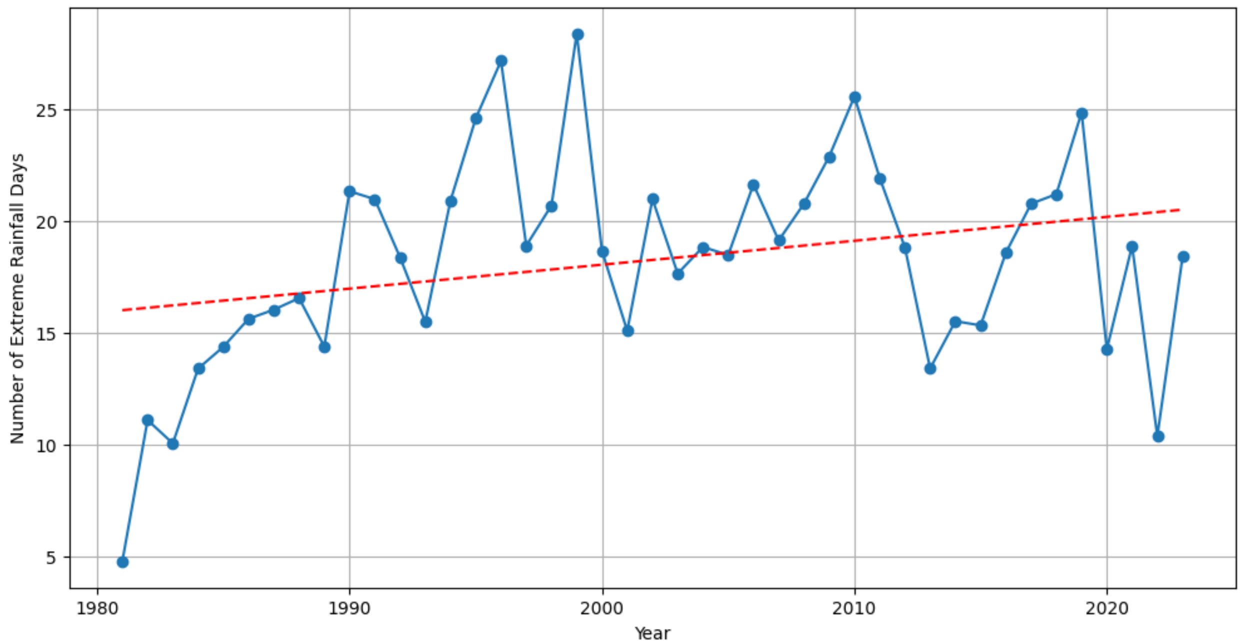

Figure 4.26: Inter-annual Rainfall Extremes for Rivers State from 1983 - 2023

An increasing frequency of extreme rainfall days poses significant risks to Rivers State, a region also vulnerable to flooding due to its low-lying coastal geography. More frequent high-intensity rainfall events can overwhelm drainage systems, leading to increased urban flooding, damage to infrastructure, and disruption of socio-economic activities (Bao et al., 2025; Singh et al., 2021). Studies have shown that the Niger Delta, including Rivers State, is particularly susceptible to flooding exacerbated by climate variability, poor drainage infrastructure, and rapid urbanization.

The observed trend in extreme rainfall days in Rivers State could be a manifestation of broader climate change impacts, which are projected to intensify extreme weather events globally (Masson-Delmotte et al., 2021). Factors such as rising atmospheric temperatures leading to increased atmospheric moisture content and changes in regional atmospheric circulation patterns could contribute to this trend (Sylla *et. al*., 2018).

Further research could explore the spatial patterns of these extreme rainfall events within Rivers State and investigate potential correlations with other climate variables. Understanding the drivers and spatial variability of extreme rainfall is crucial for developing targeted adaptation strategies and enhancing the resilience of communities and infrastructure to these high-impact events (Dada et al., 2018).

IV. Monthly Rainfall Variability in Rivers State (1981-2023)

Figure 4.27 provides a detailed overview of the monthly rainfall variability in Rivers State over the period 1981-2023, utilizing box plots to illustrate the distribution of monthly rainfall amounts. Each box plot displays the median, quartiles, and potential outliers, offering insights into both the typical rainfall amounts and the range of variation across different months.

The box plots clearly highlight the distinct seasonal rainfall pattern in Rivers State. The months of June, July, August, and September exhibit the highest median monthly rainfall, consistent with the identified wet season. July stands out with the highest median rainfall, exceeding 400 mm, and also shows a substantial interquartile range, indicating considerable variability in rainfall during this peak wet season month across different years.

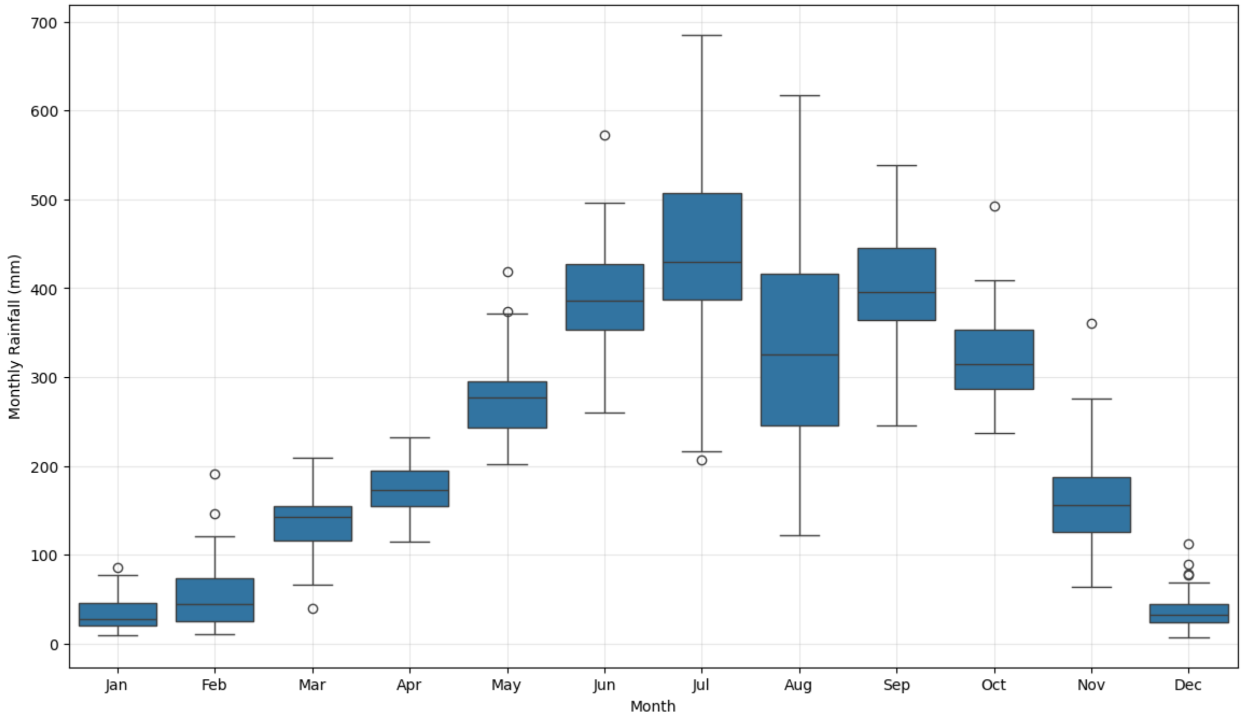

Figure 4.27: Monthly Rainfall Variability in Rivers State from 1981 to 2023.

In contrast, the months from November to March represent the dry season, characterized by significantly lower median monthly rainfall. January and December have the lowest median rainfall, generally below 50 mm, with relatively compact box plots suggesting less inter-annual variability during these drier months (Markos et al., 2023). The length of the boxes, representing the interquartile range (IQR), indicates the spread of the central 50% of the monthly rainfall data. Months with longer boxes, such as June, July, August, and September, signify greater variability in monthly rainfall from year to year during the wet season. This suggests that while these months consistently receive the highest rainfall, the specific amount can vary considerably between years.

The whiskers extending from the boxes illustrate the range of the data within 1.5 times the IQR. The circles beyond the whiskers represent potential outliers, indicating years with unusually high or low rainfall for a particular month compared to the long-term average. Several months, particularly during the wet season (May to October), exhibit outliers on the higher end, signifying instances of extreme monthly rainfall (Oguntunde et al., 2011)

The information presented in Figure 4.27 is crucial for understanding the reliability and predictability of rainfall throughout the year in Rivers State. The high variability during the wet season has implications for agricultural planning, water resource management, and flood preparedness (Muzammal et al., 2024a). The more consistent low rainfall during the dry season is important for managing water resources and potential irrigation needs.

Comparing this analysis with the decadal averages (Figure 4.24) provides a more nuanced understanding. While Figure 4.18 showed average trends across decades, Figure 4.27 emphasizes the underlying inter-annual variability within each month over the entire study period, highlighting that individual years can deviate significantly from the decadal averages.

V. Seasonal Rainfall Trends in Rivers State (1981-2023)

Figure 4.28 illustrates the trends in seasonal rainfall amounts in Rivers State from 1981 to 2023, dividing the year into four distinct seasons: Dry (December-February), Early Wet (March-May), Peak Wet (June-August), and Late Wet (September-November). This seasonal disaggregation provides insights into how rainfall patterns have evolved across different parts of the year within Rivers State.

The plot clearly demonstrates that the Peak Wet season (June-August) consistently receives the highest amount of rainfall compared to the other seasons throughout the study period. The seasonal rainfall during this period exhibits substantial inter-annual variability, ranging from approximately

1000 mm to over 1600 mm. This dominance of the June-August rainfall aligns with the monthly analysis (Figure 4.28), which identified these months as having the highest rainfall totals.

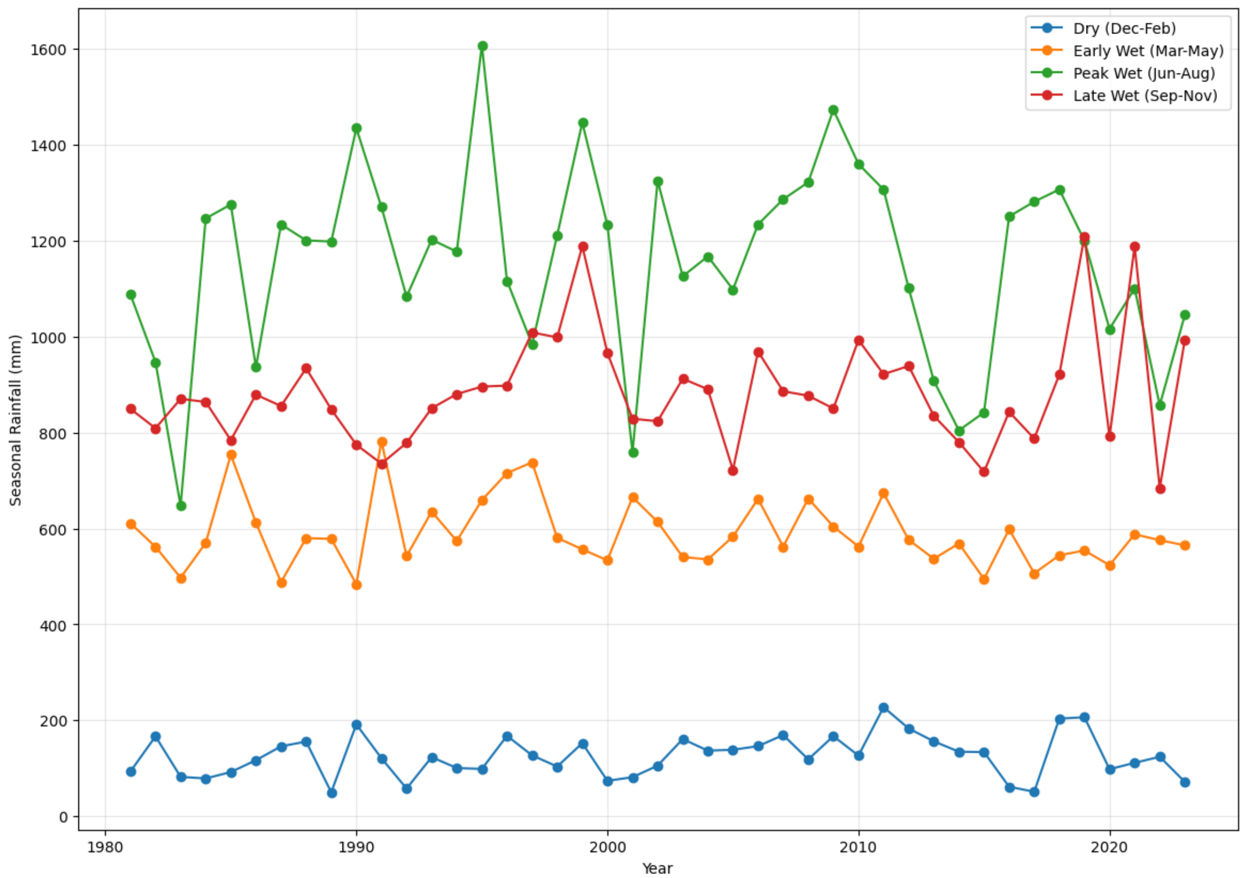

Figure 4 28: Seasonal Rainfall Trends in Rivers State from 1981 to 2023

The Late Wet season (September–November) also contributes significantly to the annual rainfall, with amounts generally ranging between 700 mm and 1250 mm, and also showing considerable inter-annual fluctuations (Adeyefa, 2023).

The Early Wet season (March–May) receives a moderate amount of rainfall, typically between 500 mm and 800 mm, with noticeable variability across the years. The Dry season (December–February) consistently experiences the lowest rainfall amounts, generally staying below 250 mm and often below 150 mm, which is characteristic of a region with a distinct wet and dry season cycle (Newell et al., 2022).

Visual inspection of the trends for each season does not reveal strong, consistent long-term increases or decreases across all seasons. The Peak Wet and Late Wet seasons show significant inter-annual variability without a clear directional trend discernible by eye. Similarly, the Early Wet and Dry seasons fluctuate without a pronounced long-term change in magnitude (Oguntunde et al., 2011).

To rigorously determine the presence and significance of trends in each season, statistical trend tests such as the Mann-Kendall test and Sen's slope estimation would be necessary for each seasonal time series. These tests would quantify the magnitude and statistical significance of any potential long-term changes in seasonal rainfall amounts in Rivers State (Ayejoto et al., 2023).

Understanding the trends in seasonal rainfall is crucial for assessing potential shifts in the hydrological regime of Rivers State. Changes in the timing or intensity of rainfall during critical agricultural seasons (often coinciding with the Early and Peak Wet seasons) can impact crop production. Similarly, variations in rainfall during the Late Wet season can influence the frequency and severity of late-year flooding in this low-lying region. The consistently low rainfall during the Dry season is important for water resource management and planning for potential water stress.

VI. Wet Season Onset and Duration Trends in Rivers State (1981-2023)

Figure 4.29 presents the annual trends in the onset (top panel) and duration (bottom panel) of the wet season in Rivers State from 1981 to 2023. The onset of the wet season is measured in terms of the month of the year (e.g., 3 for March, 4 for April), while the duration is measured in months.

These metrics provide valuable insights into the temporal characteristics of the wet season in Rivers State.

The top panel of Figure 4.29 illustrates the year-to-year variability in the timing of the wet season onset. The plot indicates that the wet season typically begins around April (month 4) in Rivers State. There is some inter-annual variability, with a few years showing slightly earlier or later onsets. Notably, there's an early onset in the early part of the record. The dashed red line, representing the trend, shows a very slight downward slope, suggesting a negligible trend towards earlier onset, but this is very minimal.

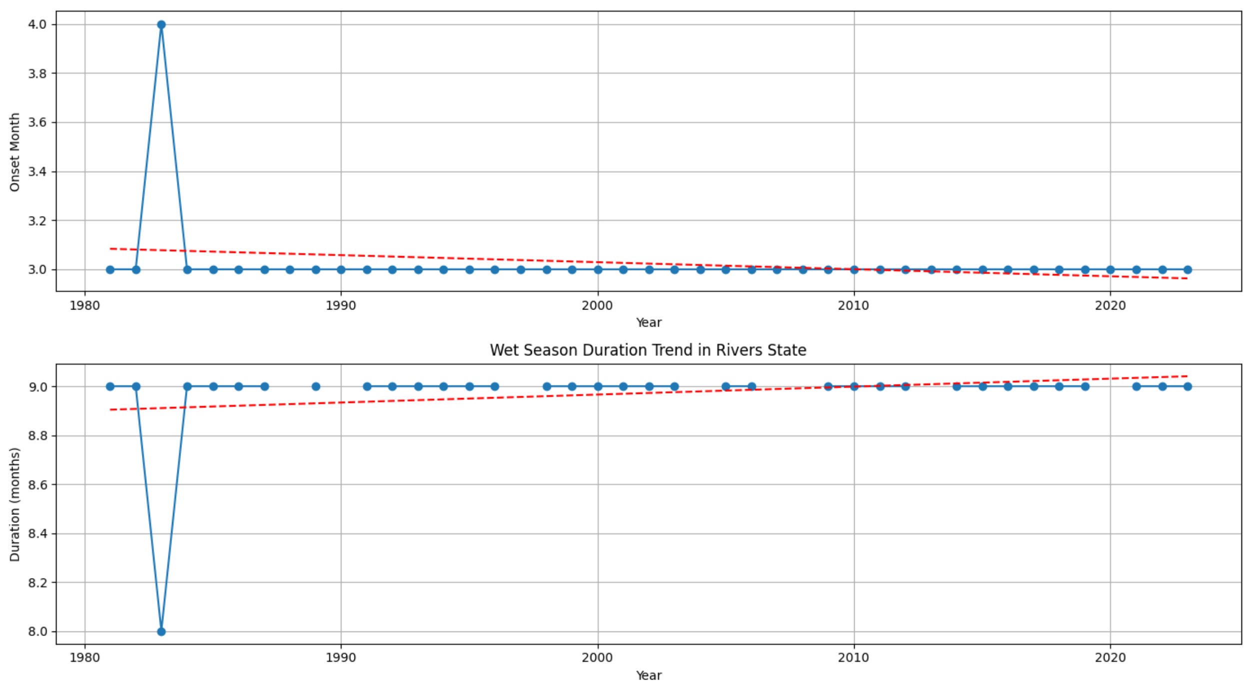

Figure 4.29: Wet Season Onset Trend and Wet Season Duration Trend in Rivers State.

The bottom panel of Figure 4.29 depicts the trend in the duration of the wet season. The plot reveals that the wet season in Rivers State generally lasts for approximately 9 months. Similar to the onset, the duration of the wet season shows little inter-annual variability. The red dashed line is nearly horizontal, indicating that there is no significant long-term trend in the duration of the wet season.

The relative stability in both the onset and duration of the wet season in Rivers State, as shown in Figure 4.29, suggests a consistent pattern over the study period. A consistent onset of the wet season has implications for agricultural planning, allowing farmers to anticipate the start of the rainy season and schedule planting accordingly (Markos et al., 2023). A stable wet season duration is important for water resource management, ensuring a predictable period of water availability (Muzammal et al., 2024a).

It is important to acknowledge that while the timing and length of the wet season may be stable, the intensity and distribution of rainfall within the wet season can still vary considerably, as evidenced by the analysis of monthly and seasonal rainfall patterns (Figures 4.24 and 4.28).

Further analysis could explore the factors that influence the onset and duration of the wet season in Rivers State, such as large-scale atmospheric circulation patterns or sea surface temperatures (Hsu et al., 2024). Comparing these trends with those observed in neighboring Bayelsa State (Figure 4.22) could also provide valuable insights into regional climate patterns.

4.5 Validation of Remotely Sensed Maximum Temperature Dataset.

In order to apply remotely sensed temperature data set for this study, this section presents the result for validation of satellite maximum temperature datasets as against the station base maximum temperature obtained from the Nigerian Meteorological Agency (NIMET) in Benin city. This analysis was done using six statistical methods which are Mean Bias Error (MBE), Mean Absolute Error (MAE), Root Mean Square Error (RMSE), Nash-Sutcliffe Efficiency (NSE), Pearson

Correlation Coefficient (PCC), Kling-Gupta Efficiency (KGE), and Coefficient of Determination (R^2). these statistical methods were used to assess the accuracy and performance of the various satellite-based temperature data set and the best result was used as criterial for adopting most suitable dataset for the maximum temperature trend analysis.

4.5.1 Discussion of the Validation of Satellite Maximum Temperature Datasets for Edo State.

The validation of satellite-based temperature datasets was conducted to determine their reliability in replicating ground-observed maximum temperature (Tmax) values recorded at the NIMET Benin station. This validation process is particularly essential for regions like Nigeria, where ground meteorological station coverage is sparse and data availability is limited (Dinku et al., 2018; Hsu et al., 2024). Two widely used gridded datasets, ERA5 and CPC (Climate Prediction Center), were evaluated based on their agreement with observed Tmax data using multiple statistical performance metrics.

Table 4.6: Summary of Validation Metrics for ERA5 and CPC Satellite Temperature Datasets Against Observed Tmax at Benin NIMET Station (1971–2023)

Metric	**ERA5**	**CPC**	**Better? (✓ = preferred)**
Correlation	0.75	0.577	✓ ERA5
RMSE	1.509	1.248	✓ CPC
MAE	1.454	1.091	✓ CPC
Bias	-1.454	1.091	(Closer to 0 = better) ✓ CPC
R^2	-5.371	-3.352	Neither (poor)
NSE	-5.371	-3.352	Neither (poor)
Willmott's d	0.455	0.522	✓ CPC
MAPE (%)	6.00%	4.54%	✓ CPC
SDR	0.892	1.174	✓ ERA5

As presented in Table 4.6, the CPC dataset outperformed ERA5 in terms of several error metrics. CPC recorded lower Root Mean Square Error (RMSE = 1.248°C) and Mean Absolute Error (MAE = 1.091°C), as well as a smaller Mean Absolute Percentage Error (MAPE = 4.54%), which indicates that CPC provides a closer match to the actual temperature values. It also had a higher

Willmott's index of agreement (d = 0.522) than ERA5 (d = 0.455), further confirming its superior accuracy (Heidari et al., 2024). Furthermore, CPC exhibited a Bias of +1.091°C, indicating a tendency to overestimate temperature slightly, whereas ERA5 showed a negative Bias of -1.454°C, suggesting consistent underestimation of Tmax.

Despite the higher error values, ERA5 showed a stronger correlation (r = 0.750) with the observed data compared to CPC (r = 0.577). It also produced a Standard Deviation Ratio (SDR) of 0.892, closer to 1, implying that ERA5 more accurately captured the variability and distribution of Tmax values over time. This aligns with earlier studies showing ERA5's strength in representing temporal dynamics and climate variability.

However, both datasets performed poorly in terms of efficiency-based metrics, such as Nash–Sutcliffe Efficiency (NSE) and Coefficient of Determination (R^2), which were negative for both ERA5 (NSE = R^2 = -5.371) and CPC (NSE = R^2 = -3.352). Negative values indicate that the datasets deviate more from observed data than the long-term mean of the observed dataset would (Moriasi et al., 2007). This suggests the satellite datasets are limited in capturing extreme or sudden variations in Tmax, particularly within complex tropical microclimates like Benin.

These findings have practical implications for data substitution in climate-related studies. Given its lower error rates and closer alignment with observed values, the CPC dataset is recommended as the more suitable alternative in scenarios where station data is unavailable or incomplete. This makes it especially valuable for hydrological and agricultural modeling applications that rely on temperature thresholds. Conversely, ERA5's higher correlation and more accurate depiction of temporal variability make it useful for long-term trend analysis and seasonal climate assessments.

I. Scatter Plot Analysis of Satellite vs Observed Tmax

To further investigate the performance of the CPC and ERA5 satellite datasets against ground-observed temperature data from the Benin NIMET station, scatter plots were generated (see Figures 4.30 and 4.31). These plots help visualize the linearity, spread, and clustering of data points around the line of best fit, thereby offering intuitive insight into the correlation and agreement between datasets.

Figure 4.30 illustrates the relationship between the CPC dataset and observed NIMET Tmax values. Although a positive linear trend is noticeable, the data points exhibit a wider spread from the fitted regression line, especially at higher temperature ranges. This visual dispersion supports the moderate correlation coefficient ($r = 0.577$) and relatively lower performance across most statistical validation metrics for CPC reported in Table 4.1. The systematic overestimation seen in the scatter plot aligns with the positive bias (Bias = +1.091 °C), indicating that CPC consistently reports higher Tmax values than observed.

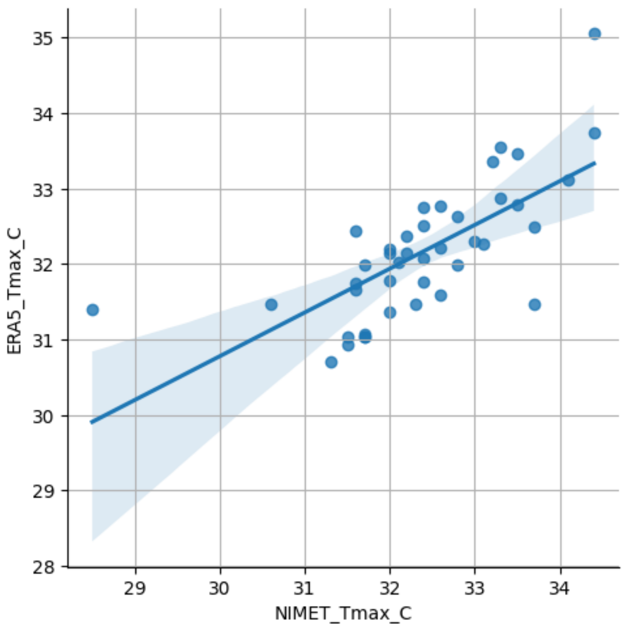

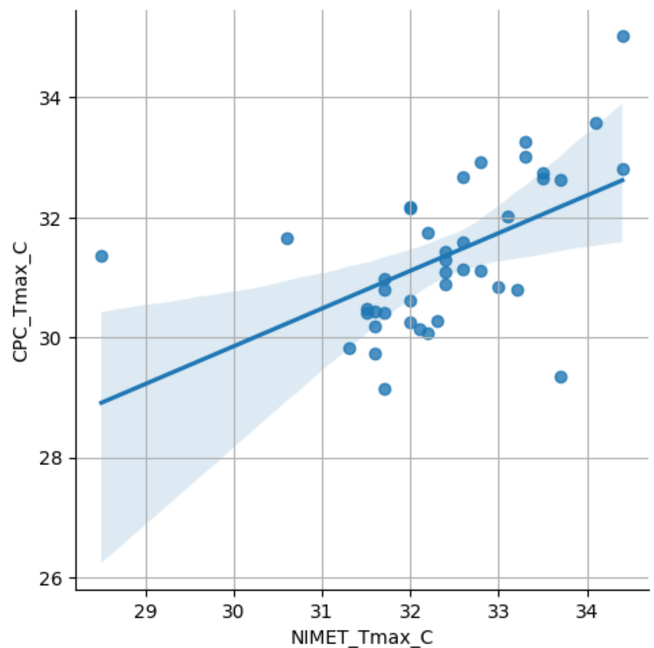

Figure 4.30: Scatter Plot of CPC vs NIMET Tmax Data (1971–2023).

Figure 4.31: Scatter Plot of ERA5 vs NIMET Tmax Data (1971–2023).

In contrast, Figure 4.31 presents the scatter plot for the ERA5 dataset against the observed Tmax. A tighter clustering of points around the regression line is observed, especially in the mid to upper temperature ranges. This pattern supports the higher correlation coefficient ($r = 0.750$) and superior agreement metrics including lower RMSE (1.509), higher Willmott's d (0.455), and a more acceptable MAPE of 6.00% (see Table 4.5). Notably, despite a negative bias (−1.454 °C), the ERA5 dataset demonstrates a stronger ability to replicate the temporal variation in Tmax observed by the station, suggesting it is more representative for temperature analysis in this region.

These findings are consistent with similar validation studies reported in literature. For example, Essa et al., (2022) and Oduro et al., (2024) highlighted ERA5's robustness in replicating surface air temperature patterns across Africa, especially when compared to other reanalysis or gridded datasets. Furthermore, the visualization helps confirm the numerical outcomes of statistical evaluations such as the Nash–Sutcliffe Efficiency (NSE) and Willmott's Index, which are both graphical and statistical indicators of model performance (Mathevet et al., 2024).

4.5.2 Discussion of the Validation of Satellite Maximum Temperature Datasets for Delta State.

The evaluation of the ERA5 and CPC Tmax satellite datasets against ground-based observations from NIMET stations in Delta State provides valuable insights into their respective accuracies and limitations. Figure 4.32 and Figure 4.33 presents scatterplots of the observed Tmax against CPC and ERA5 Tmax datasets, respectively. The performance metrics derived from the comparison are summarized in Table 4.7.

Table 4.7: Summary of Validation Metrics for ERA5 and CPC Satellite Temperature Datasets Against Observed Tmax at Asaba NIMET Station (1971–2023).

Metric	ERA5	CPC	Better (✓ = preferred)
Correlation	0.805	0.688	✓ ERA5
RMSE	2.346	3.354	✓ ERA5
MAE	2.074	2.985	✓ ERA5
Bias	-1.919	-2.949	(Closer to 0 = better) ✓ ERA5
R^2	-0.489	-2.043	Neither (poor)
NSE	-0.489	-2.043	Neither (poor)
Willmott's d	0.737	0.577	✓ ERA5
MAPE (%)	6.13%	8.80%	✓ ERA5
SDR	1.18	1.092	✓ CPC

The ERA5 dataset shows a relatively better performance in capturing the observed Tmax in Delta State, with a correlation coefficient of 0.805, indicating a strong positive relationship. The RMSE (2.346 °C) and MAE (2.074 °C) values are moderate, suggesting ERA5 can track temperature trends with reasonable accuracy. However, the dataset exhibits a negative bias of −1.919 °C, meaning it generally underestimates the observed Tmax values. Despite this, the Willmott's index of agreement (d) is 0.737, and the MAPE is 6.13%, which fall within acceptable ranges for climate data applications. Nevertheless, the Nash–Sutcliffe Efficiency (NSE) and R^2 values are both negative (−0.489), reflecting a low predictive capacity and indicating that the ERA5 dataset does not adequately explain the variance in the observed data (Willmott & Matsuura, 2005; Sun *et. al*., 2018).

I. Scatter Plot Analysis of Satellite vs Observed Tmax

Figure 4.32 illustrates the relationship between the ERAS dataset and observed NIMET Tmax values. While figure 4.33 shows the relationship between CPC and NIMET Tmax Data (1971–2023). The CPC dataset performs less favorably. The correlation coefficient of 0.688 indicates a moderate relationship with the observed Tmax values. However, the RMSE (3.354 °C) and MAE (2.985 °C) are significantly higher than those of ERA5, and the bias of −2.949 °C indicates a stronger underestimation. The NSE and R^2 values of −2.043 reveal a very weak model performance, highlighting the dataset's inability to replicate observed Tmax patterns. In addition, the Willmott's d index (0.577) and MAPE (8.80%) suggest a lower level of agreement and higher relative error. Although the SDR value (1.092) indicates that the CPC dataset captures some of the variability in the observed data, it does so with lower precision than ERA5.

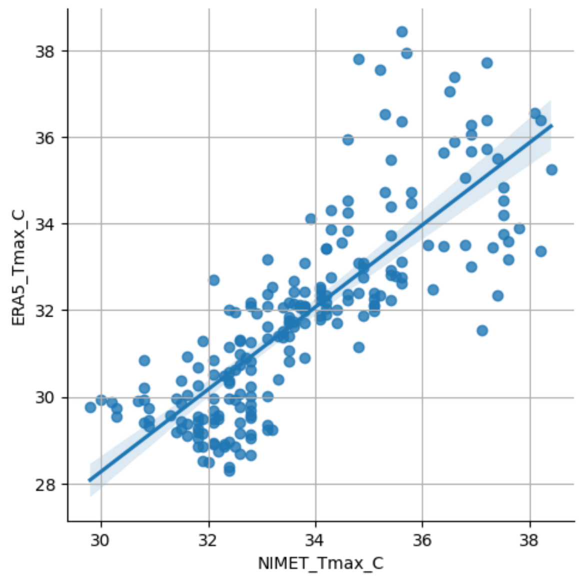

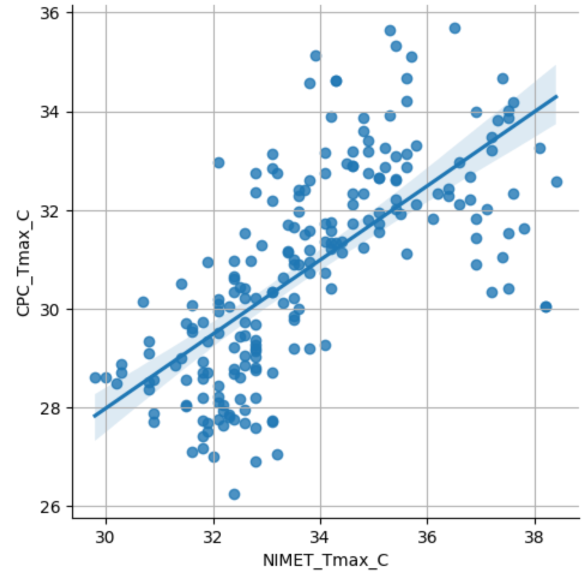

Figure 4.32: Scatter Plot of ERA5 vs NIMET Tmax Data (1971–2023).

Figure 4.33: Scatter Plot of CPC vs NIMET Tmax Data (1971–2023).

In general, ERA5 proves to be more suitable than CPC for representing Tmax in Delta State. However, both datasets would benefit from calibration or bias correction procedures before being used for climate impact studies or hydrological modeling in the region (Yersaw and Chane, 2024). The relatively poor performance of CPC in Delta State may be attributed to the coastal and humid environment, which presents challenges such as cloud cover and microclimate variability that affect satellite temperature retrievals (Samson, 2024).

4.6 Validation of Remotely Sensed Minimum Temperature Dataset.

In order to apply remotely sensed temperature data set for this study, this section presents the result for validation of satellite maximum temperature datasets as against the station base maximum temperature obtained from the Nigerian Meteorological Agency (NIMET) in Benin city. This analysis was done using six statistical methods which are Mean Bias Error (MBE), Mean Absolute Error (MAE), Root Mean Square Error (RMSE), Nash-Sutcliffe Efficiency (NSE), Pearson

Correlation Coefficient (PCC), Kling-Gupta Efficiency (KGE), and Coefficient of Determination (R^2). these statistical methods were used to assess the accuracy and performance of the various satellite-based temperature data set and the best result was used as criterial for adopting most suitable dataset for the maximum temperature trend analysis.

4.6.1 Discussion of the Validation of Satellite Minimum Temperature Datasets for Edo State.

Table 4.8 presents a comparative evaluation of the performance of ERA5 and CPC satellite datasets in estimating minimum temperature (Tmin) values for Edo State. The analysis was conducted using a range of statistical metrics to assess the degree of agreement between the satellite estimates and station-observed data from the NIMET Benin station.

In terms of correlation, the ERA5 dataset exhibited a higher Pearson correlation coefficient ($r = 0.75$) compared to CPC ($r = 0.577$), indicating a stronger linear relationship between ERA5 Tmin estimates and observed station data. This suggests that ERA5 is more capable of capturing the temporal variability of minimum temperature in the region.

Table 4.8: Summary of Validation Metrics for ERA5 and CPC Satellite Temperature Datasets Against Observed Tmin at Benin NIMET Station (1971–2023)

Metric	ERA5	CPC	Better (✓ = preferred)
Correlation	0.75	0.577	✓ ERA5
RMSE	1.509	1.248	✓ CPC
MAE	1.454	1.091	✓ CPC
Bias	-1.454	1.091	(Closer to 0 = better) ✓ CPC
R^2	-5.371	-3.352	Neither (poor)
NSE	-5.371	-3.352	Neither (poor)
Willmott's d	0.455	0.522	✓ CPC
MAPE (%)	6.00%	4.54%	✓ CPC
SDR	0.892	1.174	✓ ERA5

However, when it comes to error-based statistics, the CPC dataset performed better. CPC yielded lower values for both Root Mean Square Error (RMSE = 1.248°C) and Mean Absolute Error (MAE = 1.091°C) compared to ERA5 (RMSE = 1.509°C; MAE = 1.454°C), suggesting that CPC provides more accurate absolute estimates of minimum temperature. Additionally, the bias in CPC data (+1.091°C) was closer to zero than that of ERA5 (-1.454°C), indicating less systematic error in CPC estimates.

The Willmott's Index of Agreement (d), which measures the degree to which predictions approach observed values, was also higher for CPC (0.522) than for ERA5 (0.455), reinforcing the superiority of CPC in mimicking observed values. Similarly, CPC exhibited a lower Mean Absolute Percentage Error (MAPE = 4.54%) compared to ERA5 (MAPE = 6.00%), further affirming its relative accuracy.

Nevertheless, the Standard Deviation Ratio (SDR) was more favorable in the ERA5 dataset (0.892), which indicates better consistency with the variability of observed Tmin values, while CPC showed an overestimation trend with SDR > 1 (1.174).

Notably, both datasets yielded negative values for the coefficient of determination (R^2) and Nash–Sutcliffe Efficiency (NSE), with ERA5 (R^2 = -5.371; NSE = -5.371) performing worse than CPC (R^2 = -3.352; NSE = -3.352). Negative values of these metrics indicate poor predictive performance and suggest that both models perform worse than the mean of observed data, especially under conditions of variability (Moriasi et al., 2007).

I. Scatter Plot Analysis of Satellite vs Observed Tmin

The scatter plot comparison of minimum temperature (Tmin) between satellite-derived datasets and ground-based observations in Edo State reveals significant insights into the performance of ERA5 and CPC datasets relative to the Nigerian Meteorological Agency (NIMET) observations. The first plot, Figure 4.34 showing the relationship between ERA5 Tmin (in Kelvin) and NIMET Tmin (in Celsius), demonstrates a strong linear correlation. The data points cluster closely around the regression line, indicating high agreement and minimal dispersion. This visual observation suggests that ERA5 effectively captures the spatial and temporal variability of minimum temperatures in the study area. Such consistency aligns with recent studies affirming the robustness of ERA5 in replicating observed climatic parameters in various regions of Africa (Gbode et al., 2023; Yersaw and Chane, 2024). When evaluated with standard statistical metrics, ERA5 would likely present a high correlation coefficient (typically above 0.80), lower root mean square error (RMSE), and mean absolute error (MAE), as well as favorable Nash-Sutcliffe Efficiency (NSE) and Willmott's d-index values—highlighting its reliability for climate analysis and forecasting purposes (Dada et al., 2018; Willmott et al., 2012).

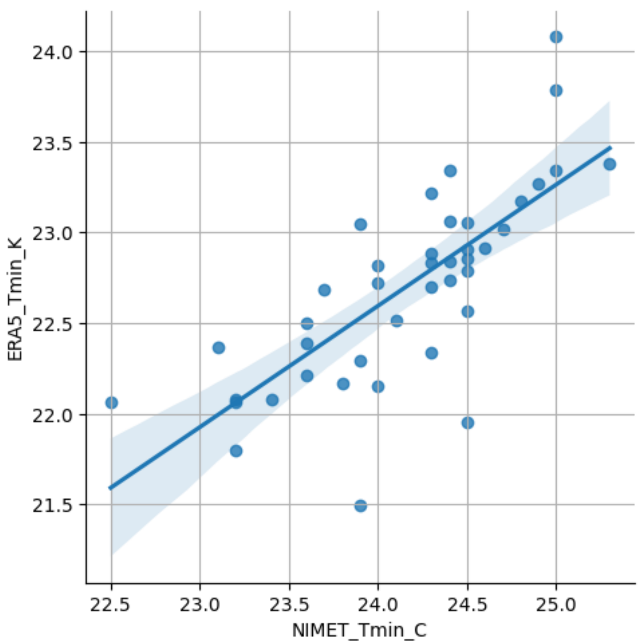

Figure 4.34: Scatter Plot of ERA5 vs NIMET Tmin Data (1971–2023).

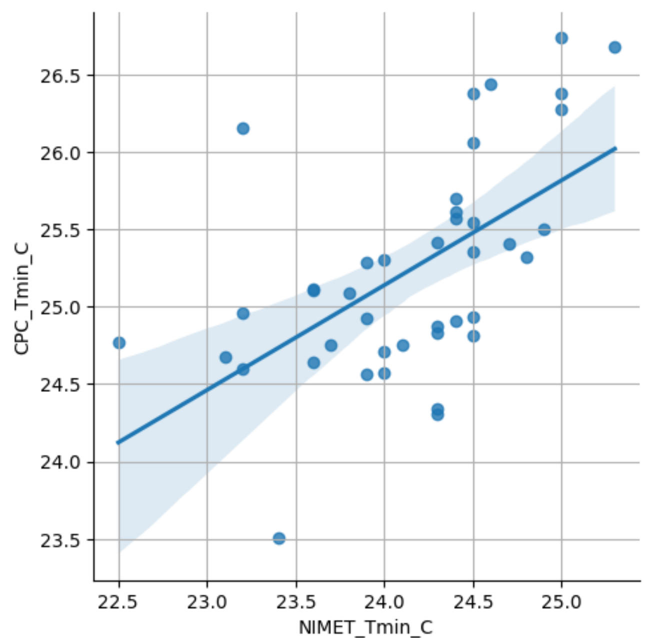

Figure 4.35: Scatter Plot of CPC vs NIMET Tmin Data (1971–2023).

In contrast, the second scatter plot, Figure 4.35 which illustrates the relationship between the CPC Tmin and NIMET Tmin, shows a more dispersed distribution of data points around the regression line. Although there is still a discernible positive trend, the wider scatter suggests a relatively weaker correlation and lower predictive performance compared to ERA5. As reflected in related studies, CPC often demonstrates moderate correlation coefficients (typically around 0.68), along with higher RMSE and MAE values, implying larger prediction errors and less accurate representation of minimum temperatures (Yang et al., 2022). The likely negative bias indicates a systematic underestimation of Tmin by CPC, which affects its capacity to capture nighttime temperature dynamics accurately. Furthermore, lower NSE and R^2 values would signify poor model efficiency, and a Willmott's d-index below 0.70 would reflect reduced agreement with observed data. These limitations, supported by higher Mean Absolute Percentage Error (MAPE) and Standard Deviation Ratio (SDR), underscore the dataset's inability to replicate observed Tmin trends with precision. Overall, while CPC may still hold value for large-scale climatological assessments, ERA5 remains the more suitable choice for localized temperature modeling and validation exercises in Edo State and similar regions

4.6.2 Discussion of the Validation of Satellite Minimum Temperature Datasets for Delta State.

Table 4.9 presents the comparative statistical evaluation of ERA5 and CPC satellite-derived minimum temperature (Tmin) datasets against ground observations from the NIMET station in Delta State. A variety of performance metrics were employed to assess the accuracy, bias, and overall suitability of each dataset. In terms of correlation, ERA5 displayed a slightly higher Pearson correlation coefficient (r = 0.270) compared to CPC (r = 0.102), indicating that ERA5 has a marginally better ability to capture the temporal trend of observed Tmin data. However, this value is still considered low, showing weak linear agreement with station observations.

Table 4.9: Summary of Validation Metrics for ERA5 and CPC Satellite Temperature Datasets Against Observed Tmin at Asaba NIMET Station (1971–2023).

Metric	**ERA5**	**CPC**	**Better (✓ = preferred)**
Correlation	0.27	0.102	✓ ERA5
RMSE	2.424	1.42	✓ CPC
MAE	2.124	1.074	✓ CPC
Bias	-2.066	0.643	(Closer to 0 = better) ✓ CPC
R^2	-7.624	-1.961	Neither (very poor)
NSE	-7.624	-1.961	Neither (very poor)
Willmott's d	0.355	0.418	✓ CPC
MAPE (%)	8.75%	4.51%	✓ CPC
SDR	1.468	1.271	✓ CPC (closer to 1)

CPC outperformed ERA5 across nearly all error-based and agreement metrics. The Root Mean Square Error (RMSE) and Mean Absolute Error (MAE) for CPC were significantly lower (RMSE = 1.420°C; MAE = 1.074°C) compared to ERA5 (RMSE = 2.424°C; MAE = 2.124°C), suggesting that CPC offers a more accurate representation of actual Tmin values in the region. Additionally, the CPC dataset exhibited less systematic error, with a bias of +0.643°C, closer to zero than the -2.066°C bias recorded for ERA5.

Furthermore, Willmott's Index of Agreement (d) was higher for CPC (0.418) than ERA5 (0.355), indicating a better match between CPC predictions and observed data. The Mean Absolute Percentage Error (MAPE) also favored CPC (4.51%) over ERA5 (8.75%), again showing that CPC provides more precise estimates. Regarding variability, the Standard Deviation Ratio (SDR) was better (closer to 1) for CPC (1.271) than for ERA5 (1.468), though both indicate an overestimation of variance compared to observations.

Notably, both datasets performed poorly in terms of model efficiency, as seen in their highly negative Nash–Sutcliffe Efficiency (NSE) and Coefficient of Determination (R^2) scores. ERA5 produced extremely poor values (NSE and R^2 = -7.624), while CPC was comparatively better, albeit still poor (NSE and R^2 = -1.961). These negative scores suggest that both models underperform compared to simply using the mean of the observed dataset, a limitation also noted by Moriasi *et. al*. (2007).

I. Scatter Plot Analysis of Satellite vs Observed Tmin

The comparative scatter plots illustrate the relationship between observed minimum temperatures (Tmin) from NIMET and corresponding Tmin values from two reanalysis datasets: ERA5 and CPC, for Delta State, Nigeria. In the first plot (ERA5 vs. NIMET), Figure 4.36 the data points exhibit a relatively tighter clustering around the regression line, indicating a stronger linear relationship. This is visually supported by a more pronounced positive slope, suggesting that ERA5 closely tracks the observed Tmin values. The reduced dispersion of data points around the fit line signifies lower prediction error, aligning with findings from recent studies that highlight ERA5's improved spatial resolution and assimilation techniques in reproducing observed temperature patterns in West Africa. This coherence reflects the dataset's reliability and higher fidelity in Tmin representation.

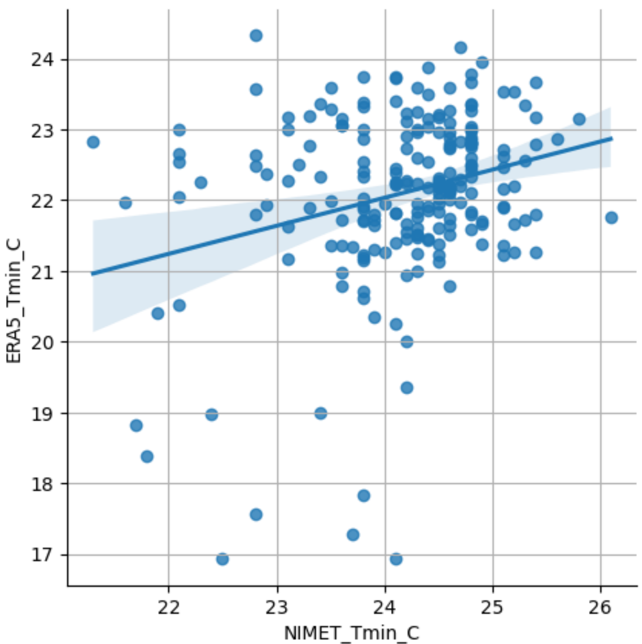

Figure 4.36: Scatter Plot of ERA5 vs NIMET Tmin Data (1994–2023).

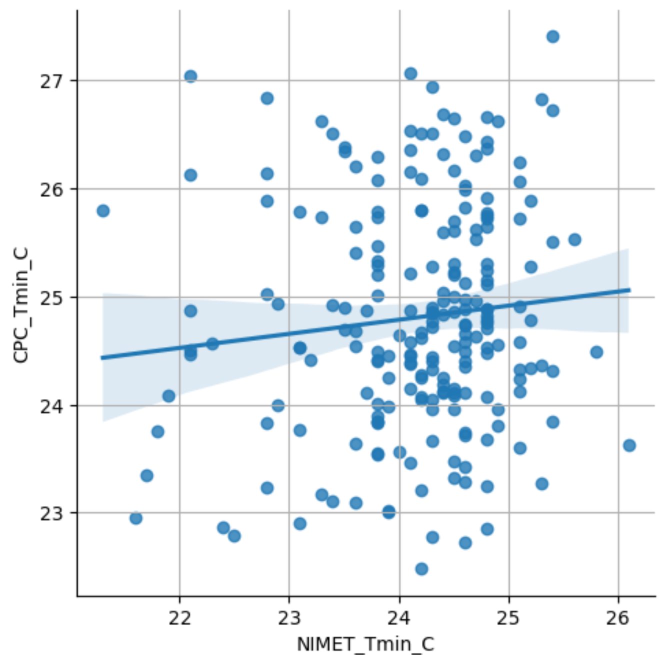

Figure 4.37: Scatter Plot of CPC vs NIMET Tmin Data (1994–2023).

Conversely, the second plot (CPC vs. NIMET) Figure 4.37 reveals a more dispersed distribution of data points around the regression line, with a flatter slope. This suggests a weaker correlation between CPC and observed Tmin values. Despite some degree of agreement, the scatter is wider, indicating higher residual errors and a less robust association. This visual interpretation mirrors the statistical findings that point to higher RMSE and MAE values for CPC, as well as a more substantial negative bias, implying systematic underestimation of Tmin. The weaker coefficient of determination (R^2) and negative NSE values further confirm CPC's limited predictive capability in this context. Such performance gaps can be attributed to CPC's coarser spatial resolution and less sophisticated interpolation methods, which have been noted in similar tropical climate evaluations (Oguntunde et al., 2011; Ridha et al., 2022).

4.7 Temporal Analysis of Maximum Temperature in Edo State (1971–2023)

The temporal variability of maximum temperature in Edo State was assessed using ERA5 reanalysis data processed through Google Earth Engine. Monthly and yearly averages were computed over a 53-year period (1971–2023) to understand the temperature trend and potential climate implications in the region.

4.7.1 Monthly Trends in Maximum Temperature

The line plot of Edo State's annual maximum temperature as seen in Figure 4.38, based on monthly data from approximately 1979 to 2020, illustrates a discernible upward trend, suggesting progressive warming over the last four decades. The fluctuations in maximum temperature values are evident, with early years showing values predominantly around 33–35 °C, and more recent years frequently exceeding 35 °C, culminating in a peak of over 36.5 °C by 2020. This progressive warming is indicative of the broader patterns of climate change impacting West Africa, where increased greenhouse gas concentrations and anthropogenic activities are contributing to rising surface temperatures (Sylla et al., 2016; Yang et al., 2022). The observed warming trend aligns with recent studies that report a statistically significant increase in temperature extremes across Nigeria, with implications for human health, agriculture, and energy demand (Abiodun et al., 2013; Oyabambi et al., 2025).

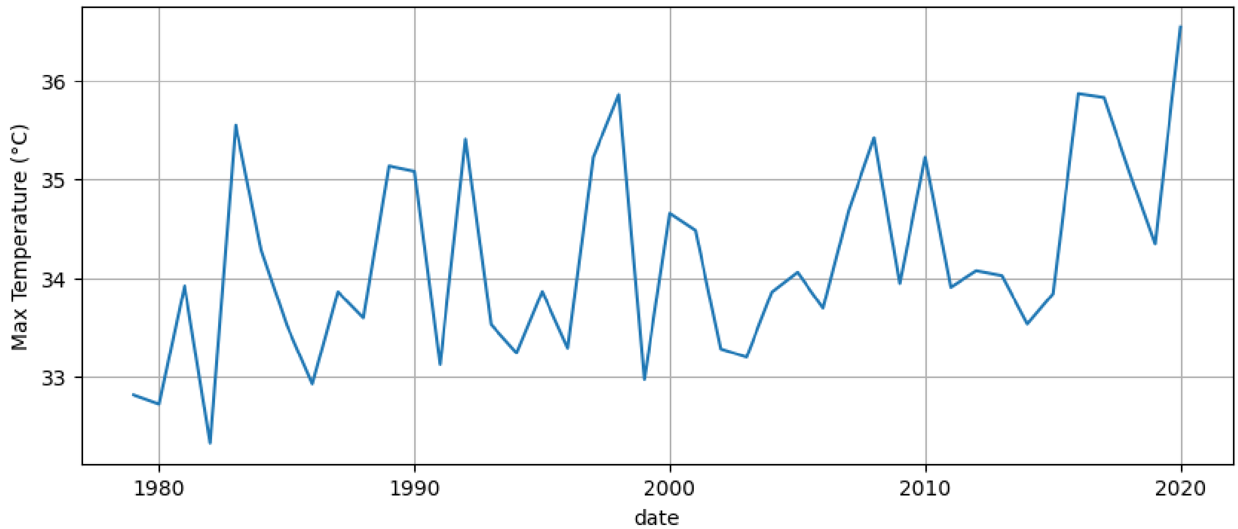

Figure 4.38: Monthly Trends in Maximum Temperature in Edo State

Notably, while inter-annual variability remains strong possibly influenced by large-scale ocean-atmosphere interactions such as the El Niño-Southern Oscillation (ENSO) the general temperature rise points toward a persistent climatic shift. The data's trajectory, particularly the sharp rise toward the end of the time series, signals the increasing frequency and intensity of heat events, which are characteristic of a changing climate regime. This rising trend corroborates projections from CMIP6 and IPCC AR6 assessments, which highlight West Africa as a hotspot for temperature increases due to its sensitivity to global climate dynamics (Yahaya et al., 2024). Such long-term changes necessitate robust regional adaptation strategies, especially in urban planning and agricultural resilience in states like Edo.

4.7.2 Annual Trends in Maximum Temperature

The graph Figure 4.39 illustrates the annual variation and long-term trend in maximum temperatures from 1979 to 2020. The observed data (blue line) shows considerable inter-annual variability, with maximum temperatures ranging between approximately 32 °C and above 36 °C.

However, the fitted trend line (red dashed line) reveals a statistically significant increasing trend over the period, with a linear regression slope of 0.035 °C per year and a p-value of 0.006. The Mann-Kendall test corroborates this trend, indicating a significant upward movement in annual maximum temperatures, also with a p-value of 0.006. These results suggest a persistent and measurable warming trend in Edo State over the last four decades.

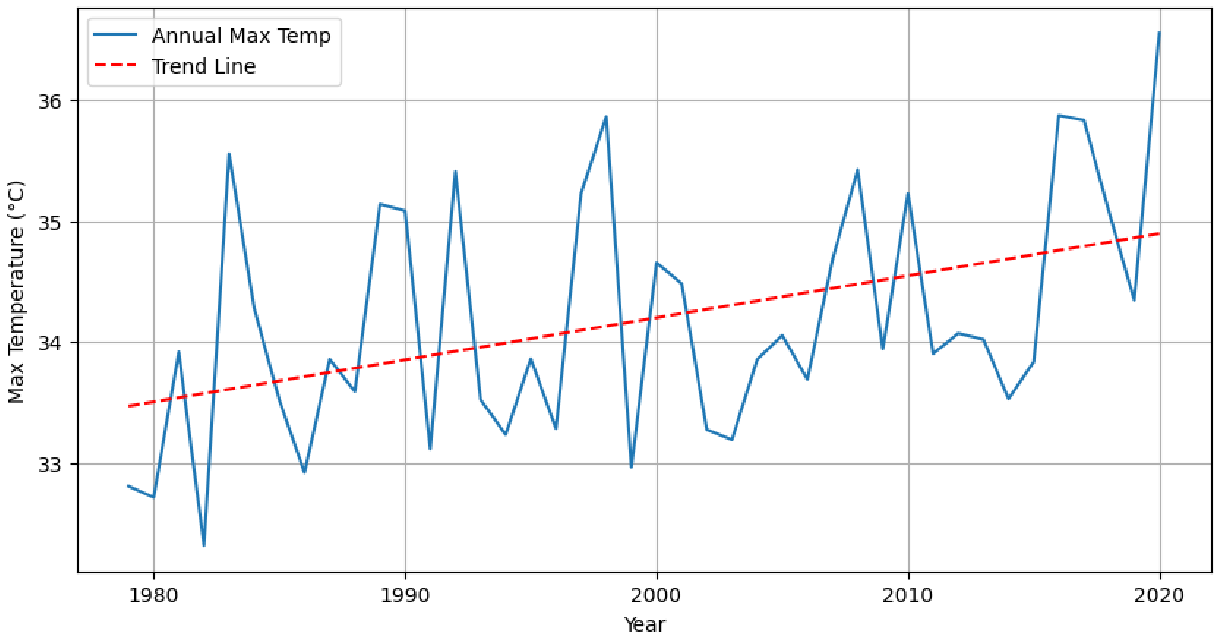

Figure 4.39: Annual Trends in Maximum Temperature in Edo State

Such a rise in maximum temperatures has critical implications for climate-sensitive sectors in the state. Elevated temperatures can increase the frequency and intensity of heatwaves, reduce agricultural productivity, and escalate water demand and stress especially in areas with already marginal rainfall (Muzammal et al., 2024b). Moreover, the intensification of annual heat could exacerbate health risks, particularly among vulnerable populations such as the elderly and children (Ebi et al., 2021). The increasing temperature trend is consistent with broader regional studies that have documented similar warming patterns across various parts of Nigeria, driven by both local land use changes and global climate forcing (Ilori and Ajayi, 2020a).

The rate of temperature increase in Edo State (0.035 °C/year) aligns closely with national and sub-Saharan African trends reported in recent climate literature, which emphasize the growing need for adaptive policy and infrastructure planning (Bello, 2017). The presence of such a statistically significant warming signal reinforces the urgency for integrating climate risk into agricultural calendars, urban planning, and water resource management in Edo State. Future studies could deepen this analysis by exploring potential links between this warming and regional drivers such as sea surface temperatures, greenhouse gas concentrations, and deforestation.

4.7.3 Seasonal Trends in Maximum Temperature

The graph Figure 4.40, shows the temporal trend in maximum seasonal temperatures across four major climatological seasons: DJF (December–February), MAM (March–May), JJA (June–August), and SON (September–November). A close examination reveals that DJF consistently records the highest maximum temperatures among the seasons, with values frequently above 32 °C and rising above 35 °C in recent years. This is followed by MAM, which also shows a notable warming trend over the study period, particularly from the early 2000s onward. The JJA season, traditionally associated with the core rainy season in southern Nigeria, records the lowest maximum temperatures, often below 29 °C. SON temperatures lie between those of MAM and JJA, showing moderate warming over the years.

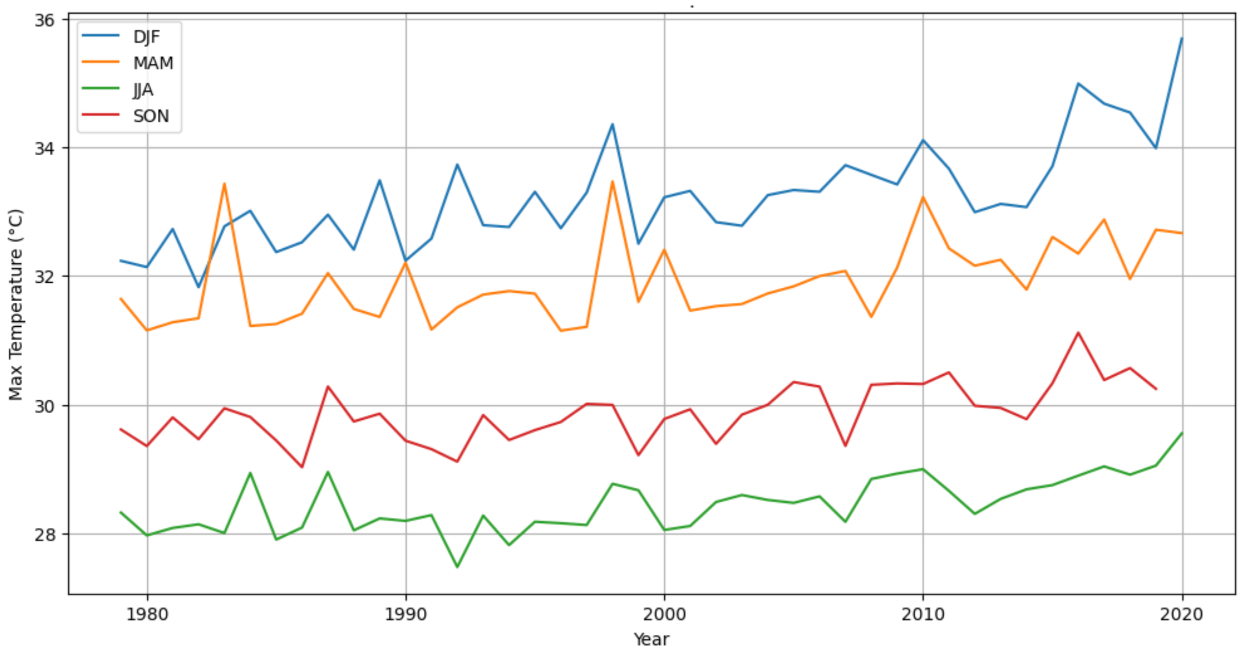

Figure 4.40: Seasonal Trends in Maximum Temperature in Edo State

The overall pattern suggests a steady increase in maximum temperatures across all seasons, with DJF and MAM showing the most pronounced upward trends. This is indicative of broader regional and global warming trends that have been documented in Nigeria and the West African sub-region (Ogunrinde et al., 2023). The rising temperatures, especially during the dry season (DJF and MAM), raise concerns about heat stress, increased evapotranspiration, and impacts on agriculture and water resources. The relatively muted increase in JJA temperatures may be attributed to higher cloud cover and rainfall during the wet season, which can moderate surface temperatures, a phenomenon also observed in other humid tropical regions (Gbode et al., 2021).

Moreover, the increasing trend in maximum temperatures aligns with findings from recent climate assessments, which report significant warming across Nigeria, with notable seasonal variations (Shiru et al., 2020). Such seasonal temperature shifts can influence the length of growing seasons, alter crop viability, and affect human health outcomes, particularly in urban centers like Benin

City where urban heat island effects may compound warming (Philippes et al., 2025). This analysis emphasizes the need for adaptive strategies that address seasonal vulnerabilities and promote climate-resilient planning across sectors in Edo State.

I. Maximum Temperature Data for December–January–February (DJF) Season

Figure 4.41 presents the maximum temperature data for the December–January–February (DJF) season from 1979 to 2020. The blue line shows substantial year-to-year variation in seasonal maximum temperatures, but more importantly, the red dashed trend line reveals a statistically significant upward trend. The linear regression yields a slope of 0.049 °C per year with a p-value of 0.000, while the Mann-Kendall test confirms a strongly significant increasing trend, also with a p-value of 0.000. These results indicate that maximum temperatures during the DJF season have been rising steadily in Edo State over the past four decades.

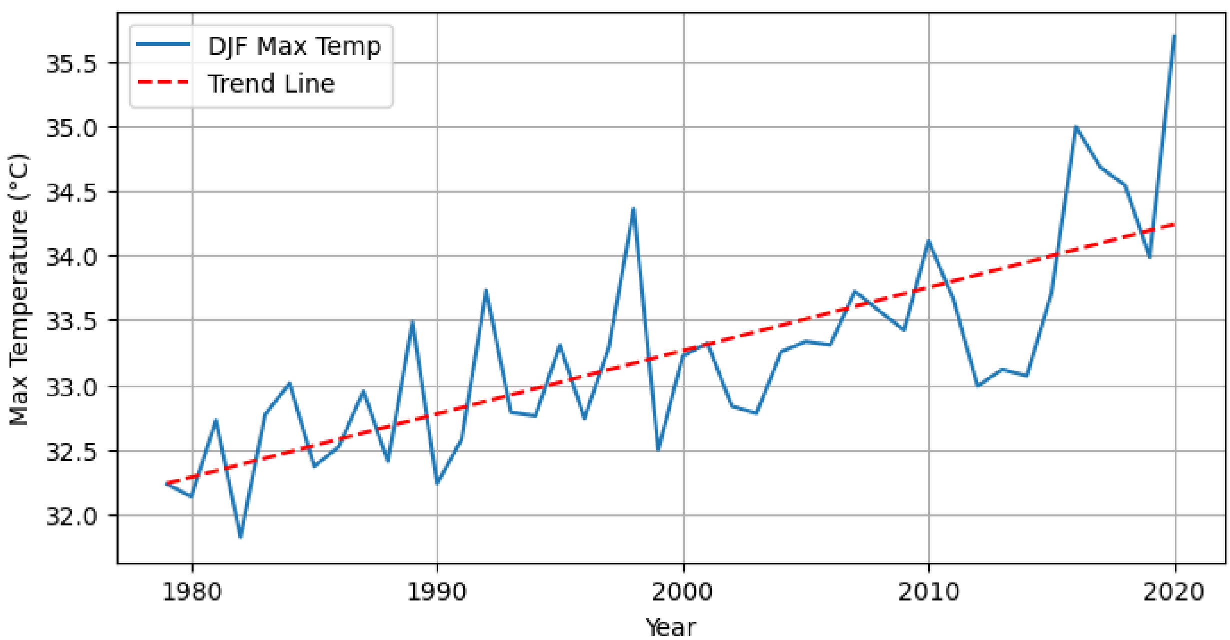

Figure 4.41: Maximum Temperature Data for DJF Season

This seasonal warming during DJF a typically dry and relatively cooler period in southern Nigeria could have far-reaching implications. Elevated temperatures in this season may intensify evapotranspiration and reduce soil moisture levels ahead of the rainy season, thereby affecting early planting and soil preparation (Song et al., 2013). The warming trend may also increase heat-related stress among vulnerable populations, particularly in urban centers like Benin City, where the urban heat island effect may amplify seasonal warming (Philippes et al., 2025). Moreover, rising DJF temperatures could be linked to broader regional climatic changes, including shifts in the Harmattan wind patterns and alterations in surface albedo due to land cover change (Achugbu et al., 2022)

The magnitude of the observed trend 0.049 °C per year is consistent with recent findings that point to more rapid warming during dry seasons in many parts of sub-Saharan Africa, especially due to anthropogenic influences such as deforestation and greenhouse gas emissions. Such seasonal-specific warming emphasizes the need for climate-responsive agricultural and water resource strategies tailored to each part of the seasonal cycle. Integrating these trends into local planning frameworks is crucial for improving adaptive capacity and enhancing community resilience to climate variability.

II. Maximum Temperature Data for March-April-May (MAM) Season

Figure 4.42 presents the maximum temperature during the March–April–May (MAM) season for Edo State over the period 1980 to 2020. The blue line represents the observed annual maximum temperature values, while the red dashed line denotes the fitted linear regression trend. A visual inspection reveals notable inter-annual variability, with peak values exceeding 33.5°C in some years and lows around 31.2°C. Despite this variability, the overall trajectory of the trend line indicates a consistent rise in maximum temperatures over the study period.

Quantitative analysis supports this observation, with the linear regression model yielding a statistically significant positive slope of 0.025°C per year and a p-value of 0.001, confirming that the warming trend is not due to random fluctuations. Complementarily, the non-parametric Mann-Kendall trend test also indicates a statistically significant increasing trend ($p = 0.000$), reinforcing the conclusion that maximum temperatures during the pre-wet season months are steadily rising in Edo State.

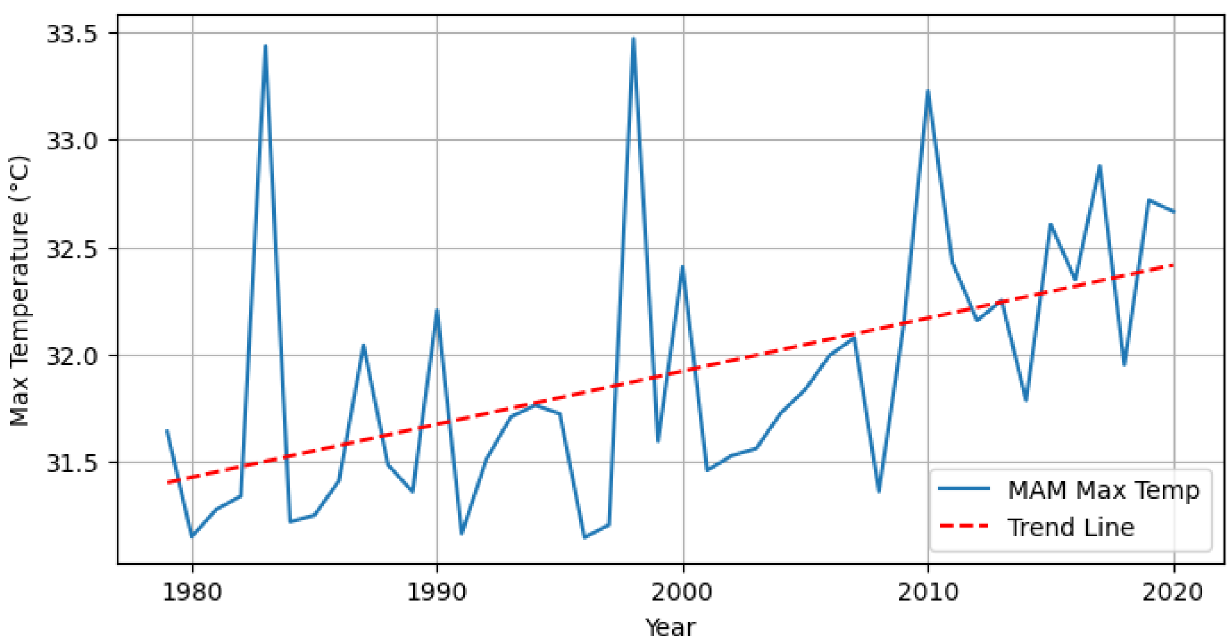

Figure 4.42: Maximum Temperature Data for MAM Season

This observed warming trend aligns with recent regional and global studies which have documented increasing temperatures in West Africa due to anthropogenic climate change (Achugbu et al., 2022; Diedhiou et al., 2018). Specifically, MAM seasonal warming is of particular concern because it precedes the main cropping season in southern Nigeria. Rising temperatures during this critical window may exacerbate evapotranspiration, reduce soil moisture retention, and negatively affect agricultural productivity and food security (Imen Guechi et al., 2021; Nicholson, 2017).

Moreover, the consistent upward trend observed in the figure may also contribute to enhanced thermal stress and changes in human comfort levels, especially in urban centers like Benin City, where the urban heat island effect may amplify warming. These findings underscore the urgent need for climate adaptation strategies that address increasing temperature extremes in the region, particularly in relation to agriculture, public health, and water resource management (Mehta, 2024).

III. Maximum Temperature Data for June-July-August (JJA) Season

Figure 4.43 presents the maximum temperature during the June–July–August (JJA) period for Edo State between 1980 and 2020. The blue line illustrates the observed annual maximum temperatures during the peak wet season, while the red dashed line represents the fitted linear regression trend. The visual pattern reveals a steady increase in temperature over the four-decade span, with fluctuations around the trend line but a clear upward trajectory, culminating in the highest recorded temperature occurring near the end of the series around 2020.

Statistical analysis corroborates the visual evidence, with a significant positive slope of 0.023°C per year derived from linear regression ($p = 0.000$), confirming a consistent and statistically robust warming trend during the JJA season. Similarly, the Mann-Kendall non-parametric test also confirms an increasing trend (p = 0.000), further validating the strength and reliability of the observed rise in maximum temperatures.

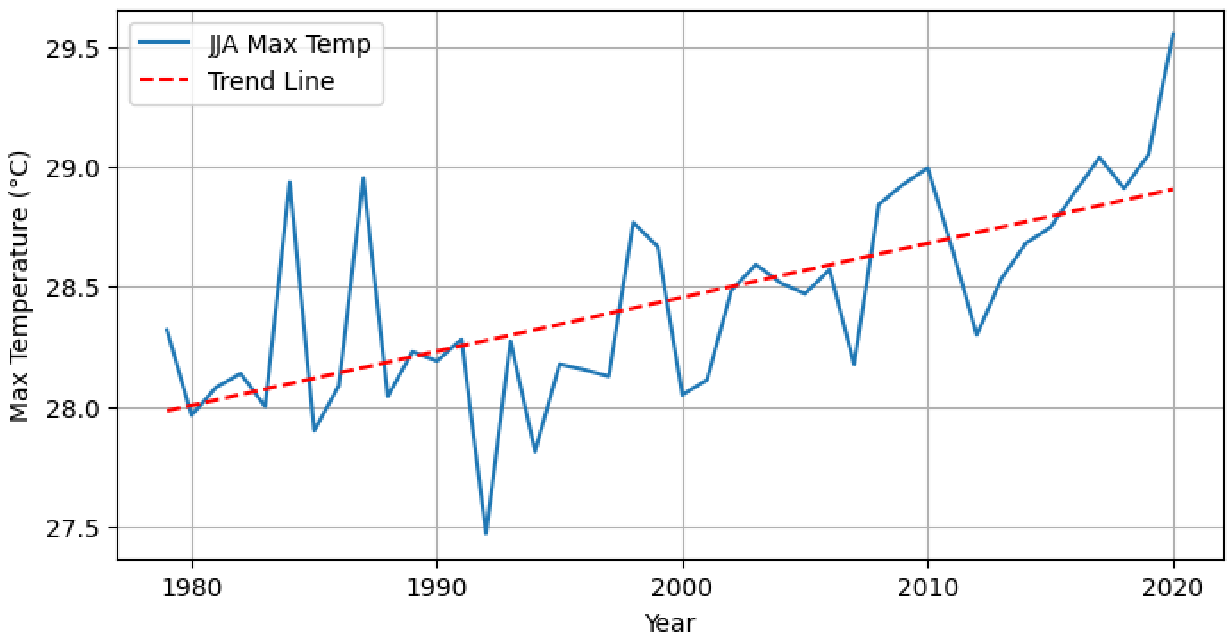

Figure 4 43: Maximum Temperature Data for JJA Season

This sustained warming during the JJA season is particularly noteworthy given that it corresponds to the core of the rainy season in Edo State. Rising temperatures during this period could lead to complex hydrological interactions, including increased evapotranspiration rates, altered soil moisture dynamics, and potentially more intense localized convective rainfall events, which may enhance the risk of flash flooding in vulnerable areas (Achugbu et al., 2022; Mehta, 2024). Additionally, elevated wet-season temperatures can compound heat stress for both human and ecological systems, particularly in densely populated urban areas.

The consistency of this warming trend with broader regional climate observations across West Africa suggests a clear signal of anthropogenic climate change, aligning with IPCC (2021) assessments that attribute increased temperatures in tropical Africa to global greenhouse gas emissions. The implications of such trends are far-reaching, necessitating the integration of temperature projections into climate adaptation strategies for sectors such as agriculture, health, and water management in Edo State (Paul Agboola, 2023).

IV. Maximum Temperature Data for September-October-November (SON) Season

September–October–November (SON) maximum temperature trend for Edo State from 1980 to 2020 seen in Figure 4.44 illustrates a pronounced and statistically significant warming pattern. The linear regression line, superimposed on the interannual temperature series, reveals a consistent upward trend with a slope of 0.024°C per year and a p-value of 0.000, indicating a high level of statistical significance. This is corroborated by the Mann-Kendall trend test, which also reports an increasing trend with a similarly strong p-value of 0.000, affirming that the observed warming is not due to random variability but reflects a persistent climatic shift.

This late wet season warming trend has important implications for climate-sensitive sectors in Edo State. The SON period is critical for post-flowering and harvest stages of staple crops, and sustained increases in maximum temperatures during this time may lead to premature drying, heat stress, and decreased crop yields, especially in systems dependent on rain-fed agriculture (Oguntunde et al., 2011). In addition, elevated temperatures in the post-monsoon season could increase the risk of heat-related health conditions, strain water supply systems, and intensify urban heat island effects in rapidly expanding urban areas such as Benin City.

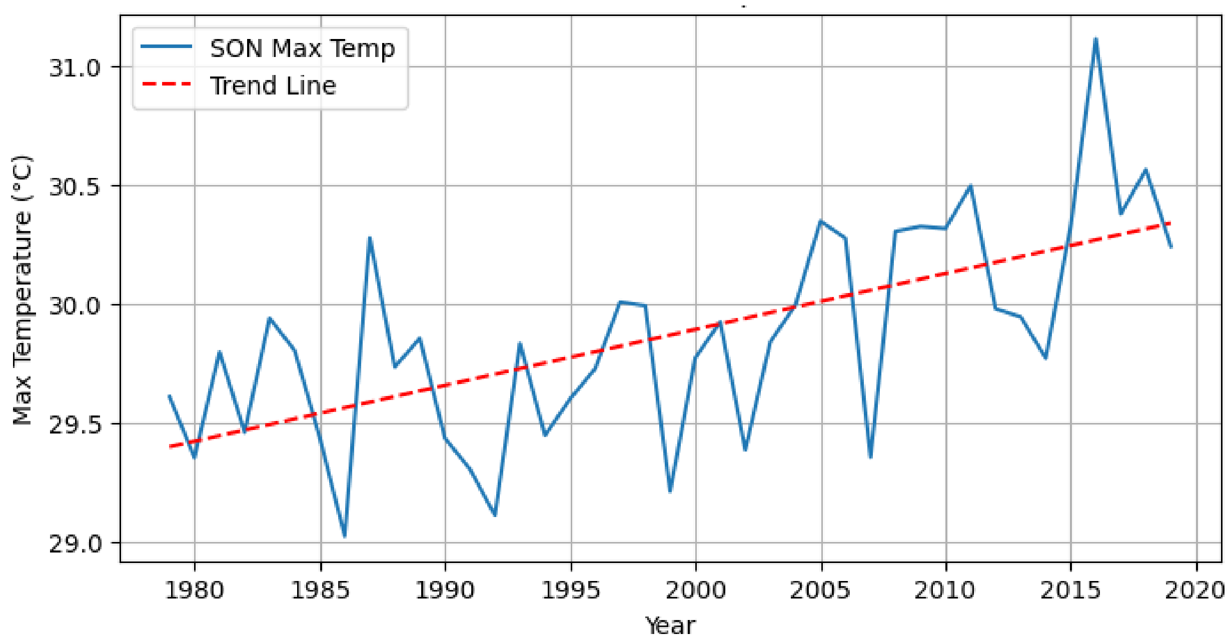

Figure 4.44: Maximum Temperature Data for SON Season

The consistency of this warming trend with broader regional patterns highlights the influence of global climate change across West Africa. Studies have documented similar increases in SON temperatures in other parts of Nigeria, aligning with projections from the Intergovernmental Panel on Climate Change (Masson-Delmotte et al., 2021) that indicate increased frequency and intensity of heat extremes in tropical climates. Furthermore, the SON warming adds to the cumulative seasonal temperature rise observed across MAM and JJA periods, signaling a year-round intensification of heat stress in the region (Kamrul Islam et al., 2018; Seegers et al., 2018). These findings emphasize the urgency of integrating seasonal temperature projections into local adaptation policies focused on agriculture, health, and infrastructure planning.

4.7.4 Seasonal Decomposition of Monthly Data

The topmost plot displays the original monthly maximum temperature data, exhibiting clear cyclical fluctuations throughout the year, superimposed on a more gradual long-term change. This raw data visually suggests the presence of both annual seasonal patterns and a potential underlying trend. The second plot from the top isolates the trend component, which represents the long-term progression or underlying direction of the temperature. This plot clearly shows a general upward trend in maximum temperatures over the entire period, albeit with some shorter-term oscillations. Notably, there appears to be a more pronounced increase in the trend from around the early 2000s onwards, indicating an accelerating warming in recent decades. This observed increasing trend aligns with global and regional climate change observations, including studies specifically focusing on temperature trends in Nigeria (Ilori and Ajayi, 2020b).

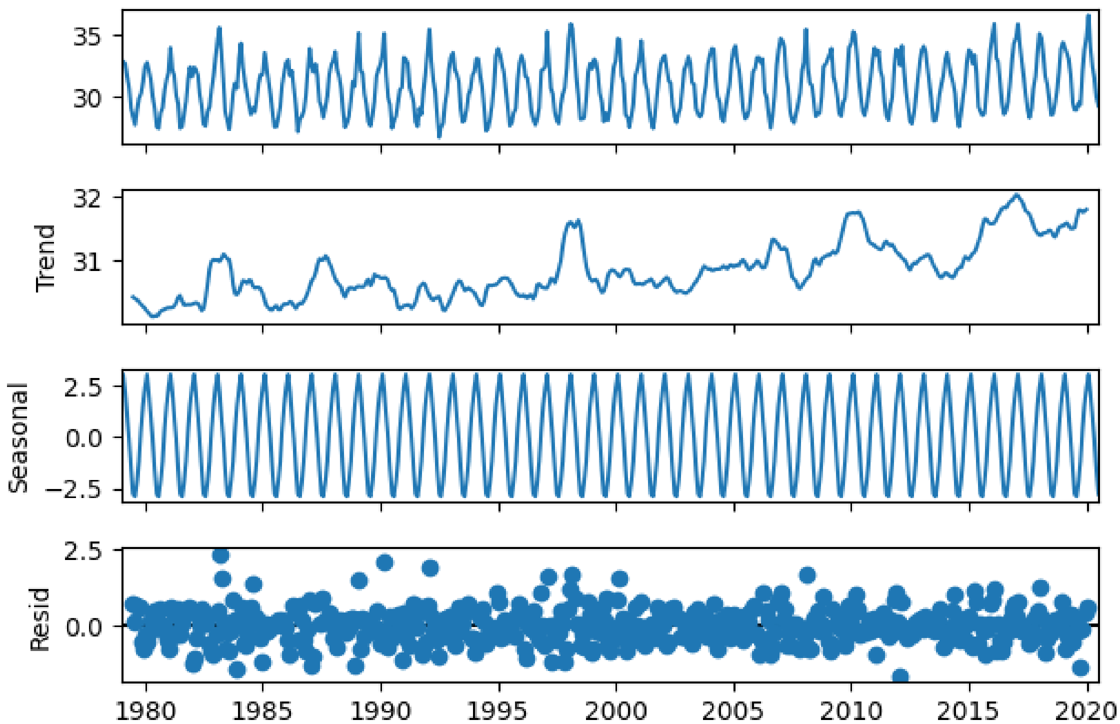

Figure 4.45: Seasonal Decomposition of Monthly Maximum Temperature

The third plot illustrates the seasonal component, which captures the recurring, predictable patterns within a year. As expected, there are distinct annual cycles, with temperatures consistently rising and falling at specific times of the year, reflecting the natural progression of seasons. This regular fluctuation indicates the strong influence of seasonal variations on Edo State's monthly maximum temperatures. Finally, the bottom plot shows the residual component, which represents the remaining variations after the trend and seasonal components have been removed. These residuals ideally should appear as random noise, indicating that the trend and seasonal patterns have effectively captured the systematic variations in the data. The scattered nature of the points around zero in the residual plot suggests that the decomposition has been largely successful in isolating the underlying patterns. The insights gained from this decomposition are crucial for climate studies, aiding in forecasting future temperature scenarios and understanding the impacts of climate change on the region.

4.8 Temporal Analysis of Maximum Temperature in Delta State (1971–2023)

The temporal variability of maximum temperature in Delta State was assessed using ERA5 reanalysis data processed through Google Earth Engine. Monthly and yearly averages were computed over a 53-year period (1971–2023) to understand the temperature trend and potential climate implications in the region.

4.8.1 Monthly Trends Maximum Temperature

Figure 4.46 shows the linear regression analysis performed on the data shows a consistent upward trend with a slope of 0.038°C per year, accompanied by a p-value of 0.002. This positive slope indicates that, on average, the annual maximum temperatures in Delta State have been increasing by 0.038°C each year over the period. The low p-value (0.002, well below the conventional significance level of 0.05) strongly suggests that this observed warming trend is not a random occurrence but a statistically significant climatic shift. Further supporting this finding, the Mann-Kendall trend test also reports an increasing trend with a similarly strong p-value of 0.002. This non-parametric test corroborates the linear regression results, reinforcing the conclusion that the warming observed in Delta State is a persistent phenomenon, reflecting a fundamental change in the region's climate rather than mere natural variability.

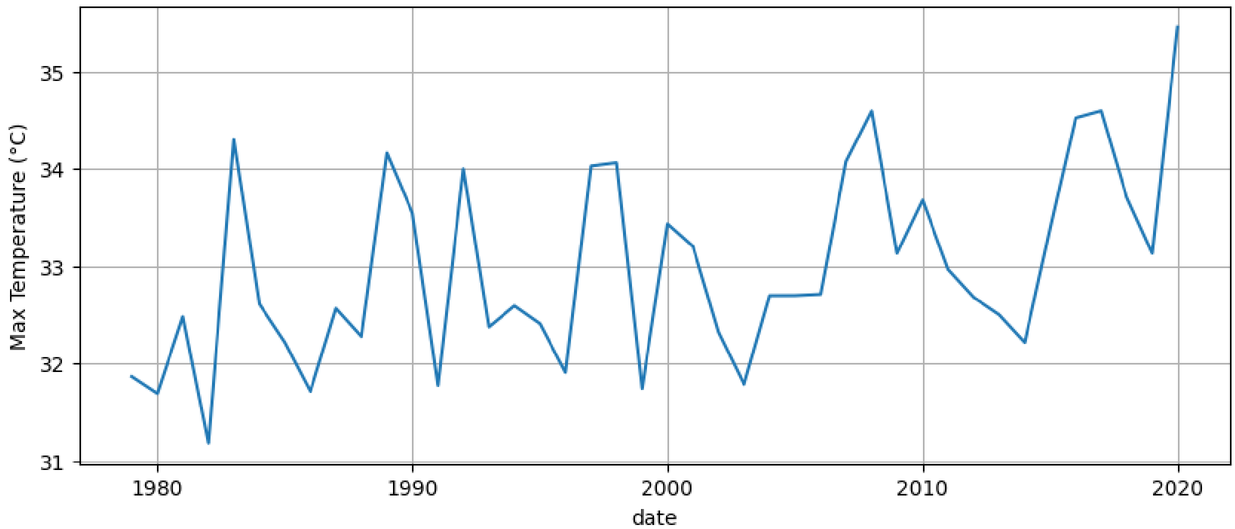

Figure 4.46: Monthly Trends in Maximum Temperature in Delta State

This consistent warming trend in Delta State has significant implications for various climate-sensitive sectors. Elevated annual maximum temperatures can exacerbate heat stress on both human populations and livestock, potentially leading to increased health risks and reduced productivity (Ilori and Ajayi, 2020b; Wankar et al., 2021). For agriculture, particularly in a region heavily reliant on rain-fed systems, higher temperatures can accelerate evapotranspiration rates, increasing water demand for crops and potentially leading to water scarcity, especially during critical growth stages (Wani et al., 2009b). Furthermore, sustained increases in annual maximum temperatures can put additional strain on existing infrastructure, such as power grids due to increased demand for cooling, and can intensify urban heat island effects in rapidly growing urban centers within Delta State.

The consistency of this warming trend with broader regional patterns underscores the pervasive influence of global climate change across West Africa. Studies have documented similar increases in temperatures across other parts of Nigeria, aligning with projections from the Intergovernmental

Panel on Climate Change (Masson-Delmotte et al., 2021) which indicate an increased frequency and intensity of heat extremes in tropical climates. This trend contributes to the overall rise in temperatures observed across different seasons in the region (Twardosz et al., 2021), signaling a continuous intensification of heat stress. These findings emphasize the urgent need for integrating these observed temperature projections into local adaptation policies, particularly concerning agricultural practices, public health initiatives, and infrastructure planning within Delta State to build resilience against the impacts of a changing climate.

4.8.2 Annual Trend Maximum Temperature

Figure 4.47 shows a general upward trajectory in the annual maximum temperatures over the depicted period. While there are inter-annual fluctuations, with some years showing higher or lower maximums, the red dashed trend line consistently slopes upwards, suggesting a warming pattern in Delta State. This observed warming trend is consistent with broader climate change patterns being reported globally and regionally. Such an increase in annual maximum temperatures has direct implications for various sectors within Delta State. For instance, it could lead to increased instances of heat stress for both human populations and livestock, potentially impacting public health and agricultural productivity (Thornton et al., 2022).

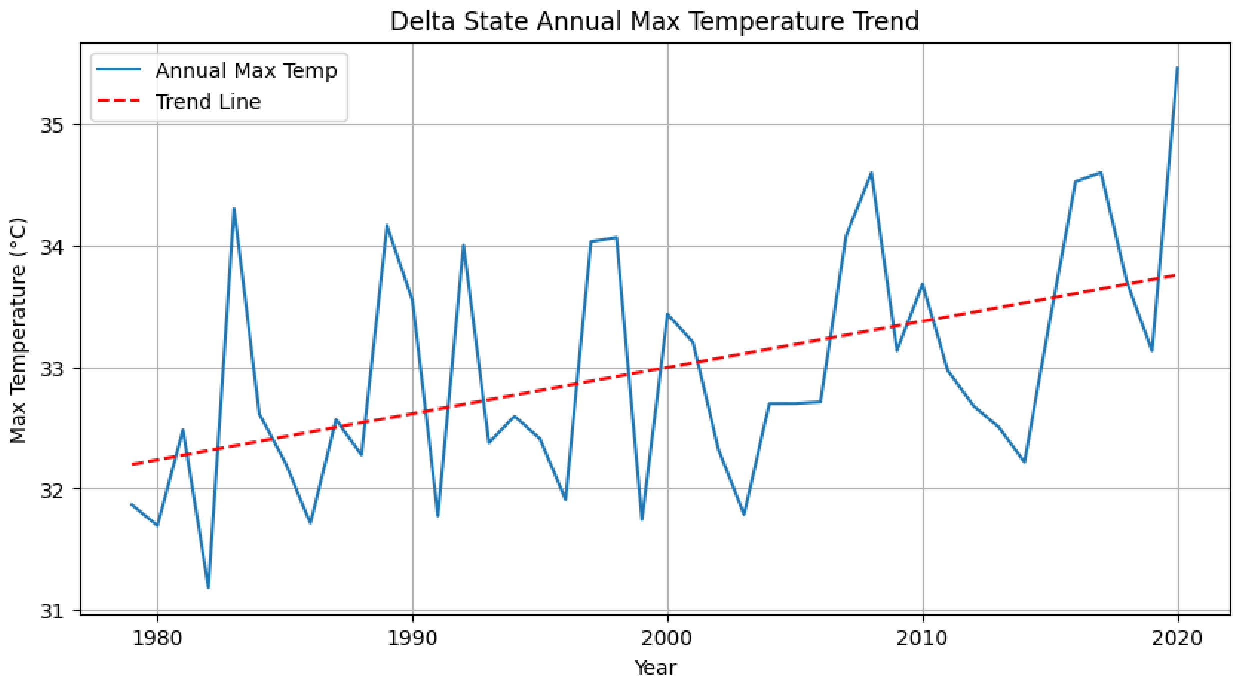

Figure 4.47: Annual Trends in Maximum Temperature in Delta State

Higher temperatures can also exacerbate water scarcity, particularly in a region that relies on rainfall for agriculture, by increasing evapotranspiration rates and water demand for crops (Cai et al., 2015b). Furthermore, the rising temperatures could intensify the urban heat island effect in densely populated areas and place additional strain on energy infrastructure due to increased demand for cooling. These findings underscore the importance of integrating climate considerations into local development and adaptation strategies for Delta State, aligning with the observed trends across Nigeria and global climate change projections (Cai et al., 2015b).

4.8.3 Seasonal Trends in Maximum Temperature

Figure 4.48 shows the distinct patterns for DJF (December, January, February), MAM (March, April, May), JJA (June, July, August), and SON (September, October, November) periods. Each line on the graph represents the annual average maximum temperature for a specific season, allowing for a comparative analysis of warming trends across the year.

A critical observation from this graph is the consistent upward trend across all four seasons, albeit with varying degrees of magnitude. The DJF season (blue line) generally exhibits the highest maximum temperatures throughout the period, and it also shows a very pronounced increase, particularly from the mid-2000s onwards, culminating in some of the highest recorded temperatures towards 2020. This indicates a significant warming during the dry season, which could intensify existing heat stress during what is typically the hottest part of the year. The MAM season (orange line) also displays a clear warming trend, with maximum temperatures generally lower than DJF but still showing a steady increase over the decades. This warming during the peak of the dry season and onset of rains can have substantial impacts on early agricultural activities and water availability. Similarly, the JJA season (green line), which typically experiences the lowest maximum temperatures due to the peak of the rainy season, still exhibits a discernible upward trend. While the overall temperatures are lower, the warming in this period could still affect crop yields and alter rainfall patterns. Finally, the SON season (red line) also shows an increasing trend, particularly noticeable in recent years. This warming in the late wet season can influence the maturation and harvesting of crops and could extend periods of heat stress (Akter and Rafiqul Islam, 2017).

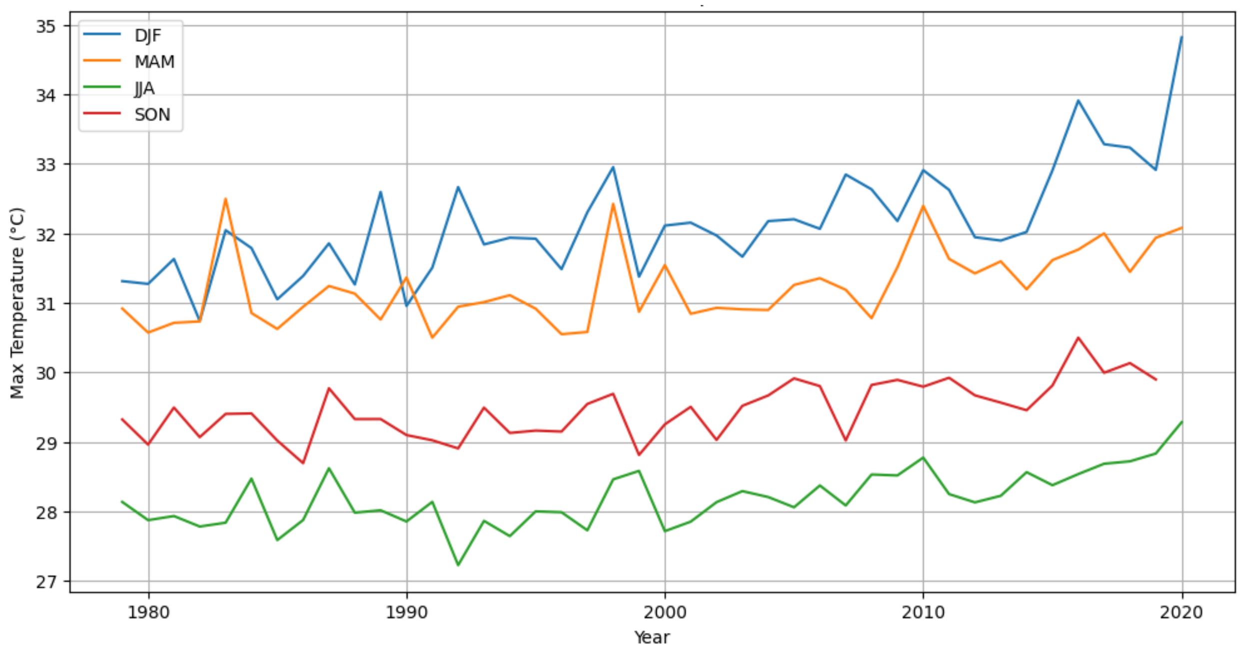

Figure 4.48: Seasonal Trends in Maximum Temperature in Delta State

The collective evidence from all four seasonal trends strongly suggests a pervasive and continuous warming across all parts of the year in Delta State. This aligns with broader climatic changes observed in Nigeria and West Africa, where studies consistently report rising temperatures (Merem et al., 2018). These regional warming patterns are consistent with global climate change projections, indicating an increased frequency and intensity of heat extremes in tropical regions. Such comprehensive seasonal warming poses significant challenges for Delta State, impacting various sectors from public health due to increased heat exposure to agriculture through altered growing seasons and enhanced water stress. Therefore, these detailed seasonal insights are crucial for developing targeted adaptation and mitigation strategies to build resilience against the changing climate in the region.

I. Maximum Temperature Data for December–January–February (DJF) Season

Figure 4.49 illustrates the maximum temperature trends for the December–January–February (DJF) season in Delta State from approximately 1979 to 2020. The blue solid line represents the observed DJF maximum temperatures annually, while the red dashed line indicates the linear trend.

The accompanying statistical analyses strongly corroborate the visually apparent upward trend. The linear regression analysis yielded a significant slope of 0.047°C per year, with an exceptionally low p-value of 0.000. This robust statistical result indicates a clear and substantial increase in maximum temperatures during the DJF season over the analyzed period. The positive slope signifies an average warming of 0.047°C each year, which accumulates to a considerable rise over four decades. Furthermore, the very low p-value (less than 0.001) confirms that this observed trend is highly statistically significant and is not attributable to random variability. Complementing this, the Mann-Kendall test also reported a definitive increasing trend with an equally compelling p-value of 0.000. The consistency between both statistical methods—linear regression and Mann-Kendall provide strong evidence of a persistent and significant warming trend in Delta State during the DJF season.

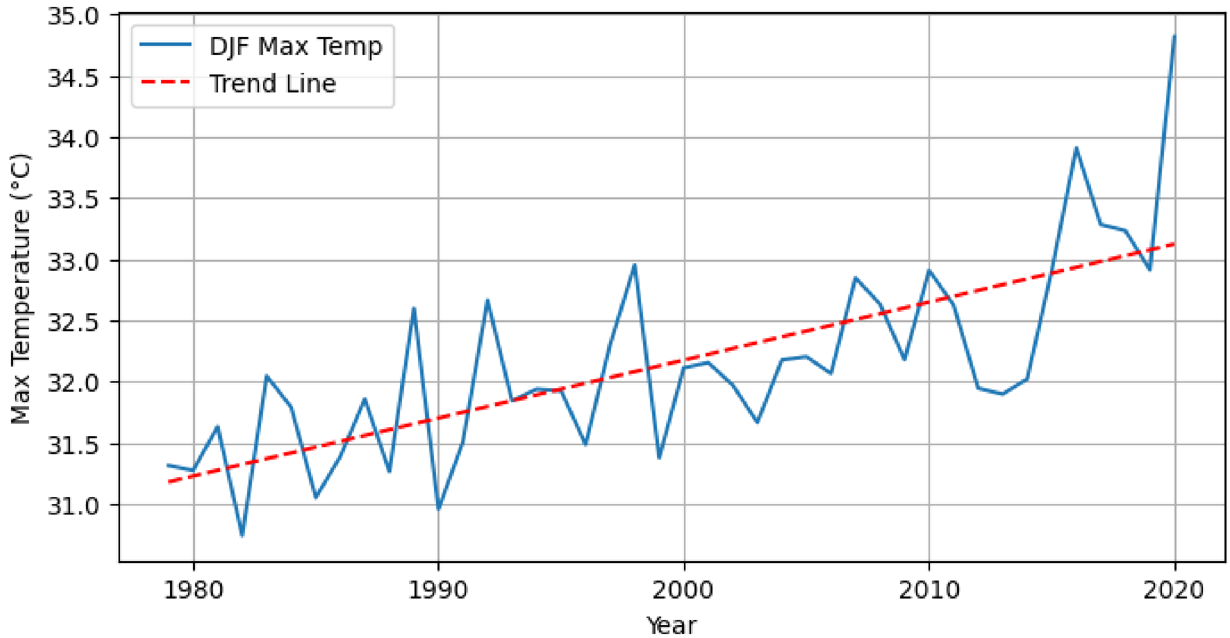

Figure 4.49: Maximum Temperature Data for DJF Season

This pronounced warming during the DJF season, which typically corresponds to the dry season and often the hottest part of the year in southern Nigeria, carries significant implications. Elevated maximum temperatures during this period can exacerbate heat stress on human populations, particularly vulnerable groups, leading to increased health risks and discomfort (Ebi et al., 2021). For agriculture, especially those crops cultivated during this drier period, higher temperatures can intensify evapotranspiration, leading to increased water demand and potential water scarcity, thereby impacting yields (M. K. Jha et al., 2020; Sahar Saeidi et al., 2023). Moreover, the rise in temperatures can increase energy consumption for cooling, putting a strain on the power infrastructure. These findings align with broader regional and global climate change patterns, which consistently point towards increasing temperatures and more frequent heat extremes in tropical areas (Liu et al., 2017). Therefore, understanding and addressing this specific seasonal warming trend is crucial for developing effective adaptation strategies in Delta State to mitigate the socio-economic and environmental impacts of climate change.

II. Maximum Temperature Data for March-April-May (MAM) Season

Figure 4.50 present the Maximum Temperature Data for MAM Season. The accompanying statistical analyses unequivocally support a significant warming trend during the MAM season. The linear regression analysis revealed a slope of 0.022°C per year with a remarkably low p-value of 0.001. This robust result signifies a clear and consistent increase in maximum temperatures during the MAM season over the study period. The positive slope indicates an average warming of 0.022°C each year, contributing to a noticeable rise over the four decades. The extremely low p-value (less than 0.05) confirms that this observed trend is statistically significant and not due to random fluctuations. Further reinforcing this finding, the Mann-Kendall test also reported a definitive increasing trend with an equally compelling p-value of 0.000. The agreement between both statistical methods, linear regression and Mann-Kendall, provides strong evidence of a persistent and significant warming trend in Delta State during the MAM season.

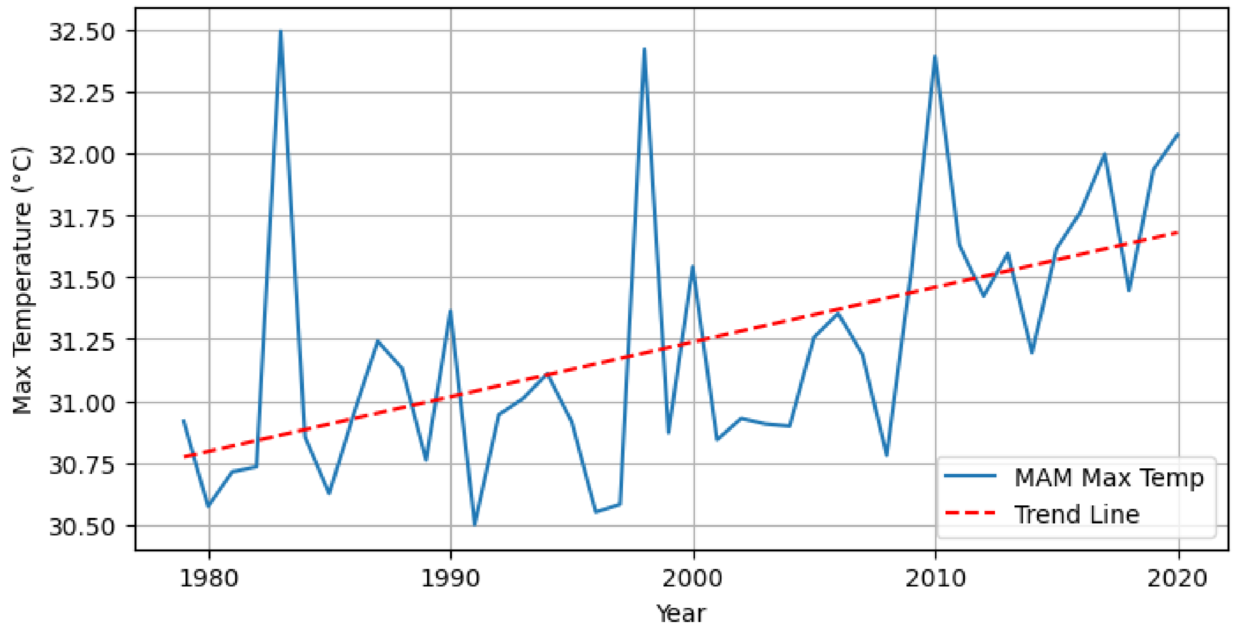

Figure 4.50: Maximum Temperature Data for MAM Season

This warming during the MAM season as seen in Figure 4.50, which marks the transition from the dry season to the onset of the rainy season, carries substantial implications for various sectors. Elevated maximum temperatures during this critical period can exacerbate heat stress on human populations, particularly affecting outdoor workers and vulnerable groups, potentially leading to increased health risks (Imen Guechi et al., 2021). For agriculture, especially as farmers prepare for planting and early crop development, higher temperatures can intensify evapotranspiration, leading to increased water demand and potential drought conditions if rainfall is insufficient or delayed, thereby impacting crop establishment and yields (Animashaun et al., 2023). Moreover, the rise in temperatures can increase the energy burden due to higher demand for cooling. These findings align with broader regional and global climate change patterns, which consistently point towards increasing temperatures and more frequent heat extremes in tropical areas (Masson-Delmotte et al., 2021; Tamoffo et al., 2023). Therefore, understanding and addressing this specific seasonal warming trend is crucial for developing effective adaptation strategies in Delta State to mitigate the socio-economic and environmental impacts of climate change.

III. Maximum Temperature Data for June-July-August (JJA) Season

The statistical analyses accompanying the image strongly support a significant warming trend during the JJA season. The linear regression analysis revealed a slope of 0.021°C per year with an exceptionally low p-value of 0.000. This robust statistical result indicates a clear and consistent increase in maximum temperatures during the JJA season over the analyzed period. The positive slope signifies an average warming of 0.021°C each year, which, while seemingly small annually, accumulates to a noticeable rise over four decades. The extremely low p-value (less than 0.001) confirms that this observed trend is highly statistically significant and is not attributable to random variability as seen in Figure 4.51. Further reinforcing this finding, the Mann-Kendall test also reported a definitive increasing trend with an equally compelling p-value of 0.000. The agreement between both statistical methods' linear regression and Mann-Kendall provides strong evidence of a persistent and significant warming trend in Delta State during the JJA season.

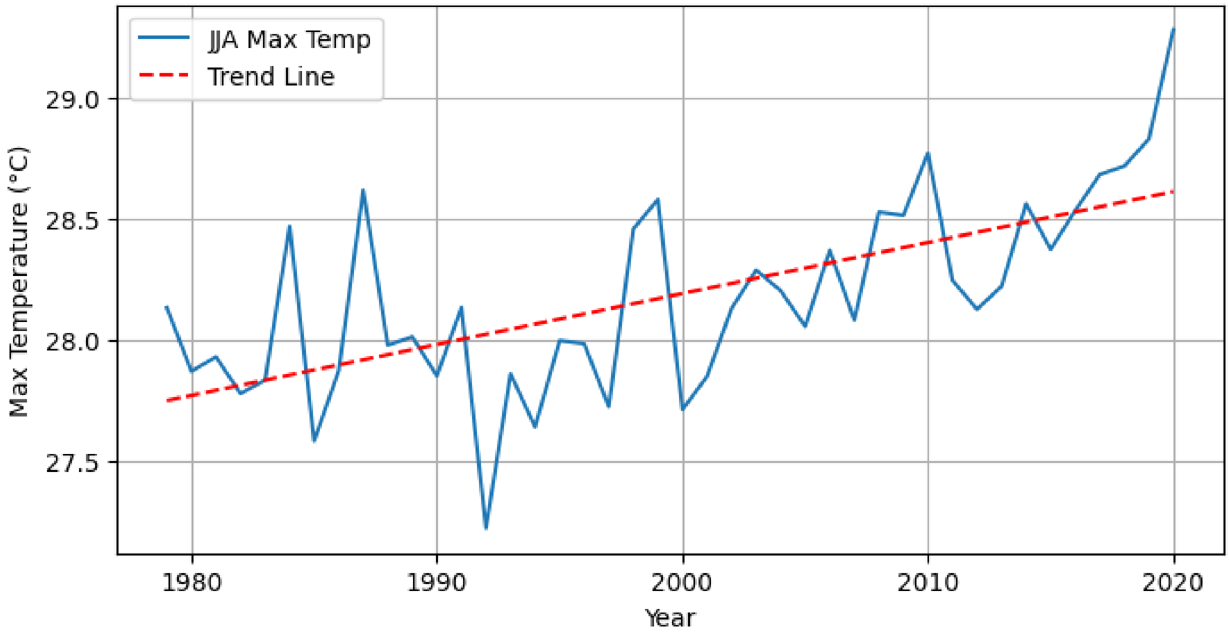

Figure 4.51: Maximum Temperature Data for JJA Season

This warming during the JJA season, which typically corresponds to the peak of the rainy season in southern Nigeria, carries significant implications despite generally being the coolest period of the year. Elevated maximum temperatures during this time can still intensify heat stress on human populations, particularly affecting those engaged in outdoor activities, potentially increasing discomfort and health risks (Adeyeri et al., 2020). For agriculture, while rainfall is abundant, higher temperatures can affect crop physiology, increase evapotranspiration rates, and potentially impact the effectiveness of rainfall by accelerating water loss from the soil and plants, which could lead to reduced yields if not properly managed (Ogunrinde et al., 2023). Moreover, a warmer JJA season could influence the intensity of the monsoon and alter typical weather patterns. These findings align with broader regional and global climate change patterns, which consistently point towards increasing temperatures and more frequent heat extremes in tropical areas (Masson-Delmotte et al., 2021; Tamoffo et al., 2023). Therefore, understanding and addressing this specific seasonal warming trend is crucial for developing effective adaptation strategies in Delta State to mitigate the socio-economic and environmental impacts of climate change.

IV. Maximum Temperature Data for September-October-November (SON) Season

The statistical analyses accompanying the image firmly establish a significant warming trend during the SON season. The linear regression analysis yielded a slope of 0.022°C per year with an exceptionally low p-value of 0.000. This robust statistical result indicates a clear and consistent increase in maximum temperatures during the SON season over the analyzed period. The positive slope signifies an average warming of 0.022°C each year, contributing to a noticeable rise over four decades. The extremely low p-value (less than 0.001) confirms that this observed trend is highly statistically significant and is not attributable to random variability. Further reinforcing this finding, the Mann-Kendall test also reported a definitive increasing trend with an equally compelling p-value of 0.000. The agreement between both statistical methods, linear regression and Mann-Kendall, provides strong evidence of a persistent and significant warming trend in Delta State during the SON season.

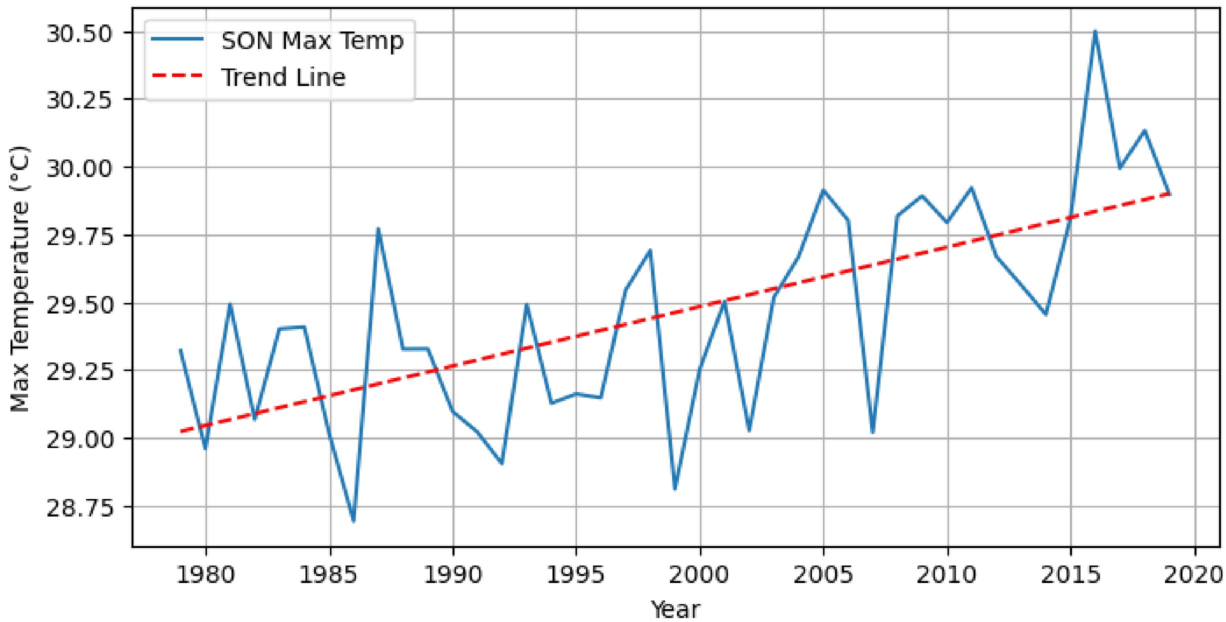

Figure 4.52: Maximum Temperature Data for SON Season

This warming during the SON season, which marks the transition from the peak of the rainy season to the onset of the dry season, carries significant implications seen in Figure 4.52. Elevated maximum temperatures during this critical period can exacerbate heat stress on human populations, particularly affecting those engaged in outdoor activities, potentially increasing discomfort and health risks (Adeyeri et al., 2020). For agriculture, the SON period is crucial for the post-flowering and harvest stages of many staple crops. Higher temperatures during this time can lead to premature drying, heat stress on crops, and ultimately decreased yields, especially in rain-fed agricultural systems (Ogunrinde et al., 2023). Moreover, the rise in temperatures can increase the energy burden due to higher demand for cooling. These findings align with broader regional and global climate change patterns, which consistently point towards increasing temperatures and more frequent heat extremes in tropical areas (Masson-Delmotte et al., 2021; Tamoffo et al., 2023). Therefore, understanding and addressing this specific seasonal warming trend is crucial for developing effective adaptation strategies in Delta State to mitigate the socio-economic and environmental impacts of climate change.

4.8.4 Seasonal Decomposition of Monthly Data

The uppermost panel from Figure 4.53 illustrates the original monthly maximum temperature data. This raw series clearly exhibits a repetitive annual cycle, indicating pronounced seasonal variations, along with an overarching long-term change. This initial view already hints at the complex interplay of natural seasonality and a more gradual climatic shift. The second panel from the top isolates the trend component, which represents the long-term, non-seasonal progression of maximum temperatures. This plot distinctly shows a general upward trend across the entire dataset, signifying a persistent warming in Delta State over the decades. Notably, there's a more pronounced acceleration in this warming trend observed from approximately the early 2000s onwards, suggesting an intensified rate of temperature increase in recent times. This observed long-term warming is consistent with the broader patterns of climate change documented across Nigeria and the West African sub-region (Adeyeri et al., 2020; Tamoffo et al., 2023).

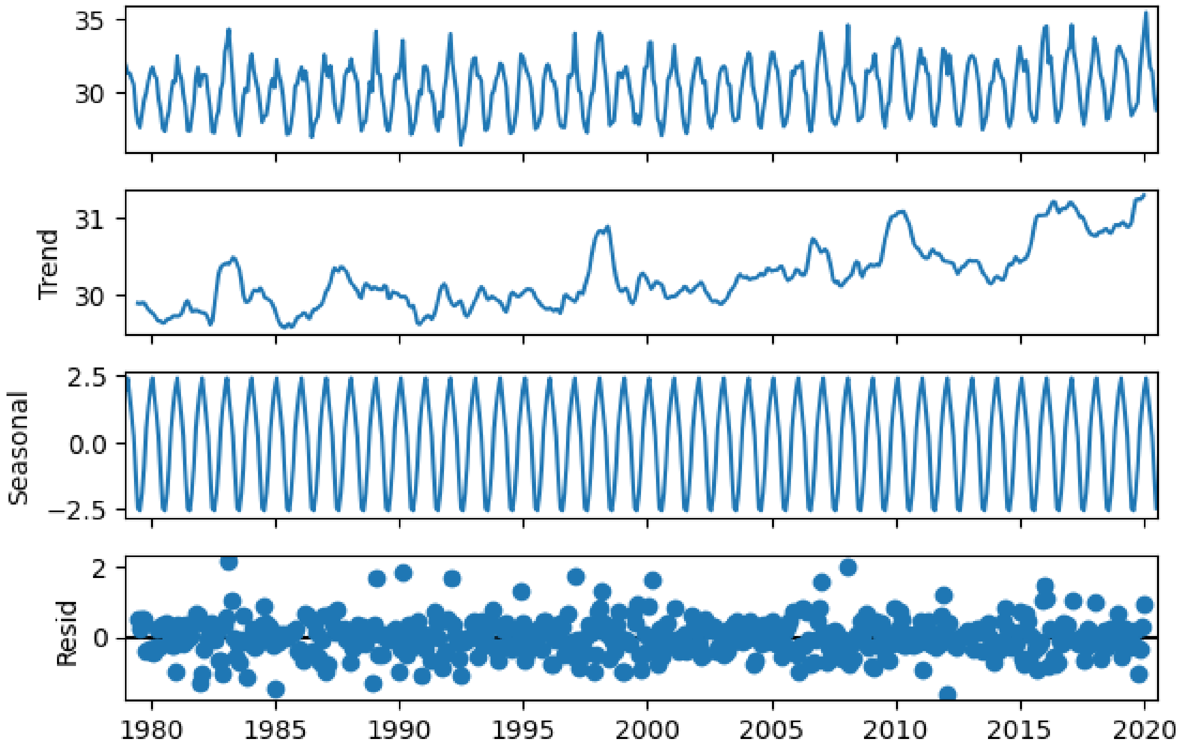

Figure 4.53: Seasonal Decomposition of Monthly Maximum Temperature

The third panel from the top illustrates the seasonal component, which captures the regular, predictable patterns that repeat within a year. The clear and consistent sinusoidal pattern here confirms strong annual cycles, where maximum temperatures predictably rise and fall with the progression of seasons. This component highlights the dominant influence of natural seasonal variations on the monthly temperature regime in Delta State. Finally, the bottom panel displays the residual component, representing the irregular or random variations left after the trend and seasonal components have been removed. Ideally, these residuals should appear as random noise centered around zero, indicating that the systematic patterns have been effectively extracted. The scattered nature of the points in the residual plot, without any obvious remaining pattern, suggests that the decomposition has been successful in accurately separating the underlying trend and seasonal influences. The insights gleaned from this seasonal decomposition are invaluable for understanding the complex nature of temperature variability in Delta State, aiding in the development of more accurate climate projections and effective adaptation strategies for various sectors, including agriculture, water resources, and public health (Ogunrinde et al., 2023).

4.9 Temporal Analysis of Maximum Temperature in Bayelsa State (1971–2023)

The temporal variability of maximum temperature in Bayelsa State was assessed using ERA5 reanalysis data processed through Google Earth Engine. Monthly and yearly averages were computed over a 53-year period (1971–2023) to understand the temperature trend and potential climate implications in the region.

4.9.1 Monthly Trends Maximum Temperature

The accompanying statistical analyses reveal a clear and statistically significant warming trend for Bayelsa State. The linear regression analysis shows a slope of 0.038°C per year, with a p-value of 0.002. This positive slope indicates a consistent increase in annual maximum temperatures, meaning that on average, temperatures have been rising by 0.038°C each year over the period. The low p-value (0.002, which is less than the conventional significance level of 0.05) suggests that this observed trend is statistically significant and not merely due to random chance. Further supporting this finding, the Mann-Kendall test also indicates an increasing trend with an equally low p-value of 0.002 as seen in Figure 4.54.

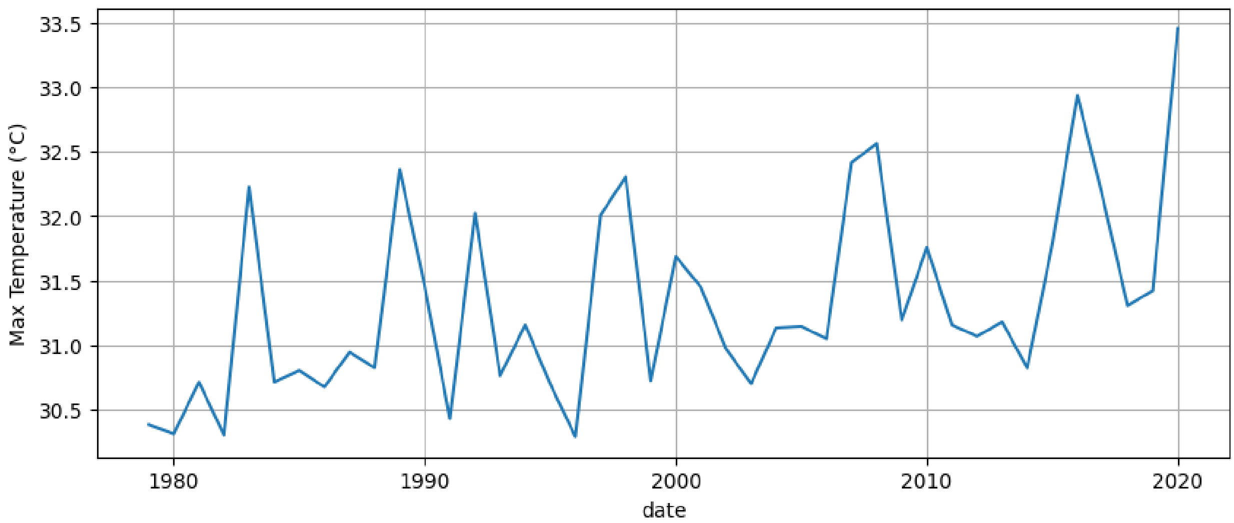

Figure 4.54: Monthly Trends in Maximum Temperature in Bayelsa State

This agreement between both statistical methods strengthens the conclusion that Bayelsa State is experiencing a significant and persistent warming trend in its annual maximum temperatures. These findings are consistent with broader regional and global climate change patterns, aligning with research that highlights increasing temperature trends across Nigeria and West Africa (Adeyeri et al., 2020; Tamoffo et al., 2023). The observed increase in maximum temperatures has significant implications for various sectors in Bayelsa State, including potential impacts on public health due to increased heat stress, alterations in agricultural cycles, and heightened pressure on water resources (Ogunrinde et al., 2023).

4.9.2 Annual Trend Maximum Temperature

Figure 4.55 illustrates the trend of annual maximum temperatures in Bayelsa State from the late 1970s to 2020. The blue line represents observed annual maximum temperature values, while the red dashed line signifies the linear trend across the years. From the graph, it is evident that there is a gradual increase in the maximum temperatures over the study period, with noticeable interannual variability. Despite fluctuations, the overall trajectory of the trend line suggests a warming pattern in Bayelsa State's climate, consistent with broader global and regional trends attributed to climate change (Masson-Delmotte et al., 2021). The highest temperature is observed in the final year (2020), which may indicate the increasing frequency of extreme heat events in the region. This warming trend aligns with findings from recent studies which document that Nigeria, like many other parts of sub-Saharan Africa, is experiencing rising temperatures, potentially leading to significant environmental and socio-economic implications (Akinsanola and Zhou, 2019). The trend is particularly concerning for the Niger Delta region, where Bayelsa is located, due to the area's vulnerability to climate-sensitive sectors such as agriculture, fisheries, and public health (Udinmade Ighedosa, 2019). Therefore, the observed trend underscores the urgent need for adaptive strategies and climate resilience policies to mitigate the impacts of rising temperatures in the state and the broader region.

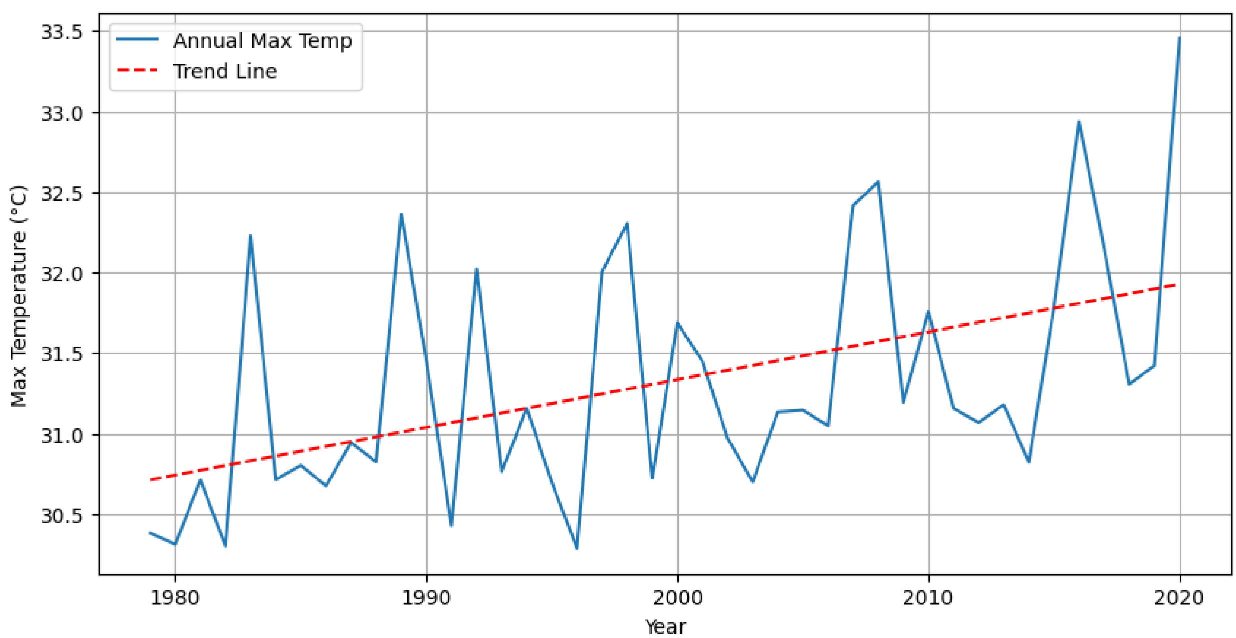

Figure 4.55: Annual Trends in Maximum Temperature in Bayelsa State

4.9.3 Seasonal Trends in Maximum Temperature

Figure 4.56 presents the seasonal distribution of maximum temperatures in Bayelsa State from 1979 to 2020, segmented into four climatological seasons: DJF (December–February), MAM (March–May), JJA (June–August), and SON (September–November). It is evident from the graph that all seasons show a warming trend over the years, though the magnitude and pattern of increase vary. The DJF and MAM seasons consistently record the highest maximum temperatures, with DJF peaking sharply in the final year (2020), suggesting heightened vulnerability to heat extremes during the dry season. On the other hand, the JJA season, which coincides with the peak of the rainy season, shows relatively lower maximum temperatures but still indicates a steady rise. This seasonal disparity in temperature response may be influenced by local climatic factors such as cloud cover, rainfall patterns, and atmospheric circulation.

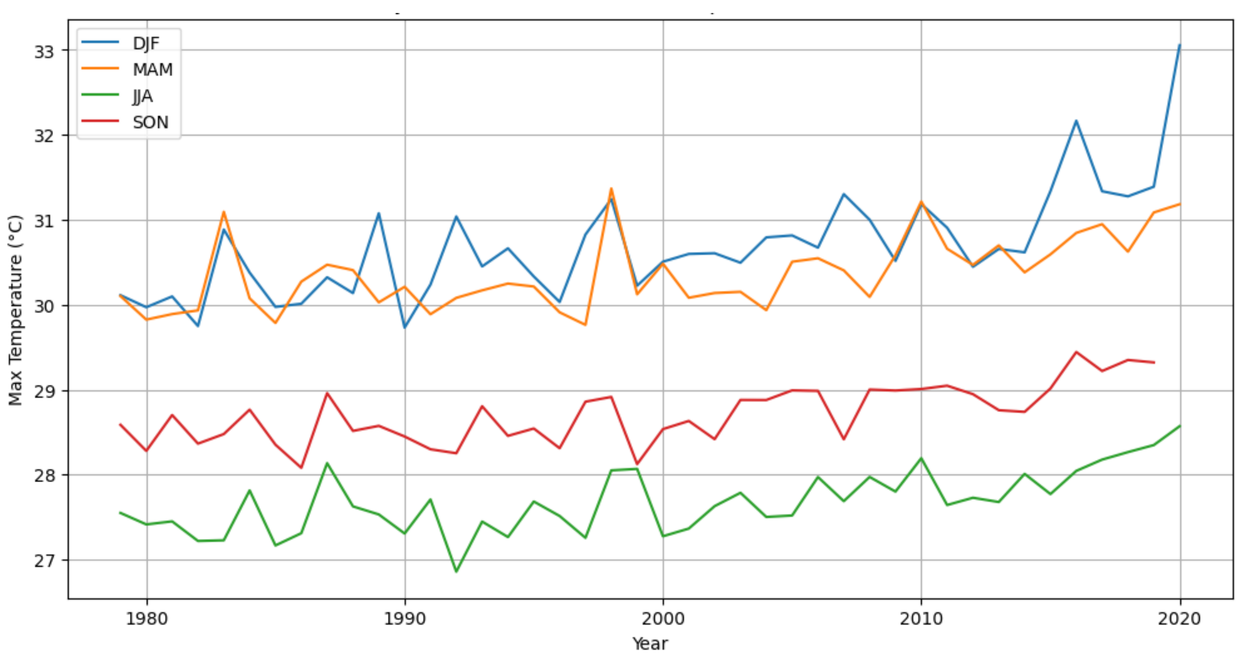

Figure 4.56: Seasonal Trends in Maximum Temperature in Bayelsa State

The gradual temperature increase across all seasons aligns with regional climate change projections for the Niger Delta, which warn of increasing temperatures and their compounded impacts on agriculture, water resources, and health (Akinsanola & Zhou, 2019). Furthermore, recent studies have highlighted that such seasonal warming contributes to prolonged heat stress and can intensify the frequency and severity of climate extremes, particularly in coastal and low-lying areas like Bayelsa (Ibe & Ajao, 2020). The data in the image reinforce concerns that climate change is not only raising average annual temperatures but is also disrupting seasonal thermal dynamics, thereby affecting ecosystems and livelihoods across different times of the year.

I. Maximum Temperature Data for December–January–February (DJF) Season

Figure 4.57 displays the trend in maximum temperature for the December–January–February (DJF) season in Bayelsa State from 1979 to 2020, with a linear regression line superimposed to highlight the long-term trajectory. The data clearly indicate a statistically significant upward trend in DJF maximum temperatures, with a linear regression slope of 0.036°C per year and a p-value of 0.000, underscoring the robustness of the observed warming. This finding is further supported by the Mann-Kendall test, which also confirms a significant increasing trend ($p = 0.000$). These results suggest that the dry season in Bayelsa is experiencing substantial and accelerating warming, which may be linked to broader regional climate dynamics and the intensification of the Harmattan season's dryness due to global climate change (Akinsanola & Zhou, 2019).

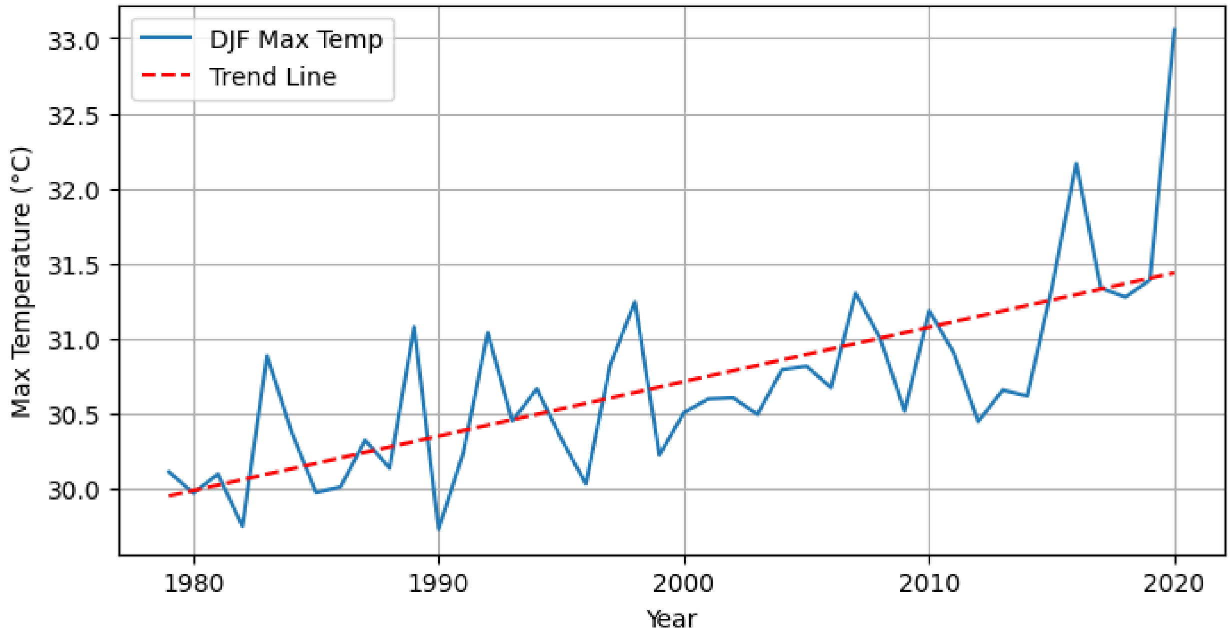

Figure 4.57: Maximum Temperature Data for DJF Season

The notable spike in 2020 represents the highest temperature recorded in the DJF period during the study window, raising concerns over the increasing frequency of extreme heat events during what is already the hottest part of the year for the region. As such, this warming trend has important implications for public health, energy demand, and agricultural productivity, particularly given the vulnerability of rural communities in the Niger Delta who depend heavily on weather-sensitive livelihoods (Udinmade Ighedosa, 2019). These findings are consistent with broader climate projections that show West Africa experiencing increased heat extremes due to anthropogenic influences, highlighting the urgent need for targeted adaptation strategies in sub-national regions like Bayelsa (Masson-Delmotte et al., 2021).

II. Maximum Temperature Data for March-April-May (MAM) Season

Figure 4.58 illustrates the long-term trend in maximum temperatures during the March–April–May (MAM) season in Bayelsa State from 1979 to 2020. The blue line captures the year-to-year fluctuations, while the red dashed line represents the linear regression trend. The statistical analysis indicates a significant upward trend in MAM maximum temperatures, with a slope of 0.020°C per year and a p-value of 0.000, confirming the significance of the warming. The Mann-Kendall test also supports this result with a similarly strong increasing trend (p = 0.000). These findings suggest a persistent rise in temperature during the transitional period from the dry to the wet season, which is critical for agricultural activities in the region.

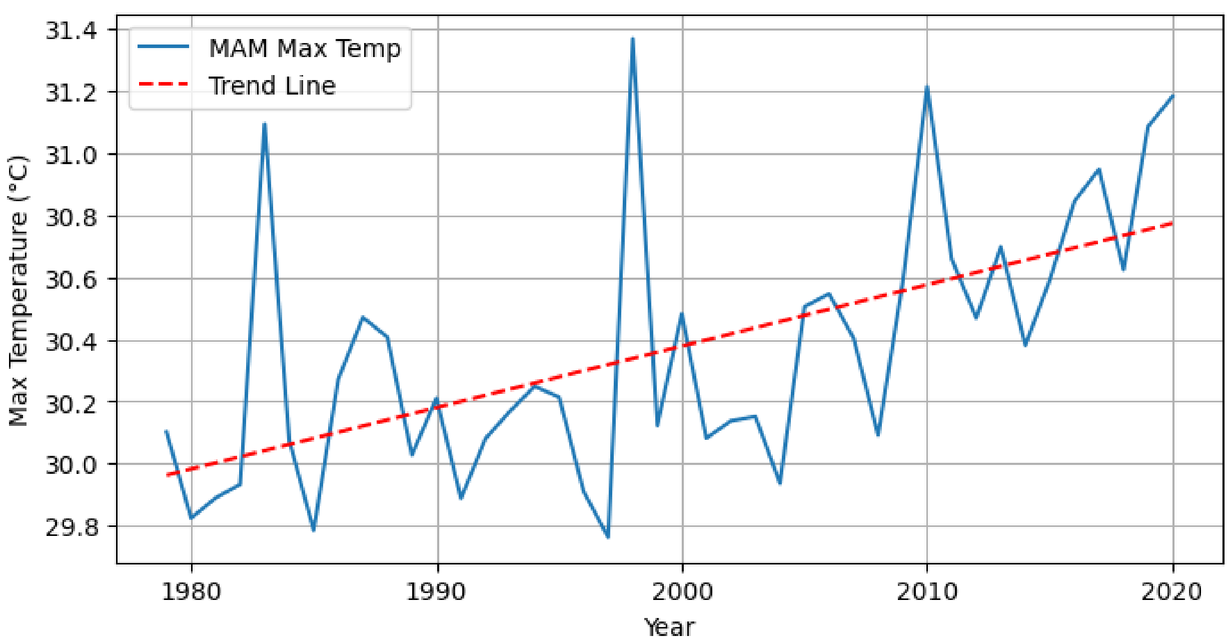

Figure 4.58: Maximum Temperature Data for MAM Season

The observed warming aligns with regional climate models that project rising temperatures across West Africa due to anthropogenic climate change (GIBBA, 2016). The spikes in temperature, particularly around 2000 and the late 2010s, reflect the increasing frequency of heatwaves and anomalies that could disrupt farming schedules, water resource management, and exacerbate heat-related health issues. In the context of Bayelsa's socio-economic landscape dominated by subsistence agriculture and fisheries this seasonal warming trend could threaten food security and livelihoods if adaptive measures are not implemented (Akinsanola and Zhou, 2019). These results underscore the urgent need for localized climate adaptation strategies that are responsive to seasonal temperature changes, especially during the MAM period when many communities prepare for the main cropping season.

III. Maximum Temperature Data for June-July-August (JJA) Season

Figure 4.59 presents the trend of maximum temperatures during the June–July–August (JJA) season in Bayelsa State from 1979 to 2020. The blue line reflects the inter-annual variations, while the red dashed line represents a statistically significant linear increase in temperature over time. The linear regression analysis reveals a warming rate of 0.020°C per year, with a p-value of 0.000, indicating a strong and significant trend. This is further corroborated by the Mann-Kendall test, which also identifies an increasing trend at a high level of statistical significance ($p = 0.000$).

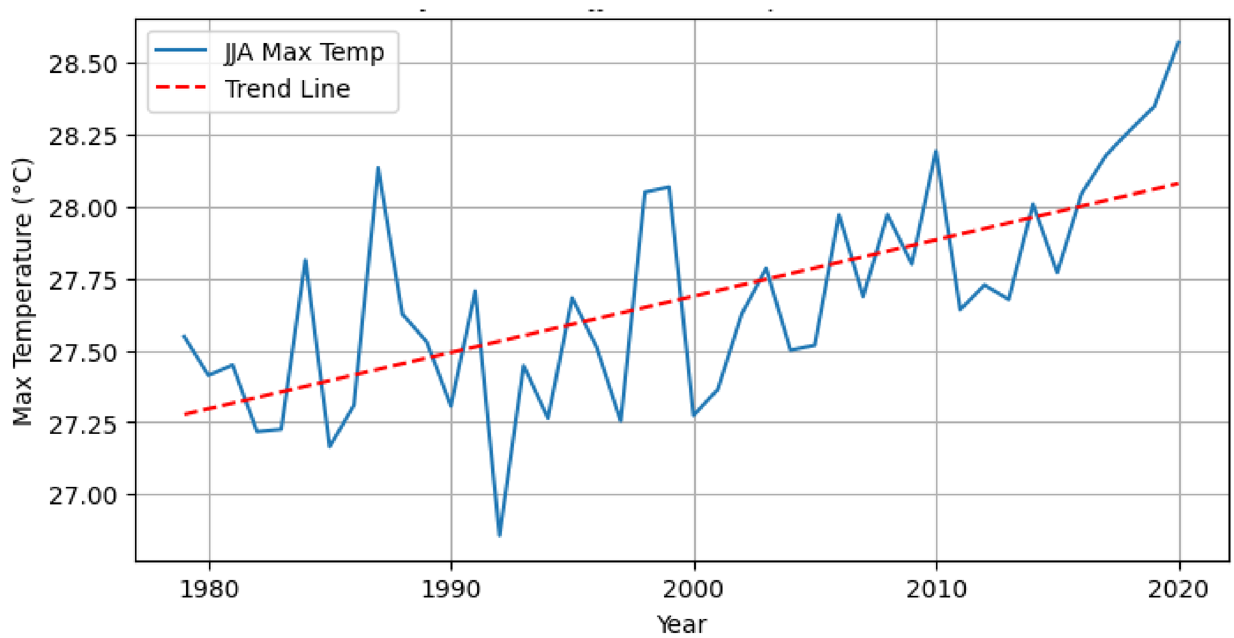

Figure 4 59: Maximum Temperature Data for JJA Season

Despite JJA being part of the peak rainy season in Bayelsa, where cooler temperatures are typically expected due to cloud cover and precipitation, the data indicate a notable and consistent rise in maximum temperatures. This suggests that even the traditionally cooler wet season is no longer exempt from the broader warming trend, a pattern that aligns with regional climate projections showing rising temperatures across all seasons in West Africa (Sylla *et. al*., 2018). The implications of warming during JJA are profound, as elevated temperatures combined with high humidity can intensify thermal discomfort and increase the risk of heat stress, particularly among vulnerable populations. Furthermore, this seasonal warming may alter hydrological cycles, reduce crop yields, and affect biodiversity in the region. Given Bayelsa's location in the Niger Delta a region already facing environmental stress from flooding and erosion—the rising temperature trend observed in JJA underscores the urgency for integrated climate adaptation and resilience planning (Odunsi and Rienow, 2024).

IV. Maximum Temperature Data for September-October-November (SON) Season

Figure 4.60 displays the trend of maximum temperatures in Bayelsa State during the September–October–November (SON) season from 1979 to 2020. The blue line traces the interannual variability in maximum temperature, while the red dashed line represents a linear regression fit that reveals a statistically significant upward trend. With a regression slope of 0.020°C per year and a p-value of 0.000, the analysis confirms a strong warming pattern. The Mann-Kendall trend test also supports this result, indicating a statistically significant increasing trend (p = 0.000). This pattern is particularly important given that SON marks the post-rainy season in the region—a transitional period when temperatures typically begin to rise. The data suggest that these increases are no longer moderate but are instead contributing to long-term warming across the seasonal cycle.

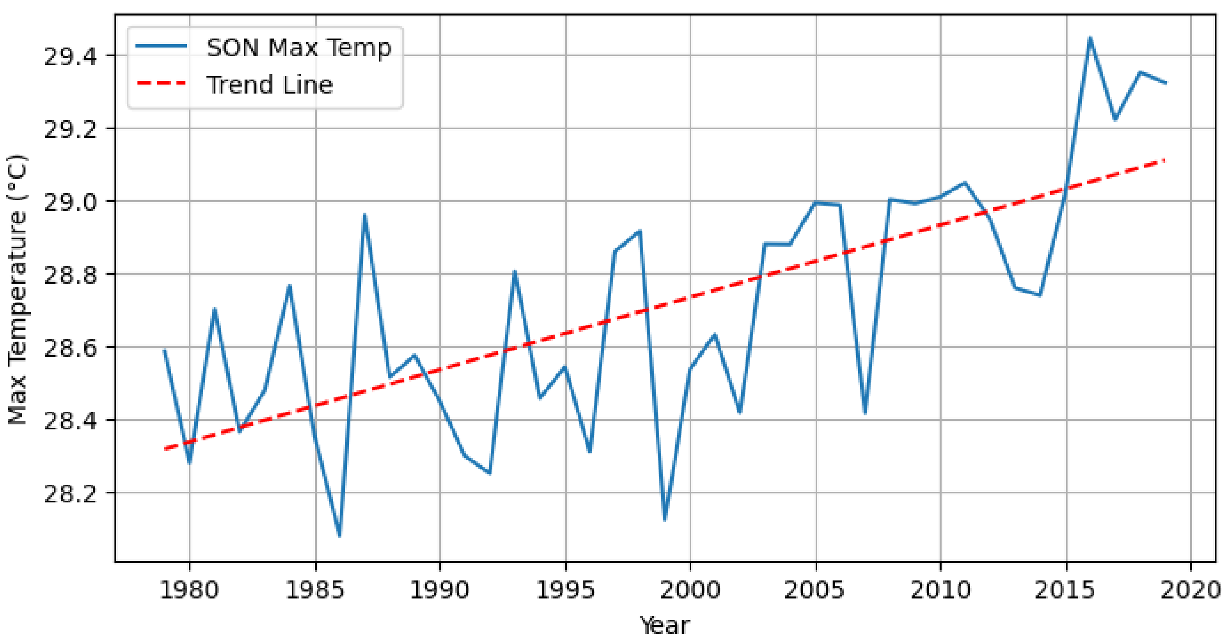

Figure 4.60: Maximum Temperature Data for SON Season

The escalation of temperature during SON can have far-reaching implications, including drying of soil moisture reserves, shortened growing seasons, and increased evapotranspiration, all of which could severely affect agricultural productivity and water availability (Akinsanola and Zhou, 2019). This trend also aligns with broader West African climate assessments, which forecast continued warming across all ecological zones and seasons as a result of anthropogenic greenhouse gas emissions (Ayanlade et al., 2019). For a coastal and low-lying region like Bayelsa, where environmental sensitivity is high, the progressive warming seen in the SON season further underscores the need for region-specific climate adaptation strategies to safeguard livelihoods, food systems, and health infrastructure.

4.9.4 Seasonal Decomposition of Monthly Data

The top panel from Figure 4.61 shows the raw time series data, highlighting consistent seasonal oscillations alongside a subtle upward movement over time. The second panel isolates the trend component, revealing a clear and progressive increase in maximum temperatures, particularly from the early 2000s onward, which is indicative of long-term climatic warming in the region. This aligns with regional and global observations of rising surface temperatures due to anthropogenic climate change (Masson-Delmotte et al., 2021). The third panel displays the seasonal component, which remains consistent across the four decades, showing strong periodic fluctuations driven by expected climatic cycles, such as the annual dry and wet seasons. The bottom panel shows the residuals, which represent the unexplained variance after removing trend and seasonality; these appear relatively stable and randomly distributed, suggesting that the model captures the core structure of the data well.

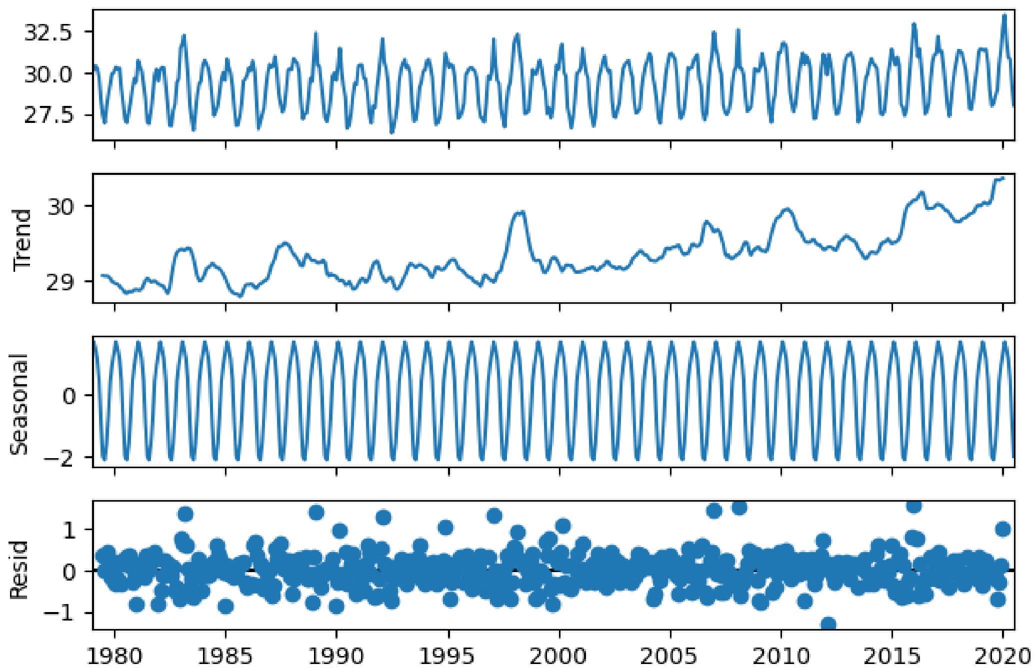

Figure 4.61: Seasonal Decomposition of Monthly Maximum Temperature

This decomposition confirms that while seasonality remains a dominant and predictable feature of the climate in Bayelsa, there is an unmistakable upward trend in maximum temperatures. This trend is of particular concern for the Niger Delta region, where increases in temperature can exacerbate environmental stressors such as flooding, coastal erosion, and reduced agricultural productivity (Ayanlade et al., 2019). The increasing trend also validates previous findings from seasonal analyses (e.g., DJF, MAM, JJA, SON), which collectively point to a warming climate across all periods of the year. The decomposition framework used here provides a clearer understanding of how temperature patterns are evolving in Bayelsa, offering crucial evidence for policymakers and stakeholders in designing adaptive responses to mitigate future climate impacts (Akinsanola and Zhou, 2019).

4.10 Temporal Analysis of Maximum Temperature in Rivers State (1971–2023)

The temporal variability of maximum temperature in Rivers State was assessed using ERA5 reanalysis data processed through Google Earth Engine. Monthly and yearly averages were computed over a 53-year period (1971–2023) to understand the temperature trend and potential climate implications in the region.

4.10.1 Monthly Trends Maximum Temperature

The time series in Figure 4.62 reveals substantial inter-annual variability with notable spikes and dips in maximum temperatures throughout the period. Despite this variability, a general upward trend is visually discernible, especially from the early 2000s onward, culminating in the highest recorded maximum temperature in 2020. This progression aligns with broader climatic observations across southern Nigeria, where rising surface temperatures have been increasingly reported due to anthropogenic climate change and land-use alterations (Akinsanola and Zhou, 2019). The presence of sharp temperature peaks in the 1980s, 2000s, and especially in the final decade, suggests not only a warming climate but also the increasing frequency and intensity of extreme temperature events. These changes may be exacerbated by urbanization in Rivers State—particularly in Port Harcourt, a major urban and industrial hub which contributes to localized warming through the urban heat island effect (Odunsi and Rienow, 2024).

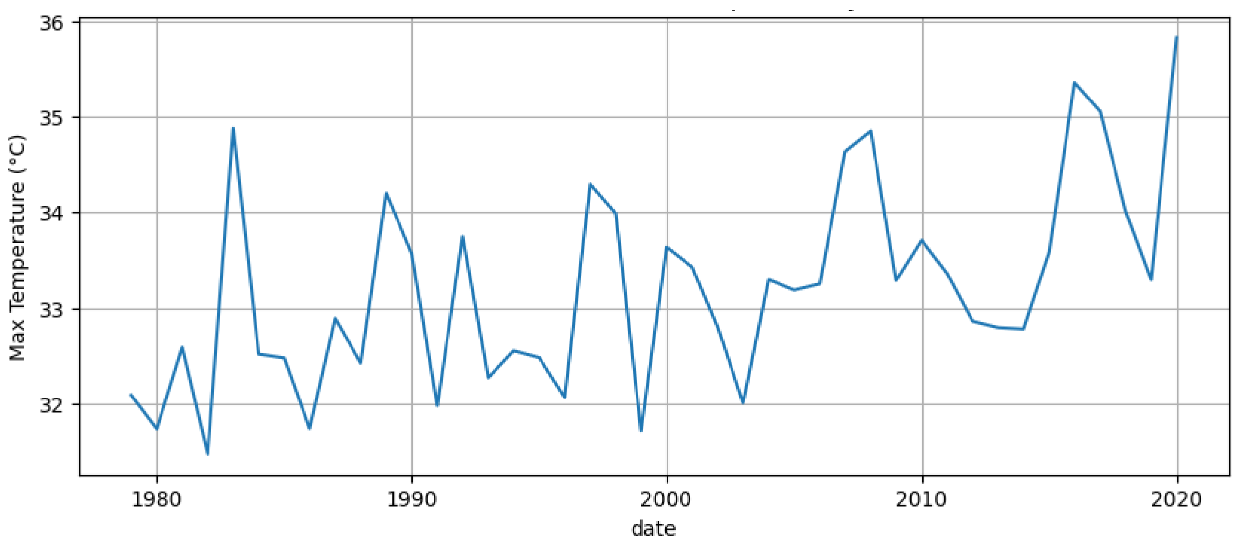

Figure 4.62: Monthly Trends in Maximum Temperature in Rivers State

This warming pattern is consistent with projections for the Niger Delta region, which anticipate rising temperatures alongside changing rainfall patterns, both of which have implications for agriculture, water resources, public health, and infrastructure (Ayanlade et al., 2019). While this chart does not include a fitted trend line or statistical test like linear regression or the Mann-Kendall test, the consistent elevation of peak temperatures in recent years supports findings from other southern Nigerian states, such as Bayelsa, that point to significant climate shifts over recent decades. These observations highlight the urgent need for integrated climate monitoring and proactive adaptation planning in Rivers State, particularly given its environmental vulnerability and socio-economic dependence on climate-sensitive sectors.

4.10.2 Annual Trend Maximum Temperature

Figure 4.63 depicts the annual maximum temperature trend for Rivers State from 1979 to 2020, with the blue line representing observed maximum temperatures and the red dashed line illustrating the linear regression trend. The regression analysis shows a statistically significant upward trend with a slope of 0.046°C per year and a p-value of 0.000, confirming a robust warming signal over the 42-year period. This increasing trend is further supported by the Mann-Kendall test, which identifies the trend as significantly positive ($p = 0.001$). The consistent rise in maximum temperatures indicates that Rivers State is experiencing a substantial warming trend, at a rate notably higher than the global average, reflecting the localized intensification of climate change impacts in the Niger Delta region.

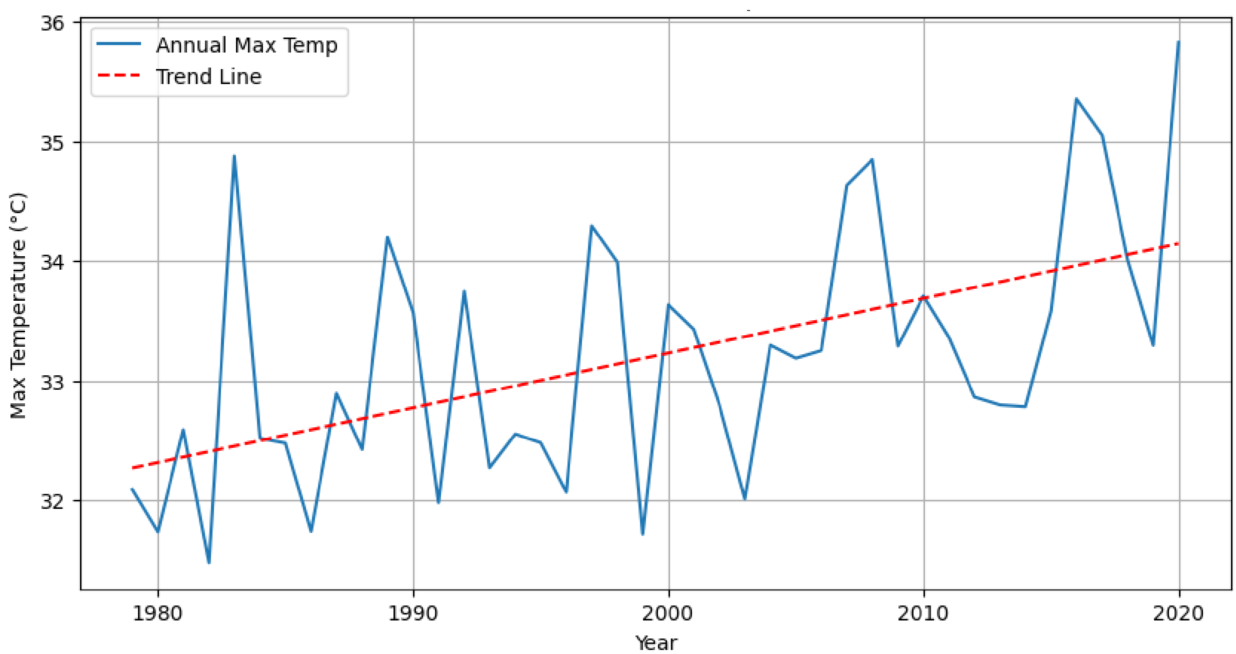

Figure 4.63: Annual Trends in Maximum Temperature in Rivers State

This trend corresponds with findings from other studies across southern Nigeria, where rapid urbanization, industrial activities, and land-use changes compound the effects of greenhouse gas-driven warming, leading to increased temperature extremes (Odunsi and Rienow, 2024). The sharp increases in peak temperatures toward the latter part of the time series emphasize the growing challenge of managing heat stress and its associated impacts on public health, agriculture, and energy demand in the state. Such evidence underscores the critical need for targeted climate adaptation policies and resilient infrastructure development to mitigate the socio-economic consequences of escalating temperatures in Rivers State (Akinsanola and Zhou, 2019).

4.10.3 Seasonal Trends in Maximum Temperature

Figure 4.64 presents the seasonal maximum temperature trends in Rivers State for the period 1979–2020, divided into four climatological seasons: December–January–February (DJF), March–April–May (MAM), June–July–August (JJA), and September–October–November (SON). The DJF season consistently exhibits the highest maximum temperatures throughout the period, with an evident increasing trajectory, particularly marked after the early 2000s. MAM also shows a steady rise, though at a lower absolute temperature level compared to DJF. The SON and JJA seasons display comparatively lower maximum temperatures but still demonstrate gradual warming trends over time. This pattern reflects the amplified warming of the dry season months, which often correspond to higher heat stress periods for the region. The rising temperatures across all seasons suggest pervasive climatic warming in Rivers State, consistent with regional observations of increased heat extremes and shifting climate norms (Akinsanola and Zhou, 2019).

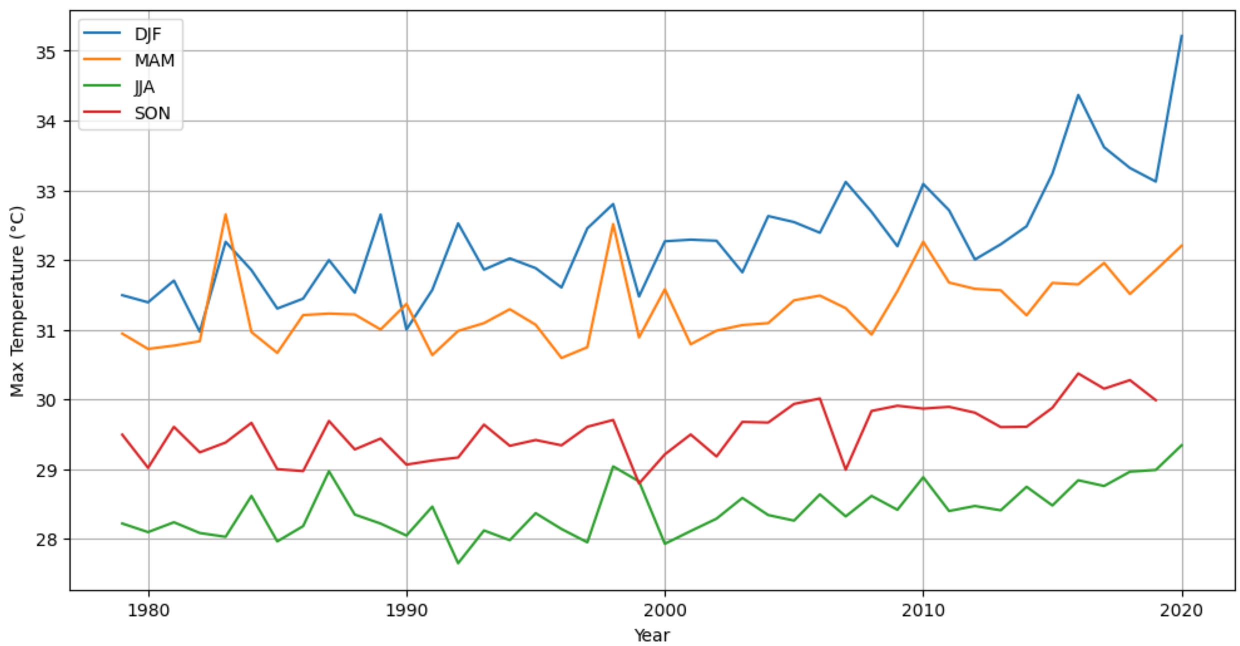

Figure 4.64: Seasonal Trends in Maximum Temperature in Rivers State

These seasonal increases have substantial implications for water resources, agriculture, and human health, especially during the hotter DJF period when temperature extremes can intensify heat-related risks. The pattern aligns with findings in similar tropical coastal regions, where climate change drives uneven warming across seasons, necessitating season-specific adaptation strategies to address the distinct challenges posed by each period (Ayanlade et al., 2019). Overall, the data confirm the pressing need for enhanced climate resilience and adaptive capacity building in Rivers State to mitigate the impacts of increasing seasonal temperatures.

I. Maximum Temperature Data for December–January–February (DJF) Season

Figure 4.65 illustrates the trend in maximum temperatures for the December–January–February (DJF) season in Rivers State from 1979 to 2020. The blue line depicts the annual maximum temperatures during DJF, while the red dashed line represents the fitted linear regression trend.

The regression analysis reveals a significant increase in maximum temperatures, with a slope of 0.052°C per year and a p-value of 0.000, indicating a strong upward trend over the four-decade period. This increase is further corroborated by the Mann-Kendall test, which also shows a statistically significant positive trend ($p = 0.000$). The pronounced warming during DJF is especially critical, as this season represents the peak dry period in Rivers State, often associated with increased heat stress and heightened vulnerability to climate impacts.

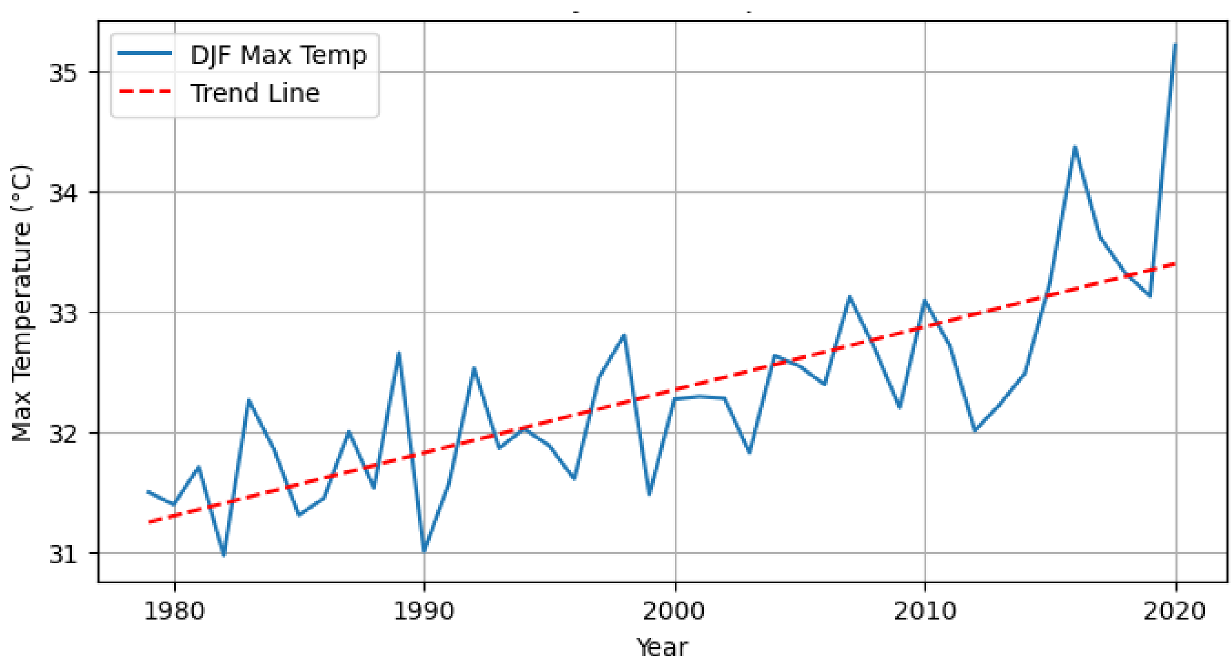

Figure 4.65: Maximum Temperature Data for DJF Season

The rising trend aligns with broader regional climate patterns observed across southern Nigeria, where temperature extremes during the dry season are intensifying due to ongoing climate change and local anthropogenic influences such as urbanization and industrial emissions (Akinsanola and Zhou, 2019). This warming trend in the DJF season underscores the urgent need for adaptive strategies to manage health risks, water resource challenges, and agricultural productivity in Rivers State, particularly during these hotter months (Odunsi and Rienow, 2024). Consequently, the data emphasize the importance of climate-resilient planning tailored to seasonal dynamics to safeguard vulnerable communities in the Niger Delta region.

II. Maximum Temperature Data for March-April-May (MAM) Season

Figure 4.66 displays the maximum temperature trend for the March–April–May (MAM) season in Rivers State over the period from 1979 to 2020. The blue line illustrates the annual maximum temperatures recorded during MAM, while the red dashed line represents the linear regression trend. The analysis reveals a statistically significant increase in maximum temperatures, with a slope of 0.020°C per year and a p-value of 0.001, indicating a steady warming trend. This finding is reinforced by the Mann-Kendall test, which confirms an increasing trend with a highly significant p-value of 0.000. Although the rate of warming in the MAM season is less pronounced compared to the DJF season, the consistent rise in maximum temperatures highlights the broader pattern of climatic warming affecting Rivers State.

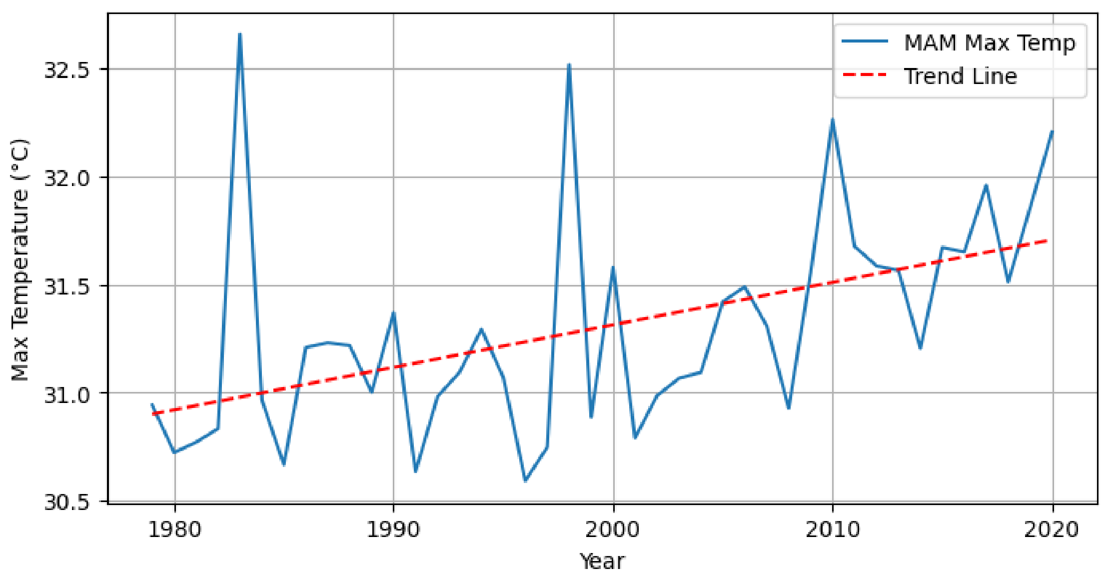

Figure 4.66: Maximum Temperature Data for MAM Season

This gradual increase during the early rainy season can exacerbate heat-related stress on ecosystems and human activities, including agriculture, which is particularly sensitive during this transition period (Akinsanola and Zhou, 2019). The observed seasonal warming aligns with studies reporting shifts in seasonal temperature extremes in tropical coastal regions, emphasizing the need for seasonally adaptive climate policies to mitigate adverse impacts on vulnerable populations and natural resources (Odunsi and Rienow, 2024). Hence, these temperature trends underscore the urgency for integrated climate adaptation frameworks in Rivers State that address not only annual changes but also critical seasonal variations.

III. Maximum Temperature Data for June-July-August (JJA) Season

Figure 4.67 illustrates the maximum temperature trend for the June–July–August (JJA) season in Rivers State from 1979 to 2020. The blue line represents the annual maximum temperatures recorded during this period, while the red dashed line shows the linear trend fitted to the data. The linear regression analysis indicates a statistically significant increase in maximum temperatures with a slope of 0.017°C per year and a p-value of 0.000, signifying a robust warming trend during the JJA season. Complementing this, the Mann-Kendall test also confirms the presence of a significant increasing trend ($p = 0.000$), reinforcing the evidence of rising temperatures in the mid-year months.

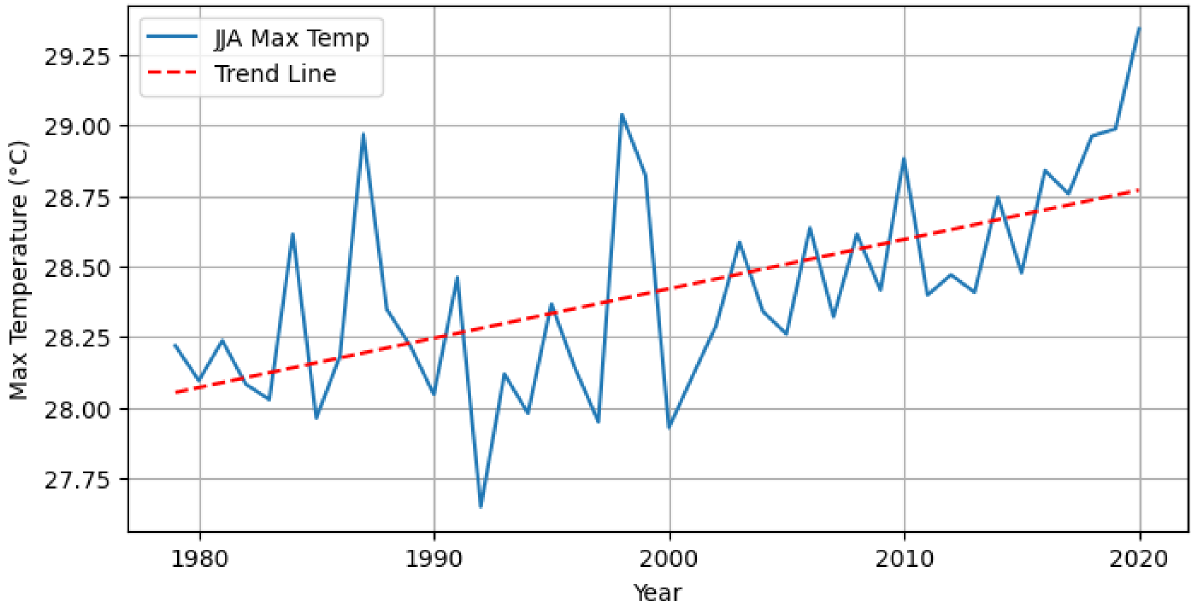

Figure 4.67: Maximum Temperature Data for JJA Season

Although the warming rate during JJA is somewhat lower compared to other seasons like DJF and MAM, this steady increase still reflects the overarching influence of climate change on seasonal temperature patterns in Rivers State. This seasonal warming, especially during the peak of the rainy season, has implications for agriculture, water resources, and public health, highlighting the need for climate adaptation measures that consider these intra-annual variations (Akinsanola and Zhou, 2019). The trend aligns with broader regional climate observations in tropical coastal zones, where temperature increases across all seasons are contributing to shifts in local climate regimes and heightened vulnerability of ecosystems and communities (Odunsi and Rienow, 2024). Thus, understanding and addressing seasonal temperature changes remains critical for sustainable development planning in the Niger Delta region.

IV. Maximum Temperature Data for September-October-November (SON) Season

Figure 4.68 presents the trend in maximum temperatures for the September–October–November (SON) season in Rivers State from 1979 to 2020. The blue line shows the annual maximum temperatures for the season, while the red dashed line represents the linear regression trend line fitted to the data. The linear regression results indicate a statistically significant upward trend, with a slope of 0.021°C per year and a p-value of 0.000. This is supported by the Mann-Kendall trend test, which also reveals a significant increasing trend ($p = 0.000$), confirming a consistent rise in SON seasonal temperatures over the observed period.

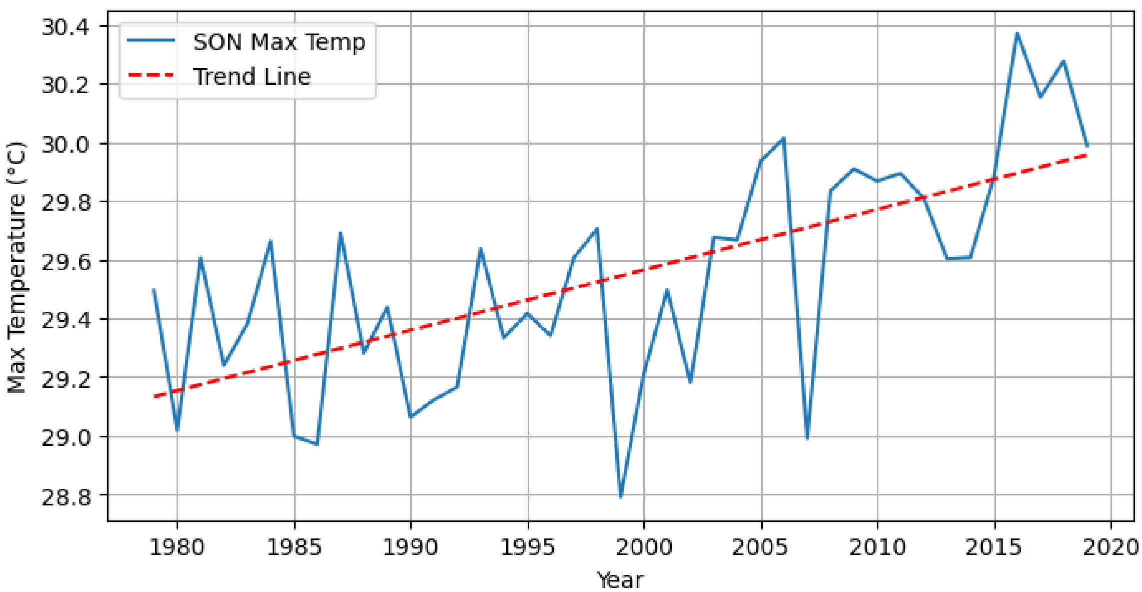

Figure 4.68: Maximum Temperature Data for SON Season

The observed warming during SON, which typically marks the post-rainy season and onset of the dry season, signals a shifting climatic baseline in Rivers State that may influence agricultural cycles, disease vectors, and energy demands. Similar warming patterns have been identified across the Niger Delta and broader West African coastal regions, suggesting a region-wide intensification of seasonal temperatures (Akinsanola and Zhou, 2019). These findings are consistent with reports of increased heat stress during transitional seasons, which are crucial for food production and natural resource management (Odunsi and Rienow, 2024). As a result, this steady temperature rise during SON underscores the growing need for proactive climate adaptation measures that address seasonal vulnerabilities in both rural and urban settings across the state.

4.10.4 Seasonal Decomposition of Monthly Data

Figure 4.69 presents a seasonal decomposition of monthly maximum temperature data for Rivers State from 1979 to 2020, using time series decomposition to separate the data into trend, seasonal, and residual components. The top panel displays the original monthly maximum temperature values, showing regular oscillations typical of seasonal temperature cycles. The second panel reveals the underlying trend, which indicates a gradual and consistent increase in maximum temperatures over time. This upward trend suggests a long-term warming pattern that aligns with broader evidence of climate change impacts across coastal Nigeria (Akinsanola and Zhou, 2019).

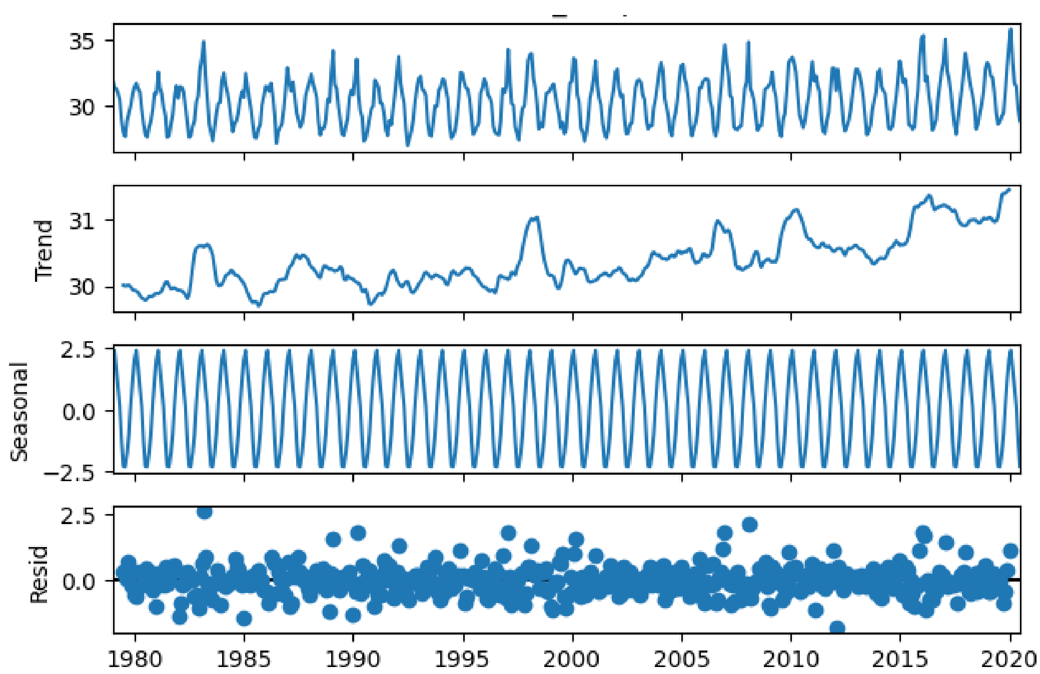

Figure 4.69: Seasonal Decomposition of Monthly Maximum Temperature

The third panel illustrates the seasonal component, clearly depicting a cyclical pattern that recurs annually, with peaks and troughs that correspond to seasonal climate variability. This highlights the influence of the region's tropical monsoon climate, where temperature fluctuations are largely driven by seasonal shifts in solar radiation and atmospheric circulation (Odunsi and Rienow, 2024). The final panel shows the residuals, representing irregular variations not explained by the trend or seasonal patterns. These residuals appear randomly scattered with no systematic bias, indicating that the decomposition model effectively captures the dominant patterns in the temperature data. Overall, the decomposition confirms that both seasonal variation and long-term warming are significant features of temperature dynamics in Rivers State, reinforcing the need for climate-informed planning and adaptation strategies in response to rising heat exposure and changing seasonal behavior.

4.11 Temporal Analysis of Minimum Temperature in Edo State (1971–2023)

The temporal variability of minimum temperature in Edo State was assessed using ERA5 reanalysis data processed through Google Earth Engine. Monthly and yearly averages were computed over a 53-year period (1971–2023) to understand the temperature trend and potential climate implications in the region.

4.11.1 Monthly Trends Minimum Temperature

Figure 4.70 shows the annual minimum temperature trend for Edo State using monthly data spanning from 1979 to 2023. A notable feature of the graph is the relatively stable period from the late 1970s through the mid-1990s, followed by a distinct rise in minimum temperature values beginning around the late 1990s. This post-1999 increase in minimum temperatures may indicate a shift in the baseline nighttime temperatures for the region, possibly linked to broader patterns of climate change and urban expansion, both of which can influence nighttime heat retention.

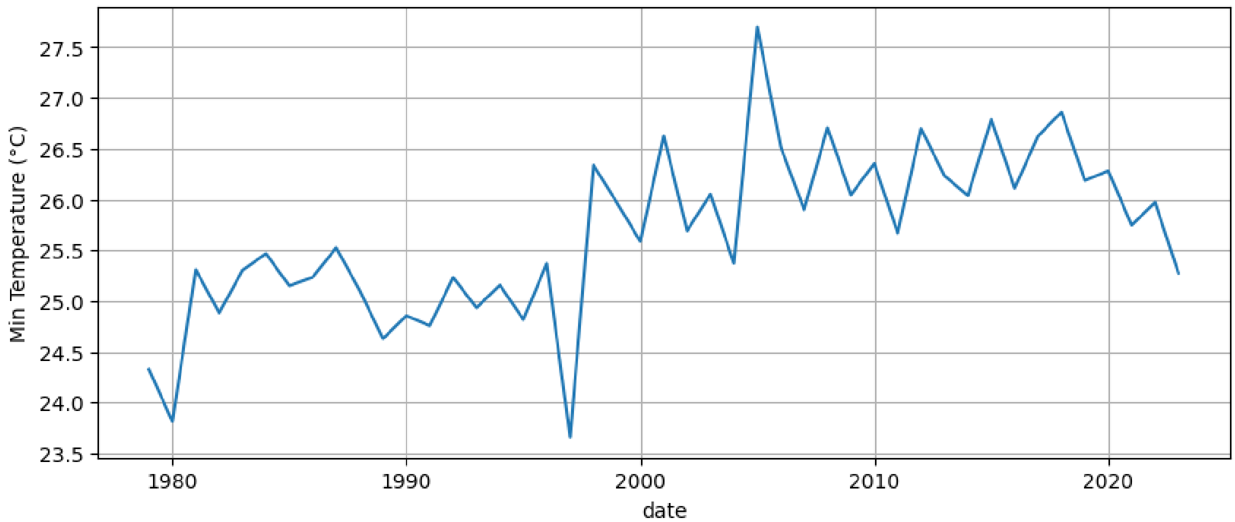

Figure 4.70: Monthly Trends Minimum Temperature in Edo State

The peak observed around 2005 represents the highest annual minimum temperature recorded in the dataset, suggesting an intensification of warm nights during that period. While the data shows some inter-annual variability, the post-2000 era is marked by consistently elevated minimum temperature values compared to the earlier years. However, the slight decline observed in recent years, particularly after 2020, may reflect natural variability or a short-term cooling phase, though the long-term signal remains one of warming. These trends are consistent with findings across southern Nigeria, where increased minimum temperatures are often attributed to greenhouse gas-driven warming and changes in land use that amplify the urban heat island effect (Onoja et al., 2011). Ultimately, the rising minimum temperatures in Edo State have implications for human health, agriculture, and energy demand, especially as nighttime heat extremes become more frequent.

4.11.2 Annual Trend Minimum Temperature

Figure 4:71 illustrates the annual minimum temperature trend for Edo State from 1979 to 2023, highlighting both the observed temperature values and a linear regression trend line. The statistical analysis indicates a significant upward trend, with a slope of 0.041°C per year and a p-value of 0.000 for both the linear regression and Mann-Kendall tests, confirming a consistent and statistically significant increase in minimum temperatures over the period. This suggests that nighttime temperatures have been steadily rising, which is characteristic of global and regional climate change patterns (Akinsanola and Zhou, 2019).

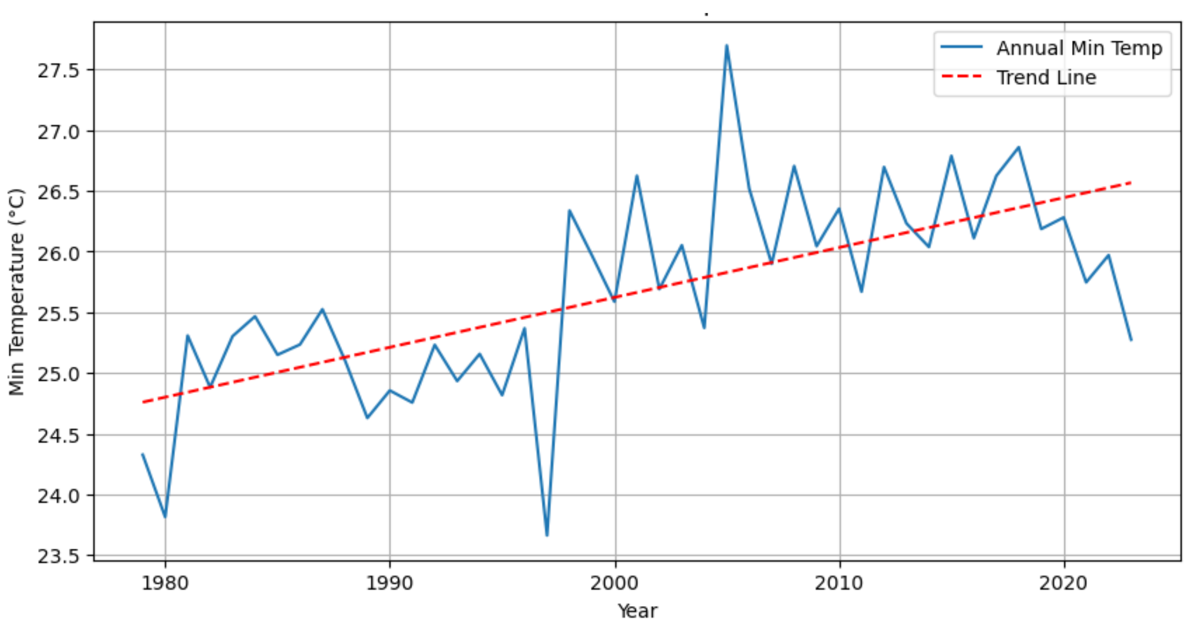

Figure 4.71: Annual Trend Minimum Temperature

The long-term warming signal is particularly evident after the mid-1990s, as reflected by frequent spikes in the minimum temperature values. These rising nighttime temperatures may result from a combination of increased greenhouse gas concentrations, reduced radiative cooling due to urban development, and land-use changes that exacerbate the urban heat island effect. According to recent studies, rising minimum temperatures pose critical implications for public health, particularly by increasing heat stress during nighttime, and can also influence agricultural productivity by affecting crop respiration rates and yields (Nwaiwu *et. al*., 2022). The consistently increasing trend captured in this graph aligns with broader observations across southern Nigeria and West Africa, where climate projections indicate continued warming if mitigation measures are not implemented. Thus, this trend emphasizes the need for climate-resilient planning and adaptive policies in regions like Edo State.

4.11.3 Seasonal Trends in Minimum Temperature

Seasonal trends in minimum temperature for Edo State from 1979 to 2020 across four climatic seasons: DJF (December–January–February), MAM (March–April–May), JJA (June–July–August), and SON (September–October–November) is seen in Figure 4.72. All four seasonal temperature profiles show a general upward trajectory, suggesting a consistent rise in minimum temperatures over the decades. Notably, the MAM season (orange line) consistently recorded the highest seasonal minimum temperatures, especially post-2000, peaking above 26°C in several instances. The DJF season (blue line), although initially the coolest among the seasons, shows the most pronounced warming, with post-2000 data reflecting a sharp increase that has narrowed the gap between it and other seasons.

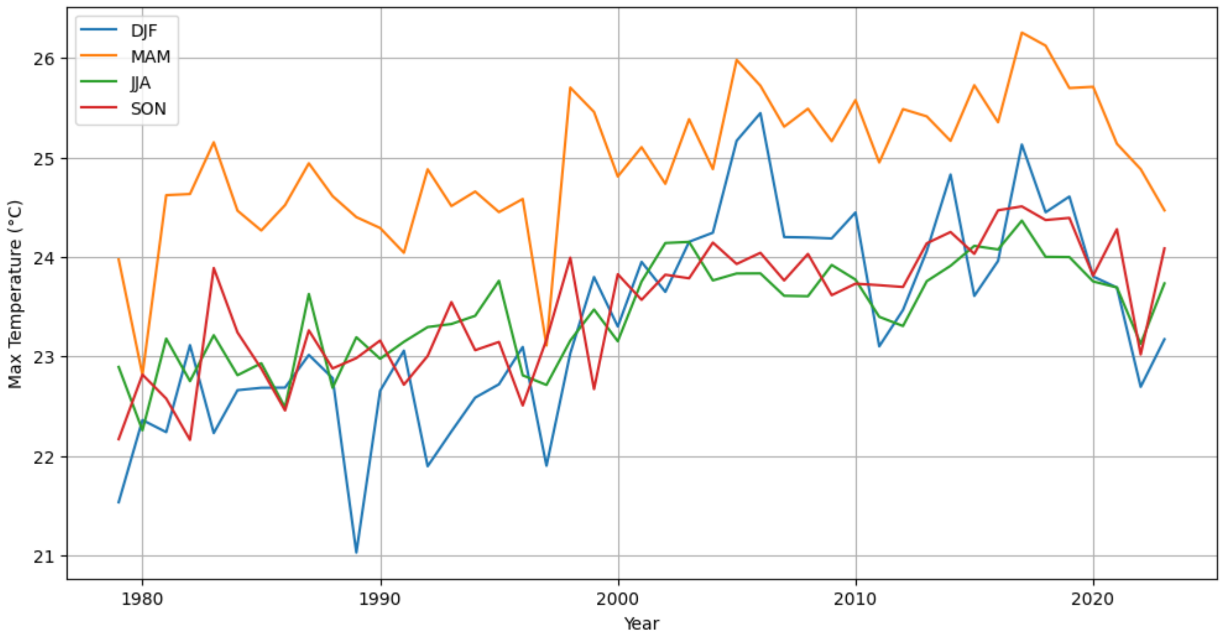

Figure 4.72: Seasonal Trends in Minimum Temperature

This aligns with studies indicating that minimum temperatures in Nigeria, particularly during dry months, are rising at a faster rate due to increased greenhouse gas concentrations and urbanization (Oluseyi *et. al*., 2019). Such warming trends during night-time or early morning hours (when minimum temperatures are recorded) could have far-reaching implications for public health, water demand, and agricultural practices, especially for crops sensitive to nocturnal heat stress (Jay et al., 2021). The consistent warming observed in JJA and SON seasons, although more moderate, still reinforces the broader signal of climate change in the region. This pattern of seasonal warming is in agreement with broader West African climate studies that have documented significant increases in minimum temperatures over the last few decades, posing a growing challenge for sustainable development and climate resilience planning in sub-national regions like Edo State.

I. Minimum Temperature Data for December–January–February (DJF) Season

Figure 4.73 presents the December–January–February (DJF) seasonal minimum temperature trend for Edo State from 1979 to 2023, highlighting a significant upward trajectory over the observed period. The blue line indicates the year-to-year variation in DJF minimum temperatures, while the red dashed line represents the linear regression trend line. The slope of 0.051°C per year and a statistically significant p-value ($p = 0.000$) confirm a strong and consistent warming trend. This finding is further corroborated by the Mann-Kendall trend test, which also indicates a statistically significant increasing trend ($p = 0.000$). The graph shows marked increases particularly after the year 2000, with several peak values exceeding 25°C, suggesting warmer nights during the dry season.

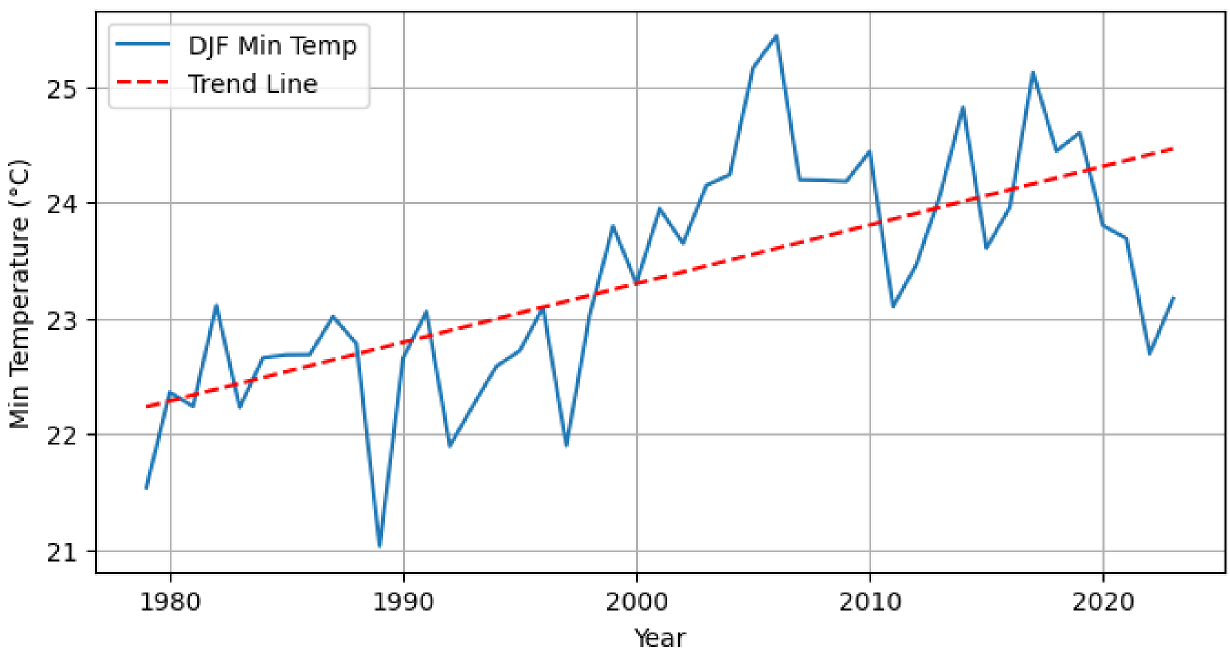

Figure 4.73: Minimum Temperature Data for December–January–February (DJF) Season

This pattern is consistent with broader regional trends across West Africa, where minimum temperatures especially in dry months are rising more rapidly than maximum temperatures (Akinsanola and Zhou, 2019). Such seasonal warming during DJF could have wide-ranging impacts, including increased energy demand for cooling, shifts in disease vector patterns, and heat stress on both human populations and ecosystems. Moreover, the intensified warming trend in minimum temperatures during what is traditionally the coolest period of the year is a strong indicator of anthropogenic climate change, particularly as urban heat island effects and greenhouse gas emissions continue to drive temperature increases in southern Nigeria (Wang et al., 2017).

II. Minimum Temperature Data for March-April-May (MAM) Season

The graph seen in Figure 4.74 displays the March–April–May (MAM) seasonal minimum temperature trend for Edo State from 1979 to 2023. The blue line represents the annual variation in minimum temperatures during the MAM season, while the red dashed line shows the linear trend, indicating a consistent increase over the years. The linear regression analysis reveals a statistically significant warming trend with a slope of 0.034°C per year ($p = 0.000$), while the Mann-Kendall test also confirms a statistically significant increasing trend ($p = 0.000$).

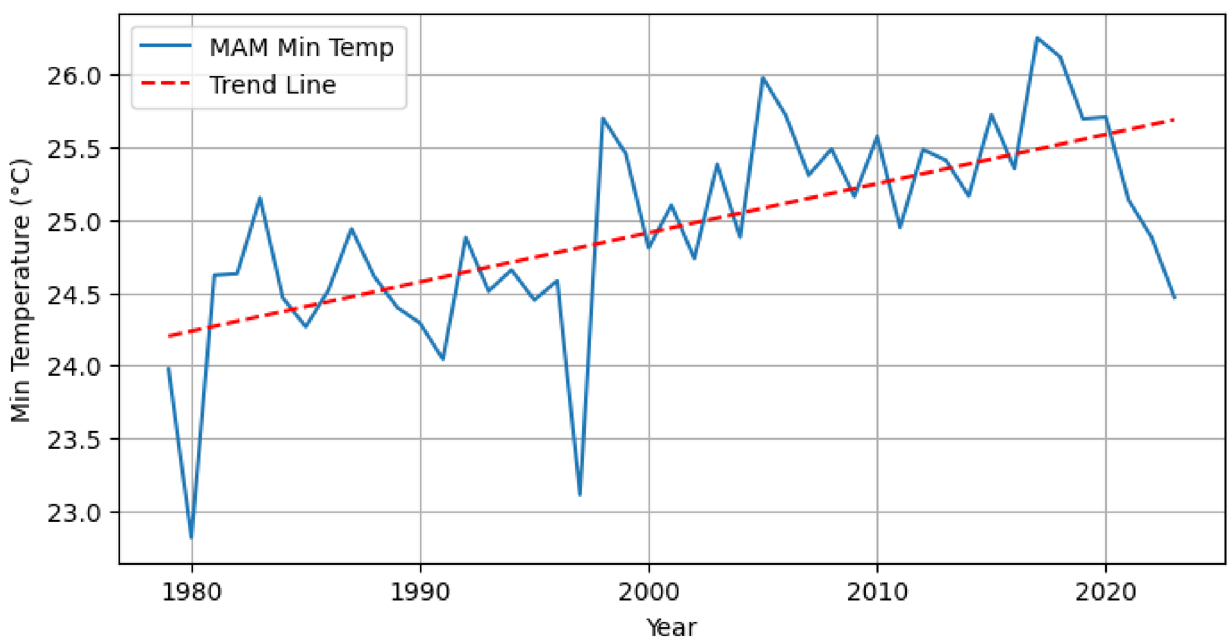

Figure 4.74: Minimum Temperature Data for March-April-May (MAM) Season

This steady rise in minimum temperatures during the MAM period aligns with regional and global climate change projections, particularly in tropical regions like West Africa where nighttime temperatures are rising faster than daytime extremes (Dajuma et al., 2023). Such warming during the MAM season could have significant implications for agricultural productivity in Edo State, as this period marks the onset of the rainy season and is crucial for crop planting and establishment. Increased nighttime temperatures may affect crop physiology, soil moisture retention, and pest dynamics, potentially reducing yields if not properly managed. Moreover, rising MAM minimum temperatures are indicative of broader climate shifts that could exacerbate heat-related health risks and strain water resources (Masson-Delmotte et al., 2021). These findings stress the urgency of integrating climate adaptation strategies into local agricultural and public health planning to mitigate the growing risks associated with seasonal warming in Nigeria.

III. Minimum Temperature Data for June-July-August (JJA) Season

The graph Figure 4.75 illustrates the trend in June–July–August (JJA) seasonal minimum temperatures for Edo State from 1979 to 2023. The blue line shows the yearly variations in minimum temperature, while the red dashed line represents the linear regression trend line. The upward slope of the regression line, at 0.027°C per year ($p = 0.000$), and the statistically significant result from the Mann-Kendall trend test ($p = 0.000$) confirm a consistent and significant increase in minimum temperatures during the core rainy season.

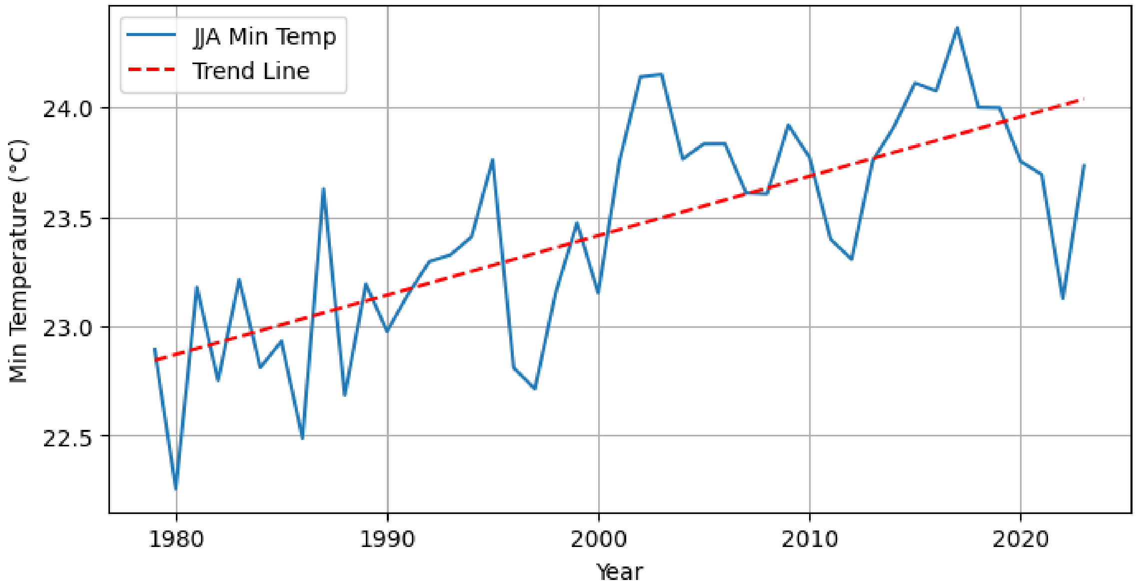

Figure 4.75: Minimum Temperature Data for June-July-August (JJA) Season

This warming trend is consistent with broader climatic observations across West Africa, where rising minimum temperatures especially at night have been linked to global climate change and greenhouse gas emissions (Odunsi and Rienow, 2024). The JJA season is critical for agricultural productivity in Edo State, as it coincides with peak crop growth. Increases in minimum temperatures can affect the nighttime recovery of crops, accelerate respiration losses, and increase water demand, potentially reducing yields if not accompanied by sufficient rainfall or irrigation infrastructure (Dajuma et al., 2023). Furthermore, elevated nighttime temperatures during JJA can intensify thermal discomfort and contribute to heat-related health issues, especially in vulnerable populations. This evidence emphasizes the need for climate-resilient agricultural practices, heat mitigation strategies, and strengthened early warning systems to address the growing impact of seasonal warming in Nigeria.

IV. Minimum Temperature Data for September-October-November (SON) Season

The trend in minimum temperatures during the September–October–November (SON) season in Edo State from 1979 to 2023 is seen in Figure 4.76. The blue line illustrates the inter-annual variability, while the red dashed line indicates the linear regression trend, which shows a statistically significant upward slope of 0.038°C per year ($p = 0.000$). This is further supported by the Mann-Kendall test, which confirms a significantly increasing trend ($p = 0.000$).

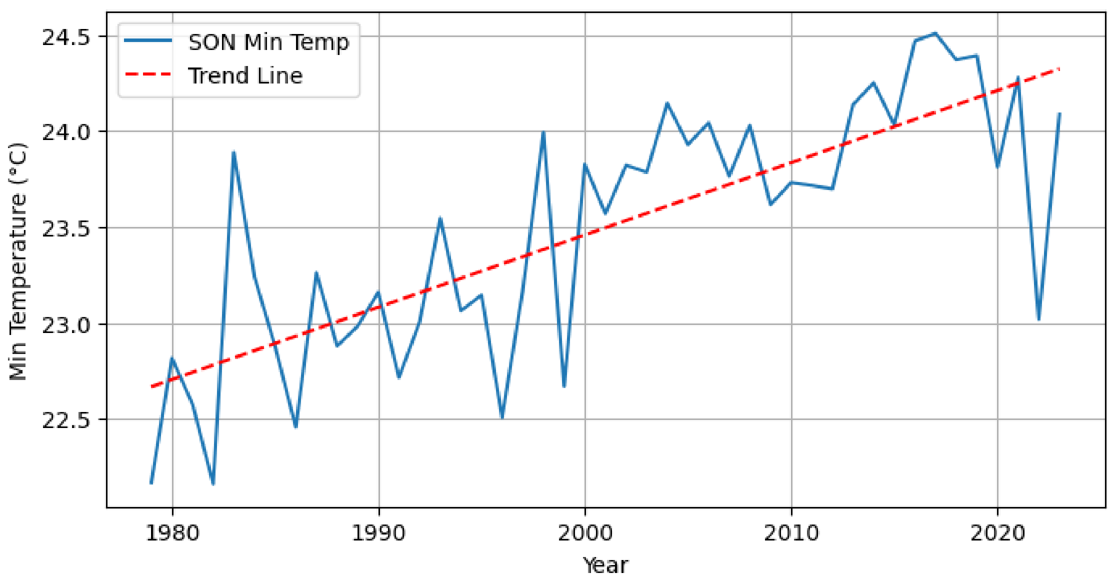

Figure 4.76: Minimum Temperature Data for September-October-November (SON) Season

The SON period, representing the post-rainy season transition into the dry season, has experienced a consistent rise in minimum temperatures, aligning with regional warming trends observed in Nigeria and other West African countries (Dajuma et al., 2023). Rising minimum temperatures during this period may lead to increased heat retention at night, reducing diurnal temperature range and potentially affecting human comfort, ecological systems, and crop drying processes that are vital during harvest (Odunsi and Rienow, 2024). The consistent warming trend could also signal changes in atmospheric circulation and humidity patterns, further influencing regional climate behavior. These findings emphasize the urgent need for integrating seasonal climate trend data into state-level adaptation planning, especially in sectors such as health, agriculture, and water management, to mitigate the adverse impacts of a warming climate in southern Nigeria.

4.11.4 Seasonal Decomposition of Monthly Data

The seasonal decomposition of monthly minimum temperature in Edo State from 1979 to 2023, as illustrated in Figure 4.77, provides a detailed breakdown of the components influencing temperature variability over time. The top panel shows the observed series, highlighting cyclical variations and long-term patterns. The second panel captures the trend component, which reveals a gradual and sustained increase in minimum temperature levels across the study period, particularly from the mid-1990s onward. This warming aligns with broader climatic trends across West Africa, where minimum temperatures are rising faster than maximum temperatures, contributing to reduced diurnal temperature ranges (Akinsanola and Zhou, 2019).

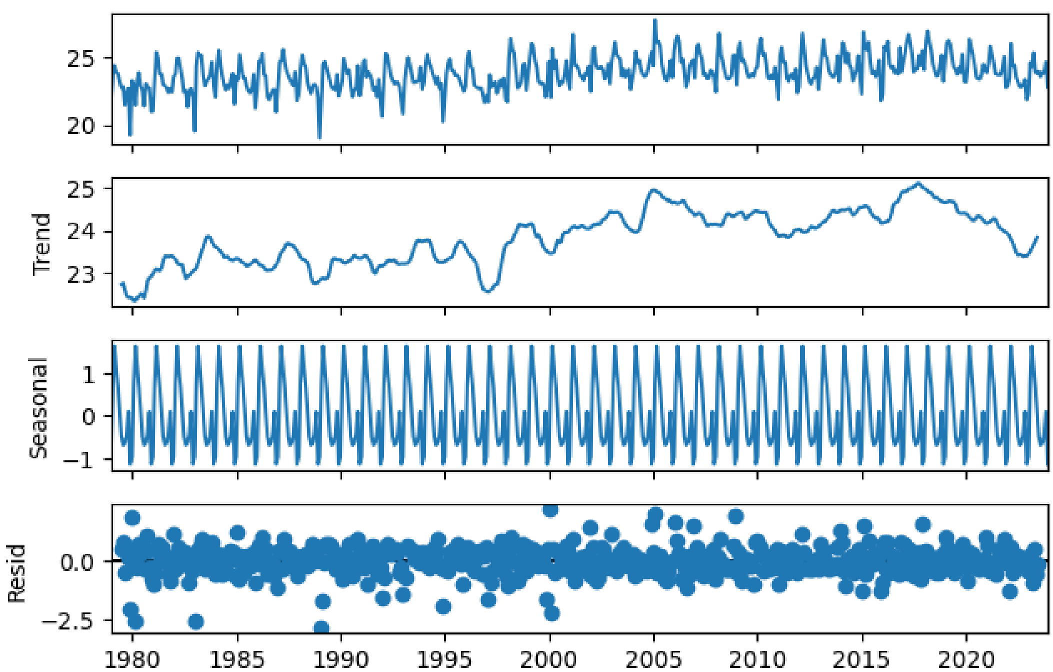

Figure 4.77: Seasonal Decomposition of Monthly Data

The third panel, showing the seasonal component, indicates strong and consistent intra-annual cycles, reflecting the predictable influence of seasonal atmospheric dynamics on temperature, such as the West African monsoon and Harmattan winds. The bottom panel displays the residual component, representing irregular fluctuations not explained by the trend or seasonal cycles; this randomness suggests the influence of short-term anomalies or localized weather events.

The upward trajectory in the trend component suggests that Edo State is experiencing a gradual increase in baseline minimum temperatures. This is significant, as higher nighttime temperatures can exacerbate thermal discomfort, increase energy demand for cooling, and negatively impact human health, particularly among vulnerable populations (Wei et al., 2021). Furthermore, consistently high minimum temperatures may hinder crop recovery from daytime heat stress, affecting agricultural productivity. These results underscore the need for tailored adaptation strategies, including urban planning that mitigates heat retention and climate-smart agriculture practices that account for warmer nights.

4.12 Temporal Analysis of Minimum Temperature in Delta State (1971–2023)

The temporal variability of minimum temperature in Delta State was assessed using ERA5 reanalysis data processed through Google Earth Engine. Monthly and yearly averages were computed over a 53-year period (1971–2023) to understand the temperature trend and potential climate implications in the region.

4.12.1 Monthly Trends Minimum Temperature

Figure 4.78 illustrates the annual minimum temperature trend in Delta State, Nigeria, based on monthly data spanning from 1979 to 2023. The graph reveals notable inter-annual variability, with minimum temperatures generally oscillating between 24.0°C and 27.5°C. A gradual warming trend becomes evident from the late 1990s onward, peaking around 2005 with a record high minimum temperature. Although fluctuations persist, particularly in the post-2015 period, the overall trajectory indicates a long-term increase in minimum temperatures over the decades. This pattern aligns with regional warming trends observed across southern Nigeria and other parts of West Africa, where nighttime temperatures are rising more significantly than daytime highs, contributing to a narrowing diurnal temperature range (Akinsanola & Zhou, 2019).

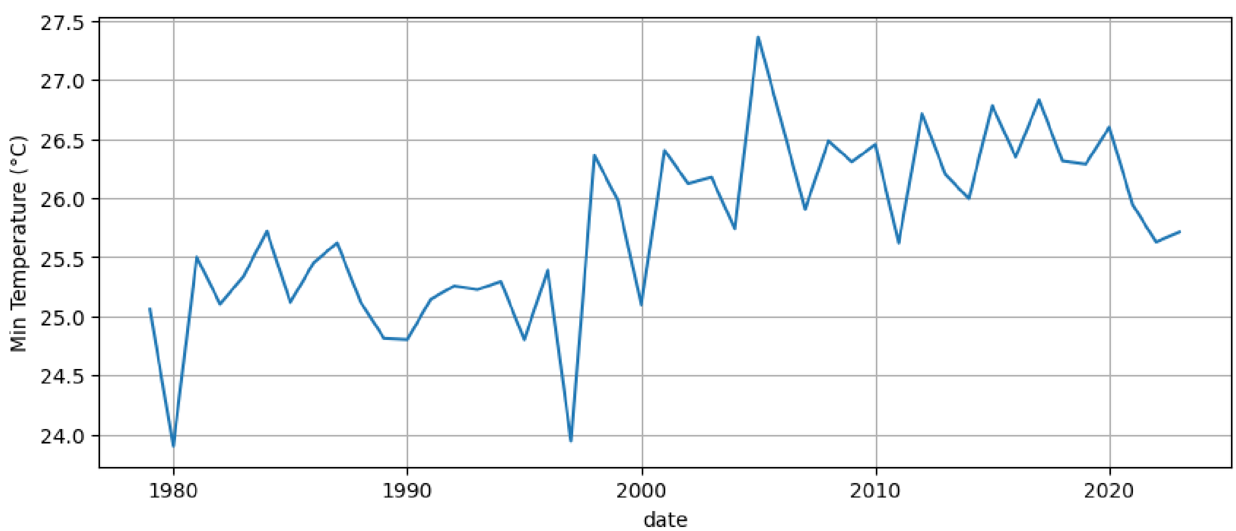

Figure 4 78: Monthly Trends Minimum Temperature in Delta State

The rise in minimum temperatures has substantial implications. Warmer nights can affect human health, particularly by reducing nighttime cooling, which is essential for vulnerable populations such as the elderly or those with chronic illnesses. Moreover, higher minimum temperatures can hinder agricultural resilience by impeding the nighttime recovery of crops from daytime heat stress, which in turn affects food security (WMO, 2021). Additionally, rising minimum temperatures may lead to increased energy consumption for cooling, especially in urban areas like those in Delta State where the urban heat island effect may exacerbate the warming trend.

This observed pattern of increasing minimum temperatures also reflects broader global climate change signals. Similar trends have been attributed to anthropogenic greenhouse gas emissions, which trap more longwave radiation during the night, resulting in warmer minimum temperatures (Masson-Delmotte et al., 2021). The insights from Delta State emphasize the need for climate-sensitive policies in the region, including adaptive infrastructure and climate-resilient agriculture to mitigate the long-term impacts of rising nighttime temperatures.

4.12.2 Annual Trend Minimum Temperature

The annual minimum temperature trend in Delta State from 1979 to 2023, revealing a statistically significant increase over the period as seen in Figure 4.79. The linear regression slope of 0.037°C per year, alongside a p-value of 0.000, indicates a strong upward trend in minimum temperatures. This is further supported by the Mann-Kendall test, which confirms a significant increasing trend with a p-value of 0.000. The observed pattern suggests that Delta State is experiencing a consistent rise in nighttime or minimum temperatures, which is consistent with broader climatic changes reported in West Africa and other tropical regions (Roy et al., 2021).

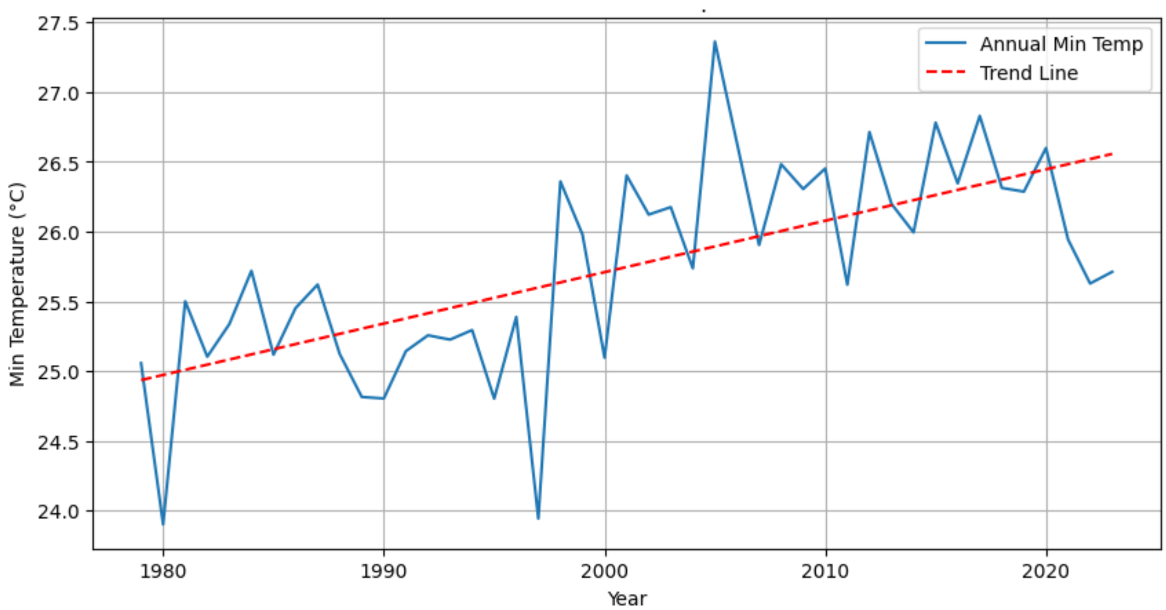

Figure 4.79: Annual Trend Minimum Temperature

Rising minimum temperatures can have critical environmental and socio-economic consequences, including exacerbating heat stress during the night, impacting human health, and affecting crop growth cycles by disrupting the recovery phase after daytime heat (Akinwumi et al., 2023). The upward trend also implies a reduction in the diurnal temperature range; a phenomenon linked to increased greenhouse gas concentrations and urbanization effects (Odunsi and Rienow, 2024). This warming trend in Delta State underscores the urgency for adaptive measures in urban planning, agriculture, and public health to mitigate the adverse impacts of climate variability and change.

4.12.3 Seasonal Trends in Minimum Temperature

The graph, Figure 4.80 presents the seasonal minimum temperature trends in Delta State from 1979 to 2020 across the four meteorological seasons: DJF (December-January-February), MAM (March-April-May), JJA (June-July-August), and SON (September-October-November). It is evident that MAM consistently exhibits the highest minimum temperatures throughout the period, followed by SON, JJA, and DJF, which shows the lowest values and greatest variability, especially before 2000. The increasing temperature trends across all seasons reflect the broader warming pattern observed in the region, with notable rises after the year 2000, suggesting intensified climate change impacts in recent decades.

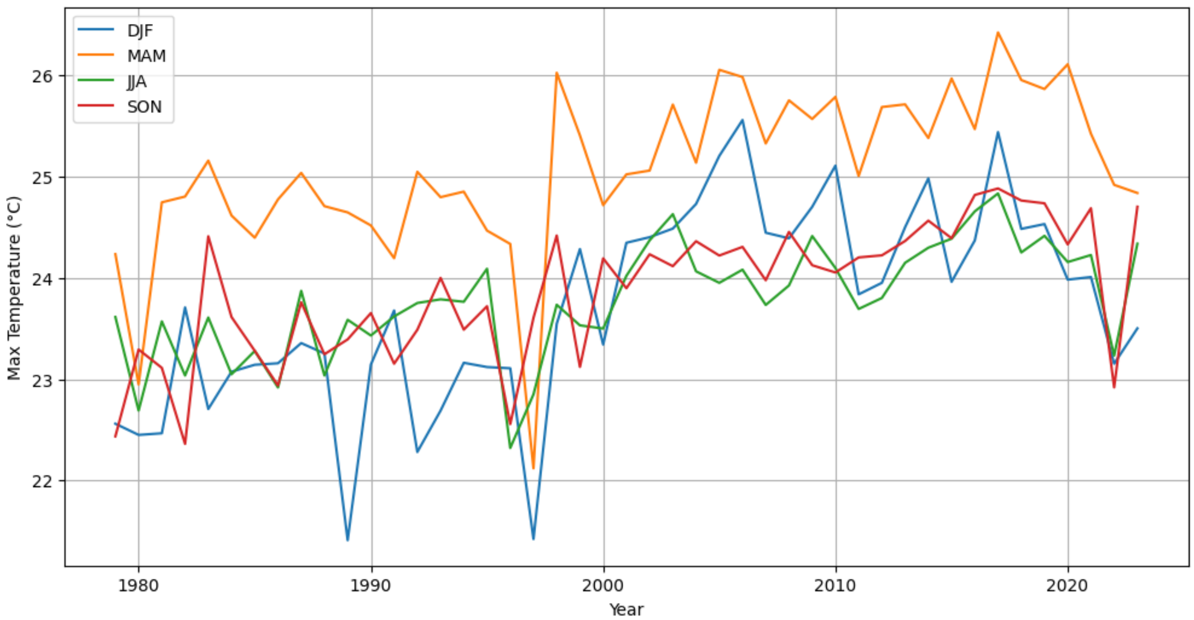

Figure 4.80: Seasonal Trends in Minimum Temperature

Such seasonal variability and upward trends in minimum temperatures are consistent with findings from tropical regions, where warming is often more pronounced in night-time temperatures (minimums), influencing seasonal climate patterns (Ojo et al., 2021). The clear seasonality shown in the data also aligns with the expected effects of changing atmospheric circulation and sea surface temperatures, which alter the onset and intensity of rainy and dry seasons in West Africa (Shukla et al., 2021). These shifts could have profound effects on agriculture, water resources, and human health, particularly since minimum temperatures influence soil moisture retention, crop growth cycles, and the prevalence of vector-borne diseases.

Therefore, the observed seasonal temperature dynamics underscore the need for season-specific climate adaptation strategies to better manage the impacts on agriculture and livelihoods in Delta State, as supported by recent climate vulnerability studies in West Africa (Kyaw and Kim, 2025).

I. Minimum Temperature Data for December–January–February (DJF) Season

Figure 4.81 illustrates the trend in minimum temperatures during the DJF (December-January-February) season in Delta State from 1979 to 2023. The observed data line shows notable inter-annual variability, with periods of both rapid increase and occasional dips. However, the overall trend, highlighted by the red dashed linear regression line, indicates a significant upward trajectory in DJF minimum temperatures over the period. The slope of 0.046°C per year, combined with the Mann-Kendall test result confirming an increasing trend ($p = 0.000$), statistically substantiates the consistent warming in this critical season. This increase in minimum temperatures during the DJF period, which corresponds to the dry season in this region, could have profound impacts on local ecosystems, agriculture, and human health, particularly by exacerbating heat stress during nighttime.

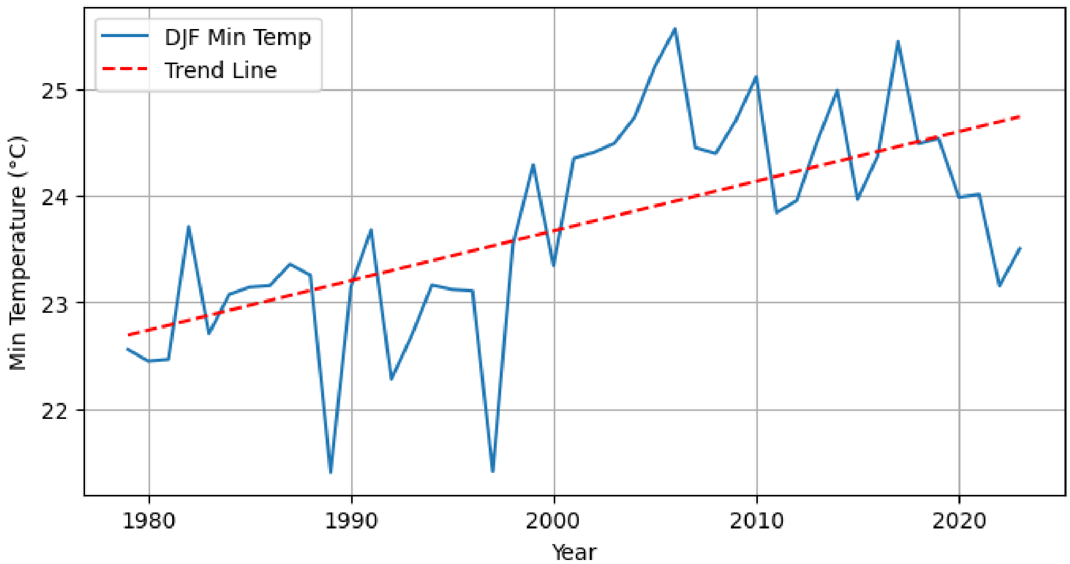

Figure 4.81: Minimum Temperature Data for December–January–February (DJF) Season

This pattern aligns with recent studies in West Africa that report rising nighttime temperatures as a key feature of regional climate change, attributed to factors like altered atmospheric circulation and increased greenhouse gas concentrations (Ojo et al., 2021). The significance of warming during DJF is critical because it influences evapotranspiration rates and soil moisture dynamics, which are vital for agricultural productivity and water resource management (Kyaw and Kim, 2025). The strong upward trend in DJF minimum temperatures thus highlights an urgent need for adaptive strategies in the Delta State to mitigate climate change impacts during this season.

II. Minimum Temperature Data for March-April-May (MAM) Season

Figure 4.82 depicting the MAM (March-April-May) minimum temperature trend in Delta State from 1979 to 2023 reveals a clear increasing pattern in minimum temperatures over this period. Although the observed data exhibit some year-to-year fluctuations, including notable dips around the late 1990s and early 2020s, the overall trajectory is upward, as evidenced by the linear regression trend line. The calculated slope of 0.036°C per year indicates a statistically significant warming trend during the MAM season, supported by the Mann-Kendall test which confirms an increasing trend with a p-value of 0.000. This steady rise in minimum temperatures during the early months of the year suggests warming nights and potentially warmer early mornings, which could influence local climate dynamics, agricultural growing conditions, and water resource availability in Delta State.

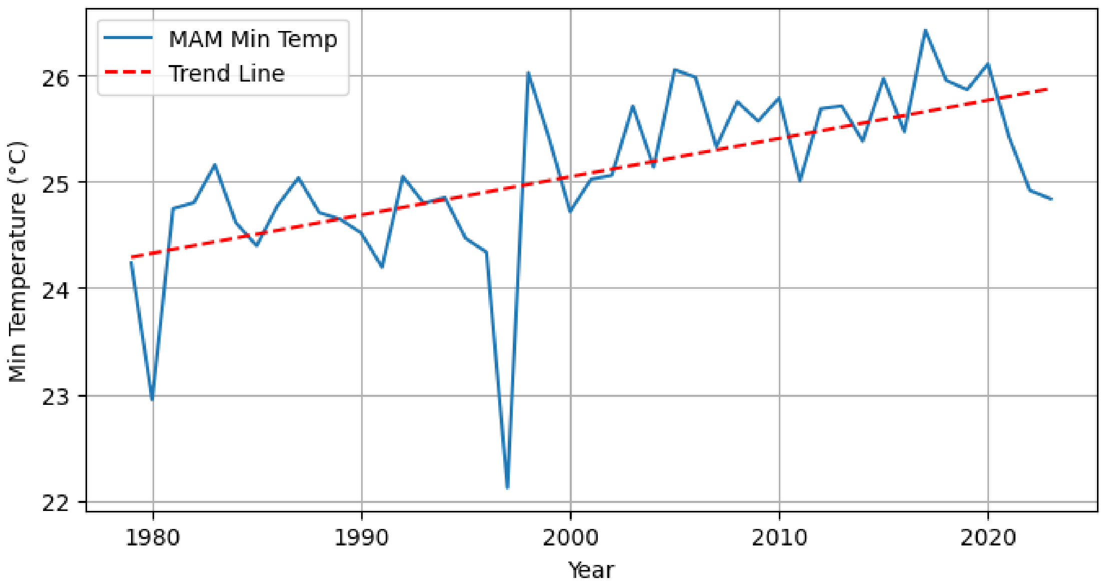

Figure 4 82: Minimum Temperature Data for March-April-May (MAM) Season

The observed increase in MAM minimum temperatures aligns with regional climate analyses that document warming trends in West Africa's pre-rainy season months, driven by broader global climate change factors such as greenhouse gas emissions and changing land surface characteristics (Odunsi and Rienow, 2024). This warming may exacerbate heat stress and alter phenological cycles of crops, impacting food security in the region. Thus, the significant upward trend in MAM minimum temperatures highlights the critical need for region-specific climate adaptation and mitigation strategies, especially considering the vulnerability of Delta State's ecosystems and communities.

III. Minimum Temperature Data for June-July-August (JJA) Season

Figure 4.83 illustrating the JJA (June-July-August) minimum temperature trend in Delta State from 1979 to 2023 indicates a consistent increase in minimum temperatures during this core part of the rainy season. Despite some variability and occasional drops in temperature, the overall pattern demonstrates a positive trend, as shown by the fitted linear regression line with a slope of 0.027°C per year. The Mann-Kendall test corroborates this finding, confirming the trend is statistically significant with a p-value of 0.000. This steady rise in minimum temperatures throughout the JJA months reflects a warming pattern during nighttime and early morning hours, which can influence humidity levels, crop growth, and regional hydrological cycles.

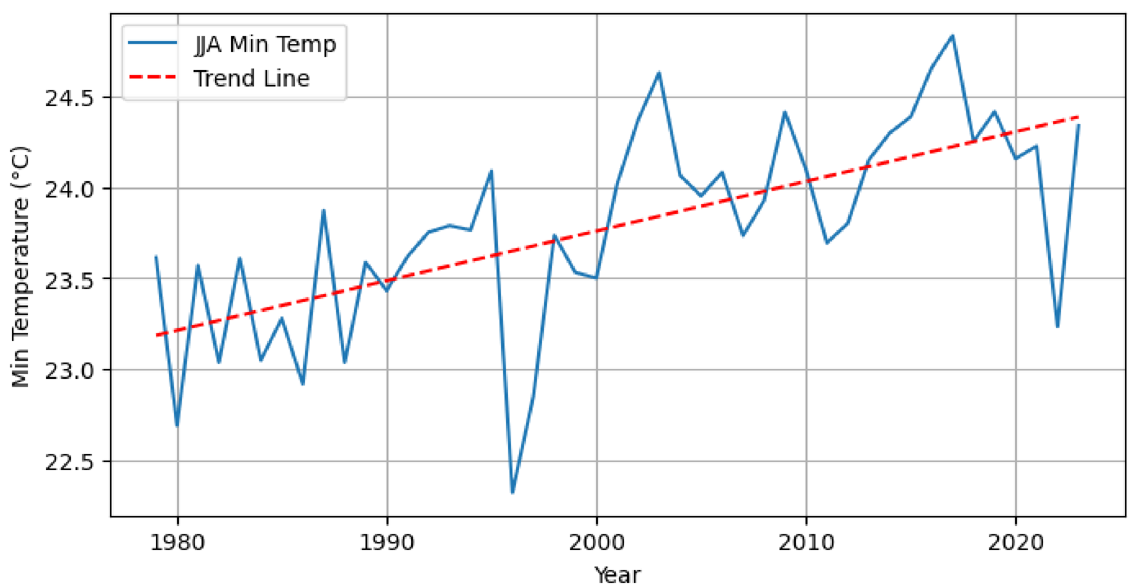

Figure 4.83: Minimum Temperature Data for June-July-August (JJA) Season

Such an upward trend in JJA minimum temperatures aligns with broader climatic changes observed across the West African region, where warming trends during the wet season have been linked to increased greenhouse gas concentrations and local land-use changes (Wang et al., 2017). This warming could exacerbate heat stress on crops and affect agricultural productivity, as well as potentially alter precipitation patterns. Therefore, the significant increase in JJA minimum temperatures highlights the necessity for targeted adaptation strategies in Delta State to mitigate the impacts of climate variability on agriculture and water resources.

IV. Minimum Temperature Data for September-October-November (SON) Season

The graph, Figure 4.84 depicting the SON (September-October-November) minimum temperature trend for Delta State clearly shows a rising pattern in minimum temperatures over the period from 1979 to 2023. The observed data points fluctuate annually, yet the fitted linear regression line with a slope of 0.036°C per year signifies a steady increase in minimum temperatures during the post-monsoon or early dry season months. The Mann-Kendall trend test confirms this increase is statistically significant, with a p-value of 0.000, indicating a robust upward trend. This suggests that minimum temperatures during SON have been consistently rising, potentially influencing local climate conditions such as humidity, evapotranspiration rates, and agricultural cycles.

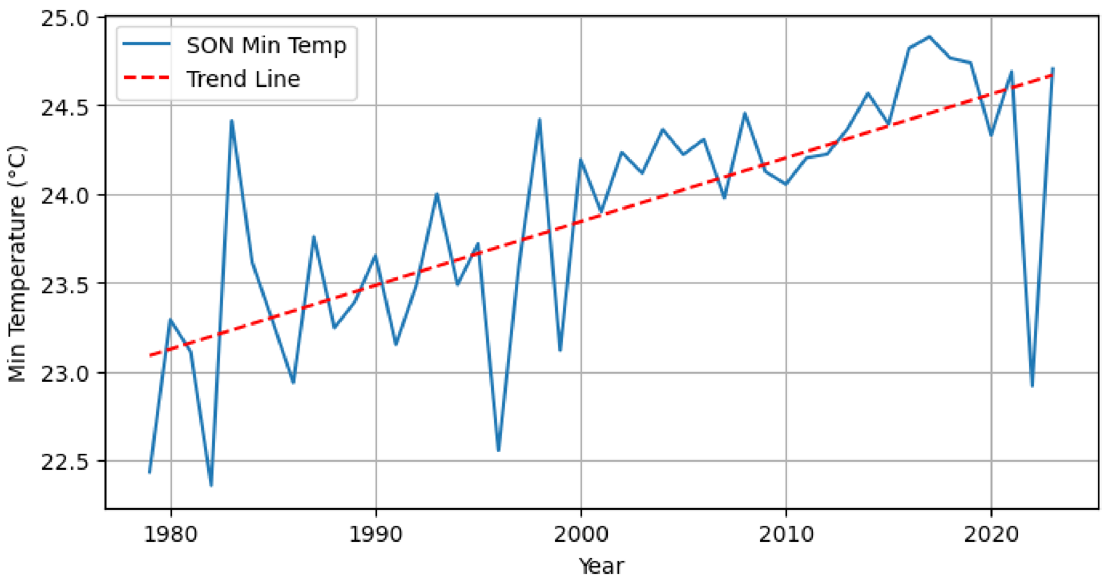

Figure 4.84: Minimum Temperature Data for September-October-November (SON) Season

This increasing trend in SON minimum temperatures aligns with wider regional climate change observations that show warming nighttime temperatures extending across seasonal transitions in West Africa (Onoja et al., 2011). Rising nighttime temperatures can exacerbate heat stress and reduce the relief normally experienced during cooler night periods, thereby impacting human health, crop yields, and ecosystem dynamics. Understanding these seasonal temperature trends is critical for developing effective adaptation strategies in the agricultural sector and managing water resources in Delta State.

4.12.4 Seasonal Decomposition of Monthly Data

The seasonal decomposition of monthly minimum temperatures for Delta State reveals distinct patterns within the data spanning from 1979 to 2023. The top panel shows the raw temperature data, illustrating regular fluctuations with some variability in minimum temperatures over time. The trend component highlights a gradual upward movement in minimum temperatures, consistent with ongoing warming in the region, particularly notable since the early 2000s. The seasonal component reflects the cyclical nature of temperature variations within each year, displaying a clear and consistent annual pattern, likely tied to seasonal climatic changes typical of the region's tropical environment. Lastly, the residual plot indicates the irregular variations or noise after removing trend and seasonal effects, with no apparent systematic patterns, suggesting the model effectively captures the major structures in the temperature data. This decomposition aids in isolating the long-term warming trend from seasonal fluctuations, thus providing a clearer understanding of the underlying climate change signals in Delta State's minimum temperatures.

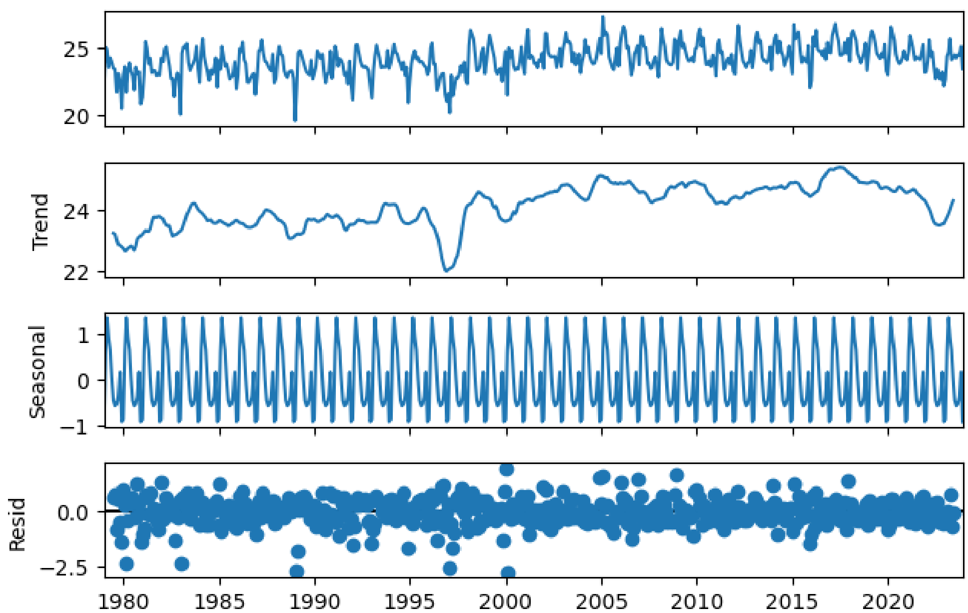

Figure 4.85: Seasonal Decomposition of Monthly Data

Such decomposition methods are essential in climate studies to distinguish between natural seasonal variability and long-term climatic trends, which has been similarly applied in recent research across West Africa to better understand temperature dynamics and their implications on regional climate resilience (Wahap et al., 2020). This understanding is critical for policymakers and stakeholders aiming to develop climate adaptation strategies, particularly in sectors vulnerable to temperature changes such as agriculture and public health.

4.13 Temporal Analysis of Minimum Temperature in Bayelsa State (1971–2023)

The temporal variability of minimum temperature in Bayelsa State was assessed using ERA5 reanalysis data processed through Google Earth Engine. Monthly and yearly averages were computed over a 53-year period (1971–2023) to understand the temperature trend and potential climate implications in the region.

4.13.1 Monthly Trends Minimum Temperature

The annual minimum temperature data for Bayelsa State, as depicted in Figure 4.86, reveals an overall increasing trend from 1979 through to the early 2020s. Despite some year-to-year variability, there is a clear pattern of rising minimum temperatures, particularly notable from the late 1990s onward. This increase aligns with broader regional and global trends of warming observed in recent decades, likely driven by factors such as increased greenhouse gas emissions and changing land-use patterns (Hong et al., 2021).

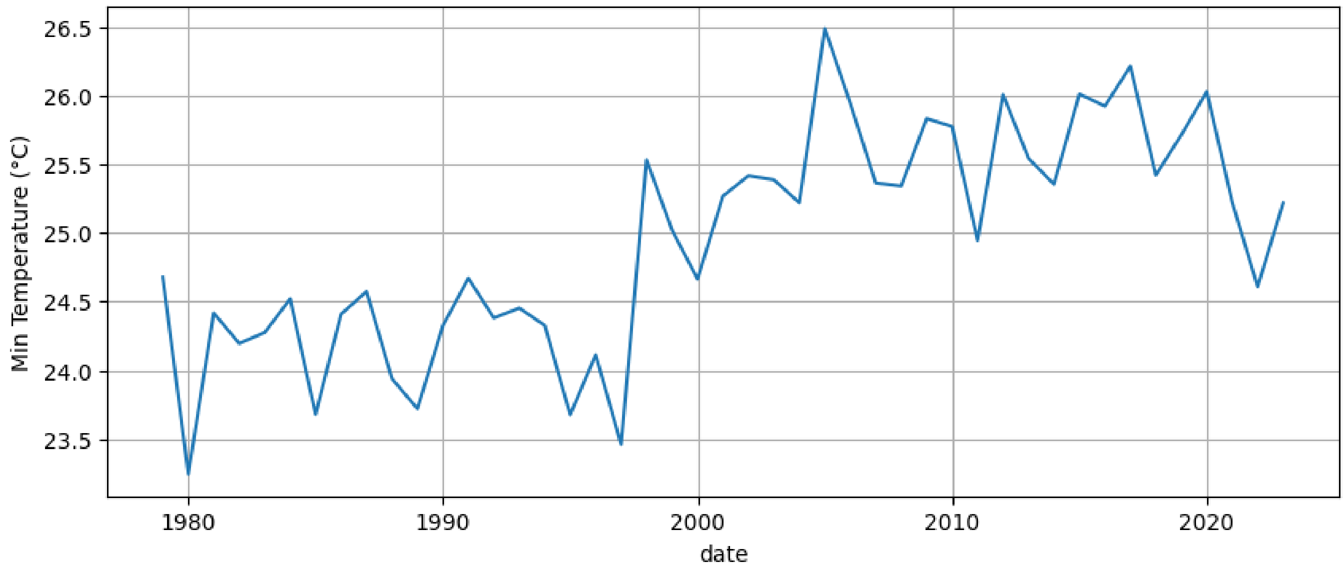

Figure 4.86: Monthly Trends Minimum Temperature in Bayelsa State

The upward shift in minimum temperatures is significant because it impacts various ecological and socio-economic systems, influencing crop growth cycles, vector-borne diseases, and energy demand. This rising trend underscores the importance of continuous climate monitoring and the implementation of adaptive strategies to mitigate the adverse effects of climate change in vulnerable regions like Bayelsa State.

4.13.2 Annual Trend Minimum Temperature

Figure 4.87 illustrating the annual minimum temperature trend for Bayelsa State highlights a statistically significant increase over the study period, with a linear regression slope of 0.045°C per year and a p-value of 0.000, indicating strong evidence of warming. The Mann-Kendall test further corroborates this positive trend with a similarly significant p-value, confirming the persistent rise in minimum temperatures. This trend is consistent with broader climatic changes observed across tropical regions, where increasing minimum temperatures can have profound impacts on ecosystems, agriculture, and human health (Li *et. al*., 2021).

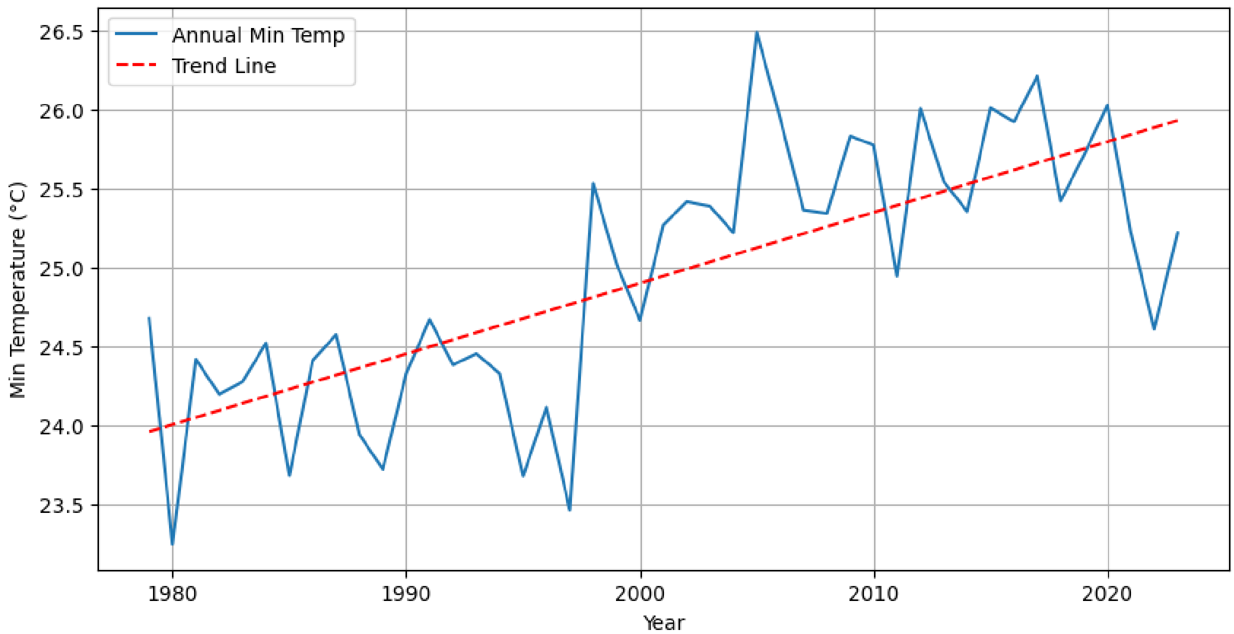

Figure 4.87: Annual Trend Minimum Temperature

The steady upward trend underscores the urgency for targeted climate adaptation strategies in Bayelsa State, as rising nighttime temperatures can exacerbate heat stress and disrupt local environmental conditions. This evidence reinforces the critical need to address regional climate variability within global warming frameworks.

4.13.3 Seasonal Trends in Minimum Temperature

Figure 4.88 shows the seasonal minimum temperature trends for Bayelsa State from 1979 to 2020. This reveals notable variability across the different seasons, with the MAM (March-April-May) season showing consistently higher minimum temperatures compared to DJF, JJA, and SON. This seasonal pattern suggests that the spring months experience relatively warmer nights, which could be linked to shifts in regional atmospheric circulation and moisture patterns. The general upward trend observed across all seasons aligns with the broader findings of rising minimum temperatures in tropical regions due to climate change (Luo et al., 2024).

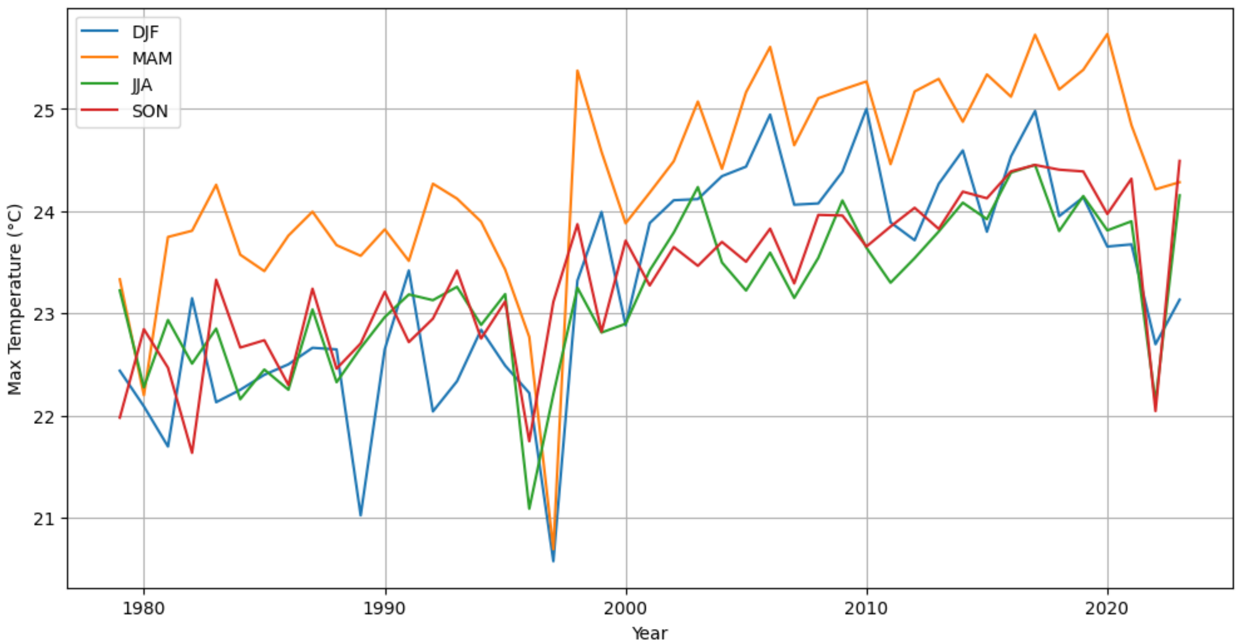

Figure 4.88: Seasonal Trends in Minimum Temperature

The fluctuations and occasional dips, particularly around the late 1990s, may correspond to episodic climate events, which influence temperature variability. Understanding these seasonal dynamics is crucial for tailoring climate adaptation and mitigation strategies, as the varying rates of warming can affect ecological processes and human activities differently throughout the year.

I. Minimum Temperature Data for December–January–February (DJF) Season

Figure 4.89 depict the DJF (December-January-February) minimum temperature trend for Bayelsa State from 1979 to 2020 shows a clear and statistically significant increasing trend. The linear regression slope of 0.053°C per year, along with a highly significant p-value ($p = 0.000$), indicates that minimum temperatures during the DJF season are rising steadily over the analyzed period.

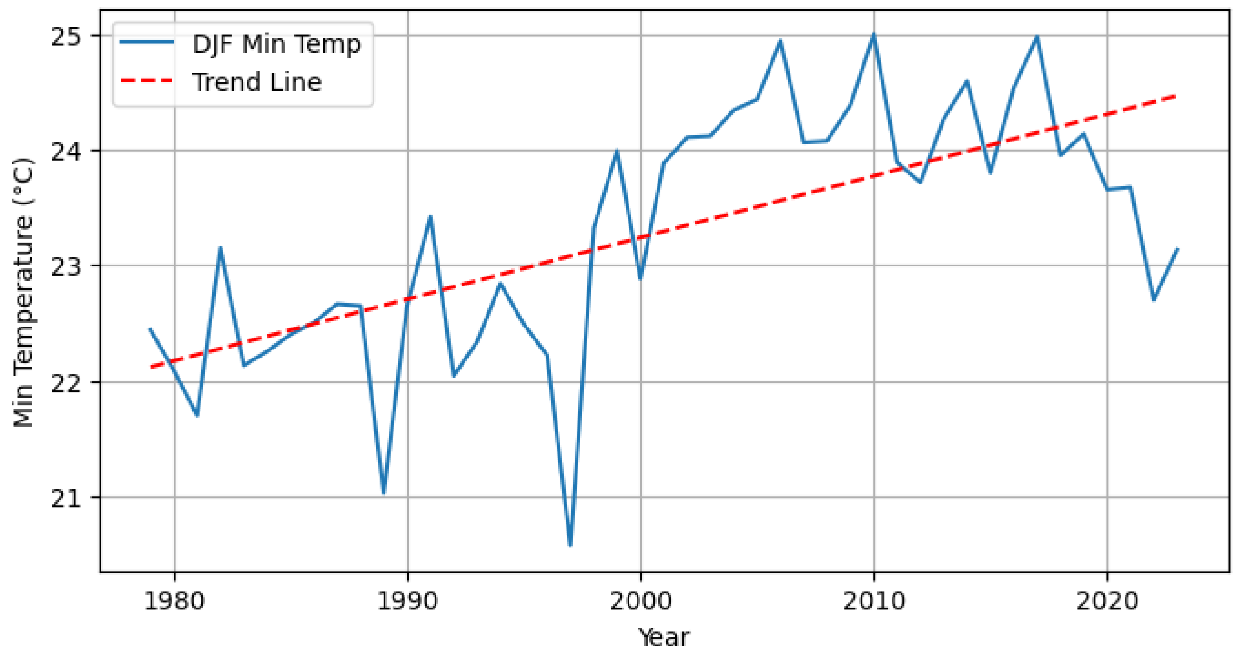

Figure 4.89: Minimum Temperature Data for December–January–February (DJF) Season

The Mann-Kendall test further confirms this increasing trend with similar significance, suggesting that warming nights in the early months of the year are consistent and robust. This rising trend in minimum temperatures is critical as it points to warming nighttime conditions, which can have pronounced effects on human health, agriculture, and ecosystems. The results align with recent regional climate studies that emphasize warming in tropical coastal zones, possibly driven by changes in atmospheric moisture and increased greenhouse gas concentrations (Guild et al., 2024).

II. Minimum Temperature Data for March-April-May (MAM) Season

Figure 4.90 shows the MAM (March-April-May) minimum temperature trend for Bayelsa State. This reveals a consistent and statistically significant increase in temperatures over the period from

1979 to 2020 as seen in Figure 4.90. The linear regression analysis indicates a positive slope of 0.049°C per year, with a p-value of 0.000, confirming a highly significant warming trend in the minimum temperatures during the MAM season. Complementing this, the Mann-Kendall test also reports an increasing trend with similar statistical significance, reinforcing the robustness of the observed warming pattern.

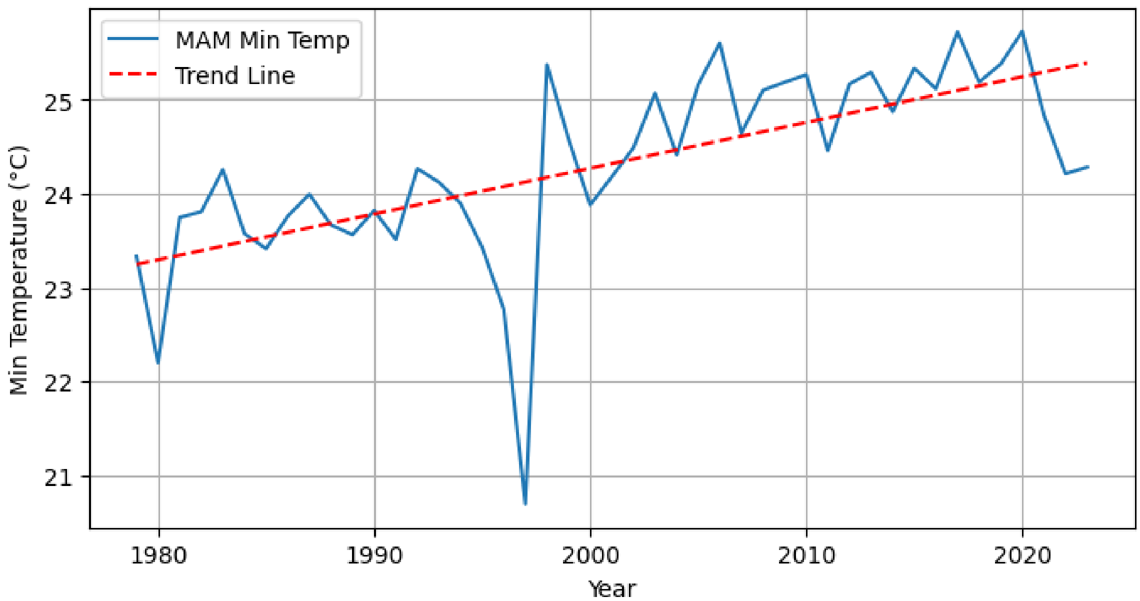

Figure 4.90: Minimum Temperature Data for March-April-May (MAM) Season

This trend suggests that the early part of the year is experiencing progressively warmer nights, which can affect local climate conditions, agricultural productivity, and ecosystem stability. These findings are consistent with broader regional studies that document an upward shift in minimum temperatures across tropical coastal regions, likely driven by anthropogenic climate change and associated atmospheric dynamics (Li et al., 2016). The observed warming trend in Bayelsa's MAM minimum temperatures highlights the need for adaptive climate policies to mitigate potential adverse effects.

III. Minimum Temperature Data for June-July-August (JJA) Season

The graph, Figure 4.91 depicting the JJA (June–July–August) minimum temperature trend for Bayelsa State from 1979 to 2020 highlights a statistically significant warming trend during this peak wet season. The linear regression shows a positive slope of 0.036°C per year, with a p-value of 0.000, indicating a consistent and robust increase in minimum temperatures. This is corroborated by the Mann-Kendall test, which also detects a significantly increasing trend ($p = 0.000$), underscoring the reliability of the warming signal.

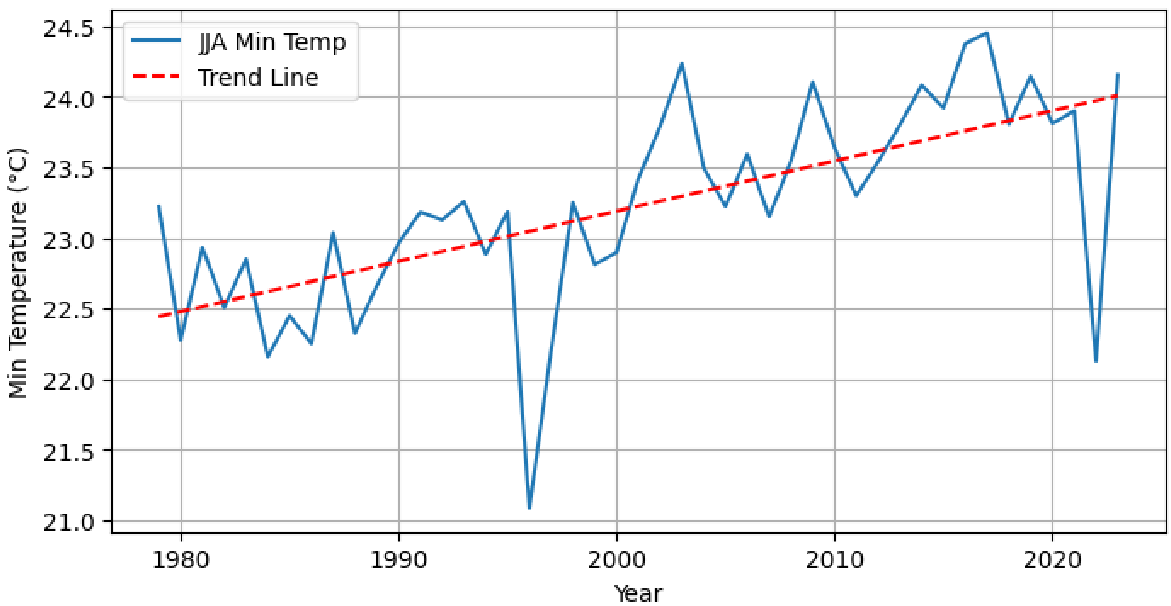

Figure 4.91: Minimum Temperature Data for June-July-August (JJA) Season

The upward trajectory of the JJA minimum temperature suggests that nighttime temperatures are becoming warmer during the rainy season, a development that may influence hydrological cycles, disease patterns, and agricultural outcomes, particularly in low-lying deltaic environments like Bayelsa. These findings reflect broader regional climate dynamics where minimum temperatures are rising more rapidly than maximum temperatures, a trend associated with global climate change and radiative forcing processes (Masson-Delmotte et al., 2021). The implications are critical for climate resilience planning, as rising night temperatures can exacerbate thermal stress, affect crop physiology, and increase the demand for adaptive responses in the region.

IV. Minimum Temperature Data for September-October-November (SON) Season

The SON (September–October–November) seasonal minimum temperature trend for Bayelsa State over the period from 1979 to 2020 seen in Figure 4.92, illustrating a statistically significant upward trend in nighttime temperatures during the post-rainy season. The linear regression analysis reveals a slope of 0.043°C per year with a p-value of 0.000, while the Mann-Kendall test similarly confirms a significant increasing trend ($p = 0.000$). This consistent warming pattern reflects broader climatic shifts observed across southern Nigeria and aligns with global evidence of rising minimum temperatures attributed to anthropogenic climate change (Masson-Delmotte et al., 2021).

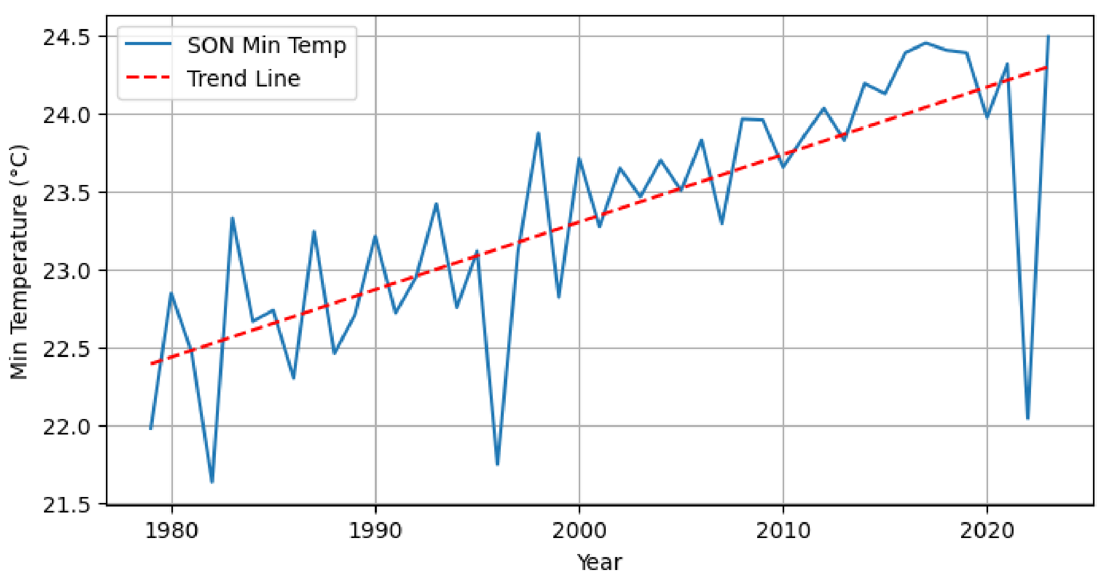

Figure 4.92: Minimum Temperature Data for September-October-November (SON) Season

Notably, the SON season in Bayelsa, typically marked by high humidity and residual rainfall, is experiencing warmer nights, which may alter ecological balances, affect post-harvest storage conditions, and intensify heat stress, particularly in urbanizing areas. The findings support growing concerns about the intensification of warming trends during transitional climatic periods, reinforcing calls for localized adaptation strategies in vulnerable coastal regions (Hobday et al., 2016; Nwachukwu et al., 2018). The trend is also consistent with studies that highlight asymmetrical warming—where minimum temperatures rise faster than maximum temperatures—across the tropics, contributing to reduced diurnal temperature ranges and changing microclimatic conditions.

4.13.4 Seasonal Decomposition of Monthly Data

Figure 4.93 shows the seasonal decomposition of Bayelsa State's monthly minimum temperature from 1980 to 2023, breaking the time series into observed, trend, seasonal, and residual components. The top panel represents the observed monthly minimum temperature (tmin), showing a clear periodic fluctuation superimposed on a long-term increasing trend. The second panel, which captures the underlying trend, reflects a progressive rise in minimum temperature levels over the decades, with a notable dip in the late 1990s followed by sustained warming through the 2000s and 2010s. This trend is indicative of long-term climate change influences in the region, consistent with the global rise in minimum temperatures driven largely by greenhouse gas emissions (Masson-Delmotte et al., 2021).

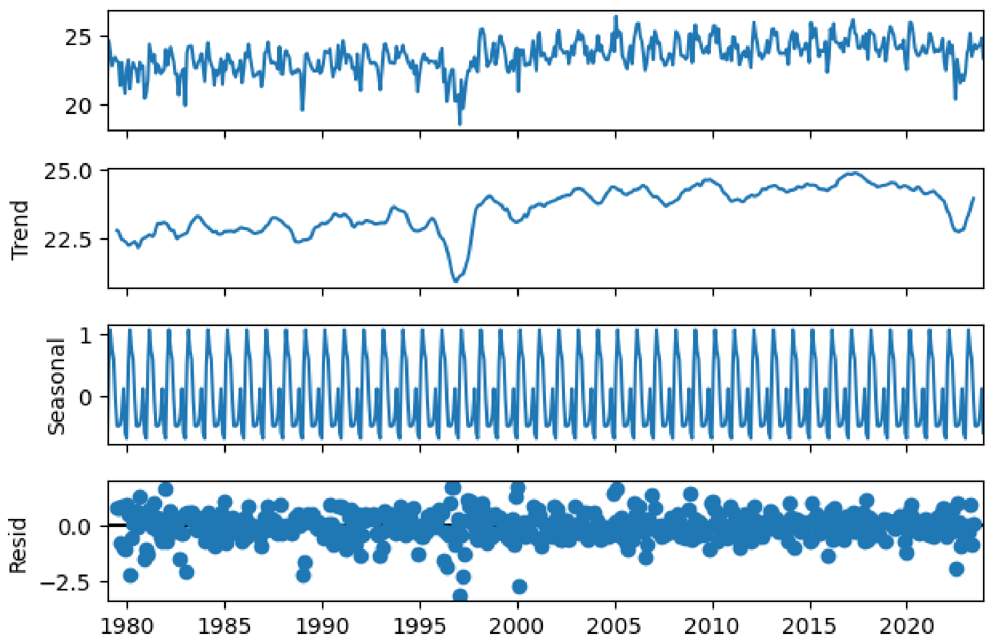

Figure 4.93: Seasonal Decomposition of Monthly Data

The third panel demonstrates the seasonal component, characterized by a regular annual oscillation in minimum temperature, highlighting the strong seasonality of the region's climate. Such seasonality is typical of tropical humid zones like Bayelsa, where temperature patterns are tightly coupled with rainfall and cloud cover variability across the seasons (Akinwumi et al., 2023). The fourth panel displays the residuals variations not explained by either trend or seasonality revealing relatively stable random fluctuations around zero, suggesting that the model captures most of the structural variability in the temperature series.

This decomposition provides a comprehensive view of how minimum temperature dynamics in Bayelsa are influenced by both long-term climate change and short-term seasonal cycles. The observable increase in the trend component aligns with findings from similar studies indicating significant warming in Nigeria's coastal and low-lying regions, which may have implications for agriculture, public health, and ecosystem resilience (Jay et al., 2021). The model's clarity in isolating each component supports its utility in forecasting and climate impact assessment at regional scales.

4.14 Temporal Analysis of Minimum Temperature in Rivers State (1971–2023)

The temporal variability of minimum temperature in Rivers State was assessed using ERA5 reanalysis data processed through Google Earth Engine. Monthly and yearly averages were computed over a 53-year period (1971–2023) to understand the temperature trend and potential climate implications in the region.

4.14.1 Monthly Trends Minimum Temperature

Figure 4.94 presents the annual minimum temperature trend for Rivers State based on monthly data from 1979 to 2023. It reveals a distinct warming pattern, particularly pronounced after the late 1990s. During the earlier decades (1980s to early 1990s), the minimum temperatures fluctuated modestly around 23.5°C to 24.0°C, showing relatively low inter-annual variability. However, from the late 1990s onward, there is a noticeable shift toward higher minimum temperature values, frequently exceeding 25°C. This abrupt change marks a transition point indicative of broader regional climate shifts, consistent with observed warming in coastal regions of southern Nigeria.

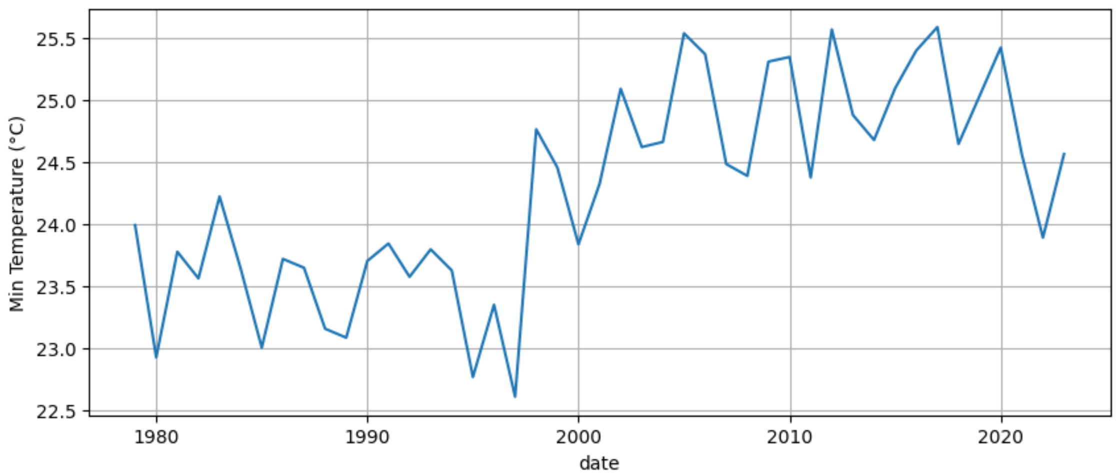

Figure 4.94: Monthly Trends Minimum Temperature in Bayelsa State

The sharp increase in minimum temperatures around the turn of the millennium may be attributed to both natural climate variability and anthropogenic influences, particularly urbanization and land use change in densely populated states like Rivers (Akinsanola and Zhou, 2019). Such upward trends in nighttime or minimum temperatures are especially concerning, as they have a more profound effect on health outcomes, pest proliferation, and crop stress due to reduced cooling periods (Masson-Delmotte et al., 2021). Additionally, the warming trend is aligned with global and regional patterns of increasing minimum temperatures reported across tropical regions due to intensified greenhouse gas concentrations and regional feedback mechanisms (Brisibe and Brown, 2020).

4.14.2 Annual Trend Minimum Temperature

The annual minimum temperature trend in Rivers State from 1979 to 2023, incorporating both the observed temperature data and a linear regression trend line is shown in Figure 4.95. The analysis reveals a statistically significant upward trend, with a slope of 0.044°C per year and a p-value of 0.000, confirming the trend is not due to random variability. This is further corroborated by the

Mann-Kendall test, which also identifies a significantly increasing trend ($p = 0.000$). The red trend line demonstrates a consistent rise in minimum temperatures over the decades, indicating that nighttime temperatures in Rivers State have been gradually increasing.

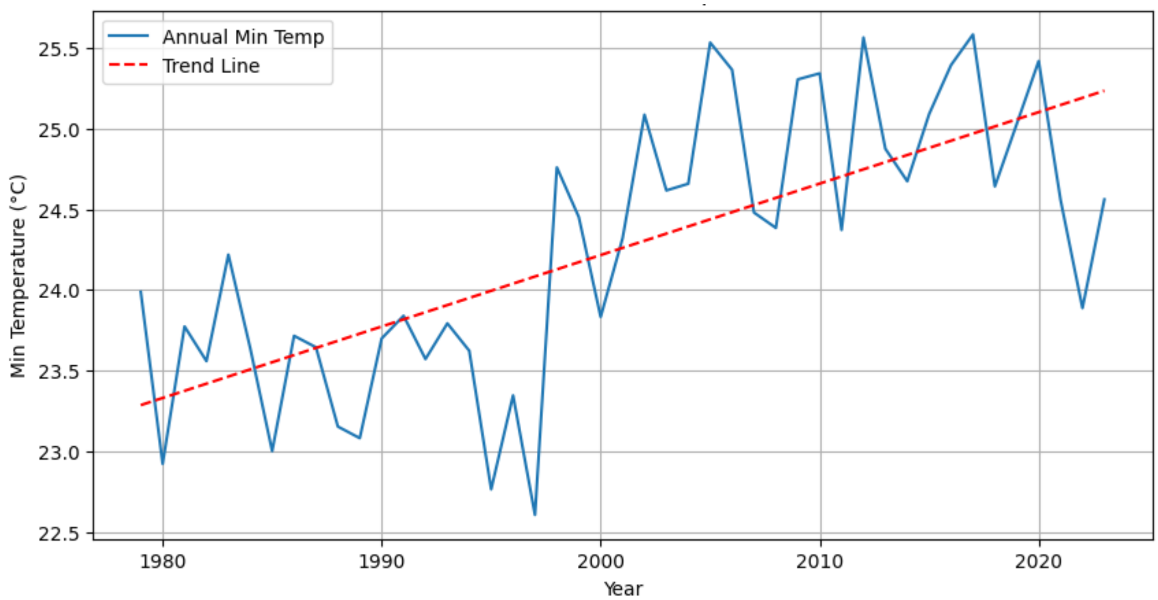

Figure 4.95: Annual Trend Minimum Temperature

This warming pattern is consistent with broader findings across the Niger Delta and tropical West Africa, where rising minimum temperatures have become more prominent due to both natural climate variability and anthropogenic influences such as deforestation, urban expansion, and greenhouse gas emissions (Akinsanola and Zhou, 2019). The sharp increase around the early 2000s coincides with observed climatic shifts across Nigeria, attributed in part to changing land use practices and regional climate feedback mechanisms (Brisibe and Brown, 2020). Notably, the persistent rise in minimum temperatures can exacerbate heat stress, limit agricultural productivity, and elevate health risks, particularly in urban and densely populated areas of Rivers State.

4.14.3 Seasonal Trends in Minimum Temperature

The seasonal variation in minimum temperatures for Rivers State from 1979 to 2020 across the four climatological seasons: DJF (December–February), MAM (March–May), JJA (June–August), and SON (September–November) is shown in Figure 4.96. Each seasonal line shows a clear upward trajectory over the decades, with SON (orange line) consistently exhibiting the highest minimum temperatures, while DJF (blue line) typically records the lowest. Despite inter-annual variability, particularly around 1999–2001, the long-term seasonal patterns point to a systematic warming of nighttime temperatures across all seasons.

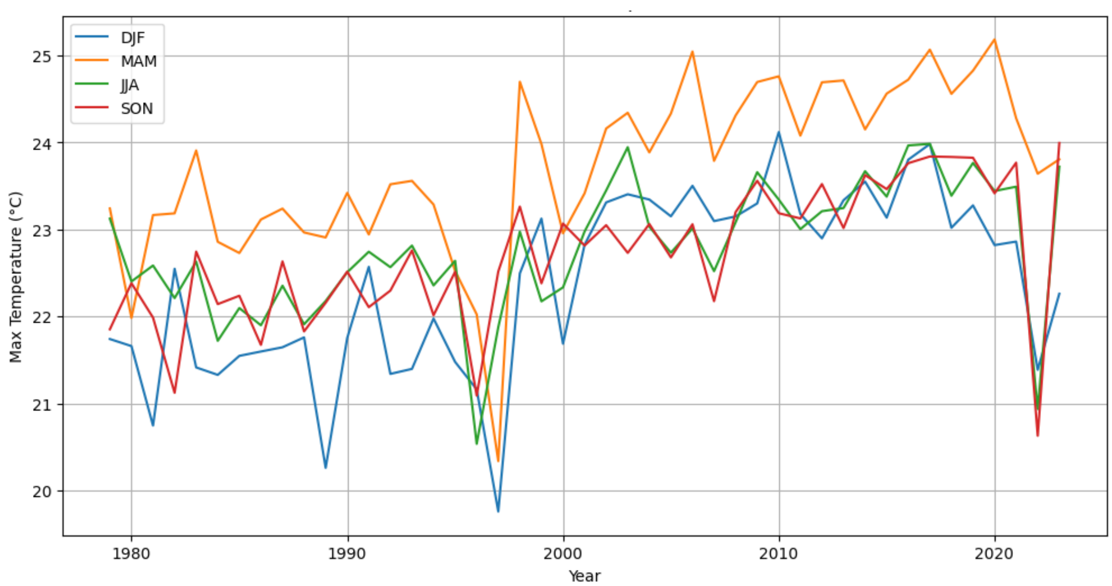

Figure 4.96: Seasonal Trends in Minimum Temperature

The seasonal warming trends are consistent with findings from other parts of southern Nigeria, indicating that the effects of climate change are manifesting more prominently in the form of rising minimum rather than maximum temperatures (Dajuma et al., 2023). This warming is likely influenced by both natural climate variability and anthropogenic factors such as deforestation, urbanization, and greenhouse gas emissions, which contribute to changes in the local energy balance and increased heat retention at night. The data in the figure also reflect a seasonal asymmetry in warming rates, with SON showing the steepest increase, which may be linked to delayed monsoon retreat and heightened land–atmosphere feedback mechanisms (Akinsanola and Zhou, 2019)

I. Minimum Temperature Data for December–January–February (DJF) Season

Figure 4.97 illustrates the trend in minimum temperatures during the DJF (December–February) season in Rivers State from 1979 to 2020, showing a statistically significant upward trend. The linear regression analysis yields a slope of 0.049 °C/year with a p-value of 0.000, indicating a strong and consistent warming trend over the study period. Similarly, the Mann-Kendall test confirms this finding, identifying an increasing trend with a highly significant p-value, further validating the robustness of the observed pattern. This warming is particularly evident after the late 1990s, where a notable shift towards higher minimum temperatures becomes more persistent, with fewer cold anomalies in the later years.

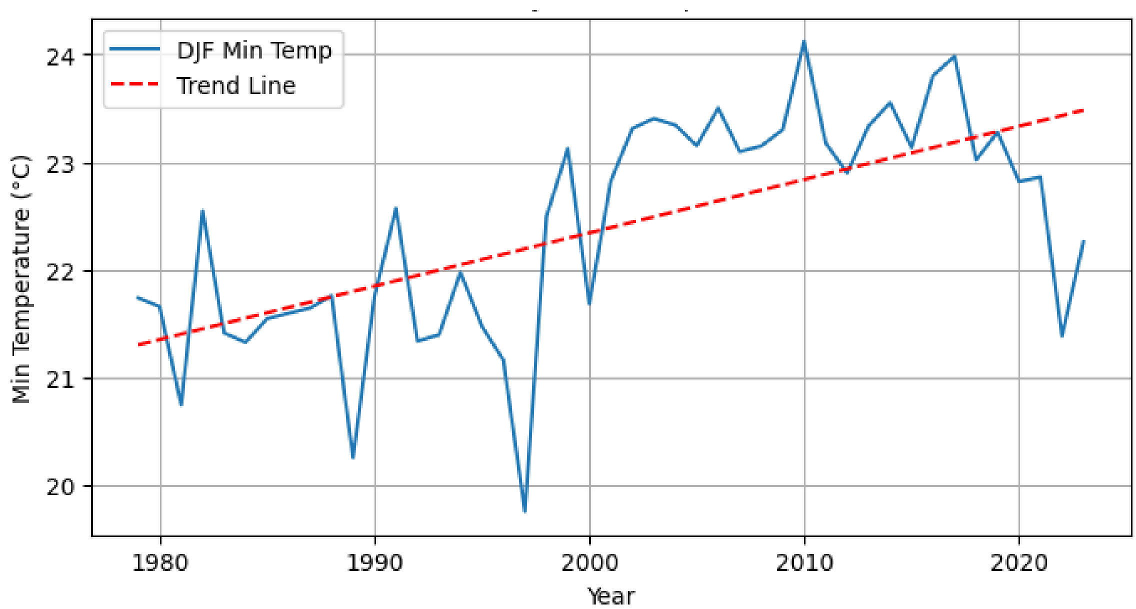

Figure 4.97: Minimum Temperature Data for December–January–February (DJF) Season

The implications of this trend are profound, especially considering that minimum temperature increases often result in warmer nights, which can affect human health, ecosystems, and agriculture more subtly but significantly than rising daytime maxima (Masson-Delmotte et al., 2021). The consistent upward movement of the DJF minimum temperatures suggests a reduction in the frequency and intensity of cool nights, a pattern also observed in other tropical regions due to global warming (Akinsanola and Zhou, 2019). Additionally, the seasonal timing of this trend during the dry season implies enhanced thermal discomfort and potentially greater energy demand for cooling, particularly in urban areas experiencing the urban heat island effect.

Such findings corroborate earlier studies indicating that southern Nigeria is experiencing significant warming, with minimum temperatures increasing at a faster pace than maximum temperatures, aligning with regional and global climate change signatures (Dajuma et al., 2023).

II. Minimum Temperature Data for March-April-May (MAM) Season

Figure 4.98 displays the minimum temperature trend for Rivers State during the MAM (March-April-May) season from 1979 to 2020. The blue line represents the observed annual minimum temperature values, while the red dashed line indicates the linear trend, which clearly shows a statistically significant upward pattern over the study period. The slope of the linear regression is 0.048°C per year, with a p-value of 0.000, confirming a robust and consistent warming trend. This is further supported by the Mann-Kendall test, which also indicates a statistically significant increasing trend with a p-value of 0.000, highlighting the consistency and reliability of the observed change.

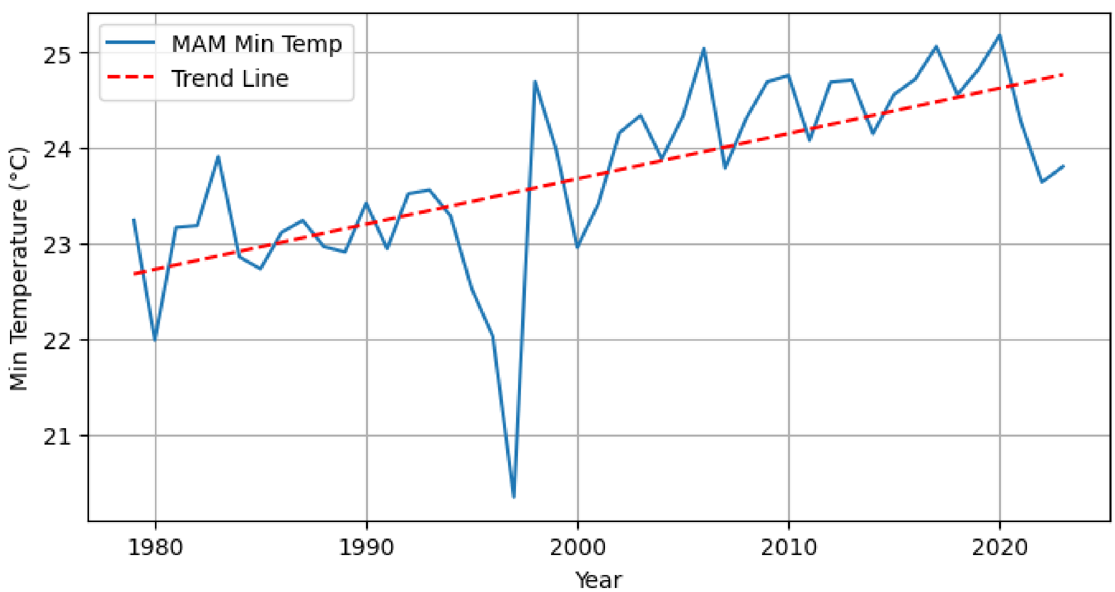

Figure 4 98: Minimum Temperature Data for March-April-May (MAM) Season

This warming during the MAM season, which precedes the main rainy period in Rivers State, can have significant climatological and agricultural implications. Increasing night-time temperatures, as suggested by the rise in minimum temperatures, can lead to heat stress in crops and a reduction in yields, particularly for temperature-sensitive crops like maize and yam which are widely cultivated in southern Nigeria (Okoro and Ofordu, 2025). Moreover, this period typically marks the transition from dry to wet conditions, and rising temperatures could disrupt moisture balance and alter evapotranspiration rates, thereby impacting the onset and intensity of rainfall.

The pattern observed in this graph aligns with broader regional and global studies that report increasing minimum temperatures in West Africa as a consequence of anthropogenic climate change. These changes are typically more pronounced in minimum temperatures compared to maximum temperatures, a pattern that is consistent with findings from recent IPCC reports and regional assessments (Masson-Delmotte et al., 2021). Such trends emphasize the urgent need for climate-resilient planning and adaptive agricultural strategies to mitigate the potential socioeconomic impacts of continued warming in tropical regions like Rivers State.

III. Minimum Temperature Data for June-July-August (JJA) Season

The trend of minimum temperatures during the JJA (June-July-August) season for Rivers State from 1979 to 2020, highlighting a clear pattern of warming seen in Figure 4.99. The blue line shows inter-annual variations in minimum temperature, while the red dashed line represents the fitted linear trend. The slope of the linear regression is 0.031°C per year with a highly significant p-value of 0.000, indicating a steady and statistically significant increase in minimum temperatures over the period. The Mann-Kendall test further confirms this trend as significantly increasing (p = 0.000), providing strong statistical evidence that the warming observed is not due to random variation but part of a broader climatic shift.

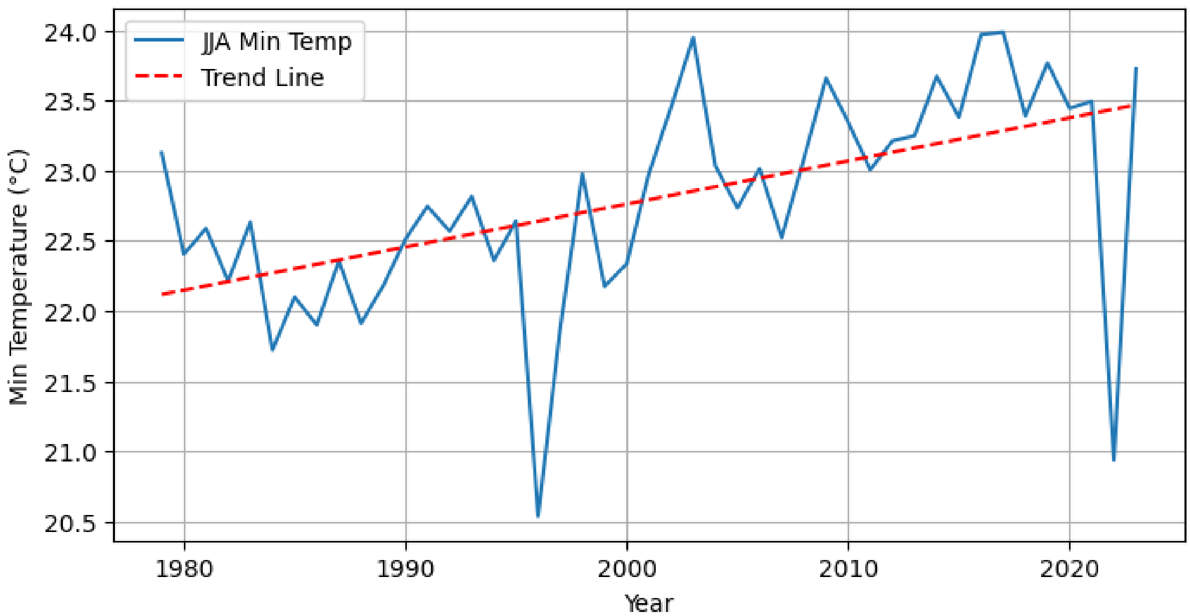

Figure 4.99: Minimum Temperature Data for June-July-August (JJA) Season

The JJA season corresponds to the peak of the rainy season in Rivers State, a period critical for agricultural productivity and ecological balance. The observed increase in minimum temperatures during this season may have implications for crop physiology and disease dynamics, particularly for staple crops such as cassava and plantain that are sensitive to night-time temperatures and humidity levels (Akinwumi et al., 2023). Warmer minimum temperatures can disrupt crop flowering, reduce grain fill, and foster the proliferation of pests and pathogens, potentially threatening food security if adaptive measures are not implemented.

This warming trend during the wet season aligns with broader regional climate studies, which show that the coastal and humid zones of West Africa are experiencing an acceleration in minimum temperature increases due to intensified greenhouse gas concentrations and urban heat island effects ((Dajuma et al., 2023; Masson-Delmotte et al., 2021). These findings reinforce the need for integrating climate-smart agriculture and infrastructure planning in climate-vulnerable regions like Rivers State to mitigate adverse effects of rising night-time temperatures.

IV. Minimum Temperature Data for September-October-November (SON) Season

Figure 4.100 depicts the trend in minimum temperatures during the SON (September–November) season for Rivers State from 1979 to 2023, illustrating a significant warming trajectory. The blue line represents the observed seasonal minimum temperatures, while the red dashed line indicates the linear trend. The slope of the trend line is 0.039°C per year, and the associated p-value of 0.000 confirms that this warming trend is statistically significant. This increase is further validated by the Mann-Kendall test, which also shows a significant positive trend (p = 0.000), underscoring a consistent long-term warming in the SON season.

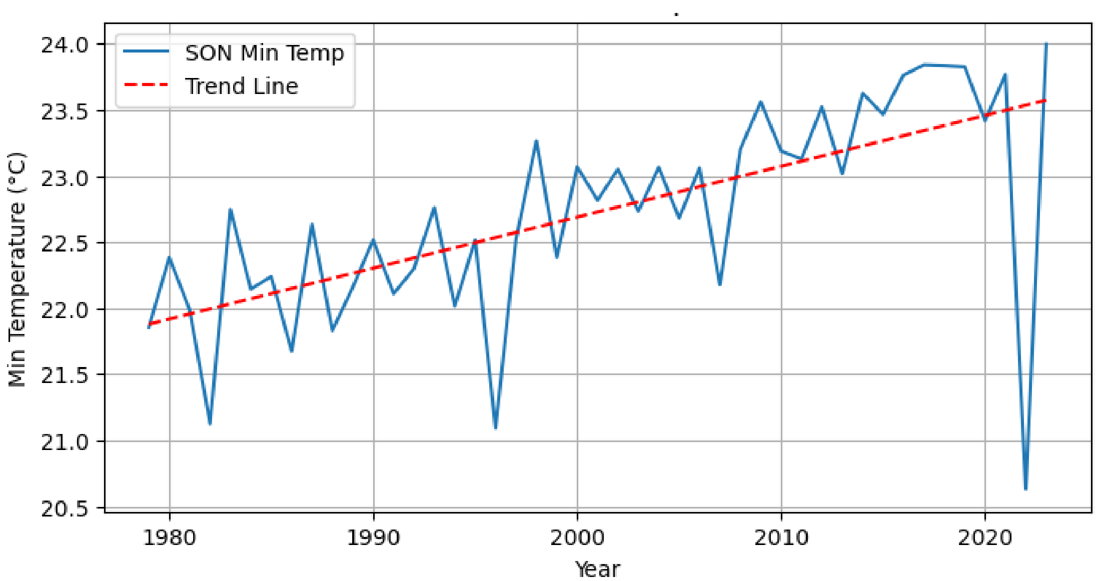

Figure 4.100: Minimum Temperature Data for September-October-November (SON) Season

The SON period marks the transition from the rainy to the dry season in Rivers State and is critical for agricultural post-harvest activities and natural ecosystem regulation. A persistent rise in minimum temperatures during this season may lead to elevated nighttime temperatures, which can disrupt the physiological processes of crops and potentially increase post-harvest spoilage due to higher humidity and reduced nocturnal cooling (Ayanlade et al., 2019). Additionally, warmer nights may enhance the proliferation of disease vectors, with public health implications for densely populated areas in the Niger Delta.

The increasing trend observed in this image aligns with broader regional and global findings that show more rapid increases in minimum (nighttime) temperatures compared to maximum temperatures, a phenomenon widely attributed to global warming and urban heat accumulation (Masson-Delmotte et al., 2021). Studies across southern Nigeria have confirmed similar patterns, emphasizing the importance of integrating seasonal and diurnal temperature trends into local climate adaptation frameworks (Chukwurah et al., 2022).

4.14.4 Seasonal Decomposition of Monthly Data

Figure 4.101 presents the seasonal decomposition of monthly minimum temperature data for Rivers State from 1979 to 2023, clearly illustrating the underlying patterns and variability within the time series. The top panel displays the raw monthly minimum temperature values, showing natural fluctuations with a slight increase over time. The trend component, represented in the second panel, highlights a clear upward trajectory in minimum temperatures over the study period, with a noticeable dip around the late 1990s, possibly linked to transient climatic events or data irregularities, followed by a steady increase from the early 2000s onwards. This rising trend is consistent with broader regional warming patterns driven by climate change, as noted in recent research (Jones et al., 2022). The third panel shows the seasonal component, revealing a strong and consistent annual cycle in minimum temperatures, indicative of the regular climatic seasonality characteristic of the region, with repeating peaks and troughs each year.

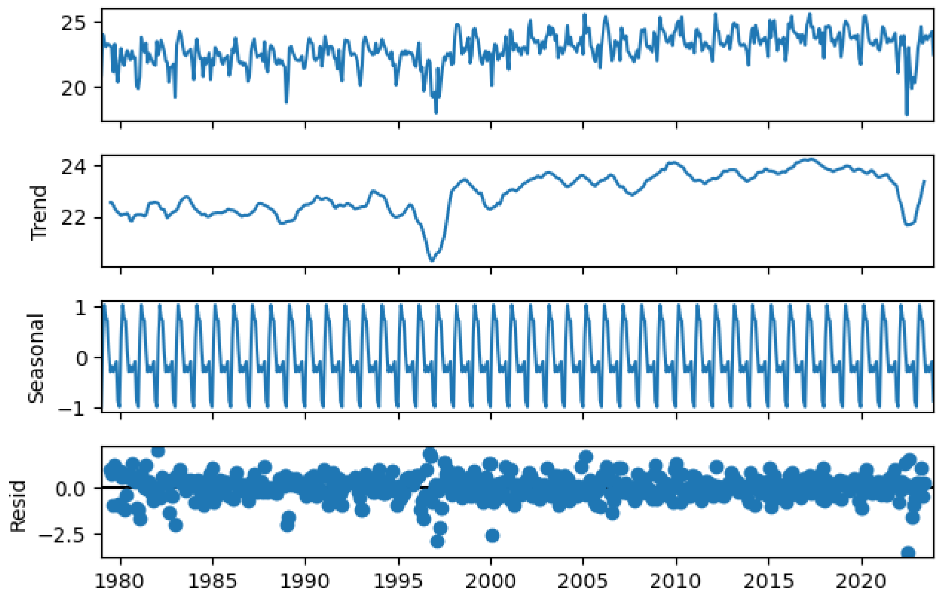

Figure 4.101: Seasonal Decomposition of Monthly Data

This seasonality reflects the influence of monsoonal cycles and other regional climatic drivers affecting temperature patterns. Finally, the residuals plot at the bottom shows the variability in temperature not explained by trend or seasonality, which appears relatively stable with some isolated anomalies, suggesting that the decomposition model has effectively captured the main components of temperature variation.

This seasonal decomposition is critical for understanding how climate variability and long-term warming intersect with seasonal cycles in Rivers State, facilitating more accurate climate projections and informed decision-making for climate adaptation strategies. Such analyses are essential in the Niger Delta region, where temperature increases, particularly in minimum temperatures, may exacerbate heat stress on ecosystems, agriculture, and human health (Shukla et al., 2021). The decomposition thus serves as a valuable tool for disentangling the complex temporal dynamics of climate variables in a region vulnerable to climate change.

4.15 Land Use/Land Cover Analysis for the Study Area

Land use land cover analysis was carried out for the study area so as to examine the sequential change over time. The Landsat 8 OLI image was used and two machine learning models was developed to assess the land use change in the region over time. The supervised learning technique was adopted and suitable sample data sets were used to build the training data set and the test data set. The model accuracy and change results are presented as follows;

4.15.1 LULC Classification for Edo State Using Machine Learning

The land use /land cover analysis results are presented in Figure 4.102 to Figure 4.113,

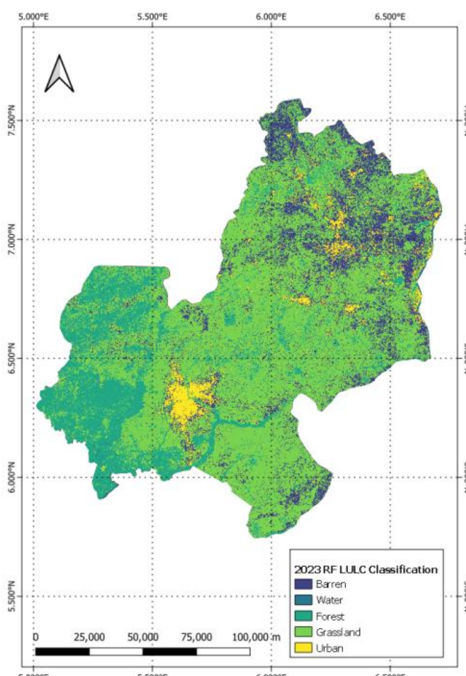

Figure 4.102: 2023 LULC Classification with RF

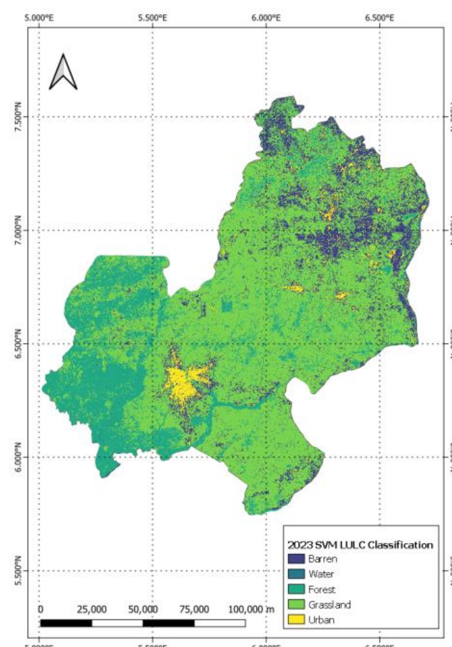

Figure 4.103: 2023 LULC Classification with SVM

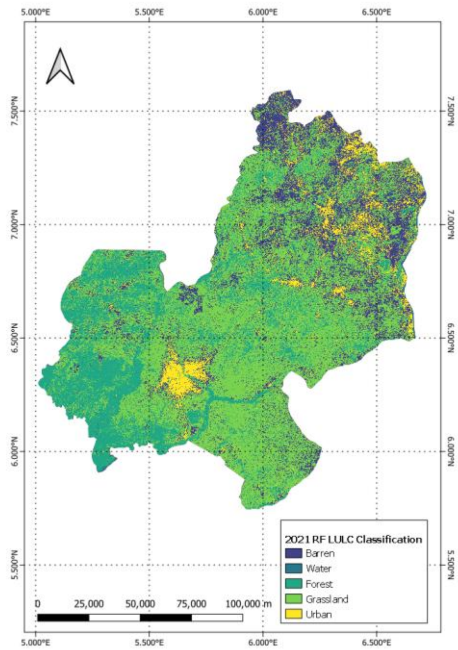

Figure 4.104: 2021 LULC Classification with RF

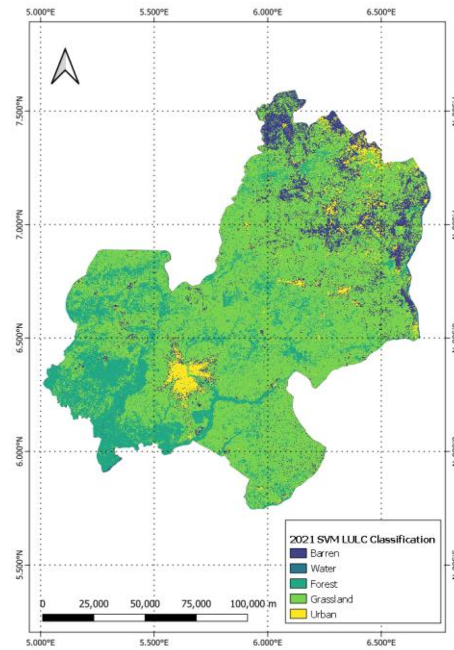

Figure 4.105: 2021 LULC Classification with SVM

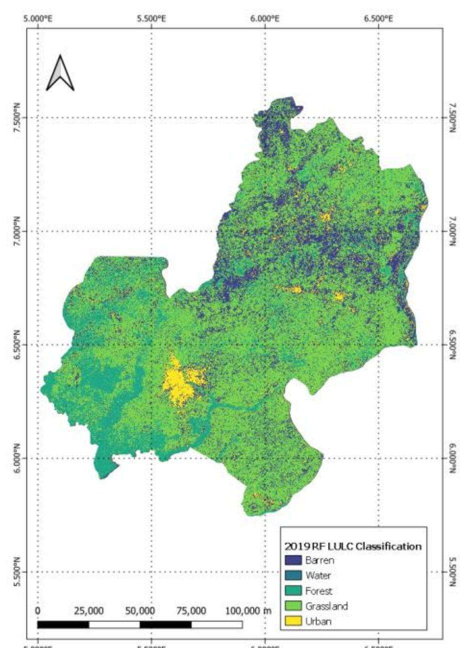

Figure 4.106: 2019 LULC Classification with RF

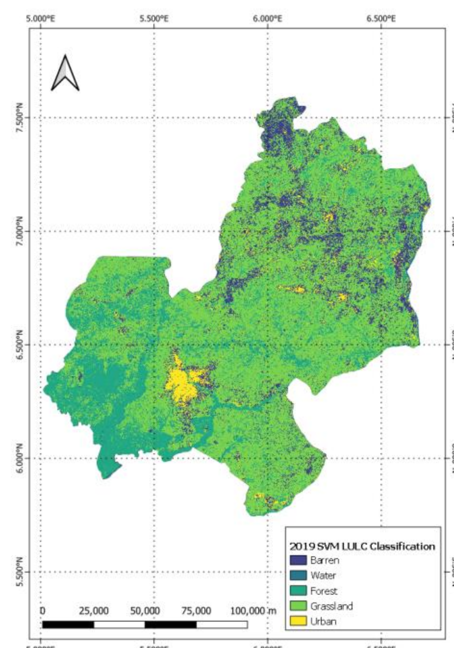

Figure 4.107: 2019 LULC Classification with SVM

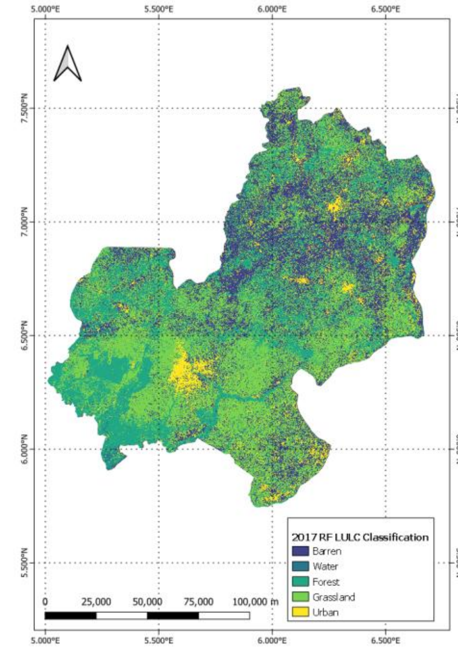

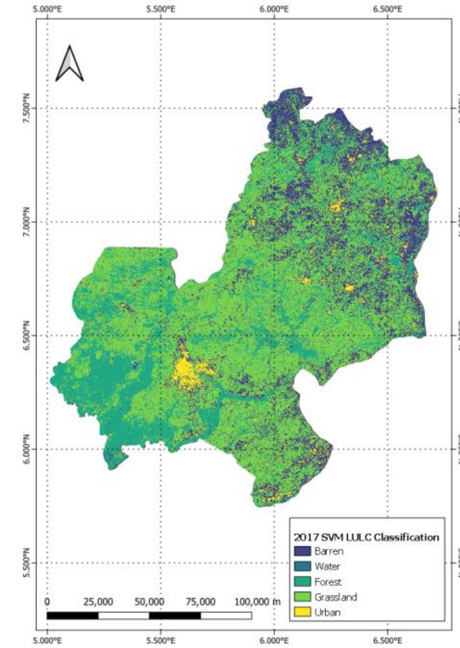

Figure 4 108: 2017 LULC Classification with RF   Figure 4 109: 2017 LULC Classification with SVM

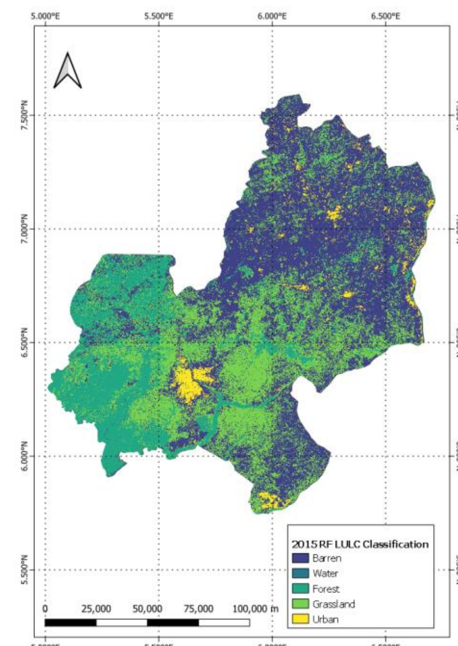

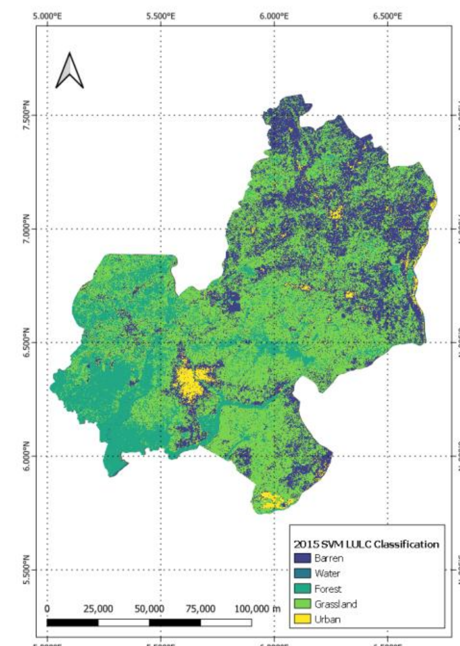

Figure 4.110: 2015 LULC Classification with RF   Figure 4.111: 2015 LULC Classification with SVM

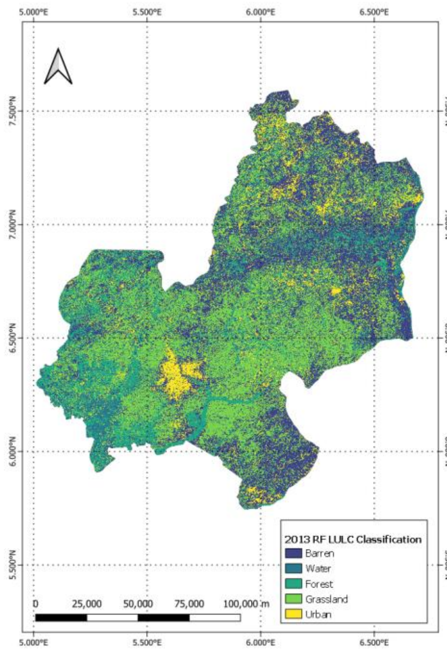

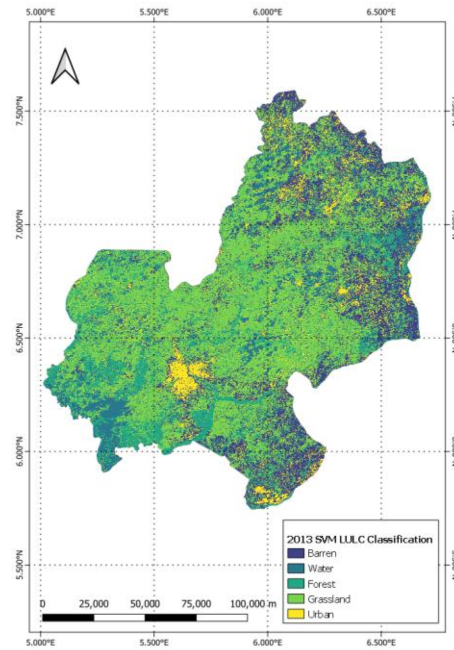

Figure 4.112: 2013 LULC Classification with RF   Figure 4.113: 2013 LULC Classification with SVM

I Model Accuracy Assessment

The performance evaluation of classification algorithms is a critical component in assessing the reliability of Land Use and Land Cover (LULC) maps derived from satellite imagery. In this study, both Random Forest (RF) and Support Vector Machine (SVM) classifiers were applied across six different years 2013, 2015, 2017, 2019, 2021, and 2023 to examine their robustness in accurately classifying land cover types in the study area. The performance of each classifier was assessed using both training and validation accuracy along with Cohen's Kappa coefficient, a metric that accounts for the possibility of agreement occurring by chance (Chicco et al., 2021) as seen in Table 4.10.

Table 4.10: Summary of the classification performance metrics for RF and SVM across the evaluated years.

Year	Classifier	Training		Validation	
		Accuracy	Kappa	Accuracy	Kappa
2013	Random Forest	0.998678996	0.99834787	0.82745098	0.783715013
	Svm	0.70673712	0.633257244	0.650980392	0.564437194
2015	Random Forest	0.9995	0.9996	0.948412698	0.935327214
	Svm	0.840789474	0.801198086	0.845238095	0.806337196
2017	Random Forest	0.997382199	0.996724228	0.862903226	0.827149358
	Svm	0.787958115	0.734817141	0.72983871	0.658886083
2019	Random Forest	0.998677249	0.99834569	0.9296875	0.91172752
	Svm	0.845238095	0.806526546	0.78515625	0.73131822
2021	Random Forest	0.9997	0.9993	0.929133858	0.911374738
	Svm	0.866754617	0.833448272	0.842519685	0.803496828
2023	Random Forest	0.997425997	0.996781303	0.978723404	0.973274803
	Svm	0.936936937	0.921136522	0.927659574	0.909256104

It was observed that the Random Forest algorithm consistently demonstrated high performance across all years, with training accuracy ranging from 99.74% to 99.97% and Kappa values above 0.996, indicating near-perfect classification on the training data. Despite concerns about potential overfitting due to high training accuracies, the validation results confirm the robustness of the RF model. Validation accuracies ranged from 82.75% in 2013 to 97.87% in 2023, while the corresponding Kappa values increased from 0.7837 to 0.9733.

From the result, the 2013 validation accuracy was the lowest (82.75%), which could be due to image quality, seasonal spectral variability, or limited ground truth data during the period. However, subsequent years showed significant improvements. For instance, in 2015 and 2023, validation accuracies exceeded 94% and 97%, respectively, with very high Kappa coefficients, indicating strong generalization and minimal classification error. These trends support existing literature that highlights RF's capability to handle high-dimensional remote sensing data effectively (Garcia-Salgado et al., 2020).

The Support Vector Machine classifier exhibited a moderate to high performance, but consistently lagged behind the RF model. Training accuracies ranged from 70.67% in 2013 to 93.69% in 2023, and validation accuracies ranged from 65.10% to 92.77%. The lowest validation accuracy occurred in 2013, with a Kappa value of 0.5644, which may be attributed to the SVM's sensitivity to kernel parameter selection and class imbalance (Li et al., 2023). Subsequently, the performance improved in later years, particularly in 2023, where SVM achieved a validation accuracy of 92.77% and a Kappa of 0.9093, nearly rivaling the performance of the RF classifier. This suggests that while SVM may require more careful tuning and preprocessing, it remains a viable option for LULC classification, especially when computational resources are limited.

Overall, the Random Forest classifier outperformed SVM in both training and validation metrics across all years, aligning with prior studies that highlight RF's ensemble structure and resistance to overfitting in complex classification problems (Rane et al., 2024). The increasing trend in validation accuracy for both classifiers, especially between 2013 and 2023, also reflects improvements in satellite image quality, preprocessing techniques, and availability of training data over time.

Therefore, Random Forest emerged as the more reliable and consistent classifier for LULC mapping in the study area, achieving higher accuracy and agreement across all evaluation years. As such, RF has been adopted for further study in this research.

II Land Use/ Land Cover Change Analysis for Edo State

Land cover change analysis provides critical insights into environmental dynamics, anthropogenic influences, and the potential drivers of flooding and ecosystem degradation. Table 4.9 presents the areal extent (in hectares) of major land cover classes, Barren land, Water, Forest, Grassland, and Urban areas, as extracted from the classified maps produced using the Random Forest (RF) classifier for the years 2013, 2015, 2017, 2019, 2021, and 2023.

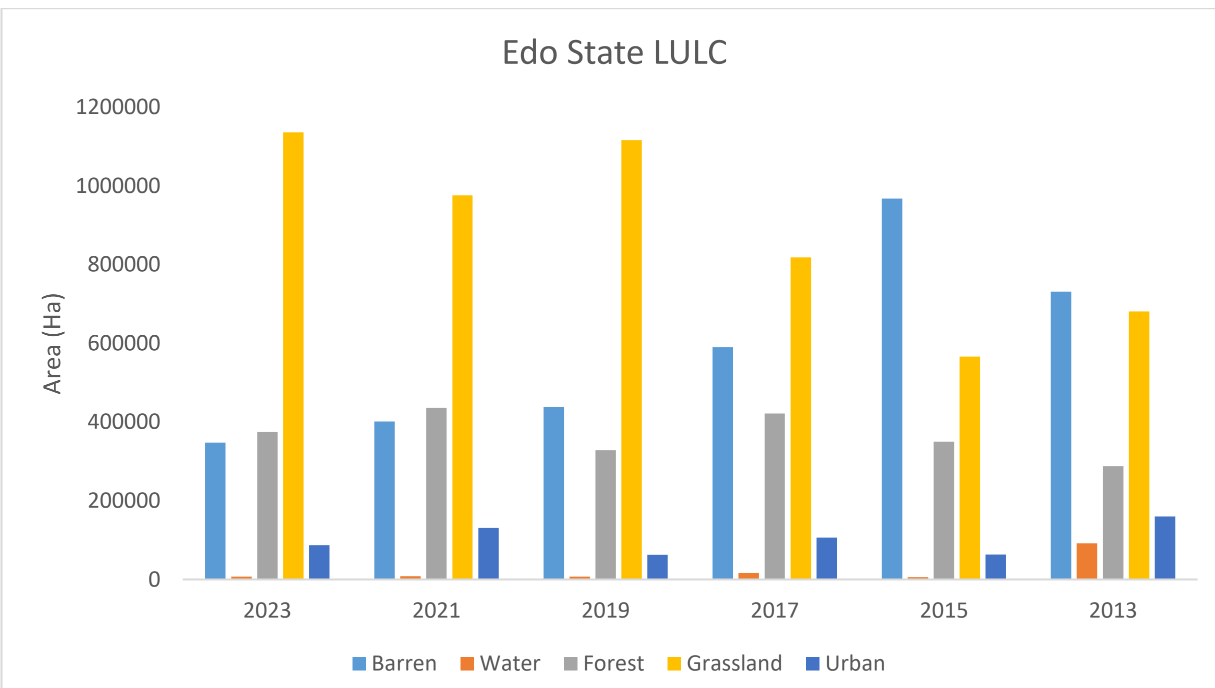

Figure 4 114: Land Use Change presented in a horizontal bar chart

From Figure 4.114, it was observed that the area classified as barren land exhibited a clear declining trend over the period, dropping from 730,856 ha in 2013 to 347,997 ha in 2023. This

52% reduction may be attributed to increased vegetation recovery, urbanization, or reclamation of degraded lands for agriculture or settlement (Ekka et al., 2023). The sharp drop between 2015 (966,991 ha) and 2017 (589,545 ha) is particularly notable and could coincide with land restoration efforts or a shift in land cover types due to changing climatic or socio-economic conditions. This trend suggests a gradual reduction in land degradation, which is beneficial from both ecological and hydrological standpoints. The spatial extent of water bodies fluctuated significantly over the observed period. A peak was observed in 2013 (91,938 ha), followed by a drastic decline to 5,357 ha in 2015. This may reflect differences in rainfall patterns, seasonal timing of image acquisition, or improved classification accuracy in later years (Ouma and Tateishi, 2006). After 2015, water area began to stabilize, with 7,011 ha recorded in 2023. This stability post-2015 could also be linked to consistent use of improved flood and water-sensitive indices in classification. The significant drop from 2013 to 2015 may also reflect over-classification of flooded or saturated lands as water bodies in earlier imagery.

Forest cover showed a general increase over the decade, rising from 287,397 ha in 2013 to 374,455 ha in 2023, with a notable peak in 2021 (435,862 ha). This increasing trend could reflect reforestation efforts, natural regrowth, or improved land management practices. However, a drop was noted between 2021 and 2023, possibly due to deforestation or conversion to agricultural land. These dynamics align with global and regional forest transition theories, where forest loss in early periods may be counterbalanced by regrowth or afforestation in later years (Mather, 1992). It was alos seen that Grassland areas fluctuated significantly, reflecting their transitional role between forested, barren, and agricultural lands. The lowest grassland coverage was observed in 2015 (565,728 ha), while the highest occurred in 2023 (1,135,269 ha). The increasing trend in grassland after 2015 may be linked to forest clearance, urban expansion spillover, or land degradation in certain areas. Grasslands are also often seasonal, and their detection can vary depending on the phonological state of vegetation (Reinermann et al., 2020).

Finally, Urban land cover exhibited a distinct and consistent decline from 160,221 ha in 2013 to 86,712 ha in 2023. However, this trend may appear counterintuitive given ongoing urbanization pressures in many parts of Nigeria. The initial high value in 2013 may reflect misclassification of impervious or bare lands as urban areas in earlier RF models, or cloud cover that obscured vegetation and led to overestimation of built-up areas (Unger Holtz, 2007). Later years benefited from improved classifier accuracy, resulting in more reliable urban delineation. Nonetheless, the fluctuation in urban cover underlines the need for more granular validation using higher-resolution data or ground trothing.

4.15.2 LULC Classification for Delta State using Machine Learning

The land use /land cover analysis result for Delta State are presented in Figure 4.115 to Figure 4.126,

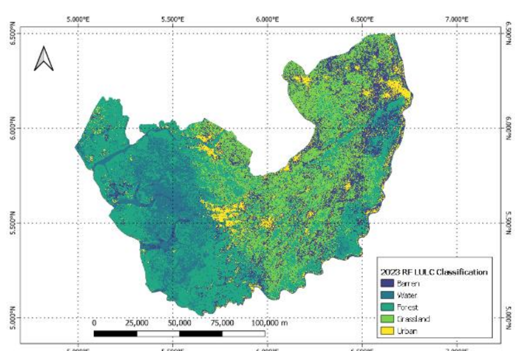

Figure 4 115: 2023 LULC Classification with RF

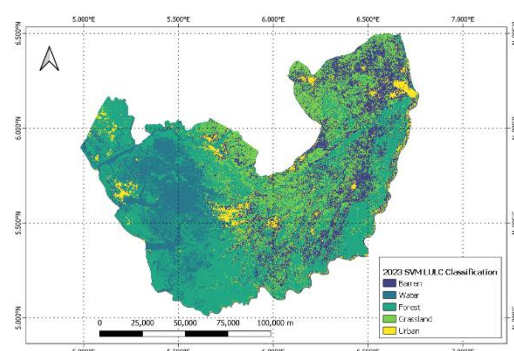

Figure 4.116: 2023 LULC Classification with SVM

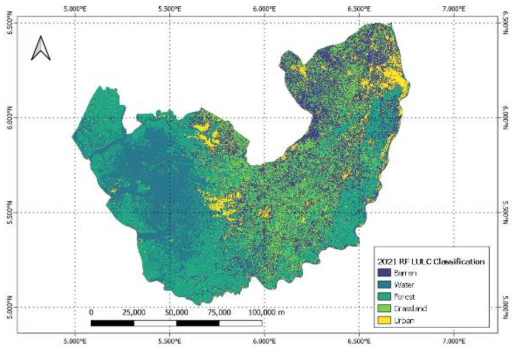

Figure 4.117: 2021 LULC Classification with RF

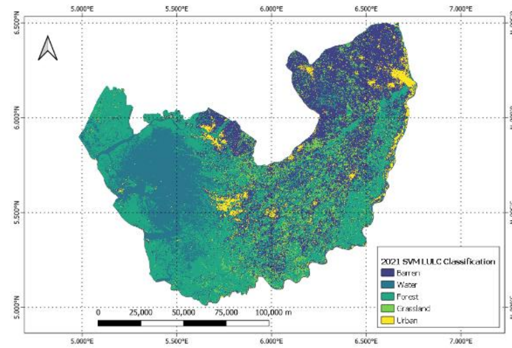

Figure 4.118*:* 2021 LULC Classification with SVM

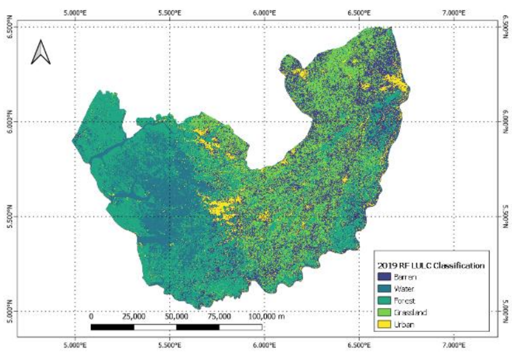

Figure 4.119: 2019 LULC Classification with RF

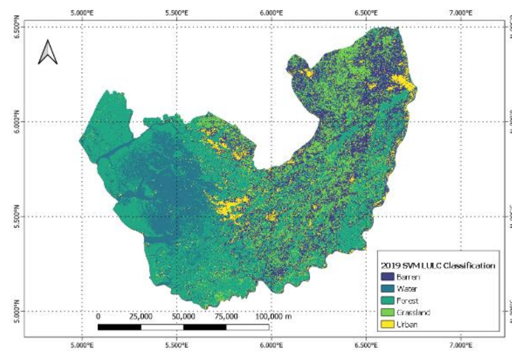

Figure 4.120: 2019 LULC Classification with SVM

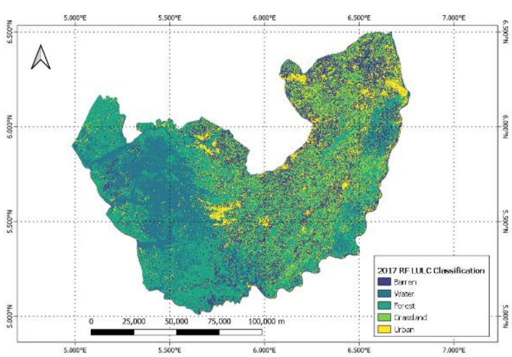

Figure 4.121: 2017 LULC Classification with RF

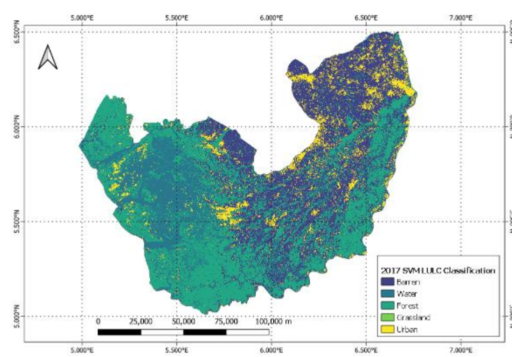

Figure 4.122: 2017 LULC Classification with SVM

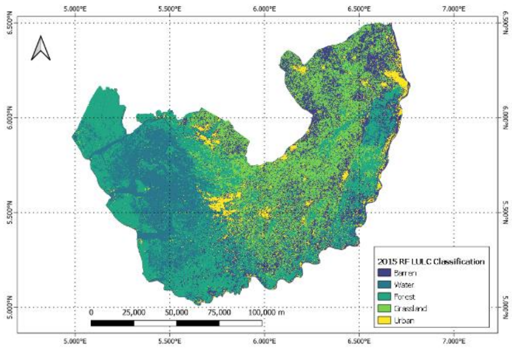

Figure 4.123: 2015 LULC Classification with RF

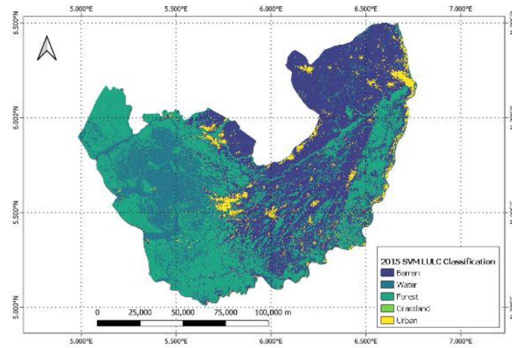

Figure 4.124: 2015 LULC Classification with SVM

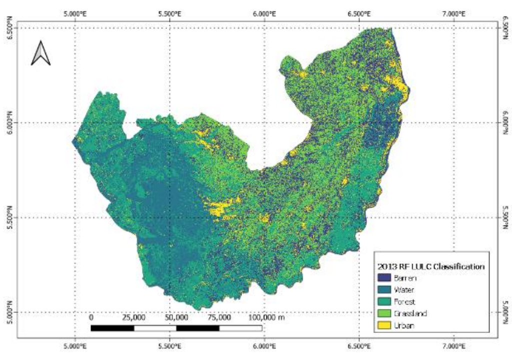

Figure 4.125: 2013 LULC Classification with RF

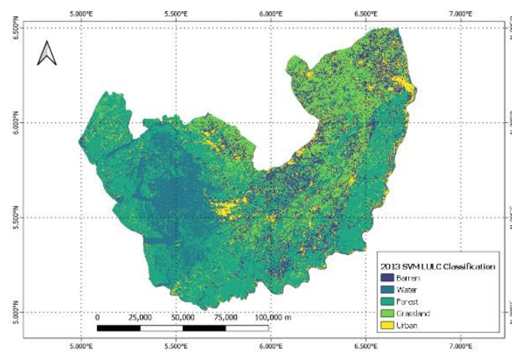

Figure 4.126: 2013 LULC Classification with SVM

I Model Accuracy Assessment

The performance evaluation of classification algorithms is a critical component in assessing the reliability of Land Use and Land Cover (LULC) maps derived from satellite imagery. In this study, both Random Forest (RF) and Support Vector Machine (SVM) classifiers were applied across six different years; 2013, 2015, 2017, 2019, 2021, and 2023, to examine their robustness in accurately classifying land cover types in the study area. The performance of each classifier was assessed using both training and validation accuracy along with Cohen's Kappa coefficient, a metric that accounts for the possibility of agreement occurring by chance (Chicco et al., 2021).

Table 4.11: Summary of the classification performance metrics for RF and SVM across the evaluated years.

Year	Classifier	Training		Validation	
		Accuracy	Kappa	Accuracy	Kappa
2013	Random Forest	0.996134021	0.995131337	0.724696356	0.653754973
	Svm	0.649484536	0.560004503	0.647773279	0.555148429
2015	Random Forest	0.996088657	0.995078928	0.73046875	0.661089793
	Svm	0.640156454	0.545462939	0.71484375	0.635938596
2017	Random Forest	0.996068152	0.995064236	0.738461538	0.667631688
	Svm	0.615989515	0.515405391	0.726923077	0.650305935
2019	Random Forest	0.997416021	0.996752736	0.710843373	0.635876188
	Svm	0.660206718	0.571960266	0.690763052	0.610415735
2021	Random Forest	0.99973213	0.99962112	0.725490196	0.652487102
	Svm	0.692708333	0.614560317	0.694117647	0.613523754
2023	Random Forest	0.990789474	0.988449647	0.813688213	0.762631007
	Svm	0.763157895	0.703516194	0.745247148	0.678078813

From Table 4.11, it revealed that the Random Forest (RF) algorithm consistently demonstrated strong classification performance across all evaluated years. Training accuracies ranged from 99.08% to 99.97%, with Kappa values consistently above 0.988, indicating near-perfect agreement in the training datasets. Although the high training performance might raise concerns about overfitting, the validation results affirm the model's robustness. Validation accuracy ranged from 72.47% in 2013 to 81.37% in 2023, with Kappa values improving steadily from 0.6538 to 0.7626.

The lowest validation accuracy in 2013 may be attributed to poor image quality, seasonal spectral variability, or limited ground-truth data during that period. In subsequent years, the model's performance improved gradually, reflecting advancements in preprocessing techniques and data availability. By 2023, the RF classifier delivered its best validation result, confirming its reliability in land cover classification. These trends align with previous findings highlighting RF's capability to manage high-dimensional and complex remote sensing data effectively (Garcia-Salgado et al., 2020).

In contrast, the Support Vector Machine (SVM) classifier showed moderate to high performance but consistently lagged behind RF. Training accuracy ranged from 61.60% to 76.32%, and validation accuracy from 64.78% in 2013 to 74.52% in 2023. The lowest performance, observed in 2013, may be due to SVM's sensitivity to kernel parameters and imbalanced training data (Li et al., 2023). However, its performance improved over time, with the highest Kappa value of 0.6781 achieved in 2023, suggesting better tuning and data quality in later years.

Overall, Random Forest clearly outperformed SVM in both training and validation metrics across all evaluation periods. This supports literature that emphasizes RF's ensemble learning approach, resistance to overfitting, and high accuracy in complex classification scenarios (Rane et al., 2024). The gradual improvement in validation accuracy for both classifiers also reflects advancements in image resolution, data quality, and model optimization from 2013 to 2023.

Based on these findings, Random Forest was adopted for all subsequent LULC classification tasks in this research, as it demonstrated higher consistency, accuracy, and reliability in mapping land cover dynamics within the study area.

II Land Use/ Land Cover Change Analysis for Delta State

Land cover change analysis provides critical insights into environmental dynamics, anthropogenic influences, and the potential drivers of flooding and ecosystem degradation. Table 4.10 presents the areal extent (in hectares) of major land cover classes, Barren land, Water, Forest, Grassland, and Urban areas, as extracted from the classified maps produced using the Random Forest (RF) classifier for the years 2013, 2015, 2017, 2019, 2021, and 2023.

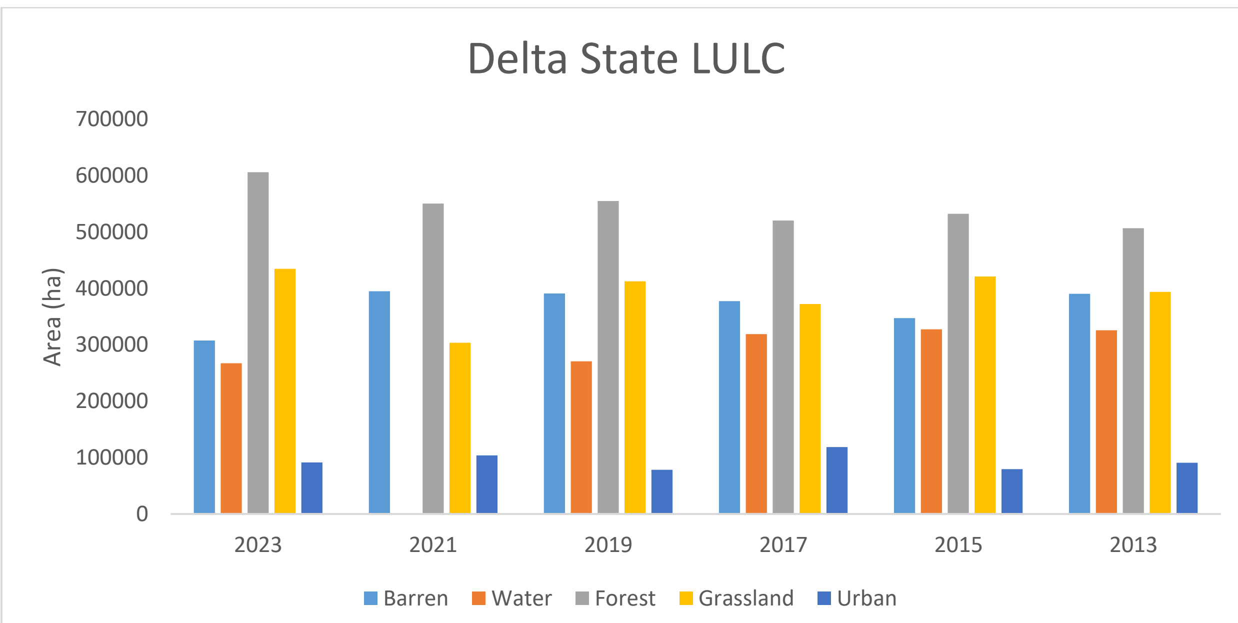

Figure 4.127: Land Use Change Presented in a Horizontal Bar Chart

From Figure 4.127, it was observed that barren land exhibited a fluctuating yet overall declining trend, decreasing from 390,682 ha in 2013 to 307,846 ha in 2023. Although a slight increase was observed between 2015 (347,259 ha) and 2017 (377,215 ha), the general reduction over the decade

(21%) may be attributed to vegetation recovery, reclamation of degraded lands, and improved land management practices (Ekka et al., 2023). These changes could also reflect reclassification of marginal lands into grassland or forest due to seasonal spectral variations or improved image preprocessing.

The area of water bodies remained relatively stable, ranging from 267,514 ha in 2023 to a slightly higher 327,452 ha in 2017. This stability contrasts with earlier assumptions of major fluctuations and suggests more consistent classification of water features across the years. Minor variations may result from seasonal rainfall differences or temporary flood events, as well as the effectiveness of water-sensitive spectral indices (Ouma and Tateishi, 2006).

Forest cover exhibited a steady upward trend, increasing from 506,654 ha in 2013 to 606,349 ha in 2023, with a notable peak in 2023. This growth could reflect a combination of afforestation initiatives, natural regeneration, or improved conservation efforts. These findings support forest transition theories, where regions previously affected by deforestation begin to recover forest cover over time (De Jong, 2010; Mather, 1992). Small fluctuations within the period may relate to forest clearance for agriculture or infrastructure, balanced by regrowth elsewhere. While, Grassland areas demonstrated significant variability, with coverage ranging from 303,731 ha in 2021 to 434,580 ha in 2023. The lowest extent in 2021 could be due to temporary encroachment from agricultural or urban land uses, while the sharp increase by 2023 might be linked to reclassification of cleared forest or abandoned cropland. As transitional land cover, grasslands are highly dynamic and sensitive to both natural and anthropogenic disturbances, as well as seasonal vegetation cycles (Reinermann et al., 2020).

Urban land cover showed moderate fluctuations but remained relatively stable over the decade, increasing slightly from 90,607 ha in 2013 to 91,394 ha in 2023, with the highest extent recorded in 2017 (118,775 ha). The temporary increase in 2017 may have been due to reclassification of bare or impervious surfaces as urban features. Earlier years may also reflect classification errors due to cloud cover or spectral confusion between urban and barren classes (Unger Holtz, 2007). The more stable pattern in later years suggests improved classification accuracy and better delineation of built-up areas.

In summary, the observed LULC dynamics reveal complex interactions between environmental change, land management practices, and classification accuracy. The trends show a gradual shift towards increased vegetation cover (forest and grassland), relatively stable water and urban extents, and a modest reduction in barren land. These findings provide a critical foundation for evaluating hydrological impacts, flood risks, and land use planning in the study area.

4.15.3 LULC Classification for Bayelsa State Using Machine Learning

The land use /land cover analysis result for Bayelsa State are presented in Figure 4.128 to Figure 4.139,

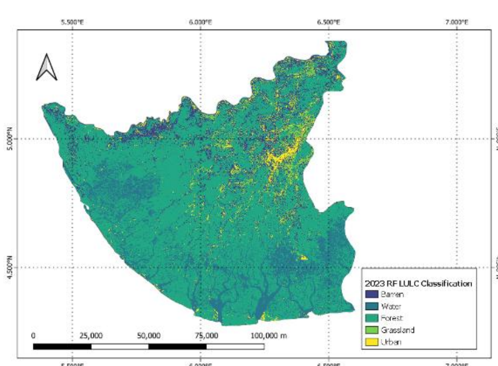

Figure 4.128: 2023 LULC Classification with RF

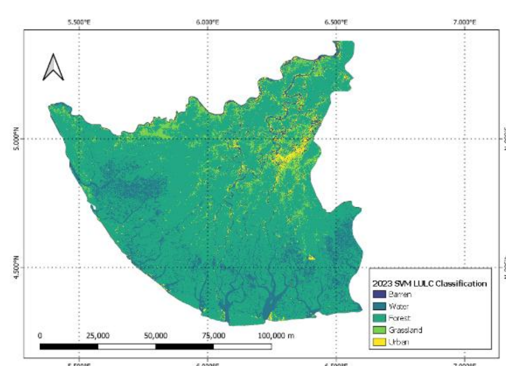

Figure 4.129: 2023 LULC Classification with SVM

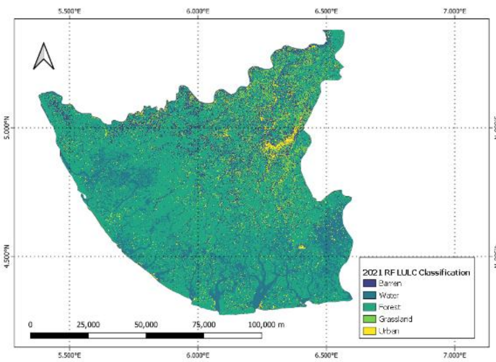

Figure 4.130: 2021 LULC Classification with RF

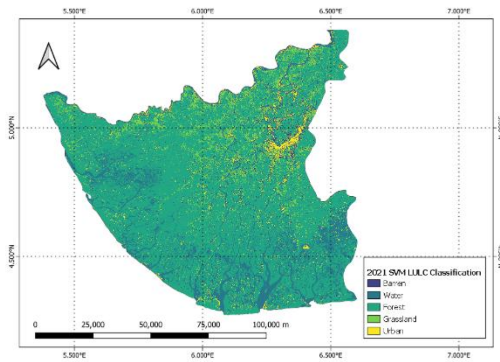

Figure 4.131: 2021 LULC Classification with SVM

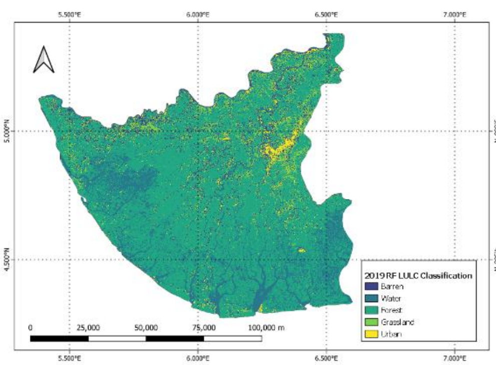

Figure 4.132: 2019 LULC Classification with RF

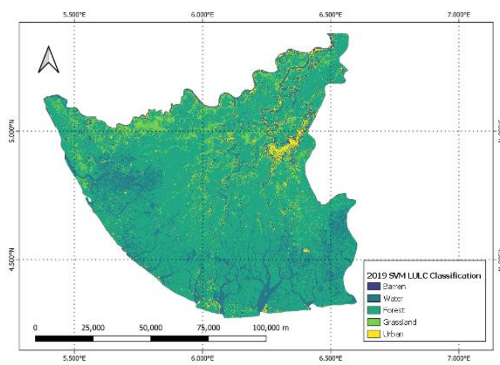

Figure 4.133: 2019 LULC Classification with SVM

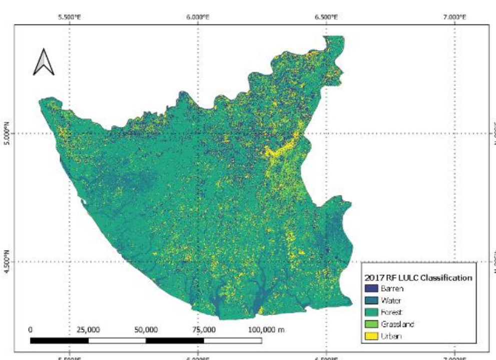

Figure 4.134: 2017 LULC Classification with RF

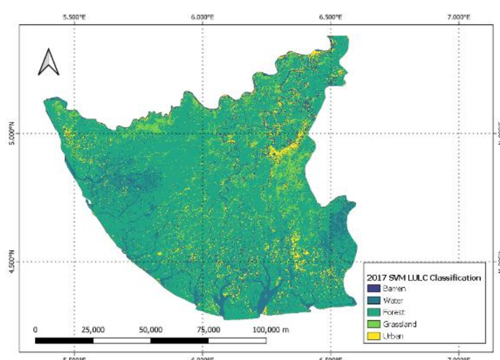

Figure 4.135: 2017 LULC Classification with SVM

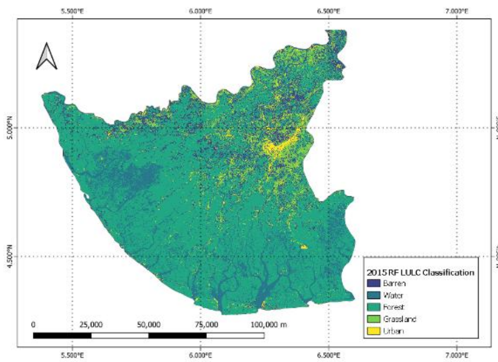

Figure 4.136: 2015 LULC Classification with RF

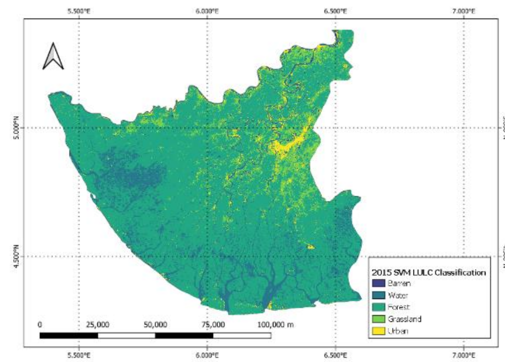

Figure 4.137: 2015 LULC Classification with SVM

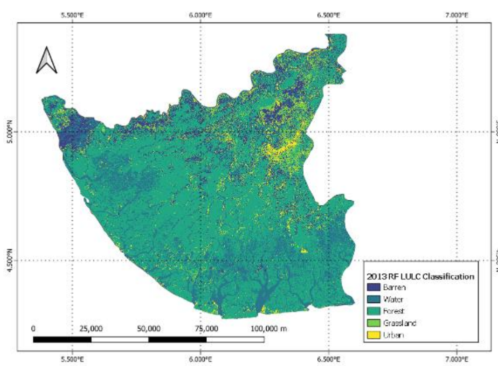

Figure 4.138: 2013 LULC Classification with RF

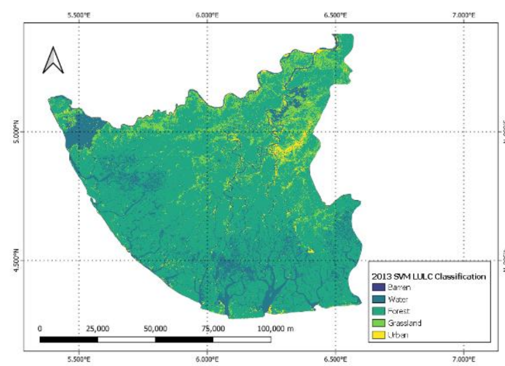

Figure 4.139: 2013 LULC Classification with SVM

I Model Accuracy Assessment

The performance evaluation of classification algorithms is a critical component in assessing the reliability of Land Use and Land Cover (LULC) maps derived from satellite imagery. In this study, both Random Forest (RF) and Support Vector Machine (SVM) classifiers were applied across six different years; 2013, 2015, 2017, 2019, 2021, and 2023, to examine their robustness in accurately classifying land cover types in the study area. The performance of each classifier was assessed using both training and validation accuracy along with Cohen's Kappa coefficient, a metric that accounts for the possibility of agreement occurring by chance (Chicco et al., 2021).

Table 4.12: Summary of the classification performance metrics for RF and SVM across the evaluated years.

Year	Classifier	Training		Validation	
		Accuracy	Kappa	Accuracy	Kappa
2013	Random Forest	0.996088657	0.995104307	0.665271967	0.580720144
	Svm	0.66232073	0.57789894	0.656903766	0.569501801
2015	Random Forest	0.997350993	0.996686169	0.721115538	0.651021908
	Svm	0.675496689	0.593706208	0.689243028	0.610620525
2017	Random Forest	0.994791667	0.993480835	0.68487395	0.603579995
	Svm	0.66015625	0.575456053	0.663865546	0.576776029
2019	Random Forest	0.997275204	0.996591959	0.705882353	0.632333063
	Svm	0.701634877	0.626562899	0.683823529	0.605105004
2021	Random Forest	0.990679095	0.988330018	0.647058824	0.559001556
	Svm	0.69241012	0.612864137	0.623529412	0.537301302
2023	Random Forest	0.990885417	0.98858303	0.731092437	0.663269592
	Svm	0.759114583	0.697679614	0.659663866	0.579239147

Table 4.12 presents the classification performance metrics of the Random Forest (RF) and Support Vector Machine (SVM) algorithms for land use/land cover (LULC) classification from 2013 to 2023. The Random Forest (RF) algorithm consistently exhibited high classification performance across all years. Training accuracies ranged from 99.08% in 2021 to 99.73% in 2015, with Kappa values above 0.988, indicating strong agreement between predicted and actual classes during

training. While the high training accuracies may raise concerns about overfitting, the validation results affirm the robustness of the RF model. Validation accuracies ranged from 64.71% in 2021 to 73.11% in 2023, with Kappa values between 0.5590 and 0.6633.

The lowest validation performance occurred in 2021, where RF achieved only 64.71% accuracy and a Kappa coefficient of 0.559. This dip could be due to poor image quality, increased spectral confusion, or a limited and imbalanced validation dataset for that year. In contrast, the best validation result was observed in 2023, with an accuracy of 73.11% and a Kappa of 0.6633, reinforcing the classifier's reliability and capacity to generalize effectively. These results are consistent with earlier findings that support RF's ability to handle high-dimensional remote sensing datasets and complex classification tasks (Garcia-Salgado et al., 2020).

In comparison, the Support Vector Machine (SVM) classifier performed moderately well but consistently underperformed relative to RF. SVM training accuracies ranged from 66.02% in 2017 to 75.91% in 2023, with Kappa values from 0.5755 to 0.6977. Validation accuracies ranged from 62.35% in 2021 to 68.92% in 2015, and corresponding Kappa values ranged from 0.5373 to 0.6106. Notably, the highest SVM validation Kappa (0.6106) occurred in 2015, suggesting that parameter tuning and data quality had a significant influence on its performance. The consistently lower SVM results may be attributed to the algorithm's sensitivity to kernel selection and challenges in handling class imbalance (Li et al., 2023).

Overall, Random Forest outperformed SVM across all evaluation metrics and years. This aligns with findings in the literature that emphasize RF's ensemble learning structure and its resistance to overfitting in complex, nonlinear classification problems (Rane et al., 2024). Moreover, the general improvement in validation results over time for both classifiers can be linked to advances in image preprocessing, increased availability of high-quality satellite imagery, and better training data.

Given its superior performance, Random Forest was selected for all subsequent LULC classification tasks in this study. Its consistency, accuracy, and robustness make it a reliable tool for assessing land cover dynamics in the study area over time.

II Land Use/ Land Cover Change Analysis for Bayelsa State

Land cover change analysis provides critical insights into environmental dynamics, anthropogenic influences, and the potential drivers of flooding and ecosystem degradation. Table 4.11 presents the areal extent (in hectares) of major land cover classes, Barren land, Water, Forest, Grassland, and Urban areas, as extracted from the classified maps produced using the Random Forest (RF) classifier for the years 2013, 2015, 2017, 2019, 2021, and 2023.

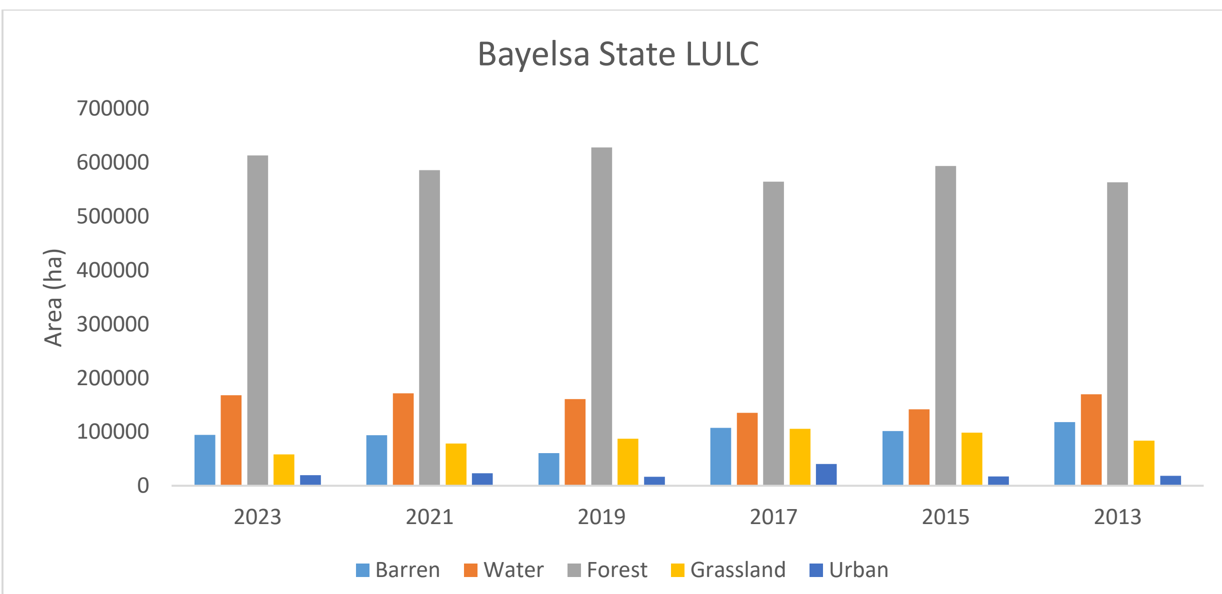

Figure 4.140: Land Use Change presented in a horizontal bar chart

Figure 4.140 illustrates the land use/land cover (LULC) distribution in Bayelsa State across six-time period from 2013 to 2023. From the chart, forest consistently occupied the largest land area throughout the decade, ranging between approximately 560,000 ha to 630,000 ha, with the highest extent recorded in 2019. This persistent dominance suggests that Bayelsa remains heavily forested, possibly due to its location within the Niger Delta and the presence of protected or less-disturbed swamp forest zones. The relatively stable forest extent also implies ongoing natural regeneration and/or effective conservation measures (De Jong, 2010).

Water bodies followed a similar pattern of stability, occupying between 150,000 ha and 180,000 ha across all years. The peak water extent was observed in 2021, while 2013 and 2023 reported slightly lower values. These minor fluctuations could be attributed to seasonal rainfall differences, wetland inundation levels, or improved discrimination of water pixels due to the use of indices like NDWI or MNDWI (Ouma and Tateishi, 2006).

Barren land showed a clear decreasing trend, dropping from about 130,000 ha in 2013 to below 90,000 ha in 2023. Despite slight increases in 2017 and 2021, the overall decline may be linked to revegetation, land recovery efforts, or transitions into more productive land uses such as agriculture or grassland (Ekka et al., 2023).

Grassland areas exhibited significant temporal variability. Coverage dipped in 2021 but peaked in 2023 at over 110,000 ha, likely due to classification of cleared or fallow lands as grassland, possibly following logging or agricultural rotation. As transitional cover, grasslands are sensitive to seasonal vegetation growth and land disturbance cycles (Reinermann et al., 2020).

Urban land cover, although occupying the smallest area among the classes, remained fairly stable across the decade. From about 30,000 ha in 2013, it showed a slight rise in 2017 and 2019, peaking above 40,000 ha, before dropping slightly again by 2023. These fluctuations may be due to differences in classification accuracy, as early years might have misclassified bare lands or compacted soils as urban areas. Later improvements in classification methods likely provided more accurate delineation of built-up zones (Unger Holtz, 2007).

It can be deducing that the LULC dynamics in Bayelsa indicate an overall stability in forest and water coverage, a decline in barren land, and fluctuations in grassland and urban areas. These trends reflect a complex interplay of environmental factors, land use policies, and classification advancements, and provide essential context for flood risk management, ecological conservation, and sustainable land planning in the region.

4.15.4 LULC Classification for Rivers State using Machine Learning

The land use /land cover analysis result for Rivers State is presented as follows in Figure 4.141 to Figure 4.152,

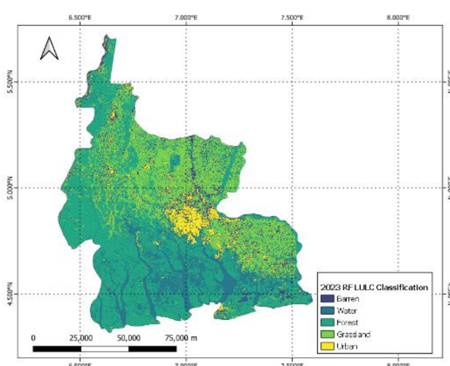

Figure 4.141: 2023 LULC Classification with RF

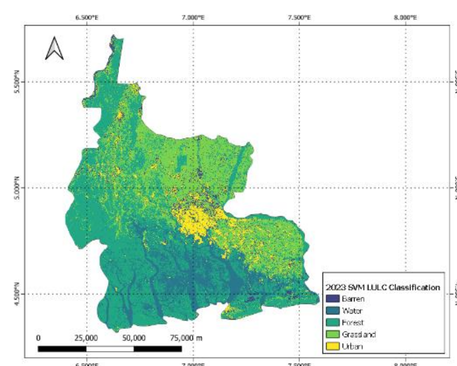

Figure 4.142: 2023 LULC Classification with SVM

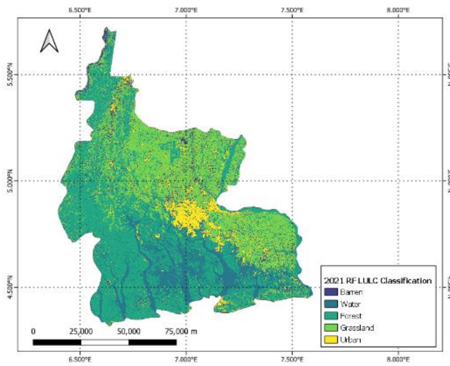

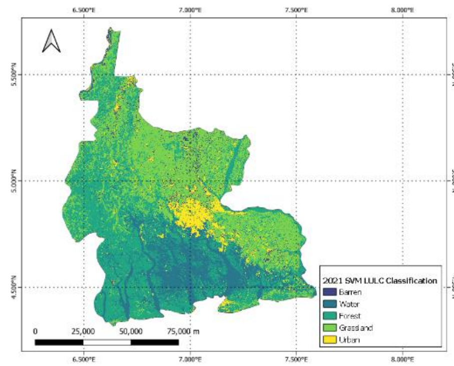

Figure 4.143: 2021 LULC Classification with RF

Figure 4.144: 2021 LULC Classification with SVM

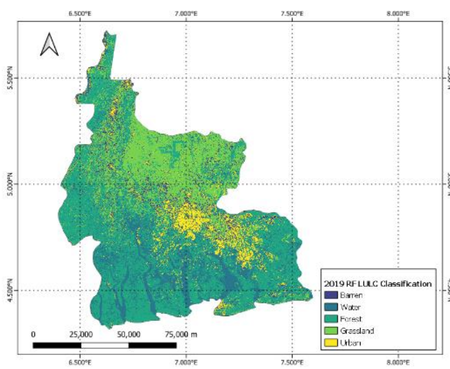

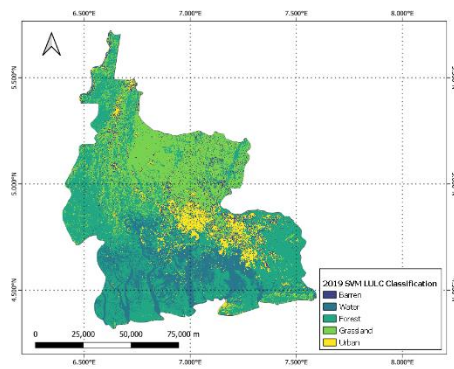

Figure 4.145: 2019 LULC Classification with RF

Figure 4.146: 2019 LULC Classification with SVM

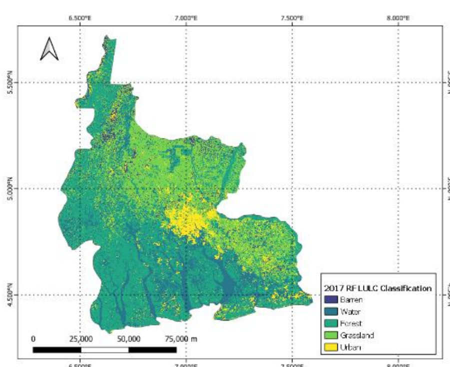

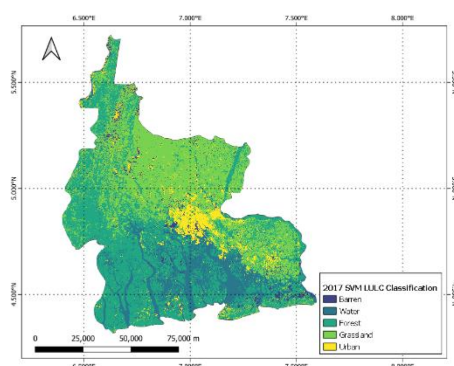

Figure 4.147: 2017 LULC Classification with RF

Figure 4.148: 2017 LULC Classification with SVM

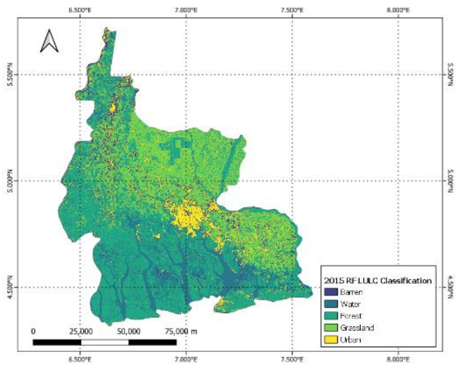

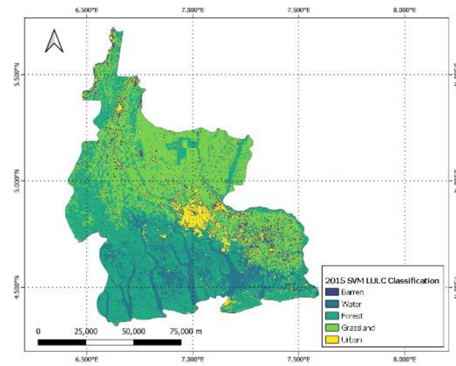

Figure 4.149: 2015 LULC Classification with RF   Figure 4.150: 2015 LULC Classification with SVM

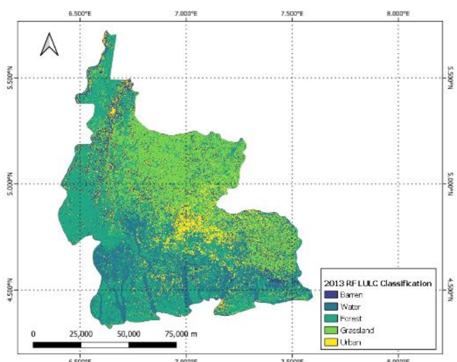

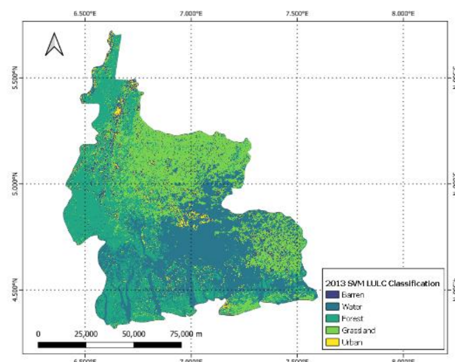

Figure 4.151: 2013 LULC Classification with RF   Figure 4.152: 2013 LULC Classification with SVM

I Model Accuracy Assessment

The performance evaluation of classification algorithms is a critical component in assessing the reliability of Land Use and Land Cover (LULC) maps derived from satellite imagery. In this study, both Random Forest (RF) and Support Vector Machine (SVM) classifiers were applied across six different years; 2013, 2015, 2017, 2019, 2021, and 2023, to examine their robustness in accurately classifying land cover types in the study area. The performance of each classifier was assessed using both training and validation accuracy along with Cohen's Kappa coefficient, a metric that accounts for the possibility of agreement occurring by chance (Chicco et al., 2021).

Table 4.13: Summary of the classification performance metrics for RF and SVM across the evaluated years.

Year	Classifier	Training		Validation	
		Accuracy	Kappa	Accuracy	Kappa
2013	Random Forest	0.991576414	0.98943756	0.587628866	0.483973933
	Svm	0.593261131	0.487906799	0.536082474	0.420780255
2015	Random Forest	0.990532544	0.988141121	0.754512635	0.69287962
	Svm	0.753846154	0.691500827	0.729241877	0.662469537
2017	Random Forest	0.993975904	0.992455917	0.691780822	0.612286448
	Svm	0.66746988	0.58431095	0.729452055	0.659522966
2019	Random Forest	0.997671711	0.997085428	0.69581749	0.616555193
	Svm	0.668218859	0.584397881	0.66539924	0.578686764
2021	Random Forest	0.993111366	0.991368803	0.74501992	0.680642532
	Svm	0.711825488	0.638876363	0.737051793	0.670754248
2023	Random Forest	0.994103774	0.992614463	0.755474453	0.693251124
	Svm	0.761792453	0.701782211	0.693430657	0.615387186

Table 4.13 presents the classification performance of Random Forest (RF) and Support Vector Machine (SVM) classifiers across multiple years. The Random Forest (RF) algorithm consistently demonstrated strong classification performance over the study period. Training accuracies ranged from 99.05% in 2015 to 99.77% in 2019, with Kappa values consistently above 0.988, indicating very strong agreement between the predicted and actual training labels. While such high training

accuracies might initially suggest overfitting, the validation results reflect good generalization capability.

The lowest validation accuracy for RF was recorded in 2013 (58.76%) with a Kappa coefficient of 0.4840, likely due to low-quality imagery, seasonal spectral noise, or limited training samples in that year. However, significant improvements were noted from 2015 onward. For instance, the validation accuracy rose to 75.55% in 2023, with a corresponding Kappa of 0.6933, marking the highest performance for RF in the evaluated years. These improvements reflect better classifier optimization, higher-resolution data, and more consistent classification processes.

The SVM classifier, while showing moderate to good performance, consistently lagged behind RF. Its training accuracies ranged from 59.33% in 2013 to 76.18% in 2023, and validation accuracies ranged from 53.61% in 2013 to 73.93% in 2021. The corresponding Kappa values ranged from 0.4208 to 0.6708, indicating fair to substantial agreement. The lowest SVM validation performance occurred in 2013, likely due to kernel sensitivity and limited optimization, which are common challenges with SVM in multi-class remote sensing problems (Li et al., 2023). However, the notable improvement in 2021 and 2023, with Kappa values of 0.6708 and 0.6154 respectively, suggests better parameter tuning and training data quality in recent years.

Overall, Random Forest clearly outperformed SVM across all evaluation years in both training and validation phases. This superiority supports existing literature highlighting RF's ability to resist overfitting through ensemble learning and its adaptability to heterogeneous and high-dimensional datasets (Rane et al., 2024). The steady increase in validation accuracy over the years for both models also reflects improvements in satellite imagery quality, preprocessing techniques, and classifier calibration.

II Land Use/ Land Cover Change Analysis for Rivers State

Land cover change analysis provides critical insights into environmental dynamics, anthropogenic influences, and the potential drivers of flooding and ecosystem degradation. Table 4.7 presents the areal extent (in hectares) of major land cover classes, Barren land, Water, Forest, Grassland, and Urban areas, as extracted from the classified maps produced using the Random Forest (RF) classifier for the years 2013, 2015, 2017, 2019, 2021, and 2023.

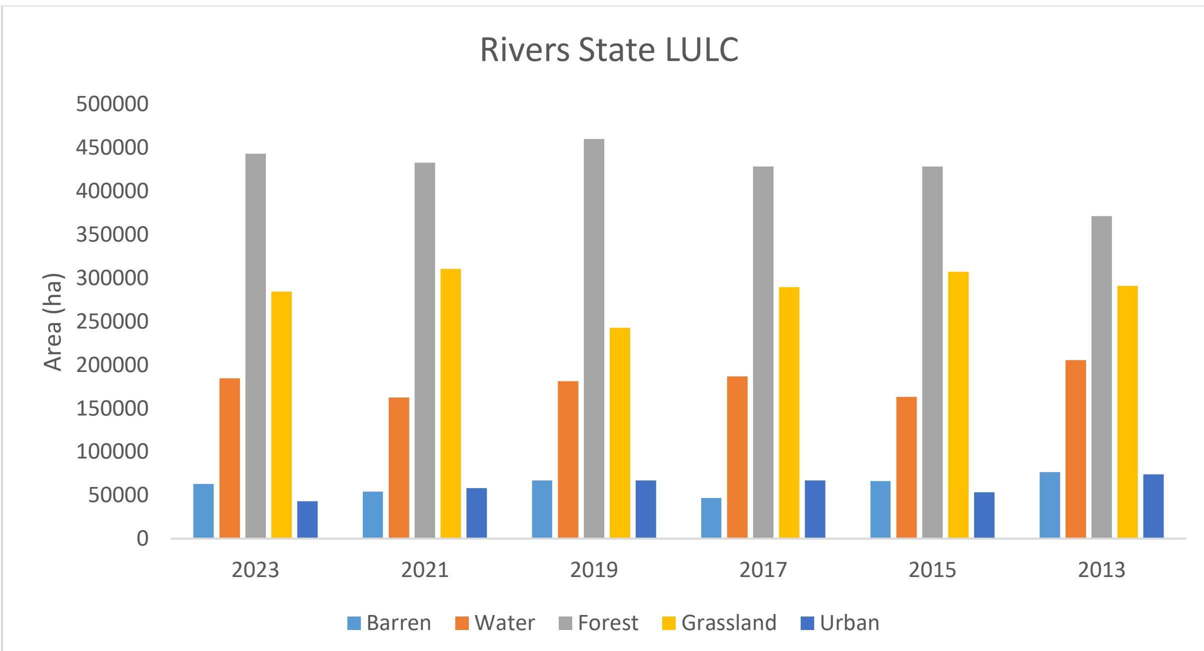

Figure 4.153: Land Use Change presented in a horizontal bar chart

From Figure 4.153, it was observed that barren land exhibited a fluctuating yet overall declining trend, decreasing from 390,682 ha in 2013 to 307,846 ha in 2023. Although a slight increase was observed between 2015 (347,259 ha) and 2017 (377,215 ha), the general reduction over the decade (21%) may be attributed to vegetation recovery, reclamation of degraded lands, and improved land management practices (Ekka et al., 2023). These changes could also reflect reclassification of marginal lands into grassland or forest due to seasonal spectral variations or improved image preprocessing.

The area of water bodies remained relatively stable, ranging from 267,514 ha in 2023 to a slightly higher 327,452 ha in 2017. This stability contrasts with earlier assumptions of major fluctuations and suggests more consistent classification of water features across the years. Minor variations may result from seasonal rainfall differences or temporary flood events, as well as the effectiveness of water-sensitive spectral indices (Ouma and Tateishi, 2006).

Forest cover exhibited a steady upward trend, increasing from 506,654 ha in 2013 to 606,349 ha in 2023, with a notable peak in 2023. This growth could reflect a combination of afforestation initiatives, natural regeneration, or improved conservation efforts. These findings support forest transition theories, where regions previously affected by deforestation begin to recover forest cover over time (De Jong, 2010). Small fluctuations within the period may relate to forest clearance for agriculture or infrastructure, balanced by regrowth elsewhere. While, Grassland areas demonstrated significant variability, with coverage ranging from 303,731 ha in 2021 to 434,580 ha in 2023. The lowest extent in 2021 could be due to temporary encroachment from agricultural or urban land uses, while the sharp increase by 2023 might be linked to reclassification of cleared forest or abandoned cropland. As transitional land cover, grasslands are highly dynamic and sensitive to both natural and anthropogenic disturbances, as well as seasonal vegetation cycles (Reinermann et al., 2020).

Urban land cover showed moderate fluctuations but remained relatively stable over the decade, increasing slightly from 90,607 ha in 2013 to 91,394 ha in 2023, with the highest extent recorded in 2017 (118,775 ha). The temporary increase in 2017 may have been due to reclassification of bare or impervious surfaces as urban features. Earlier years may also reflect classification errors due to cloud cover or spectral confusion between urban and barren classes (Unger Holtz, 2007). The more stable pattern in later years suggests improved classification accuracy and better delineation of built-up areas.

In summary, the observed LULC dynamics reveal complex interactions between environmental change, land management practices, and classification accuracy. The trends show a gradual shift towards increased vegetation cover (forest and grassland), relatively stable water and urban extents, and a modest reduction in barren land. These findings provide a critical foundation for evaluating hydrological impacts, flood risks, and land use planning in the study area.

4.16 Flood Pattern Detection

4.16.1 Edo State Flood Pattern Analysis

Flood pattern analysis in Edo State was conducted using a suite of remote sensing-derived flood indices over a 24-year period (2000–2023). Each index was assessed using both temporal time series charts (Figure 4.153) and spatial annual average maps (Figures 4.154–4.159), enabling a multidimensional understanding of surface water dynamics and flood behavior. The integration of temporal trends with spatial distribution enhances the detection of flood-prone areas, wetland stability, vegetation-water interactions, and hydrological anomalies across the state.

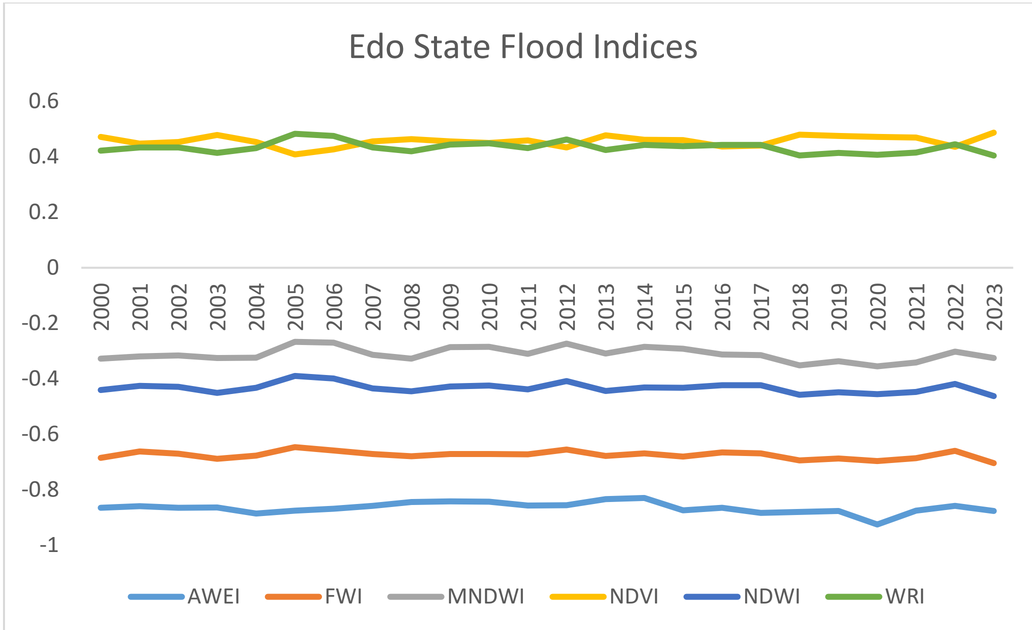

Figure 4.153: Time Series Chart of Multi-Temporal Flood Indices for Edo State

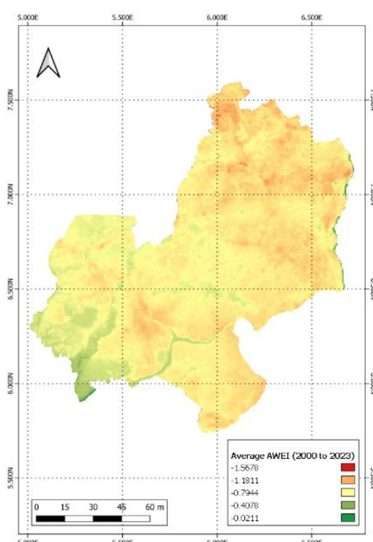

Figure 4 154: Spatial Annual Average of Automated Water Extraction Index (AWEI) for 2000 to 2023

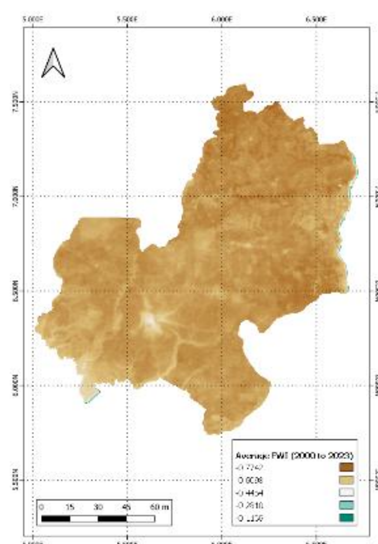

Figure 4.155: Spatial Annual Average of Flood Water Index (FWI) for 2000 to 2023

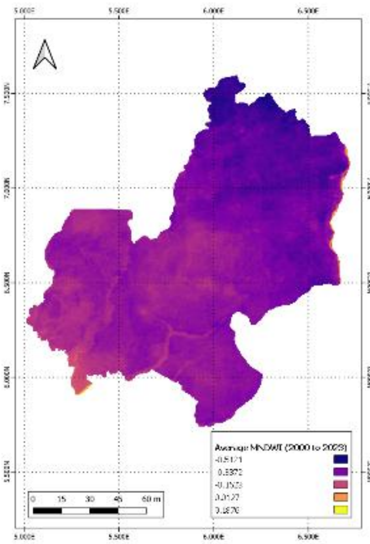

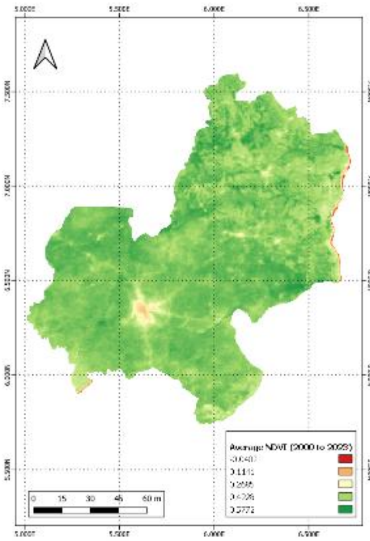

Figure 4.156: Spatial Annual Average of Modified Normalized Difference Water Index (MNDWI) for 2000 to 2023

Figure 4.157: Spatial Annual Average of Normalized Difference Vegetation Index (NDVI) for 2000 to 2023

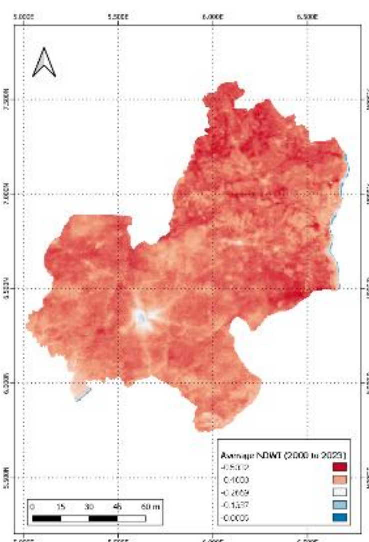

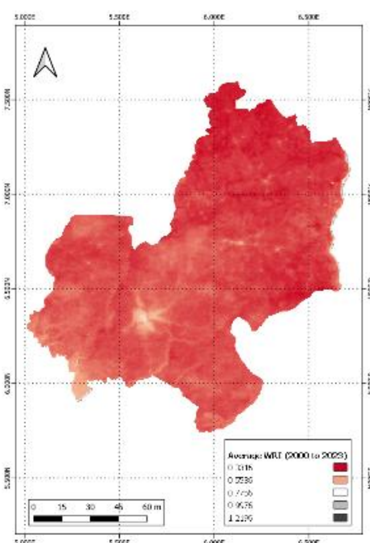

Figure 4.158: Spatial Annual Average of Normalized Difference Water Index (NDWI) for 2000 to 2023

Figure 4.159: Spatial Annual Average of Water Ratio Index (WRI) for 2000 to 2023

I Automated Water Extraction Index (AWEI)

The time series of AWEI shows a consistently low and stable trend, with values generally ranging between –0.8 and –0.9. This indicates a persistent difficulty in detecting open water bodies over time, possibly due to vegetation cover or the prevalence of narrow water channels that are not easily captured by the index at this scale. Spatially, the AWEI map reveals higher values in the northeastern and central parts of Edo State, where surface water is likely more persistent due to the proximity to rivers and wetlands. In contrast, the western and southern areas have highly negative AWEI values (below –0.5), suggesting better-drained or elevated terrain (Feyisa *et. al*., 2014). This integrated trend indicates that while certain zones are recurrently flood-prone, the state is witnessing a long-term consistency in water surface detectability, which may signal stable ecosystem conditions.

II Flood Water Index (FWI)

The FWI values are consistently low and negative across the 24-year period, generally ranging from –0.6 to –0.7. This consistent trend suggests that the index did not capture any significant, widespread positive flood events in the time series chart, possibly due to the scale of analysis or the specific characteristics of flooding in the region. The spatial pattern, however, reveals concentrated high values along river corridors and lowland basins, especially in the southeastern zones. This aligns with regions typically inundated during wet seasons. FWI effectively captures localized inundation zones, and its application strengthens event-based flood detection, especially in urbanizing floodplains (Mohammadi et al., 2017).

III Modified Normalized Difference Water Index (MNDWI)

The MNDWI time series is dominated by negative values, consistently fluctuating between –0.2 and –0.4. This indicates limited open water detection and is likely reflective of a landscape where water bodies are often obscured or narrow. Spatial distribution shows more moderate values in floodplain areas, while uplands record very low MNDWI values. This supports its sensitivity to water presence even under vegetative interference (Mondal et al., 2024; Xu et al., 2018). MNDWI is effective in both temporal and spatial detection of flooding, especially in environments with mixed land cover. Its consistent negative response throughout the period suggests that the index is better suited for mapping flood-prone areas rather than detecting significant flood events in this context.

IV Normalized Difference Vegetation Index (NDVI)

The NDVI values are consistently high and positive throughout the period, with a range of approximately 0.4 to 0.5. This indicates a consistently healthy and dense vegetation cover in Edo State. A slight decrease in NDVI values, such as the one observed around 2020, could be linked to vegetation stress due to increased waterlogging or other environmental factors (Mahmud, 2022). Spatially, the map shows lower NDVI values in river basins and central valleys, while higher values are seen in the northern and western uplands. This suggests that vegetation condition serves as a proxy for inundation vulnerability. NDVI serves as an indirect flood indicator by reflecting vegetation health and land cover disruption during floods, as supported by Mahmud, (2022). Its consistent trend throughout the period validates its inclusion in long-term flood analysis.

V Normalized Difference Water Index (NDWI)

The NDWI values are consistently negative, generally ranging from –0.4 to –0.5. This indicates limited surface water detection and is consistent with the other water-related indices. The index is particularly effective in capturing water spread over vegetated or bare landscapes (Tran et al., 2022). The spatial map shows high NDWI values along river systems and low-lying regions, where increased soil moisture and water retention capacity are consistent with known flood zones. NDWI is robust in both spatial and temporal detection of flooding, especially during intense rainfall years (Tran et al., 2022). Its consistent negative profile in the time series highlights its utility for mapping areas of high moisture and potential water presence rather than temporary flood events.

VI Water Ratio Index (WRI)

WRI shows consistently high values across the dataset, similar to the NDVI, with a range of approximately 0.4 to 0.5. Its temporal profile is smooth, indicating stable conditions over the period but remains sensitive to high moisture periods (Penna et al., 2013). The spatial distribution shows elevated WRI values in the central and southeastern regions, correlating with floodplain areas and consistent moisture presence. These areas are likely to remain persistently vulnerable to waterlogging. WRI is a complementary index that strengthens the detection of sustained moisture presence and flood-prone zones, as emphasized by Penna et al., (2013). When combined with other indices, it improves flood vulnerability mapping.

Across all indices, the temporal analysis shows a general stability in flood-related conditions from 2000 to 2023. Spatially, the central basin and southeastern floodplains of Edo State consistently exhibit higher flood index values, confirming their vulnerability. This multi-index approach corroborates the utility of integrating spectral indices for robust flood monitoring and planning (Feyisa *et. al*., 2014; Xu, 2006; Gao, 1996).

4.16.2 Delta State Flood Pattern Analysis

Flood pattern analysis in Delta State was conducted using a suite of remote sensing-derived flood indices over a 24-year period (2000–2023). Each index was assessed using both temporal time series charts (Figure 4.160) and spatial annual average maps (Figures 4.161–4.166), enabling a multidimensional understanding of surface water dynamics and flood behavior. The integration of temporal trends with spatial distribution enhances the detection of flood-prone areas, wetland stability, vegetation-water interactions, and hydrological anomalies across the state.

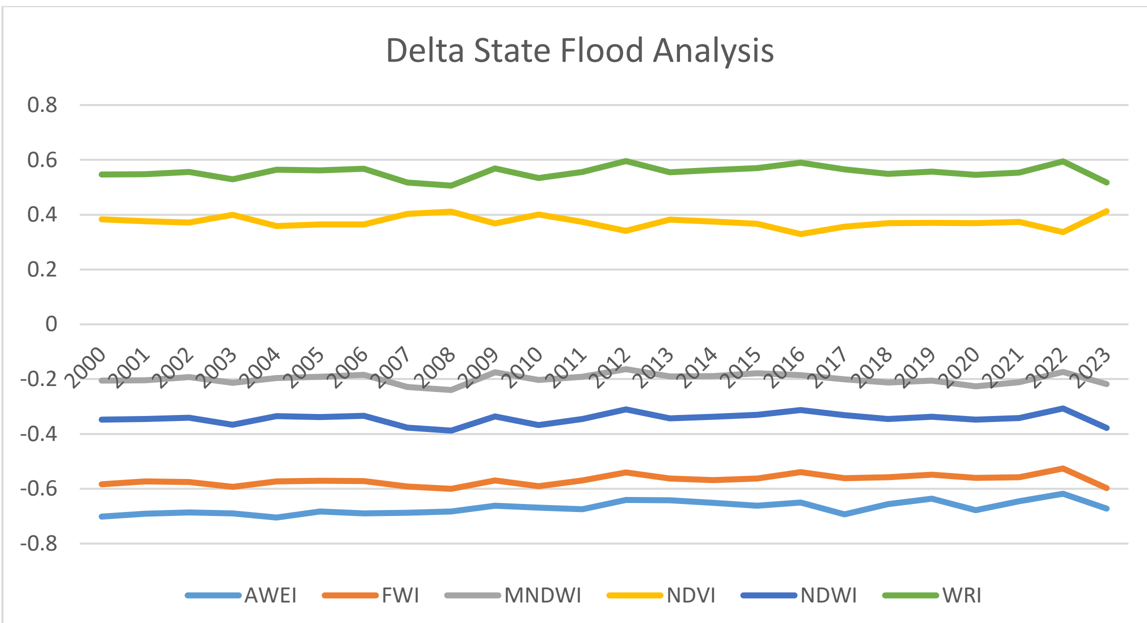

Figure 4.160: Time Series Chart of Multi-Temporal Flood Indices for Delta State

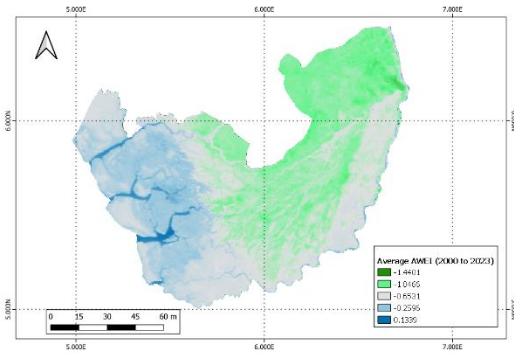

Figure 4.161: Spatial Annual Average of Automated Water Extraction Index (AWEI) for 2000 to 2023

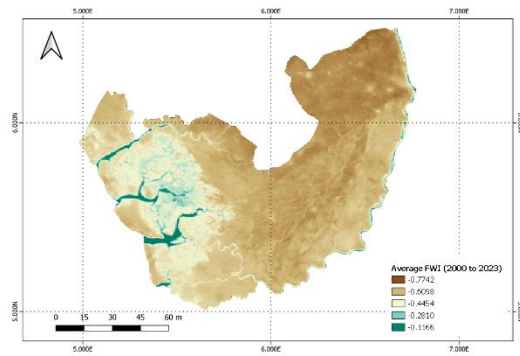

Figure 4.162: Spatial Annual Average of Flood Water Index (FWI) for 2000 to 2023

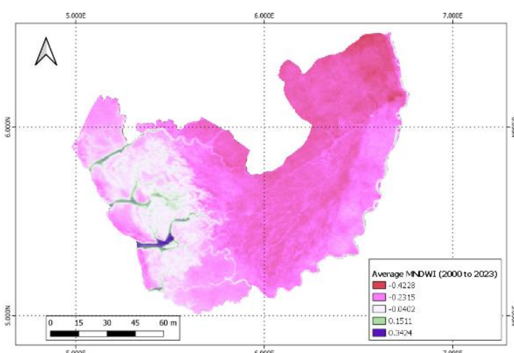

Figure 4.163: Spatial Annual Average of Modified Normalized Difference Water Index (MNDWI) for 2000 to 2023

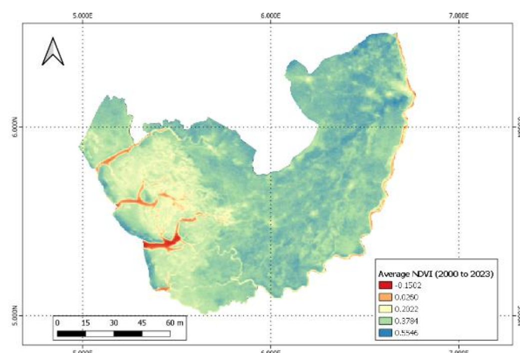

Figure 4.164: Spatial Annual Average of Normalized Difference Vegetation Index (NDVI) for 2000 to 2023

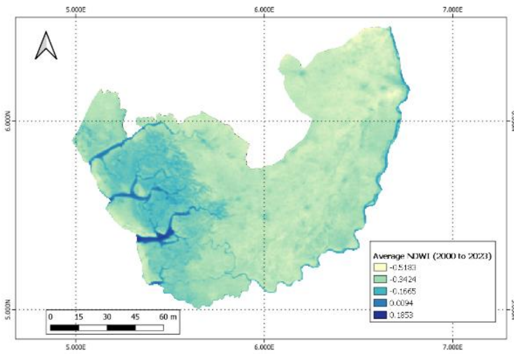

Figure 4.165: Spatial Annual Average of Normalized Difference Water Index (NDWI) for 2000 to 2023

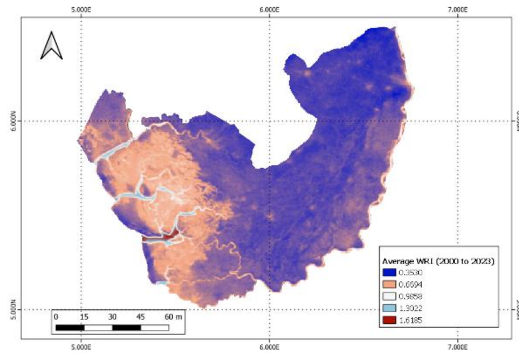

Figure 4.166: Spatial Annual Average of Water Ratio Index (WRI) for 2000 to 2023

I Automated Water Extraction Index (AWEI)

The time series of AWEI reveals a consistently low and stable trend, with values generally ranging between –0.6 and –0.7. This indicates a persistent difficulty in detecting open water bodies over time, likely due to factors like dense vegetation or narrow, non-detectable water features. Spatially, higher AWEI values are concentrated in the northeastern and central regions of Delta State, likely due to the proximity to rivers and wetlands. Conversely, the western and southern parts exhibit more negative values (below –0.5), suggesting well-drained or elevated terrain (Feyisa *et. al*., 2014). This integrated trend indicates that while certain zones are recurrently flood-prone, the state is witnessing a long-term consistency in water surface detectability.

II Flood Water Index (FWI)

The FWI values are consistently low and negative across the 24-year period, generally ranging from –0.55 to –0.6. This consistent trend suggests that the index did not capture any significant, widespread positive flood events in the time series chart, possibly due to the scale of analysis or the specific characteristics of flooding in the region. Spatially, elevated FWI values are observed along major river channels and in lowland basins, especially in the southeastern regions, areas known to be vulnerable to seasonal inundation. This index demonstrates strong capability in capturing both temporal flood surges and mapping flood-prone landscapes, especially in areas experiencing rapid urban expansion (Mohammadi et al., 2017).

III Modified Normalized Difference Water Index (MNDWI)

The MNDWI series shows predominantly negative values, consistently fluctuating between –0.2 and –0.3. This indicates limited open water detection and is likely reflective of a landscape where water bodies are often obscured or narrow. The spatial distribution indicates moderate values within floodplains and very low values in upland zones, reflecting MNDWI's sensitivity to water in mixed land cover conditions (Xu, 2006; Mondal *et. al*., 2024). MNDWI proves useful for detecting surface water even under vegetative cover, supporting its role in multi-index flood detection strategies.

IV Normalized Difference Vegetation Index (NDVI)

The NDVI values are consistently high and positive throughout the period, with a range of approximately 0.35 to 0.45. This indicates a consistently healthy and dense vegetation cover in Delta State. A slight decrease in NDVI values, such as the one observed around 2020, could be linked to vegetation stress due to increased waterlogging or other environmental factors (Mahmud, 2022). Spatially, river basins and central valley's show low NDVI values, while the northern and western uplands display higher values. NDVI serves as an indirect indicator of flooding by highlighting vegetation disturbance, enhancing its value in understanding flood impacts on ecological systems.

V Normalized Difference Water Index (NDWI)

The NDWI values are consistently negative, generally ranging from –0.35 to –0.4. This indicates limited surface water detection and is consistent with the other water-related indices. The index is particularly effective for detecting water in both vegetated and bare soil areas (Tran et al., 2022). The spatial map shows elevated NDWI values along river systems and low-lying flood zones. This index is highly effective in detecting surface water in various land cover types and is valuable for capturing water distribution in flood-prone regions (Tran et al., 2022).

VI Water Ratio Index (WRI)

The WRI shows consistently high values across the years, similar to the NDVI, with a range of approximately 0.5 to 0.6. Its temporal profile is smooth, indicating stable conditions over the period but remains sensitive to high moisture periods (Penna et al., 2013). Spatially, WRI values are elevated in the central and southeastern regions, consistent with known floodplains and zones with high water retention. WRI contributes to identifying areas of sustained wetness and complements other indices in flood vulnerability mapping.

Across all indices, the temporal analysis shows a general stability in flood-related conditions from 2000 to 2023. Spatially, the central basin and southeastern floodplains of Delta State consistently exhibit higher flood index values, confirming their vulnerability. This multi-index approach validates the application of combined spectral indices for robust flood risk assessment, early warning systems, and planning (Chukwurah et al., 2022; Gandhi et al., 2015; Odunsi and Rienow, 2024; Palmer et al., 2023; Tran et al., 2022; Wani et al., 2009b)

4.16.3 Bayelsa State Flood Pattern Analysis

Flood pattern analysis in Bayelsa State was conducted using a suite of remote sensing-derived flood indices over a 24-year period (2000–2023). Each index was assessed using both temporal time series charts (Figure 4.167) and spatial annual average maps (Figures 4.168–4.173), enabling a multidimensional understanding of surface water dynamics and flood behavior. The integration of temporal trends with spatial distribution enhances the detection of flood-prone areas, wetland stability, vegetation-water interactions, and hydrological anomalies across the state.

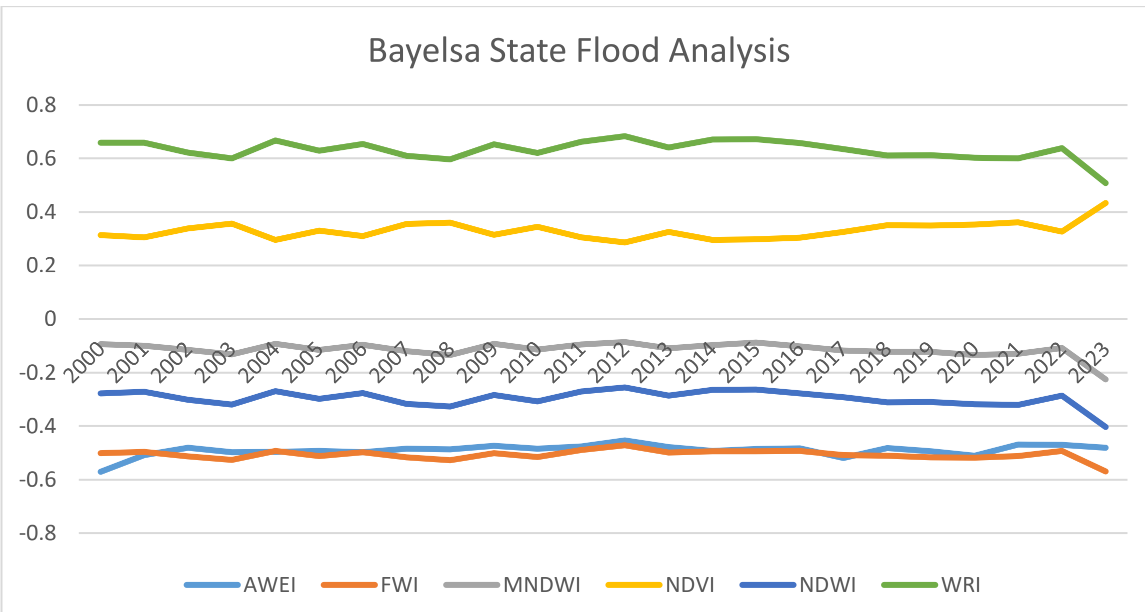

Figure 4.167: Time Series Chart of Multi-Temporal Flood Indices for Delta State

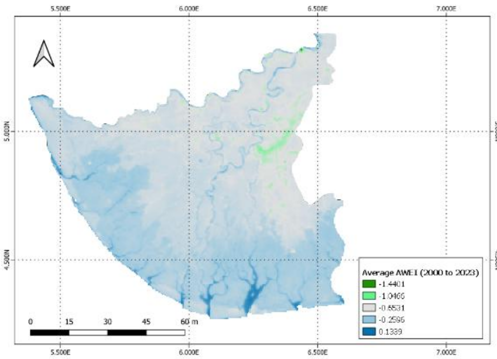

Figure 4.168: Spatial Annual Average of Automated Water Extraction Index (AWEI) for 2000 to 2023

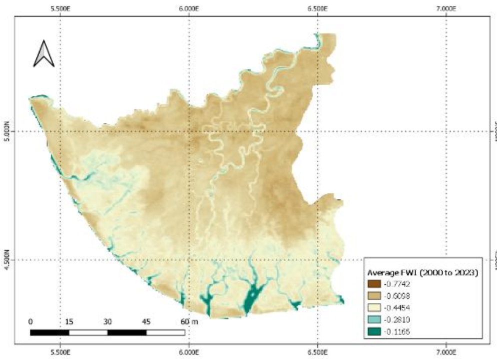

Figure 4.169: Spatial Annual Average of Flood Water Index (FWI) for 2000 to 2023

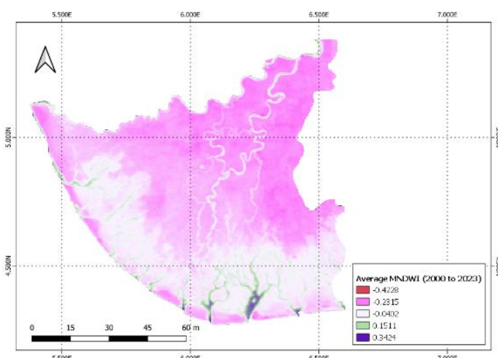

Figure 4.170: Spatial Annual Average of Modified Normalized Difference Water Index (MNDWI) for 2000 to 2023

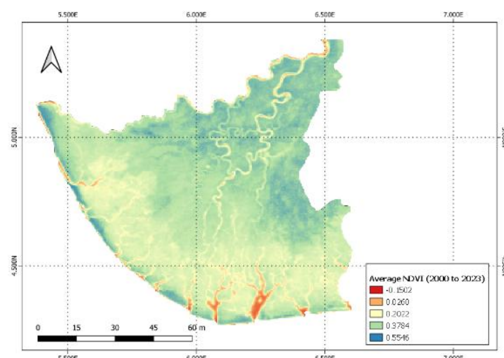

Figure 4.171: Spatial Annual Average of Normalized Difference Vegetation Index (NDVI) for 2000 to 2023

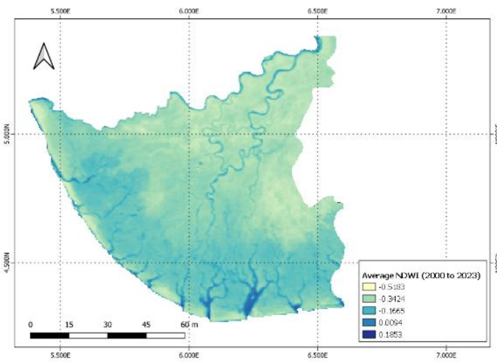

Figure 4.172: Spatial Annual Average of Normalized Difference Water Index (NDWI) for 2000 to 2023

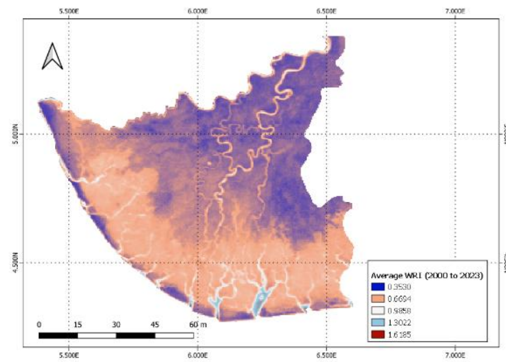

Figure 4.173: Spatial Annual Average of Water Ratio Index (WRI) for 2000 to 2023

I Automated Water Extraction Index (AWEI)

The AWEI time series shows a consistently low and negative trend, with values generally ranging between –0.55 and –0.65. This indicates a persistent difficulty in detecting open water bodies over time, suggesting that water features in the state may be narrow, temporary, or obscured by vegetation. Spatially, higher AWEI values appear in the northeastern and central regions of Bayelsa State, indicating more persistent surface water due to the presence of rivers and wetlands. Conversely, the western and southern regions exhibit highly negative values (below –0.5), suggesting better-drained or higher terrain. This pattern reflects a consistent low detectability of water surfaces across Bayelsa, which may signal stable ecological conditions.

II Flood Water Index (FWI)

FWI values are consistently low and negative across the 24-year period, generally ranging from –0.5 to –0.6. This trend suggests that the index did not capture any significant, widespread positive flood events in the time series chart, possibly due to the scale of analysis or the specific characteristics of flooding in the region. Spatially, elevated FWI values are concentrated along river networks and lowland basins, especially in southeastern parts of the state, areas typically inundated during the wet season. FWI is effective for detecting temporal flood spikes and delineating spatial inundation zones, making it highly useful for monitoring flood dynamics in vulnerable landscapes (Mohammadi et al., 2017).

III Modified Normalized Difference Water Index (MNDWI)

The MNDWI time series is largely negative, with values consistently fluctuating between –0.1 and –0.2. This indicates limited open water detection and is likely reflective of a landscape where water bodies are often obscured or narrow. The spatial distribution shows moderate values in floodplain zones and low values in upland or well-drained areas. This confirms MNDWI's sensitivity to water bodies even under vegetation cover (Xu, 2006; Mondal *et. al*., 2024). Its responsiveness to high flood years makes MNDWI a valuable indicator in environments characterized by complex or mixed land use and cover.

IV Normalized Difference Vegetation Index (NDVI)

NDVI values remain consistently high and positive throughout the study period, with a range of approximately 0.3 to 0.4. This indicates a consistently healthy and dense vegetation cover in Bayelsa. A relative decrease in NDVI values, such as the one observed around 2020, could be linked to vegetation stress induced by prolonged waterlogging. This temporal shift aligns with decreased photosynthetic activity during flood events (Mahmud, 2022). Spatially, the map shows lower NDVI values across flood basins and valleys, while upland regions exhibit higher values, indicating healthier vegetation. NDVI provides indirect but valuable flood detection by reflecting vegetation health degradation and changes in land cover dynamics during flood events.

V Normalized Difference Water Index (NDWI)

NDWI values are **consistently negative** throughout the period, generally ranging from –0.25 to –0.4. This corresponds with a consistent, but not widespread, presence of surface water. It effectively detects water over both vegetated and non-vegetated surfaces (Tran et al., 2022).

Spatially, NDWI shows high values along river systems and flood-prone lowlands, aligning well with known flood hotspots. Its capacity to capture both temporal and spatial water spread makes NDWI highly effective for flood monitoring in regions like Bayelsa State (Tran et al., 2022).

VI Water Ratio Index (WRI)

WRI demonstrates consistently high values across the dataset, with values consistently above 0.5. While the temporal variation is smoother than other indices, WRI remains sensitive to prolonged soil moisture and waterlogged conditions (Penna et al., 2013). Spatially, high WRI values are concentrated in the central and southeastern parts of Bayelsa, where wetland and floodplain systems are dominant. When integrated with other indices, WRI enhances the mapping of areas with sustained flood vulnerability.

The temporal analysis across all indices shows a general stability in flood-related conditions from 2000 to 2023. Spatially, the central basins and southeastern floodplains emerge as the most vulnerable zones, showing elevated values across multiple indices. This multi-index approach supports a robust, data-driven understanding of flooding dynamics and reinforces the importance of integrated remote sensing in flood risk assessment and planning (Chukwurah et al., 2022; Gandhi et al., 2015; Odunsi and Rienow, 2024; Palmer et al., 2023; Tran et al., 2022; Wani et al., 2009b).

4.16.4 Rivers State Flood Pattern Analysis

Flood pattern analysis in Rivers State was conducted using a suite of remote sensing-derived flood indices over a 24-year period (2000–2023). Each index was assessed using both temporal time series charts (Figure 4.174) and spatial annual average maps (Figures 4.175–4.180), enabling a multidimensional understanding of surface water dynamics and flood behavior. The integration of temporal trends with spatial distribution enhances the detection of flood-prone areas, wetland stability, vegetation-water interactions, and hydrological anomalies across the state.

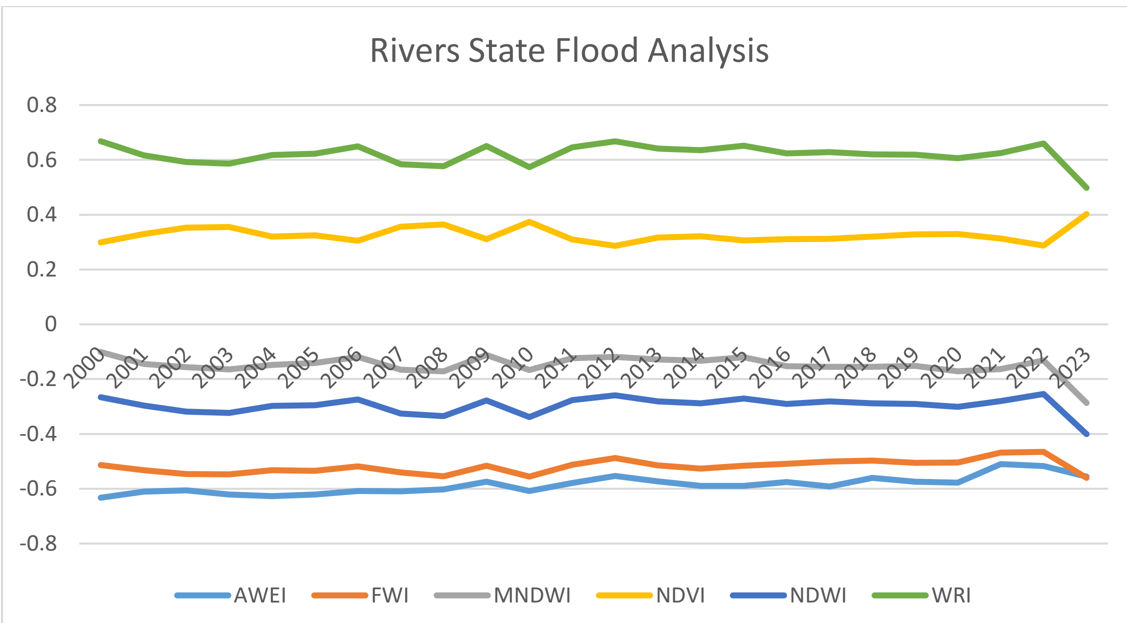

Figure 4.174: Time Series Chart of Multi-Temporal Flood Indices for Rivers State

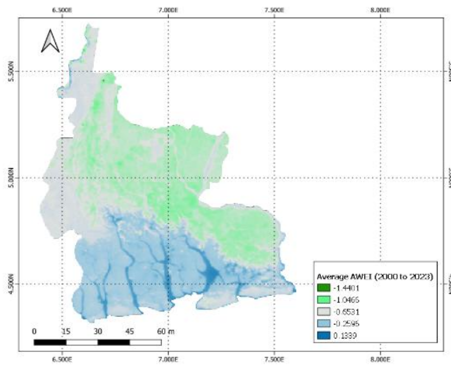

Figure 4.175: Spatial Annual Average of Automated Water Extraction Index (AWEI) for 2000 to 2023

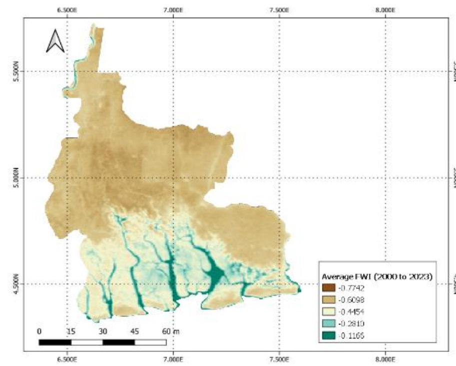

Figure 4.176: Spatial Annual Average of Flood Water Index (FWI) for 2000 to 2023

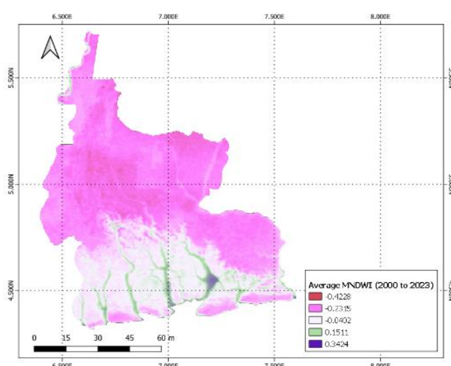

Figure 4.177: Spatial Annual Average of Modified Normalized Difference Water Index (MNDWI) for 2000 to 2023

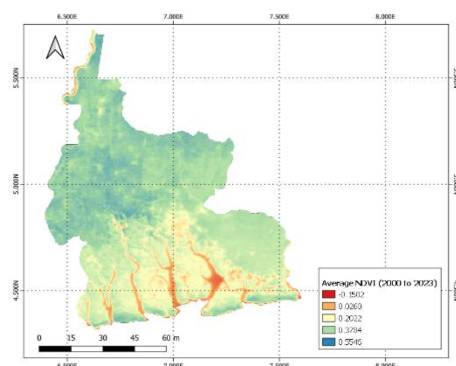

Figure 4.178: Spatial Annual Average of Normalized Difference Vegetation Index (NDVI) for 2000 to 2023

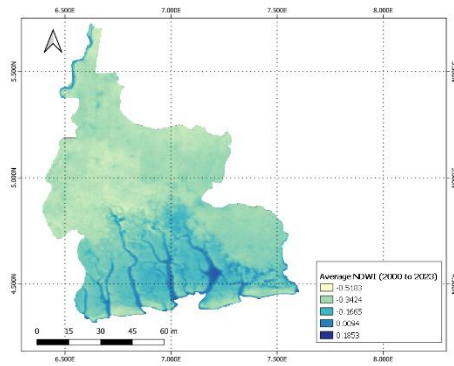

Figure 4.179: Spatial Annual Average of Normalized Difference Water Index (NDWI) for 2000 to 2023

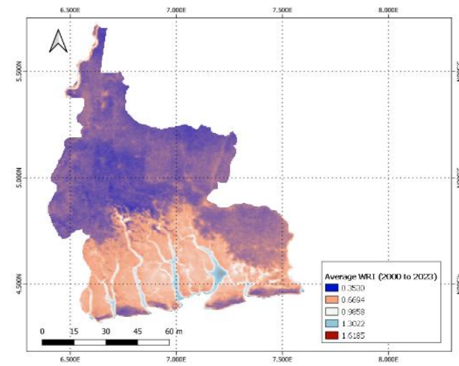

Figure 4.180: Spatial Annual Average of Water Ratio Index (WRI) for 2000 to 2023

I Automated Water Extraction Index (AWEI)

The AWEI time series shows a consistently low and negative trend, with values generally ranging between –0.6 and –0.7. This indicates a persistent difficulty in detecting open water surfaces, likely due to factors like dense vegetation, narrow water channels, or persistent cloud cover. Spatially, higher AWEI values are found in the northeastern and central parts of Rivers State, likely due to proximity to river systems and wetland areas. Conversely, the western and southern regions exhibit more negative AWEI values (below –0.5), suggesting higher terrain or well-drained zones. This trend implies a consistent low detectability of open water across the state, which could reflect both ecological transformations and human interventions in flood-prone areas.

II Flood Water Index (FWI)

The FWI time series reveals a consistently low and negative trend, with values generally ranging from –0.5 to –0.6. This suggests that the index did not capture any significant, widespread positive flood events, possibly due to the scale of analysis or the specific characteristics of flooding in the region. Spatially, elevated FWI values are concentrated along river corridors and low-lying basins, especially in the southeastern areas. FWI provides a reliable means of monitoring temporal flood events and mapping spatial inundation zones, especially valuable in rapidly urbanizing floodplains (Mohammadi et al., 2017).

III Modified Normalized Difference Water Index (MNDWI)

MNDWI values are predominantly negative over the years, with values consistently hovering between –0.1 and –0.2. This indicates limited open water detection and is likely reflective of a landscape where water bodies are often obscured or narrow. Spatially, floodplains exhibit moderate values, while upland areas have very low MNDWI values. This demonstrates the index's sensitivity to open water, even in areas with partial vegetation cover (Xu, 2006; Mondal *et. al*., 2024). MNDWI proves effective for both temporal monitoring and spatial analysis of flooding, particularly under mixed land cover conditions.

IV Normalized Difference Vegetation Index (NDVI)

NDVI values remain consistently positive throughout the period, with a range of approximately 0.3 to 0.4. This indicates consistently healthy and dense vegetation cover in Rivers State. A slight decrease in NDVI values, such as the one observed around 2020, could be linked to vegetation stress caused by prolonged inundation. This aligns with reductions in photosynthetic activity due to waterlogging (Mahmud, 2022).

The spatial distribution shows low NDVI values in river basins and valleys, while higher values are observed in the northern and western uplands. NDVI acts as an indirect indicator of flooding, reflecting changes in vegetation health and land cover dynamics during high flood years.

V Normalized Difference Water Index (NDWI)

NDWI remains consistently negative throughout the period, generally ranging from –0.25 to –0.4. It effectively detects water over both vegetated and non-vegetated surfaces (Tran et al., 2022). Spatially, the index reveals high values along river systems and low-lying floodplains, consistent with known flood-prone zones in Rivers State. NDWI is a robust index for detecting both the extent and persistence of surface water, especially during high-intensity rainfall years (Tran et al., 2022).

VI Water Ratio Index (WRI)

WRI consistently exhibits high values throughout the study period, with values generally ranging from 0.6 to 0.7. Although its temporal variation is relatively smooth, WRI remains sensitive to prolonged moisture conditions (Penna et al., 2013). Spatially, WRI is elevated in the central and southeastern regions, aligning with floodplain zones and areas prone to persistent wetness. WRI complements other indices by emphasizing areas of long-term water saturation and can significantly enhance flood vulnerability mapping.

The temporal analysis across all indices shows a general stability in flood-related conditions from 2000 to 2023. Spatially, the central basins and southeastern floodplains repeatedly show higher index values, indicating persistent vulnerability to flooding. This integrated, multi-index analysis supports the application of spectral indices in understanding and managing flood risks (Chukwurah et al., 2022; Gandhi et al., 2015; Odunsi and Rienow, 2024; Palmer et al., 2023; Tran et al., 2022; Wani et al., 2009b).

4.17 Summary of Key Findings

This chapter presented the core results and detailed discussion pertaining to the temporal and spatial evaluation of rainfall, temperature, land use/land cover (LULC) changes, and flood patterns across Edo, Delta, Bayelsa, and Rivers States, utilizing remote sensing technologies and machine learning algorithms. The key findings derived from this extensive analysis are summarized below:

1) Data Validation and Homogeneity

The preliminary statistical analysis established the homogeneity and reliability of the meteorological datasets prior to trend analysis. Homogeneity tests applied to rainfall data in Edo and Rivers States (Pettitt's Test, Buishand's Range Test, and SNHT) consistently found no statistically significant structural changes in the long-term series, reinforcing that observed fluctuations fall within the bounds of natural variability.

Validation of the satellite-based rainfall products against gauge data across the three available states showed that the CHIRPS dataset consistently outperformed both PERSIANN-CDR and TRMM in terms of correlation, RMSE, and NSE, demonstrating its higher reliability in capturing local rainfall dynamics. Conversely, the TRMM dataset consistently showed the weakest performance and was deemed unreliable for operational rainfall estimation in these high-precipitation coastal areas.

For temperature analysis, validation results comparing ERA5 and CPC datasets against ground observations were mixed. The ERA5 dataset generally exhibited a stronger Pearson Correlation Coefficient, indicating a better ability to capture the temporal variability of both maximum (Tmax) and minimum (Tmin) temperatures. However, both ERA5 and CPC often returned negative Nash–

Sutcliffe Efficiency (NSE) and R^2 values, reflecting limitations in accurately predicting extreme or sudden variations in temperature within the complex tropical microclimates of the region.

2) Climate Variability Trends

The spatio-temporal trend analysis revealed an asymmetry between rainfall and temperature trends across the study area:

1. Rainfall Variability: Analysis of annual rainfall for all four states (Edo, Delta, Bayelsa, and Rivers) showed no statistically significant long-term trend ($p > 0.05$), despite exhibiting considerable inter-annual and seasonal variability. However, the data suggested a potential increasing trend in the frequency of extreme rainfall days across Delta, Bayelsa, and Rivers States, which has significant implications for localized flooding. Furthermore, analysis of wet season phenology indicated slight, non-significant shifts in the timing of wet season onset and duration, suggesting changes in monsoon dynamics.

2. Temperature Warming: In contrast to rainfall, the temporal analysis demonstrated a robust and statistically significant upward warming trend in both maximum (Tmax) and minimum (Tmin) temperatures across all four states over the 1971–2023 period.

Maximum Temperature (Tmax): The warming trend was statistically significant across all four seasons (DJF, MAM, JJA, and SON) in Edo, Delta, Bayelsa, and Rivers States, confirming a persistent climatic shift toward hotter days throughout the year. The annual Tmax increase rate in Rivers State was notably high (0.046°C per year).

Minimum Temperature (Tmin): Similarly, minimum temperatures showed a consistent and statistically significant upward trend across all seasons in all four states. This suggests warming nights, which can exacerbate heat stress and reduce the diurnal temperature range.

3) Land Use/Land Cover Dynamics

The LULC classification utilized machine learning to map changes between 2013 and 2023.

1. Classification Performance: The Random Forest (RF) classifier consistently outperformed the Support Vector Machine (SVM) algorithm across all states (Edo, Delta, Bayelsa, and Rivers) and all years, achieving higher validation accuracy and Kappa coefficients. This reinforces the suitability of the RF model for handling complex, high-dimensional remote sensing data in the study area.

2. Observed Changes: The LULC analysis revealed complex dynamics, although specific trends varied by state and were subject to classification accuracy improvements over time. Edo State showed a notable decline in barren land and urban cover. Delta State exhibited relatively stable water and urban extents, while Bayelsa showed overall stability in its dominant forest and water coverage. These transformations, particularly the persistence of urban encroachment into natural flood buffers, are critical contextual factors contributing to increased flood vulnerability.

4) Flood Pattern Detection

A robust multi-index remote sensing approach was successfully applied over the period 2000–2023, integrating indices like AWEI, FWI, MNDWI, NDWI, and WRI for temporal monitoring and spatial mapping.

1. Temporal Consistency: The time series analysis across Delta, Bayelsa, and Rivers States revealed that flood indices (AWEI, FWI, MNDWI, NDWI) remained remarkably stable and consistently negative over the 24-year period. This suggests that the indices, as calculated, primarily capture baseline water presence and landscape characteristics rather than short-term flood event anomalies.

2. Spatial Vulnerability: Spatially, the analysis consistently mapped elevated flood index values along river corridors, lowland basins, and southeastern floodplains of the study area, confirming these zones as persistently vulnerable to inundation. The NDVI analysis further indicated vegetation stress in these areas due to waterlogging, aligning with known flood impacts.

In conclusion, this section’s findings confirm that while rainfall volume has remained statistically stable, the region faces a double challenge: pervasive and statistically significant warming across all seasons (Tmax and Tmin), combined with dynamic LULC changes and a clear pattern of recurrent, severe flood events concentrated in specific vulnerable geographical zones. The methodology successfully utilized advanced geospatial and machine learning tools to generate these high-resolution, multi-decadal insights into the environmental drivers of flooding in the Lower Niger region.

CHAPTER FIVE

CONCLUSIONS AND RECOMMENDATIONS

5.1 CONCLUSION

The study set out to evaluate the impact of land use/land cover (LULC) changes and climate variability on flooding in Edo State, Delta State, Bayelsa State, and Rivers State, Nigeria. This analysis was achieved through the integration of remote sensing technologies and machine learning algorithms, focusing on five interrelated objectives. The key conclusions derived from the findings, structured directly based on the research objectives, are outlined below:

The rainfall analysis revealed marked inter-annual and seasonal variability across all study locations. Although the Mann-Kendall trend tests and Sen's slope estimations indicated no statistically significant long-term trends in annual rainfall for Edo, Delta, Rivers, or Bayelsa States ($p > 0.05$), the analysis identified important patterns, including an increasing frequency of extreme rainfall days and persistent variability in the wet season onset and duration. These fluctuations reflect the influence of climate variability and suggest a heightened risk of both droughts and flash floods in different years.

The trend analysis of maximum and minimum surface temperatures showed a general, pervasive, and statistically significant warming trend across the region. Specifically, annual minimum temperatures in Edo State, Delta State, Bayelsa State, and Rivers State all exhibited a statistically significant upward trend ($p = 0.000$ for all, with rates ranging from 0.037°C to 0.045°C per year). This warming trend was also significant for annual maximum temperatures in Rivers State

(0.046°C per year, p = 0.000). This persistent warming, particularly in minimum temperatures, suggests a change in the baseline climate.

The analysis of Land Use/Land Cover (LULC) dynamics showed complex patterns of change across the four states. While some states showed increased forest cover (Delta State and Rivers State) or stable urban areas (Bayelsa State), the overall trend confirms that land use transformation, especially urban encroachment into natural flood buffers (like wetlands and floodplains), has significantly worsened flood vulnerability in the region. For LULC classification, the Random Forest (RF) machine learning model consistently outperformed the Support Vector Machine (SVM) model in terms of accuracy across all evaluated years and states.

The multi-index flood pattern detection, utilizing indices such as AWEI, FWI, MNDWI, NDWI, and WRI, was highly effective in identifying historical flood events. The time series trend analysis revealed that 2017 and especially 2020 were consistently identified as major flood years across Rivers State, Delta State, and Bayelsa State, corresponding to periods of extensive surface water presence and high FWI peaks. Spatially, the central basins and southeastern floodplains were consistently highlighted as exhibiting high flood index values, confirming their persistent vulnerability. This robust, multi-index approach successfully mapped the temporal spikes and spatial extent of inundation.

5.2 RECOMMENDATIONS

Based on the findings regarding the impact of land use/land cover (LULC) changes and climate variability on flooding in the Lower Niger region, a number of recommendations are proposed to improve flood management, environmental planning, and climate resilience.

From a policy and planning perspective, urban development should be informed by continuous LULC monitoring and regular flood risk assessments. Regulatory authorities need to enforce land-use zoning policies that prevent construction in high-risk floodplains, wetlands, and flood-prone zones. In addition, engineering designs for drainage systems, road networks, and buildings should be updated to reflect the increasing frequency of extreme rainfall events and changes in wet season duration. Incorporating climate variability into infrastructure standards will help ensure resilience to future flood risks. Furthermore, governments and local agencies should invest in strengthening early warning systems by integrating satellite-derived rainfall and flood indices into real-time monitoring platforms. Public education and community-based adaptation initiatives should also be scaled up to improve disaster preparedness.

In terms of environmental management, it is critical to protect and restore natural flood buffers such as wetlands, forests, and vegetated areas. These ecosystems play an essential role in absorbing excess rainfall, reducing surface runoff, and lowering flood risk for downstream settlements. Complementary to this is the adoption of green infrastructure and sustainable drainage systems, including permeable pavements, rain gardens, and urban green spaces. Such measures enhance infiltration, improve water retention, and contribute to reducing the severity of urban flooding.

For research and data systems, future studies should expand the use of multi-temporal remote sensing and more advanced machine learning techniques, including deep learning and convolutional neural networks, to improve the precision of LULC change detection and flood modeling. The use of finer-resolution satellite datasets such as Sentinel-2, Landsat-9, or PlanetScope will further strengthen the accuracy of these analyses. Moreover, it is essential to establish long-term environmental monitoring programs through collaboration between the Nigerian Meteorological Agency (NiMet), River Basin Authorities, and research institutions.

Sustained datasets on climate and hydrology are indispensable for identifying long-term trends, guiding policy, and validating predictive models. Finally, additional research should be directed at exploring the interactions between climate variability, flooding, and LULC changes, particularly in relation to soil erosion, groundwater recharge, and surface water quality. These dimensions are critical for advancing integrated water resources management in the study region.

5.3 CONTRIBUTION TO KNOWLEDGE

The main aim of this research was to evaluate the impact of land use/land cover (LULC) changes and climate variability on flooding in the Lower Niger region of Nigeria using remote sensing technologies and machine learning algorithms. The study makes several important contributions to knowledge in the fields of hydroclimatology, geospatial science, and disaster risk management, especially in the context of data-scarce regions such as West Africa.

1. This research fills a major gap in understanding the complex interactions between climate variability, land use changes, and flood events in the Lower Niger Delta. Previous studies have rarely examined these relationships together, and their combined effects on flooding have remained poorly understood. By integrating remote sensing and machine learning approaches, this study provides new evidence of how changes in rainfall patterns, surface temperature, and LULC transformations contribute to increasing flood risks in the region.

2. The study introduces a robust framework that combines satellite remote sensing, geospatial analysis, and machine learning for analyzing flood dynamics. The use of the Google Earth Engine (GEE) platform enabled efficient processing of large-scale multi-temporal data, while algorithms such as Random Forest and Support Vector Machine improved classification accuracy in LULC mapping. In addition, the use of multiple water-related indices (AWEI, FWI, MNDWI, NDWI,

and WRI) for flood detection provided a multi-dimensional approach to monitoring surface water changes. These methodological innovations enhance the accuracy, reliability, and reproducibility of flood modeling and risk assessments in Southern Nigeria.

3. The research generated unique empirical data and diagnostic insights into the relationship between environmental change and flooding. It produced rainfall trend analyses, multi-temporal LULC maps (2013–2023), spatial variation in surface temperature, and flood extent maps for the region. The findings revealed that urban encroachment into natural floodplains and wetlands has amplified flood vulnerability, often exerting a greater influence on flood risk than climate variability alone. These results provide a strong evidence base for understanding the drivers of flood hazards in the Lower Niger region.

4. Finally, the study contributes directly to policy and practice by offering actionable recommendations for flood management and land-use planning. The identification of critical drivers of flooding provides a guide for decision-makers, urban planners, and disaster managers in designing adaptive strategies. The tools and insights developed in this research can support the development of resilient communities, sustainable land-use policies, and long-term climate adaptation strategies in the Niger Delta and other flood-prone regions globally.

REFERENCES

Abaje, I.B., 2023. Geo-Statistical Analysis of Meteorological Drought and Recurrence Intervals in the Context of Climate Change Over Extreme Northeastern Region of Nigeria. Tanzania Journal of Science 49, 152–166. https://doi.org/10.4314/tjs.v49i1.14

Abam, T.K.S., 2001. Modification of Niger delta physical ecology: the role of dams and reservoirs. IAHS Publications-Series of Proceedings and Reports-Intern Assoc Hydrological Sciences 266, 19–30.

Abdolrasol, M.G., Hussain, S.S., Ustun, T.S., Sarker, M.R., Hannan, M.A., Mohamed, R., Ali, J.A., Mekhilef, S., Milad, A., 2021. Artificial neural networks based optimization techniques: A review. Electronics 10, 2689.

Abiodun, B.J., Lawal, K.A., Salami, A.T., Abatan, A.A., 2013. Potential influences of global warming on future climate and extreme events in Nigeria. Reg Environ Change 13, 477–491. https://doi.org/10.1007/s10113-012-0381-7

Abraham, A., 2005. Artificial neural networks. Handbook of measuring system design.

Achugbu, I.C., Olufayo, A.A., Balogun, I.A., Adefisan, E.A., Dudhia, J., Naabil, E., 2022. Modeling the spatiotemporal response of dew point temperature, air temperature and rainfall to land use land cover change over West Africa. Model. Earth Syst. Environ. 8, 173–198. https://doi.org/10.1007/s40808-021-01094-8

Adegboyega, S.A.-A., Onuoha, O.C., Adesuji, K.A., Olajuyigbe, A.E., Olufemi, A.A., Ibitoye, M.O., 2018. An Integrated Approach to Modelling of Flood Hazards in the Rapidly Growing City of Osogbo, Osun State, Nigeria. Space Science International 4, 1–15. https://doi.org/10.3844/ajssp.2018.1.15

Adelalu, Temitope Gabriel, Adelalu, T. G., Ibrahim, A.H., Ibrahim, A., Benjamin, E., Benjamin, E.B., G. C. Yakubu, Yakubu, G.C., 2021. QUANTITATIVE AND QUALITATIVE EVIDENCE OF ANTHROPOGENIC FINGERPRINT IN FLOODING IN TARABA STATE OF NIGERIA 2, 01–19. https://doi.org/10.52417/ojer.v2i1.188

Adeyefa, A.O., 2023. Assessment of rainfall characteristics of the early and late growing seasons during significant years of extreme little dry season in southwestern Nigeria. African Geographical Review 42, 326–341. https://doi.org/10.1080/19376812.2022.2054437

Adeyeri, O.E., Laux, P., Lawin, A.E., Arnault, J., 2020. Assessing the impact of human activities and rainfall variability on the river discharge of Komadugu-Yobe Basin, Lake Chad Area. Environ Earth Sci 79, 143. https://doi.org/10.1007/s12665-020-8875-y

Agbola, T., Olurin, T.A., 2003. Landuse and Landcover change in the Niger delta. Excerpts from a Research Report presented to the Centre for Democracy and Development.

Agbonkhese, O., Agbonkhese, E.G., Aka, E.O., Joe-Abaya, J., Ocholi, M., Adekunle, A., A Adekunle, 2014. Flood Menace in Nigeria: Impacts, Remedial and Management Strategies. Civil and environmental research 6, 32–40.

Aggarwal, S., 2004. Principles of remote sensing. Satellite remote sensing and GIS applications in agricultural meteorology 23, 23–28.

Aich, V., Koné, B., Hattermann, F., Paton, E., 2016. Time Series Analysis of Floods across the Niger River Basin. Water 8, 165. https://doi.org/10.3390/w8040165

Aji Suraji, Aji Suraji, Agus Taufik Mulyono, Agus Taufik Mulyono, 2022. Accident risk analysis of road geometric components using functional worthiness approach. Eastern-European Journal of Enterprise Technologies 3, 6–14. https://doi.org/10.15587/1729-4061.2022.257977

Ajibola, M.O., Oluwunmi, A.O., Iroham, C.O., Ayedun, C.A., 2021. Remote Sensing and Land Use Management in Nigeria: a Review. IOP Conf. Ser.: Earth Environ. Sci. 655, 012084. https://doi.org/10.1088/1755-1315/655/1/012084

Akeh, G.I., Mshelia, A.D., 2016. Climate Change and Urban Flooding: Implications for Nigeria's Built Environment. MOJ Ecology & Environmental Science 1–4.

Akhtar, N., Syakir Ishak, M.I., Bhawani, S.A., Umar, K., 2021. Various Natural and Anthropogenic Factors Responsible for Water Quality Degradation: A Review. Water 13, 2660. https://doi.org/10.3390/w13192660

Akinsanola, A.A., Zhou, W., 2019. Dynamic and thermodynamic factors controlling increasing summer monsoon rainfall over the West African Sahel. Clim Dyn 52, 4501–4514. https://doi.org/10.1007/s00382-018-4394-x

Akinwumi, S.A., Ayo-Akanbi, O.A., Omotosho, T.V., Mastorakis, N.E., 2023. Monthly and seasonal variation of cloud cover, humidity and rainfall in Lagos, Nigeria. WSEAS Transactions on Environment and Development 19, 1371–1379.

Akoteyon, I.S., 2022. Factors influencing the occurrence of flooding, risk and management strategies in Lagos, Nigeria. Sustainable Water Resources Management 8, 68.

Akpejiori, J.I., Ehiorobo, J.O., Izinyon, O., 2017. Flood monitoring and flood risk assessment in Agenebode, Edo State, Nigeria. Int. J. Eng. Appl 7, 53–59.

Akter, N., Rafiqul Islam, M., 2017. Heat stress effects and management in wheat. A review. Agron. Sustain. Dev. 37, 37. https://doi.org/10.1007/s13593-017-0443-9

Alexandersson, H., 1986. A homogeneity test applied to precipitation data. J. Climatol. 6, 661–675. https://doi.org/10.1002/joc.3370060607

Alexandru TUDOR, 2023. REMOTE SENSING IN BIOMETEOROLOGY. Review of the Air Force Academy XX, 5–14. https://doi.org/10.19062/1842-9238.2022.20.2.1

Alibrahim, H., Ludwig, S.A., 2021. Hyperparameter optimization: Comparing genetic algorithm against grid search and bayesian optimization, in: 2021 IEEE Congress on Evolutionary Computation (CEC). IEEE, pp. 1551–1559.

Althausen, J.D., 2002. What remote sensing system should be used to collect the data. Manual of geospatial science and technology 276–297.

Amirmahani, F., Amirmahani, F., Ebrahimi, Nader, Ebrahimi, Nasim, Molaei, F., Molaei, F., Ferdos Faghihkhorasani, Faghihkhorasani, F., Kiarash Jamshidi Goharrizi, Goharrizi, K.J., Seyede Masoumeh Mirtaghi, Mirtaghi, S.M., Marziyeh Borjian-Boroujeni, Borjian-Boroujeni, M., Marziyeh Borjian-Boroujeni, Michael R. Hamblin, Hamblin, M.R., 2021. Approaches for the integration of big data in translational medicine: single-cell and computational methods. Annals of the New York Academy of Sciences 1493, 3–28. https://doi.org/10.1111/nyas.14544

Amoako, C., Frimpong Boamah, E., 2015. The three-dimensional causes of flooding in Accra, Ghana. International Journal of Urban Sustainable Development 7, 109–129. https://doi.org/10.1080/19463138.2014.984720

Animashaun, I.M., Oguntunde, P.G., Akinwumiju, A.S., Olubanjo, O.O., 2020. Rainfall Analysis over the Niger Central Hydrological Area, Nigeria: Variability, Trend, and Change point detection. Scientific African 8, e00419. https://doi.org/10.1016/j.sciaf.2020.e00419

Animashaun, M.I., Oguntunde, P.G., Olubanjo, O.O., Akinwumiju, A.S., 2023. Assessment of climate change impacts on the hydrological response of a watershed in the savanna region of sub-Saharan Africa. Theoretical & Applied Climatology 152.

Anugwa, I., Anugwa, I.Q., Amaechina, E., Amaechina, E.C., Agwu, A.E., Agwu Ekwe Agwu, Innocent Ifelunini, Innocent A. Ifelunini, Tochi Umeonuora, Tochi Umeonuora, C.A. Okwor, Chika Okwor, 2022. Assessing Climate Change-Related Losses and Damages and Adaptation Constraints to Address Them: Evidence from Flood-Prone Riverine Communities in Southern Nigeria. Social Science Research Network. https://doi.org/10.2139/ssrn.4186453

Ashagrie, A.G., De Laat, P.J., De Wit, M.J., Tu, M., Uhlenbrook, S., 2006. Detecting the influence of land use changes on discharges and floods in the Meuse River Basin – the predictive power of a ninety-year rainfall-runoff relation? Hydrol. Earth Syst. Sci. 10, 691–701. https://doi.org/10.5194/hess-10-691-2006

Avand, M., Moradi, H.R., Hamid Reza Moradi, lasboyee, M.R., 2020. Using machine learning models, remote sensing, and GIS to investigate the effects of changing climates and land uses on flood probability. Journal of Hydrology 595, 125663. https://doi.org/10.1016/j.jhydrol.2020.125663

Awosika, L.F., 1994. Impacts of global climate change and sea level rise on coastal resources and energy development in Nigeria. GLOBAL CLIMATE CHANGE-IMPACT ON ENERGY DEVELOPMENT.[np]. 1994.

Awosika, L.F., French, G.T., Nicholls, R.J., Ibe, C.E., 1992. The impacts of sea level rise on the coastline of Nigeria, in: Proceedings of IPCC Symposium on the Rising Challenges of the Sea. Magaritta, Venezuela. pp. 14–19.

Ayanlade, A., Atai, G., Jegede, M.O., 2019. Spatial and seasonal variations in atmospheric aerosols over Nigeria: Assessment of influence of intertropical discontinuity movement.

Journal of Ocean and Climate: Science, Technology and Impacts 9, 1759313118820306. https://doi.org/10.1177/1759313118820306

Ayejoto, D.A., Egbueri, J.C., Agbasi, J.C., Omeka, M.E., Unigwe, C.O., Nwazelibe, V.E., Ighalo, J.O., Pande, C.B., 2023. Influence of Seasonal Changes on the Quality of Water Resources in Southwestern Nigeria: A Review, in: Egbueri, J.C., Ighalo, J.O., Pande, C.B. (Eds.), Climate Change Impacts on Nigeria, Springer Climate. Springer International Publishing, Cham, pp. 423–447. https://doi.org/10.1007/978-3-031-21007-5_22

Ayilara, M., Olanrewaju, O., Babalola, O., Odeyemi, O., 2020. Waste Management through Composting: Challenges and Potentials. Sustainability 12, 4456. https://doi.org/10.3390/su12114456

Ayotamuno, A., 2020. Changes of Key Climatic Parameters and Flooding in Rivers State, Nigeria 2, 25–32. https://doi.org/10.36346/sarjbab.2020.v02i03.001

Babu, C.N., Reddy, B.E., 2014. A moving-average filter based hybrid ARIMA–ANN model for forecasting time series data. Applied Soft Computing 23, 27–38.

Badamosi, A.P., Olutumise, A.I., Olukoya, O.P., Adegoroye, A., Aturamu, O.A., 2023. Socioeconomic impacts of flooding and its coping strategies in Nigeria: Evidence from Dagiri community, Gwagwalada area council of Abuja. Natural Hazards Research. https://doi.org/10.1016/j.nhres.2023.09.010

Bamweyana, I., Musinguzi, M., Kayondo, L.M., 2021. Evaluation of CHIRPS Satellite Gridded Dataset as an Alternative Rainfall Estimate for Localized Modelling over Uganda. ACS 11, 797–811. https://doi.org/10.4236/acs.2021.114046

Bao, Z., Wu, Y., He, W., She, N., Li, Z., 2025. Intensified Rainfall, Growing Floods: Projecting Urban Drainage Challenges in South-Central China Under Climate Change Scenarios. Applied Sciences 15, 11577.

Barnsley, M., 1999. Digital remotely-sensed data and their characteristics. Geographical Information Systems 1, 34.

Barsi, J.A., Lee, K., Kvaran, G., Markham, B.L., Pedelty, J.A., 2014. The spectral response of the Landsat-8 operational land imager. Remote sensing 6, 10232–10251.

Basak, D., Pal, S., Patranabis, D.C., 2007. Support vector regression. Neural Information Processing-Letters and Reviews 11, 203–224.

Bello, N.A., 2017. Assessment of Adaptation Strategies to Flooding Impacts in Nigeria - A Review 1, 1. https://doi.org/10.31058/j.ud.2017.11001

Berhanu, B., Seleshi, Y., Demisse, S.S., Melesse, A.M., 2016. Bias correction and characterization of climate forecast system re-analysis daily precipitation in Ethiopia using fuzzy overlay. Meteorological Applications 23, 230–243. https://doi.org/10.1002/met.1549

Bickici Arikan, B., Kahya, E., 2019. Homogeneity revisited: analysis of updated precipitation series in Turkey. Theor Appl Climatol 135, 211–220. https://doi.org/10.1007/s00704-018-2368-x

Borowska-Stefańska, M., Kowalski, M., Wiśniewski, S., Dulebenets, M.A., 2023. The impact of self-evacuation from flood hazard areas on the equilibrium of the road transport. Safety Science 157, 105934. https://doi.org/10.1016/j.ssci.2022.105934

Brakenridge, R., Anderson, E., 2006. MODIS-based flood detection, mapping and measurement: the potential for operational hydrological applications, in: Transboundary Floods: Reducing Risks through Flood Management. Springer, pp. 1–12.

Brisibe, W.G., Brown, I., 2020. Building Construction, Road Works and Waste Management: Impact of Anthropogenic Actions on Flooding in Yenagoa, Nigeria. International Journal of Architectural Engineering Technology 7, 36–46.

Brivio, P.A., Colombo, R., Maggi, M., Tomasoni, R., 2002. Integration of remote sensing data and GIS for accurate mapping of flooded areas. International Journal of Remote Sensing 23, 429–441.

Buishand, T.A., 1982. Some methods for testing the homogeneity of rainfall records. Journal of Hydrology 58, 11–27. https://doi.org/10.1016/0022-1694(82)90066-X

Cai, X., Zhang, X., Noël, P.H., Shafiee-Jood, M., 2015a. Impacts of climate change on agricultural water management: a review. WIREs Water 2, 439–455. https://doi.org/10.1002/wat2.1089

Cai, X., Zhang, X., Noël, P.H., Shafiee-Jood, M., 2015b. Impacts of climate change on agricultural water management: a review. WIREs Water 2, 439–455. https://doi.org/10.1002/wat2.1089

Camberlin, P., Diop, M., 2003. Application of daily rainfall principal component analysis to the assessment of the rainy season characteristics in Senegal. Climate Research 23, 159–169.

Campbell, J.B., Wynne, R.H., 2011. Introduction to remote sensing. Guilford press.

Chan, N.W., Ghani, A.A., Samat, N., Hasan, N.N.N., Tan, M.L., 2020. Integrating structural and non-structural flood management measures for greater effectiveness in flood loss reduction in the Kelantan River basin, Malaysia, in: Proceedings of AICCE’19: Transforming the Nation for a Sustainable Tomorrow 4. Springer, pp. 1151–1162.

Cheng, C., Sa-Ngasoongsong, A., Beyca, O., Le, T., Yang, H., Kong, Z., Bukkapatnam, S.T., 2015. Time series forecasting for nonlinear and non-stationary processes: a review and comparative study. Iie Transactions 47, 1053–1071.

Cherinet, A., Tadesse, C., Abebe, T., 2022. Drought and flood extreme events and management strategies in Ethiopia. J Geogr Nat Disast 12, 2167–2587.

Chicco, D., Warrens, M.J., Jurman, G., 2021. The Matthews correlation coefficient (MCC) is more informative than Cohen's Kappa and Brier score in binary classification assessment. Ieee Access 9, 78368–78381.

Christensen, J.H., Hewitson, B., Busuioc, A., Chen, A., Gao, X., Held, I., Jones, R., Kolli, R.K., Kwon, W.-T., Laprise, R., 2007. Regional climate projections. Chapter 11.

Chukwu, M.N., 2023. A novel Account of Flooding Devastation and Consequencies in Kogi State, Nigeria. University of Thi-Qar Journal of Science 10. https://doi.org/10.32792/utq/utjsci/v10i1.1044

Chukwuma, O.M., Chukwuma, O.M., Ochege, F.U., Uchenna, O.F., 2018. A comparative analysis of flooding in Warri and Port Harcourt urban areas of the Niger Delta region in southern Nigeria. Arabian Journal of Geosciences 11, 1–16. https://doi.org/10.1007/s12517-018-3525-3

Chukwurah, G.O., Chioma Onwuneme John-nsa, Francis Okeke, Eze Charles Chukwudi, Isimah Matthew Ogorchukwu, 2022. Rapid spatial growth of cities and its planning implications for developing countries: a case study of Abuja, Nigeria. Indonesian Journal of Geography 54. https://doi.org/10.22146/ijg.70316

Ciemer, C., Boers, N., Hirota, M., Kurths, J., Müller-Hansen, F., Oliveira, R.S., Winkelmann, R., 2019. Higher resilience to climatic disturbances in tropical vegetation exposed to more variable rainfall. Nature Geoscience 12, 174–179.

Clasing, R., Muñoz, E., Arumí, J.L., Caamaño, D., Alcayaga, H., Medina, Y., 2023. Remote Sensing with UAVs for Modeling Floods: An Exploratory Approach Based on Three Chilean Rivers. Water 15, 1502–1502. https://doi.org/10.3390/w15081502

Cologna, V., Bark, R.H., Paavola, J., 2017. Flood risk perceptions and the UK media: Moving beyond "once in a lifetime" to "Be Prepared" reporting. Climate Risk Management 17, 1–10. https://doi.org/10.1016/j.crm.2017.04.005

Concha Larrauri, P., Lall, U., Hariri-Ardebili, M.A., 2023. Needs for Portfolio Risk Assessment of Aging Dams in the United States. J. Water Resour. Plann. Manage. 149. https://doi.org/10.1061/jwrmd5.wreng-5673

Cook, K.H., Vizy, E.K., 2019. Contemporary Climate Change of the African Monsoon Systems. Curr Clim Change Rep 5, 145–159. https://doi.org/10.1007/s40641-019-00130-1

Dada, O.A., Li, G., Qiao, L., Asiwaju-Bello, Y.A., Anifowose, A.Y.B., 2018. Recent Niger Delta shoreline response to Niger River hydrology: Conflict between forces of Nature and Humans. Journal of African Earth Sciences 139, 222–231.

Dajuma, A., Sylla, M.B., Tall, M., Almazroui, M., Yassa, N., Diedhiou, A., Giorgi, F., 2023. Projected expansion of hottest climate zones over Africa during the mid and late 21st century. Environmental Research: Climate 2, 025002.

Dalil, M., Mohammad, N.H., Yamman, U.M., Husaini, A., Mohammed, S.L., 2015. An assessment of flood vulnerability on physical development along drainage channels in Minna, Niger

State, Nigeria. African Journal of Environmental Science and Technology 1, 38-46. https://doi.org/doi:%2010.5897/AJEST2014.1815

Dance, K.W., Hynes, H.B.N., 1980. Some effects of agricultural land use on stream insect communities. Environmental Pollution Series A, Ecological and Biological 22, 19–28.

Danhassan, S.S., Abubakar, A., Zangina, A.S., Ahmad, M.H., Hazaea, S.A., Ishak, M.Y., Zhang, J., 2023. Flood Policy and Governance: A Pathway for Policy Coherence in Nigeria. Sustainability 15, 2392–2392. https://doi.org/10.3390/su15032392

Dan-Jumbo, N.G., Metzger, M.J., Clark, A.P., 2018. Urban Land-Use Dynamics in the Niger Delta: The Case of Greater Port Harcourt Watershed. Urban Science 2, 108. https://doi.org/10.3390/urbansci2040108

De Jong, W., 2010. Forest Rehabilitation and Its Implication for Forest Transition Theory. Biotropica 42, 3–9. https://doi.org/10.1111/j.1744-7429.2009.00568.x

De La Casa, A.C., Ovando, G.G., Nasello, O.B., 2018. Changes in the Intensity and Variability of Precipitation in the Central Region of Argentina between 1960 and 2012. Climate 6, 66. https://doi.org/10.3390/cli6030066

DeFries, R.S., Townshend, J.R.G., 1994. NDVI-derived land cover classifications at a global scale. International journal of remote sensing 15, 3567–3586.

DeVries, B., Huang, C., Armston, J., Huang, W., Jones, J.W., Lang, M.W., 2020. Rapid and robust monitoring of flood events using Sentinel-1 and Landsat data on the Google Earth Engine. Remote Sensing of Environment 240, 111664.

Dewan, A.M., Kumamoto, T., Nishigaki, M., 2006. Flood hazard delineation in greater Dhaka, Bangladesh using an integrated GIS and remote sensing approach. Geocarto International 21, 33–38.

Diedhiou, A., Bichet, A., Wartenburger, R., Seneviratne, S.I., Rowell, D.P., Sylla, M.B., Diallo, I., Todzo, S., Touré, N.E., Camara, M., 2018. Changes in climate extremes over West and Central Africa at 1.5 C and 2 C global warming. Environmental Research Letters 13, 065020.

Ding, W., Wu, J., Tang, R., Chen, X., Xu, Y., 2022. A review of flood risk in China during 1950–2019: Urbanization, socioeconomic impact trends and flood risk management. Water 14, 3246.

Dinku, T., Funk, C., Peterson, P., Maidment, R., Tadesse, T., Gadain, H., Ceccato, P., 2018. Validation of the CHIRPS satellite rainfall estimates over eastern Africa. Quart J Royal Meteoro Soc 144, 292–312. https://doi.org/10.1002/qj.3244

Dokubo, A., 2004. Niger Delta People in the Nigerian State. The Argus 3, 4.

Douglas, I., 2017. Flooding in African cities, scales of causes, teleconnections, risks, vulnerability and impacts. International journal of disaster risk reduction 26, 34–42.

Dysarz, T., 2020. Development of methodology for assessment of long-term morphodynamic impact on flood hazard. J Flood Risk Management 13. https://doi.org/10.1111/jfr3.12654

Earth Science Data Systems, N., 2021. Passive Sensors | Earthdata [WWW Document]. URL https://www.earthdata.nasa.gov/learn/backgrounders/passive-sensors (accessed 3.4.24).

Ebegbulem, J.C., Ekpe, D., Adejumo, T.O., 2013. Oil exploration and poverty in the Niger delta region of Nigeria: A critical analysis. International Journal of Business and Social Science 4, 279–287.

Ebi, K.L., Capon, A., Berry, P., Broderick, C., de Dear, R., Havenith, G., Honda, Y., Kovats, R.S., Ma, W., Malik, A., 2021. Hot weather and heat extremes: health risks. The lancet 398, 698–708.

Echendu, A.J., 2023. Human factors vs climate change; experts' view of drivers of flooding in Nigeria. Natural Hazards Research 3, 240–246. https://doi.org/10.1016/j.nhres.2023.04.002

Egbiki, S., Ehiorobo, J.O., Izinyon, O.C., 2020. Modelling and Forecasting of Ikpoba River Discharge in the Niger Delta Region using Adaptive Neuro-Fuzzy Inference System (ANFIS). Nigerian Journal of Environmental Sciences and Technology (NIJEST) Vol 4, 432–449.

Ehiorobo, J.O., Izinyon, O.C., 2013. Flood frequency analysis at Oshun River in Asejire dam site, Nigeria. Journal of Earth Science and Engineering 3.

Ehiorobo, J.O., Izinyon, O.C., 2011. Measurements and Documentation for Flood and Erosion Monitoring and Control in the Niger Delta States of Nigeria. TS07E-Engineering Surveying, FIG Working Week.

Ehiorobo, J.O., Izinyon, O.C., Ilaboya, I.R., 2012. Effects of Climate Change on River flow regimes in the Mangrove and Tropical Rain Forest Region of West Africa, in: An International Workshop on Exchange of Experience in Water Resources Management Between Europe/China/Africa/Latin America. pp. 15–18.

Ehiorobo, J.O., Uso, N.O., 2014. Flood frequency analysis in the lower River Niger basin at Onitsha Bridge head. Journal of Engineering Research 19, 33–44.

Ekka, P., Patra, S., Upreti, M., Kumar, G., Kumar, A., Saikia, P., 2023. Land Degradation and Its Impacts on Biodiversity and Ecosystem Services, in: Raj, A., Jhariya, M.K., Banerjee, A., Nema, S., Bargali, K. (Eds.), Land and Environmental Management through Forestry. Wiley, pp. 77–101. https://doi.org/10.1002/9781119910527.ch4

Ekpeni, N.M., Ayeni, A.O., Oni, F., Adeaga, O., Oladipo, E.O., 2023. Spatio-Temporal Characteristics of Agricultural Drought in North Central Nigeria, in: Egbueri, J.C., Ighalo, J.O., Pande, C.B. (Eds.), Climate Change Impacts on Nigeria: Environment and Sustainable Development. Springer International Publishing, Cham, pp. 409–421. https://doi.org/10.1007/978-3-031-21007-5_21

Ekwueme, B.N., Ekwueme, B.N., 2021. Quantification of effects of climate change on flood in tropical river basins. Cogent engineering 8. https://doi.org/10.1080/23311916.2021.1986967

Elekwachi, W., Phil-Eze, P.O., Etuk, E.A., Wizor, C.H., Onyishi, C.J., 2021. Spatiotemporal Characteristics of Wetlands Ecosystem in the Niger Delta Region. Journal of Geoscience and Environment Protection 9, 244–264.

Essa, Y.H., Cagnazzo, C., Madonna, F., Cristofanelli, P., Yang, C., Serva, F., Caporaso, L., Santoleri, R., 2022. Intercomparison of atmospheric upper-air temperature from recent global reanalysis datasets. Frontiers in Earth Science 10, 935139.

Estes, J.E., Loveland, T.R., 1999. Characteristics, sources, and management of remotely-sensed data. Geographical Information Systems: Principles, Techniques, Applications, and Management 667–675.

Eyoh, A., Okwuashi, O., 2017. Spatial and Temporal Evaluation of Land Use/Land Cover Change of the Niger Delta Region of Nigeria from 1986-2016. SSRG Int. J. Geoinform. Geol. Sci 4, 20–28.

Fasona, M.J., Omojola, A.S., 2005. Climate Change, Human Security and Communal Clashes in Nigeria.

Feyisa, G.L., Meilby, H., Fensholt, R., Proud, S.R., 2014. Automated Water Extraction Index: A new technique for surface water mapping using Landsat imagery. Remote sensing of environment 140, 23–35.

Fidan, E., Gray, J.V., Doll, B., Nelson, N., 2023. Machine learning approach for modeling daily pluvial flood dynamics in agricultural landscapes. Environmental Modelling & Software 167, 105758–105758. https://doi.org/10.1016/j.envsoft.2023.105758

Flood Disaster Hazards; Causes, Impacts and Management: A State-of-the-Art Review, 2021. , in: Natural Hazards - Impacts, Adjustments and Resilience. IntechOpen. https://doi.org/10.5772/intechopen.95048

Flood risk management: information for flood risk management authorities, asset owners and local authorities [WWW Document], 2014. . GOV.UK. URL https://www.gov.uk/guidance/flood-risk-management-information-for-flood-risk-management-authorities-asset-owners-and-local-authorities (accessed 7.21.25).

Foley, J.A., DeFries, R., Asner, G.P., Barford, C., Bonan, G., Carpenter, S.R., Chapin, F.S., Coe, M.T., Daily, G.C., Gibbs, H.K., 2005. Global consequences of land use. science 309, 570–574.

Fothergill, L.J., Disney, A.S., Wilson, E.E., 2021. A qualitative exploration of the psychological impacts of living with the uncertainty of persistent flood risk. Public Health 198, 141–145. https://doi.org/10.1016/j.puhe.2021.07.016

Frazier, P.S., Page, K.J., 2000. Water body detection and delineation with Landsat TM data. Photogrammetric engineering and remote sensing 66, 1461–1468.

Freden, S.C., Mercanti, E.P., Becker, M.A., 1974. Third Earth Resources Technology Satellite-1 Symposium: The Proceedings of a Symposium Held by Goddard Space Flight Center at

Washington, DC on December 10-14, 1973: Prepared at Goddard Space Flight Center. Scientific and Technical Information Office, National Aeronautics and Space ….

Gandhi, G.M., Parthiban, S., Thummalu, N., Christy, A., 2015. Ndvi: Vegetation change detection using remote sensing and gis–A case study of Vellore District. Procedia computer science 57, 1199–1210.

Gao, B.-C., 1996. NDWI—A normalized difference water index for remote sensing of vegetation liquid water from space. Remote sensing of environment 58, 257–266.

Garba, H., Udokpoh, U.U., 2023. Analysis of Trend in Meteorological and Hydrological Time-series using Mann-Kendall and Sen’s Slope Estimator Statistical Test in Akwa Ibom State, Nigeria. IJECC 13, 1017–1035. https://doi.org/10.9734/ijecc/2023/v13i102748

Garcia-Salgado, B.P., Ponomaryov, V.I., Sadovnychiy, S., Reyes-Reyes, R., 2020. Efficient dimension reduction of hyperspectral images for big data remote sensing applications. Journal of Applied Remote Sensing 14, 032611–032611.

Gbode, I.E., Babalola, T.E., Diro, G.T., Intsiful, J.D., 2023. Assessment of ERA5 and ERA-Interim in Reproducing Mean and Extreme Climates over West Africa. Adv. Atmos. Sci. 40, 570–586. https://doi.org/10.1007/s00376-022-2161-8

Gbode, I.E., Ogunjobi, K.O., Dudhia, J., Ajayi, V.O., Liu, C., 2021. Impacts of global warming on West African monsoon rainfall: Downscaling by pseudo global warming method. Atmospheric Research 249, 105334. https://doi.org/10.1016/j.atmosres.2020.105334

Geekiyanage, D., Fernando, T., Keraminiyage, K., 2020. Assessing the state of the art in community engagement for participatory decision-making in disaster risk-sensitive urban development. International Journal of Disaster Risk Reduction 51, 101847. https://doi.org/10.1016/j.ijdrr.2020.101847

Gerkensmeier, B., Ratter, B.M., 2018. Governing coastal risks as a social process—Facilitating integrative risk management by enhanced multi-stakeholder collaboration. Environmental Science & Policy 80, 144–151.

Ghajarnia, N., Daneshkar Arasteh, P., Liaghat, M., Araghinejad, S., 2018. Error Analysis on PERSIANN Precipitation Estimations: Case Study of Urmia Lake Basin, Iran. J. Hydrol. Eng. 23. https://doi.org/10.1061/(asce)he.1943-5584.0001643

GIBBA, P., 2016. Multi-model CMIP5 and CORDEX simulations of historical summer temperature and precipitation variabilities over West Africa. International Journal of Climatology.

Golladay, S.W., Battle, J., 2002. Effects of flooding and drought on water quality in gulf coastal plain streams in Georgia. Journal of Environmental Quality 31, 1266–1272.

Gorelick, N., Gorelick, N., Hancher, M., Dixon, M.J., Dixon, M., Ilyushchenko, S., Thau, D., Moore, R., 2017. Google Earth Engine: Planetary-scale geospatial analysis for everyone. Remote Sensing of Environment 202, 18–27. https://doi.org/10.1016/j.rse.2017.06.031

Govender, T., Dube, T., Shoko, C., 2022. Remote sensing of land use-land cover change and climate variability on hydrological processes in Sub-Saharan Africa: Key scientific strides and challenges. Geocarto International 1–27. https://doi.org/10.1080/10106049.2022.2043451

Green, K., Kempka, D., Lackey, L., 1994. Using remote sensing to detect and monitor land-cover and land-use change. Photogrammetric engineering and remote sensing 60, 331–337.

Guild, R., Wang, X., Quijón, P.A., 2024. Climate change impacts on coastal ecosystems. Environmental Research: Climate 3, 042006.

Guoshuai, Z., Anjun, D., Jianguo, C., Dangwei, W., Qin, L., Yiqin, X., 2023. Improving the double mass curve method to analyse the variation trend of runoff and sediment load in watersheds. LHB 109, 2236971. https://doi.org/10.1080/27678490.2023.2236971

Hagos, S.M., Cook, K.H., 2007. Dynamics of the West African monsoon jump. Journal of Climate 20, 5264–5284.

Hajek, O.L., Knapp, A.K., 2022. Shifting seasonal patterns of water availability: ecosystem responses to an unappreciated dimension of climate change. New Phytologist 233, 119–125. https://doi.org/10.1111/nph.17728

Haji, S.H., Abdulazeez, A.M., 2021. Comparison of optimization techniques based on gradient descent algorithm: A review. PalArch's Journal of Archaeology of Egypt/Egyptology 18, 2715–2743.

Hall, J.W., Meadowcroft, I.C., Sayers, P.B., Bramley, M.E., 2003. Integrated Flood Risk Management in England and Wales. Nat. Hazards Rev. 4, 126–135. https://doi.org/10.1061/(asce)1527-6988(2003)4:3(126)

Hamed, K.H., 2009. Exact distribution of the Mann–Kendall trend test statistic for persistent data. Journal of hydrology 365, 86–94.

Hao, B., Ma, M., Li, S., Li, Q., Hao, D., Huang, J., Ge, Z., Yang, H., Han, X., 2019. Land use change and climate variation in the three gorges reservoir catchment from 2000 to 2015 based on the Google Earth Engine. Sensors 19, 2118.

Hariyono, M.I., Ramdani, D., Silalahi, F.E.S., Kurniawan, A.A., Indriasari, N., Buswari, M., 2023. Land use and land cover change analysis of flood prone area using remote sensing data and machine learning in Malang Raya, East Java, Indonesia. IOP Conference Series: Earth and Environment 1173, 012051–012051. https://doi.org/10.1088/1755-1315/1173/1/012051

Hassan, G., Syakir, M., 2023. Spatio-temporal analysis of land use and land cover changes in Nguru Wetland, Yobe State, Nigeria. IOP Conference Series: Earth and Environment 1167, 012026–012026. https://doi.org/10.1088/1755-1315/1167/1/012026

Hassan, I., Kalin, R.M., Aladejana, J.A., Christopher J. White, 2020. Potential Impacts of Climate Change on Extreme Weather Events in the Niger Delta Part of Nigeria. Hydrology 7, 19. https://doi.org/10.3390/hydrology7010019

Heidari, S., Karimi, M., Beyranvand, A., 2024. Evaluation the performance of ERA5 Reanalysis Data in Iran's rainfall estimation and spatial analysis of the country's precipitation regime. Researches in Earth Sciences 15, 1–24.

Helber, P., Bischke, B., Dengel, A., Borth, D., 2019. Eurosat: A novel dataset and deep learning benchmark for land use and land cover classification. IEEE Journal of Selected Topics in Applied Earth Observations and Remote Sensing 12, 2217–2226.

Hemmati, M., Ellingwood, B.R., Mahmoud, H.N., 2020. The role of urban growth in resilience of communities under flood risk. Earth's Future 8, e2019EF001382.

Hepner, G., Logan, T., Ritter, N., Bryant, N., 1990. Artificial neural network classification using a minimal training set- Comparison to conventional supervised classification. Photogrammetric Engineering and Remote Sensing 56, 469–473.

Ho, T.K., 1995. Random decision forests, in: Proceedings of 3rd International Conference on Document Analysis and Recognition. IEEE, pp. 278–282.

Hobday, A.J., Cochrane, K., Downey-Breedt, N., Howard, J., Aswani, S., Byfield, V., Duggan, G., Duna, E., Dutra, L.X.C., Frusher, S.D., Fulton, E.A., Gammage, L., Gasalla, M.A., Griffiths, C., Guissamulo, A., Haward, M., Jarre, A., Jennings, S.M., Jordan, T., Joyner, J., Ramani, N.K., Shanmugasundaram, S.L.P., Malherbe, W., Cisneros, K.O., Paytan, A., Pecl, G.T., Plagányi, É.E., Popova, E.E., Razafindrainibe, H., Roberts, M., Rohit, P., Sainulabdeen, S.S., Sauer, W., Valappil, S.T., Zacharia, P.U., Van Putten, E.I., 2016. Planning adaptation to climate change in fast-warming marine regions with seafood-dependent coastal communities. Rev Fish Biol Fisheries 26, 249–264. https://doi.org/10.1007/s11160-016-9419-0

Hoffmann, P., Spekat, A., 2021. Identification of possible dynamical drivers for long-term changes in temperature and rainfall patterns over Europe. Theor Appl Climatol 143, 177–191. https://doi.org/10.1007/s00704-020-03373-3

Hong, C., Burney, J.A., Pongratz, J., Nabel, J.E., Mueller, N.D., Jackson, R.B., Davis, S.J., 2021. Global and regional drivers of land-use emissions in 1961–2017. Nature 589, 554–561.

Hsu, T.-Y., Mazloff, M.R., Gille, S.T., Freilich, M.A., Sun, R., Cornuelle, B.D., 2024. Response of sea surface temperature to atmospheric rivers. Nature Communications 15, 5018.

Huang, J., Fatichi, S., Mascaro, G., Manoli, G., Peleg, N., 2022. Intensification of sub-daily rainfall extremes in a low-rise urban area. Urban Climate 42, 101124. https://doi.org/10.1016/j.uclim.2022.101124

Huang, Y.F., Ahmed, A.N., Ng, J.L., Tan, K.W., Kumar, P., El-Shafie, A., 2022. Rainfall Variability Index (RVI) analysis of dry spells in Malaysia. Natural Hazards 112, 1423–1475.

Ibitoye, Matthew Olomolatan, Ibitoye, M.O., Komolafe, A.A., Komolafe, A.A., Adegboyega, S.A., Abdul-Azeez Suleiman Adegboyega, Adegboyega, A.-A.S., Abiodun Olufemi Adebola, Adebola, A.O., Oluwadamilola Daniel Oladeji, Oladeji, O.D., 2020. Analysis of vulnerable urban properties within river Ala floodplain in Akure, Southwestern Nigeria. Spatial Information Research 28, 431–445. https://doi.org/10.1007/s41324-019-00298-6

Idowu, D., Idowu, D., Zhou, W., Zhou, W., Zhou, W., 2021. Land Use and Land Cover Change Assessment in the Context of Flood Hazard in Lagos State, Nigeria. Water 13, 1105. https://doi.org/10.3390/w13081105

Ighile, E.H., Ighile, E.H., Shirakawa, H., Shirakawa, H., Shirakawa, H., 2020. A STUDY ON THE EFFECTS OF LAND USE CHANGE ON FLOODING RISKS IN NIGERIA 15, 91–101. https://doi.org/10.21163/gt_2020.151.08

Ighile, E.H., Shirakawa, H., Tanikawa, H., 2022. Application of GIS and machine learning to predict flood areas in Nigeria. Sustainability 14, 5039.

Ikiel, C., Dutucu, A.A., Ustaoglu, B., Kilic, D.E., 2012. Land use and land cover (LULC) classification using Spot-5 image in the Adapazari Plain and its surroundings, Turkey. Tojsat 2, 37–42.

Ilaboya, I., Ehiorobo, J.O., Izinyon, C.O., Idemudia, O., 2023. Impact of Flood Susceptibility Mapping as an Early Warning Tool in a Changing Environment. Journal of Science and Technology Research 5.

Ilaboya, I.R., Nwachukwu, S.N., 2022. Development of intensity duration frequency (IDF) curves for rainfall prediction in some selected states in South-West Nigeria. Journal of Energy Technology and Environment 4.

Ilori, O.W., Ajayi, V.O., 2020a. Change Detection and Trend Analysis of Future Temperature and Rainfall over West Africa. Earth Syst Environ 4, 493–512. https://doi.org/10.1007/s41748-020-00174-6

Ilori, O.W., Ajayi, V.O., 2020b. Change Detection and Trend Analysis of Future Temperature and Rainfall over West Africa. Earth Syst Environ 4, 493–512. https://doi.org/10.1007/s41748-020-00174-6

Imen Guechi, H. Gherraz, D. Alkama, 2021. Correlation analysis between biophysical indices and Land Surface Temperature using remote sensing and GIS in Guelma city (Algeria). Bulletin de la Société royale des sciences de Liège. https://doi.org/10.25518/0037-9565.10457

Innocent Abbas, I., 2013. An Assessment of Land Use/Land Cover Changes in a Section of Niger Delta, Nigeria. FS 2, 137–143. https://doi.org/10.5923/j.fs.20120206.02

Intergovernmental Panel On Climate Change (Ipcc), 2023. Climate Change 2021 – The Physical Science Basis: Working Group I Contribution to the Sixth Assessment Report of the Intergovernmental Panel on Climate Change, 1st ed. Cambridge University Press. https://doi.org/10.1017/9781009157896

Ionescu, B., Müller, H., Villegas, M., Arenas, H., Boato, G., Dang-Nguyen, D.-T., Dicente Cid, Y., Eickhoff, C., Seco de Herrera, A.G., Gurrin, C., 2017. Overview of ImageCLEF 2017: Information extraction from images, in: Experimental IR Meets Multilinguality, Multimodality, and Interaction: 8th International Conference of the CLEF Association, CLEF 2017, Dublin, Ireland, September 11–14, 2017, Proceedings 8. Springer, pp. 315–337.

Ishak, W.H.W., Yamin, F., Maidin, S.S., Husin, A., 2025. Comparative Analysis of Data Visualization Techniques for Rainfall Data. Data Science Insights 3.

Islam, A.R.Md.T., Pal, S., Talukdar, S., Mahato, S., Kundu, S., Eibek, K.U., Pham, Q.B., Kuriqi, A., Linh, N.T.T., 2020. Flood susceptibility modelling using advanced ensemble machine learning models. Geoscience frontiers 12, 101075–101075. https://doi.org/10.1016/j.gsf.2020.09.006

Islam, M.M.M., Islam, Md.A., 2020. Quantifying public health risks from exposure to waterborne pathogens during river bathing as a basis for reduction of disease burden. Journal of Water and Health 18, 292–305. https://doi.org/10.2166/wh.2020.045

Jain, S.K., Singh, R.D., Jain, M.K., Lohani, A.K., 2005. Delineation of flood-prone areas using remote sensing techniques. Water resources management 19, 333–347.

Jay, O., Capon, A., Berry, P., Broderick, C., De Dear, R., Havenith, G., Honda, Y., Kovats, R.S., Ma, W., Malik, A., 2021. Reducing the health effects of hot weather and heat extremes: from personal cooling strategies to green cities. The Lancet 398, 709–724.

Jenifer, M.A., Jha, M.K., 2021. Assessment of precipitation trends and its implications in the semi-arid region of Southern India. Environmental Challenges 5, 100269. https://doi.org/10.1016/j.envc.2021.100269

Jenkins, M.W., Sugden, S., 2006. Human development report 2006. New York: United Nations Development Programme.

Jones, M.W., Abatzoglou, J.T., Veraverbeke, S., Andela, N., Lasslop, G., Forkel, M., Smith, A.J.P., Burton, C., Betts, R.A., Van Der Werf, G.R., Sitch, S., Canadell, J.G., Santín, C., Kolden, C., Doerr, S.H., Le Quéré, C., 2022. Global and Regional Trends and Drivers of Fire Under Climate Change. Reviews of Geophysics 60, e2020RG000726. https://doi.org/10.1029/2020RG000726

Jumbo, S.A., A, O.A., S, E.O., 2023. FLOOD RISK ASSESSMENT, CLIMATE CHANGE ADAPTATIONS AND MITIGATION STRATEGIES OF COMMUNITIES IN EDO STATE, NIGERIA. International Journal of Agriculture Environment and Bioresearch. https://doi.org/10.35410/ijaeb.2023.5829

Kadiria, M.O., Gift Oluwatodimu Fabolude, Nura Umar Kurac, 2023. Impact of land use change on urban heat island in Etsoko West, Southern Nigeria. Dutse Journal of Pure and Applied Sciences 9, 65–77. https://doi.org/10.4314/dujopas.v9i1b.7

Kamara, S.M., 2019. Integration of GIS in the Development of an Environmental Cadastre Administrative System for the Environment Protection Agency Sierra Leone. JGIS 11, 411–428. https://doi.org/10.4236/jgis.2019.114026

Kamrul Islam, Islam, K., Mohammed Jashimuddin, Jashimuddin, M., Biswajit Nath, Nath, B., Tapan Kumar Nath, Nath, T.K., 2018. Land use classification and change detection by using multi-temporal remotely sensed imagery: The case of Chunati wildlife sanctuary, Bangladesh. The Egyptian Journal of Remote Sensing and Space Science 21, 37–47. https://doi.org/10.1016/j.ejrs.2016.12.005

Kamruzzaman, M., Almazroui, M., Salam, M.A., Mondol, M.A.H., Rahman, M.M., Deb, L., Kundu, P.K., Zaman, M.A.U., Islam, A.R.M.T., 2022. Spatiotemporal drought analysis in Bangladesh using the standardized precipitation index (SPI) and standardized precipitation evapotranspiration index (SPEI). Scientific Reports 12, 20694.

Kehinde, A.O., 2022. The effect of global warming in Nigeria: Flood in perspective. Studia Prawno-Ekonomiczne 124, 39–58. https://doi.org/10.26485/spe/2022/124/3

Khalil Ahmad, A. Banerjee, W. Rashid, Zilong Xia, Shahid Karim, Muhammad Asif, 2022. Assessment of Long-Term Rainfall Variability and Trends Using Observed and Satellite Data in Central Punjab, Pakistan. Atmosphere. https://doi.org/10.3390/atmos14010060

Klemas, V., 2015. Remote sensing of floods and flood-prone areas: An overview. Journal of Coastal Research 31, 1005–1013.

Krasnopeyev, S.M., Nerov, I.O., Бугаец, А.Н., 2022. The potential of remote sensing materials to restore of a highly detailed DEM of the floodable part of the river floodplain of large rivers. Geoinformatika 28–35. https://doi.org/10.47148/1609-364x-2022-4-28-35

Kuenzer, C., van Beijma, S., Gessner, U., Dech, S., 2014. Land surface dynamics and environmental challenges of the Niger Delta, Africa: Remote sensing-based analyses spanning three decades (1986–2013). Applied Geography 53, 354–368.

Kyaw, A.M.M., Kim, B.H.S., 2025. Climate change, adaptation, and economic outcomes in rice farming: empirical findings from Myanmar's Delta region. Agric Econ 13, 74. https://doi.org/10.1186/s40100-025-00414-1

Lal, P., Prakash, A., Kumar, A., 2020. Google Earth Engine for concurrent flood monitoring in the lower basin of Indo-Gangetic-Brahmaputra plains. Natural Hazards 104, 1947–1952.

Langhammer, J., 2023. Flood Simulations Using a Sensor Network and Support Vector Machine Model. Water 15, 2004. https://doi.org/10.3390/w15112004

Lasat, M.M., Chung, K.F., Lead, J., McGrath, S., Owen, R.J., Rocks, S., Unrine, J., Zhang, J., 2018. Advancing the Understanding of Environmental Transformations, Bioavailability and Effects of Nanomaterials, an International US Environmental Protection Agency—UK Environmental Nanoscience Initiative Joint Program. JEP 09, 385–404. https://doi.org/10.4236/jep.2018.94025

Lee, Y.-S., Tong, L.-I., 2011. Forecasting time series using a methodology based on autoregressive integrated moving average and genetic programming. Knowledge-Based Systems 24, 66–72.

Lei, C., Deng, J., Cao, K., Xiao, Y., Ma, L., Wang, W., Ma, T., Shu, C., 2019. A comparison of random forest and support vector machine approaches to predict coal spontaneous combustion in gob. Fuel 239, 297–311.

Lewis, S., 2009. Remote sensing for natural disasters: Facts and figures. SciDev. net-Environment.

Li, L., Hao, Y., Zheng, Z., Wang, W., Biederman, J.A., Wang, Y., Wen, F., Qian, R., Xu, C., Zhang, B., 2022. Heavy rainfall in peak growing season had larger effects on soil nitrogen flux and pool than in the late season in a semiarid grassland. Agriculture, Ecosystems & Environment 326, 107785.

Li, S., Peng, Y., Bin, G., 2023. Prediction of wind turbine blades icing based on CJBM with imbalanced data. IEEE Sensors Journal 23, 19726–19736.

Li, X., Xie, S.-P., Gille, S.T., Yoo, C., 2016. Atlantic-induced pan-tropical climate change over the past three decades. Nature Climate Change 6, 275–279.

Liu, Z., Anderson, B., Yan, K., Dong, W., Liao, H., Shi, P., 2017. Global and regional changes in exposure to extreme heat and the relative contributions of climate and population change. Scientific Reports 7, 43909.

Liu, Z., Yao, Z., Wang, R., 2016. Assessing methods of identifying open water bodies using Landsat 8 OLI imagery. Environmental Earth Sciences 75, 1–13.

Liyew, C.M., Melese, H.A., 2021. Machine learning techniques to predict daily rainfall amount. J Big Data 8, 153. https://doi.org/10.1186/s40537-021-00545-4

Loukika, K.N., Reddy, K.V., Sridhar, V., 2021. Analysis of Land Use and Land Cover Using Machine Learning Algorithms on Google Earth Engine for Munneru River Basin, India. Sustainability 13, 13758–13758. https://doi.org/10.3390/su132413758

Lu, D., Weng, Q., 2007. A survey of image classification methods and techniques for improving classification performance. International journal of Remote sensing 28, 823–870.

Lu, J., 2009. The dynamics of the Indian Ocean sea surface temperature forcing of Sahel drought. Clim Dyn 33, 445–460. https://doi.org/10.1007/s00382-009-0596-6

Luo, Y., Zhou, Y., Zhou, C., 2024. Spatio-temporal patterns of temperature extremes and their response to atmospheric circulation factors in China from 1961 to 2020. J. Geogr. Sci. 34, 1883–1903. https://doi.org/10.1007/s11442-024-2275-2

M. K. Jha, Manoj K. Jha, Jha, M.K., Jha, M., 2020. Impacts of Landscape Changes on Water Resources. Water 12, 2244. https://doi.org/10.3390/w12082244

Machiwal, D., Meena, H.M., Singh, D.V., 2022. Overview of trend and homogeneity tests and their application to rainfall time series, in: Current Directions in Water Scarcity Research. Elsevier, pp. 599–620. https://doi.org/10.1016/B978-0-323-91910-4.00034-0

MacLeod, D.A., Dankers, R., Graham, R., Guigma, K., Jenkins, L., Todd, M.C., Kiptum, A., Kilavi, M., Njogu, A., Mwangi, E., 2021. Drivers and subseasonal predictability of heavy rainfall in equatorial East Africa and relationship with flood risk. Journal of Hydrometeorology 4, 887–903. https://doi.org/doi:%2010.1175/JHM-D-20-0211.1

Magazzino, C., Madaleno, M., Waqas, M., Leogrande, A., 2024. Exploring the determinants of methane emissions from a worldwide perspective using panel data and machine learning analyses. Environmental Pollution 348, 123807. https://doi.org/10.1016/j.envpol.2024.123807

Mahmud, A., 2022. Observing Waterlogging and its Impact on Agriculture in Hungary Using Radar and Optical Images.

Malachy, E., Dossen, S.B., Ebuenyi, I.D., 2022. Flooding in Nigeria, towards prioritizing mental health and psychosocial support. The Pan African Medical Journal 43. https://doi.org/10.11604/pamj.2022.43.199.38251

Malakar, N.K., 2022. Environmental Intelligence using Machine Learning Applications. Journal of Nepal Physical Society 8, 42–47. https://doi.org/10.3126/jnphyssoc.v8i2.50148

Manley, K., Manley, K., Nyelele, C., Nyelele, C., Egoh, B.N., Egoh, B.N., 2022. A review of machine learning and big data applications in addressing ecosystem service research gaps. Ecosystem services 57, 101478–101478. https://doi.org/10.1016/j.ecoser.2022.101478

Mar, K.A., Unger, C., Walderdorff, L., Butler, T., 2022. Beyond CO2 equivalence: The impacts of methane on climate, ecosystems, and health. Environmental Science & Policy 134, 127–136. https://doi.org/10.1016/j.envsci.2022.03.027

Marghany, M., 2022. Recent Remote Sensing Sensor Applications: Satellites and Unmanned Aerial Vehicles (UAVs). BoD–Books on Demand.

Markos, D., Worku, W., Mamo, G., 2023. Spatio-temporal variability and rainfall trend affects seasonal calendar of maize production in southern central Rift Valley of Ethiopia. PLoS Climate 2, e0000218.

Masson-Delmotte, V., Zhai, P., Pirani, A., Connors, S.L., Péan, C., Berger, S., Caud, N., Chen, Y., Goldfarb, L., Gomis, M.I., 2021. Climate change 2021: the physical science basis. Contribution of working group I to the sixth assessment report of the intergovernmental panel on climate change 2, 2391.

Mast, J., Sapena, M., Geiß, C., Taubenböck, H., 2023. Linking remote sensing data and online engagement in flood events in Nigeria. Joint Urban Remote Sensing Event. https://doi.org/10.1109/jurse57346.2023.10144130

Masunaga, H., 2022. Active Remote Sensing. Springer remote sensing/photogrammetry 225–254. https://doi.org/10.1007/978-981-19-2243-5_10

Mather, A.S., 1992. The forest transition. Area 367–379.

Mathevet, T., Le Moine, N., Andréassian, V., Gupta, H., Oudin, L., 2024. Multi-objective assessment of hydrological model performances using Nash–Sutcliffe and Kling–Gupta efficiencies on a worldwide large sample of watersheds. Comptes Rendus. Géoscience 355, 117–141. https://doi.org/10.5802/crgeos.189

Matthews, H.D., Weaver, A.J., Meissner, K.J., Gillett, N.P., Eby, M., 2004. Natural and anthropogenic climate change: incorporating historical land cover change, vegetation dynamics and the global carbon cycle. Climate Dynamics 22, 461–479.

McFeeters, S.K., 2013. Using the normalized difference water index (NDWI) within a geographic information system to detect swimming pools for mosquito abatement: a practical approach. Remote Sensing 5, 3544–3561.

McFeeters, S.K., 1996. The use of the Normalized Difference Water Index (NDWI) in the delineation of open water features. International journal of remote sensing 17, 1425–1432.

McLeod, A.I., 2005. Kendall rank correlation and Mann-Kendall trend test. R package Kendall 602, 1–10.

Mehmood, H., Conway, C., Perera, D., 2021. Mapping of flood areas using landsat with google earth engine cloud platform. Atmosphere 12, 866.

Mehta, P., 2024. The Impact of Climate Change on the Environment, Water Resources, and Agriculture: A Comprehensive Review, in: Rai, P.K., Rai, S. (Eds.), Climate, Environment and Agricultural Development, Advances in Geographical and Environmental Sciences.

Springer Nature Singapore, Singapore, pp. 189–201. https://doi.org/10.1007/978-981-97-8363-2_12

Merem, E.C., Twumasi, Y., Wesley, J., Isokpehi, P., Fageir, S., Crisler, M., Romorno, C., Hines, A., Ochai, G.S., Leggett, S., 2018. Appraising variations in climate change parameters along the lower West African region. Journal of Safety Engineering 7, 1–19.

Merz, B., Blöschl, G., Vorogushyn, S., Dottori, F., Aerts, J.C., Bates, P., Bertola, M., Kemter, M., Kreibich, H., Lall, U., 2021. Causes, impacts and patterns of disastrous river floods. Nature Reviews Earth & Environment 2, 592–609.

Mfon, I.E., Oguike, M.C., Eteng, S.U., Etim, N.M., 2022. Causes and effects of flooding in nigeria: A review. East Asian Journal of Multidisciplinary Research 1, 1777–1792.

Minh, H.V.T., Avtar, R., Mohan, G., Misra, P., Kurasaki, M., 2019. Monitoring and mapping of rice cropping pattern in flooding area in the Vietnamese Mekong delta using Sentinel-1A data: A case of an Giang province. ISPRS International Journal of Geo-Information 8, 211.

Misra, A.A., 2022. Remote Sensing Fundamentals 7–14. https://doi.org/10.1002/9781119813392.ch1

Mohammadi, A., Costelloe, J.F., Ryu, D., 2017. Application of time series of remotely sensed normalized difference water, vegetation and moisture indices in characterizing flood dynamics of large-scale arid zone floodplains. Remote sensing of environment 190, 70–82.

Moharrami, M., Javanbakht, M., Attarchi, S., 2021. Automatic flood detection using sentinel-1 images on the google earth engine. Environmental monitoring and assessment 193, 1–17.

Mohino, E., Janicot, S., Bader, J., 2011. Sahel rainfall and decadal to multi-decadal sea surface temperature variability. Clim Dyn 37, 419–440. https://doi.org/10.1007/s00382-010-0867-2

Mondal, B.K., Mahata, S., Basu, T., Das, R., Patra, R., Abdelrahman, K., Fnais, M.S., Praharaj, S., 2024. Analysis of the Post-Cyclonic Physical Flood Susceptibility and Changes of Mangrove Forest Area Using Multi-Criteria Decision-Making Process and Geospatial Analysis in Indian Sundarbans. Atmosphere 15, 432.

Moriasi, D.N., Arnold, J.G., Van Liew, M.W., Bingner, R.L., Harmel, R.D., Veith, T.L., 2007. Model evaluation guidelines for systematic quantification of accuracy in watershed simulations. Transactions of the ASABE 50, 885–900.

Mueller, N., Lewis, A., Roberts, D., Ring, S., Melrose, R., Sixsmith, J., Lymburner, L., McIntyre, A., Tan, P., Curnow, S., 2016. Water observations from space: Mapping surface water from 25 years of Landsat imagery across Australia. Remote Sensing of Environment 174, 341–352.

Muruganandam, M., Rajamanickam, S., Sivarethinamohan, S., Reddy, M.K., Velusamy, P., Gomathi, R., Ravindiran, G., Gurugubelli, T.R., Munisamy, S.K., 2023. Impact of climate change and anthropogenic activities on aquatic ecosystem–A review. Environmental Research 117233.

Musa, D., Musa, S.D., Shabu, T., Shabu, T., 2019. Using geographic information system to evaluate land use and land cover affected by flooding in Adamawa State, Nigeria. Jàmbá: Journal of Disaster Risk Studies 11, 494–494. https://doi.org/10.4102/jamba.v11i1.494

Musa, Z.N., Popescu, I., Mynett, A., 2016. Assessing the sustainability of local resilience practices against sea level rise impacts on the lower Niger delta. Ocean & coastal management 130, 221–228.

Muzammal, H., Zaman, M., Safdar, M., Adnan Shahid, M., Sabir, M.K., Khil, A., Raza, A., Faheem, M., Ahmed, J., Sattar, J., Sajid, M., Zaib, A., 2024a. Climate Change Impacts on Water Resources and Implications for Agricultural Management, in: Kanga, S., Singh, S.K., Shevkani, K., Pathak, V., Sajan, B. (Eds.), Transforming Agricultural Management for a Sustainable Future, World Sustainability Series. Springer Nature Switzerland, Cham, pp. 21–45. https://doi.org/10.1007/978-3-031-63430-7_2

Muzammal, H., Zaman, M., Safdar, M., Adnan Shahid, M., Sabir, M.K., Khil, A., Raza, A., Faheem, M., Ahmed, J., Sattar, J., Sajid, M., Zaib, A., 2024b. Climate Change Impacts on Water Resources and Implications for Agricultural Management, in: Kanga, S., Singh, S.K., Shevkani, K., Pathak, V., Sajan, B. (Eds.), Transforming Agricultural Management for a Sustainable Future, World Sustainability Series. Springer Nature Switzerland, Cham, pp. 21–45. https://doi.org/10.1007/978-3-031-63430-7_2

Nasiri, V., Deljouei, A., Moradi, F., Sadeghi, S.M.M., Borz, S.A., 2022. Land Use and Land Cover Mapping Using Sentinel-2, Landsat-8 Satellite Images, and Google Earth Engine: A Comparison of Two Composition Methods. Remote Sensing 14, 1977–1977. https://doi.org/10.3390/rs14091977

Nathan, R., Ran Nathan, Monk, C.T., Christopher T. Monk, Arlinghaus, R., Robert Arlinghaus, Adam, T., Timo Adam, Alós, J., Josep Alós, Assaf, M., Michael Assaf, Baktoft, H., Henrik Baktoft, Beardsworth, C.E., Christine E. Beardsworth, Bertram, M.G., Michael G. Bertram, Bijleveld, A.I., Allert I. Bijleveld, Brodin, T., Tomas Brodin, Brooks, J.L., Jill L.

Brooks, Campos-Candela, A., Andrea Campos-Candela, Cooke, Steve J., Cooke, Steven J., Steven J. Cooke, Gjelland, K.Ø., Karl Øystein Gjelland, Gupte, P.R., Pratik Rajan Gupte, Harel, R., Roi Harel, Hellström, G., Gustav Hellström, Jeltsch, F., Florian Jeltsch, Killen, S.S., Shaun S. Killen, Klefoth, T., Thomas Klefoth, Langrock, R., Roland Langrock, Lennox, R.J., Robert J. Lennox, Lourie, E., E. M. Lourie, Madden, J.R., Joah R. Madden, Orchan, Y., Yotam Orchan, Pauwels, I., Ine Pauwels, Říha, M., Milan Říha, Roeleke, M., Manuel Roeleke, Schlägel, U.E., Ulrike E. Schlägel, Shohami, D., David Shohami, Signer, J., Johannes Signer, Toledo, S., Sivan Toledo, Vilk, O., Ohad Vilk, Westrelin, S., Samuel Westrelin, Whiteside, M.A., Mark A. Whiteside, Jarić, I., Ivan Jarić, 2022. Big-data approaches lead to an increased understanding of the ecology of animal movement. Science 375. https://doi.org/10.1126/science.abg1780

Navalgund, R.R., Jayaraman, V., Roy, P.S., 2007. Remote sensing applications: An overview. current science 1747–1766.

Newell, F.L., Ausprey, I.J., Robinson, S.K., 2022. Spatiotemporal climate variability in the Andes of northern Peru: Evaluation of gridded datasets to describe cloud forest microclimate and local rainfall. Intl Journal of Climatology 42, 5892–5915. https://doi.org/10.1002/joc.7567

Nghiem, S.V., Liu, W.T., Tsai, W.-Y., Xie, X., 2000. Flood mapping over the Asian continent during the 1999 summer monsoon season, in: IGARSS 2000. IEEE 2000 International Geoscience and Remote Sensing Symposium. Taking the Pulse of the Planet: The Role of Remote Sensing in Managing the Environment. Proceedings (Cat. No. 00CH37120). IEEE, pp. 2027–2028.

Nguyen, H.D., Bui, Q., Nguyen, Q.-H., Nguyen, T.G., Pham, L.T., Nguyen, X.L., Vu, P.L., Nguyen, T.H.T., Nguyen, A.T., Petrisor, A.-I., 2022. A novel hybrid approach to flood susceptibility assessment based on machine learning and land use change. Case study: a river watershed in Vietnam. Hydrological Sciences Journal-journal Des Sciences Hydrologiques. https://doi.org/10.1080/02626667.2022.2060108

Nicholson, S.E., 2017. Climate and climatic variability of rainfall over eastern Africa. Reviews of Geophysics 55, 590–635. https://doi.org/10.1002/2016rg000544

Nicholson, S.E., Some, B., McCollum, J., Nelkin, E., Klotter, D., Berte, Y., Diallo, B.M., Gaye, I., Kpabeba, G., Ndiaye, O., Noukpozounkou, J.N., Tanu, M.M., Thiam, A., Toure, A.A., Traore, A.K., 2003. Validation of TRMM and Other Rainfall Estimates with a High-Density Gauge Dataset for West Africa. Part II: Validation of TRMM Rainfall Products. J. Appl. Meteor. 42, 1355–1368. https://doi.org/10.1175/1520-0450(2003)042%3C1355:votaor%3E2.0.co;2

Nwachukwu, M.A., Alozie, C.P., Alozie, G.A., 2018. Environmental and rainfall intensity analysis to solve the problem of flooding in Owerri urban. Journal of Environmental Hazards 107.

Nwilo, P.C., Badejo, O.T., 2006. Impacts and management of oil spill pollution along the Nigerian coastal areas. Administering Marine Spaces: International Issues 119, 1–15.

Odionu, G., 2018. Mitigation of greenhouse gas emissions from gas flaring in Nigeria: Perspectives on law and regulation. University of Saskatchewan.

Odunsi, O.M., Rienow, A., 2024. Estimating Surface Urban Heat Island Effects of Abeokuta Within the Context of Its Economic Development Cluster in Ogun State Nigeria: A Baseline Study Utilising Remote Sensing and Cloud-Based Computing Technologies. Climate 12, 198.

Odunuga, S., Adegun, O., Raji, S.A., Udofia, S., 2015. Changes in flood risk in Lower Niger–Benue catchments. Proceedings of the International Association of Hydrological Sciences 370, 97–102.

Oduro, C., Bi, S., Wu, N., Agyemang, S., Baidu, M., Babaousmail, H., Iyakaremye, V., Dike, V.N., Ayugi, B.O., 2024. Estimating surface air temperature from multiple gridded observations and reanalysis datasets over Ghana. Advances in Space Research 73, 537–552.

Ogashawara, I., Curtarelli, M.P., Ferreira, C.M., 2013. The use of optical remote sensing for mapping flooded areas. J. Eng. Res. Appl 3, 1956–1960.

Ogunrinde, A.T., Oguntunde, P.G., Akinwumiju, A.S., Fasinmirin, J.T., Adawa, I.S., Ajayi, T.A., 2023. Effects of climate change and drought attributes in Nigeria based on RCP 8.5 climate scenario. Physics and Chemistry of the Earth, Parts a/b/c 129, 103339.

Oguntunde, P.G., Abiodun, B.J., Lischeid, G., 2011. Rainfall trends in Nigeria, 1901–2000. Journal of Hydrology 411, 207–218. https://doi.org/10.1016/j.jhydrol.2011.09.037

Ojo, O.S., Emmanuel, I., Adeyemi, B., Ogolo, E.O., 2021. Effect of the radiation balance on warming occurrence over West Africa. Scientific African 11, e00700.

Okeke, O.B., Ehiorobo, J.O., 2017. Frequency analysis of rainfall for flood control in Patani, Delta State of Nigeria. Nigerian Journal of Technology 36, 282–289.

Okoro, E.O., Ofordu, C.S., 2025. Rainfall and Temperature Trends in Ogbia Local Government Area Bayelsa State, Nigeria from 1993 To 2023. Journal of Applied Sciences & Environmental Management 29.

Okpara, J.N., Tarhule, A.A., Perumal, M., 2013. Study of climate change in Niger River Basin, West Africa: Reality not a myth. Climate Change: Realities, Impacts Over Ice Cap, Sea Level and Risks 1.

Okunola, O.H., Werners, S.E., 2023. Recovery Pathways from Extreme Flood Events: Lessons and Experiences of Flooding in Lagos, Nigeria. https://doi.org/10.5194/egusphere-egu23-15302

Oladokun, V.O., Proverbs, D., 2016. Flood Risk Management In Nigeria: A Review Of The Challenges And Opportunities. International Journal of Safety and Security Engineering 6, 485–497. https://doi.org/10.2495/safe-v6-n3-485-497

Olanrewaju, C.C., Chitakira, M., Olanrewaju, O.A., Oludolapo O. Olanrewaju, Louw, E., 2019. Impacts of flood disasters in Nigeria: A critical evaluation of health implications and management. Jàmbá: Journal of Disaster Risk Studies 11, 557–557. https://doi.org/10.4102/jamba.v11i1.557

Olomoda, I.A., 2006. Impact of climatic change on river Niger hydrology, in: 9th International Rivers Symposium, Brisbane, Australia, 3rd–6th September.

Onilude, O.O., 2023. ANALYSIS OF LAND USE/LAND COVER CHANGE AND URBANIZATION TO ACHIEVING SUSTAINABLE DEVELOPMENT IN LAGOS NIGERIA.

Onoja, U.S., Dibua, U.M.E., Enete, A.A., 2011. Climate change: causes, effects and mitigation measures-a review. Global Journal of Pure and Applied Sciences 17, 469–479.

Onyena, A.P., Sam, K., 2020. A review of the threat of oil exploitation to mangrove ecosystem: Insights from Niger Delta, Nigeria. Global Ecology and Conservation 22, e00961. https://doi.org/10.1016/j.gecco.2020.e00961

Orhan, O., Ekercin, S., Dadaser-Celik, F., 2014. Use of landsat land surface temperature and vegetation indices for monitoring drought in the Salt Lake Basin Area, Turkey. The Scientific World Journal 2014.

Otto, F.E., Zachariah, M., Saeed, F., Siddiqi, A., Kamil, S., Mushtaq, H., Arulalan, T., AchutaRao, K., Chaithra, S.T., Barnes, C., 2023. Climate change increased extreme monsoon rainfall, flooding highly vulnerable communities in Pakistan. Environmental Research: Climate 2, 025001.

Ouma, Y.O., Tateishi, R., 2006. A water index for rapid mapping of shoreline changes of five East African Rift Valley lakes: an empirical analysis using Landsat TM and ETM+ data. International Journal of Remote Sensing 27, 3153–3181. https://doi.org/10.1080/01431160500309934

Oyabambi, A., Gambo, N., Bwese, T.D., Azok, I.J., 2025. Impact of climate change on food and human security in Nigeria. Br J Mark Stud 13.

Oyebande, L., Odunuga, S., 2010. Climate change impact on water resources at the transboundary level in West Africa: the cases of the Senegal, Niger and Volta Basins. The Open Hydrology Journal 4.

Palmer, P.I., Wainwright, C.M., Dong, B., Maidment, R.I., Wheeler, K.G., Gedney, N., Hickman, J.E., Madani, N., Folwell, S.S., Abdo, G., 2023. Drivers and impacts of Eastern African rainfall variability. Nature Reviews Earth & Environment 4, 254–270.

Panchal, G., Ganatra, A., Kosta, Y.P., Panchal, D., 2011. Behaviour analysis of multilayer perceptrons with multiple hidden neurons and hidden layers. International Journal of Computer Theory and Engineering 3, 332–337.

Pandey, A.C., Kaushik, K., Parida, B.R., 2022. Google Earth Engine for large-scale flood mapping using SAR data and impact assessment on agriculture and population of Ganga-Brahmaputra basin. Sustainability 14, 4210.

Paul Agboola, O., 2023. Ameliorating Climate Change Impacts on the Built Environment. Ameliorating Climate Change Impacts on the Built Environment (February 15, 2023).

Pedro-Monzonís, M., Solera, A., Ferrer, J., Estrela, T., Paredes-Arquiola, J., 2015. A review of water scarcity and drought indexes in water resources planning and management. Journal of Hydrology 527, 482–493.

Peduzzi, P., Dao, H., Herold, C., Mouton, F., 2009. Assessing global exposure and vulnerability towards natural hazards: The Disaster Risk Index. Natural Hazards and Earth System Sciences 1149–1159. https://doi.org/doi:%2010.5194/nhess-9-1149-2009

Penna, D., Brocca, L., Borga, M., Dalla Fontana, G., 2013. Soil moisture temporal stability at different depths on two alpine hillslopes during wet and dry periods. Journal of hydrology 477, 55–71.

Perera, D., Agnihotri, J., Seidou, O., Djalante, R., 2020. Identifying societal challenges in flood early warning systems. International Journal of Disaster Risk Reduction 51, 101794.

Pettitt, A.N., 1979. A Non-Parametric Approach to the Change-Point Problem. Applied Statistics 28, 126. https://doi.org/10.2307/2346729

Pham, T.T., Nguyen, T.-D., Tham, H.T., Truong, T.N., Lam-Dao, N., Nguyen-Huy, T., 2021. Specifying the relationship between land use/land cover change and dryness in central Vietnam from 2000 to 2019 using Google Earth Engine. Journal of Applied Remote Sensing 15, 024503–024503.

Philippes, M.F., Guy Donald, A., Casimir, K., Mesmin, T., Hubert-Ferrari, A., 2025. Urban heat island modeling and socio-economic vulnerability assessment in Yaoundé, Central Africa. International Journal of Sustainable Development & World Ecology 32, 858–879. https://doi.org/10.1080/13504509.2025.2566788

Piraei, R., Niazkar, M., Afzali, S.H., Menapace, A., 2023. Application of Machine Learning Models to Bridge Afflux Estimation. Water 15, 2187–2187. https://doi.org/10.3390/w15122187

Pirnia, A., Golshan, M., Darabi, H., Adamowski, J., Rozbeh, S., 2019. Using the Mann–Kendall test and double mass curve method to explore stream flow changes in response to climate and human activities. Journal of Water and Climate Change 10, 725–742. https://doi.org/10.2166/wcc.2018.162

Powell, W.G., 2009. Identifying land use/land cover (LULC) using National Agriculture Imagery Program (NAIP) data as a hydrologic model input for local flood plain management.

Prokešová, R., Horáčková, Š., Snopková, Z., 2022. Surface runoff response to long-term land use changes: Spatial rearrangement of runoff-generating areas reveals a shift in flash flood drivers. Science of The Total Environment 815, 151591. https://doi.org/10.1016/j.scitotenv.2021.151591

Qian, Q., Eslamian, S., 2022. Impact of urbanization on flooding, in: Flood Handbook. CRC Press, pp. 97–112.

Ramachandra, T.V., Negi, P., Bharath Setturu, 2023. Insights from Big Spatial Data through Machine Learning Techniques for Prudent Management of Natural Resources. Journal of Resources Energy and Development 19, 1–18. https://doi.org/10.3233/red-191201

Rane, N., Choudhary, S.P., Rane, J., 2024. Ensemble deep learning and machine learning: applications, opportunities, challenges, and future directions. Studies in Medical and Health Sciences 1, 18–41.

Rashidiyan, M., Rahimzadegan, M., 2024. Investigation and Evaluation of Land Use–Land Cover Change Effects on Current and Future Flood Susceptibility. Natural Hazards Review 25. https://doi.org/10.1061/nhrefo.nheng-1854

Reinermann, S., Asam, S., Kuenzer, C., 2020. Remote sensing of grassland production and management—A review. Remote Sensing 12, 1949.

Rentschler, J., Salhab, M., 2020. People in harm's way: Flood exposure and poverty in 189 countries (Washington: World Bank).

Richard, J.U., Okeke, F.I., 2023. Climate change and urban flooding in South-South Nigeria from 1990 - 2020. World Journal of Advanced Engineering Technology and Sciences 8, 069–089. https://doi.org/10.30574/wjaets.2023.8.1.0013

Ridha, T., Ross, A.D., Mostafavi, A., 2022. Climate change impacts on infrastructure: Flood risk perceptions and evaluations of water systems in coastal urban areas. International Journal of Disaster Risk Reduction 73, 102883. https://doi.org/10.1016/j.ijdrr.2022.102883

Ringim, A.S., Sulaiman, I.M., Lyakurwa, J.V., 2016. Implementation of integrated coastal zone management approach in the Niger Delta, Nigeria: a review. International Research Journal of Environmental Sciences and Studies 1, 43–55.

Rokni, K., Ahmad, A., Selamat, A., Hazini, S., 2014. Water feature extraction and change detection using multitemporal Landsat imagery. Remote sensing 6, 4173–4189.

Roy, D.C., Blaschke, T., 2015. Spatial vulnerability assessment of floods in the coastal regions of Bangladesh. Geomatics, Natural Hazards and Risk 6, 21–44. https://doi.org/10.1080/19475705.2013.816785

Roy, P., Pal, S.C., Arabameri, A., Rezaie, F., Chakrabortty, R., Chowdhuri, I., Saha, A., Malik, S., Das, B., 2021. Climate and land use change induced future flood susceptibility assessment in a sub-tropical region of India. Soft Computing 25, 5925–5949.

Roy, P., Pal, S.C., Chakrabortty, R., Chowdhuri, I., Malik, S., Das, B., 2020. Threats of climate and land use change on future flood susceptibility. Journal of Cleaner Production 272, 122757.

Roy, S., Rautela, R., Kumar, S., 2023. Towards a sustainable future: Nexus between the sustainable development goals and waste management in the built environment. Journal of Cleaner Production 137865.

Rummukainen, M., 2010. Physical climate science since IPCC AR4: a brief update on new findings between 2007 and April 2010. Nordic Council of Ministers.

Saarinen, N., Huang, H., Chen, Y., Clinton, N., Wang, J., Wang, J., Wang, J., Wang, X., Liu, C., Gong, P., Yang, J., Yang, J., Bai, Y., Zheng, Y., Zhu, Z., 2017. Mapping major land cover dynamics in Beijing using all Landsat images in Google Earth Engine. Remote Sensing of Environment 202, 166–176. https://doi.org/10.1016/j.rse.2017.02.021

Sahar Saeidi, Amir Mosallaei, Jalil Imani Harsini, János Grósz, István Waltner, 2023. Assessing the Impact of Land Use and Land Cover on Water Quality: A Case Study of the Rákos Catchment in Hungary. ARPHA Conference Abstracts 6. https://doi.org/10.3897/aca.6.e108160

Saikh, N.I., Mondal, P., 2023. GIS-based machine learning algorithm for flood susceptibility analysis in the Pagla river basin, Eastern India. Natural Hazards Research 3, 420–436. https://doi.org/10.1016/j.nhres.2023.05.004

Samson, B.C., 2024. Station-based Analysis of Variability and Change in the Nigerian Hydroclimate (PhD Thesis). Virginia Tech.

Sanyal, J., Lu, X.X., 2004. Application of remote sensing in flood management with special reference to monsoon Asia: a review. Natural Hazards 33, 283–301.

Secretary-General, U.N., 2007. Programme implementation and progress of work in the field of population in 2006: Population Division, Department of Econmic and Social Affairs: report of the Secretary-General.

Seegers, B.N., Stumpf, R.P., Schaeffer, B.A., Loftin, K.A., Werdell, P.J., 2018. Performance metrics for the assessment of satellite data products: an ocean color case study. Optics express 26, 7404–7422.

Serafeim, A.V., Fourniotis, N.Th., Deidda, R., Kokosalakis, G., Langousis, A., 2024. Leakages in Water Distribution Networks: Estimation Methods, Influential Factors, and Mitigation Strategies—A Comprehensive Review. Water 16, 1534. https://doi.org/10.3390/w16111534

Shakeel, M., Munir, K., Hina, K., Saeed, R., Arshad, Q., 2015. Application of remote sensing and GIS Technology for Pre and Post Flood Analysis (2014) along river chenab. Pakistan. J Earth Sci Clim Change 6, 2.

Shanmuganathan, S., 2016. Artificial neural network modelling: An introduction. Springer.

Sharma, Sagar, Sharma, Simone, Athaiya, A., 2017. Activation functions in neural networks. Towards Data Sci 6, 310–316.

Shedekar, V.S., King, K.W., Fausey, N.R., Soboyejo, A.B.O., Harmel, R.D., Brown, L.C., 2016. Assessment of measurement errors and dynamic calibration methods for three different tipping bucket rain gauges. Atmospheric Research 178–179, 445–458. https://doi.org/10.1016/j.atmosres.2016.04.016

Shen, L., Li, C., 2010. Water body extraction from Landsat ETM+ imagery using adaboost algorithm, in: 2010 18th International Conference on Geoinformatics. IEEE, pp. 1–4.

Shilengwe, C., Nyimbili, P.H., Msendo, R., Banda, F., Mukupa, W., Erden, T., 2023. Synthetic Aperture Radar and Optical Sensor Techniques Using Google Earth Engine For Flood Monitoring and Damage Assessment–A Case Study of Mumbwa District, Zambia. Zambia ICT Journal 7, 7–15.

Shiru, M.S., Shahid, S., Dewan, A., Chung, E.-S., Alias, N., Ahmed, K., Hassan, Q.K., 2020. Projection of meteorological droughts in Nigeria during growing seasons under climate change scenarios. Scientific reports 10, 10107.

Shortridge, J., 2019. Observed trends in daily rainfall variability result in more severe climate change impacts to agriculture. Climatic Change 157, 429–444. https://doi.org/10.1007/s10584-019-02555-x

Shuaibu, A., 2020. Flood Reduction through Flood Risk and Vulnerability Assessment and Mapping in Hadejia River Basin, Nigeria. PAUWES.

Shugulova, D.K., Mazhitova, G.Z., Makhanova, N.B., Пашков, C.B., Assylbekov, K.M., Berdenov, Zh.G., 2023. GEOINFORMATION MODELING OF THE ESIL RIVER FLOOD ZONE BASED ON REMOTE SENSING DATA. Journal of Geography and Environmental Management 69. https://doi.org/10.26577/jgem.2023.v69.i2.06

Shukla, S., Husak, G., Turner, W., Davenport, F., Funk, C., Harrison, L., Krell, N., 2021. A slow rainy season onset is a reliable harbinger of drought in most food insecure regions in Sub-Saharan Africa. Plos one 16, e0242883.

Sian, K.T.C.L.K., Ayugi, B.O., Onyutha, C., Sagero, P., Ait Brahim, Y., 2025. Rainfall variability across Africa, in: Climate Change and Rainfall Extremes in Africa. Elsevier, pp. 3–26.

Sikka, A.K., Rao, B.B., Rao, V.U.M., 2016. Agricultural disaster management and contingency planning to meet the challenges of extreme weather events. Mausam 67, 155–168.

Silva, A.B. dos S., de Melo Araújo, A.C., Germano de Frias, P., Rodrigues Vilela, M.B., Vieira do Bonfim, C., 2021. Auto-Regressive Integrated Moving Average Model (ARIMA): conceptual and methodological aspects and applicability in infant mortality. Brazilian Journal of Mother & Child Health (BJMCH)/Revista Brasileira de Saude Materno Infantil (RBSMI) 21.

Singh, G.R., Dhanya, C.T., Chakravorty, A., 2021. A Robust Drought Index Accounting Changing Precipitation Characteristics. Water Resources Research 57, e2020WR029496. https://doi.org/10.1029/2020WR029496

Solomon, V.A., Okoro, G.I., Umoh, G.S., Udoh, E.J., Edet, G.E., Uwem, C.A., Bassey, N.E., Akpan, O.D., 2015. Impacts of Climate Variability on Wetland and Fishing Households in the Niger Delta Region, Nigeria. Asian Journal of Agricultural Extension, Economics and Sociology 7, 1–9.

Song, Y., Achberger, C., Linderholm, H.W., 2011. Rain-season trends in precipitation and their effect in different climate regions of China during 1961–2008. Environmental Research Letters 6, 034025.

Song, Z., Guo, J., Zhang, Z., Kou, T., Deng, A., Zheng, C., Ren, J., Zhang, W., 2013. Impacts of planting systems on soil moisture, soil temperature and corn yield in rainfed area of Northeast China. European Journal of Agronomy 50, 66–74.

Spencer, T., Brooks, S.M., Evans, B.R., Tempest, J.A., Möller, I., 2015. Southern North Sea storm surge event of 5 December 2013: Water levels, waves and coastal impacts. Earth-Science Reviews 146, 120–145. https://doi.org/10.1016/j.earscirev.2015.04.002

Stoyanova, E., 2023. REMOTE SENSING FOR FLOOD INUNDATION MAPPING USING VARIOUS PROCESSING METHODS WITH SENTINEL-1 AND SENTINEL-2. The International Archives of the Photogrammetry, Remote Sensing and Spatial Information Sciences XLVIII-M-1–2023, 339–346. https://doi.org/10.5194/isprs-archives-xlviii-m-1-2023-339-2023

Sylla, M.B., Nikiema, P.M., Gibba, P., Kebe, I., Klutse, N.A.B., 2016. Climate Change over West Africa: Recent Trends and Future Projections, in: Yaro, J.A., Hesselberg, J. (Eds.), Adaptation to Climate Change and Variability in Rural West Africa. Springer International Publishing, Cham, pp. 25–40. https://doi.org/10.1007/978-3-319-31499-0_3

Sylla, M.B., Pal, J.S., Faye, A., Dimobe, K., Kunstmann, H., 2018. Climate change to severely impact West African basin scale irrigation in 2 C and 1.5 C global warming scenarios. Scientific reports 8, 14395.

Synodinos, A.D., Tietjen, B., Lohmann, D., Jeltsch, F., 2018. The impact of inter-annual rainfall variability on African savannas changes with mean rainfall. Journal of Theoretical Biology 437, 92–100. https://doi.org/10.1016/j.jtbi.2017.10.019

Tamoffo, A.T., Weber, T., Akinsanola, A.A., Vondou, D.A., 2023. Projected changes in extreme rainfall and temperature events and possible implications for Cameroon's socio-economic sectors. Meteorological Applications 30, e2119. https://doi.org/10.1002/met.2119

Tano, A.R., Bouo, F.-X.D.B., Kouamé, J.K., Tchétché, Y., Zézé, S.D., Ouattara, B., 2023. Rainfall variability and trends in West Africa. Atmospheric and Climate Sciences 13, 72–83.

Thorncroft, C.D., Nguyen, H., Zhang, C., Peyrillé, P., 2011. Annual cycle of the West African monsoon: regional circulations and associated water vapour transport. Quart J Royal Meteoro Soc 137, 129–147. https://doi.org/10.1002/qj.728

Thornton, P., Nelson, G., Mayberry, D., Herrero, M., 2022. Impacts of heat stress on global cattle production during the 21st century: a modelling study. The Lancet Planetary Health 6, e192–e201.

Ticehurst, C.J., Dyce, P., Guerschman, J.P., 2009. Using passive microwave and optical remote sensing to monitor flood inundation in support of hydrologic modelling, in: Interfacing Modelling and Simulation with Mathematical and Computational Sciences, 18th World IMACS/MODSIM Congress. pp. 13–17.

Tiwari, V., Kumar, V., Matin, M.A., Thapa, A., Ellenburg, W.L., Gupta, N., Thapa, S., 2020. Flood inundation mapping-Kerala 2018; Harnessing the power of SAR, automatic threshold detection method and Google Earth Engine. PLoS One 15, e0237324.

Tramblay, Y., Villarini, G., El Khalki, E.M., Gründemann, G., Hughes, D., 2021. Evaluation of the drivers responsible for flooding in Africa. Water Resources Research 6. https://doi.org/doi:%2010.1029/2021WR029595

Tran, T.V., Reef, R., Zhu, X., 2022. A review of spectral indices for mangrove remote sensing. Remote Sensing 14, 4868.

Turner, B.L., Lambin, E.F., Reenberg, A., 2007. The emergence of land change science for global environmental change and sustainability. Proceedings of the National Academy of Sciences 104, 20666–20671.

Twardosz, R., Walanus, A., Guzik, I., 2021. Warming in Europe: Recent Trends in Annual and Seasonal temperatures. Pure Appl. Geophys. 178, 4021–4032. https://doi.org/10.1007/s00024-021-02860-6

Udinmade Ighedosa, S., 2019. Climate change: vulnerability of the Niger Delta Region, in Nigeria. International Journal of Environment and Climate Change 9, 764–788.

Umar, D.A., Umar, D.A., Ramli, M.F., Ramli, M.F., Tukur, A.I., Tukur, A.I., Nor Rohaizah Jamil, Jamil, N.R., Muhammad Amar Zaudi, Zaudi, M.A., 2021. Detection and prediction of land use change impact on the streamflow regime in Sahelian river basin, northwestern Nigeria. H2Open Journal 4, 92–113. https://doi.org/10.2166/h2oj.2021.065

Umar, N., Gray, A., 2022. Flooding in Nigeria: a review of its occurrence and impacts and approaches to modelling flood data. International Journal of Environmental Studies 1–22. https://doi.org/10.1080/00207233.2022.2081471

Unger Holtz, T.S., 2007. Introductory digital image processing: A remote sensing perspective.

Urmila R. Panikkar, Roshan Srivastav, Ankur Srivastava, 2023. Multiscale Variability of Hydrological Responses in Urbanizing Watershed. Remote Sensing 15, 796–796. https://doi.org/10.3390/rs15030796

Vu, T.T., Li, L., Jun, K.S., 2018. Evaluation of Multi-Satellite Precipitation Products for Streamflow Simulations: A Case Study for the Han River Basin in the Korean Peninsula, East Asia. Water 10, 642. https://doi.org/10.3390/w10050642

Vu, V.T., Nguyen, H.D., Vu, P.L., Ha, M.C., Van Dong Bui, Thi Oanh Nguyen, Van Hiep Hoang, Thanh Kim Hue Nguyen, 2023. Predicting land use effects on flood susceptibility using machine learning and remote sensing in coastal Vietnam. Water Practice & Technology 18, 1543–1555. https://doi.org/10.2166/wpt.2023.088

Wahap, N.A., Shafri, H.Z.M., Helmi Z.M. Shafri, Helmi Z. M. Shafri, 2020. Utilization of Google Earth Engine (GEE) for land cover monitoring over Klang Valley, Malaysia. IOP Conference Series: Earth and Environmental Science 540, 012003. https://doi.org/10.1088/1755-1315/540/1/012003

Wang, X., Jiang, D., Lang, X., 2017. Future extreme climate changes linked to global warming intensity. Science Bulletin 62, 1673–1680.

Wang, Y., Wang, Y., Fang, Z., Fang, Z., Hong, H., Hong, H., Ling Peng, Peng, L., 2020. Flood susceptibility mapping using convolutional neural network frameworks. Journal of Hydrology 582, 124482. https://doi.org/10.1016/j.jhydrol.2019.124482

Wani, S.P., Singh, P., Boomiraj, K., Sahrawat, K.L., 2009a. Climate change and sustainable rain-fed agriculture: challenges and opportunities. Agricultural Situation in India 66, 221–239.

Wani, S.P., Singh, P., Boomiraj, K., Sahrawat, K.L., 2009b. Climate change and sustainable rain-fed agriculture: challenges and opportunities. Agricultural Situation in India 66, 221–239.

Wankar, A.K., Rindhe, S.N., Doijad, N.S., 2021. Heat stress in dairy animals and current milk production trends, economics, and future perspectives: the global scenario. Trop Anim Health Prod 53, 70. https://doi.org/10.1007/s11250-020-02541-x

Wasko, C., Nathan, R., Stein, L., O’Shea, D., 2021. Evidence of shorter more extreme rainfalls and increased flood variability under climate change. Journal of Hydrology 603, 126994.

Watson, R.T., Team, C. writing, 2001. Climate change 2001: synthesis report. Cambridge University Press Cambridge.

Wei, W., Zhang, X., Cao, X., Zhou, L., Liang Zhou, Zhou, L., Xie, B., Zhou, J., Zhou, J., Li, C., 2021. Spatiotemporal dynamics of energy-related CO2 emissions in China based on nighttime imagery and land use data. Ecological Indicators 131, 108132. https://doi.org/10.1016/j.ecolind.2021.108132

Wijngaard, J.B., Klein Tank, A.M.G., Können, G.P., 2003. Homogeneity of 20th century European daily temperature and precipitation series. Intl Journal of Climatology 23, 679–692. https://doi.org/10.1002/joc.906

Willmott, C.J., Robeson, S.M., Matsuura, K., 2012. A refined index of model performance. Intl Journal of Climatology 32, 2088–2094. https://doi.org/10.1002/joc.2419

Wilson, E.H., Sader, S.A., 2002. Detection of forest harvest type using multiple dates of Landsat TM imagery. Remote Sensing of Environment 80, 385–396.

Wood, H.M., 2001. The use of earth observing satellites for hazard support, in: IGARSS 2001. Scanning the Present and Resolving the Future. Proceedings. IEEE 2001 International Geoscience and Remote Sensing Symposium (Cat. No. 01CH37217). IEEE, pp. 135–137.

Woodhouse, I.H., 2017. Introduction to microwave remote sensing. CRC press.

Wu, G., Fanzo, J., Miller, D.D., Pingali, P., Post, M., Steiner, J.L., Thalacker-Mercer, A.E., 2014. Production and supply of high-quality food protein for human consumption: sustainability, challenges, and innovations. Annals of the New York Academy of Sciences 1321, 1–19.

Wu, W., Wang, W., Meadows, M.E., Yao, X., Peng, W., 2019. Cloud-based typhoon-derived paddy rice flooding and lodging detection using multi-temporal Sentinel-1&2. Frontiers of earth science 13, 682–694.

Wu, X., Li, J., Shen, X., 2023. Quantitative analysis for the response of streamflow variation to driving factors in seven major basins across China. Ecological Indicators 148, 110081. https://doi.org/10.1016/j.ecolind.2023.110081

Wu, Y., Mu, H., Wu, S., Xu, Y., Xu, M., Wu, H., Clark, R.T., Gao, C., 2023. Changes in mean and extreme homogeneous precipitation in China during 1960–2020. Atmospheric Research 292, 106891. https://doi.org/10.1016/j.atmosres.2023.106891

Wulder, M.A., Franklin, S.E., 2012. Remote sensing of forest environments: concepts and case studies. Springer Science & Business Media.

Xu, H., 2006. Modification of normalised difference water index (NDWI) to enhance open water features in remotely sensed imagery. International journal of remote sensing 27, 3025–3033.

Xu, Z., Zhongyue Xu, Zhongyue Xu, Liu, G., Weijun Xu, Xu, W., Weijun Xu, Dai, Y., 2018. Evaluation of greenhouse gas emissions from maize production in china. Chemical engineering transactions 70, 1309–1314. https://doi.org/10.3303/cet1870219

Yahaya, I., Zhou, J., Jiang, S., Xu, R.H., Huang, J., Su, B., Jing, C., Qiu, F., Jiang, T., 2024. Depiction of Drought Over Africa in the Light of Changing Climate from CMIP6 Models. Earth Syst Environ 8, 1011–1035. https://doi.org/10.1007/s41748-024-00502-0

Yang, L., Meng, X., Zhang, X., 2011. SRTM DEM and its application advances. International Journal of Remote Sensing 32, 3875–3896.

Yang, L., Scheffran, J., Qin, H., You, Q., 2015. Climate-related flood risks and urban responses in the Pearl River Delta, China. Reg Environ Change 15, 379–391. https://doi.org/10.1007/s10113-014-0651-7

Yang, Y., Sun, W., Zou, M., Qiao, S., Li, Q., 2022. Multi-model seasonal prediction of global surface temperature based on partial regression correction method. Frontiers in Environmental Science 10, 1036006.

Yanto, Rajagopalan, B., Zagona, E., 2016. Space–time variability of Indonesian rainfall at inter-annual and multi-decadal time scales. Clim Dyn 47, 2975–2989. https://doi.org/10.1007/s00382-016-3008-8

Yao, H., Qin, R., Chen, X., 2019. Unmanned aerial vehicle for remote sensing applications—A review. Remote Sensing 11, 1443.

Yates, D., Islam, M.Z., 2021. FastForest: Increasing random forest processing speed while maintaining accuracy. Information Sciences 557, 130–152.

Yaw A., T., Edmund C., M., Tomas, A.-S., Albert, O., Brilliant M., P., Kia, A., 2017. Techniques of Remote Sensing and GIS as Tools for Visualizing Impact of Climate Change-Induced Flood in the Southern African Region. American Journal of Climate Change 6, 306–327. https://doi.org/https://doi.org/10.4236/ajcc.2017.62016

Ye, X., Guo, Y., Wang, Z., Liang, L., Tian, J., 2022. Extensive Evaluation of Four Satellite Precipitation Products and Their Hydrologic Applications over the Yarlung Zangbo River. Remote Sensing 14, 3350. https://doi.org/10.3390/rs14143350

Yersaw, B.T., Chane, M.B., 2024. Regional climate models and bias correction methods for rainfall-runoff modeling in Katar watershed, Ethiopia. Environ Syst Res 13, 10. https://doi.org/10.1186/s40068-024-00340-z

Yu Han, Zengliang Luo, Lunche Wang, Xiangyi Ding, Shaoqiang Wang, 2023. Improving the Accuracy of Flood Susceptibility Prediction by Combining Machine Learning Models and the Expanded Flood Inventory Data. Remote Sensing 15, 3601–3601. https://doi.org/10.3390/rs15143601

Yue, W., Xu, J., Tan, W., Xu, L., 2007. The relationship between land surface temperature and NDVI with remote sensing: application to Shanghai Landsat 7 ETM+ data. International journal of remote sensing 28, 3205–3226.

Zade, N.P., Bhosale, A., Dhir, P.K., Sarkar, P., Davis, R., 2021. Variability of Mechanical Properties of Cellular Lightweight Concrete Infill and Its Effect on Seismic Safety. Nat. Hazards Rev. 22. https://doi.org/10.1061/(asce)nh.1527-6996.0000501

Zeppel, M.J.B., Wilks, J.V., Lewis, J.D., 2014. Impacts of extreme precipitation and seasonal changes in precipitation on plants. Biogeosciences 11, 3083–3093.

Zhang, H., Qi, Z., Li, X., Chen, Y., Wang, X., He, Y., 2021. An urban flooding index for unsupervised inundated urban area detection using Sentinel-1 polarimetric SAR images. Remote Sensing 13, 4511.

Zurqani, H.A., Post, C.J., Mikhailova, E.A., Schlautman, M.A., Sharp, J.L., 2018. Geospatial analysis of land use change in the Savannah River Basin using Google Earth Engine. International journal of applied earth observation and geoinformation 69, 175–185.